JOURNAL OF

METALS

TWO SECTIONS — SECTION 1

February 1954

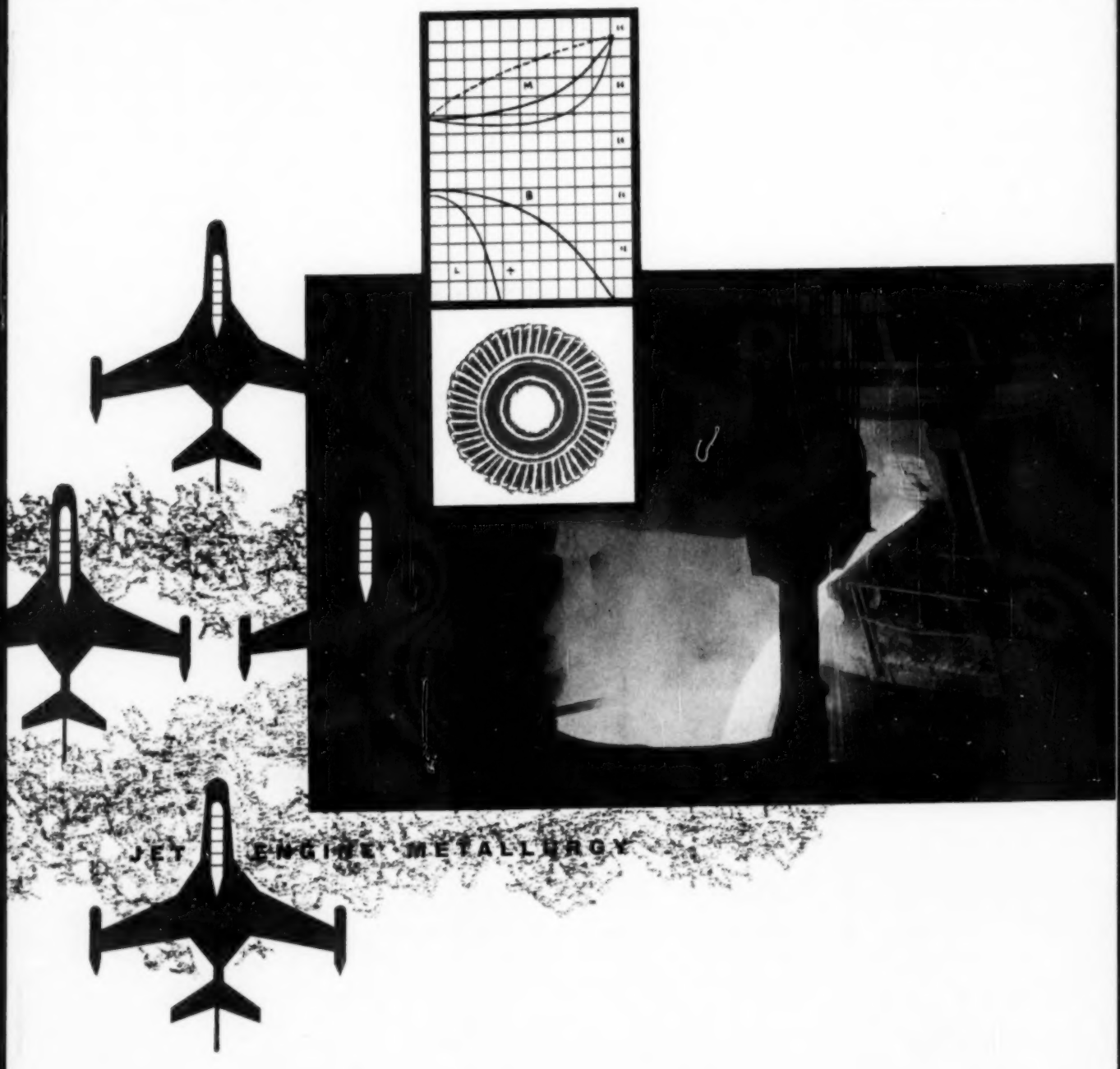

JET ENGINE METALLURGY

Why are half of all the coil springs in American cars made of

U·S·S Carilloy steel?

THE REASON IS SIMPLE. While ordinary hot rolled bars require extensive grinding to remove harmful seams, pits, and decarburization, Carilloy Precision Rolled Coil Spring Rounds require very little grinding; in fact, they are often used *as furnished* with no grinding at all. That's because they are rolled on a special mill to half of standard tolerances and with very little decarburization. As a result, it costs less to make *high quality* coil springs from Carilloy Precision Rolled Rounds.

These cost-saving spring rounds are an exclusive development of the United States Steel Corporation. We are continually searching out ways to make steel better, discovering better ways to fabricate steel, and finding new and better uses for steel.

By contacting our nearest sales office and consulting frequently with U·S·S Service Metallurgists you can keep in touch with our latest discoveries. Then, as we find ways to simplify, speed up, or lower the cost of your production, these men can pass the information along to you.

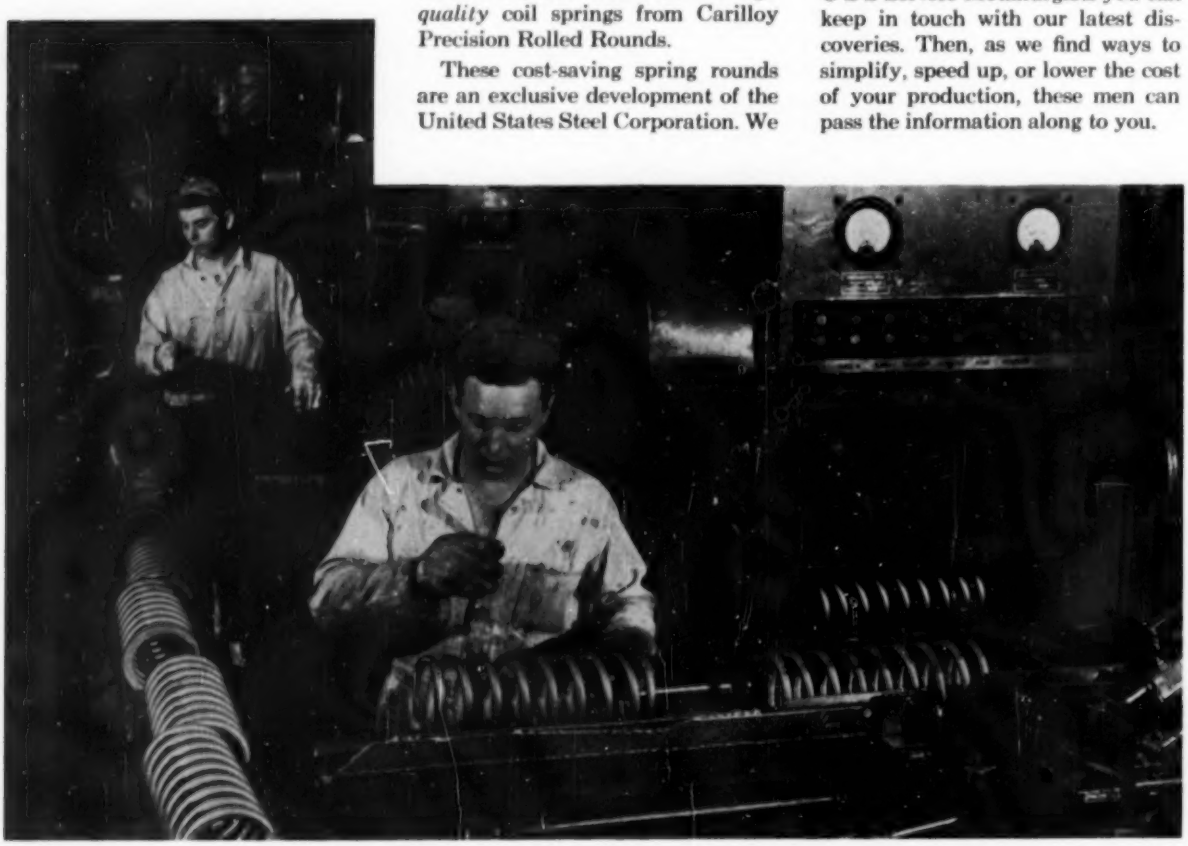

UNITED STATES STEEL CORPORATION, PITTSBURGH · COLUMBIA-GENEVA STEEL DIVISION, SAN FRANCISCO
TENNESSEE COAL & IRON DIVISION, FAIRFIELD, ALA. · UNITED STATES STEEL SUPPLY DIVISION, WAREHOUSE DISTRIBUTORS
UNITED STATES STEEL EXPORT COMPANY, NEW YORK

Carilloy USS Steels

ELECTRIC FURNACE OR OPEN HEARTH — COMPLETE PRODUCTION FACILITIES IN CHICAGO OR PITTSBURGH

3-2260

UNITED STATES STEEL

JOURNAL OF

METALS

VOL. 6, NO. 2 FEBRUARY, 1954

Published to provide a continuing, authoritative, and up-to-date record of technological, engineering, and economic progress in all branches of the metals industry by the Metals Branch American Institute of Mining and Metallurgical Engineers, Inc. 29 West 39th Street, New York 18

• • •

ALVIN S. COHAN
Manager of Publications
Editor, JOURNAL OF METALS

• • •

D. G. GARRETT M. A. MATZKIN
E. M. WEISS G. M. ZILL
Assistant Editors

GRACE PUGSLEY Production Manager
W. J. SEWING Asst. Prod. Mgr.

• • •

METALS BRANCH COUNCIL
K. C. McCutcheon Chairman
E. O. Kirkendall Secretary
M. Cohen IMD Chairman
T. J. McLaughlin ISD Chairman
R. R. McNaughton EMD Chairman
W. A. Dean R. D. Parks
T. D. Jones D. S. Eppelsheimer

EDITORIAL ADVISORY COMMITTEE
J. S. Smart, Jr. Chairman
W. A. Dean Evan Just
J. C. Kinnear, Jr. John Marsh
T. D. Jones M. Tenenbaum

TECHNICAL PUBLICATIONS COMMITTEES
Robert Aborn AIME Chairman
Otto Zmeskal ISD Chairman
S. J. Dickinson EMD Chairman
W. R. Hibbard, Jr. IMD Chairman
E. J. Kennedy, Jr. Secretary

• • •

JAMES A. STANGARONE
Advertising Manager
FRED STANLEY
Eastern Representative

• • •

The AIME Publishes:
Journal of Metals
Mining Engineering
Journal of Petroleum Technology

COVER

America's air supremacy depends directly on the skill of the metallurgist to provide durable materials for jet planes to fly higher, faster, and farther. One aspect of this problem, the story of high performance jet engine materials requirements, is told on p. 113.

NEWS

Meet the Authors	97	Drift of Things	108
Employment Service	98	Journal of Metals Reporter	111
Books for Engineers	99	Annual Meeting Program	128
New Products	101	AIME News	161
Industrial Notes	104	Coming Events	165
Trends	106	Personals	166

TECHNICAL FEATURES

High Performance Jet Engine Design Dependent Upon Metallurgical Ingenuity I. Perlmutter 113

Titanium Alloys Give Promise of High Temperature Applications F. A. Crossley, H. D. Kessler 119

Poland and China Expand Steel Capacities 122

Sources of Inclusions from Pouring Refractories Investigated M. P. Fedock 125

TRANSACTIONS

Regenerator Efficiency and Air Preheat in the Open Hearth B. M. Larsen 129

Chromium Distribution Between Liquid Iron and Molten Basic Slags N. J. Grant, E. C. Roberts, J. Chipman 145

Wustite Phase in Partially Reduced Hematite G. Bitsianes, T. L. Joseph 150

Theoretical Analysis of Diffusion of Solutes During the Solidification of Alloys C. Wagner 154

This issue of JOURNAL OF METALS is in two Sections:
Section 1—Magazine Section 2—Transactions Section

Published the first day of each month by the American Institute of Mining and Metallurgical Engineers, Inc., 29 West 39th Street, New York 18, N. Y. Telephone: PEnnsylvania 6-9220. Subscription $8 per year for non-AIME members in United States and North, South and Central America; $10, foreign; $6 for AIME members, or $4 additional in combination with a subscription to "Mining Engineering" or "Journal of Petroleum Technology." Single copies, 75 cents; single copies foreign, $1.00; special issues, $1.50 . . . The AIME is not responsible for any statement made or opinion expressed in its publications . . . Copyright 1954 by the American Institute of Mining and Metallurgical Engineers, Inc. . . . Registered cable address, AIME New York . . . Indexed in Engineering Index, Industrial Arts Index and Chemical Abstracts . . . Reentered as second-class matter Sept. 21, 1949, at the post office at New York, N. Y., under the Act of March 3, 1879. Additional entry established at Manchester, N. H.

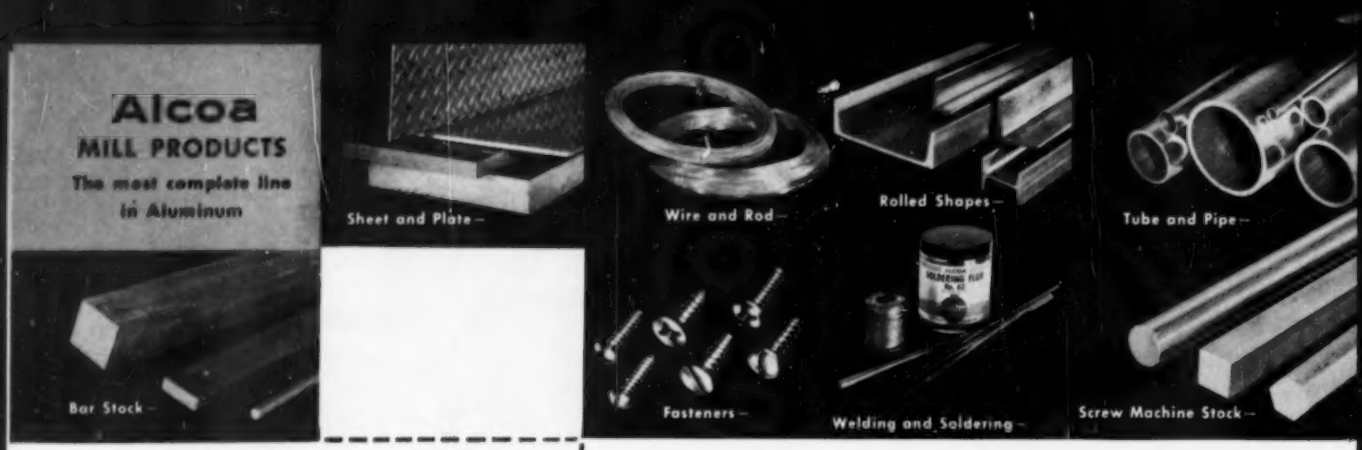

Built-up parts are no bargain; riveting and welding demand too many costly man-hours.

That's why production costs drop when you use aluminum extruded shapes. They take the handcuffs off your designer and allow him to distribute the metal where it's needed. Parts that would be prohibitively expensive to produce by assembly become practical. And while extrusion is not a precision process, tolerances are so close that only surface finishing is ordinarily required. Lengths run to 80 feet, maximum weights up to 600 pounds per piece.

Alcoa operates the world's largest light metal extrusion facilities with 50 presses in five plants. With the experience of 50 years to draw on, Alcoa can show you how to take advantage of a broad line of standard extruded shapes or help you design for your own specialized requirements. Call your local Alcoa sales office or write: ALUMINUM COMPANY OF AMERICA, 878-B Alcoa Building, Pittsburgh 19, Penna.

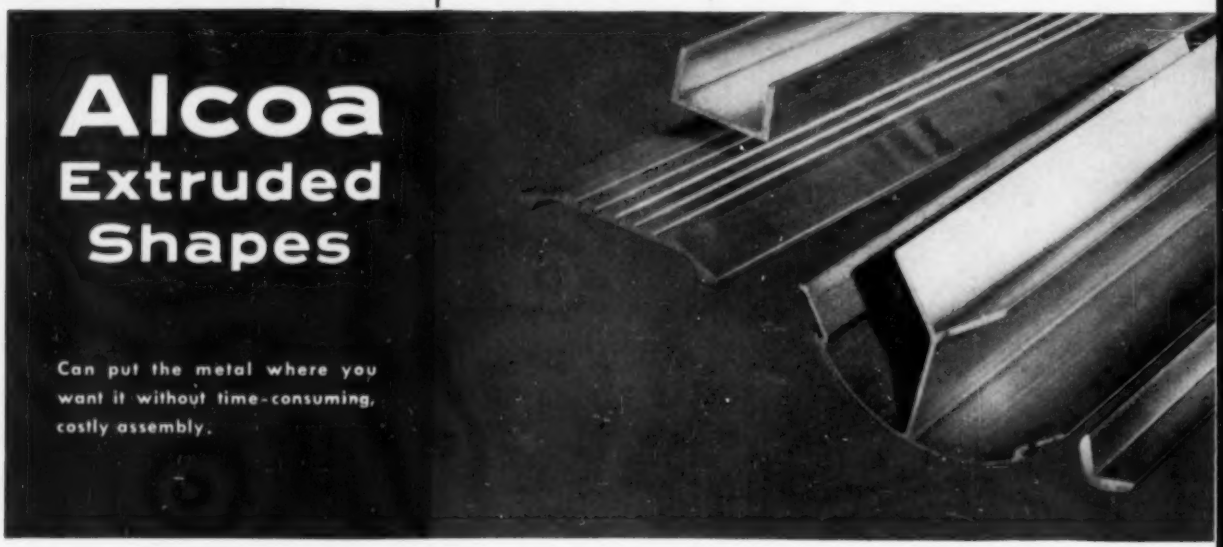

YOUR ALCOA DISTRIBUTOR HAS ALCOA STANDARD WAREHOUSE ITEMS IN STOCK

ALCOA ON TV brings the world to your armchair with "SEE IT NOW" featuring Edward R. Murrow, Tuesday evenings on most CBS-TV stations.

ALCOA ALUMINUM

ALUMINUM COMPANY OF AMERICA

Reduce plate weight *10%*

. . . insure unvarying quality

To inspect pressure and bulk storage vessels J. B. Beaird Co. uses two OX-250 x-ray units. These versatile units can be mounted on stationary jib cranes, mobile jib cranes, truck-type, or semi-automatic production type housings.

100% x-ray inspection results in higher quality products with substantial savings

When the J. B. Beaird Co., Inc., of Shreveport, La., introduced 100% x-ray inspection, they reduced the plate thickness of their pressure and bulk storage vessels by 10%. This is permissible because ASME and API-ASME codes state that a 10% higher weld efficiency factor can be used when welds are 100% x-ray inspected.

The resulting savings in steel alone amount to several tons per tank, with a consequent reduction in shipping costs. In addition, Beaird now uses less welding time and materials.

Allowing for films, chemicals, operator's time and equipment amortization and upkeep — the use of two OX-250 x-ray units permits substantial savings on each vessel produced. More important, Beaird customers are assured unvarying high quality.

No matter what your non-destructive testing needs, there's a General Electric x-ray unit to match your requirements. Your G-E x-ray representative can base his recommendation on 25 models, ranging from 140,000 to 15,000,000 volts. Call him today, or write X-Ray Department, General Electric Company, Milwaukee 1, Wis., Rm. AY 24.

Like all G-E x-ray apparatus — OX-250 can be yours — without initial capital investment — on the Maxiservice® rental plan.

You can put your confidence in —

GENERAL ELECTRIC

Need Vacuum-Melted Metals in 1000-pound Quantities?

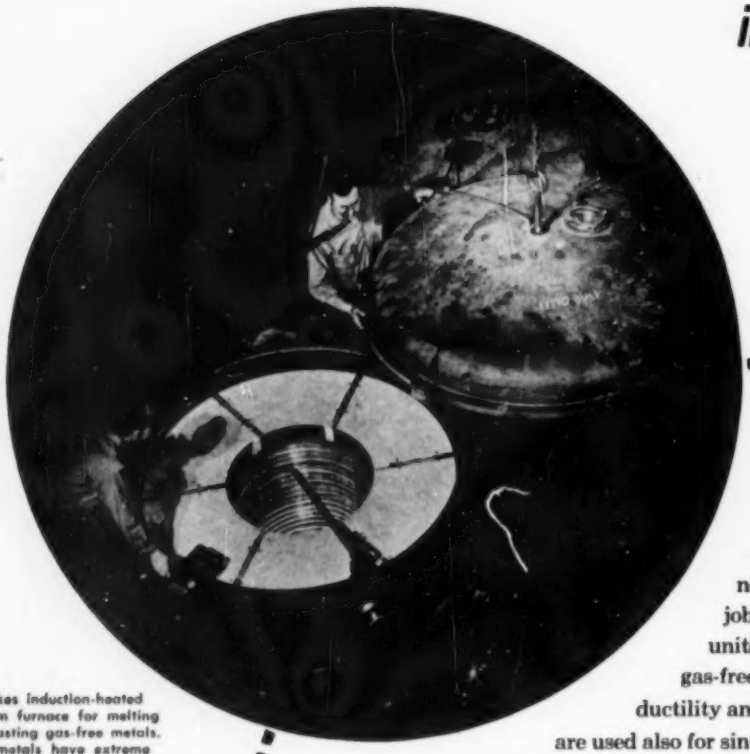

A Stokes induction-heated vacuum furnace for melting and casting gas-free metals. Such metals have extreme purity, high ductility, great impact and rupture strength, improved creep resistance and exceptional performance qualities.

Stokes is *building* practical vacuum furnaces to supply that need . . . *designing* for 2000-pound jobs . . . *planning* for 5000-pound units . . . for melting and casting gas-free metals of extreme purity, high ductility and great strength. These furnaces are used also for sintering, annealing and degassing.

You can have Stokes vacuum furnaces for top or bottom pouring, for single or multiple ingots, for centrifugal castings. We build tilting type induction-heated melting furnaces of 10 to 1000 pounds capacity; movable retort resistance-heated furnaces for degassing and annealing in 10, 20 and 30-inch retort sizes; resistance-heated furnaces with removable heat source or with bell-type retort; two-zone furnaces with movable boat, and others.

We supply complete, integrated "package" units engineered completely and specifically to meet the particular need for vacuum pumping capacity, heating input and any mechanical actuation required to control operations in the vacuum chamber.

Most important . . . we bring to every vacuum furnace problem the value of 40 years' *practical* experience in building vacuum equipment and guiding its installation and adjustment to efficient operation in the field.

F. J. Stokes Machine Company, Philadelphia 20, Pa.

STOKES

STOKES MAKES: High Vacuum Equipment, Vacuum Pumps and Gages / Industrial Tabletting, Powder Metal and Plastics Molding Presses / Pharmaceutical Equipment

Meet The Authors

I. Perlmutter (p. 113) received his B.S. in metallurgy from Massachusetts Institute of Technology. From 1936 to 1941 he was a metallurgist with the Carnegie-Illinois Steel Corp., South Chicago. He was with the U. S. Bureau of Mines for a short time and then joined the materials laboratory, directorate of research, Wright Air Development Center where he is presently located.

I. PERLMUTTER

M. E. NICHOLSON

M. E. Nicholson (p. 185) was born in Indianapolis and graduated from Massachusetts Institute of Technology. Dr. Nicholson is presently assistant professor at the Institute for the Study of Metals, University of Chicago. While undertaking his graduate studies, he was called for duty to the Springfield Armory, Mass., where he was a metallurgist and administrative officer. For approximately three years Dr. Nicholson was with the engineering research dept. of the Standard Oil Co. (Ind.). Since 1950 he has been with the University of Chicago. He holds membership in AIME, Chicago Section and is also active in the Scouts as an adult leader.

M. C. Udy (p. 207) is a graduate of Lehigh and Ohio State Universities (B.S., M.S., Ph.D.). He joined Battelle as a research fellow in 1939, was promoted to research engineer in 1941, and is now an assistant div. chief. In addition to being an AIME Member, he is a member of AFS, ACS, AIChE, and ASM. Dr. Udy is active in church affairs and also tries his hand at cooking. In the way of sports, he enjoys bowling and swimming. He has also presented various papers before AIME.

Karl M. Weigert (p. 233) is a native of Stettin, Germany, where he graduated from the University of Goettingen in 1933, (Ph.D.). From 1934 to 1937 he was located in Istanbul, Turkey testing ores for the Cyprus copper mine. For two years he was on the staff of the chemistry dept. of the Johns Hopkins University. From 1939 to 1942 he was engaged in working on various heavy chemicals. Dr. Weigert was in the U. S. Army for 19 months stationed near the Persian Gulf. Since 1946 he has been with Goldsmith Bros. Smelting & Refining Co., Chicago. As his hobbies he enjoys special photographic work, sound recording, and hiking. He is also a member of the Chicago AIME Local Section.

M. C. UDY

K. M. WEIGERT

Francis W. Boulger (p. 207) is a div. chief at Battelle Memorial Institute. Born in Minneapolis he holds degrees from the University of Minnesota and Ohio State University. From 1934 to 1936 he was an editorial assistant with the Associated Press. He joined Republic Steel Corp. for one year where he was an open hearth observer. Mr. Boulger has been with Battelle since 1938. His varied hobbies include golf, poker, and gardening.

...it takes
"KNOW-HOW"
to do an Expert Job!
FURNACE TEAR OUTS
SALAMANDER OR SLAG REMOVAL
MATERIAL HANDLING
Prepared to serve you with maximum efficiency ANYWHERE – at ANYTIME!
CONSULT US ON YOUR NEXT BLASTING PROBLEM
CHICAGO CONCRETE BREAKING CO.
EDWARD GRAY, President
GENERAL OFFICES:
12233 Avenue O, Chicago 33, Ill
BAyport 1-8400
PITTSBURGH 19, PA.
Suite 704, 550 Grant St.
ATlantic 1-4674
Serving the Steel Industry for Over 30 Years

— Personnel Service —

THE following employment items are made available to AIME members on a nonprofit basis by the Engineering Societies Personnel Service, Inc., operating in cooperation with the Four Founder Societies. Local offices of the Personnel Service are at 8 W. 40th St., **New York 18;** 100 Farnsworth Ave., **Detroit;** 57 Post St., **San Francisco;** 84 E. Randolph St., **Chicago 1.** Applicants should address all mail to the proper key numbers in care of the New York office and include 6c in stamps for forwarding and returning application. The applicant agrees, if placed in a position by means of the Service, to pay the placement fee listed by the Service. AIME members may secure a weekly bulletin of positions available for $3.50 a quarter, $12 a year.

MEN AVAILABLE

Mining Engineer, 29, family. Sales and service experience top steel company. Desire opportunity, not necessarily as engineer, in metals business, equipment sales, service, advertising, export in or primarily around New York. Consider anything with potential. Business and personal references. M-120.

POSITIONS OPEN

Metallurgist, young, graduate, preferably with some experience in nonmetallic flotation. Duties to include direction of control laboratory, test work and operating metallurgy. Salary open. Location, South. Y9523.

Metallurgists. (a) Metallurgists, recent graduates, for research laboratory, for work involving routine analysis and research assistance until men develop sufficiently to handle product development work. Location, Ohio. (b) Metallurgists, recent graduates, for plant metallurgy departments. Will be placed in a training program that would sufficiently inform them of products, processes and metallurgical problems so that they can handle metallurgical control work in these operating divisions. Location, Pennsylvania and Maryland. Y9518.

Metallurgical Engineer with a minimum of a B.S. degree for work involving the study and development of the various processes for the agglomeration of iron ore with an emphasis at the present time on sintering ore for blast furnace use. Opportunity to study for advanced degree. Salary open. Location. Pennsylvania. Y9513.

Assistant Metallurgists, B.S. degrees in metallurgical engineering required for work involving quality control problems connected with stainless steel operations. Excellent opportunity for young men to establish in large and progressive organization. Location, Maryland. Y9483.

Professor in physical metallurgy, experienced in research direction and graduate instruction. Ph.D. or equivalent, to head educational option in physical metallurgy and direct thesis and contract research. Excellent opportunity for expansion in an outstanding center in the middle Atlantic region. Y9482.

Process Engineer for nonferrous mill. Metallurgical engineer preferred, but not essential. Must have had at least three years industrial experience. Age, 25 to 40. Knowledge of inspection techniques and statistical methods of research required. Salary open. Location, Pennsylvania. Y9459.

PROFESSIONAL SERVICES

Limited to AIME members, or to companies that have at least one AIME member on their staffs. Rates $40 per year per inch.

SCIENTISTS
CONSULTANTS
METALLURGISTS

Small Jobs Welcomed

SAM TOUR & CO., INC.

Laboratories and offices
44 Trinity Place, New York 6, N. Y.

Testing—Certifying
American Standards
Testing Bureau, Inc.

HANS NEUBERT

PRECISE *PROMPT*
TECHNICAL TRANSLATIONS FROM GERMAN, SPANISH, FRENCH INTO ENGLISH FIRST TWO TYPEWRITTEN PAGES $3.00 EACH INTRODUCTORY PRICE. REGULAR PRICE THEREAFTER 3 CENTS PER WORD.
31 Hilltop Ave. Clark-Rahway, N. J.

MAX STERN
Consulting Engineer
Expert for Scrap Recovery and Shipwrecking — Modernization of Plants and Yards for Ferrous and Nonferrous Metal Scrap
149 Broadway New York 6, N. Y.

METALLURGIST

RESEARCH
SUPERVISION ADMINISTRATION

REQUIREMENTS—Metallurgy or Physical Chemistry or Chemical Engineering at doctorate level with experience preferred.

Management positions in leading ferrous industry. Duties entail planning, coordinating, and developing profitable research programs in:

REDUCTION & REFINING PHYSICAL METALLURGY
SURFACE TREATMENTS RAW MATERIALS

Excellent opportunities in conjunction with expansion of research staff and facilities. Salary open. Located in Midwest. State in detail personal history, education, experience, and occupational interests. All replies confidential.

B-5, AIME, 29 W. 39th St., New York 18, N. Y.

NONFERROUS METALLURGIST

Opportunities for professional growth and advancement involving alloy research and development studies. Situations independent of government projects. Only incidental travel from New Jersey location. Give full details, including salary desired.

Box B-3 AIME
29 W. 39th St.
New York 18, N. Y.

EXECUTIVE TRAINEES. Degree in metallurgical or chemical engineering, nonferrous experience. Well established firm in Philadelphia suburb. Salary about $6000, annual increases. Complete benefits.

B-4, AIME
29 W. 39th St., New York 18, N. Y.

WANTED: Back volumes of Periodicals A.S.M. Transactions To Buy for Cash.

Ashley, 24 E. 21 St., New York

Books for Engineers

Structure and Properties of Solid Surfaces, edited by Robert Gomer and Cyril Stanley Smith. *The University of Chicago Press.* $8.50, 491 pp., 1953.—Material for this book was drawn from a conference organized by the Committee on Solids of the National Research Council. Contents may be divided into four main groups: Thermodynamics and theories of surface forces; the structure of a surface and means of determining it; growth processes of and on surfaces; and processes on surfaces which leave them relatively unaltered. Discussion follows each paper and forms an integral part of book. Some of the papers cut across current opinion and efforts have been made to include differing viewpoints.

Stress Concentration Design Factors, by R. E. Peterson. *John Wiley & Sons, Inc.* $8.50, 155 pp., 1953.—It is the purpose of this book to place in the designer's hands information which will enable him to improve his design calculations, to the end that failure will be less prevalent and better balanced designs achieved. The book is primarily a working tool and is not intended to be a textbook in the usual sense. Enough background and references are presented to enable the reader to explore further if he so chooses.

Welding Engineering, by Boniface E. Rossi. *McGraw Hill Book Co.* $8.00, 786 pp., 1954.—The book furnishes student or beginner with fundamental facts about welding, in addition to giving those already in the field a wider understanding, and providing a useful reference source to draftsman, engineer, designer, and researcher. Section one covers various welding processes. Section two deals with metals, their metallurgy, and weldability. Section three discusses pertinent design and fabrication considerations such as welded design and its field of application. Section four treats the testing and inspection of welds.

The Atomisation of Liquid Fuels, by E. Giffen and A. Muraszew. *John Wiley & Sons, Inc.* $6.00, 246 pp., 1953.—This book, based on a survey of published information, is an attempt to picture the whole process by which an initially continuous liquid jet is broken up into a great number of small droplets—a process widely used with liquid fuels for internal combustion engines and furnaces. It deals with the process of disintegration; characteristics of fuel sprays and the effect on these of the atomizer, the liquid, the gaseous medium and injection pressure; the theory of the swirl atomizer; and experimental study methods.

Engineering Law, fourth edition, by R. E. Laidlaw and C. R. Young. *University of Toronto Press.* $5.25, 394 pp., 1951.—Using a minimum of technical legal language, the book offers a simple presentation of those phases of Canadian law that relate to engineering. It covers contracts and specifications, arbitration, expert evidence, compensation, patents and inventions, and a wide range of engineering activities. Extracts from reports of typical cases have been added for illustration to the new edition.

Nuclear Physics, by W. Heisenberg. *Philosophical Library.* $4.75, 224 pp., 1953.—This book is for those with no training in physics but with familiarity with physical ideas. Opening with a historical introduction, chapters of the book deal with structures of molecules and atoms, radioactivity, atomic nuclei, nuclear forces and reactions, and instruments and procedures of the nuclear physicist. A final chapter deals with applications.

Principles of Transistor Circuits, edited by Richard F. Shea. *John Wiley & Sons, Inc.* $11.00, 535 pp., 1953—Claimed to be the first comprehensive treatment of the subject, the book is divided into three parts; low frequency, high frequency, and large signal non-linear applications. Each part includes the presentation and analysis of equivalent circuits, analysis of the mathematical relationship, and development of the applicable circuits. Basic semi-conductor principles are discussed. The treatment throughout enables the engineer with vacuum tube experience to utilize the material.

ORDER YOUR BOOKS THROUGH AIME—Address Irene K. Sharp, Book Department. Ten per cent discount given whenever possible. Order Government publications direct from the agency concerned.

Symposium on Tin. *American Society for Testing Materials.* $2.50, 111 pp., 1953.—This symposium presents organized information on various aspects of tin as a preliminary to the establishment of standards and specifications relating to tin. Information presented includes: Production and resources; tin coatings; use of tin in the container industry and in automobile bodies; the effect of impurities in tin and their determinations; and the analysis of tin in general.

Alternating Current Measurements, third edition, by David Owen. *John Wiley & Sons, Inc.* $2.00, 120 pp., 1953.—A brief account is presented of the measurement of resistance, inductance, and capacitance by use of alternating current, mainly at low frequencies, but including a chapter on radio-frequencies. Special attention is paid to the alternating current potentiometer and its applications.

Cambridge Elementary Statistical Tables, by D. V. Lindley and J. C. P. Miller. *Cambridge University Press.* $1.00, 35 pp., 1953.—The book contains a set of 10 tables of the commoner statistical functions and tests of significance for users of statistical methods in scientific research, technology, and industry.

Superior
BLAST FURNACE
COPPER CASTINGS
Hot Blast Valves and Valve Seats
Blast Furnace Tuyeres. Licensed Manufacturers of all Leading Designs
Cooling Plates of all kinds including Heavy Mass Super Cooled Bosh Plates
SMEETH-HARWOOD COMPANY
8824 Vincennes Ave., Chicago 20, Ill.
In Canada—The William Kennedy & Sons, Ltd., Owen Sound, Ontario
Blast Furnace Copper Castings—also Brass and Bronze Mill Castings

Packed in Bags and Shipped on Pallets

Each bag holds 25 lb. of contained vanadium, so additions can be made without weighing. Bags prevent contamination and are shipped on pallets for easy and economical handling.

Use this New, Easy Method

. . . FOR ADDITIONS OF VANADIUM

You can handle additions of vanadium conveniently and economically with ELECTROMET ferrovanadium packed in bags.

Check these advantages:

- *Convenient Packaging*—The alloy is packed in strong five-ply, paper bags. These bags have a wide blue band across the middle, as well as blue edges and bottom, for positive identification. The bags prevent contamination and preclude any chance of mix up with other alloys.
- *No Weighing*—Each bag (25 lb. of contained vanadium) can be added without weighing.
- *Handling Costs Reduced*—Pallet shipments are available at no extra charge. Each pallet holds about 4,000 lb. of ferrovanadium—2,200 or 3,000 lb. of contained vanadium, depending on the analysis. Pallets can be conveniently unloaded and handled in your plant by lift truck or overhead crane. Handling costs are reduced and inventory-taking is simplified. And you don't have to return the pallets.
- *High-Quality Material for Every Need*—ELECTROMET ferrovanadium is uniform in analysis, closely graded, correctly sized, and physically clean. It is furnished in these grades:

	Vanadium	Silicon max.	Carbon max.
High-Speed Grade	50 to 55% or 70 to 75%	1.50%	0.20%
Special Grade	50 to 55% or 70 to 75%	2%	0.50%
Open-Hearth Grade	50 to 55%	8%	3%
Foundry Grade	50 to 55%	approx. 10%	3%

* **Immediate Delivery**—Vanadium is readily available and can frequently be used in engineering steels to replace part, if not all, of certain scarcer alloys.

The term "Electromet" is a registered trade-mark of Union Carbide and Carbon Corporation.

* **Engineering Service**—Our staff of experienced metallurgical engineers is always ready to furnish technical assistance in the use of vanadium. Phone, wire, or write one of ELECTROMET's offices for additional information.

ELECTRO METALLURGICAL COMPANY
A Division of Union Carbide and Carbon Corporation
30 East 42nd Street UCC New York 17, N. Y.
OFFICES: Birmingham • Chicago • Cleveland • Detroit
Houston • Los Angeles • New York • Pittsburgh • San Francisco

In Canada: Electro Metallurgical Company, Division of Union Carbide Canada Limited, Welland, Ontario

Electromet
Trade Mark
Ferro-Alloys and Metals

New Products

New Products | New Literature | New Services

For Further Information or Literature on any Product, Fill in the Coupon and Send to JOURNAL OF METALS
Students are Requested to Apply Directly to Manufacturers for Bulletins and Information

1—DUSTPROOF MOTOR: *Elliott Co.* has announced a taconite dustproof motor. It is of particular use

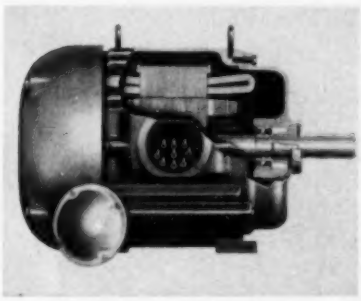

in ore refining plants using taconite beneficiation process where crushing, mixing, and drying operations produce an atmosphere burdened with fine magnetic dust.

2—THERMOCOUPLE WELL: A thermocouple protecting tube has been announced by *Bristol Co.* It combines the thermal conductivity and shock resistance of metal with the oxidation and deformation resistance of ceramics. Available in lengths of 12, 18, and 24 in., it has a wall thickness of ⅛ in.

3—MICRO BALANCE: A single pan constant sensitivity micro ballance has been designed and is available from *Fisher Scientific Co.* It embodies the features in the 200-g Gram-atic and 100-g Semi-Micro Gram-atic balances: High accuracy (±0.002 mg) and high speed (5-min weighings are cut to 35 sec).

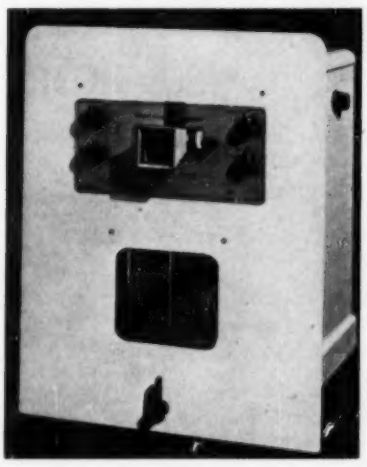

4—GRINDING WHEELS: Carboflex depressed center grinding wheels for rough grinding, cut off and slotting operations for ferrous and nonferrous metals and nonmetallics are available. The wheels come in sizes of 7 and 9⅛ in. diam; ⅛, 3/16, and ¼ in. thick and contain a ⅞ in. arbor. *Carborundum Co.*

5—BRINELL TESTING: A semiautomatic Brinell testing machine

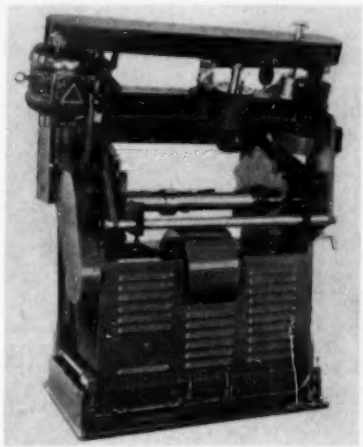

has been announced by the *Detroit Testing Machine Co.* It automatically indexes test pieces through both spot grinding and Brinell testing stations. It has a 30 in. work opening and is hydraulically operated.

6—SPEED CONTROL: A new style variable speed control for lathes and other machines, powered by fractional and 1 hp dc motors, has been introduced by *Electro Products Laboratories.*

7—SPECTROSHELL MOLDS: New spectroshell molds offer a new facility for the production of sample pins for better emission spectrographic analysis. Single unit spectroshell molds measure 2x4x3½ in. overall and afford capacity for four pins each ¼x2¼ in. *Baird Associates.*

8—HOSE: Greater lightness, flexibility, and retractability are incorporated in this new CWS Flexaust hose introduced by the *Flexaust Co.* It is made of Neoprene impregnated cotton drill in which spiral wire reinforcement is imbedded. Standard sizes range from 1¼ to 8 in. ID.

9—ENAMEL COATING: A porcelain enamel coating with a full matte, acid resisting finish is available from *Bettinger Corp.*

10—SOLVENT CEMENT: Used for bonding a wide variety of lightweight materials to wood, metal, glass, rubber, and many plastics, this general purpose rubber and resin solvent cement is available from the *Flintkote Co.* It adheres to light fabrics, felts, and insulation materials and may be applied by brush.

11—HP MOTORS: A new line of integral horsepower motors has been announced by the electric motor div., *A. O. Smith Corp.* Production is in 1 and 1½ and 2 hp ratings. This line will supplement the present which extends from ½ to 150 hp.

12—GRINDER AND MILLER: The *Newage International, Inc.* hand air turbine grinder and miller comes in

three sizes to perform grinding, milling, and polishing operations at speeds to 85,000, 70,000, and 55,000 rpm. The tools are designed for operation on air pressure from 60 to 100 psi.

13—SCINTILLOMETER: This Scintillometer is used for making production checks in radioactive ore processing and for field and laboratory radioactive ore assaying. It weighs 7 lb with batteries. Maximum detection sensitivity and radiation determination is obtained by the use of a 10 stage photomultiplier tube type 5819 optically coupled to a gamma sensitive crystal. *Radiac Co.*

Free Literature

20—CARBIDE TOOLS: A wide variety of carbide tipped single point cutting tools is described in brochure published by the *DoAll Co.* Standard unground carbide tips as well as carbide tips for threading tools, reamers, scrapers, etc., are also shown.

21—TESTING MACHINES: Illustrations and complete specifications of more than six different types of Brinell hardness testers are included in catalog issued by *Steel City Testing Machines, Inc.*

22—GLASS BLOCKS: Information on physical performance, technical data on light transmission, insulation values, and other pertinent data are given. *Pittsburgh Corning Corp.*

23—PURCHASING GUIDE: Booklet issued by *Continental Copper & Steel Industries, Inc.*, lists the products made by all divisions. Included are wire cloth, wire and cable, tool steels, and welded pipe, among others.

24—CORROSION DATA: Folder TDC 160 contains information on comparative corrosion resistance of stainless steels to corrosive media. It presents data on six widely used stainless tubing steels and several hundred corrosive media at various temperatures and concentrations. *Babcock & Wilcox Co.*

25—CARBONITRIDING PRACTICE: Bulletin available from *Armour & Co.* is a survey of industrial carbonitriding practice. Table of contents includes: Nature of carbonitriding process; typical carbonitrided structures; sources and nature of data; parts carbonitrided and steels used; furnaces; quenching and cleaning, tempering and finishing, and several other important factors.

26—STRAIN GAGE: Features and specifications of hand type, dial micrometer instrument for 2 and 10-in. gage lengths are given in brochure issued by *Baldwin-Lima-Hamilton Corp.*

27—CAST HIGH ALLOYS: Reprint of a technical article that discussed the cast corrosion resistant alloys most generally used for process equipment in the chemical industries is obtainable from *Copper Alloy Foundry Co.*

28—PRECISION INSTRUMENTS: A complete presentation of the precision instruments manufactured by the *Chicago Dial Indicator Co.* is available. Geneva dial indicators, bench center set, dial snap gages, and depth gages are just a few of the instruments manufactured.

29—FURNACE CONTROLS: The latest edition of furnace and oven controls is available from *Minneapolis-Honeywell Regulator Co.* Specifications and prices on temperature controllers, program controllers, valves and accessories, and combustion safeguard equipment are listed.

30—CALROD: The 1954 edition of the *General Electric Co.* catalog on Calrod electric heaters and heating devices has been announced by the company. The 60-page catalog describes the units in terms of application, special features, installation, and pricing. It also contains methods for determining power requirements and heat losses for many applications.

31—BLAST CLEANING: The purpose of this booklet is to supply nontechnical information to those interested in the possibilities of blast cleaning. The three basic advantages of the process are discussed and an analysis of where it can be used and how the abrasive is forcibly propelled. *Pangborn Corp.*

32—VOLUME PUMPS: Bulletin on air powered controlled volume pumps shows how these pumps are used to solve low capacity flow control problems. A graphic presentation of pump operating principles and capacity-pressure and air consumption tables is included. *Milton Roy Co.*

33—HYDRAULIC PRESSES: Brochure on representative hydraulic presses and equipment manufactured by *R. D. Wood Co.* is available. Basic hydraulic press specifications in addition to representative high pressure hydraulic valves, hydraulic accumulators, and hydraulic shock alleviators are given.

34—RESEARCH INSTRUMENTS: *North American Philips Co., Inc.*, has issued a reference book on research and control instruments, X-ray and analytical equipment. X-ray diffraction, spectrometry, and spectrography, tubes, rectifiers, and cameras are covered in the book. Some space is also devoted to accessory equipment.

35—MN STEEL: General catalog describing complete line of castings made of "the toughest steel known," has been released by *American Manganese Steel Div.* A complete discussion of the impact and abrasion resistant characteristics of Amsco 13 pct manganese steel under each product category is also contained.

36—PLATING ANODES: Information on copper, lead, zinc, tin, tin-lead, cadmium, cadmium oxide, and brass plating anodes is contained in catalog published by federated metals div., *American Smelting & Refining Co.* Sizes, shapes, and compositions are included.

37—PUNCHES AND DIES: Money saving tips on punches and dies are contained in booklet prepared by *F. J. Stokes Machine Co.* Do's and don'ts that should be followed in keeping tools in condition are listed.

38—PLASTIC SHEETS: Applications of clear cast thermoset Cocor sheets are described in catalog issued by *Cast Optics Corp.* Properties such as high abrasion and heat resistance are featured. Technical properties are included.

39—ROLLING MILLS: The complete line of low cost precision built laboratory and production rolling mills is illustrated in bulletin available from *Stanat Mfg. Co.*

Journal of Metals
29 West 39th St.
New York 18, N. Y.

February

Please send me { ☐ More Information ☐ Free Literature ☐ Price Data } on items indicated.

Not Good After May 1, 1954

1	2	3	4	5	6	7	8	9	10
11	12	13	14	15	16	17	18	19	20
21	22	23	24	25	26	27	28	29	30
31	32	33	34	35	36	37	38	39	40
41	42	43	44	45	46	47	48	49	50

Name _____ Title _____

Company _____

Street _____

City and Zone _____ State _____

FERROCARBO + STEEL = PLUS STEEL

For the story of FERROCARBO in quality steelmaking, mail the coupon today—or phone or write the FERROCARBO distributor nearest you. You'll learn why steel deoxidized with FERROCARBO is "plus steel."

KERCHNER, MARSHALL & CO.
PITTSBURGH • Cleveland • Buffalo
Philadelphia • Birmingham • Los Angeles

MILLER & COMPANY
CHICAGO • St. Louis • Cincinnati

WILLIAMS & WILSON
TORONTO • Montreal • Windsor

THE CARBORUNDUM COMPANY, Dept. JM 84-31
Niagara Falls, New York

Gentlemen:

I would like to have the FERROCARBO story—no obligation on my part.

NAME AND TITLE

COMPANY

STREET AND NUMBER CITY ZONE STATE

FERROCARBO

TRADE MARK

by CARBORUNDUM

"Carborundum" and "Ferrocarbo" are trademarks which are registered in the U. S. by The Carborundum Company, Niagara Falls, New York, and in Canada by Canadian Carborundum Company, Ltd., Niagara Falls, Ontario.

84-939

Industrial Notes

• Despite softening markets in the latter months of 1953, domestic production of ferroalloys for the year was more than 2.3 million net tons, compared with about 2 million tons for the previous year, according to William C. Keeley, president of Vanadium Corp. of America. Mr. Keeley stated that his firm substantially increased its sales over the previous 1952 record of $38,875,247.

• A $238,500 fund for grants to colleges and universities to further the teaching of science has been established by the Du Pont Co. The company has made the grant to advancement of teaching the largest in its aid-to-education program. It has authorized a total of more than $700,000 for the entire program for the 1954-55 academic year.

• *A new aluminum fabricating plant is under construction at Alicante, Spain, according to Aluminium Ltd. of Canada. Constructing the plant is Aluminio Iberico, formed by Aluminium Ltd. and a Spanish group about two years ago. The plant is being designed to fabricate between 18 and 20,000 tons of aluminum products per year from ingot to be supplied by smelting subsidiaries of Aluminium Ltd.*

• U. S. Air Force selected Bridgeport Brass Co. to operate its $50 million Adrian, Mich. aluminum extrusion plant. Bohn Aluminum & Brass Corp., present plant operator, terminates its contract with the Air Force, May 1, 1954.

• Harrisburg Steel Corp. has acquired all physical assets of Taylor-Wharton Iron & Steel Co. Purchase was made through a Harrisburg Steel subsidiary. Taylor-Wharton was established in 1742 and has plants at High Bridge, N. J.; Easton, Pa.; Cincinnati; and Birmingham, Ala. These operations will continue without change in location, personnel, or management.

• Three firms have joined to expand activities of the Borolite Corp., recently formed to pursue study and development of various metal borides for high temperature military and civilian applications. The three firms are: Firth Sterling, Inc., Pittsburgh; American Electro Metal Corp., Yonkers, N. Y.; and the Carborundum Co., Niagara Falls, N. Y. Joint statement by the three companies said that the Borolite Corp. was formed to concentrate funds and facilities for faster and broader development. In initial stages the participating companies will manufacture borolite products to be marketed by the Borolite Corp., Niagara Falls, N. Y.

• *With recent Government decision to release atomic energy to private industry, small atom smashers with their stainless steel parts and accessories are already at work in some industrial laboratories. Chromium-nickel stainless is used in the atom smashing equipment because of nonmagnetic properties and strength. Strength of steel is needed to hold coils in place against electrically induced forces developed while energizing atomic particles. A nonmagnetic steel is also necessary to avoid short circuiting or dissipating the magnetic field. Walls of the raceway through which atomic particles speed are also made of stainless steel.*

• Elgiloy, the cobalt-base spring alloy developed by Elgin National Watch Co., has been placed back on the commercial market. The alloy was removed from the market in 1950 because of Government cobalt and nickel restrictions. According to Elgin, Elgiloy consists of cobalt, 40 pct; chromium, 20 pct; and nickel, 15 pct, and is noted for high hardness, toughness, tensile strength, corrosion, set, and fatigue resistance.

For maximum efficiency in the production of specimens in the metallurgical laboratory the Buehler cabinet type polishing table with companion storage cabinets represents the latest modern development of this type of equipment.

The convenience of this streamlined polishing equipment saves time and encourages the operator to produce the highest quality of polished sample.

Item No. 1511 is a two-unit polishing table with Formica top approximately 60" long x 27" deep by 30" high to table top. Two 12" swing spouts, drain, 8" diameter wash bowl, plumbing and wiring.

Recommended accessories to complete an efficient set up for maximum convenience are: No. 1512 storage cabinet with recessed light and No. 1513 supporting panel for installation above polishing desk. Or, No. 1514 floor model storage cabinet. Both these cabinets can be used together to advantage in most laboratories.

The Formica top and back on the table and cabinet is installed with a smooth Formica edge that eliminates all metal rims that may form pockets for water and dirt. Covers are held in place on the back by magnetic holders. The large 8" wash bowl is a new feature that enables the operator to use both hands in washing specimens.

All metal construction finished in hammer tone grey makes a very attractive appearance. Prompt delivery can be made on these new items.

The Buehler Line of Specimen Preparation Equipment Includes . . . Cut-Off Machines • Specimen Mount Presses • Power Grinders • Emery Paper Grinders • Hand Grinders • Belt Surfacers • Mechanical and Electro Polishers • Polishing Cloths • Polishing Abrasives

Buehler Ltd. METALLURGICAL APPARATUS
2120 Greenwood Avenue, Evanston, Illinois

Our NEW RareMeT Compound

is Now TWICE as Heavy

Years of experience with rare earth materials, constant research and application of our product assure you of the best results.

Our new RareMeT Compound is evidence of our progress. Now the new RareMeT Compound is twice as heavy, requires less handling and provides more uniform results.

Hot workability in many types of steels is being improved with small additions of this already established product. For example, in stainless steel, excellent results in both hot workability and increased yield have been obtained, as published in MCA's current literature and the trade magazines.

As recognized authorities in the application of Molybdenum, Tungsten, Boron, Cerium and its derivatives both as alloys and chemicals, MCA assures confidential and immediate response to inquiries.

Write today for free Progress Report Number 1, "Rare Earths in Melting."

MOLYBDENUM

CORPORATION OF AMERICA

Grant Building **Pittsburgh 19, Pa.**

Offices: Pittsburgh, Chicago, Detroit, Los Angeles, New York, San Francisco
Sales Representatives: Edgar L. Fink, Detroit; Brumley-Donaldson Co., Los Angeles, San Francisco
Subsidiary: Cleveland Tungsten, Inc., Cleveland *Plants:* Washington, Pa., York, Pa.

MCA

THE research div. of National Research Corp. believes that it has a "sound and commercially feasible" method for the melting, handling, and casting of titanium. According to the corporation the process is simple and employs few procedures not generally practiced in foundries manufacturing stainless steel and alloy castings.

Five steps are involved in preparation of the pattern and the mold flask. As usual, the pattern is made to size based on shrinkage factors of the metal and mold. The mold is made by mixing powdered refractory with a liquid binder and pouring resulting slurry over the pattern. The slurry forms one half the mold by solidifying on the pattern. The other half of the mold is prepared similarly. A strong cohesive mold is produced by a low temperature bakeout followed by high temperature firing. During the foregoing steps the mold is given special treatment enabling it to withstand the action of molten titanium. Finally, the mold is assembled with the necessary gates, risers, and pour blocks and held together by clamps or jigs.

In premelting operations, the mold is placed, at room temperature, into the furnace and titanium sponge or scrap is loaded into the crucible. After sealing from the atmosphere, the furnace is evacuated to a low pressure, 1 to 10 microns, or 0.001 to 0.01 mm Hg. Argon is introduced into the furnace to provide suitable pressure for melting and casting phase. At the start of melting and casting, power is applied to the electrode, starting the arc. Melting of titanium in the crucible begins.

Power is cut off when enough metal is melted, and the electrode removed from the path of the molten stream. The melt is poured into the mold gate below and in line with the crucible pouring lip. The mold is cooled in the furnace under argon or vacuum for half hour to an hour, giving the titanium in mold and crucible time to cool below the temperature at which it reacts with the atmosphere.

Titanium castings shown are about 40 pct of actual size. The large casting is a cover plate produced on purchase order for the U. S. Army Ordnance Corps of Watertown Arsenal, using the National Research method.

The small furnace in operation at National Research can produce 4 or 5-lb castings. Melting capacity limits production of larger castings. It is believed by National Research that good castings up to 100 lb can be produced by the process in a larger furnace. Finish is equivalent to that of good sand castings, according to National Research, and castings have a high degree of soundness.

The combination vacuum and inert atmosphere arc furnace is the essential equipment not ordinarily found in the foundry. The furnace consists of a skull melting type crucible in a chamber evacuated by vacuum pumps. Titanium is contained in a graphite crucible backed by refractory ramming mix, all in a stainless steel shell. Carbon pickup from the graphite shell is minimized and can be contained below 0.15 to 0.20 pct in the finished cast shape by limiting melting to a center pool. National Research is prepared to grant non-exclusive licenses on this process to qualified foundries.

◆◆◆◆◆◆

THE Special Subcommittee on Minerals, Materials and Fuels Economics of the Committee on Interior and Insular Affairs has just issued the first part of its report after hearings in Washington, D. C.; Seattle; and Henderson, Nev. Other hearings are scheduled for Los Angeles, Salt Lake City, and again in Washington. It has heard testimony from engineers, producers, and Government officials. While some of the hearings were held in executive session because of security requirements, the committee states in its initial report that testimony revealed a "shocking" shortage of certain strategic materials. This shortage of strategic critical materials is to be investigated in separate hearings.

The report states that: "We have become dependent upon foreign nations across one or both major oceans for many of the materials without which we cannot fight a war or support our economic structure."

It is also stated that the stockpile program, scheduled for completion by 1951, was extended to 1953. It is now doubtful that the program can be completed by 1958, the report said. Contracts for strategic materials, it was disclosed in secret sessions, show that terms were more favorable to foreign producers than to "domestic American producers." The report of the subcommittee finds that the terms of these contracts are contrary to stockpile law and national security. During hearings, several military strategists stated disbelief in the possibility of keeping long sea lanes open during time of war.

The committee recorded complaints that have reached them relative to domestic production to be:

Trade agreements made by the State Dept. under the 1934 Trade Agreements Act; Taxes, direct and indirect; Regulations governing venture capital by the Securities and Exchange Commission; Favoritism toward purchase of foreign materials over domestic sources under the Stockpile Act; and currency manipulation and participation for trade advantage by foreign governments both in the U. S. and abroad.

◆◆◆◆◆◆

KENNECOTT Copper Co. is entering the aluminum field via a minority investment in an already established major producer—Kaiser Aluminum & Chemical Corp. Kaiser ranks third on the U. S. aluminum scale. Kennecott confirmed Kaiser's announcement that it is buying $16.25 million worth of a new series of convertible preferred stock "for investment." The shares will carry a 5½ pct dividend and be convertible into common stock for 20 years at $30 per share. If all the shares are converted, Kennecott will acquire about 451,666 shares of common.

Kennecott is also buying 100,000 outstanding shares of common from a group of Kaiser Aluminum founders. Sellers are Henry J. Kaiser Co., General Construction Co., J. F. Shea Co., and Pacific Bridge Co. The founder companies are selling in proportion to ownership in Kaiser Aluminum. There are more than 3.7 million shares outstanding.

About a year ago Anaconda Copper Mining Co. entered the aluminum business with the start of construction of a primary aluminum producing plant in Montana.

◆◆◆◆◆◆

FALCONBRIDGE Nickel is expanding facilities at its Norway plant to provide 45 million lb of nickel per year, but its eventual goal for overall operations is 60 million lb by 1960. One report has it that the additional plant to furnish the 15 million lb may be located in the Sudbury district of Canada. The company has a new pyrrhotite treatment process which is said to show promise of fitting into future plans. The *Northern Miner* reports that foundations for the plant are being poured and deliveries of structural steel are scheduled to start. Plans are to divert 200 tons per day of pyrrhotite from the Sudbury smelter to the new plant.

The plant is being built on the slag dump of the smelter. While recovery of nickel is the prime factor, there are indications that a salable iron ore will be produced as a byproduct. According to the *Northern Miner* some completely new principles are being used in the new process which also lends itself to treatment of other complex base metal ores. Tests are reported to indicate that metal recoveries are greater than those from selective flotation on some difficult ores and with moderate cost. It is concluded that plant investment would be no greater than for an electrolytic refinery of equal capacity. While neither Falconbridge nor International Nickel, who also has a pyrrhotite method, have disclosed process details, it is believed there are significant differences.

◆◆◆◆◆◆

CERRO Bolivar, Orinoco Mining Co.'s Venezuelan iron ore venture, shipped its first ore to the U. S. last month. The shipment is the culmination of a great development effort on the part of the U. S. Steel Corp. subsidiary, which started when F. H. Kihlstedt, Orinoco mining engineer first climbed the slopes of Cerro Bolivar—then called La Parida. JOURNAL OF METALS carried the first story ever printed on the discovery in the February 1950 issue. Kihlstedt saw lavish ore exposures as high as 200 ft. Average grade of the ore by dry analysis is about 63.50 pct iron. Natural iron content is calculated to be approximately 58 pct. The ore is practically free of overburden, according to W. W. Wanamaker, chief engineer of Orinoco.

The ore will be shipped from Puerto Ordaz. Orinoco performed a monumental dredging operation to make the port usable. Only one crusher is being installed at the port for the present. Dumping cycle and apron feeder are adjusted to provide a capacity of 3000 tons per hr, although all components are designed to handle as much as 6000 tons per hr. It is anticipated that some 2 million tons will be shipped during 1954, but by the end of the year output is expected to reach a 5 million ton annual rate. The ore handling system is geared to handle 67 ore cars per hr, with initial stockpile capacity 700,000 tons. A tunnel conveyor provides economical reclaiming from stockpile to dockside traveling shiploaders.

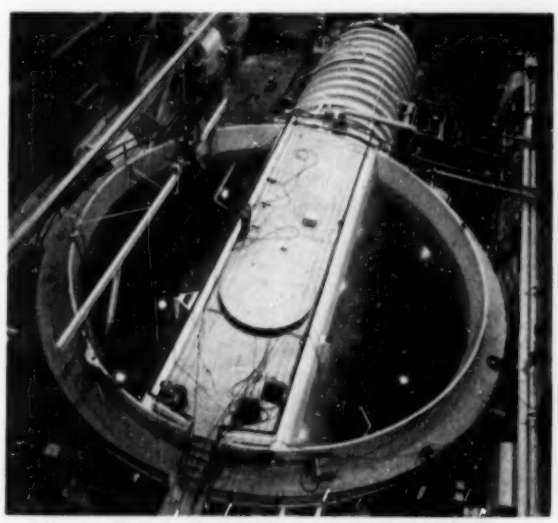

This is the land locked submarine at the National Reactor Testing Station, Idaho, containing the Mark I nuclear power plant, prototype of the one in the U.S.S. *Nautilus*, launched last month.

Drift of Things

NO doubt to the casual observer the life of an Institute President is "just a bowl of cherries," but we have accumulated a few facts on the duties that indicate that this is not necessarily so. Beginning with September 10 and following through the month of October, we find that President Andrew Fletcher had a pretty rough schedule:

Sept. 10. Arrived at Sydney, Nova Scotia and traveled by automobile to Keltic Lodge at Ingonish Beach for the Industrial Minerals Div. Fall Meeting. Spoke at the dinner.

Sept. 11. Attended meeting activities.

Sept. 12. Traveled from Ingonish Beach to Antigonish, Nova Scotia, receiving an honorary degree of Doctor of Laws and delivering the Convocation address.

Sept. 13. Left Halifax, Nova Scotia to return to New York.

Sept. 18. Attended a meeting of the Oregon Section at Portland. Eighty men and wives attended and President Fletcher spoke to the group.

Sept. 19. Met with Seattle AIME Members with an attendance of 50 people.

Sept. 21-24. Attended American Mining Congress meeting at Seattle and presided over an AIME Board meeting.

Sept. 25. Attended a meeting of AIME Members at the Consolidated Mining & Smelting Co. plant at Trail, B. C.

Sept. 26. Attended a joint meeting of the Canadian Institute of Mining and Metallurgy and members of the Spokane Subsection at Trail, B. C.

Sept. 27. Visited Metalline Falls, Idaho and toured Pend O'Reille Lead & Zinc Co.

Sept. 28. Addressed the Northwest Mining Assn. at Spokane at a luncheon meeting. Attended an evening meeting of the Spokane Subsection with an attendance of 125.

Sept. 29. Visited major operations in the Coeur d'Alene district and met with AIME Members in Kellogg, Idaho.

Oct. 1. Stopped at the Anaconda smelter at Anaconda, Mont., where a special AIME luncheon was held for the President. A dinner meeting of the Montana Section was held in Butte at the Finlen Hotel.

Oct. 13. Visited Phelps Dodge operations at Morenci, Ariz., and attended an evening meeting with the Morenci Subsection.

Oct. 14. Inspiration and Miami companies held a special dinner honoring the President at Globe, Ariz. Seventy-six AIME members attended from Ray, Inspiration, Miami, Superior, and Globe.

Oct. 15. Special meeting of the Ajo Subsection—62 attended.

Oct. 16. Phelps Dodge Corp. held a luncheon for the President in Ajo.

Oct. 20. Toured in Tucson and visited the new operations at San Manuel.

Oct. 21. Met with students of the University of Arizona at a gathering sponsored by Arizona Section Woman's Auxiliary, where Mr. and Mrs. Andrew Fletcher were guests of honor.

Oct. 22. Visited Phelps Dodge smelter at Douglas, Ariz.

Oct. 23. Dinner dance at Bisbee, Ariz. under the auspices of the Bisbee and Douglas Subsections.

Oct. 24. Attended a luncheon at Silver City, N. Mex. given by Kennecott Copper Co. and attended an evening meeting with the Southwestern New Mexico Section at Silver City.

Oct. 26. Visited International Minerals & Chemical Co. and U. S. Potash plants at Carlsbad, N. Mex., and attended a special meeting and dinner given by the Carlsbad Section.

Oct. 27. Arrived at El Paso and attended the Fall Meeting of the Mining, Geology, and Geophysics Div. and International Mining Days.

We probably shouldn't print this—it's apt to scare off the upcoming Presidents, and future ones to be chosen—but it does give a little better idea of the work load that comes with the AIME Presidency. Rewards are the kind that go with doing a terrific job well—knowing that in the year of office one has performed a duty for which the membership is grateful. It takes the kind of men who have led the Institute in the past and who are already set to lead it in the future. Leo Reinartz will be President in 1954. His past and present lend themselves well to the task at hand. This issue of JOURNAL OF METALS contains a brief sketch of Mr. Reinartz as the editors see him. (C. M. C.)

MEMBERS planning to come to the Annual Meeting in New York by air will find that the airlines bus terminal at Park Ave. and 42d St. has been replaced by a new terminal at 1st Ave. and 37th to 38th Sts., about 15 minutes' walk from the former location. To get from LaGuardia or Idlewild airports to midtown Manhattan requires a bus ride to the terminal and a taxi ride from there to one's hotel. Passengers deplaning at Newark Airport are more fortunate in that the airport bus, on its way to the 1st Ave. terminal, will stop at 8th Ave. and 42d St. and at Grand Central.

Passengers with only light baggage, alighting at LaGuardia for midtown Manhattan, may find it quicker and certainly cheaper to take the city bus from the front of the Administration Building to its terminal at 74th St. and Roosevelt Ave. There they may walk upstairs to an elevated train which brings them to Grand Central or Times Square; or they may walk downstairs to the subway and take an "F" train which stops at Lexington Ave. and Fifth Ave. on 53d St., and at 50th, 42d, and 34th St. on 6th Ave. (Avenue of the Americas). The city bus fare is 13¢, the elevated or subway fare 15¢, a total of 28¢ compared with the airport bus fare of $1.25 plus a taxi fare of 50 to 75¢. (E.H.R.)

This rubber "tire" talks to you

Bell Laboratories engineers have developed a new and highly economical way to record sound magnetically.

Instead of tape or wire they use a mixture of rubber and iron oxides which is formed into a band and mounted on a wheel. This simple and very rugged "talking rubber" can play back messages clearly millions of times.

Talking rubber is already at work for the Bell System announcing weather and answering customers who call vacant or disconnected numbers. It promises to have many other uses. In a new machine, it answers your telephone in your own voice when you are away—and takes a message for you in the voice of your caller.

Many businesses, too, other than telephone, are expected to find a variety of ways to use talking rubber—especially whenever a message must be given quickly to many people.

Talking rubber proves again the downright practicality of Bell Laboratories' research to improve telephone service.

One of a bank of recorder-reproducers operated by the New York Telephone Company for the New York Stock Exchange. They give instant stock quotations to brokers who dial a code number. Recording and pickup heads are shown above wheel.

BELL TELEPHONE LABORATORIES

Improving telephone service for America provides careers for creative men in scientific and technical fields.

Product Purity and sterility are easy to maintain in this metering pump, because head and inlet and outlet fittings are constructed of Type 303 chromium-nickel stainless steel. Maisch Metering Pumps are built by Mechanical Products Corp., Chicago 7, Ill.

An example of Corrosion Resistance
...and maintenance of accuracy...
provided by Type 303 Stainless

Manufacturers of equipment designed to protect product purity and assure sanitation find it pays to use chromium-nickel stainless steel for corrosion resistance and other money-saving properties.

For instance, the makers of Maisch metering pumps . . . widely used for precise dispensing in biological and industrial fields . . . specify Type 303 Stainless. They fabricate pump heads and inlet and outlet fittings from Type 303 to provide properties that help users maintain product purity, sterility and sanitation, as well as permanent accuracy under very diverse service conditions.

Type 303 is the free-machining grade of the austenitic chromium-nickel stainless steels which are immune to most organic and a great many inorganic chemicals.

INCO

This improved machinability, combined with resistance to galling and seizing, make Type 303 stainless particularly useful for gears, heads, fittings and other machined products.

You can also trim bulk and deadweight by using correct types of chromium-nickel stainless. They are strong yet tough, and also resistant to wear and abrasion. At elevated temperatures they resist creep, scaling and oxidation, while at low temperatures they offer exceptional resistance to impact.

Investigate all the economies you can obtain by using stainless steel for your products or equipment. Send us your inquiries on the use of cast or wrought stainless alloy steels containing nickel, and details of your problems for our suggestions.

Chromium-Nickel Stainless Steel Type 303 . . . and precision construction . . . contribute to the permanent accuracy of this biological metering pump. Maisch pumps are adjustable, and permit dispensing from 0 to 9,000 cubic centimeters per minute.

Sanitation in dispensing hot or cold, viscous or non-viscous liquids is advanced by use of Type 303 stainless. Maisch industrial pumps are available, single or duplex, with fixed capacities from 10 to 290 gph.

THE INTERNATIONAL NICKEL COMPANY, INC. 67 WALL STREET NEW YORK 5, N. Y.

A 300-ton per day oxygen unit is supplying oxygen to International Nickel Co., Inc.'s new oxygen flash smelting process for copper concentrates at Copper Cliff. The flash smelting process uses 7.5 million cu ft of oxygen per day and eliminates the need for other fuels used for copper smelting. Built by Canadian Liquid Air Co., Ltd., the unit separates oxygen from air by liquefaction.

Edward F. Mansure, general services administrator, announced that $43 million has been assigned to expansion of the Government-owned nickel plant at Nicaro, Cuba. The fund includes $1 million for research. Appropriation of the money came after Office of Defense Mobilization certified that Nicaro expansion is essential to national defense. The plant is now producing at a rate of nearly 28,000 lb of nickel per year. The new program calls for a 75 pct capacity expansion and also envisages the use of mineral resources of eastern Cuba.

The U. S. steel industry established a new production record in 1953 with 111,600,445 net tons. It was 18,432,406 tons more than produced in 1952 and 6.4 million tons higher than the previous record year, 1951. U. S. output represented 44 pct of estimated world production of about 255 million tons in 1953. In addition, U. S. ingot capacity was estimated to be 124,330,410 net tons on the first day of 1954, 5.8 pct more than the 117,547,470 tons at the outset of 1953.

Canada's steel production for 1953 was an estimated 4.75 million tons, double that of 1946 when only 2,252,000 tons were produced. Current capacity is about 5 million tons, compared with 3,532,750 in 1945.

Development of an unusual ion source at Oak Ridge National Laboratory, through use of the calutron--a mass spectrograph--has made possible separation of usable quantities of isotopes of ruthenium, palladium, iridium, and platinum. Operated by Union Carbide & Carbon Corp. for the AEC, the laboratory developed ion source operates at temperatures from about 3800° to 5070°F. Temperatures are obtained by electron bombardment of the graphite oven containing one of the elements in the form of metal.

U. S. Bureau of Mines announced that mineral production in the Continental U. S. during 1953 had an estimated value of $14,346 million, the greatest in history and 7 pct higher than in 1952. Iron ore production led the metal mining industry with a total of 117 million long tons shipped, another record. Production of all ferroalloy metals mined in the U. S. except cobalt, was substantially higher than in 1952. However, domestic mine production of zinc was the smallest since 1938.

The new Sherritt-Gordon mine at Lynn Lake, Man., made its first shipment of concentrates, 280 tons, to Fort Saskatchewan. The concentrate will be stockpiled in preparation for start of operations of the new processing plant.

Radiamatic pyrometers

for your "hard to get" temperatures

Temperature of moving tube coming from a continuous reheating furnace is measured by *Radiamatic* pyrometer.

WHEN your important temperatures prove difficult to measure, call on *Radiamatic* Pyrometers. They're ideal for applications where temperatures are too high . . . atmosphere too destructive . . . or vibration too severe for thermocouples. And they do many jobs impossible for other pyrometers, such as measuring temperatures of moving objects and surface temperature of work in furnaces.

These features assure you accurate measurement and ready adaptability to any application:

Reproducible Calibration: As interchangeable as thermocouples . . . calibrated to a fixed standard.

Easy Sighting: you can aim it accurately at the desired target . . . as simply as looking through a telescope.

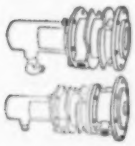

Versatile Mounting: varied mounting accessories include air-cooled and water-cooled fittings; safety shutter protects the element against backfiring flames.

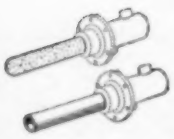

Selection of Sighting Tubes: open-end and closed-end types of ceramics and heat-resistant alloys.

Temperature Compensated: needs no cooling devices for high ambient temperatures.

Radiamatic elements and *ElectroniK* recorders to work with them are available in ranges from 125 to 7000° F. Your nearest Honeywell engineer will be glad to discuss your plant's applications. Call him today . . . he is as near as your phone.

MINNEAPOLIS-HONEYWELL REGULATOR Co., *Industrial Division*, 4573 Wayne Ave., Philadelphia 44, Pa.

● **REFERENCE DATA: Write for Catalog 9300, "*Radiamatic* Pyrometers"**

MINNEAPOLIS
Honeywell
BROWN INSTRUMENTS
First in Controls

The Boeing RB-47E Stratojet is the world's fastest day or night long-range photo ship. It is capable of speeds in excess of 600 mph and has a service ceiling of more than 40,000 ft.

High Performance Jet Engine Design Dependent Upon Metallurgical Ingenuity

by I. Perlmutter

THE requirements for high performance propulsion systems are increasing at rapidly expanding rates as airplane speeds enter the supersonic range. Because military aviation is one of the most competitive enterprises in the world, these requirements must be met if U. S. airpower is to maintain its leadership. The challenge to the engine designer is in turn reflected to the metallurgist in his ability to provide the suitable materials and special design data which the designer will require.

Fig. 1 is a view of a typical axial flow jet engine. Air enters the compressor where it is compressed to a definite ratio through a series of stages. The compressor rotor consists of a number of bladed discs mounted on a shaft which is driven by the turbine wheel. The air is led from the compressor through passages in the compressor rear frame into combustion chambers where it is mixed with fuel and combustion takes place. The hot gas is allowed to expand through a turbine, then passes through the tail cone, the tail pipe, and finally escapes through a jet nozzle, providing thrust for propulsion.

I. PERLMUTTER is Assistant Chief, Metals Branch, Materials Laboratory, Directorate of Research, Wright Air Development Center, Dayton. This paper was presented at the AIME Electric Furnace Steel Conference, Cincinnati, Dec. 2 to 4, 1953.

Higher speed and altitude may be attained by increasing the thrust which in the basic jet requires an increase in turbine inlet temperature. However, Fig. 2 shows that as turbine inlet temperature goes up, thermal efficiency (which is in inverse proportion to specific fuel consumption) decreases.[1] This is not the case in a true gas turbine where the kinetic energy is converted to shaft horse power and thermal efficiency increases with increasing temperature. In a turbo jet engine the gas escapes from a nozzle and provides thrust by its momentum. The reaction is absorbed by the various parts of the engine. Since kinetic energy increases as the square of the velocity of the gas, whereas momentum increases in direct proportion to the velocity, thermal efficiency will decrease with increasing temperature in the jet engine. How then can the associated drop in efficiency which would, of course, be reflected in increased specific fuel consumption and hence in reduced range, be restored?

Fig. 3 shows[2] that at a given turbine inlet temperature, both thrust and efficiency (i.e., decrease in specific fuel consumption) can be raised by increasing the pressure ratio. Since for each inlet temperature the thrust curve reaches a maximum, whereas the specific fuel curve continuously decreases, the

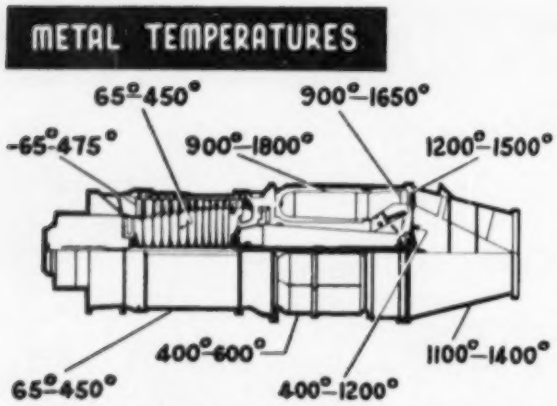

Fig. 1—Metal temperatures of the component parts of an axial flow jet engine are shown in this diagrammatic view.

selection of the optimum design point is generally based on the purpose of the aircraft, i.e., speed and altitude vs range and load.

Compressor Conditions

The increase in pressure ratio has a direct and far reaching influence in the choice of engine materials, particularly those for compressor construction. Major increases in pressure ratio in axial flow compressors are generally attained by raising the number of stages of bladed discs. Since the higher pressures raise the load which the turbine must take during expansion it becomes necessary to increase the number of turbine stages. Moreover, other components such as the combustion system and the compressor casing and rear frame, operating at higher pressure, must be more rugged. From these considerations it is apparent that increasing the pressure ratio will involve an increase in weight at least part of which must be offset by increasing allowable stresses or the use of lighter alloys with acceptable strength.

The combined effect of higher speed and high pressure ratio on compressor temperatures is shown in Fig. 4 in which are plotted some calculated values of compressor inlet and outlet temperatures at various air speeds at an altitude of 35,000 ft and air temperature of −67°F. It will be noted that at Mach 2 (twice the speed of sound) the ram or inlet air temperature is 250°F and that at the outlet of a 10:1 compressor the value rises to 1000°F. The same value of compressor discharge temperature could also be attained with a lower pressure ratio at a higher speed under the same ambient conditions. It is important to note that this is within the range of highest operating temperatures of current steam turbines. Moreover, if such a compressor is to be an efficient one it must also have rather small clearances between blade tips and casing. Thus, from a materials point of view, it differs from the steam turbine in that a life of 1000 hr instead of 100,000 hr is required at much higher allowable stresses.

It has been customary in discussing materials for jet engines to stress the high temperature problems in the turbine section only since compressor outlet temperatures seldom exceeded 500°F. However, the combined effects of higher pressures and higher temperatures in a high performance jet engine compressor greatly magnify certain problems which in current jet engines are either non-existent or have adequate solutions. For example, under present compressor discharge conditions, hot air leakage to the interior of the engine, particularly the highly stressed thrust bearing and lubrication system, is greatly reduced by the use of labyrinth seals which decrease the pressure by turbulence. Such measures may not

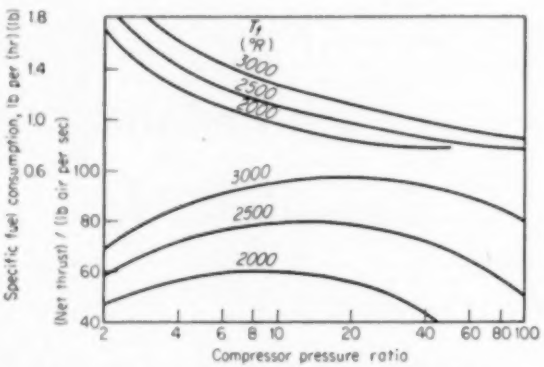

Fig. 3—At a given turbine inlet temperature both thrust and efficiency can be raised by increasing the pressure ratio. This is reflected in a decrease in fuel consumption and hence in increased range.

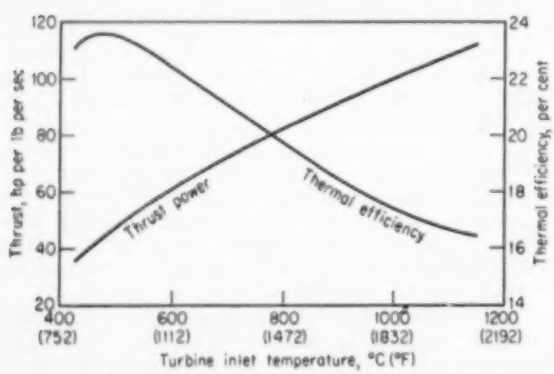

Fig. 2—Thrust and turbine inlet temperature relationships at a fixed pressure ratio indicate a decrease in thermal efficiency with increasing temperature in the jet engine.

be adequate at the very high pressures which may require friction seals with their concomitant materials problems of wear, lubrication at high rotating speeds, and high heat generation. Consider also that in current engines there are almost 2000 compressor blades and a maximum outlet temperature of 450°F, whereas in the high performance compressor 2500 to 3000 blades operate at a maximum outlet temperature of 1000°F and that failure of a single blade is nearly always disastrous. The emergence of the compressor as a major problem in heat resistant materials can, therefore, not be over-emphasized.

Because it receives no cooling whatever and presents the largest area subject to high stress at elevated temperature, the compressor wheels in the hot stages of the compressor constitute a serious materials problem. In addition to having adequate creep strength the compressor wheels must be resistant to corrosion by marine atmosphere and free from notch sensitivity. As a compromise between compressor efficiency and allowance for expansion in the casing, it is estimated that the maximum total permis-

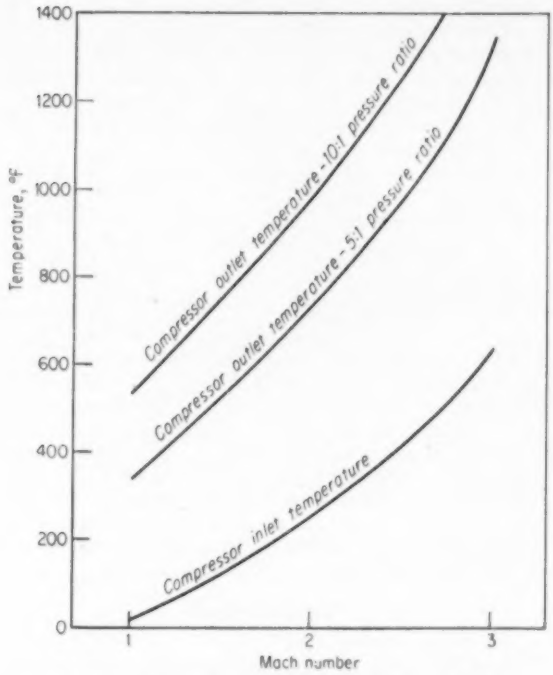

Fig. 4—Calculated values of compressor inlet and outlet temperatures at various air speeds at an altitude of 35,000 ft and an air temperature of —67°F show the combined effect of higher speed and high pressure ratio on compressor temperatures. Mach 1 is the speed of sound.

sible creep in the wheels should be in the range 0.1 pct to 0.2 pct per 1000 hr.

Compressor Materials

Table I gives the nominal composition* for commercially available materials now used in compressors. The temperature-stress relations for 0.1 pct and 0.2 pct creep per 1000 hr for these materials are plotted in Fig. 5. The ferritic or martensitic heat resistant steels fall into two classes, the low alloy and the 12 pct Cr or stainless types. The principal advantage of low alloy steels is their relatively low alloy content in relation to their high creep strength and their freedom from susceptibility to stress-corrosion cracking. The wide range of creep strength and ductility is attained by heat treatment.

The main disadvantage of the low alloy steels is their lack of corrosion resistance. Thus, if they are to be used in a compressor at high temperatures, they must be given surface protective treatment which must also be stable at the operating temperature. Under current investigation are ceramic coatings, plating, aluminizing, and heat resistant paints.

If very high allowable stresses in compressor wheels in the 1000° to 1100°F range are required, the iron base austenitic precipitation hardening alloys offer possibilities. This type of alloy is currently being applied for turbine wheels in air force jet engines and turbo-superchargers.

The ferritic steels are used extensively abroad in jet engine turbine wheels at rim temperatures up to 1100°F, but the rest of the wheel is much cooler. The encouraging results of active research on the modification of the ferritic steels by the addition of boron and titanium indicate that the level of high temperature strength given for these materials in Fig. 5 will soon be surpassed.

The 12 pct Cr or stainless type of creep resistant steels are modifications of Type 403 (which is now used in compressor blades and wheels) with additions of molybdenum, vanadium, tungsten, or columbium. They can be heat treated to approximately the same creep strength level as the low alloy steels by quenching and drawing. Their chief advantage over the low alloy steels is their higher corrosion resistance which obviates the difficult problem of surface protection. Their principal drawback is their susceptibility, at higher strength levels, to stress-corrosion cracking, which has now been observed in compressor blades by two engine manufacturers and has been definitely identified by the air force as the cause of at least two major accidents. In both instances the stress-corrosion cracks at the edges of the blades nucleated fatigue cracks which led to blade fracture and subsequent complete wreckage of compressor and engine. While the exact nature of the phenomenon is not well understood, it appears to be characteristic of Type 403 stainless steel and its modifications when they are tempered in the range 900° to 1050°F. Material heated over 1100°F appears to be free from this susceptibility, but unfortunately the fatigue strength of the steel tempered in this manner may fall too short of that required for the rather long blades in the type of compressor considered here.

Titanium alloys are a *natural* so far as compressor blades and wheels are concerned because of their

Table I. Nominal Composition of Available Compressor Materials, Pct

Material	C	Mn	Si	Cr	Mo	V	W
Low Alloy Steels							
17-22AV	0.30	0.70	0.60	1.3	0.50	0.85	—
H-40	0.30	0.50	0.30	3.0	0.50	0.85	0.50
12 Pct Cr Type							
Rex 448*	0.10	1.0	0.50	11.0	0.8	0.20	—
C-422	0.23	0.6	0.20	13.0	1.0	0.25	1.0
Iron Base Austenitic Precipitation Hardening Alloy							
A-286**	0.05	1.1	0.85	15.0	1.25	0.30	—
Titanium Alloys							
	Fe	Cr	Al	Mo			
Ti 155A	1.0	2.0	5.0	1.0			
3AL-5Cr	—	5.0	3.0	—			

* In addition contains 0.50 pct Cb.
** In addition contains 26.0 pct Ni.

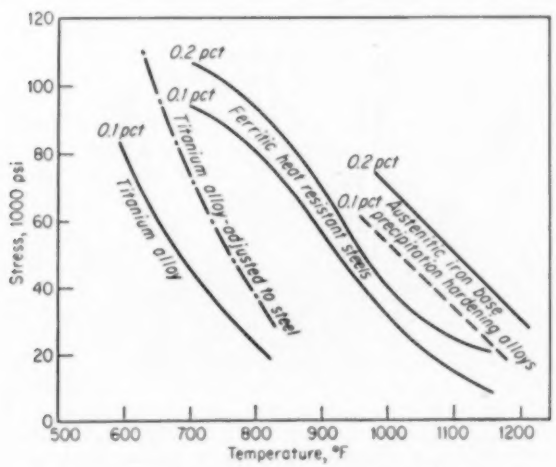

Fig. 5—Maximum stress for 0.1 pct and 0.2 pct creep in 1000 hr for commercially available materials used currently in jet engines.

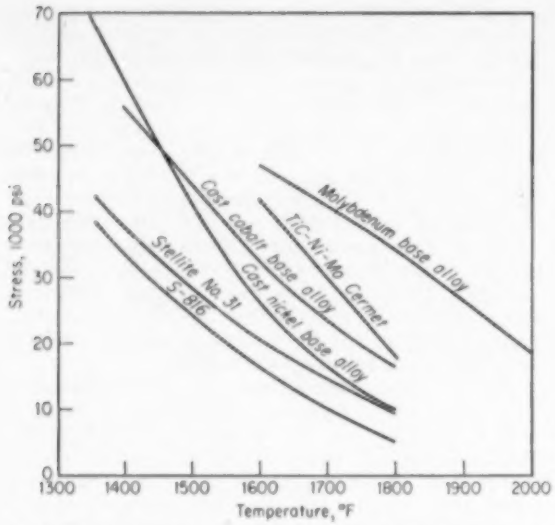

Fig. 6—A comparison of four experimental materials with S-816 and Stellite No. 31 now used in turbine buckets is presented on the basis of stress to rupture in 100 hr. The wrought molybdenum base alloy and the cermet have been adjusted to S-816.

high strength-to-weight advantage. Moreover, they are free from the stress-corrosion susceptibility of the 12 pct Cr steels, and the low corrosion resistance of the low alloy steels. As noted in Fig. 5, the commercially available titanium alloys lose their strength very rapidly above 700°F, but the encouraging results obtained on a 6 pct Al - 0.5 pct Si alloy, developed by the air force, indicate that this is only a temporary situation.

However, titanium alloys possess certain characteristics which may handicap their application, particularly for rather long compressor blades. One disadvantage is their low modulus of elasticity which is about half that of steel. This property, in conjunction with the rather long blades would be reflected in vibrational frequencies which are well within the operational range of the engine, thus posing a problem in resonant fatigue. The galling tendency of titanium may cause difficulties at the mating surfaces in the fastenings between the blade and the wheel since fatigue failures of steel blades by this mechanism have already been encountered. The titanium alloys are also characterized by a high degree of first stage creep which must be taken into consideration in using creep data for design purposes.

A possible application of titanium alloys, second in importance only to the compressor wheels and blades, is the compressor stator casing. In current engines, this part is made of a cast aluminum alloy, which in the high performance compressor, would be quite inadequate for the high temperature and pressure requirements. To meet the latter specifications would require that the part be made of steel. The present commercially available titanium alloys offer possibilities as a light weight substitute for the cooler portions of this component.

The most critical requirement in the high performance jet engine is in the compressor blades where high fatigue strength is needed to cope with the high vibrational stresses. This is brought about by the necessity for higher air flow and reduced drag in the compressor which in turn require rather long blades. The blades are also simultaneously subjected to creep stresses due to the centrifugal forces and the higher temperature. These requirements represent a drastic departure from those for current blades which are shorter (hence involve lower vibrational stresses) and are subject to steady (centrifugal) stresses at temperatures where no measurable creep takes place. The conventional creep, tensile, and fatigue data are no longer adequate for design purposes. Unfortunately there is no information at all on the combined effects of static and dynamic (vibratory) stresses (Goodman diagram) on creep or rupture strength of any of the materials available for compressor blades.

Concomitant with the need for fatigue strength is resistance to corrosion, for a rust pit can initiate a fatigue failure, and it requires the fracture of only one out of 2500 blades to produce severe damage, if not complete disaster. To reduce the possibility of such damage, the compressor blade material should also be free from notch sensitivity and have acceptable impact resistance in the range —75°F to the maximum compressor outlet temperature. Finally, it is very important that at the highest strength level at which the material is to be applied it should not be susceptible to stress-corrosion cracking.

Turbine Buckets

It can be readily shown that to obtain high performance in an engine having a high compressor outlet temperature, the turbine inlet temperature will also have to be high, probably at least 75° to 100°F higher than those in current engines in which, for appreciable bucket life, maximum temperatures do not exceed the 1550° to 1575°F range. To meet the requirements of higher turbine inlet temperatures there are two main approaches; air cooling, and improvement of solid buckets by development of materials having the required strength at the higher temperatures. While the former is beyond the scope of this discussion, it can be stated that it offers the possibility of very high turbine inlet temperatures (higher, in fact, than could be withstood by the strongest of the experimental heat resistant materials) with conventional alloys. Such a design, involving hollow wheels, would also save weight. Its principle disadvantages are the associated complications in designing to provide the hollow bucket with resistance to fatigue and assuring passage of cooling

Fig. 7—A comparison of the standard fir tree root with some experimental designs is shown. The essential feature of the experimental designs is that by avoiding the stress concentrations at the fir tree serrations, the strength of the attachment in relation to applied centrifugal load can be appreciably improved.

North American Aviation's F-100, the *Super Sabre*, is powered by Pratt & Whitney Aircraft's J-57 axial flow jet engine. It was the first combat plane designed to find an open door through the sound barrier.

air to the critical regions at the trailing and leading edges. Some efficiency is also sacrificed in bleeding the cooling air from the compressor.

Fig. 6 presents a comparison, on the basis of stress to rupture in 100 hr, of a casting and forging alloy in current turbine bucket application in a number of air force engines with four experimental materials which have acceptable strength at temperatures considerably above the 1550° to 1575°F range. The latter consist of a cast nickel base alloy, a cast cobalt base alloy, a wrought molybdenum base alloy and a nickel-bonded titanium carbide cermet alloyed with molybdenum. At present these constitute the leading possibilities for attaining high turbine inlet temperatures with solid buckets.

It will be noted in Fig. 6 that certain molybdenum alloys, even after correction for their density, have the highest rupture strength of all the materials that have been considered for high temperature turbine buckets. These molybdenum alloys, which are chiefly of the solid solution type, derive their strength by being worked below their very high recrystallization temperature. The application of this principle to jet engine materials has an excellent precedent in the hot-cold worked 16-25-6 alloy which has now been in continuous use in turbo-supercharger and jet engine wheels for 11 yr. The ductility of molybdenum alloys at temperatures below 400°F is very strain rate sensitive, and in a molybdenum alloy bucket this might constitute a problem in stress concentration at the root in the fastening or at any indentation in the air foil section as the engine is brought up to speed.

By far the most serious shortcoming of molybdenum and its alloys is the rapid rate at which they oxidize even at moderately elevated temperatures. While considerable progress has been made in the development of ceramic and metallic protective coatings, each having its particular advantages and disadvantages, to date there is no reliable surface treatment or coating which will consistently stand up under conditions of jet engine operation including possible impact by foreign bodies. For this reason molybdenum alloys must be ruled out, at least for the present, as a means of attaining high turbine inlet temperature.

In addition to the high strength indicated in Fig. 6, the nickel bonded titanium carbide cermets (and their modifications with molybdenum, columbium, and tantalum) are light (requiring thinner wheel rims to which they are fastened) and have acceptable resistance to thermal shock and oxidation. They also represent a lower investment in critical metals than any other bucket alloy. Their disadvantages are very low ductility and low impact strength. The former is a major handicap, particularly at the root section where the possibility of stress-concentration is highest. The latter, low impact strength, is the most serious limiting factor in the application of the cermets for buckets. In current jet engines, impact by fragments of liners and broken buckets generally produces deformation or indentation of the operating buckets, which will nevertheless continue to operate. However, experience with jet engine rotors, fitted either partially or entirely with cermet buckets, has shown that failure of any one part invariably results in destruction of most of the cermet buckets. This is further aggravated by the fact that there is no nondestructive method of inspecting cermets.

The effort to develop and establish the metal bonded carbides as a turbine bucket material has taken two main directions, increasing ductility and suitable design. Since a cermet combines the high hot strength of the brittle carbide with the ductility of the metal, some ductility can be gained by compromising in favor of the metal bond at the sacrifice of some high temperature strength. Further modifications of composition, improved techniques in compacting, and increased metal content in the root are also being investigated. However, to the main problem of impact brittleness at temperature, there appears to be no immediate solution.

The other approach to the low ductility problem has been to circumvent or reduce the requirement for ductility in the bucket material by modification of the current fir tree root as shown in Fig. 7. This effort has been very fruitful for it has developed concepts of root design which, as applied to certain alloys, now constitutes the most promising means of attaining the immediate goal. In this connection, the excellent work of the National Advisory Committee for Aeronautics should be cited. Fig. 7 presents a comparison of the standard fir tree root with some experimental designs proposed for cermet buckets. The essential feature of the latter is that by avoiding the stress concentrations at the fir tree serrations,

the strength of the attachment, in relation to the applied centrifugal load, can be appreciably enhanced. The strength of the attachment can be further effectively increased by partially compensating for the lack of ductility in the cermet through the insertion of ductile shims or retaining pins of metal at the mating surfaces either of which provides for a better load distribution.

Casting Alloys

Fig. 6 compares the materials mentioned previously with a cast cobalt and a cast nickel base alloy. These two are representative of a group of casting alloys which are characterized by higher rupture strength than the current materials shown in Fig. 6 but with low ductility (3 pct or less) at room and intermediate temperatures. However, at elevated temperatures (1500°F or higher) their ductility is quite adequate, and thus under engine operating conditions it is not expected that they would have low impact resistance. Because of their low ductility at the lower temperatures, these alloys have hitherto received relatively little attention, particularly as the more ductile forging and casting alloys have been giving adequate performance at current operating temperatures. In view of the inadequacies of the molybdenum alloys and the carbide cermets, it appears desirable to review the properties of these cast cobalt and nickel base alloys, particularly in the light of the fruitful research which has been carried out on root design and ductility requirements and to extend those findings to these alloys.

Such considerations strongly indicate that the application of the low ductility cast cobalt and nickel base alloys to a bucket provided with a root having a minimum of stress concentrations and cushioned in its fastening by a shim of ductile metal can extend turbine inlet temperature to an appreciably higher level. Such buckets would be free from the impact brittleness of the cermets and the low oxidation resistance of the molybdenum alloys.

Progress Reviewed

Table II lists chronologically the alloys[4] used in aircraft turbines since 1918, the year of the first turbo-supercharger, and the approximate temperature for rupture at 100 hr at 20,000 psi. The first three materials, through 1933 as shown in Table III, were respectively a chromium-vanadium spring, intake valve, and exhaust valve steels.

It will be noted in Table II that the progress attained in the first 24 yr (as measured by the increase in temperature for the indicated conditions of time and stress) is more than matched by that accomplished in the short time comprising the war and the first few postwar years. The corresponding temperatures for the group of experimental materials indicates that this rate of development can be maintained or even surpassed, but unfortunately what the tabulations do not show is that between this group and the other materials there is a broad gap, involving the philosophy of the relations between design and metallurgy, and that if this is not overcome, only a small part of the indicated potential progress will be realized.

The alloys indicated in the first group of Table II (1918 to 1948) were accepted by the designer because they fitted into his framework of design concepts. Since it has been possible to meet his demands for various combinations of mechanical and other properties by developing new compositions or by modifying existing ones, the basis for his requirements has seldom been challenged. It is, therefore, natural that he became conservative in his requirements for certain properties in the consciousness that the metallurgist would always meet them and looked with distrust and suspicion on any new material which fell short of his demand, regardless of how attractive its functional or operational properties might appear.

The end for this state of affairs lies between the two groups of materials in Table II. The designer must recognize that the very high temperature materials are endowed by nature with certain limitations. He must base his design on the properties of these materials taking into consideration their natural limitations as well as their high temperature strength. As he gains experience and skill in dealing with such materials and becomes thoroughly familiar with their behavior and their level of properties, he will gain more confidence in them provided that the metallurgist does his best to assure that the level of properties is consistent and uniform. Only through such cooperation can the full potential of these materials for high performance engines be realized.

Table II. Chronological List of Materials Used in Aircraft Turbines and Temperature for Rupture in 100 Hr at 20,000 psi

Date of Use	Material	Temperature	Use
1918 to 1922	SAE 6150	1050°F	Turbo-supercharger
1922 to 1928	Silchrome No. 1	1100°F	
1928 to 1933	KE 965	1225°F	
1933 to 1942	17W	1300°F	
1942	Stellite No. 21	1525°F	
1946	S-816	1550°F	Jet Engines
1948	Stellite No. 31	1600°F	
	Cast Ni-base	1650°F	Experimental
	Cast Co-base	1740°F	
	TiC-Ni-Mo-Cermet	1780°F	
	Molybdenum-Base Alloy	1970°F	

Table III. Nominal Composition of Turbine Bucket Materials, Pct

Material	C	Mn	Si	Ni	Cr	Co	Mo	W	V	Cb
SAE 6150	0.45	—	—	—	1.0	—	—	—	0.25	—
Silchrome No. 1	0.45	—	3.0	—	9.0	—	—	—	—	—
KE 965	0.45	0.60	0.60	14.0	14.0	—	—	2.5	—	—
17W	0.45	0.60	0.60	19.0	14.0	19.0	—	2.5	—	—
Stellite No. 21	0.20	—	—	2.0	27.0	64.8	6.0	—	—	—
S-816	0.40	—	—	20.0	20.0	43.0	4.0	4.0	—	4.0
Stellite No. 31	0.40	0.60	0.70	10.0	25.0	56.3	—	7.0	—	—

References

[1] S. L. Bragg: Influence of Operating Temperature on the Design and Performance of Gas Turbines. *Iron and Steel Institute Report No. 43* (1951) London, p. 23.

[2] R. V. Hensley, N. D. Sanders, and R. P. Krebs: Performance of the Turbojet Engine. Preprint No. 148. Institute of Aeronautical Sciences.

[3] Resume on High-Temperature Investigation Conducted During 1951-52. Timken Roller Bearing Co. Canton, Ohio.

[4] The 1943 Supercharger Symposium Lecture Book. General Electric Co. Riverworks, West Lynn, Mass. p. 68.

Titanium Alloys Give Promise Of High Temperature Applications

by F. A. Crossley and H. D. Kessler

INTEREST in titanium base alloys for elevated temperature use is based upon the belief that they can be substituted for steels and aluminum alloys to gain significant savings in weight. The application for which the greatest effort in titanium alloy development is being directed is that of jet engine components. It is in this area that weight reduction is especially important and even mandatory for aerial superiority. A pound saved in the engine means additional pounds saved in supporting members.

Requirements for jet engine components place most severe demands on properties of alloys for elevated temperature application. While selection of materials for use in jet engines is based primarily on elevated temperature properties, properties at normal and low temperatures are also of importance. Because military aircraft must be designed to operate in all climates, parts must have the ability to withstand stress conditions imposed at normal and subnormal temperatures. The properties most important at these lower temperatures are ductility and impact strength. It is generally required that compressor blade materials have a minimum of 10 pct tensile elongation at room temperature.

Elevated temperature properties which must be evaluated for alloys in jet engines are: A—Stress-rupture strength, B—resistance to creep, C—resistance to corrosion by jet engine gaseous environments, and D—fatigue strength. Because of the allotropic nature of titanium, three distinct types of alloys can be produced—the alpha, beta, and alpha-beta alloys. Single-phase alloys such as the alpha or beta alloys offer considerable advantage for use at elevated temperatures from the standpoint of stability at high temperatures. On the other hand the alpha-beta alloys, although they may not be stable at the high temperatures, may actually be more creep resistant if precipitation occurs at a low enough rate.

Rather than detail the complex story of the alloy development program in progress at the Armour Research Foundation, several of the better experimental alloys representing the various types have been selected for comparison with several of the more prominent commercial titanium base alloys. The various points of comparison among the three types of alloys to be brought out will cover the short-time tensile properties, creep and stress-rupture properties, and structural stability.

F. A. CROSSLEY and H. D. KESSLER are Research Metallurgist and Supervisor of Nonferrous Metallurgy, respectively, Armour Research Foundation, Chicago. This article is an abstract of a paper presented at the AIME Institute of Metals Div. meeting, Cleveland, Oct. 21 to 23, 1953.

Short-Time Tensile Properties

The data in Table I indicate that two alloys do not have a room temperature tensile elongation of at least 10 pct desired for compressor blade applications. These are MST 3Al-5Cr and Ti-8Al-4Mo. There is little question that the former or Mallory alloy, if properly heat treated and with the proper adjustment of interstitially soluble elements, could be brought within the required tensile ductility range. However, it would be quite difficult to achieve a consistent 10 pct or better elongation in the Ti-8Al-4Mo alloy. Armour's alloy development program has shown that, although aluminum additions to binary or more complex titanium alloys greatly improve the elevated temperature properties, aluminum contents in the range of 8 pct result in low ductility at room temperature.

The elevated temperature tensile properties of the various alloys are shown in Fig. 1. Of the commercial alloys, only the MST 3Al-5Cr was included in this comparison. Data presently available show that the MST 3Al-5Cr has tensile and yield strengths

Table I. Room Temperature Tensile Properties of Titanium Base Alloys

Alloy	Type	Heat Treatment	Ultimate Tensile Strength Psi	Yield Strength (0.2 Pct Offset) Psi	Elongation* Pct	Source of Data
Ti-6Al	α	1200°F-1 hr-AC	121,000	110,000	15	Armour
Ti-6Al-0.5Si	α— complex	1110°F-24 hr-AC	153,000	140,000	12	Armour
		1560°F-3 hr-AC	147,000	128,000	19	Armour
Ti-150A	$\alpha + \beta$	—	150,000	120,000	12**	Titanium Metals Corp.[1]
RC-130B	$\alpha + \beta$	—	145,000	135,000	16 (2 in.)	Rem-Cru[2]
Ti-8Al-4Mo	$\alpha + \beta$	As-forged	170,000	140,000	8	Armour
MST 3Al-5Cr	$\alpha + \beta$	Hot forged 97 pct	170,000	160,000	5 (2 in.)	Mallory-Sharon[3]
Ti-30Mo	β	As-forged	131,000	130,000	16	Armour

* In 1-in. gage length unless otherwise specified.
** Minimum specification.

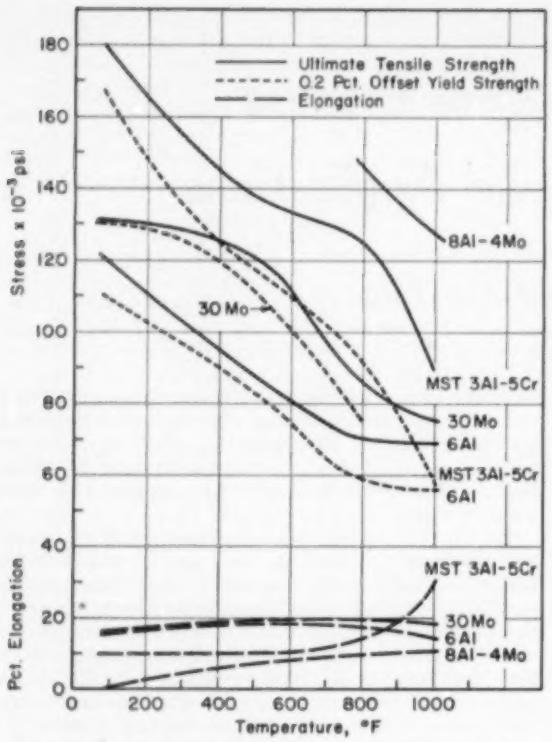

Fig. 1—The elevated temperature tensile properties of various titanium base alloys are compared.

superior to those of other commercial alloys at all temperatures up to 1000°F. It may be noted that at 800°F the beta alloy Ti-30Mo has better tensile properties than the alpha alloy Ti-6Al. However, the beta alloy has roughly 20 pct greater density than the alpha alloy and consequently must be 20 pct stronger to be equivalent on a strength-weight basis. Also noteworthy is the high ultimate tensile strength of the Ti-8Al-Mo alloy at elevated temperatures. These data were obtained for the alloy as annealed at 1290°F for 24 hr. This heat treatment rendered the alloy brittle at room temperature as compared to 8 pct elongation obtained for the alloy in the as-forged condition as shown in Table I.

Creep and Stress-Rupture Properties

The properties of most importance in the evaluation of alloys for use in jet engine components are creep and stress-rupture strengths. Fig. 2 illustrates the superior creep resistance of commercially pure titanium, RC 70, at 400° and 600°F when compared on a strength-weight basis to two representative high strength aluminum base alloys.

Table II compares stress-rupture data for four experimental alloys studied at the Armour Research Foundation, two commercial alloys, and Type 410 (12.5 pct Cr) stainless steel. At 800°F the alloys, except Ti-150A, have excellent 1000-hr rupture strength and compare very favorably with the stainless steel. On the basis of 1000-hr rupture strength at 800°F, the three strongest alloys are ranked in the order: A—Ti-8Al-4Mo, B—Ti-30Mo, and C—Ti-6Al-0.5Si. At 1020°F, Ti-150A and MST 3Al-5Cr, both alpha-beta alloys, fail to compare favorably with Type 410 in stress-rupture strength. The significance of these data are better illustrated in Fig. 3. This figure shows that on a strength-weight basis titanium alloys offer a definite advantage over the stainless steel at 1020°F.

Creep data on titanium base alloys for temperatures of 800° and 1000°F are not complete enough to make a detailed comparison with Type 410 stainless steel. However, some observations based on Armour's researches can be reported. Of the alloys compared in Table II, the beta alloy Ti-30Mo is the most creep resistant at 800°F. The alpha-complex alloy Ti-6Al-0.5Si ranks closely behind followed by the alpha-beta alloy Ti-8Al-4Mo. This order is contrary to that observed for 1000-hr rupture strength at 800°F and indicates that stress-rupture data cannot be relied upon to show the relative merit of alloys when the differences in their rupture strengths is not great. On the basis of creep resistance, Ti-30Mo, Ti-6Al-0.5Si, and Ti-8Al-4Mo alloys offer considerable advantage over the stainless steel at 800°F. At 1000°F, the Ti-8Al-4Mo definitely and the Ti-6Al-0.5Si probably offer advantage over Type 410 stainless steel.

Structural Stability

Stability is especially important if the requirement of 10 pct minimum room temperature tensile elongation is expected to be maintained throughout service life. Indications are that titanium base alloys after proper heat treatment when exposed to elevated temperatures for long periods, but not under stress, are quite stable. However, exposure under stress may cause structural changes. For example, observation of the microstructure of the so-called *stable* beta Ti-30Mo alloy after over 900 hr exposure at a stress of 75,000 psi at 800°F indicates a fine dispersion of alpha throughout the structure. The specimen failed in a brittle manner while it was being extracted from the creep testing machine. Although this *stable* beta alloy was ductile prior to testing, it became extremely brittle while stressed at 800°F. It would seem that more than

Table II. Stress-Rupture Data for Titanium Base Alloys

Alloy	Type	Heat Treatment	Stress at 800°F for Rupture			Stress at 1020°F* for Rupture			Source of Data
			100 Hr	500 Hr	1000 Hr	100 Hr	500 Hr	1000 Hr	
6Al	α	1200°F-1 hr-AC	79,000	77,000	76,000	32,000	26,000**	24,000**	Armour
6Al-0.5Si	α-complex	1560°F-3 hr-AC	—	—	85,000†	40,000	34,000	28,000**	Armour
30 Mo	Stable β	1200°F-1 hr-AC	—	—	95,000†	38,000	26,000	22,000**	Armour
8Al-4Mo	$\alpha + \beta$	—	105,000	104,000	103,000**	56,000	44,000	40,000**	Armour
Ti-150A	$\alpha + \beta$	—	42,000	35,000	33,000†	12,000	10,000	8,400**	TMC[1]
MST 3Al-5Cr	$\alpha + \beta$	1830°F-1 hr-FC-1200°F-24 hr-AC	—	—	80,000†	38,000	19,300**	12,000**	Armour
Type 410	Stainless Steel	1830°F-½ hr-AC-1200°F-1 hr-AC	70,000	61,000	58,000	30,000	26,000	24,000	Armour††

* Ti-150A data taken at 1000°F. ** Extrapolated data. † Estimated from limited data.
†† These data give higher values than those reported by US Steel Corp. for this alloy.

30 pct molybdenum would be required to prevent alpha precipitation and consequent embrittlement at 800°F or lower. Unfortunately, all beta stabilizing elements are heavier than titanium so that very large additions to produce truly stable alloys would seriously reduce the weight saving advantage of titanium. For this reason it appears that truly stable beta alloys do not offer much promise of being useful for elevated temperature applications.

All the commercial alpha-beta alloys contain additions which form a binary eutectoid system with titanium. The tensile and yield strength vs temperature plots for MST 3Al-5Cr in Fig. 1 and the log rupture strength vs log time plots in Fig. 3 at 1020°F indicate that eutectoid decomposition occurs in this alloy in a fairly short time under stress. Time-temperature-transformation studies on a similar composition, Ti-8Al-4Cr, alloy showed the initiation of eutectoid decomposition in about 20 hr at 930°F. There are indications that Ti-150A and RC 130B decomposed eutectoidally when exposed to elevated temperatures under stress.

The Ti-8Al-4Mo alloy does not decompose eutectoidally as neither aluminum nor molybdenum are eutectoid formers. However, there is microscopic evidence that the beta phase precipitates alpha at temperatures for application. It is believed that this is the reason for the difference in room temperature ductility in the as-forged and annealed conditions. As-forged, this alloy shows 8 pct tensile elongation against 0 pct annealed at 1290°F for 24 hr.

Summary

There is little doubt that the titanium base alloys will be applied with success up to 1000°F for exposures of approximately 1000 hr. At least one ductile experimental alloy, Ti-6Al-0.5Si, has greatly superior creep resistance and rupture strength compared to Type 410 stainless steel at 800°F. At least one experimental alloy, Ti-8Al-4Mo, is greatly superior in creep rupture and in creep resistance to Type 410 at 1000°F. This last named alloy is not ductile. However, by modification of composition some of the strength could be sacrificed to give a ductile alloy which could be applied with advantage at 1000°F. To go beyond this temperature two barriers must be crossed. The first of these is adequate creep resistance; the second is improved corrosion resistance. Raising the temperature limit of application of titanium base alloys could be made considerably less difficult if designers could learn to use an alloy having something less than 10 pct tensile elongation at room temperature. If the alloys must have high room temperature ductility after exposure to stress and heat, then the alloy development work should be directed away from the alpha-beta toward the alpha type, particularly toward the precipitation hardenable alpha-complex alloys.

The so-called *stable* beta alloys do not offer much promise for elevated temperature applications because extremely large additions of the heavy beta stabilizing elements are required to produce alloys truly stable under stress at elevated temperatures.

Aluminum additions to alpha alloys or to alpha-beta alloys seem to confer the best elevated temperature strength properties. Alloys for service above 800°F should contain in the range of from 6 to 8 pct Al. However, the aluminum content must be kept at the lowest possible level to obtain sufficient room temperature ductility. One of the desirable properties of the alpha alloys, unlike the alpha-beta alloys, is that they are ductile as welded and require no post welding heat treatment.

Although little information is available at the present time on the elevated temperature corrosion resistance of titanium alloys, preliminary work at Armour indicates that aluminum additions reduce the corrosion rate in air at intermediate temperature levels. Diffusion or alloying of the interstitially soluble elements oxygen and nitrogen and resulting embrittlement is of greater importance than scaling at temperatures of 900° to 1300°F. There is a definite need for information on the influence of alloying elements on elevated temperature corrosion resistance of titanium.

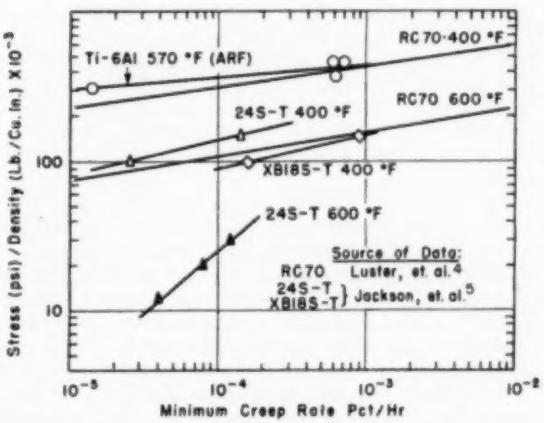

Fig. 2—Creep rate comparison on a strength-weight basis is shown between commercially pure titanium, RC 70, and two representative high strength aluminum base alloys.

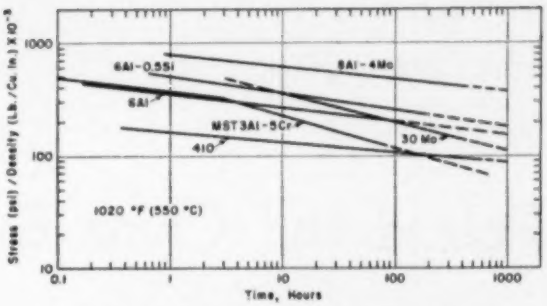

Fig. 3—Stress-rupture comparison of titanium base alloys with Type 410 stainless steel indicates that on a strength-weight basis titanium alloys offer a definite advantage.

References

[1] *Handbook on Titanium Metal.* 5th Ed. (1952) Titanium Metals Corp. of America. New York.

[2] *Rem-Cru Titanium And Titanium Alloys.* 2nd Ed. (1952) Rem-Cru Titanium, Inc. Midland, Pa.

[3] *Properties of Titanium and Titanium Alloys.* (1953) Mallory-Sharon Titanium Corp. Niles, Ohio.

[4] D. R. Luster, W. W. Wentz, and D. W. Kaufman: Creep Properties of Titanium. *Materials and Methods* (June 1953) **37**, p. 100.

[5] L. R. Jackson, H. C. Cross, J. M. Berry: Tensile, Fatigue and Creep Rupture Properties of Forged Aluminum Alloys at Temperatures up to 800°F. Tech. Note 1469 (March 1948) National Advisory Committee for Aeronautics.

Iron Curtain Report—

Poland and China Expand Steel Capacities

Poland's Steel Industry Destined for Russian Dependency

WITHIN Poland's present borders, the two districts of Silesia and Dabrowa remain her most important steel-making area. Most of the present day steelworks of Silesia and the Bankowa plant in Dabrowa were established in the first half of the last century. Other plants came into being in Dabrowa in the 1880's and 1890's as a result of political and economic pressure by neighboring states. There are, however, three plants in the Radom-Kielce district, one of which, at Ostrowiec, was built in the latter part of the last century with French capital.

The absorption by Poland of German Upper and Lower Silesia after the war gave her the steel plants at Bobrek, Stalin (Laband), Gliwice, Ozimek (Malapana), Andreaj, and Zabrze (Hindenburg). Poland also acquired the coke ovens and blast furnaces at Stettin (Szczecin). This new area of postwar Poland soon became dominated by Russian influence, and reconstruction was planned on the Soviet model. Public ownership of large scale industry became effective during 1946, followed by a more gradual process of nationalization of smaller concerns and of trade during the Three-Year Plan of 1947 to 1949.

By the time the Six-Year Plan of 1950 to 1955 was introduced, the integration of industry on Soviet lines had been completed. Publication of statistics had been progressively reduced, and the changing of place-names made comparison with the area of prewar Poland very difficult. Under the latest plan, Poland is in the process of building two completely new steel works at Czestochowa and Nowa Huta, near Kraków, each with an annual capacity of over 1 million metric tons, while a new special steel plant is under construction in the Warsaw area.

New Iron and Steel Plants

Nowa Huta is now the magic word in Poland, and news of development of the new town and steelworks is continually being brought before the public. Up to 1949, the site of the present constructional activity was simply green fields; now it has already some 35,000 inhabitants and is proclaimed as the first Polish socialist town. The whole town is built around a steelworks which, when completed, will produce more steel than did the whole of Poland in 1937. Under the present plan, the town will eventually house 120,000 people, and nationwide propaganda took the line that is was "an essential and urgent task for the National Front to unite the nation around the building of Nowa Huta." The siting of the town is some 50 miles to the east of Poland's main coal deposits and it covers a 6-mile arc along the bank of the River Vistula. The river port, which will be of paramount importance to the steelworks, is already almost complete. Finished products from the plant will be sent by river to Warsaw and Gdynia, while ultimately the major part of Nowa Huta's ore supplies will come by river barge from the Russian Krivoi Rog ore field via the Dnieper-Bug-Vistula waterway.

The equipment scheduled for the plant includes four blast furnaces each of 800 metric tons daily output, ten open hearth furnaces with combined annual output of 1½ million metric tons, and rolling mill capacity of 1 million metric tons a year including structural steel, plates, and sheets. The initial stage of the plan aims at completing only half the proposed coke oven plant, two blast furnaces, and about half the open hearth furnaces, as well as the blooming mill and sheet mill. Production at Nowa Huta was expected to begin before the end of 1953, but the works may not be fully completed even by the end of the Six-Year Plan in 1955. Another plant which is under construction is the Warsaw Special Steel Works. Situated on the left bank of the Vistula, it is to be the largest special steel works in Poland.

Scheduled for expansion under the Six-Year Plan is the Stalin Works (previously known as the Laband Works), which has steel melting shops and rolling mills. This plant, situated some few miles to the northwest of Gliwice, was not very large in prewar days, although some modern equipment had been installed between the years 1936 and 1938, but during the war the Germans expanded it considerably for war purposes. In 1946, the Russians took much of the equipment as reparations, although later reports indicate that it was reinstalled. One of the largest Polish works is the ex-German plant at Bobrek. This was also subjected to

These articles were abstracted from the *Iron & Coal Trades Review*, Vol. 167, Nov. 27 and Dec. 11, 1953, London.

Russian demands for reparations, but again most of the dismantled equipment was later returned.

Development Plans

In steelmaking, the emphasis is upon building large units. The new open hearth furnaces at Czestochowa appear to have a productive capacity of some 110 to 140 metric tons per heat, while it has recently been announced that the Nowa Huta shop will have furnaces of 185 and 370 metric tons capacity. The pig iron charge in steelmaking is planned to increase to 75 pct so as to relieve the present acute shortage of scrap. This compares with a figure of under 55 pct in 1949. Targets in 1955 under the Six-Year Plan are as follows: Coal—100,000,000; coke—12,800,000; iron ore—3,000,000; pig iron—3,500,000; steel ingots—4,600,000; and rolled products—3,200,000 metric tons.

The 1955 prospects for Poland in steel seem to depend on her ability to obtain Swedish ore by offering coal cheaper than other European producers. But in the long run she will probably become more dependent on Russian ore, especially in view of the intention to build a second iron and steel plant at Nowa Huta of similar capacity to the one already under construction. The second Nowa Huta plant, also requiring Krivoi Rog ore, would make a Bug canalization scheme almost a necessity, and it would result in the Polish industry becoming almost entirely dependent on Russian ore. Ultimately, almost the entire Polish economy and prosperity would thus be controlled by Moscow.

Red China Strives For Increased Steel Production

COMMUNIST China's massive exhibition pavilion at the 1953 Leipzig Fair in eastern Germany afforded the opportunity to see products and learn of present conditions in the Chinese mineral industries. It was estimated that crude steel production would be approximately 3 million metric tons in 1953, nearly twice the 1943 record. Coal output, however, is only now reaching the pre-Communist peak. This was 54 million metric tons for the entire country (excluding Formosa) in 1943, and 25 million metric tons in Manchuria alone. Pig iron production was thought to have exceeded the wartime maximum of some 2.5 million metric tons.

Official Chinese sources have claimed that production increases in 1952 were 40 pct for pig iron, coal 29 pct, crude steel 40 pct, and rolled steel 49 pct over 1951. By the end of 1953, the first year of the Five-Year Plan, which concentrates on building up heavy industry, pig iron output was planned to rise 13 pct, ingot steel 22 pct, and rolled steel 35 pct.

All the main iron works in China were said to be making top quality basic pig iron for steel production. According to one government report, basic pig iron in 1952 accounted for 90 pct of the pig iron output at Anshan, China's principal steel center. Low grade iron ore was stated to be used extensively there, and the production of basic pig from sintered ore was described as one of the outstanding achievements of the iron and steel industry.

Manchurian Industry

Northeast China (Manchuria) continues to be the country's major industrial base with construction and investment priorities going to Anshan. The integrated iron and steel works there was built by the Japanese with German assistance. At its peak during the war it had a huge coke oven plant in operation, nine blast furnaces with individual daily outputs varying from 350 to 700 metric tons, steel furnaces with an annual output of 1.3 million tons, and rolling mills. Anshan was largely destroyed in the final weeks of the world war and the subsequent civil war and partly dismantled by the USSR, but it is now being rebuilt and expanded. This work was pushed ahead last winter despite an average temperature of 0°F.

Largest projects at Anshan have been the construction of several blast furnaces and the erection of new rolling mills and a seamless tube mill. The Chinese maintain that much of the equipment for these installations was provided by Russia, and that Soviet engineers and technicians have assisted greatly in the work in everything from original designs to training and advising the workers.

Seventy-five miles northeast of Fushun, expansion of China's principal coal center is being pressed. The open pit mine is believed to be the largest of its kind and to have the thickest seams of bituminous coal in the world. Seam depth averages 130 ft but extraction in the past was largely by hand. One open pit mine has now been mechanized and several vertical shafts opened up. A plant for producing high grade carbon black has also been established. The Fushun steelworks is said to be producing 13 kinds of stainless, heat resisting, and high speed steels while local factories are making mining machinery according to Russian designs.

Second Industrial Area

After the Northeast, Taiyuan in Shansi province is China's number two industrial base. The iron and steel works is being modernized, and a new sheet mill, forge shop, and electric furnace dept. have recently been installed. Products are chromium, stainless, and silicon sheet steel.

At the allied heavy engineering plant, machinery is now going in for the manufacture of rolling mills, coke ovens, and other metallurgical equipment, as well as large traveling cranes. Facilities are to be expanded by the construction of a new foundry, steelmelting shop, and gas plant.

At Tientsin, the integrated iron and steel works is now turning out rods and wire, and a machine-tool plant covering 20 acres started production at the beginning of the year. Mechanization of the Tatung colliery, North China's richest coalfield, has begun, and three abandoned pits with seams up to 65 ft thick are to be restored. The Tangshan steel plant claims to be converting its acid Bessemer process to basic Bessemer with more pig and less scrap being used for the production of rails and plates.

Production program at Shanghai steel mills is reported to include light rails, structural steel, railway wheels, *Alnico*, and rimmed, tool, and high manganese steels. While Shanghai has been dependent until recently on the distant Northeast area for most of its pig iron supplies, pig smelted from local ore at the nearby Maanshan iron works is now becoming available. Two renovated blast furnaces started operation last autumn, and the first pig iron was delivered to Shanghai on Oct. 27, 1953. By the end of 1953 it was hoped, with the restoration of five more blast furnaces at Maanshan, that all of Shanghai's needs could be met from this source.

Hankow has become the hub of the industrial area in Central China. The integrated iron and steel works, now being renovated and expanded, is linked by river and rail with the Pinghsiang coal mines and Tayeh ore fields. The Tayeh metallurgical plant itself now includes Bessemer converters, electric furnaces, and rolling mills.

In the Southwest, the Chungking steel mills accounted for most of the rails used in the recently completed line from that city to Chengtu and is said to be China's largest producer of rails. Other factories there are making rock drills, mining machinery, steel cables, and machine tools.

Northwest China

A new industrial base in the remote Northwest area is taking shape in Singkiang province with an iron and steel mill and several machinery factories already operating in Tihwa. The railway line from the China coast has now reached Lanchow, and there are grandiose plans for extending it 2000 miles further inland through Yumen to Tihwa, and then on to the trans-Siberian line in Soviet Asia.

Extensive mineral prospecting is being undertaken throughout the country. In the Northwest, the Reds claim that rich deposits of coal, iron, and copper ore, as well as zinc, manganese, tungsten, beryllium, and bismuth have been discovered. Prospecting in Yunnan, the principal tin mining province, is being intensified. Preliminary drilling is reported to have begun this year at a large coalfield discovered in the Pinghsiang area. In the Tayeh iron region, proved ore reserves are stated to have been greatly extended, and deposits of magnetic iron ore and manganese found there. Estimates of coal reserves in the Northeast have been multiplied by ten as a result of geological surveys conducted during the past few years, and further iron ore deposits have been discovered north of Peking.

Training

China's industrial ambitions run far ahead of the present supply of skilled personnel, although many Chinese have received training in Russia. A group of steel workers recently completed a year's apprenticeship at the Novotagil mills in the Urals, returning to Anchan, which has become the main training center for the iron and steel industry. Full time courses in engineering established there are expected to turn out 35,000 skilled technicians and workers during the next five years. In addition, part-time courses at the technical university as well as evening classes have been established.

Similar training facilities are being created in Chungking where the existing educational system is being reorganized with a strong shift in emphasis to technical subjects. New schools include those for the iron and steel industry, geology, coal mining, highway and building construction, and communication. In Taiyuan, Peking, Dairen, Port Arthur, and other industrial centers, top priority has been given to courses in metallurgy, mechanical and civil engineering, geology, mining, and communications.

The Five-Year Plan

China's Five-Year Plan, entered upon in 1953, calls for reaching industrial levels, which, it is claimed, took western countries 30 to 50 years to attain. The tempo of development will be particularly severe in the iron, steel, and nonferrous industries, machine-building, coal mining, petroleum, electric power, and defense.

China's National Day in October 1953 was the occasion for a flood of speeches, official communiques, and special articles in which past accomplishments and future prospects were reviewed. One document, dealing in part with scientific achievements, stated that, "notable work has been done in research into the production and methods of use of nodular graphite cast iron; the experimental manufacture of hard alloys; heat treatment of *Alnico;* the dressing of poor ores of iron and manganese, molybdenum sands, and graphite. . . . Thanks to the scientists, 64 pct of the tremendous deposits of inferior iron ores in the Northeast can now be extracted. This is done by introducing a wet dressing method, i.e. by mixing fatty acids derived from soy beans with soft water, and is found to be even better than the more costly method of magnetic dressing."

Developments in 1952

At the same time, the State Statistical Bureau, in its survey of developments during 1952, reported, "Branches of State owned industry still had many defects in their rehabilitation and development. Many enterprises had not established perfect production planning, and management systems and responsibility systems were not able to carry on production systematically in accordance with their plans.

"In the production of some products consideration was still not given to the balance between production and distribution, so that some were in short supply while others were not kept in stock. The potential of production in many enterprises had not been fully utilized; their equipment was not fully used; the accumulation of stocks of material and liquid funds was still common, and business accounting was not sufficiently established among many enterprises.

"The cost of production in some enterprises was too high and there was a tendency to neglect quality for quantity, the ratio of second-rate and defective products was high, and reduction in costs of production and the rise in the quality of the products did not keep pace with the increasing demands of economic construction."

Sources of Inclusions From Pouring Refractories Investigated

by M. P. Fedock

IN any investigation of inclusions in basic electric melted steel, the pouring refractories—ladle brick, sleeves, nozzles and fireclay mortar—are the most fertile sources of inclusion material. It is generally assumed that inclusions from these sources are the result of mechanical erosion and that a *clean* ladle is one that has no loose or projecting accumulations of fireclay patching material or slag which may be easily eroded. It is acknowledged that mechanical erosion can and does contribute to refractory inclusion material found in ingots. However, the source of such mechanically eroded material has not been definitely established.

Recent studies have shown that in addition to simple fusion, spalling, and mechanical erosion of the refractories, metal-refractories reactions also occur. The products of such reaction are fluid MnO-Al_2O_3-silicates which can contribute serious amounts of inclusion material to the steel. McCance,[1] Rait[2] and Post and Luerssen[3] have stressed particularly the important role of manganese or the manganese-silicon ratio on the cleanliness of steels. Rait concluded that for bottom cast acid open hearth steels of a constant manganese-silicon ratio, an aluminous refractory is less eroded, and thus contributes fewer troublesome inclusions than does a more siliceous refractory. He concluded that aluminous pouring refractories are required for minimizing refractory inclusions in steel. Post and Luerssen have likewise drawn attention to the highly significant reactions between basic electric melted steel and pouring refractories and consequent large rejections of steel caused by inclusions if the manganese-silicon ratio is large. Their solution to the problem was to suggest changes in the steel composition, within metallurgical limits, to a lower manganese-silicon ratio. These authors presumably based all their conclusions on observations made when using conventional, siliceous, bloating-type, pouring refractories.

In the course of an investigation of inclusions occurring in 52100 steel intended for bearing applications, close examination was made of the amount and pattern of pouring refractory erosion, various scums produced, and characteristic inclusion material. Sufficient data was obtained to question the generally held impression of what constitutes a clean ladle and the area in the ladle from which inclusion material originates.

M. P. FEDOCK is a Ceramic Engineer, Republic Steel Corp., Canton, Ohio. This paper was presented at the AIME Electric Furnace Steel Conference, Cincinnati, Dec. 2 to 4, 1953.

Ladle Erosion

The studies reported in this paper were conducted in the period 1944 to 1946 on a double pouring arrangement used exclusively for pouring 18-ton heats of basic electric melted heats of 52100 steels. Fig. 1 represents the double pouring arrangement used. The primary ladle is of 18-tons capacity and the secondary ladle is of 4-tons capacity. Both ladles are lined with conventional, eastern, bloating-type ladle brick laid up with an appropriate fireclay mortar. Conventional clay-graphite stopper heads and clay sleeves and nozzles were used. The blackened portions of the ladle linings indicate the extent

Table I. Analyses of Ladle and Ingot Scums Obtained by Varying Age of Ladle Linings

Ladle Combinations		Analyses in Percent						
Primary	Secondary	MnO	Al_2O_3	SiO_2	CaO	MgO	FeO	Cr_2O_3
Secondary Ladle								
New	New	5.30	14.71	47.09	3.04	0.30	5.61	4.68
Used	New	11.42	12.79	38.85	5.90	0.80	6.32	7.75
New	Used	6.71	10.63	43.04	24.11	0.32	3.31	2.53
Used	Used	5.81	12.58	44.85	17.45	3.03	4.11	2.70
Ingot								
New	New	13.80	9.19	30.42	2.98	0.37	12.60	12.78
Used	New	12.48	26.08	37.40	5.37	0.94	7.21	8.94
New	Used	11.77	16.39	36.60	7.84	0.34	9.65	7.39
Used	Used	11.67	12.80	35.60	7.18	1.99	7.49	6.66
Used	Single Ladle	10.32	13.79	38.79	5.60	0.76	4.38	4.88
Glazed Coating Secondary Ladle								
	Sidewalls	10.92	9.36	46.04	15.48	—	4.68	3.54
	Bottom	1.76	7.60	34.66	37.41	9.67	0.94	0.51

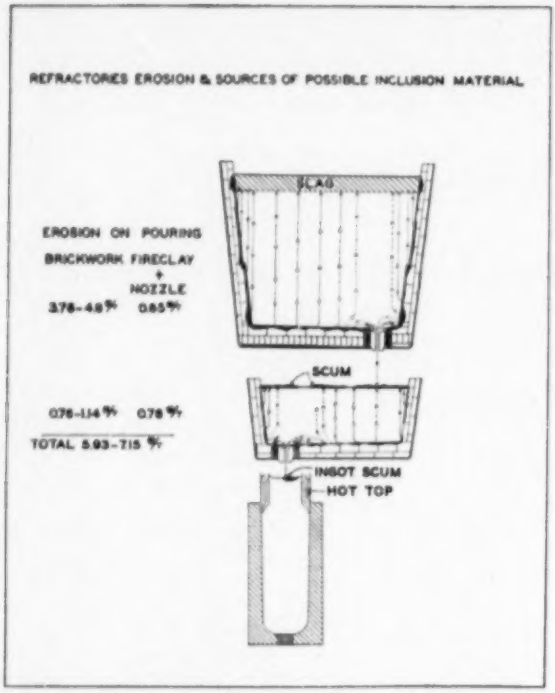

Fig. 1—Double pouring arrangement used in determining the pattern and extent refractory lining erosion. The primary and secondary ladles are of 18-ton and 4-ton capacity respectively.

and pattern of wear observed for the linings after pouring from 15 to 18 heats.

From Fig. 1 it can be seen that the lining is worn most at three distinct areas: A—At the slag line, B—at the offset in the sidewall, and C—at the bottom and bottom sidewalls. It was concluded the very marked erosion at the slag line was due to the constant heat size handled by the ladle. For one such pouring arrangement the actual amount of refractory material consumed was measured by weight loss and also calculated from measurements on the lining after service. These results are indicated on the left in Fig. 1. The values on the amount of brickwork erosion are respectively that obtained by actual weight loss measurements on the ladle and that obtained from calculations based on measurements of the thickness of the lining after service. From analyses and calculations on the changes in composition of the tap and ladle slags, it was concluded that most of such eroded refractory finds its way into the slag.

Scums

While studying ladle erosion and pouring, the incidence of a slag or scum on the metal in the secondary ladle was observed to form even when relatively clean ladles were used in the pouring arrangement. A similar scum was also observed at times on the top surfaces of the ingots. The amount of secondary ladle scum material was usually greater than could be attributed to metal oxidation and eroded refractory material carried down from the primary ladle. On closer study the amount, behavior, and composition of this scum appeared to be related to the age of the secondary ladle lining (age in terms of heats on the lining). For a newly lined ladle a small amount of scum is formed. As the age of the ladle lining increased, the amount of scum observed increased. For an old ladle lining the amount of scum was observed to grow continuously while steel was being poured. The occurrence and amount of ingot scum also appeared to be related to the age of the secondary ladle lining.

Petrographic analyses showed these scums to be essentially glassy and of variable composition. The glass composition ranged from that of a contaminated alumina-silicate glass, similar to that resulting from fusion of the pouring refractories, to a complex composition containing MnO, CaO, FeO, Al_2O_3 and SiO_2. Detailed examination showed the contaminated alumina-silicate glass with its associated mullite and undissolved quartz crystals to be fused pouring refractory material. The complex glass composition was a fused mixture of furnace slag oxidized metallics and fluxed fireclay refractory. The alumina-silicate glasses were most prominent in scums from newly lined ladles and the complex glasses most prominent in scums from old ladles. These scums had a fusion point which averaged 2275°F. Samples of the glazed coating on the surfaces of the secondary ladle lining were similar in composition and fusion point to the secondary ladle scum.

Chemical analyses of ladle and ingot scums collected for different combinations in the age of the two ladle linings are shown in Table I. Table II shows the progressive change in composition of ingot scums when newly lined ladles were used in the pouring arrangement of one heat.

From the above observations the following sources were identified as contributing to the observed secondary ladle scum:

A—Spalled or eroded pieces of refractory close to and including the nozzle washed down from the primary ladle and eroded refractories from the secondary ladle which rise to the surface.

B—Fusion and subsequent erosion of the furnace slag coating on the ladle lining from previous heats in close proximity to the nozzle well in the primary ladle and all such slag and scum coating on the secondary ladle lining which melts and rises to the surface of the molten steel. This is apparent from the increase in CaO and MgO content of the scum as the age of the ladle linings increases.

C—Atmospheric oxidation of the metal stream and oxidation of the exposed metal in the secondary ladle. This is indicated by the MnO, FeO, and Cr_2O_3 of the scums.

D—Deoxidation products which float out of the metal. This is indicated by the presence of significant amounts of CaO when newly lined ladles are used. Such CaO originates from the CaSi deoxidation of the steel in the primary ladle.

E—Reaction products of the steel with the refractories. Essentially and most significantly this involves the reaction Mn (in steel) + SiO_2 (in refractories) ⇌ MnO + Si. The MnO so produced readily fluxes the fireclay pouring refractories. The MnO

Table II. Progressive Scum Analyses Using New Primary and New Secondary Ladle Linings, Pct

Sample	MnO	Al_2O_3	SiO_2	CaO	MgO	FeO	Cr_2O_3
Sec. ladle	18.85	6.12	25.32	0.52	1.14	10.94	15.48
1st ingot	18.72	13.92	23.16	3.42	0.64	2.38	5.67
2nd ingot	14.79	15.00	30.60	2.38	1.13	5.40	5.67
3rd ingot	18.46	12.66	38.42	1.92	1.14	4.82	7.03
4th ingot	16.38	5.26	42.48	1.84	1.09	3.89	3.69
5th ingot	18.07	11.49	38.96	1.12	1.75	3.17	5.16

Table III. Tracing Transport of Nonmetallic Material from Ladles During Steel Pouring Using Cobalt Tracer

Area of Lining Investigated	No. of Tests	Secondary Ladle Scum*	Ingot Scum*
Primary Ladle			
Fireclay for nozzle setting	4	+,—,—,—	—,—,—,—
Direct pour, secondary ladle not used	2	—	+,+
Fireclay mortar joints for brick adjacent to nozzle well	4	—,—,—,—	—
Fireclay patch of eroded brickwork 12 to 15 in. from well	3	+,+,—	—,—,—
Secondary Ladle			
Nozzle	1	—	+
Fireclay for nozzle setting	5	—,—,—,—,—	+,+,+,+,+,+
Fireclay rim at junction of sidewall and bottom of ladle varying from 8 in. to 4 ft from well	3	+,—,—	+,—,—
Brickwork adjacent to well	3	—	—,—,—
Fireclay bottom patch, 6 in. from well	2	—	+,+ for 3 of 5 ingots poured
Fireclay bottom patch, 12 in. from well	4	?,—,?,?	—,?,+,+
Fireclay bottom patch, 18 in. from well	2	—,—	—,+
Cobalt oxide fused into scum coating by means of acetylene torch in area 12 in. from well	2	—,—	+,+ on 4th ingot—no scum on other 4 ingots poured
Cobalt nitrate solution painted onto glazed scum coating 6 in. from nozzle well	5	?,—,—,—,—	+,+,+,—,—
Cobalt nitrate solution painted onto glazed scum coating 12 in. from nozzle well	6	6 —	?,—,+,—,—
As above but 14 to 18 in. from nozzle well	3	—,—,—	—,—,?

* + indicates positive evidence; — indicates no evidence; ? indicates indefinite evidence of transport.

content of these scums indicates that this reaction does occur.

Paralleling this, the following sources were identified as contributing to the ingot scums: A—Spalled and eroded pieces of refractory from the secondary ladle washed down by the metal stream, B—fusion and erosion of the slag-scum coating close to the nozzle well in the secondary ladle. Also, detached portions of this material which are caught in the metal stream, C—spalled pieces of the hot top, D—atmospheric oxidation of the metal stream, and E—deoxidation products which float out of the steel in the ingot.

The above observations on scums and their behavior was explained as follows: On pouring steel from the primary to the secondary ladle some erosion of the refractories occurs. This is particularly pronounced for the raw fireclay used for setting the nozzle and the nozzle itself. In addition, some of the slag from previous heats coating the refractories close to the nozzle is eroded. This material, together with suspended deoxidation products, is transported by the stream to the secondary ladle. There much of this material rises to the surface of the metal as scum. If the secondary ladle has been used previously, the slag-scum coating on the refractories with a fusion point of some 2275°F becomes molten, detaches from the brickwork and also rises to the surface. On pouring from the secondary ladle to the molds, the transport of material is repeated as above. The observed growth in amount of scum with the age of the ladles can therefore be interpreted as the additive effect of slag and scum from previous heats coating the refractories and becoming detached when the following heat is poured into the ladle. Therefore, although the ladle gives a glazed, clean appearance when cold, the glazed coating is not permanent at service temperatures.

Sources of Potential Inclusions

The composition of the ingot scums from repeated examinations bears a striking similarity to the composition of inclusion material found in the ingots. Some of the scum material therefore remains in the ingot. Also the scum material is transported by the pouring stream only from a critical area of unknown extent in the ladle close to the nozzle well. Knowledge of the extent of this critical area would therefore be helpful in any attempts at eliminating inclusions of pouring refractories origin.

To determine the extent of this critical area, a tracer technique was used. It was recognized that the tracer element must have very distinctive properties and, after considering all possible elements, cobalt as the oxide or nitrate was selected because it was readily available and convenient to use. The procedure consisted simply of impregnating the area under investigation with the cobalt tracer. Ladle and ingot scums obtained on the subsequent pour were collected and then analyzed spectroscopically for strong indications of the presence of cobalt. By treating 4-in. wide circular areas progressively further from the nozzle, the extent of the critical area as regards potential inclusion material was established. Table III summarizes the results of these tests. Indications of cobalt in the secondary ladle scum were not strong, probably because of the frequently large amount of scum present and consequent dilution of the cobalt tracer.

The results show that spalled, fused, and eroded material within an 18 to 22-in. radius from the nozzle is carried along by the pouring stream. Tentatively it is concluded the most fruitful investigation of inclusions of pouring refractories origin is limited to this area of the ladle lining. These observations can be used as a guide for any future work involving radioactive tracers for investigating sources of inclusions from pouring refractories.

References

[1] A. McCance: Nonmetallic Inclusions: Their Constitution and Occurrence in Steel. *Jour. British Iron and Steel Institute* (1918) **97**, p. 239.

[2] J. R. Rait: Casting Pit Refractories as a Source of Nonmetallic Inclusions in Steel. *Trans. British Ceramic Society* (1943) **42**, p. 57.

[3] Carl A. Post and G. V. Luerssen: The Interaction of Liquid Steel with Ladle Refractories. *Trans.* AIME (1940) **185**, p. 15.

AIME Annual Meeting Program, Feb. 13 to 18, 1954

Hotels Statler and McAlpin, New York

Names of Divisions and Subdivisions are coded as follows: MIED—Mineral Industry Education Div. MED—Mineral Economics Div. M—Mining Subdiv. G—Geology Subdiv. Geophys.—Geophysics Subdiv. NM—(nonmetallics) Industrial Minerals Div. Coal—Coal Div. MBD—Minerals Beneficiation Div. EMD—Extractive Metallurgy Div. IMD—Institute of Metals Div. ISD—Iron & Steel Div. Petroleum Branch—Named as such. SEG—Society of Economic Geologists.

All Metals Branch sessions will be held in the Hotel McAlpin, and all Mining and Petroleum Branch sessions will be held at the Hotel Statler.

SATURDAY, FEBRUARY 13

10 am
Council of Section Delegates

SUNDAY, FEBRUARY 14

2 pm
Board of Directors

2:30 pm
IMD, MIED—Columbia Univ.

5 pm
IMD Program Committee

7:30 pm
IMD, MIED

MONDAY, FEBRUARY 15

8 am
Registration

9 am
Petroleum Branch—*Executive Committee*

9:45 am
EMD—*Aluminum*
EMD—*Arc Furnace Copper Melting*

9:45 am
ISD—*Surface Quality of Bars*

9:45 am
IMD—*Semi-Conductors*

10 am
NM—*Fluorspar*
M—*Drilling Problems*
NM—*Dimension Stone and Slate* (closed session)
MBD—*General Business Session*
Coal, CIMM—*Mining Methods in Relation to Recovery*
Metals Branch Council Meeting

12 noon
Welcoming Luncheon
Grayson Kirk, president, Columbia University

2 pm
Petroleum Branch—*Technical Session*
M—*Drilling Problems*
G—*Base Metal Deposits*

2:30 pm
G—SEG
NM—*Ceramics Raw Materials*
NM, MBD—*Cement, Lime, Gypsum*
MBD—*Materials Handling*
MBD, MIED
Coal—*Preparation, Coarse Coal*
EMD—*Aluminum*
EMD—*Arc Furnace Copper Melting*
ISD—*Open Hearth Combustion*
IMD—*Semi-Conductors*
IMD—*Deformation*

3 pm
Peele Award Committee
JOURNAL OF METALS Editorial Advisory Board

4 pm
MGGD Executive Committee

4:30 pm
IMD Membership Committee

6 pm
Cocktail Party

8 pm
Dinner-Smoker

TUESDAY, FEBRUARY 16

7:30 am
EMD Executive Committee Breakfast
IMD Titanium Committee Breakfast

8 am
MBD Scotch Breakfast

9 am
Petroleum Branch—*Technical Session*
M—*Block Caving*
M—*Stratified Mining*
G, SEG, NM—*Radioactive Materials*
NM—*Careers in Industrial Minerals*
NM, SEG, G—*Rare Minerals*
MBD—*Crushing and Grinding*
MBD—*Operating Control*
Coal, CIMM—*Preparation, Fine Coal*
Geophys
EMD—*Lead-Zinc*
EMD—*Hydrometallurgy—Physical Chemistry*
ISD—*Use of Rare Earths*
IMD—*Deformation*

10 am
Mining Branch Council

11 am
Howe Memorial Lecture
by C. D. King

12 noon
MGGD Luncheon
Coal Luncheon

12:15 pm
IMD Executive Committee Luncheon

2 pm
Petroleum Branch—*Economic, Geological, Political Factors of World Oil Production*
NM—*Rare Minerals*
MBD—*Concentration*
Coal—*Mining Methods*
EMD—*Lead-Zinc-Cadmium*
EMD, MBD—*Hydrometallurgy*—Statler
ISD—*Ingot Examination and New European Practices*
IMD—*Constitution*
IMD—*High Temperature Properties*

2:30 pm
MGGD
Jackling Lecture

6 pm
Metals Branch Cocktail Party
Petroleum Branch Cocktail Party and Dinner

7 pm
Metals Branch Annual Dinner

9 pm
Informal Dance, AIME

WEDNESDAY, FEBRUARY 17

7:30 am
ISD Executive Committee Breakfast

9 am
M—*Greater Butte Project*
G, Geophys
NM—*Special Sands and Abrasives*
MBD—*Concentration*
MBD—*Solids-Fluids Separation*
Coal—*Continuous Mining*
EMD, IMD—*Physical Chemistry of Extractive Metallurgy*
EMD—*Titanium*
ISD—*Physical Chemistry*
IMD—*Solidification*

9:30 am
Petroleum Branch—*Technical Session*

11 am
IMD Annual Lecture
by Bruce Chalmers

12 noon
NM Luncheon
MIED Luncheon

12:15 pm
EMD Stag Luncheon and Business Meeting

2 pm
M—*Underground Mining Problems*
G—*Porphyry Copper Deposits*
MED
NM
EMD—*Physical Chemistry of Extractive Metallurgy*
EMD—*Copper*
ISD—*Blast Furnace*
IMD—*Constitution*
IMD—*Titanium*

2:30 pm
Geophys, G
MBD—*Pyrolysis and Agglomeration*
Coal—*Air and Water Pollution*
Coal—*Strip Mining*

4:30 pm
NM Executive Committee

7 pm
Annual Banquet
President's Reception

THURSDAY, FEBRUARY 18

9 am
M—*Support of Mine Workings*
MGGD, NM—*Industrial Waters*
MBD—*What's New in Milling*
Coal—*Utilization*
EMD—*Uncommon Metals*
IMD—*Steel*
IMD—*Powder Metallurgy*

12 noon
MBD Luncheon

12:15 pm
IMD Powder Metallurgy General Luncheon

2 pm
MGGD, NM—*Industrial Waters*
MBD—*Clean-up Session*
Coal—*Utilization*
IMD—*Powder Metallurgy Seminar*

Regenerator Efficiency and Air Preheat In the Open Hearth

by B. M. Larsen

A discussion based on three commercial furnace tests and electrical analogue calculations is presented. It shows that while regenerator efficiency is mainly dependent on loading or relative amount of heat exchange surface plus the heat transfer coefficients as effected by flow velocity, the actual air preheat temperature can be high or low, largely independent of regenerator efficiency, mainly due to the diluting or unbalancing effects of cold air leakage into various parts of the furnace system.

THERE are many signs of a renewal of interest in the heat regeneration aspect of the open hearth process, among them being the recent paper by Marsh,[1] the introduction of auxiliary checkers in the stacks of the Isley furnace design, and a number of recent installations of two-pass checkers in new and old furnaces. However, there are also signs of yielding to the usual temptation of oversimplifying a problem. Faced with the job of obtaining better draft on a furnace, for example, a good designer always recognizes that focusing attention on some one factor, such as height of the stack or capacity of the exhaust fan, does not make his problem any easier; rather he must look at the whole system, including such items as valve resistances, bends in the flues, and flow resistance in the waste heat boiler; then he must make his design in relation to the available draft so as to avoid any serious bottleneck in the system. Yet this example is really much simpler than the problem of air preheating, and again, the latter problem is not really made easier by concentrating on air temperature in uptakes and on the more obvious methods for making this air as hot as possible. Also to be considered are such things as the total amount of air needed theoretically for complete combustion at any selected fuel rate, together with that needed for oxygen absorbed into the bath and for burning the combustible gases given out from the bath, plus some excess air. Furthermore, how does this total air requirement relate to the regenerator efficiency at various loadings? How much of the total air equivalent in stack gases will come from preheated air passed through the whole length of the incoming regenerator and how much from air leakage into various zones of the whole furnace system? Does the effect of leakage air differ depending on whether it leaks into the ingoing regenerator, the furnace above floor level, the outgoing regenerator, or the stack zone?

Over a number of years we have in this Laboratory experimented with methods for measuring hot gas temperatures; we have measured, approximately, the efficiency of a few regenerators on commercial furnaces and we have developed an electrical analogue[2] for calculations of regenerator efficiency. The whole problem is too complex to cover in one paper even with a more complete background of data than we possess, but we can attempt here to clarify certain aspects in a general way, hoping to assist specific plant studies on individual furnaces. Some of our earlier experience has been incorporated into chaps. 4, 19, 20, and 21 in the book "Basic Open Hearth Steelmaking,"[3] and on the assumption that this text is available to most readers, this discussion has been shortened by references to that book. The most recent design of a flowing-gas thermocouple which we are now using for measurement

B. M. LARSEN, Member AIME, is associated with the Research Laboratory, United States Steel Corp., Kearny, N. J.

Discussion on this paper, TP 3701C, may be sent, 2 copies, to AIME by April 1, 1954. Manuscript, Oct. 27, 1953. New York Meeting, February 1954.

Paper presented at Birmingham Regional Technical Meeting, American Iron and Steel Institute, October 1953.

The Transactions papers appearing in the Journal of Metals during 1954 will subsequently appear in AIME Transactions Volume 200, and may be permanently referenced to that volume.

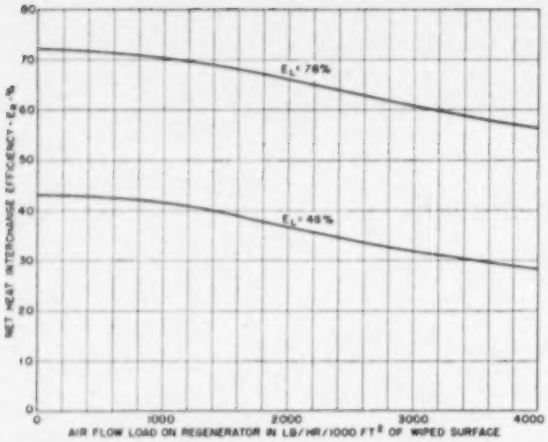

Fig. 1—Effect of load rate on net regenerator efficiency (E_R) for two extreme values of efficiency limit (E_L = 46 and 78 pct).

of gas and air temperatures in regenerative zones is described briefly in the Appendix.

Some Background on Furnace and Regenerator Design

Although the open hearth furnace is about eighty years old, many furnaces are now being operated with regenerators of design and capacity quite inadequate to preheat approximately all of their normal air requirements to a desirable temperature level. It may be interesting, and perhaps helpful, to sketch here some background and some of the reasons for the existence of this situation in a process of such predominant industrial importance.

The very early furnaces of 20 to 30 tons capacity needed checker chambers which, with reasonably adequate surface area for heat exchange, were still small enough to be located largely underneath the melting chamber. This helped to give minimum heat losses and air leakage in a blocky design of minimum external surface. With furnace capacities growing to 40 to 60 tons, the increased size, together with certain design and operating factors, favored the location of the checker chambers out under the charging floor, pointed toward flues and stack, that is, about at right angles to the melting chamber. This gave more exposed surface for heat loss out and for leakage of cold air in, but many operators eventually learned how to use insulating and sealing coatings on all exposed surfaces below floor level to keep most of the heat in and the cold air out. In this size range, up to perhaps 60 tons, a checker of moderate length still suffices to give an adequate total perimeter* of heat exchange surface.

* The perimeter of a checker setting is defined as the total length of all brick-to-gas intersection over a given horizontal cross section, that is, the sum of lengths of all the sides of all the open flues.

If the charging floor is also placed at a reasonable height above normal maximum ground water levels, the checker can be about as deep as it is long, so that the distribution of gas and air flows can remain fairly uniform over all the flue openings.

As furnace sizes increased to over 100 tons, the needed checker surface would have demanded, for the same chamber length, a checker depth so great that serious engineering problems of digging deep flues and sealing against ground water were involved. The simple alternative was to lengthen these checker settings, until extremes of only 8 to 10 ft of depth combined with 25 to 30 ft of length were attained in some shops. The gases and air could not be expected to flow anywhere near uniformly down all the flue openings over this great length of checker setting. This "channeling" of gas and air flows will not be discussed here, but it can be assumed that it is serious enough so that these long single-pass checker chambers do not give the increase in efficiency which should result from their proportional increase in total heat exchange surface. One simple proof of this lies in the fact that at various times operators have blocked off some 8 or 10 ft of checker openings at the far end of the settings with no noticeable decrease, or even a slight increase, in furnace sharpness.

As average furnace size increased, many older shops obtained a net gain in costs per ton by increasing the capacity of their smaller, older furnaces. Baths were lengthened or widened or deepened and fuel input rates increased, and while heat times tended to increase, there was a net gain in labor and overhead costs. Regenerator and flue capacities were harder to increase so, in general, they remained about constant, and became less and less adequate for the loads placed upon them. Although precise data are lacking, it is a fairly safe guess that in most shops, instead of a gradual gain in heat regeneration efficiency with real improvements obtained by insulation, sealing, checker cleaning, burner and port design, and furnace controls, this efficiency has been falling off somewhat over the years. The changes have developed gradually, it is true, yet it still remains a puzzle as to why the relative decrease in regeneration efficiency has not been given more attention by the industry as a whole. One probable reason lies in the shape of the curve of regenerator efficiency with increasing size. One form of this is given in Fig. 21-2 in ref. 3 (similar to Fig. 6 here) in which increasing depth at constant perimeter* and constant gas flow is plotted against net efficiency for two widely different values of drift ratio (or leakage confined to the melting chamber parts between regenerative zones**).

* See asterisk footnote in first column.

** The relations between "drift ratio" and leakage in various zones of the furnace system are explained in a later section, as well as the E_L values in Fig. 1.

Roughly speaking, it can be seen from the curves that for any given constant value of cross section and drift ratio** the first 8 to 10 ft of checkerwork depth gives around 80 pct of the net efficiency that should be obtained from a setting around 20 ft deep. Or, from another angle, the curves** in Fig. 1 show net efficiency against increasing load, that is, increasing rates of air flow for the same regenerative system. As nearly as can be estimated, most of the older, enlarged furnaces are operating about in the middle of these curves near the range of 2000 to 3000 on the horizontal scale. Thus, the lowering of efficiency with more overloading is not too rapid.

Furthermore, as will be shown below, by certain methods of operation, including excess fuel input and wastage of heat into the stack zone coupled with air leakage above furnace sill level, inefficient, overloaded regenerators can be made to preheat a limited amount of air to very high temperatures in the uptakes to give a sharp, intense flame. Relatively more high temperature heat moves downstairs and the downtake, slag pocket, and fantail portion of the system take on more of the air heating.

In brief, as this drift toward inadequate regeneration of heat developed over the years in older fur-

naces, there was not a catastrophic loss in steelmaking rates. There was only a gradual, moderate loss of furnace sharpness, with longer heats and greater stack losses being countered by savings in overhead and labor as well as from waste heat boiler recovery, and by the effects of more insulation and better combustion and control methods.

However, the relative inefficiency of the larger, longer, shallow regenerators was apparently recognized early by a few people. Dyrrsen[4] suggested the idea of a metallic preheater between checkers and stack and this idea is paralleled in the stack checkers of the present Isley[5] furnace. Even earlier, in a book by Groume-Grjimailo,[6] a drawing is shown of a regenerator tried by the Pennsylvania Steel Co. of a design very nearly the same as the modern two-pass regenerator chambers. Yet after all this time specific data on the efficiency of various regenerator designs are still needed. There seems to be some lack of understanding of the many-factored problems involved in air preheat and of certain related operating difficulties with double-pass regenerators.

Limitations of the Present Discussion

The division of the furnace system into: 1—melting chamber zone or "working chamber," 2—regenerator zones, and 3—stack zone, as described in chap. 21 and Fig. 21-1 of ref. 3, is satisfactory for our purpose because it concentrates attention on regenerative zones of heat interchange, largely independent of the melting chamber, with the latter regarded merely as the supply source for heating gases. However, certain effects in the melting chamber do relate to, or affect, the air preheat temperature and the regenerator efficiency.† Although some of these are not treated adequately in the literature, to discuss them properly here would make this paper even longer and more cumbersome than it already is. So we will ask the reader to take the following points, if not on faith, at least as tentative assumptions correlative to the later discussion of air preheating.

† The reason for listing these as two separate factors will perhaps become more obvious from the discussion later on.

1—Flame radiation intensity depends not only on air preheat temperature, but also on the pattern of fuel-air mixing and related port design and, with liquid fuels, on burner design and position and atomizing agent used. These latter factors, however, are essentially separate from the regenerator problem. Also, the air temperature is the main factor determining flame intensity, as partly substantiated by the measurements shown in Fig. 2, all made on one furnace. Since flame radiation and air preheat are rapidly varying things, difficult to express accurately in integrated or effective mean values, the correlation indicated is considered good.

2—There are many areas of flame zone in the open hearth which can hardly be seen at all. The main flame zone, from which hot carbon-rich particles radiate intensely in the short wave lengths of visible light, is easily seen, even against the glare from hot and reflecting wall or slag surfaces. But any carbon monoxide or hydrogen tailing out away from this easily visible flame can, wherever it burns, radiate almost no energy except in longer wave lengths invisible to the eye. The large volumes of carbon monoxide and the small amount of hydrogen evolved from the bath give a similar "thin" flame which is almost invisible against a bright background. Unless there is a large excess of air supply to the melting chamber, some of this "invisible combustion" will occur in downtakes and even over top checkers, partly by virtue of cold air leakage directly into this zone. This effect raises appreciably both the "top" or "100 pct" temperature level (Tg_t) of any selected regenerative zone and its total quantity of heat supply.

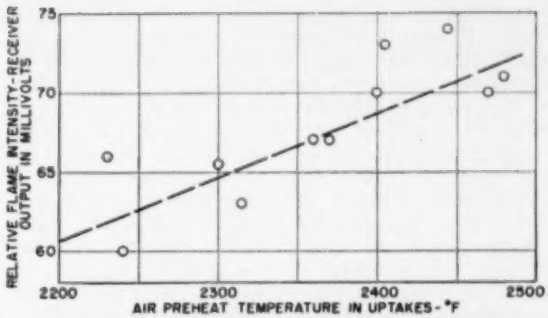

Fig. 2—Correlation between air preheat temperature in uptakes and the apparent flame intensity as measured by the output of a radiation receiver at one wicket hole pointed at the most intense flame zone. All values measured on furnace A.

3—The open hearth process differs from the bessemer in that its main source of oxidation comes from ore and limestone. But it is also more like the bessemer than is often thought, because it can obtain a great deal of oxidation from heated air with useful effect. Much iron can be burned during meltdown of exposed scrap, thereby providing much heat and storing liquid oxide in the bath for later reaction. The slag can absorb oxygen directly as the gases above it have more oxygen available. The gas from the carbon monoxide boil requires large quantities of excess air to burn it.

4—As air oxidation can be increased and the charge and feed ore decreased, the net heat requirement of the bath from external sources can decrease by a large percentage, especially as heat can be absorbed from burning boil gases over the slag in the melting chamber instead of down in the regenerative zones. Also, in this regenerative system, even the excess air,†† which never burns anything, has more or less of its heat extracted and returned to the working chamber, depending on the net regenerative efficiency. Thus in general the furnace process can utilize "extra" air to good effect, in such large quantities as would be very bad in boiler or reheating furnaces, where the work is inactive to the combustion process. This excess of air can come either from that ingoing through checkers or from direct cold air leakage, and its relation to regenerator efficiency may become obvious from the examples in a later section.

†† Throughout this paper, "theoretical air" is calculated as that required to burn all fuel input plus any carbon monoxide from bath, or oxygen absorbed into the bath, insofar as these could be measured. This theoretical air is then taken as the 100 pct basis (usually in lb per hr over any given test period) and values for "pct excess air" or "pct air leakage" are in reference to the theoretical requirement. Excess air is that present in excess of combustion requirement, so that a gas weight and composition will give it for any sampling point. Air leakage is the total equivalent of air present at any sampling point, minus the air input through the ingoing regenerator. When given in percentage values, the air leakage is again referred to the same theoretical air as the 100 pct basis.

Some Points of Reference

The brick surfaces of downtakes, slag pockets, and fantails contribute a very appreciable part of the total gas cooling and air heating. Measurements

show that the air temperature rise in this "upper zone" of the whole system of heat interchange or regeneration may be anywhere from 200° to 500°F. Although the largest part of the air heating is done by the regenerator chamber surfaces of checkers, rider walls, arches, etc., this last 300°F or more of air heating in the "upper zone" is very important to the "flame sharpness" and must be kept in mind.

Therefore, to make any sort of definition or measurement of regenerator efficiency in a real open hearth system, certain boundary conditions must be defined. The cold end of the regenerator zone is quite definitely separated from the stack zone at the air dampers and reversing valves, especially if these are reasonably tight, but the hot end of the zone of heat interchange shades into the working or combustion zone in the port ends. However, the top of the downtakes can be used as the dividing point, with reasonable preciseness. There is some heat interchange above this point, and there is also some direct radiation flow into the downtakes, which means some heat supply which does not come from the actual gas flowing through this upper downtake zone, but these two effects tend to cancel each other.

In making a measurement of heat interchange efficiency in an actual furnace, there are several reasons for omitting the upper zone:

1—Outgoing gases are poorly mixed as they enter the downtakes and they tend to have somewhat variable velocity and temperature. There may be, frequently, a variable amount of "tail end combustion" of carbon monoxide and hydrogen coming from the flame or from the boil gases. It is thus very difficult to measure mean values of temperature and composition and to calculate the rate of heat supply which is essential to the fixing of a definite value for heat interchange efficiency.

2—The variable and indefinite pattern of gas and air velocities near the wall surfaces of this "upper regenerative zone" makes it very difficult to interpret the process of heat interchange. Mean flow rates are apparently not very high, and the amount of brick surface is not very large in this zone, which would probably result in low efficiency. The fact that a very appreciable amount of air heating occurs here must be due to the rather large temperature differences between brick surface and air and to a considerable turbulence in the air stream; there is also good heat transfer from combustion gases to brick surface due to a large radiation transfer effect.

3—The opportunity for variable design to improve efficiency in the checkerwork setting is very limited in the design of this upper zone. Its design is fixed largely by various problems of engineering and brickwork construction plus the limitations of available refractories under the high temperature and slagging encountered in this zone. In fact, its design is always a compromise between conditions favorable to effective air heating and the largely opposite conditions favorable to outgoing gas flow with a minimum of damage to refractories.

For these reasons, in the tests to be discussed, the checker chamber zone of the regenerator system has been "isolated" by measuring gas composition and air temperatures at: 1—the bridgewall between checker chamber and fantail, and 2—the flues just below checkerwork or at the exits from the regenerator chamber. The gas stream is usually well mixed at both points and the rates of flow of gas and air can be rather accurately calculated for points in the checkerwork setting. Thus, from the data on heat-transfer coefficients given in Fig. 20-7 of ref. 3, the mean values of heat transfer rate in various checker zones can be estimated, which helps to interpret the results obtained. The discussion of these heat-transfer curves in chap. 20, ref. 3 shows how the radiation factor causes the heat transfer coefficient‡ for gas-to-brick to vary with both temperature and gas flow velocity, while the coefficient for brick-to-air varies only with air flow velocity because the air is transparent to radiation and can absorb heat only by convection, that is, only by actually "wiping" the heat off the hot surfaces.

‡ This is the Btu transferred between air or gas and one square foot of exposed brick surface, per hour, per degree of temperature difference between gas stream and brick surface or between this surface and the air stream.

Before discussing specific cases it is useful to list all the factors which affect the temperature of the air stream at any instant as it arrives at a given point, such as the burner port or the checker bridgewall, as follows:

1—General temperature level of the whole furnace system.

2—Distribution in the furnace system of the zone, or zones, of combustion of fuel and of gases from the bath boils.

3—Rate of fuel input and excess air, that is, the loading rate on any given regenerative zone.

4—Time of period between reversals; also the time in the reversal period.

5—Uniformity of flow distribution of gases and air over various cross sections in the regenerative zone.

6—Cleanliness, or freedom from insulating dust coatings, of checker surfaces.

7—Air leakage directly *into* regenerator zones.

8—The ratio between heat capacity of ingoing air stream and outgoing stream of combustion gases plus excess air, determined mainly by the amount of air leakage above door sill level, that is, *between* regenerator zones.

9—Relative size and design of the regenerator zone.

The first factor, or the general temperature level of the whole furnace system, expresses the fact that the "spillover" temperature level of gases leaving the working chamber is not constant, even if the second factor is held constant, that is, the combustion zone is kept short and in the same relative position. This "critical temperature level" averages out to somewhere around 2800°F or higher over the whole heat cycle, but it varies considerably with the stage of the heat, the rate of fuel input, and especially with the rate at which charged scrap or bath is absorbing heat. The resulting effect on air preheat in uptakes may sometimes be quite confusing. For example, consider one of those periods in which the bath "goes dead" or gets covered with a foamy or very heavy lime-lump-filled slag. Heat flow rate into the bath drops off quickly to a few percent of normal, the chamber heats up rapidly, and combustion gases enter regenerator zones at a temperature level perhaps 200°F higher than before. On one or more reversal periods the resulting preheat air temperature may be very high, at a time when the fur-

nace is "working" very poorly, leading to a possible absurd interpretation if the variable factor involved is not recognized. Again, a furnace using only coke-oven-gas fuel with a flame of low radiation intensity would tend to give a higher spillover temperature leading to a higher air preheat for given regenerative zone conditions.

The second factor is related to the first, in that with a long flame plus heavy bath boils the combustion zone may extend down into the regenerative zone. Spillover gas temperature will be higher, but there will also be an extra heat supply, just as though some auxiliary fuel was injected into the slag pocket or over the checkers, and air preheat temperature may rise, at the expense of heat not effectively used in the working chamber. If such a condition is intense for only a short period, there may result an extra high "skin temperature" on brick surfaces in slag pocket and fantail (not soaked in very far into the brick), and the following reversal period might show an extra high air preheat just after reversal which would drop off more rapidly during the air period.

Factor No. 3 is a matter of loading rate of heating and cooling gases relative to a given regenerator size or capacity. It was alluded to previously in connection with the curves of Fig. 1 and it will be discussed again below. The insulating effect of dust on checker surfaces in factor No. 6 is recognized in most shops, but it is still another variable to be remembered. Factor Nos. 7, 8, and 9 will, it is hoped, become clarified during the discussion on the measurement of heat interchange efficiency in specific furnaces.

The general point to be made here is that the mere measurement of air preheat temperature in uptakes does not furnish a simple measuring stick for all the thermal problems of an open hearth. It may serve as one useful aid in such diagnoses but useful results will not be favored by oversimplifying the problem, ignoring some of the many factors involved. The curves given in Fig. 3 represent air temperatures in one uptake at sill level on only one end during most of the air periods of one heat following finish charge on a fairly sharp modern 220 ton furnace. The variable mean temperature and variable rate of drop-off of air temperature illustrate the general effect of some of the above factors even in a single furnace, although there is encouragement in the greater regularity during the finishing period. Granting that such measurements have at least some limited usefulness in operations control, it is even more important to try to understand some of the underlying factors involved between regenerator design, heat interchange efficiency, and control and operating practice.

Before coming to specific regenerator efficiency measurements, a few of the main design factors involved in the heat interchange efficiency of a regenerator for a given rate of loading will be reviewed. In actual furnace practice, the optimum reversal period is essentially limited between 7 and 15 min per half cycle. For all commercial fire-clay brick materials, the useful thickness for effective in-and-out heat flow in such time periods is between about ½ and 1.0 in. behind the gas-to-brick surface, as illustrated by the curves of Fig. 20-8, in chap. 20 of ref. 3. Since practical, stable checker settings seem to require brick between 2 and 3 in. thick (with brick layer wiped on both sides by gas flow) this means that behind each square foot of brick surface

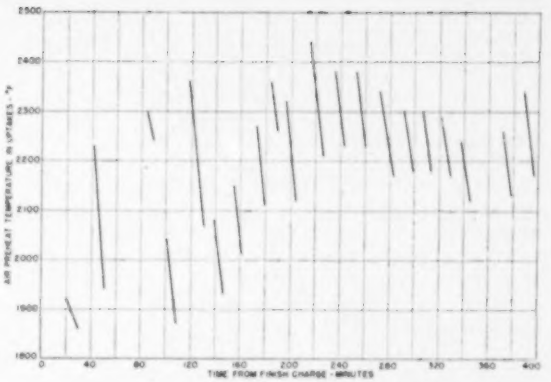

Fig. 3—Air preheat temperature in uptake at sill level on one end of one furnace, over most of the air periods on one heat from finish charge to tap.

swept over by gas and air streams, there is always enough thickness or mass of refractory to absorb and give out all the heat that can be interchanged in these half cycle periods. And this in turn means that the *total effective exposed area* of brick surface in the regenerators at each furnace end is the main fundamental factor involved in regenerator efficiency. To utilize this surface with full effectiveness, the gas and air streams must flow at somewhere near a uniform rate over all this surface, that is, approximately uniformly over the whole checker cross section. In order to get both maximum "wiped surface" and maximum weight of brick, or maximum heat storage capacity, most checker settings are now made with simple solid flues so that the perimeter*

* See asterisk footnote, p. 130.

multiplied by the depth of checkerwork gives the exposed surface, except for a small percentage increase from rider wall and arch surfaces (omitting the "upper regenerative zone" surfaces in fantails, slag pockets, etc.).

The only other important factor is the coefficient of heat transfer, which, as shown by the curves of Fig. 20-7 in ref. 3, depends essentially on the rates of gas and air flow. For any given effective surface area in checkerwork, the only way to increase heat transfer is to arrange this surface more in series and less in parallel, so that the gas or air streams flow over the same surface area in the same time but at a faster flow rate so that more effective heat transfer is obtained from each square foot of brick surface. Normally, in actual design this can be done only by deepening the chambers, that is, by increasing the height of the charging floor above the base of the underground flues. If such deepening of the checker setting is not practicable, about the only way to obtain this effect is to use the two-pass design, as indicated by the diagrams of Fig. 4. In these diagrams, the two-pass chamber is shown about enough longer to accommodate the blind pass. If chamber length must remain unchanged with the two-pass setting, the blind pass uses up much more chamber length than it adds in surface area. The cold pass only accumulates a fine, powdery dust deposit which is easily blown off and it is therefore practicable to use thinner brick with smaller flues to give a larger surface area in a relatively smaller cold pass, as is indicated in Fig. 4. In this way, a given length of chamber can be changed to the two-pass design, retaining somewhere near the same effective surface

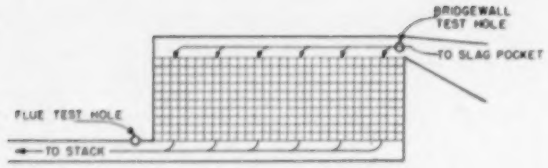

SINGLE-PASS CHECKER CHAMBER

Fig. 4a—Approximate layout of typical single-pass regenerator chamber.

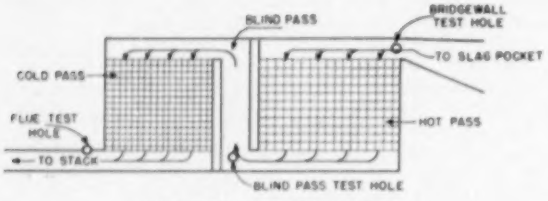

TWO-PASS CHECKER CHAMBER

Fig. 4b—Approximate layout of typical double-pass regenerator chamber.

area. The flow rates increase to somewhat above twice the values in the single-pass design, giving a large increase in coefficients of heat transfer. At the same time, the two-pass design favors greater uniformity of flow distribution over the cross section in each pass.

Heat Interchange Efficiency Studies on Commercial Furnaces

Data obtained for three commercial regenerators that will be described illustrate many of the variable conditions that have been discussed. In all cases, the measurements were made under conditions approaching as close to steady state as was possible under commercial operations. Most of the measurements were made during refining, with the bath on a steady boil with no additions to the bath. For a few reversal periods, the furnace would be undisturbed, no doors opened, no changes in control settings, etc. The fuel input rates were measured carefully by recently checked meters, and the rate of carbon drop in a known weight of bath was measured accurately. The fuel analysis was checked. From these data the weight of carbon in the outgoing gases per unit of time could be calculated. The rate of atomizing steam or air input was measured and with the known air humidity, the rate of input of hydrogen plus water vapor was calculable. The outgoing gases in flues at checker exits were analyzed for oxygen and carbon dioxide content by Orsat meters (in some cases also at the checker bridgewall), with checks at different points in the flue or flues for uniformity. These data made it possible to calculate the true analysis of the gas stream, including water content, and to calculate its total equivalent air content.

In the natural draft furnace (*A*) the air input rate was measured by a special meter‡‡ and in the two forced-air furnaces (*B* and *C*) the orifice plates for measurement of air input rate were checked. Thus the input rates of air were known with reasonable accuracy and by difference from the total air equivalent in outgoing gases the *total* air leakage to the system was known. The *distribution* of this leakage presented a problem, which is discussed below for each case.

‡‡ A Thomas meter was installed over one air inlet.

Temperatures of both gas and air streams were accurately measured by flowing-gas thermocouples (see Appendix) at both checker bridgewall and checker exit points over the whole reversal cycle involved, so that mean gas and air temperatures could be calculated. A convenient "dodge" in plotting or in certain efficiency calculations was resorted to by setting the mean gas temperature at bridgewall as 100 and mean air temperature below checkers as zero, other temperatures becoming percentages of this range.

A Natural-Draft Furnace with Overloaded Single-Pass Regenerators: This old furnace, no longer in service, was designed for 30 to 35 ton heats, and, over the years, had been enlarged to make heats of around 55 tons. The practice described represents extreme conditions, not found normally in modern open hearth furnaces, but of value for purposes of comparison in this paper. The checkerwork depth of 8.3 ft above rider walls was probably about the same as in the original furnace. In the test period the results indicated that the load rate on ingoing air was 2860 lb per hr per 1000 sq ft of effective checker chamber surface, a very heavy loading, as may be seen by comparison in Table I. The values in Table II indicate the flow rates in the test period, with the total theoretical air required for combustion (of the oil input of 170 gal per hr or 1385 lb per hr plus the carbon monoxide rate of 315 lb per hr; total, 1700 lb per hr) being taken as 100 pct in the percentage figures of the second column.

Before discussing this high excess air operation, the main test results will be completed, Table III; remembering that the checkers and rider arches are being "isolated" in this case, excluding even the rider walls and flues near the checkers, temperatures being measured just over the checkerwork and just beneath the rider arch supports.

Perhaps some evidence should be given of the consistency of the results in view of the obvious difficulties in a test of this sort on a commercial operating furnace. If steady state was approached, the amount of heat absorbed by the ingoing air should be just a very little less than that given up by the gases, considering that the checker chamber walls were very tight and well insulated so that external heat loss was very low in this particular zone of the

Table I. Partial Comparative Data on Regenerator Tests in Three Commercial Open Hearths

	Furnace		
	A	B	C
Size of heat, tons	55	260	240
Regenerator type	Single pass	Double pass	Single pass
Exposed regenerator surface, one end, sq ft	7,030	56,000	39,700
Combustion gas flow, lb per hr	41,600	78,960	151,030
Preheated air ingoing, lb per hr	20,100	61,870	71,820
Total theoretical air for combustion, lb per hr	23,000	58,600	83,410
Total air leakage between regenerators, pct of theoretical	86.1	17.4	82.4
Combustion gas temperature, flue exit, T_{g_L}, °F		1,110	1,420
Net regenerative efficiency, E_R, pct	32.4	64.5	(35.0)?
Efficiency limit, $E_L = \frac{Ca}{Cg} \times 100$, pct	45.1	73.2	44.1
Air load rate on heating surface, lb per hr per 1000 sq ft	2,860	1,100	1,800

Table II. Flow Rates in the Test Period, Furnace A

	Flow Rate, Lb per Hr	Pct Based on Theoretical Air = 100
Total combustion gases into checker, Wg	41,600	
Fuel oil plus carbon monoxide from bath	1,700	
Total air (equivalent in combustion gases)	39,900	173.6
Preheated air ingoing through checker, Wa	20,100	87.5
Total air leakage between regenerators	19,800	86.1
Total air	39,900	173.6
Total theoretical air for combustion	23,000	100.0
Excess air entering outgoing checker	16,900	73.6

furnace system. The mean heat capacities of the gases and air over the temperature ranges above are as follows:

Sg (1770°–2370°F) = 0.305 Btu per lb per °F.

Sa (380°–1840°F) = 0.263 Btu per lb per °F.

Heat absorbed from gases will be $Cg\ (Tg_2-Tg_1) = (Wg)\ (Sg)\ (Tg_2-Tg_1)$

$= (41{,}600)\ (0.305)\ (2370°-1770°) =$

7.61×10^6 Btu per hr.

Heat absorbed by the air; $Ca(Ta_2-Ta_1) = (Wa)\ (Sa)\ (Ta_2-Ta_1)$

$= (20{,}100)\ (0.263)\ (1840°-380°) =$

7.72×10^6 Btu per hr.

This agreement is as good as would be expected; the error may be either in the measurements or in a small departure from steady state.

In calculating the net efficiency of any given portion of the whole regenerature zone such as is under test here, the Ta_1 temperature (of the air entering the test zone) is taken as sea-level or 0 pct level and the net efficiency is simply

$$E_R = \frac{\text{Btu per hr carried by air stream from zone toward furnace, above } Ta_1}{\text{Btu per hr carried by gases into this zone, also above } Ta_1}$$

$$\text{or, } E_R = \frac{(Wa)\ (Sa)\ (Ta_2-Ta_1)\times 100}{(Wg)\ (Sg)\ (Tg_2-Ta_1)} =$$

$$\frac{(20{,}100)\ (0.263)\ (1840°-380°)\ \times 100}{(41{,}600)\ (0.288)\ (2370°-380°)} = 32.4 \text{ pct.}$$

As discussed in ref. 3 (chap. 21, p. 843), in order to have a logical concept of regenerator efficiency, consideration must be given to the limiting efficiency (E_L), or the net efficiency that would be obtained from a perfect regenerator under the same flow conditions. Such a regenerator could obviously do no more than heat the air stream up to the Tg_2 temperature so that in this case,

$$E_L = \frac{(Wa)\ (Sa)\ (Tg_2-Ta_1)\times 100}{(Wg)\ (Sg)\ (Tg_2-Ta_1)} =$$

$$\frac{Ca}{Cg}\times 100 = \frac{(20{,}100)\ (0.269)\ (100)}{(41{,}600)\ (0.288)} = 45.1 \text{ pct,}$$

and the absolute efficiency

$$E_A = \frac{E_R\times 100}{E_L} = \frac{100\times 32.4}{45.1} = 71.8 \text{ pct}$$

or the efficiency relative to the performance of a perfect heat interchanger *under the existing flow conditions.*

The flow rate data listed above show that only 87.5 pct of the theoretical air requirements was actually passed through the regenerator ingoing to be preheated. In the other half cycle, an almost equal amount (or 86.1 pct) of air leaked into the furnace somewhere between the two checker bridgewalls, so that an abundance of total air was available for the burning, leaving an excess of 73.6 pct still present when the gases reached the top checker brick outgoing. This degree of unbalance between the two heat capacity flows (Ca/Cg), to which the term "drift ratio" has been given, is what is also expressed (simply multiplied by 100) by the above E_L value of 45.1 pct.

Although the *total air leakage* (86.1 pct) in this furnace is known, the *distribution* of this leakage is not so easily found. It is very important, however, to know whether the air leak is into the melting chamber zone above sill level or into the upper regenerator zones between top of downtakes and the top checker courses. In both cases, the volume of gas flow in checkers is increased, but in the latter case, *its temperature is also lowered.* In furnace *A*, although the leakage distribution could not be measured directly, from various observations it was known that it was very largely confined to the melting chamber and the end zones above the sill level. Because of the relatively heavy outgoing gas flow, under this rather heavy fuel input plus a low drift ratio, the furnace ends, slag pockets, and top checkers ran very hot, with top checkers often up to 2500°F. Silica brick was used, even in chamber arches, and the high temperature and fluxing conditions almost insured a tight sealing together of the brick near their inner surface. Some cracks would of course open up, but the operators were especially careful in watching for, and sealing any such cracks below floor level, being helped by the fact that the furnaces were small and easily accessible downstairs.

The draft control level, however, was normally at *zero or atmospheric pressure at the roof crown level* so that there was a positive suction inward at all lower levels and air leakage was continuous through all openings in and around all doors. There was also some leakage in ends (around burners, etc.) but most of this was also above the top of the downtakes. The important point here is that most of this large air leakage *became well heated before it entered the outgoing regenerative zone.* The result was that, although the checker surface was heavily burdened in both halves of reversal cycle, yet, with a drift ratio (Ca/Cg) of 0.451, it was fed with a *heating-up supply in gases outgoing of more than twice the heat absorbing capacity of the air ingoing,* so the resulting air stream to the ingoing port could be made very hot even by such an inadequate regenerator. Of course, the large air leakage

Table III. Temperature of Gases, Furnace A

	Range Over Half-Cycle, °F	Mean Temperature, °F
Temperature of gases entering, Tg_2	2400–2300	2370
Temperature of gases leaving, Tg_1	1810–1700	1770
Temperature of air entering, Ta_1	320–480	380
Temperature of air leaving, Ta_2	1800–1920	1840

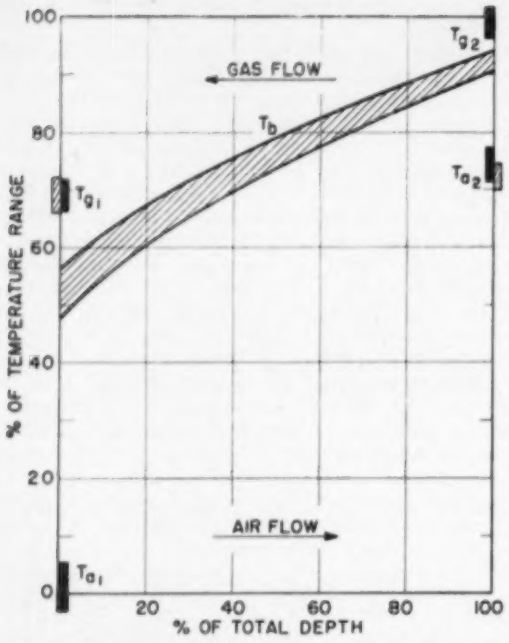

Fig. 5—Diagram of temperature measurements on furnace A. Total depth equals checkers plus rider arches equals 9 ft. Temperature range, (T_{g2} — T_{a1}). Cross-hatched band, T_b: temperatures of brick surface over reversal cycle. Solid bars: ranges as directly measured for T_{g1}, T_{g2}, T_{a1}, and T_{a2}. Cross-hatched bars: ranges for T_{a2} and T_{g1} as calculated on electrical analogue.

also robbed a large amount of useful high temperature heat from the melting chamber and carried much of it out to the waste-heat boilers (gases immediately below checkerwork were at 1770°F, and in flues usually around 1500°F or above). This condition will be referred to again below.

In this test, a few thermocouples were placed at various levels in the checker setting, so the temperature swings of the brick surfaces were measured fairly accurately. The shaded band in Fig. 5 shows the range of brick surface temperatures over the swings of, in this case, a reversal cycle of 30 min, or reversal every 15 min. The abscissae are in percentage of checkerwork depth with the zero level at left being on top of rider walls, so movement through the checkerwork is from left to right (clay brick, 2½ in. thick, solid flue setting). The ordinate scale is in percentage of the actual temperature range of the test zone involved, that is, zero represents 380°F or Ta_1 and 100 represents 2370°F, or Tg_2. The gas flow downward is from right to left and the air flow upward is from left to right. The gas and air temperatures were not measured at intermediate depths but the solid block bars in the figure represent the range of variation just above and below the checkerwork, marked as Tg_1, Ta_2, etc.

Calculations Based on the Test of Furnace A: The mathematics involved in rigorous calculations of steady state and efficiency of heat interchange in regenerators is so complex[4,5] as to be almost unworkable except by machine methods. At the time of this test, however, we had in the laboratory an electrical analogue of the regenerator[3] which could be used as a calculating machine to determine results quickly with variable values of loading, checker depth, drift ratio, etc. We first set up the same conditions of flow rate, surface area, etc., as existed at the time of the above test on furnace *A*, using the heat transfer coefficients of Fig. 20-7 in ref. 3. This gave the ranges of outgoing gas (Tg_1) and preheated air (Ta_2) temperatures (in percentage of the Tg_2—Ta_1 temperature range) shown by the cross-hatched bars in Fig. 5; the agreement to within 2 to 3 pct gave assurance that practically useful curves could be obtained for the effects of different variables. The load curves of Fig. 1 show the effect, so calculated, of varying load (that is, of varying the air flow rate with gas flow in proportion to give a certain E_L), with checker depth and surface area held constant. The lower curve is for E_L (that is, drift ratio or $Ca/Cg \times 100$) held at 46 pct as in the above test. The value of 2860 lb air per hr per 1000 sq ft of surface on abscissae and 32.5 pct efficiency represents the furnace *A* test conditions which gave the net efficiency value of 32.4 pct by direct measurement. The upper curve for E_L at 78 pct represents about the results to be expected in an "ideal furnace," that is, one in which excess air is very small and with practically no cold air allowed to leak in at any point in the whole furnace system. This curve indicates that on fuels not preheated, such as oil, tar, natural gas, etc., the maximum possible net regenerator efficiency is around 70 pct.

Fig. 6 gives curves of net efficiency (E_R) for variable checker depth and various E_L values, but with the heavy load conditions of furnace *A*, which are probably characteristic of many of our present older furnaces. By dividing the ordinates by the corresponding E_L values, E_A is obtained, which is a measure of relative air preheat temperature. It will be noticed that as the drift ratio, or E_L, decreases, E_A increases for the same size or depth of checker-

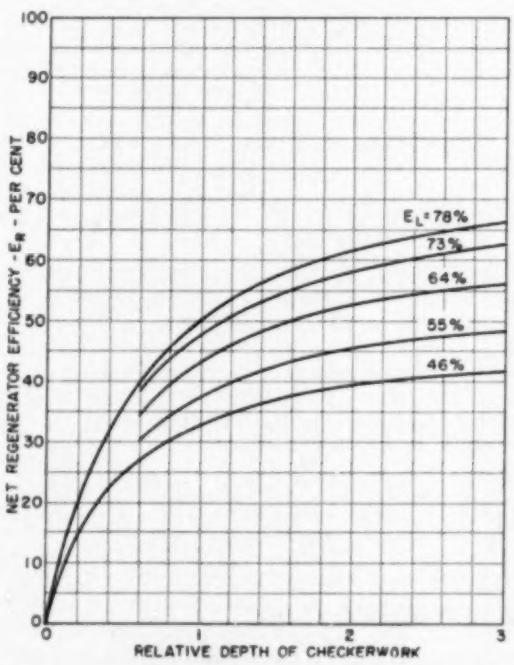

Fig. 6—Net regenerator efficiency (E_R) for increasing checkerwork depth (at constant perimeter) for several values of E_L.

work, a reflection of the conditions which produced a high air preheat temperature in furnace *A* with a heavily overloaded regenerator system. A corrolary which requires no additional curves, is that if the excess air and cold air leakage above had been directly into the regenerative zones instead of into the furnace above sill level, the dilution effect on temperature levels would have lowered both preheat temperatures and heat interchange efficiencies.

The reader may well be confused at this point by the many factors involved in regenerator efficiency and we should perhaps turn to a few direct practical considerations. This same furnace *A* gave the air preheat temperatures in uptakes at sill level and flame intensity levels plotted in Fig. 2. The range for both abscissae and ordinates is at a high level such as has been observed in only a very few modern furnaces, with relatively large and efficient regenerators and much less overloading with respect to charge and fuel input rates. It strongly indicates how air preheat temperatures measured in uptakes have no necessary relation to adequacy of regenerator size and design, and that high flame intensities should be obtainable in almost any commercial open hearth if properly managed. Also, it shows that such a result, if regenerators are too small, too inefficient, or too heavily loaded, is obtained at the cost of excess fuel, partly wasted in the form of an excessive volume and temperature in the combustion gases flowing to stack or waste heat boilers.

Thus, the reader may very logically be wondering how this extreme practice condition of furnace *A* developed, and how well it worked in terms of production rate and rebuild costs. This sort of thing cannot be answered in specific terms, with the confusion of factors involved in furnace output and refractories life. In general, this practice probably gave the best results obtainable with existing handicaps. Charge-to-tap time on all-cold charges using the worst kind of miscellaneous scrap involving rarely less than 5 hr for charging time was usually 10 to 11 hr, but frequently between 8.5 and 9.5 hr. Rebuild and refractory costs were about normal, except that checker brick had to be largely replaced on each rebuild because of high temperatures and excessive fluxes from miscellaneous scrap. Fuel consumption, because of a relatively high output rate, was not excessive for cold charge practice, at 4.5 to 5.0 million Btu per ton, and naturally a very high waste heat steam output was obtainable with efficient waste heat boilers.

The practice described really developed as an "adaptation to environment" over years of trial and error. The natural draft was not adequate to supply more air ingoing through checkers, and the checkers were inadequate to heat even this much air without the low E_L value. This may be illustrated, somewhat diagrammatically, by curves of Fig. 7. Although based indirectly on some quantitative data, these two diagrams represent only in a relative way what would happen throughout the whole length of a heavily loaded regenerative system (like the one above) operated with a high leakage above sill level and a low drift ratio (diagram *A*), if draft pressures were then changed (diagram *B*) so that the leakage above sill level was reduced to a minimum at around 10 to 15 pct, thus raising the drift ratio (Ca/Cg) from around 0.45 to 0.50 to around 0.65 to 0.72. It is assumed that for both cases the cold air leakage directly into regenerative zones is kept to

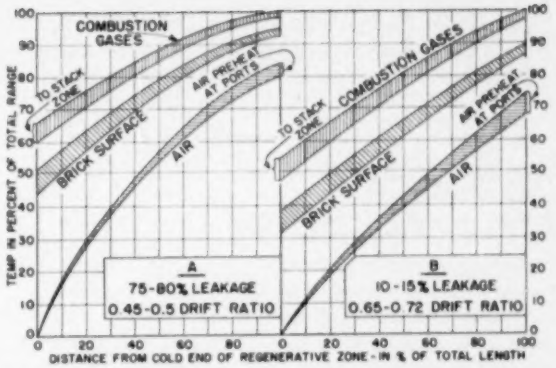

Fig. 7—Approximate temperature distribution over total regenerative zone for two values of drift ratio and air leakage above sill level.

the absolute practicable minimum. The effect here with the increased drift ratio in *B* is to markedly lower the temperature of combustion gases to the stack zone. This means that with these gases reduced in both volume and temperature the net efficiency of heat interchange, E_z, is markedly increased in case *B*. However, the *level of air preheat temperature in uptakes* is also definitely *decreased*, and in spite of an increased thermodynamic or static efficiency of the whole system, the flame intensity would drop and the furnace would slow down. It will be noted (in diagram *A*) that with the low drift ratio, the heat "soaks back" into the regenerative zone, giving a flatter gradient and higher temperature levels in the upper regenerative zone and top checkers. With the high drift ratio (diagram *B*) the whole range of brick surface temperature drops and the gradient becomes steeper so that top checkers are much cooler; also, the air preheat not only drops but becomes somewhat more variable during a reversal period.

In some remarks, above, we asked the reader to take on faith, at least tentatively, the idea that an open hearth can make good use of a large amount of excess air, partly to accentuate air oxidation in bath reactions. Perhaps the most significant aspect of furnace *A* practice is that even with as much as 70 pct excess air above fuel and bath requirements, the furnace performance was on the whole quite good, with some fuel wastage held to a reasonable amount by furnace speed. While not inherently desirable (it would have been much better to provide adequate regenerators for these furnaces) this practice indicates that excess air can be used with much greater freedom in the open hearth than some operators and fuel engineers have thought permissible. This has an important bearing on the operating problems with a more efficient double-pass checker furnace (such as is discussed in the following section) where the hot-pass checkers tend to run at excessively high temperatures.

A Furnace with Highly Efficient Double-Pass Checkers: This is a modern furnace adequately designed for about 240 tons, and operated at about 260 tons capacity. The double-pass regenerator design follows roughly the lower diagram in Fig. 4, with extra chamber length sufficient to accommodate the blind pass and about 14 ft or more of actual checkerwork depth above supporting arches in both passes. To give one actual checker test period as an example, it can be seen in Table I that the furnace *B*

Table IV. Flow Rates in Test on Furnace B

	Flow Rate, Lb per Hr	Pct Based on Theoretical Air
Total combustion gases into checker, Wg	78,960	
Oil input plus CO from bath	5,010	
Atomizing steam	1,800	
Total air (equivalent in combustion gases)	72,150	123.0
Preheated air ingoing through checker, Wa	61,810	105.6
Total air leakage between regenerators	10,280	17.4
Total air	72,150	123.0
Total theoretical air for combustion	58,600	100.0
Excess air entering outgoing checker	13,550	23.0

regenerator was much more lightly loaded than the regenerator in furnace *A*. Total heat interchange surface, in regenerator chamber only, at each furnace end was 56,000 sq ft as compared to the 7000 sq ft in the smaller furnace *A*, a difference of 8 to 1 as compared to about a 4.5 to 1 difference in size of heat. The fuel input rate could also be relatively smaller in this efficient furnace so that in this one test period the 5920 lb waste gases per hour per 1000 sq ft of surface for furnace *A* is reduced to 1410 lb per hr per 1000 sq ft in furnace *B*, and on air flow the 2860 lb per hr per 1000 sq ft is reduced to 1100 lb per hr per 1000 sq ft. On the load curves of Fig. 1, this air load rate falls within the relatively flat region approaching zero flow,¶ so that on this factor alone, the efficiency of the regenerators of furnace *B* would be expected to approach a much higher level.

¶ These load curves are really an approximation. The load rates in Fig. 1 should be based on total heat capacities, rather than total weights, of air or gases, per unit time. However, taking air load rate alone, the two are very nearly proportional.

Flow rates in this test on furnace *B* during a refining period with only a low rate of carbon drop, excess air demand above that required for the fuel input of 550 gal oil per hour being small, are given in Table IV.

In this test, Tg_1 and Ta_1 were measured at the flue just outside the chamber, instead of directly beneath the checkerwork as in furnace *A*. This accounts for the lower Ta_1 temperature in the values in Table V.

As another means of checking consistency, two values can be calculated for net efficiency, 1—E_{L_g}, the efficiency of removing heat from the gases, and 2—E_{L_a}, the efficiency in storing heat in the air:

$$E_{L_g} = \frac{Sg\ (Tg_2 - Tg_1) \times 100}{Sg\ (Tg_2 - Ta_1)} =$$

$$\frac{0.311\ (2550° - 1110°) \times 100}{0.290\ (2550° - 210°)} = 66.0 \text{ pct.}$$

(The weight of gases cancels out, Sg must be adjusted for the temperature range.)

$$E_{L_a} = \frac{(Wa)\ (Sa)\ (Ta_2 - Ta_1) \times 100}{(Wg)\ (Sg)\ (Tg_2 - Ta_1)} =$$

$$\frac{(61{,}870)\ (0.267)\ (2240° - 210°) \times 100}{(78{,}960)\ (0.290)\ (2550° - 210°)} = 63.0 \text{ pct.}$$

At steady state, and with negligible heat loss, these two values should check, so the errors in this case are reasonably small. The net efficiency here is twice that of the 32.4 pct for furnace *A*. This large difference is partly due to the lower load rate, and to the much higher coefficient of heat transfer from brick surface to air due to the higher flow rates in the double-pass design. However, it also depends largely on the much higher drift ratio due to the low air leakage value of 17.4 pct total between regenerators:

$$E_L = \frac{Ca}{Cg} \times 100 = \frac{(Wa)\ (Sa)\ (Tg_2 - Ta_1) \times 100}{(Wg)\ (Sg)\ (Tg_2 - Ta_1)} =$$

$$\frac{(61{,}870)\ (0.271) \times 100}{(78{,}960)\ (0.290)} = 73.2 \text{ pct.}$$

From the load-efficiency curves of Fig. 1, it is possible to interpolate approximately for this case. At the air load rate of 1070 lb per hr per 1000 sq ft and interpolating for $E_L = 73$ pct, an E_B value of around 65 to 67 pct would be obtained, which is in good agreement with the above values of 63.0 and 66.0 pct. This indicates that Fig. 1 is a good approximation for regenerators in which, 1—roughly all the heat interchange surface is actually swept by both gas and air streams, and, perhaps, 2—there is a minimum of air leakage directly into the regenerator zones involved.

Furnace *B* had a minimum of air leakage below floor level, similar to furnace *A*. Its draft pressure at the main roof (+0.07 to 0.09 in. water), however, was such that most door frames and peepholes were blowing out and there was much less leakage above floor level than in furnace *A*. Instead of the 87.5 pct of theoretical air in furnace *A*, 105.6 pct of theoretical air was passed through the regenerator ingoing in the more efficient furnace *B*. The resulting drift ratio of 73.2 pct compared to the 45.1 pct of furnace *A* is the essential difference between these two furnace control practices. The absolute efficiency,

$$E_A = \frac{64.5}{73.2} = 88 \text{ pct,}$$

is much above the 71.8 pct for furnace *A*, corresponding to the respective 2240° and 1840°F for air preheat at the bridgewall.

Air preheat temperatures *in uptakes* were about the same in both *A* and *B* practices, however, (around 2300° to 2400°F or sometimes higher) simply because in furnace *B* with the longer, more efficient regenerative zone, the "upper zone" was a smaller proportion of the total heat interchange effect. That is, the air temperature rose around 200°F from bridgewall to uptakes in furnace *B*, but around 500°F in furnace *A* in the same zone. On the other hand, the more heavily burdened checkers in furnace *A* had to have a larger difference in temperature between top checker brick surfaces and the air passing over them, so they would sometimes get about as hot as those in the hot pass of furnace

Table V. Temperature of Gases

	Mean Temperature, °F
Temperature of gases entering regenerator chamber, Tg_2	2550
Temperature of gases leaving regenerator chamber, Tg_1	1110
Temperature of air entering regenerator chamber, Ta_1	210
Temperature of air leaving regenerator chamber, Ta_2	2240

Table VI. Flow Rate and Temperature Conditions, Furnace B

	Flow Rate, Lb per Hr		Pct Based on Theoretical Air
Total combustion gases into checker, Wg	58,420		
Oil input plus CO from bath	3,340		
Atomizing steam	1,900		
Total air (equivalent in combustion gases)	53,280		136.0
Preheated air ingoing through checker, Wa	50,400		128.6
Total air leakage between regenerators	2,880		7.4
Total air	53,280		136.0
Total theoretical air for combustion	39,170		100.0
Excess air entering outgoing checker	14,110		36.0
Temperature of gases entering regenerator, Tg_2		2550°F	
Temperature of gases leaving regenerator, Tg_1		1100	
Temperature of air entering regenerator, Ta_1		170	
Temperature of air leaving regenerator, Ta_2		2120	

B. Nevertheless, it can be seen that this hot pass could get overheated much more easily. The top checkers in furnace A got hot only because of the low E_L value and could easily be cooled by decreasing air leakage above sill level. In furnace B, the top checkers can only be kept from overheating¶¶ by, 1—keeping the leakage above sill level to a minimum, and then if necessary, by 2—decreasing fuel input, and by 3—increasing the amount of excess air ingoing so that cooling effect on checkers is still further increased relative to heating effect on the other half of the reversal cycle.

¶¶ That is, assuming that one does not wish to resort to the rather ridiculous alternative of wall openings for intentional air leakage placed somewhere in the upper regenerative zone.

For example, in one other test period during refining on furnace B, it happened that bath action was small and the bath was hot, so heat absorption was small and outgoing gas temperatures tended to rise. The fuel input was therefore decreased to 355 gal oil per hour, a low rate for such a large furnace. The ingoing air rate was kept relatively high, giving the flow rate and temperature conditions shown in Table VI.

With only 7 pct air leakage and nearly 30 pct excess air ingoing, the E_L value was raised to 80.5 pct. Gas temperatures shown remained about the same as in the case above (with 550 gal oil per hour but faster heat absorption in the bath), air preheat temperature at bridgewall dropping somewhat with this higher E_L value. In proportion to furnace size, fuel input never needed to be as high in the more efficient furnace B as in furnace A, and had to be lowered to less than half the relative value in periods such as that described here. It should be obvious that with more fuel and with E_L values much lower than around 70 pct, the hot pass checkers in furnace B would have become seriously overheated.

Air preheat temperature in any type of furnace is limited not by regenerator efficiency but by the practical limiting operating temperatures for refractories, mainly in top checker courses. It may also now be evident why regenerator efficiency and air preheat temperature were referred to as two more or less independent factors. In A and B furnace practices, the two extremes in relative adequacy of regenerative equipment are illustrated, yet by proper adjustment of air input and of amount and distribution of air leakage, both furnaces gave about the same high air preheat levels and flame radiation intensities.

One might logically question, then, why the bother with larger and more complex and more efficient regenerative equipment? The difference here lies in 1—a capacity to provide a *higher rate* of preheated air supply in furnace B, and 2—the avoidance of wastage of high temperature heat into stack zone involved in the cold air leakage of furnace A practice. The latter effect can be illustrated by comparing the relative percentages of high temperature or available heat per unit of fuel input in the two practices as shown in Table VII.

Even throttled down to a fuel input of only 355 gal of oil per hour, furnace B was able to deliver more heat actually useful to the melting chamber process (per unit of bath weight) than furnace A with a fuel rate more than twice as large in proportion to heat size. The load rate of furnace B is in this case only about 900 lb air on the scale of Fig. 1 and it can more than double its fuel rate without losing much regenerative efficiency or air preheat and flame intensity. In general, the chief operating problem with furnace B is to "hold it down" by keeping a moderate flame length and fuel rate, keeping cold air leakage to a minimum *in both melting and regenerative zones* and also supplying *plenty of excess air through checkers ingoing* so that the E_L value is always high. Comparisons of performance are not really accurate, as has been indicated, but very roughly furnace B with its efficient double pass checker can give a speed somewhat greater than furnace A in comparable practice and do this with probably not much more than one half the fuel rate per ton of ingots.

To try to explain why furnace A, with such a relatively low efficiency (20 pct) in high temperature heat delivery and such large cold air leakage and excess air levels, could perform as well as it did is a more puzzling problem and would lead us too far afield from our subject of regenerator efficiency and air preheat. We would suggest, however, that as we have mentioned above, the open hearth bath process can use excess air to good advantage even, apparently, when it comes from cold air leakage directly into the melting chamber. Since in many of our older furnaces the regenerator capacities are rather low, it is almost certainly possible, by operating with somewhat lower values of E_L, to increase air preheat temperatures and flame intensity levels. These conditions will naturally coincide with more

Table VII. Comparison of Efficiency in Furnaces A and B

	Furnace A	Furnace B
Heat size, tons	55	260
Fuel input in test periods, lb oil per hr	1,385	2,750
Heat of combustion, per lb oil, Btu	18,400	18,800
Heat in air ingoing, per lb oil, Btu	9,000	11,300
Total heat input, per lb oil, Btu	27,400	30,100
Heat in outgoing gases, per lb oil, Btu	23,800	16,900
Available heat, per lb oil, Btu	3,600	13,200
Available heat to melting chamber, pct	19.6	70.2
Btu per hr per ton in bath, available heat	90,000	148,000

Table VIII. Flow Rate and Temperature Conditions, Furnace C

	Flow Rate, Lb per Hr		Pct Based on Theoretical Air
Total combustion gases into checker, Wg	151,030		
Tar input plus CO from bath	8,580		
Atomizing steam	1,980		
Total air (equivalent in combustion gases)	140,470		168.5
Preheated air ingoing through checker, Wa	71,820		86.1
Total air leakage between regenerators	68,650		82.4
Total air	140,470		168.5
Total theoretical air for combustion	83,410		100.0
Excess air entering outgoing checker	57,060		68.5
Temperature of gases entering regenerator, Tg_2		2350°F	
Temperature of gases leaving regenerator, Tg_1		1420	
Temperature of air entering regenerator, Ta_1		190	
Temperature of air leaving regenerator, Ta_2		1680	

excess air over the bath, and performance may be thus improved in many cases.

A Furnace with Large Single-Pass Regenerators but Bad Distribution of Leakage: A checker efficiency test on furnace *C* is included here chiefly because the furnace during the test period happened to have a bad leakage condition which is rather typical of conditions at various times in many operating furnaces. In fact, a certain amount of this type of air leakage is probably so common as to be more representative of average shop practice than either *A* or *B* furnace practices. Furnace *C* is a fairly new and modern design, with single-pass regenerators, about 14 ft in checkerwork depth above supports, and a chamber length of about 30 ft resembling closely the upper diagram in Fig. 4. Total potential "wiped surface" area for heat interchange in regenerators (between bridgewall and flue exits) is close to 39,700 sq ft at each furnace end. In the test period described here, the load rate on air flow was about 1800 lb per hr per 1000 sq ft of wiped surface area, this being anywhere from 70 to 100 pct more load than on furnace *B*, but a considerably lighter load than that on furnace *A* (see Table I). Under optimum conditions, its performance should not be very much below that of furnace *B*.

The flow rates in one test period during refining are listed in Table VIII.

The E_z values from the data of Table VII are

$$E_{z_2} = \frac{0.312\ (2350°-1420°) \times 100}{0.290\ (2350°-190°)} = 46.2 \text{ pct.}$$

$$E_{z_1} = \frac{(71{,}820)\ (0.265)\ (1680°-190°) \times 100}{(151{,}030)\ (0.290)\ (2350°-190°)} = 30.0 \text{ pct.}$$

The drift ratio was

$$\frac{Ca}{Cg} = \frac{(71{,}820)\ (0.268)}{(151{,}030)\ (0.289)} = 0.441, \text{ that is, } E_L = 44.1 \text{ pct.}$$

It could be argued that this data should have been thrown away and new tests made. However, the time required to get accurate integrated values for Tg_2 and Ta_1 above the bridgewall was not practicable under the existing flow condition on a commercial furnace; also, we knew the conditions existing, such that we could usefully interpret the results in spite of the large inconsistency between the two E_z values. Two complicating factors were present: 1—a large air leakage into the upper regenerative zone (fantails, etc.); and 2—some channeling of gas and air flows in this long, single-pass chamber. As a result, it is very probable that in this data, the Tg_2 value is too high and the Ta_2, or perhaps the Tg_1, value is too low. On fairly reasonable assumptions, we calculated that the true E_z value here was about 34 to 37 pct. For $E_L = 44.1$ pct, and for the air load rate of 1800 lb, on the abscissae of Fig. 1, the corresponding E_z value by extrapolation is about 35.5 pct.

Direct measurement of leakage distribution was hardly practicable in this test, but from observation, we can say with fair certainty that roughly 90 pct of this total air leakage of 82 pct between regenerators was *into the upper regenerator zones*, rather than directly into the melting chamber above sill level, as in furnace *A*. Most of this leakage was into the outgoing zone. Visual observation showed that the fantail arches were very leaky, and rather large temperature differences could be seen inside the fantail zone. In trying to maintain a certain draft pressure at the main roof arch, the draft fan was in effect acting like a pump trying to pull a slight vacuum in a chamber to which it was connected by a very leaky tube. The regenerator chamber itself was rather tight, but between bridgewall and uptake large cold air leaks occurred. Draft pressure at roof arch could hardly be lowered below about +0.09 to +0.10 in. of water so that suction around doors at sill level was small and not much air leaked above sill level. With the bad thermal condition of the whole system, some excess fuel was used as an offsetting factor. Ingoing preheated air was only 86 pct of theoretical, similar to furnace *A* practice. But the leakage, mainly between furnace end and checker bridgewall outgoing, was so large that total equivalent air in outgoing gases was 168 pct of theoretical. Handling this large volume of gases required about the maximum pull of the fan, so that the suction at points below sill level increased to favor more leakage.

The very large volume of exit gases (151,000 lb per hr) and the flue temperature above 1400°F, meant that an excessive amount of heat was being delivered to the waste heat boiler. Reasoning from argument based on furnace *A*, however, a compensating advantage would be expected from this heat waste and the low E_z value of 44.1 pct (even lower than in the furnace *A* practice). Apparently this low drift ratio should have given even higher air preheat temperatures and flame intensities than either furnace *A* or *B*, considering the fairly moderate air flow loading on the regenerator surface. However, the air leakage which produced this unbalanced drift ratio *was in the wrong zone of the system*, which is the main point we want to bring out from this test. In furnace *A* the leakage was above sill level, which meant that it: 1—supplied extra air to help generate useful heat by oxidation effects above the bath or on melting scrap surfaces, and 2—the excess air borrowed heat from the combustion and from hot surfaces so that it entered the regenerative zone at about the full "spillover temperature" level. In furnace *C*, the air leak was mostly below sill level, into the upper regenerative zone outgoing. There it: 1—helped to complete any "tail-end combustion" (caused at times by the combination of high fuel rate, lack of air ingoing,

and heavy CO evolution from bath boils), or it 2—simply cooled the gas stream so that temperature potential for heat interchange from brick surface was lowered.

The last effect was undesirable since it resulted in directly lowering air preheat. The first effect was also bad in part in that it involved little or no excess air over the bath and loss of some available heat evolution in the melting chamber where it could have done the most good.

On the other hand, the high fuel rate and the extra heat from this "tail-end combustion" directly in upper regenerative zones at least in certain periods of the heat did have a compensating effect toward raising the air preheat temperature. The air leaving the checkerwork was rarely above about 1750° to 1800°F, but when it reached the port end, it was frequently 550° to 600°F hotter, giving preheat levels of 2300°F and above *in certain periods.*

In brief, the writer regards the practice on furnace *C* during the test period as representing a fairly sick furnace; although total air leakage was also excessive in amount, its worst feature was that of being in the wrong place, being below sill level, instead of above it as in the furnace *A* practice. Its performance was noticeably below that of other furnaces in the shop, but with high fuel input the difference would not be too obvious, partly because the other furnaces would often suffer from variable amounts of the same bad leakage distribution.

In trying to diagnose such a condition, simple gas analyses for CO_2 and O_2 at the flue exit, plus accurate values for fuel input, carbon drop, and rates of atomizing steam and ingoing air flow would give the basis for calculating the flow rates and percentages of total leakage and excess air as tabulated above. These data, plus the measured pressure at roof arch and visual observations, would often suffice to indicate, approximately, the distribution of the air leakage, although measurements of air temperature ingoing and of draft pressures outgoing, at various points, might be helpful. However, suppose the diagnosis on this furnace had depended entirely on a few preheat air temperatures measured only in uptakes about at sill level. If these measurements happened to coincide with periods of high temperature level in melting chamber with little bath activity, or immediately following heavy boil periods in the bath, coupled with high fuel input, temperatures of 2250° to 2350°F probably would have been obtained and there would have been little reason to suspect or to look for the very serious leakage condition actually present below floor level.

In correcting this practice on furnace *C* we would presumably begin by making the structure as tight as possible at all points below floor level, perhaps with special attention to fantail arches, even to the point of redesign and rebuilding if necessary to make tight sealing more practicable. With each outgoing zone made tight from stack or fan to top of uptakes, we would now "have control" in the sense of a decreased outgoing gas volume and the ability to obtain any desired draft effect above sill level. In furnace *C*, the regenerator capacity is reasonably good so that the optimum E_L value would probably be somewhere between the two extremes represented by furnaces *A* and *B* (Table I). One might begin by adjusting the pressure at roof arch to a level such as to blow out at three or four doors and suck in at No. 1 ingoing. This would give a minimum of leakage above sill level, and the air ingoing would be adjusted to the theoretical for the fuel or at a moderate excess. This would presumably give too high an E_L value, top checkers would not get very hot and air preheat temperatures would be too low. The pressure at roof level would then be lowered to allow leakage in two or three doors; with mean air rate ingoing kept the same or lower, E_L would be decreased; top checkers and air preheat would both increase in temperature level. Gradual lowering of the roof pressure over several heats for the same mean air rate ingoing should lower E_L and raise top checker brick temperature until it would approach perhaps 2300° to 2400°F at certain periods in most heats. This should give a maximum practicable air preheat level in uptakes, and furnace sharpness should be about at its best for a reasonable refractory and rebuild cost. In theory, at least, this should bring furnace *C* to about the same peak of performance, for the existing furnace equipment, as we believe to have obtained in the furnace *A* and *B* practices. We do not mean to imply that this is a complete "recipe" for open hearth control, because, whether our interpretation of the problem is correct or not, many details may be different in various furnaces in such a complex process. However, it represents the broad outlines of the general method for adjusting any furnace to its best performance for its given equipment in regenerator capacity, based on the tests on the three furnaces given above.

Any such "adjustment" to lower E_L values to get high air preheat from more or less inefficient regenerative equipment is of course a compromise to get maximum speed at the expense of some waste of fuel. The very reasonable consequence is, obviously, that only if the regenerators approach maximum efficiency can the best *combination of both high production rate and low fuel consumption* be obtained. The above tests indicate that furnace *B* did approach this condition, with a high regenerative efficiency that could hardly be appreciably increased. In furnace *A* the only solution would have been a costly enlargement of checker chambers and changes in flue layout. In furnace *C*, the 30 ft checker chambers are so long that they might be modified to a double-pass design within the boundaries of existing chamber walls with no changes in flue layout. This involves, in the space required for the passages and walls of the blind pass, a much larger proportion of the length than is contributed in heat exchange surface. But by making a number of larger passages in the blind pass with a rather high flow rate and by using thinner brick and smaller checker flues in the cold pass, it might be possible to end up with the same or a slight increase in total heat exchange surface. This is perhaps a rough guide on the question of such a modification to double pass design; that is, if the resulting two-pass chamber has about as much total effective surface, then the higher brick-to-air heat transfer coefficients due to flow rates more than 100 pct higher and a better utilization of the total effective surface from less channeling of gas and air flows, should combine to give perhaps a worthwhile increase in efficiency.

A Few Ideas on A Method for Open Hearth Control

During the course of a development several years ago in this Laboratory of a method[10] for automatic open hearth reversal control, a general idea of the

simplest means of furnace control was evolved which seems to have been confirmed by later experience such as the tests included above. As a part of this reversal method, radiation receivers were assumed to be kept sighted on the hottest area of top checker brick at either end of the furnace. These maximum top checker surface temperatures registered, at least during gas cycles, on a recorder having an adjustable maximum temperature setting. As an emergency method of reversal, any brick temperature in excess of this setting, which might be around 2400°F, would actuate a relay to reverse the furnace, this occurring, of course, only when the normal reversal impulse was not actuated before this maximum desired checker temperature was reached. This scheme, besides giving the first helper a continuous indication of his highest checker brick temperatures, would, when he was too busy to observe them, start reversing the furnace on shorter cycles to give protection and a warning to him of this condition so he could either decrease his fuel rate or increase his ingoing air rate. However, the idea behind it was also that such temperature levels *should be reached* one or more times during a heat whenever the furnace was properly tuned up to maximum speed. Therefore in a furnace which rarely or never attains this practical maximum of checker temperatures, one should begin to look for leakage below floor level, for E_L values too high, etc., until checker temperatures become high enough so that this reversal impulse is actuated at least occasionally, perhaps at least once in each heat.

This is probably not the whole answer to the complex control problem, but the writer still believes that it represents about the most practical general basis for such control toward maximum furnace speed with safe conditions below floor level where the first helper can normally make few, if any, direct observations. Direct measurement of air preheat temperatures in uptakes is much less useful for day-to-day control. Such measurements are desirable, at least occasionally, since the difference between air temperature and top checker temperature will vary considerably due to cold air leakage, air rate ingoing, etc. But they are difficult to make, and as has been indicated, are often puzzling to interpret with the many factors involved. They are often useful as one auxiliary tool for occasional diagnosis, along with gas analysis, draft pressures at various points, etc., but for regular day-to-day operation control, the above method of recording and reversal on maximum checker temperatures seems a more practical tool if given proper maintenance and repair.

Summary and Conclusions

In conclusion, we summarize briefly the rather involved argument above, for which the only excuse is the one at the beginning of the paper, namely, that in any such complex problem as is involved in air preheat vs regenerator efficiency, the problem cannot really be clarified unless about all of the essential factors are included.

First, we confirm the logical concept that for the best *combination* of furnace speed *and* low fuel rate, net regenerative efficiency (E_R) should be as high as possible. The theoretical maximum for this appears to be around 70 to 72 pct. The most practical and reasonably simple design capable of approaching such a level of E_R that has been developed to date appears to be the double-pass design, for which an example is shown in furnace *B*, which gave an E_R value of around 64 to 66 pct. It should have a checkerwork depth of around 15 to 16 ft and sufficient heat exchange surface so that the load rate on ingoing air is down to around 900 to 1100 lb air per hr per 1000 sq ft of effective wiped surface in the regenerator between the checker bridgewall and the flue exit.

However, in the general problem for the industry as a whole, we are up against the fact that only a few existing furnaces have sufficient effective regenerative capacity to yield E_R values approaching this level. Most of the older furnaces have greatly overloaded regenerative surface, probably above 2000 lb air per hr per 1000 sq ft of surface, and many of the newer furnaces with very long single-pass chambers do not get fully effective use of the surface area due to channeling and low flow rates, giving lower average brick-to-air heat transfer coefficients. In a number of such cases, as indicated above, it may be possible to obtain some improvement by modifying these long chambers to the double-pass design. However, at best, for the industry as a whole, it should be helpful to know more about possible methods for obtaining higher air preheat from more or less inadequate regenerative capacity.

The discussion above boils down to the thesis that by allowing more air leakage above sill level (always with leakage near the absolute minimum below sill level; also, with ingoing preheated air rate held at about theoretical or even below) the drift ratio or E_L value is decreased, unbalancing the two flow rates (air up vs gases down) so that checker brick temperatures rise toward the practical maximum of around 2300° to 2400°F. At some optimum level of E_L, almost any existing regenerator, at the cost of some fuel waste to stack or boilers, can yield the practical maximum of air preheat and flame intensity levels. The chain of reasoning involved in this conclusion can be summarized as follows:

1—As a basis for argument, the reader is asked to assume that excess air in rather large amounts, even above the combustion requirements for both fuel and bath reactions, can be used in the open hearth without serious handicap to melting and general heat transfer rates to the bath. In all active bath periods this amounts to around 30 to 70 pct above fuel requirement alone, or even higher. A full discussion of this proposition would involve another paper, although the practice on furnace *A* affords a certain amount of evidence for it.

2—As a consequence, we must first distinguish between three sources of such excess air; a—extra air input through the regenerator ingoing, b—leakage air directly into regenerator zones either ingoing or outgoing, especially between checker bridgewall and top of uptakes, and c—leakage into the melting chamber zone above sill level as controlled by the pressure at roof arch. Effect (a) tends to raise E_L and lower checker temperatures, being therefore in the wrong direction for overloaded regenerators. Effect (b) tends to lower air preheat and checker temperatures except at times when it may burn excess combustibles, but then it will also be bad for maximum heating effect over the bath. Effect (c) unbalances the drift ratio and lowers E_L in the desired direction.

3—It is therefore of first importance to tighten up the furnace system against leakage below sill

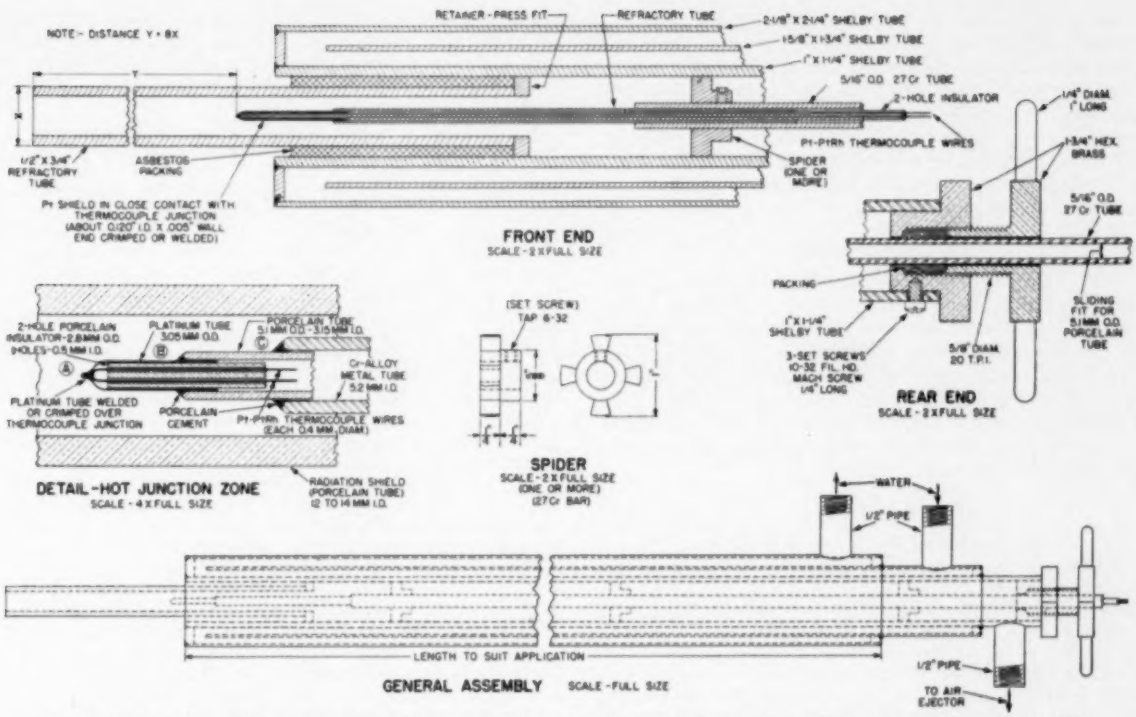
NOTE - DISTANCE Y = 8X
RETAINER - PRESS FIT
REFRACTORY TUBE
2-1/8" X 2-1/4" SHELBY TUBE
1-5/8" X 1-3/4" SHELBY TUBE
1" X 1-1/4" SHELBY TUBE
5/16" O.D. 27 Cr TUBE
2-HOLE INSULATOR
1/4" DIAM. 1" LONG
Pt-PtRh THERMOCOUPLE WIRES
SPIDER (ONE OR MORE)
1-3/4" HEX. BRASS
1/2" X 3-1/4" REFRACTORY TUBE
ASBESTOS PACKING
Pt SHIELD IN CLOSE CONTACT WITH THERMOCOUPLE JUNCTION (ABOUT 0.120" I.D. X .005" WALL END CRIMPED OR WELDED)
FRONT END
SCALE - 2 X FULL SIZE
PACKING
1" X 1-1/4" SHELBY TUBE
3-SET SCREWS 10-32 FIL. HD. MACH SCREW 1/4" LONG
5/8" DIAM. 20 T.P.I.
SLIDING FIT FOR 5.1 MM O.D. PORCELAIN TUBE
REAR END
SCALE - 2 X FULL SIZE
(SET SCREW) TAP 6-32
2-HOLE PORCELAIN INSULATOR - 2.8 MM O.D. HOLES - 0.5 MM I.D.
PLATINUM TUBE 5.05 MM O.D.
PORCELAIN TUBE 5.1 MM O.D. - 3.15 MM I.D.
Cr-ALLOY METAL TUBE 5.2 MM I.D.
PLATINUM TUBE WELDED OR CRIMPED OVER THERMOCOUPLE JUNCTION
PORCELAIN CEMENT
Pt-PtRh THERMOCOUPLE WIRES (EACH 0.4 MM DIAM.)
DETAIL - HOT JUNCTION ZONE
SCALE - 4 X FULL SIZE
RADIATION SHIELD (PORCELAIN TUBE) 12 TO 14 MM I.D.
SPIDER
SCALE - 2 X FULL SIZE (ONE OR MORE) (27 Cr BAR)
WATER
1/2" PIPE
LENGTH TO SUIT APPLICATION
1/2" PIPE
TO AIR EJECTOR
GENERAL ASSEMBLY
SCALE - FULL SIZE

Fig. 8—Design of an aspirating or velocity thermocouple. Horizontal dimension reduced approximately 75 pct for reproduction.

level to the maximum degree possible, not merely to eliminate certain bad effects of leakage into regenerative zones, but also to bring the system under control, enabling the exhaust fan to produce any desired lower pressure at the roof arch. Usually, the critical zones will be at the hard-to-get-at places between checker bridgewall and uptakes, such as fantail arches, which may need redesign to favor better sealing.

4—As leakage air around doors, etc., above sill level increases, relative to the rate of preheated air flow ingoing, the whole of the regenerative zones gets more heating and less cooling in the reversal cycle. Exit gas temperature rises and E_R decreases, but as illustrated in diagram *A* of Fig. 7, the heat "soaks back" farther into the regenerator zones, thus increasing preheat air temperatures in uptakes as the E_L value is lowered.

5—At some such decreased E_L value, the top checker brick will presumably be running too hot relative to cleaning or checker maintenance costs, indicating that E_L is now somewhat below its optimum value. Such optimum E_L values would lie somewhere between 68 and 46 pct, rarely if ever as low, however, as in the practice on furnace *A*. Optimum values of checker temperature at their hottest periods are not too well known, but may be in the range of 2350° to 2450°F.

As a direct consequence of this argument, however, it follows also that on furnaces with *highly efficient, lightly loaded regenerators*, as for example most of those equipped with the double-pass design, the main problem may be the opposite one of guarding against excessive temperature in the top checkers of the hot pass, the following methods being indicated by the above discussion:

1—Moderate fuel rates, with more fuel cutting at times when the bath is not absorbing heat. Good atomization and moderate flame length.

2—Plenty of excess air supply (up to 40 to 60 pct in certain boil periods) for bath reactions or when top checker surfaces approach 2350° to 2450°F.

3—Good sealing *both below and above sill level* with a higher roof pressure for minimum leakage, so that nearly all excess air above fuel requirement *is supplied through the regenerator ingoing*, thus keeping E_L as high as possible.

The large number of effects, often confusing, which determine air temperature in uptakes at a given instant makes the interpretation of measured air temperatures, as with the velocity couple[1] often very difficult, especially when these values are unaccompanied by other related data. In the long run, it may be easier and more profitable to make such measurements of gas composition, etc., as were involved in the tests for regenerator efficiency summarized above, among which velocity couple measurements of air or gas stream temperature at various points may be very useful. By whatever methods that may be used for measurement, however, what is needed are reasonably accurate values for the rates of flow of gases down and of air up in the regenerators and of the amount of leakage air, also, a knowledge of the locations in the system into which most of it is leaking; the demand for excess air should be known with respect to fuel and bath reaction oxidation requirements and perhaps the top checker brick temperatures. It may then usually be possible to interpret the situation rationally and to make a more intelligent choice of more frequent routine measurements or observations.

It is suggested that for day-to-day control, one useful tool for the first helper is a continuous temperature record on zones of maximum temperature in checker brick at each furnace end, coupled with automatic reversal whenever some set temperature limit is exceeded. The shorter reversal period can

then be a warning to indicate the need for either a higher ingoing air or a lower fuel rate, or both. Also, when such a maximum safe temperature is seldom or never approached, it may serve to indicate the need for more air leakage above sill level to lower the E_L or drift ratio in regenerative zones, assuming always that air leakage below sill level is frequently checked and held always at the very lowest possible amount.

Acknowledgments

This paper represents several years of work and tests made in many plants of the U. S. Steel Corp. as well as at this Laboratory. The writer is indebted for help and cooperation to many of the open hearth operators. Former members of the laboratory staff who contributed were J. W. Bain, K. Heindlhofer and C. Siddall. Present staff members L. O. Sordahl and J. B. Wagstaff are responsible for much of the work involved.

Appendix

An Aspirating Thermocouple Design

The paper by Marsh[1] discusses some of the problems in measuring gas temperatures in the open hearth system, as well as a good design for an aspirating or velocity thermocouple for such measurement. In spite of certain more or less inherent disadvantages of this method, it seems to be the only accurate and reasonably practical technique yet available for measuring the more or less rapidly changing temperatures of either gas or air streams in the system. This has been made somewhat easier by the development of high speed recorders which can accurately follow and record a temperature which may occasionally be changing by as much as one or more degrees Fahrenheit per second. But the real difficulty is still that of measuring the true gas temperature instead of getting values which may be closer to the higher or lower temperatures of the surrounding wall surfaces. This is especially true in the case of the preheated air stream at such points as above the checker bridgewall or near the top of the uptakes, where visible surfaces are often hotter than the air stream by several hundred degrees Fahrenheit. These visible surfaces can pour out heat rapidly by radiation, whereas the air can only give up its heat by actual contact with the measuring couple.

Any design of aspirating or velocity thermocouple, of which there have been dozens reported in the literature, is usually a compromise between the requirements for accuracy or maximum temperature range, and for convenience in use, the latter being especially important around an open hearth furnace. The design shown in Fig. 8 has been found to be fairly simple to assemble and repair, which is the main reason for describing it briefly here.

This design is the result of trials with several different arrangements, one of the earlier ones having been described in a paper[11] in a Symposium on Gas Temperature Measurement conducted by the British Institute of Fuel in 1939. This design was used in the earlier tests on furnace *A* described above. The later design shown in Fig. 8, which gives probably no more accurate results but is more convenient to use and maintain and usually gives more measurements before replacements of parts are required, was used in the tests on furnaces *B* and *C*. This design, which is largely self-explanatory from the diagram, was pointed mainly toward the following effects: 1—to give the portion adjacent to the hot junction a high rate of heat absorption by convection and a low heat capacity, and 2—to enable the use of only one simple shield tube.

The diagrammatic enlarged detail of the hot junction zone will illustrate these points. The last length of two-hole porcelain insulator here is of minimum size for 0.4 mm couple wires; this, plus the wires and the thin platinum tube sheath total to a small heat capacity. Also the platinum tube surface tends to absorb and conduct heat rapidly by convection transfer, and is in good thermal contact with the couple junction, to give effect No. 1.

For effect No. 2, the bright surface of the platinum tube has a low emmissivity so that it should reflect some 80 to 85 pct of the radiant energy coming from the inner surface or the open end of the single porcelain shield tube. This single shield tube cannot block out quite all the radiant energy but by the combination of the reflectivity of the platinum tube and its rapid heat interchange with the sucked-in air or gas stream, the error, with only a rather moderate gas velocity, appears to be down to a few degrees, although we have not attempted any absolute check on its accuracy. A double shield tube, with the sucked-in stream flowing between the two tubes as well as inside the inner one, would reduce the error, but the single shield tube, which here is simply packed into the water-cooled tube in a concentric position with asbestos rope, is much easier to remove and replace.

The hot junction need only project about 1 in. or a little less beyond the end of the water-cooled metal tube (we have used anywhere from 6 to 14 ft of free length of water-cooled tube, depending on the accessibility of the point to be measured in the furnace). Thus the porcelain shield tube need only project about 5 in. This part is fragile, however, and can also be cracked by thermal shock with too rapid heating or cooling. When used in part on outgoing gases, the platinum tube sheath should be cleaned and polished a little, occasionally, to maintain its reflectivity.

We have used one unit on both air and combustion gases for a few dozen reversal periods without appreciable damage, where temperatures did not exceed about 2550°F. Measurement of outgoing gases in downtakes, up to around 2900° to 3000°F, caused rapid blackening of the platinum tube and some deterioration of the shield tube, and the couple would soon deteriorate at its hot end, so that this higher range above about 2600°F on gases is not very practicable except for a few occasional readings at risk of some replacement. On air streams up to perhaps around 2800°F, the design seems to give rather good life, with some experience in handling.

References

[1] J. S. Marsh: Significance of Air Temperature in Open Hearth Operation. *Yearbook* Amer. Iron and Steel Inst. (1951) pp. 185-207.

[2] K. Heindlhofer and B. M. Larsen: An Electrical Analogue of the Flow of Heat in a Regenerator System. *Trans.* AIME (1945) **162**, pp. 15-36.

[3] *Basic Open Hearth Steelmaking.* (1951) 2nd Edition. Physical Chemistry of Steelmaking Committee, AIME.

[4] W. Dyrrsen: Preheaters for Open Hearth Furnaces and Their Relation to Waste Heat Boilers. *Mining and Metallurgy* (January 1928) **9**, pp. 12-17.

[5] W. W. Kompart: Economics of a 500-ton Open Hearth Furnace. *Proc.* Assoc. Iron and Steel Engrs. (1951) pp. 145-147.

[6] W. E. Groume-Grjimailo: *The Flow of Gases in Furnaces.* (1923) Fig. 51 and pp. 93, 97. New York. John Wiley and Sons.

[7] Chap. 21, p. 840 of ref. 3.

[8] W. Nusselt: The Theory of Air Preheaters. *Ztsch. ver. deut. Ing.* (1927) **71**, pp. 85-91.

[9] W. Nusselt: The Steady State in the Air Preheater. *Ztsch. ver. deut. Ing.* (1928) **72**, pp. 1052-1054.

[10] B. M. Larsen and W. E. Shenk: A Completely Automatic Control of Open-Hearth Reversal. *Trans.* AIME (1945) **162**, pp. 37-48.

[11] B. M. Larsen, C. Siddall, and K. Heindlhofer: A Modified Aspirating Thermocouple for Gas Temperatures. *Journal*, Inst. Fuel (British), Gas Temperature Measurement Special Issue (March 1939) **12**, pp. S55-56.

Chromium Distribution Between Liquid Iron and Molten Basic Slags

by Nicholas J. Grant, Earl C. Roberts, and John Chipman

An equilibrium study was made of the distribution of chromium and oxygen between liquid iron, containing less than 1 pct Cr, and simple slags of the $CaO(MgO)$-SiO_2-FeO-Cr_2O_3 type in the temperature range 1526° to 1734°C. The effects of slag oxidation, temperature, and basicity were observed.

IN spite of the fact that chromium is one of the most important alloying elements in steel, and exists in almost all steels as a significant residual element, little research has been done to determine its behavior in basic steelmaking processes. Considerably more work has been done under silica-saturated acid slag conditions. Körber and Oelsen,[1] Herasymenko,[2] and others have generally agreed that in acid steelmaking practice the chromium in the slag behaved as if it were present as the chromous ion (CrO). Work by Hilty[3] in high chromium slags also indicated that chromium may exist as CrO.

In basic slag systems no equilibrium data exist. Based on individual studies of basic open hearth and electric furnace practice, Bardenheuer,[4] Rockrohr,[5] and Hauck[6] concluded that: 1—chromium recovery increased with decreasing basicity, and 2—chromium recovery increased with increasing temperature, although the effect was small. In similar studies Yavioskii and Dzemyen[7] concluded that: 1—slag FeO is the most important variable, 2—the basicity of the slag has no effect on chromium recovery, and 3—slag viscosity is not high even when 20 pct Cr_2O_3 is present. Lapitskii[8] concluded that chromium recovery improved as the basicity of the slag decreased and increased with increasing manganese in the metal.

Regarding the effectiveness of Cr_2O_3 as a base or acid in basic slags, both Kristoffersen[9] and Trojer[10] reported that Cr_2O_3 was an acidic component requiring neutralization as $2CaO \cdot Cr_2O_3$.

N. J. GRANT and J. CHIPMAN, Members AIME, are Associate Professor and Professor of Metallurgy, respectively, Massachusetts Institute of Technology, Cambridge, Mass., and E. C. ROBERTS, formerly Research Assistant, Dept. of Metallurgy, MIT, is now Assistant Professor of Metallurgy, Montana School of Mines, Butte, Mont.

Discussion on this paper, TP 3731C, may be sent, 2 copies, to AIME by April 1, 1954. Manuscript, Aug. 6, 1953. New York Meeting, February 1954.

Experimental Procedure

The experimental apparatus and procedure used for the present research were similar in most details to those used by Winkler and Chipman[11] and were described in detail by them. A magnesia crucible was used, holding 60 to 80 lb of Armco iron which was decarburized with hydrogen to about 0.010 pct C. Since all the metal samples solidified without gas evolution, this carbon level was assumed not to be significant. Synthetic slags made by mixing pure oxides were used throughout the study.

Temperatures were measured by means of calibrated W-Mo thermocouples and were checked by Pt-Pt-Rh thermocouples. The range of temperatures covered in this study was from 1526° to 1734°C.

The chromium content of the iron was in the range 0.032 to 0.82 pct, although the bulk of the tests showed 0.04 to 0.2 pct.

The slags were of the $CaO(MgO)$-SiO_2-FeO-Cr_2O_3 type in which the Cr_2O_3 content was from about 2 to 20 pct, although most of the slags showed from about 2 to 10 pct. The FeO range was from about 10 to 65 pct. CaO and SiO_2 were in the range of about 5 to 45 pct each, yielding a rather wide range of basicity values.

The first 12 heats were made without a sulphur addition, and with only 30 min allowed for slag-metal equilibrium to be reached. In previous research it had been shown that less than 30 min was adequate to achieve equilibrium in slags free of Cr_2O_3.[11, 12, 13] A study of the present data indicated that some of the tests may not have reached equilibrium in this time; accordingly four additional heats were made in which at least 1 hr was permitted for equilibrium to be reached. For reaching

Table I. Summary of Slag-Metal Chemistry and Temperature Data

Heat Sample No.	Temperature, °C	Metal Analyses			Slag Analyses, Percent						
		O*	Cr†	S	CaO	MgO	SiO_2	FeO	Fe_2O_3	Cr_2O_3	S
86-11	1580	0.153	0.050	—	26.09	6.00	15.28	43.96	5.13	2.34	—
87-9	1826	0.130	0.038	—	24.97	6.29	17.06	39.62	8.60	1.43	—
88-3	1854	0.140	0.048	—	20.81	5.34	12.80	48.79	8.24	3.82	—
88-9	1542	0.114	0.041	—	24.22	3.98	14.44	43.31	8.19	5.70	—
88-15	1564	0.157	0.049	—	21.45	2.65	16.36	42.32	10.80	6.17	—
88-17	1583	0.137	0.057	—	24.88	4.24	17.74	39.98	8.29	4.68	—
88-23	1593	0.183	0.058	—	18.81	4.55	13.14	52.43	7.87	3.21	—
89-4	1646	0.194	0.099	—	22.66	6.52	14.34	44.26	5.56	4.90	—
89-6	1704	0.236	0.175	—	20.41	7.64	13.22	44.11	5.72	7.32	—
89-8	1619	0.187	0.067	—	21.65	6.88	14.26	45.32	5.96	4.31	—
89-14	1600	0.178	0.066	—	20.53	6.05	13.78	47.15	6.53	4.34	—
89-16	1646	0.181	0.095	—	18.52	6.86	13.34	37.41	11.22	10.64	—
89-18	1613	0.161	0.084	—	26.17	4.55	16.34	39.75	6.28	4.85	—
89-24	1542	0.128	0.036	—	21.14	4.82	16.42	44.77	6.89	4.43	—
89-26	1570	0.144	0.053	—	20.84	5.15	17.20	43.36	6.58	5.40	—
91-10	1668	0.278	0.004	—	10.39	8.50	13.30	55.78	6.98	3.73	—
91-12	1584	0.174	0.042	—	10.53	7.66	15.50	56.77	4.93	3.39	—
91-16	1663	0.243	0.069	—	14.40	8.61	14.10	53.99	4.55	3.67	—
91-20	1632	0.180	0.078	—	13.56	8.72	16.52	43.68	6.07	9.62	—
94-6	1625	0.171	0.090	—	14.83	6.70	12.34	42.49	8.39	13.78	—
94-8	1551	0.146	0.037	—	14.96	5.95	13.54	38.89	10.92	13.33	—
94-14	1636	0.172	0.104	—	25.73	5.26	12.64	42.82	7.07	4.44	—
94-16	1666	0.188	0.143	—	26.10	5.21	13.42	38.92	6.11	8.29	—
94-18	1577	0.137	0.072	—	23.20	5.35	12.18	33.37	10.45	13.30	—
94-20	1610	0.158	0.078	—	25.53	2.25	18.38	19.13	11.87	21.00	—
94-22	1603	0.156	0.079	—	27.32	3.46	18.02	28.48	9.02	12.30	—
94-24	1591	0.145	0.061	—	25.04	3.61	16.70	27.33	10.45	14.50	—
95-4	1586	0.151	0.068	—	24.27	4.40	13.22	41.56	8.79	7.26	—
95-6	1608	0.156	0.069	—	24.46	4.63	13.80	41.41	6.07	7.49	—
95-8	1697	0.219	0.170	—	22.58	5.16	13.50	41.13	6.94	9.92	—
95-14	1577	0.136	0.061	—	20.13	6.22	14.40	26.60	10.07	20.60	—
95-16	1608	0.150	0.099	—	31.46	3.19	21.10	26.05	8.18	9.72	—
95-18	1613	0.148	0.087	—	30.00	3.89	20.18	30.63	5.59	7.44	—
95-20	1652	0.179	0.108	—	29.32	3.14	17.82	32.61	8.29	7.94	—
95-24	1710	0.211	0.183	—	25.03	4.99	21.02	34.84	5.66	5.61	—
96-2	1690	0.229	0.125	—	11.84	5.56	5.18	62.55	6.55	6.42	—
96-8	1537	0.144	0.032	—	12.62	6.06	8.64	49.02	11.84	10.78	—
96-10	1604	0.174	0.063	—	19.77	5.19	9.16	51.34	8.05	5.68	—
96-12	1640	0.169	0.092	—	20.13	4.44	7.92	51.04	8.17	6.56	—
96-14	1630	0.167	0.093	—	21.24	5.03	7.74	45.73	11.67	6.80	—
96-20	1581	0.127	0.076	—	26.73	4.97	7.68	45.27	8.79	4.56	—
96-22	1615	0.135	0.110	—	27.32	4.73	7.70	44.15	9.10	5.53	—
96-28	1593	0.110	0.116	—	31.52	4.36	8.14	40.25	8.73	5.24	—
96-30	1648	0.138	0.140	—	29.93	4.59	8.76	40.12	8.28	6.45	—
96-32	1654	0.132	0.210	—	33.30	4.61	9.57	36.18	8.50	6.58	—
96-34	1573	0.096	0.131	—	33.65	4.51	10.32	33.65	9.34	7.23	—
97-4	1641	0.174	0.092	—	28.88	6.33	16.78	36.40	5.76	4.96	—
97-6	1631	0.142	0.101	—	32.40	6.28	13.80	33.95	8.62	3.60	—
97-14	1651	0.137	0.149	—	29.20	3.83	8.00	42.90	7.55	7.33	—
97-18	1734	0.211	0.268	—	21.32	6.84	12.28	39.85	5.66	11.94	—
97-24	1614	0.182	0.068	—	20.47	3.11	17.08	36.97	8.95	11.95	—
97-28	1549	0.129	0.042	—	36.45	1.14	25.94	28.70	3.89	2.05	—
97-30	1597	0.133	0.101	—	33.75	2.61	31.34	27.30	2.55	2.88	—
97-38	1597	0.100	0.166	—	13.37	2.84	39.51	19.58	22.54	4.70	—
98-2	1570	0.131	0.070	—	34.13	10.20	24.02	23.45	3.98	2.67	—
98-8	1615	0.102	0.169	—	20.84	18.18	32.70	19.78	4.20	3.29	—
98-10	1591	0.093	0.183	—	14.31	17.92	37.70	19.46	6.98	3.23	—
98-16	1608	0.068	0.475	—	40.74	6.88	38.36	9.89	0.87	2.85	—
98-22	1589	0.048	0.621	—	39.18	2.56	39.76	10.25	1.67	5.27	—
98-24	1573	0.047	0.642	—	34.55	3.32	44.54	10.11	2.50	5.62	—
98-28	1642	0.065	0.822	—	30.56	5.80	40.38	13.02	2.99	7.01	—
99-2	1568	0.176	0.028	—	5.01	3.60	7.64	66.53	9.26	7.63	—
99-4	1600	0.193	0.042	—	5.06	5.07	10.72	65.81	7.27	5.36	—
99-8	1618	0.228	0.048	—	4.17	6.33	13.10	58.63	8.30	7.61	—
99-10	1621	0.211	0.050	—	4.28	7.44	15.94	59.56	6.31	6.25	—
99-12	1639	0.231	0.055	—	4.05	7.88	17.62	57.76	5.91	6.20	—
99-14	1610	0.190	0.049	—	3.84	9.58	20.68	54.53	5.61	4.12	—
99-16	1612	0.172	0.058	—	3.42	10.58	24.47	52.09	5.43	3.69	—
99-20	1594	0.153	0.059	—	2.58	7.46	32.14	46.85	4.43	4.85	—
99-24	1615	0.160	0.091	—	5.21	9.42	29.56	45.26	3.42	5.21	—
99-26	1610	0.128	0.133	—	4.88	10.90	29.34	42.25	4.27	6.70	—
99-28	1625	0.141	0.096	—	14.39	9.91	28.80	38.08	3.21	3.33	—
99-30	1630	0.159	0.102	—	20.39	9.85	27.36	32.57	5.97	3.13	—
99-34	1619	0.144	0.127	—	22.22	8.67	28.60	32.76	3.05	3.31	—
100-2	1580	0.079	0.207	0.095	40.24	9.15	34.76	13.61	0.04	1.58	0.093
100-6	1590	0.073	0.252	0.094	39.99	10.64	34.92	11.78	0.07	2.25	0.055
100-8	1612	0.067	0.520	0.094	38.19	11.57	37.74	9.56	0.07	2.72	0.042
100-10	1620	0.073	0.510	0.094	31.63	14.88	38.62	11.43	0.07	3.09	0.031
100-16	1618	0.064	0.635	0.093	35.83	9.54	39.81	10.11	0.04	3.66	0.032
100-18	1658	0.092	0.580	0.093	33.95	11.60	37.77	13.14	0.07	3.86	0.036
101-2	1548	0.128	0.053	0.111	33.39	5.57	21.75	32.99	3.28	2.77	0.20
101-4	1592	0.151	0.074	0.113	32.81	6.15	21.14	32.56	3.04	4.43	0.19
101-6	1635	0.158	0.109	0.111	33.04	6.54	19.60	33.83	3.08	3.32	0.235
101-8	1645	0.160	0.130	0.107	34.39	6.79	18.06	34.73	2.76	3.74	0.273
101-10	1625	0.152	0.115	0.107	33.39	6.99	17.57	35.85	2.56	3.66	0.275
101-14	1590	0.129	0.063	0.109	30.06	6.18	18.68	34.88	3.08	6.94	0.22
101-20	1582	0.117	0.104	0.112	18.85	9.28	32.22	33.80	0.08	4.51	0.058
102-2	1635	0.218	0.036	0.135	7.97	4.48	3.36	78.14	4.66	3.47	0.56
102-4	1600	0.199	0.041	0.137	8.48	4.43	3.54	74.47	5.76	3.22	0.56
102-6	1600	0.184	0.040	0.132	12.82	4.23	3.42	71.62	5.07	2.89	0.61
102-8	1602	0.153	0.080	0.129	18.54	3.80	3.18	61.49	6.85	6.11	0.67
102-10	1605	0.140	0.091	0.120	23.39	3.63	3.04	55.42	7.87	6.45	0.75
102-12	1622	0.114	0.150	0.112	28.22	3.29	2.66	48.30	7.58	9.76	0.85
102-16	1583	0.113	0.109	0.104	26.76	3.20	2.08	50.06	9.13	7.90	0.81
102-18	1605	0.133	0.105	0.104	23.58	3.34	2.08	55.27	8.15	7.25	0.72
103-4	1625	0.205	0.067	0.127	16.12	4.43	11.70	53.79	4.01	9.69	0.30
103-8	1601	0.178	0.064	0.131	14.18	7.12	15.80	52.22	3.20	7.62	0.225
103-10	1611	0.196	0.053	0.128	13.46	5.45	15.20	56.06	3.93	6.25	0.27
103-12	1595	0.171	0.059	0.128	11.08	5.91	14.66	57.87	3.69	6.28	0.26
103-14	1602	0.194	0.046	0.127	10.07	5.78	13.26	59.71	3.93	7.16	0.27
103-16	1605	0.025	0.053	0.125	9.10	5.54	13.78	61.82	3.65	5.95	0.28

* Oxygen was determined by vacuum fusion.
† Total chromium (soluble plus insoluble).

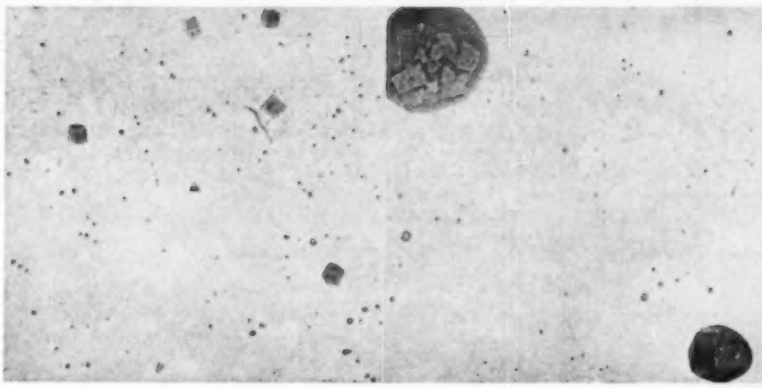

Fig. 1 (left)—Chromite inclusions (angular) and iron oxide (rounded) in metal sample 96-34. X750.

Fig. 2 (center)—Two-phase oxide inclusions, chromite in iron oxide, in metal sample 91-10. X750.

Fig. 3 (upper right)—Chromite phase in slag sample 99-32. X750.

Fig. 4 (lower right)—Chromite phase in slag sample 94-24 showing a metal button inside the chromite. X750.

equilibrium 1 hr was noted to be adequate. Sulphur was added to these heats in order that the sulphur distribution ratio might be used as a measure of the acidic or basic nature of Cr_2O_3 in basic slags.

Table I lists the metal and slag compositions as well as the temperatures of the bath at the time of sampling.

Experimental Results and Discussion

Microexamination of Slag and Metal Phases: A large number of slag and metal samples were examined microscopically in an effort to obtain evidence of existing phases. The results were difficult to interpret but did present some interesting structures.

Fig. 1 shows a micrograph of an iron sample. The spherical particles are of the iron oxide, wüstite, phase. It will be noted that the size of the particles varies from extremely minute spheres to very large ones. The angularly shaped particles are chromite inclusions. These particles are extremely uniform in size, suggesting that this phase separated out in a narrow temperature range.

Fig. 2 shows two-phase oxide inclusions in an iron sample as well as smaller wüstite inclusions, again over a range of particle sizes. From the geometry of the included phase it is concluded that it is chromite which lies in the wüstite phase. Such a combination of wüstite and chromite suggests that the chromite may have served as a nucleus on which the wüstite could precipitate and grow; this does not explain why the chromite particles are larger than when wüstite is absent. It seems more probable that there is appreciable solubility between wüstite and chromite at high temperatures, as was suggested by Trojer.[10] In the latter case the chromite precipitated within the droplets of nonmetallic liquid first formed and conditions may have been more favorable for growth.

Fig. 3 shows one of the slags. The angular phase is chromite which exists in wüstite. Some dicalcium-silicate was also identified. Fig. 4 shows an interesting and not too rare instance wherein a metallic button exists within the chromite phase. The analysis of the metal was not obtained, unfortunately, because of the smallness of the particles. A satisfactory explanation for the occurrence of this metallic particle in the chromite has not been found.

Cr_2O_3 as a Basic Component in Basic Slags: One of the primary aims of the research was to determine the acidic or basic contribution of Cr_2O_3 in basic open hearth type slags. Efforts to determine this on the first 12 heats were completely unsuccessful, due to the lack of an adequate criterion.

Accordingly, the four sulphur-containing heats were examined, using the "desulphurization standard line" determined by Grant and Chipman[18] as a reference. It will be recalled that the strongly acidic nature of Al_2O_3 in basic open hearth type slags was determined in this same manner.

A value of "excess base" was calculated according to the method of Grant and Chipman for each slag. In the first set of calculations the Cr_2O_3 (mols per 100 gram of slag) was considered as an acid requiring 1 mol of CaO for neutralization. A plot of the desulphurization ratio, $(\%S)/[\%S]$, against excess base was then made as shown in Fig. 5. It is seen that in general the points lie above the standard curve, indicating that for a given desulphurization ratio, the slags, as calculated, are too acid.

A similar set of calculations was made next in which Cr_2O_3 was assumed to be neutral (similar to FeO). This resulted in higher calculated basicity values for the slags than was obtained above, but the points were still too far above the curve.

In a third set of calculations the Cr_2O_3 was assumed to be a base, contributing to the basicity equally with CaO, MgO, and MnO, on a molar basis. It was noted that the points fit the standard curve about as well as the points for slags not containing

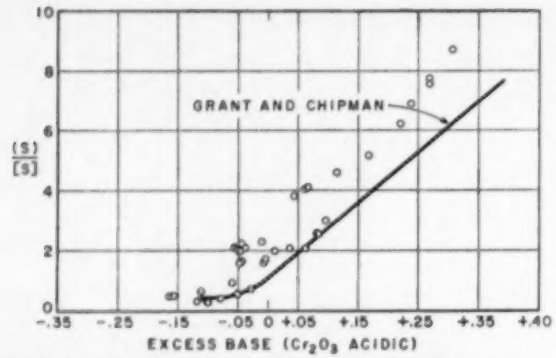

Fig. 5—Desulphurization ratio vs excess base. Cr_2O_3 assumed to be acidic. Note poor agreement with standard desulphurization curve.

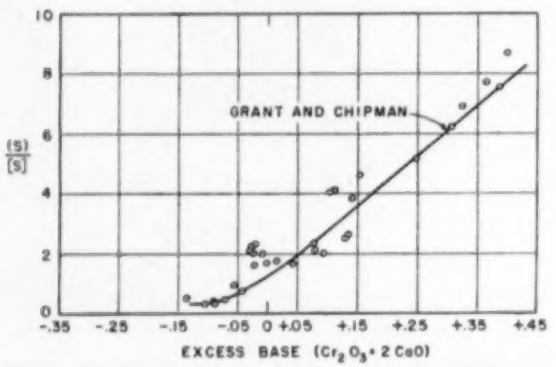

Fig. 6—Desulphurization ratio vs excess base. Cr_2O_3 assumed to be equivalent to 2CaO. Note good agreement with standard desulphurization curve.

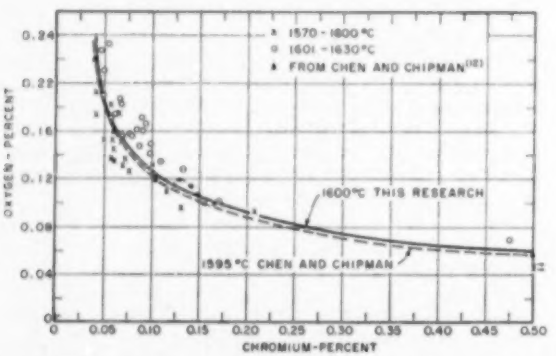

Fig. 7—Oxygen content of low chromium-iron melts in equilibrium with chromite saturated slags at 1600°C. Note good agreement with curve of Chen and Chipman.[12]

Cr_2O_3, previously reported.[12] In a fourth calculation it was assumed that 1 mol of Cr_2O_3 is equivalent to 2 mols of CaO. The result of such a calculation is almost indistinguishable from that of assuming that chromium is divalent and equivalent in basic properties to calcium. The results of this calculation are shown in Fig. 6 in which it is seen that the individual points are in very good agreement with the "standard curve" previously reported.

The Chromium Oxidation Reaction: Wentrupp and Knapp[11] reported that with up to about 8 pct Cr in the metal the chromium is in equilibrium with chromite ($FeO \cdot Cr_2O_3$) in the slag. Chen and Chipman[12] also reported chromium to be in equilibrium with chromite but placed the upper limit at about 5.5 pct Cr. Furthermore, the data of Chen and Chipman showed that with up to 1 pct Cr in the metal the effect of chromium on the oxygen activity was small. When solid chromite is present, the following reaction may be assumed to take place:

$$FeO \cdot Cr_2O_3 \text{ (solid)} = Fe \text{ (liquid)} + 2\,\underline{Cr} + 4\,\underline{O}$$

where the underlined values indicate elements in solution in the liquid iron.

Then

$$K' = [\%\ Cr]^2 \times [\%\ O]^4.$$

A plot of percent oxygen against percent chromium is shown in Fig. 7, utilizing two groups of points based on the temperature ranges 1571° to 1600°C and 1601° to 1630°C. The solid curve best represents the oxygen-chromium relationship at 1600°C and is compared to the curve obtained by Chen and Chipman.[12] The agreement is extremely good.

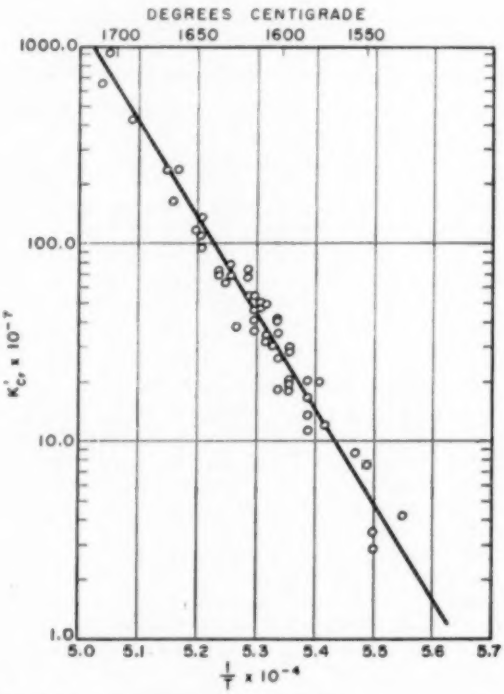

Fig. 8—Plot of K'_{Cr} vs the reciprocal of the temperature for the chromite reaction in liquid iron.

Fig. 8 is a plot of K' for the above reaction against the reciprocal of the absolute temperature. From this curve, K' at 1595°C is 2.55×10^{-4} in agreement with 2.44×10^{-4} from the data of Chen and Chipman. The straight line is represented by the expression

$$\log K' = -49{,}000/T + 20.6.$$

The close agreement of all of the data with the lines representing K' in Figs. 7 and 8 has a significance with respect to the experimental conditions which should not be overlooked. It shows that in every case the slag was saturated with respect to chromite. The results are therefore comparable with what would be expected on a chromite hearth.

Moreover, the chromium content of the metal is completely controlled by oxygen and by temperature. Under such conditions any "distribution ratio" of chromium between slag and metal has little significance.

The slag analyses may be used to establish a minimum value for the solubility of chromite in slags of the type used. This can be only a minimum rather than a true solubility because all the slags contained an undetermined amount of chromite in suspension. Plots of base/acid ratio vs Cr_2O_3 content of the slag (from Table I) showed that the minimum observed values at 1550°, 1600°, 1650°, and 1700°C are respectively about 2.0, 2.7, 3.5, and 5.0 pct by weight of Cr_2O_3. Above this minimum the scatter of the data is so great (due largely to the presence of suspended chromite) that the effects of FeO and basicity cannot be evaluated. These plots,

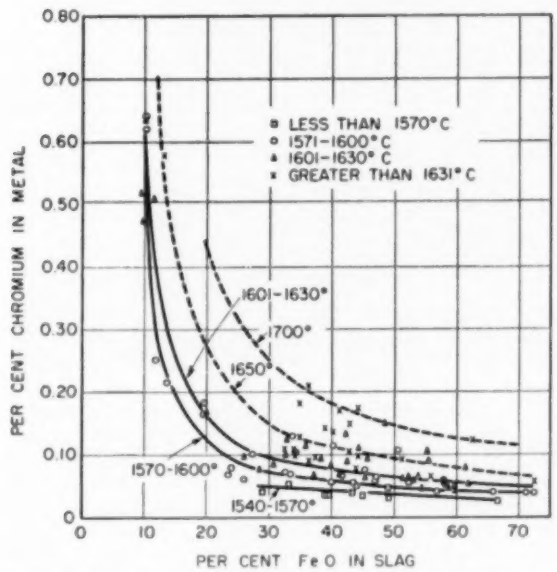

Fig. 9—Relationship of chromium in the metal to slag FeO as a function of temperature for chromite saturated slags.

omitted for the sake of brevity, indicated that the slags showing the lowest chromite solubility are principally those of intermediate basicity having V-ratios between 1.5 and 2. There are indications that solubilities approximately double the above minima may occur at very low V-ratios.

Of more practical significance, Fig. 9 shows a plot of percent chromium in the metal vs percent FeO in the slag, taken directly from Table I. The points shown in Fig. 9 were examined with respect to temperature and slag basicity. The following items, based directly on Fig. 9, deserve mention:

1—Above about 30 pct FeO, the effect of FeO is relatively small and temperature plays the leading role in controlling the chromium content of the liquid bath under a slag saturated with chromite.

2—With less than about 30 pct FeO, the slag FeO is the most important factor, residual chromium increasing as FeO decreases. This is in agreement with the findings of Yavioskii and Dzemyen,[7] whereas item 1 is in disagreement.

3—The effect of temperature is important at all levels of oxidation, chromium recovery increasing with increasing temperature. Previous investigators had indicated that this effect would be small.[4-6]

In a supplementary plot, where the slags were differentiated with respect to basicity, only a small effect of slag basicity on chromium recovery was noted. This is overshadowed by the large effects of oxidation and temperature. The disagreement in previous work on the role of basicity, based on non-equilibrium data,[4-6] is thus easily understood.

Conclusions

Based on equilibrium studies between liquid iron and simple slags in the system $CaO(MgO)$-SiO_2-FeO-Cr_2O_3, and with chromium contents up to 0.82 pct in the metal, the following conclusions may be made:

1—Equilibrium is reached more slowly than in chromium-free slags, and some chromite remains suspended in the slag.

2—Cr_2O_3 appears to behave as a basic oxide in slags of the open hearth type being approximately as effective in desulphurization as CaO, MgO, and MnO.

3—The solubility of chromite in slags is estimated to correspond to about 2 to 5 pct Cr_2O_3 at temperatures of 1550° to 1700°C and somewhat higher in slags of very low V-ratio.

4—The reaction of chromium with oxygen at low chromium contents in the presence of chromite-saturated slags is best represented as follows:

$$FeO \cdot Cr_2O_3 \text{ (solid)} = Fe \text{ (liquid)} + 2\,\underline{Cr} + 4\,\underline{O}$$

$$K' = [\%\ Cr]^2 \times [\%\ O]^4;\ \log K' = -49{,}000/T + 20.6.$$

This agrees with the results of Chen and Chipman at 1595°C.

5—For metal containing less than 1 pct Cr, recovery of chromium in remelting is favored by high temperature and low FeO. The effects of basicity are less clear.

Acknowledgments

The authors are indebted to Mr. Donald Guernsey for his capable and careful analyses and to the American Iron and Steel Institute for sponsoring the research program.

References

[1] Körber and Oelsen: *Mitt. Kaiser Wilhelm Inst. Eisenforschung* (1935) **17**, pp. 231-245.

[2] Herasymenko: *Trans.* Faraday Soc. (1938) **34**, p. 1254.

[3] Hilty: *Trans.* AIME (1949) **185**, pp. 91-95; JOURNAL OF METALS (February 1949).

[4] Bardenheuer: *Verein Deutscher Eisenhüttenlaute* (December 1942) No. 39.

[5] Rockrohr: *Stahl und Eisen* (1941) **61**, pp. 203-209.

[6] Hauck: *Stahl und Eisen* (1947) **61**, pp. 201-202.

[7] Yavioskii and Dzemyen: *Stahl* (1947) **1**, pp. 302-309.

[8] Lapitskii: *Teoriya i Prakt. Met.* (1937) No. 8, pp. 42-47.

[9] Kristoffersen: *Kjemi, Bergresen og. Metallurgi* (1941) **1**, No. 5, pp. 75-82.

[10] Trojer: *Radex Rundschau* (April 1948) No. 1-2, pp. 27-37.

[11] Winkler and Chipman: *Trans.* AIME (1946) **167**, pp. 111-133; METALS TECHNOLOGY (April 1946).

[12] Chen and Chipman: *Trans.* ASM (1947) **38**, pp. 70-113.

[13] Grant and Chipman: *Trans.* AIME (1946) **167**, p. 134; METALS TECHNOLOGY (April 1946).

[14] Wentrupp and Knapp: *Technische Mitt. Krupp, A. Forschungsberichte* (1941) **4**, pp. 237-256.

[15] Fetters and Chipman: *Trans.* AIME (1941) **145**, pp. 95-112.

The Wustite Phase in Partially Reduced Hematite

by Gust Bitsianes and T. L. Joseph

THE layered structure of partially reduced iron ore was described in a previous paper.[1] Reduction by hydrogen was found to take place at well-defined interfaces between layers of the solid phases. In the present investigation, a detailed study was made of the wüstite phase that had formed during the partial reduction of a cylindrical compact of chemically pure hematite. An unusually wide band of wüstite permitted a rather detailed study of this phase.

The specimen was made from Baker's C.P. hematite in the form of a cylinder 1.5 cm in diameter and 1.8 cm long. A dense ore structure with about 6 pct porosity was attained by heating the specimen in air at 1100°C for 3 hr. To confine reduction to the top surface, a ceramic coating was applied to the bottom and sides of the cylindrical compact. The specimen was then partially reduced in hydrogen at 850°C and subjected to a coordinated sequence of macro-, micro-, and X-ray examinations.

A section of the partially reduced cylinder is shown in the macrograph, Fig. 1. Four layers consisting of metallic iron, wüstite, magnetite, and unreduced hematite are clearly shown. The effort to force reduction to proceed downward in topochemical fashion was only partly successful, as some reduction occurred along one side and bottom of the cylinder. A rather wide layer of dark wüstite phase had formed, however, and permitted sampling for X-ray studies as indicated.

To supplement previous work and to study the wüstite layer in more detail, ten separate layers were removed for X-ray examination. Broad and diffuse patterns were obtained with the as-filed powders, especially with those of iron and wüstite, and the condition indicated a cold-working and variable composition effect within the respective layers. This condition was corrected by annealing the entire series of powders at an appropriate temperature. For the annealing treatment, the ten powder samples were wrapped in silver foil, sealed under vacuum in small quartz tubes, and heated at 750°C for 16 hr. The specimens were then drastically quenched in cold water to preserve the annealed condition. These annealed specimens were X-rayed in turn and the compiled patterns are shown in Fig. 2. The standard patterns for iron and its oxides have been interjected at appropriate positions for purposes of comparison and phase identification.

All of the patterns obtained were clearcut and concise so that positive identifications could be made for all of the phases. The outermost layers *A*, *B*, and *C* were composed almost entirely of iron with a small amount of wüstite being detectable at the X-ray limit of phase detection. Layer *D* from the iron-wüstite interface showed both of these phases. The next four layers *E*, *F*, *G*, and *H* were all in the dark phase band which had been tentatively identified as wüstite by the macroexamination, Fig. 1. The diffraction data with their single-phase patterns of wüstite for these layers checked the visual evidence. Continuing the X-ray analyses after layer *H*, the macrograph (Fig. 1) shows that layer *I* came largely from the magnetite zone but included some fringes of the wüstite-magnetite interface. The diffraction pattern for the sample confirmed this observation. Layer *J* came from the unreduced core of the specimen and its diffraction pattern indicated a preponderance of hematite phase. The reduction behavior of synthetic compacts has thus been found to be similar to natural dense iron ore.

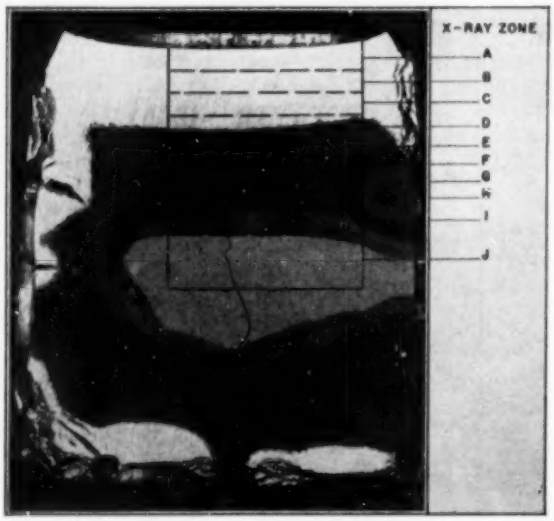

Fig. 1—Macrostructure of partially reduced synthetic ore, cylinder No. 9. Reduced in hydrogen at 850°C for 70 min. X6.5. Area reduced approximately 60 pct for reproduction.

The previous results were supplemented with measurements of the diffraction films and calculations of the respective unit parameters. These X-ray data are summarized in Table I and offer some interesting correlations as to the compositions of the various phases undergoing reduction.

The iron layers that were analyzed gave lattice parameters close to that of pure iron at 2.8664Å. Evidently this iron was present in layers *A* through *D* as a pure phase with little or no oxygen dissolved in its lattice.

With the wüstite layers an entirely different situation prevailed in that there was a definite and

G. BITSIANES and T. L. JOSEPH, Members AIME, are Assistant Professor and Professor, respectively, School of Mines and Metallurgy, University of Minnesota, Minneapolis, Minn.

Discussion on this paper, TP 3729C, may be sent, 2 copies, to AIME by April 1, 1954. Manuscript, Nov. 6, 1953. New York Meeting, February 1954.

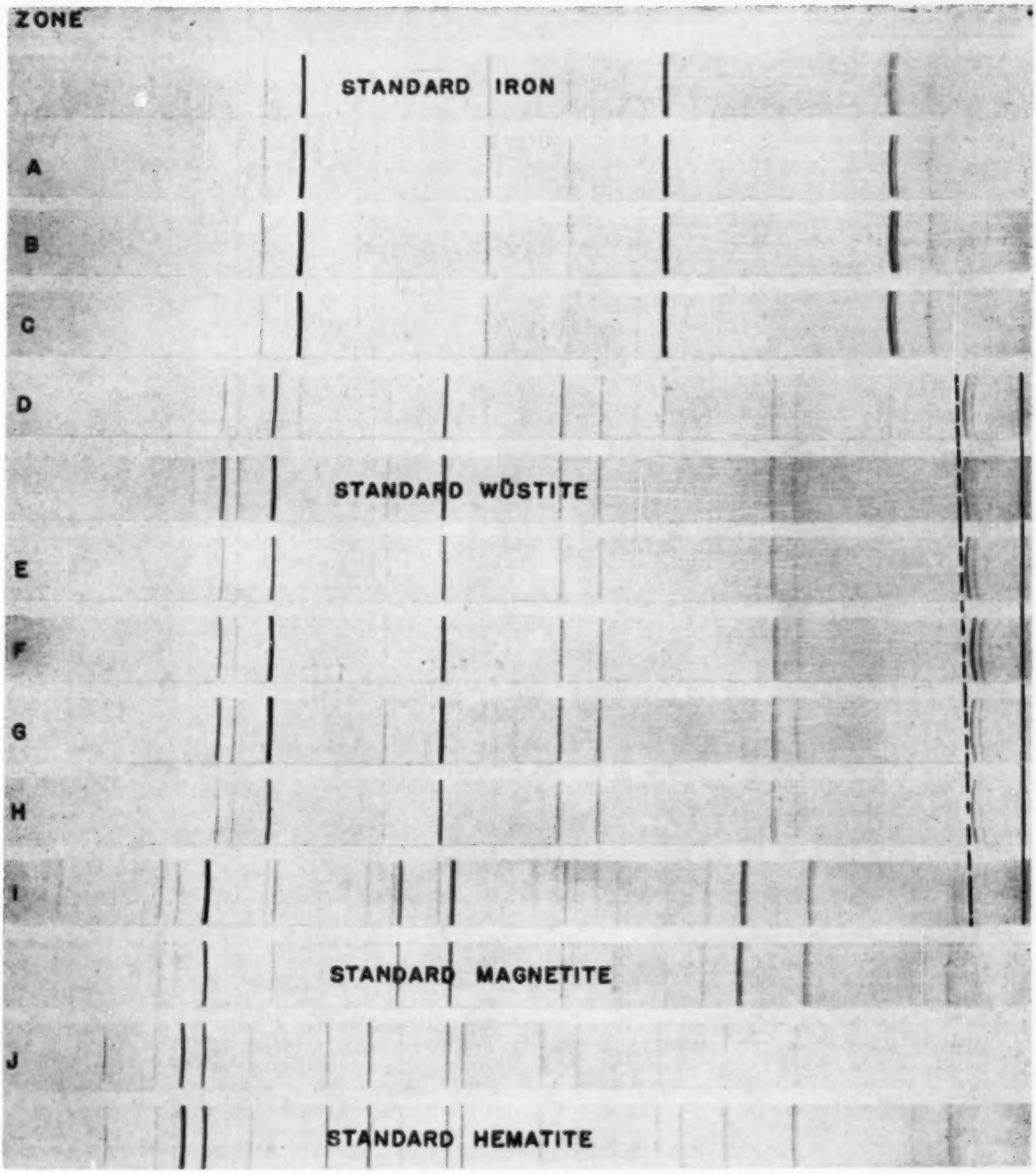

Fig. 2—X-ray study of cylinder No. 9. X0.5.

sizable lattice parameter change from one extremity of the field to the other. The effect can be seen in the X-ray pattern compilation of Fig. 2. The wüstite doublet on the extreme right, corresponding to the 331 line, had shifted gradually to the right with increasing depth of penetration. Such a change involving a solid solution can only mean that the lattice parameter of the wüstite had changed across the breadth of the field. The data of Table I for the wüstite field give quantitative proof of the directional change in parameter and show it to have been a *decrease*. Under the conditions of reduction, the wüstite nearest the iron phase should have been lower in oxygen content than that next to the magnetite. It may thus be concluded that the wüstite formed on reduction had an increasing oxygen content as a function of depth and at the same time exhibited a decreasing lattice parameter. These findings are in direct agreement with the work of Jette and Foote[5, 6] who found that the parameter of their grade of wüstite decreased regularly with increasing oxygen content.

The change in wüstite parameter could not be correlated directly with the composition of the various layers as insufficient material was available for chemical analysis. Jette and Foote,[5, 6] however, have published a curve relating the composition (oxygen content) of wüstite with its X-ray parameter. This curve was used to correlate oxygen content with X-ray data obtained in the present investigation.

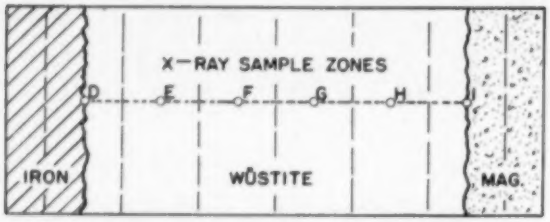

Fig. 3—Schematic representation of layer sampling technique used on the wustite field of cylinder No. 9.

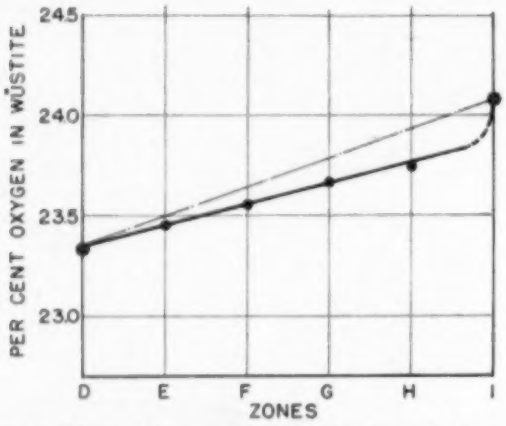

Fig. 4—Wustite field compositions as a function of depth of penetration for cylinder No. 9. *D* and *I* are the determined equilibrium points.

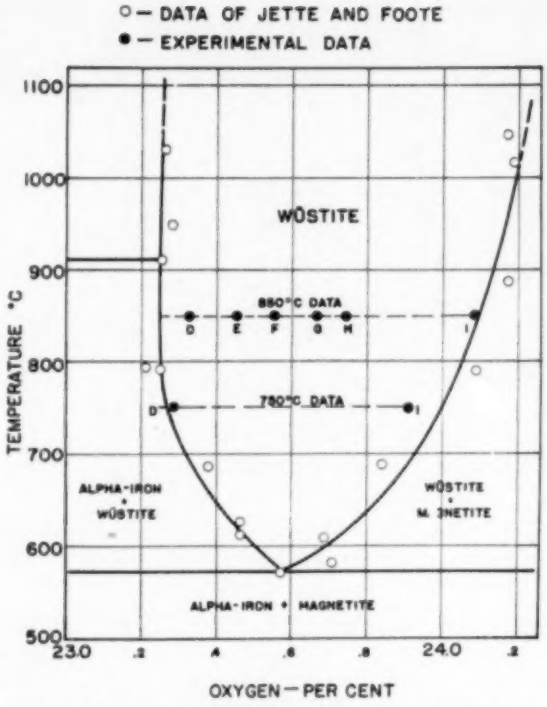

Fig. 5— Correlation of wustite field compositions for cylinder No. 9. *D* and *I* represent wustite equilibrium points with iron and magnetite, respectively.

The first correlation has been concerned with the changes in composition of the wüstite field with depth. Fig. 3 is a schematic representation of the location of the samples used for X-ray analyses. Six layers were filed as uniformly as possible and the broken vertical lines represent the probable boundaries of the separate layers. Each layer was then annealed to a homogeneous composition at an effective temperature of 850°C and the resultant X-ray parameters and oxygen analyses could be taken to represent the mid-points of the respective layers. The *D* and *I* layers, however, contained iron and magnetite, respectively, and thus represented the equilibrium conditions for wüstite at 850°C.

Fig. 4 shows how the oxygen content of the wüstite phase varies across the wüstite field. The four points *E*, *F*, *G*, and *H* represent the dynamic condition at the time of reduction and determine the curve fixing the oxygen concentration across the wüstite field. The curve starts at the equilibrium composition on the iron-wüstite interface, increases in linear fashion across the width of the wüstite field, and finally increases sharply to the equilibrium composition on the wüstite-magnetite interface. This behavior would indicate that a steady-state condition prevailed across the wüstite layer in which a diffusional effect was operating in conjunction with an interfacial resistance to control the process. The diffusional effect was probably one involving the counterdiffusion of hydrogen and water vapor molecules through the porous layer of wüstite grains. The actual reduction of the individual wüstite grains, however, could have been carried on by the solid lattice-type of diffusion involving iron ions.

The second correlation has been made with Jette

Table I. X-Ray Data Compilation for Synthetic Cylinder No. 9

Layer	Annealing Temperature, °C	Phases Present: Iron		Wüstite		Magnetite		Hematite	
		*I**	a_o†	*I*	a_o	*I*	a_o	*I*	a_o
A	750	vs	2.867(0)	vvw					
B									
C									
D	750	ms	2.867(1)	vs	4.308(5)				
	850	ms	2.866(6)	vs	4.306(8)				
E	750			vs	4.302(9)				
F	750			vs	4.300(0)				
G	750			vs	4.296(6)				
H	750			vs	4.294(9)				
I	750			s	4.290(3)	vs	8.397(4)		
	850			s	4.285(6)	vs	8.395(5)		
J	750					vw	8.39(5)	vs	a_{rh} = 5.42(5) α = 55°18′

* Relative intensity (*I*) scale: s, strong; m, medium; w, weak; v, very.
† a_o in angstrom units: probable accuracy of four significant figures.

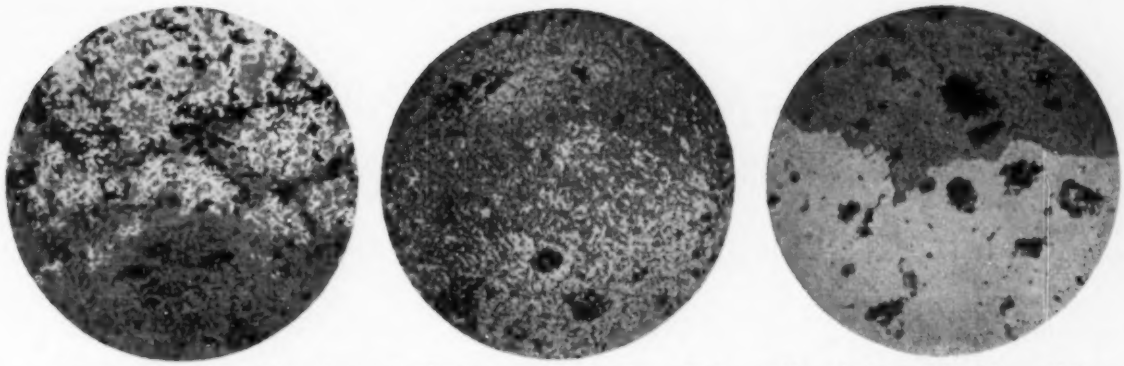

a—Iron-wustite interface. White phase, iron; gray phase, wustite; black areas are pores.

b—Wustite-magnetite interface. Dark gray phase, wustite; light gray phase, magnetite.

c—Magnetite-hematite interface. Light gray phase, magnetite; white phase, hematite; some dark pore areas.

Fig. 6—Reduction interfaces of synthetic ore, cylinder No. 9. Reduced in hydrogen at 850°C for 70 min. Etched. X500. Area reduced approximately 50 pct for reproduction.

and Foote's[2, 3] representation of the wüstite field. Their data and those of the authors are shown in Fig. 5 with the *D* and *I* points representing equilibrium compositions at either extremity of the wüstite field. These equilibrium points are in good agreement with Jette and Foote's values but they cannot be regarded as independent checks as the analytical results were obtained with the aid of the previous authors' calibration curve. The X-ray data, however, appear to have been fairly consistent. Within the wüstite field the oxygen content of the intermediate layers increased progressively and uniformly with depth of penetration.

The parameters obtained for the phases in layers *I* and *J* were very close to those for the pure magnetite and hematite standards. The magnetite layer *I* was actually too thin for an extensive sampling treatment and the parameter data could well represent an average layer condition.

As a further means of study, the specimen was microexamined and the results are summarized in the micrographs of Fig. 6. The reduction interfaces in the synthetic specimen were substantially the same as those observed in a natural iron ore. The same phases were present in the same orientation, and the occurrence of progressively narrower interfaces with depth of penetration was again observed. There are some differences which should be noted in the reduction behavior of synthetic and natural material. The first difference is in the porosity of the iron layers which have a tendency to sinter.

Sintering, in general, occurs in any sponge iron layer provided that it is held above 650°C for sufficient time. In the synthetic specimen the iron layer has undergone a remarkable sintering action to create a distinctive type of macroporosity. Fig. 6a illustrates the case and shows that the iron grains have grown together and produced large, branching pore areas. In contrast, the reduction of natural ore is characterized by a minimum of sintering action and thus by iron layers with a uniform distribution of pore space. These results along with other evidence would indicate that the purer materials have the greater tendency to sinter.

A second difference in the reduction behavior of synthetic material has been noted in that many of the wüstite grains are not completely reduced at the iron-wüstite interface but persist well out into the ferrite layer. In Fig. 6a these isolated grains are shown encased by agglomerated masses of sponge iron, and the microinspection has shown that the distribution of residual wüstite decreases uniformly out on the edge of the specimen. This "wüstite retention" effect has been noted in most synthetic material and is directly related to the size of the wüstite grains and to the iron sintering action.

Summary and Conclusions

An unusually wide band of wüstite was found in a partially reduced cylinder of chemically pure hematite which had been fired to produce a dense, homogeneous, and thermally stable structure. Six samples which represented layers of varying depths of penetration were filed from the wüstite band and annealed prior to X-ray analysis. A change of composition across the wüstite field was indicated by a *decrease* of lattice parameter.

Using the work of Jette and Foote to fix oxygen content from X-ray data, results from the present study at 850°C showed that the oxygen content *increased* across the wüstite field. The curve started at the equilibrium composition on the iron-wüstite interface (23.35 pct O) and increased in linear fashion across the wüstite field to a value slightly below the equilibrium composition on the wüstite-magnetite interface (24.10 pct O).

Work on fired compacts of chemically pure hematite confirmed earlier work on iron ore as to the existence of four well-defined phase layers in samples partially reduced with hydrogen above 570°C.

Microscopic examination of the iron layer formed by reduction of pure hematite showed a tendency for the iron grains to coalesce leaving pores or open areas. This sintering action encased certain grains of wüstite with ferrite, retarded their reduction at the moving iron-wüstite interface, and permitted their retention well out into the ferrite layer. The effect was not characteristic of the reduction of dense iron ore.

References

[1] G. Bitsianes and T. L. Joseph: Solid Phase Identification in Partially Reduced Iron Ore. *Trans.* AIME (1953) **197**, pp. 1641-1647; JOURNAL OF METALS (December 1953).

[2] E. R. Jette and F. Foote: A Study of the Homogeneity Limits of Wüstite (FeO) by X-Ray Methods. *Trans.* AIME (1933) **105**, pp. 276-289.

[3] E. R. Jette and F. Foote: An X-Ray Study of the Wüstite (FeO) Solid Solutions. *Journal of Chemical Physics* (1933) **1**, pp. 29-36.

Theoretical Analysis of Diffusion of Solutes During The Solidification of Alloys

by Carl Wagner

When an alloy solidifies and the composition of the solid differs from the composition of the liquid, atoms of the alloying elements rejected at the solid-liquid interface have to diffuse toward the bulk liquid. Diffusion may be supported by convection. Theoretical calculations have been made for a liquid without convection, for a liquid involving natural convection, and for solidification of a liquid alloy at the surface of a rotating disk as an example of forced convection.

WHEN an alloy solidifies, the equilibrium composition of the originating solid phase differs in general from the composition of the liquid phase. Thus, segregation may take place, i.e., the composition of the solid phase formed at different times differs from the bulk composition. The degree of segregation depends on several factors such as the partition ratio of the alloying elements between the liquid and the solid phase, the rate of solidification, and convection. To clarify, a theoretical analysis has been worked out. The following presuppositions are made:

1—Calculations are confined to the solidification of binary alloys in which the concentration of component A (solvent) is much greater than that of component B (solute).

2—The equilibrium concentration of the alloying element B is assumed to be lower in the solid phase than in the coexisting liquid phase.

3—At the solid-liquid interface, partition equilibrium is assumed.

4—The dependence of the partition ratio of the solute between the liquid and the solid phase on concentration and temperature is disregarded since only small concentrations of the solute are considered.

5—The concentration of the alloying element B in the solid phase is supposed to be lower than the saturation concentration for the formation of a second solid phase.

6—Diffusion in the solid phase is disregarded, since diffusion rates in the solid state are comparatively low.

When the partition ratio of the solute between the liquid and the solid phase is greater than unity, a part of the solute is rejected at the solid-liquid interface and has to diffuse toward the bulk liquid. Thus there is necessarily a concentration difference in the liquid between the solid-liquid interface and the bulk liquid as has been pointed out by Hayes and Chipman,[1] Rutter and Chalmers,[2] Tiller, Jackson, Rutter, and Chalmers,[3] and others (see Fig. 1). In view of the concentration gradient in the liquid phase, the ratio of the concentration of the solute in the solid phase to that in the bulk liquid differs from the equilibrium ratio, although at the solid-liquid interface, partition equilibrium is assumed. Under certain limiting conditions, the solid may even have virtually the composition of the bulk liquid as is shown below.

C. WAGNER, Member AIME, is Visiting Professor, Dept. of Metallurgy, Massachusetts Institute of Technology, Cambridge, Mass.

Discussion on this paper, TP 3698DE, may be sent, 2 copies, to AIME by April 1, 1954. Manuscript, Aug. 27, 1953. New York Meeting, February 1954.

General Equations

Let u be the linear crystallization velocity in cm per sec, D the diffusion coefficient of component B in the liquid phase in $cm^2\ sec^{-1}$, c'_s and c''_s the concentrations of component B in the liquid and the solid phase, respectively, in mol per cm^3, and s the distance from the solid-liquid interface toward the bulk liquid at a given time t. The partition ratio is assumed to be equal to a partition constant K. Thus,

$$c''_s/c'_s = K \text{ at } s = 0. \qquad [1]$$

The difference in the specific volume between the liquid and the solid phase may be disregarded. In view of the discontinuity of the concentration of the solute at the interface according to Eq. 1, $u(c'_s - c''_s)_{s=0} = uc'_s\ (s = 0)(1 - K)$ gram-atoms B per unit area per unit time are rejected at the interface and have to diffuse toward the bulk liquid. From Fick's first law it follows that

$$uc'_s(s = 0)(1 - K) = -D(\partial c'_s/\partial s)_{s=0} \qquad [2]$$

The concentration profile in the liquid near the interface depends on the interplay of diffusion and convection as is discussed in the following sections. A schematic concentration profile is shown in Fig. 1. The "effective thickness of the diffusion boundary

layer" δ_{eff} may be defined as the distance of the intersection of the tangent line on the c'_B vs s curve at $s = 0$ and the extrapolated horizontal plateau of the bulk concentration $c'_{B(b)}$. Thus, according to Fig. 1,

$$\left(\frac{\partial c'_B}{\partial s}\right)_{s=0} = \frac{c'_{B(b)} - c'_B(s=0)}{\delta_{eff}} \quad [3]$$

Transformation of Eq. 3 yields the following analytical definition of δ_{eff}:

$$\delta_{eff} = \left[\frac{1}{c'_{B(b)} - c'_B(s=0)}\left(\frac{\partial c'_B}{\partial s}\right)_{s=0}\right]^{-1} \quad [4]$$

Upon substituting Eq. 3 in Eq. 2 and eliminating $c'_B(s=0)$ with the aid of Eq. 1, the ratio of the concentration of B in the solid phase to that in the bulk liquid is obtained as

$$\frac{c''_B}{c'_{B(b)}} = \frac{K}{1 - (\delta_{eff}u/D)(1-K)} \quad [5]$$

Since the difference in the specific volumes of the two phases is disregarded, the concentration ratios on the left-hand side of Eqs. 1 and 5 may be replaced by the corresponding mol fraction or weight fraction ratio in order to express results in a more usual manner. Thus

$$\frac{N''_B}{N'_{B(b)}} = \frac{[\%B]''}{[\%B]'_{(b)}} = \frac{K}{1 - (\delta_{eff}u/D)(1-K)} \quad [6]$$

where N''_B and $N'_{B(b)}$ are the mol fractions and $[\%B]'$ and $[\%B]''_{(b)}$ are the weight percents of component B in the solid and in the bulk liquid, respectively.

To apply Eqs. 5 and 6, the linear solidification rate u must be known. The value of u is related to the mass rate of solidification, dm''/dt, by the equation

$$dm''/dt = \rho'' A u \quad [7]$$

where ρ'' is the density of the solid and A is the solid-liquid interface area. In many cases the mass rate of solidification is determined by the heat conducted away from the interface per unit time. In some cases, the interface area A is given by the geometry of the experimental set-up, especially when the solid-liquid interface is virtually plane, e.g., during the growth of single crystals. In many cases, however, the solid-liquid interface area is not plane and may, therefore, be much larger than estimated from the geometry of the container. This is especially true when dendrites are formed. In the following calculations, a virtually plane interface is presumed. Limitations of this approach are discussed below.

If the composition of the solid differs from that of the liquid from which it is formed, the composition of the liquid varies with the advancement of solidification. Likewise the composition of the solid formed at different stages of the solidification process varies. Hence, there result local concentration differences in the solid after the solidification has been completed. This is called segregation. The greater the deviation of the ratio $c''_B/c'_{B(b)}$ from unity at a given time, the greater, in general, will be the local differences in composition of a solidified ingot. Thus, it follows from Eq. 6 that segregation is favored by: 1—a small value of the partition constant K, 2—a low linear solidification rate, 3—a high value of the diffusion coefficient D, and 4—a low value of the effective thickness of the diffusion boundary layer.

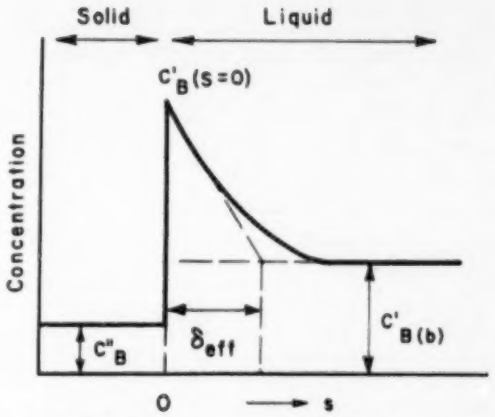

Fig. 1—Schematic concentration distribution of component B near the solid-liquid interface.

Convection of the liquid may lead to a nearly uniform distribution of the rejected portion of solute B in the liquid and thus to a gradually increasing concentration $c'_{B(b)}$. This causes macrosegregation. Without convection, microsegregation prevails.

Attention is called to the following apparent paradox. Stirring minimizes concentration differences within the liquid and thus virtually equilibrium between solid and bulk liquid may be reached. This, however, results in a maximum concentration difference between the bulk liquid and the outer layer of the solid corresponding to the value of K given by the phase diagram. On the other hand, without convection, there may be a considerable concentration difference between the bulk liquid and the liquid near the solid-liquid interface, but the composition of the outer layer of the solid may be virtually equal to the composition of the bulk liquid. Thus, an ingot solidified under conditions causing the uttermost state of nonequilibrium in the liquid may have an almost uniform composition.

In many cases, the value of δ_{eff} is not computable from first principles. Then Eq. 6 may be used to calculate δ_{eff} from observed values of N''_B and $N'_{B(b)}$ or $[\%B]''$ and $[\%B]'_{(b)}$ if u is known. Thus,

$$\delta_{eff} = \frac{D}{u}\,\frac{1 - K(N'_{B(b)}/N''_B)}{1-K} \quad [8]$$

From Eq. 8 it follows that there is a maximum value $\delta_{eff(max.)}$ if the difference in concentration between the solid and the bulk liquid vanishes, i.e., if $N''_B = N'_{B(b)}$. Hence

$$\delta_{eff(max.)} = D/u\,. \quad [9]$$

The existence of a maximum value of δ_{eff} is a rather unusual feature in contradistinction to other boundary layer problems.

Upon substitution of Eq. 9 in Eq. 6, it follows that

$$\frac{N''_B}{N'_{B(b)}} = \frac{[\%B]''}{[\%B]'_{(b)}} = \frac{K}{1 - (\delta_{eff}/\delta_{eff(max.)})(1-K)}\,. \quad [10]$$

The degree of segregation is, therefore, determined by the value of K and the ratio $\delta_{eff}/\delta_{eff(max.)}$. Convection leads to significant segregation only if convection is sufficiently vigorous in order to yield

Table I. Distribution of $SrCl_2$ between Solid and Liquid KCl for Different Rates of Growth According to Kelting and Witt[2]

Mol Fraction of $SrCl_2$ in Bulk Liquid	Mol Fraction of $SrCl_2$ in Solid	
	$u = 5 \times 10^{-4}$ cm/sec	$u = 1.7 \times 10^{-3}$ cm/sec
3×10^{-4}	0.8×10^{-4}	0.4×10^{-4}
6×10^{-4}	1.5×10^{-4}	0.7×10^{-4}

a value of δ_{eff} which is substantially less than the value of $\delta_{eff(max.)} = D/u$ according to Eq. 9.

In liquid metallic solutions the diffusion coefficient is of the order of 3×10^{-5} cm² per sec. If the rate of solidification is 1 cm per min, or $u = 0.017$ cm per sec, the value of $\delta_{eff(max.)}$ equals 1.8×10^{-3} cm. This indicates a rather small thickness of the diffusion boundary layer under most conditions.

In the following sections, the concentration distribution in the liquid is calculated for special conditions. Thus the value of δ_{eff} is eliminated from the foregoing equations in order to obtain the concentration ratio $c''_B/c'_{B(b)}$ in terms of the significant macroscopic variables.

Solidification without Convection

Solidification without convection in the liquid will be considered first. Natural convection will not take place if the solid-liquid interface is horizontal and the alloying element B increases the density so that the liquid alloy at the solid-liquid interface has a higher density than the bulk liquid above. If a liquid metal with a temperature slightly above its melting point T_f is poured into a flat mold with a very thick wall, the rate of solidification is essentially determined by heat conduction in the wall, the heat capacity of the wall, and its initial temperature T_w. In the limiting case of an infinitely thick wall, the solid-liquid interface advances proportionally to the square root of time as has been derived theoretically by Feild,[4] Lightfoot,[5] Schwarz,[6] Ruddle,[7] and others. Thus the distance Y of the solid-liquid interface from the wall of the mold as a function of time may be assumed to be given as

$$Y = (\alpha t)^{1/2} \qquad [11]$$

where α is a constant having the dimension length²/time, e.g., cm²/sec.

Under these conditions atoms of type B which are rejected at the solid-liquid interface remain in the boundary layer whose thickness increases proportionally to the square root of time. The composition of the bulk liquid remains unchanged until the very end of the solidification when finally the thickness of the boundary layer becomes of the order of the thickness of the bulk liquid.

The concentration ratio $c''_B/c'_{B(b)}$ for a plane solid-liquid interface has been calculated by a straightforward solution of the diffusion differential equation (see Appendix A). It is independent of time and determined by the equilibrium constant K in Eq. 1 and the ratio of the constant α in Eq. 1 to the diffusion coefficient D of the liquid alloy. The following limiting result is noteworthy:

$$\frac{c''_B}{c'_{B(b)}} \cong \frac{1}{1 + 2[(1-K)/K](D/\alpha)} \qquad [12]$$

if $\frac{1}{2}\alpha/D >> 1$.

Table II. Distribution of Constituent B Due to Natural Convection*

u, Cm/Sec	$c''_B/c'_{B(b)}$ for			
	$K = 0.8$	$K = 0.5$	$K = 0.2$	$K = 0.1$
0.001	0.96	0.82	0.44	0.24
0.003	1.00	1.00	0.83	0.67
0.01	1.00	1.00	1.00	1.00

* The following values are assumed: height of solid-liquid interface 1 cm; $D = 3 \times 10^{-5}$ cm² per sec; kinematic viscosity of liquid $\nu = 0.1$ cm² per sec; relative density difference $|\rho' - \rho'_0|/\rho'_0 = \beta c'_{B(b)} = 0.03$, where ρ' is the density of the bulk liquid and ρ'_0 is the density of pure liquid metal A.

For the solidification of steel ingots, Chipman and FonDersmith[8] have reported a value of $\alpha = 0.083$ cm² per sec, which is much greater than the diffusion coefficient of alloying elements in steel ($D \cong 3 \times 10^{-5}$ cm² per sec). Under these conditions, no noticeable segregation without convection can be expected except for very small values of K. This result may be generalized. The value of α will always be much greater than the value of D if the temperature of the mold is several hundred degrees lower than the melting point, since the heat conductivity of nonmetallic molds and the other values determining α except for the temperature difference between alloy and mold are always of the same order of magnitude. In principle, the temperature difference can be made sufficiently small so that α becomes of the order of D. If $\alpha = D = 3 \times 10^{-5}$ cm² per sec is assumed, it follows from Eq. 11 that 1 cm of solid metal is obtained after a time as long as 10 hr. This indicates that in general α will be much greater than D.

Very low solidification rates occur when single crystals are grown. Usually a constant solidification rate is maintained. Tiller, Jackson, Rutter, and Chalmers[9] have suggested a solution, which may be qualitatively correct but cannot be considered as a rigorous solution because Eq. 7 of their paper does not satisfy Fick's second law and the boundary condition at the solid-liquid interface stated above in Eq. 2. The most characteristic feature is the fact that the distribution ratio depends on time and finally tends to unity.

Although solidification rates used for the growth of single crystals are relatively small, the distribution ratio of a solute between solid and bulk liquid may differ from the equilibrium ratio as is indicated by the dependence of the experimental distribution ratio on the rate of solidification (see Table I).

Natural Convection

In the case of a vertical solid-liquid interface, natural convection plays a decisive part. If the alloying element B enriched at the solid-liquid interface increases the density ρ' of the liquid, a downward flow along the solid-liquid interface takes place. Conversely, a lower density of the boundary layer leads to an upward flow. The velocity v of the flow parallel to the interface is a function of the distance s from the interface and the distance x from the upper or lower end of the interface where the flow starts. The velocity and the concentration distribution may be calculated from differential equations similar to those for natural convection in the case of heat transfer (see Appendix B). The ratio of the concentrations in the solid and the bulk liquid is determined by the value of K and a dimensionless group ξ (see Fig. 2).

Numerical values compiled in Table II indicate that natural convection leads to significant concentration differences between the solid and the liquid phase only if the solidification rate is relatively low.

Convection Due to Ascending Gas Bubbles

In rimmed steel ingots, segregation is more pronounced than in killed steel ingots.[10] This indicates that ascending gas bubbles formed by the reaction C (in liquid Fe) + O (in liquid Fe) = CO (gas) decrease the effective thickness of the diffusion boundary layer. A straightforward theoretical analysis of conditions in a boundary layer involving ascending gas bubbles is not available.

A similar situation occurs if magnesium is dissolved in an aqueous solution of hydrochloric acid. Roald and Beck[11] have shown that diffusion of HCl to the metal-solution interface is the controlling factor. For magnesium rods revolving with high speed (6400 rpm), the dissolution rate is proportional to the HCl concentration, i.e., the effective thickness of the diffusion boundary layer is determined essentially by the rotation of the rod. In the case of magnesium rods at rest, however, the dissolution rate increases proportionally to a power of the HCl concentration greater than unity, because the effective thickness of the diffusion boundary layer decreases with increasing gas evolution. Since the volume of gas evolved per unit area per unit time is not the only factor determining the effective thickness of the diffusion boundary layer, no direct correlation to rimmed steel ingots is possible.

It is also known that ascending gas bubbles increase the rate of heat transfer from a solid wall to a boiling liquid. The geometrical conditions for heat transfer, however, differ substantially from those for the aforementioned problems of mass transfer, because vaporization takes place at the gas-liquid interface of a bubble and thus heat conduction from the solid-liquid interface to the liquid-gas interface is decisive, whereas for the solidification of an alloy or dissolution of magnesium in acid, mass transfer between the solid-liquid interface and the bulk liquid is the controlling factor. Heat transfer from a wall to a boiling liquid is, therefore, not analogous to mass transfer between the liquid-solid interface of a solidifying alloy and the bulk liquid.

Forced Convection

The effective thickness of the diffusion boundary layer may also be decreased by forced convection of the liquid, e.g., by stirring as usually applied in thermal analysis. Vigorous stirring may preclude marked concentration differences across the boundary layer so that the composition of the originating solid phase is virtually the equilibrium composition corresponding to the bulk liquid.

The concentration ratio $c''_B/c'_{B(b)}$ may be calculated theoretically for solidification of an alloy at the surface of a rotating disk. For laminar flow the hydrodynamic equations have been solved by von Kármán[12] and Cochran.[13] The thickness of the hydrodynamic boundary layer is determined by the angular velocity ω of the disk and the kinematic viscosity of the liquid and is independent of the distance from the axis. A straightforward calculation yields the concentration of B as a function of the distance from the solid-liquid interface. Hence it follows that

$$\frac{c''_B}{c'_{B(b)}} = \frac{K}{1-(1-K)f(\gamma)} \qquad [13]$$

where

$$f(\gamma) = \int_0^\infty \exp\left(-\tau - 0.171\,\tau^3/\gamma^3\right) d\tau \qquad [14]$$

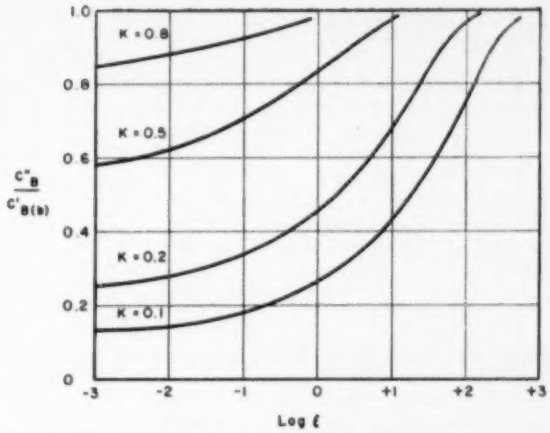

Fig. 2—Concentration ratio $c''_B/c'_{B(b)}$ as a function of the dimensionless group

$$\xi = \frac{45\,\nu\,u'x}{8g\,\beta c'_{B(b)}\,D^2}$$

where ν is the kinematic viscosity of the liquid, x is the distance from the leading edge of the boundary layer, g is gravitational acceleration, and $\beta = |\partial \ln \rho' / \partial c'_B|$.

with τ as a variable of integration and the dimensionless group γ defined as

$$\gamma = u\nu^{1/6}/D^{2/3}\omega^{1/2}. \qquad [15]$$

From Eq. 13 it follows that rather high angular velocities are required in order to obtain a distribution ratio close to the equilibrium value K. For instance, for $K = 0.5$, $u = 0.01$ cm per sec, $\nu = 0.1$ cm^2 per sec, and $D = 3\text{x}10^{-5}$ cm^2 per sec, an angular velocity of $\omega = 75$ sec^{-1} corresponding to 12 revolutions per second is needed in order to obtain halfway equilibrium between solid and bulk liquid, i.e., $c''_B/c'_{B(b)} = 0.75$. In view of Eqs. 13 to 15, the required angular velocity is inversely proportional to the square of the rate of solidification u and therefore decreases rapidly if a lower solidification rate is used.

Stability Problems

The foregoing analysis shows that the composition of the solid will be close to the composition of the bulk liquid unless the linear rate of solidification is very low, or vigorous stirring is provided. This seems to be contradictory to general experience since significant segregation does occur in many cases. To resolve this apparent conflict, it is necessary to take into consideration the stability of the boundary layer. It will be shown that a boundary layer involving a concentration difference higher than about one atomic percent is not stable.

Rutter and Chalmers[2] have pointed out that different local concentrations of solute B in the liquid correspond to different solid-liquid equilibrium temperatures according to the phase diagram. When solute B is enriched at the solid-liquid interface, the equilibrium temperature at the interface is therefore lower than the equilibrium temperature at any point remote from the interface. The following cases are to be considered:

1—If there is a steep temperature gradient in the liquid and the solute concentration is very low, the actual local temperature in the liquid may everywhere be higher than the local equilibrium solidification temperature (see Fig. 3a). In this case no

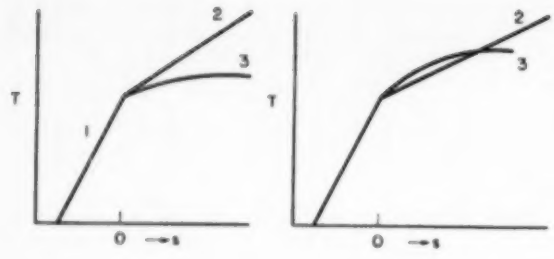

a—For a stable state of the boundary layer.

b—For a metastable state of the boundary layer.

Fig. 3—Temperature distribution and local equilibrium solidification temperature at the solid-liquid interface. Curve 1—Local temperature of the solid. Curve 2—Local temperature of the liquid. Curve 3—Local equilibrium solidification temperature.

part of the liquid will solidify except at the interface.

2—If the solute concentration is higher, there will be a region where the actual local temperature is below the local equilibrium solidification temperature (see Fig. 3b). Such a state is unstable but not impossible. The rate of nucleation of the solid phase is significant only when the degree of supercooling Θ, defined as the difference between the actual temperature and the equilibrium solidification temperature, exceeds a critical value ΔT_n, which in most alloys is of the order of several degrees. In view of the high heat conductivity of metallic phases, temperature differences within the boundary layer, i.e., over a distance of 10^{-4} to 10^{-5} cm, are always small, in general less than 1°C, and may be disregarded in most cases. The degree of supercooling $\Theta(s)$ at distance s from the solid-liquid interface is, therefore, proportional to the difference between the concentration of solute B at the solid-liquid interface and the local concentration

$$\Theta(s) = [N'_B(s=0) - N'_B(s)] \times |dT/dN'_B| \quad \text{if } dT/ds \cong 0 \qquad [16]$$

where $|dT/N'_B|$ is the absolute value of the slope of the liquidus. Thus

1—If $\Theta < \Delta T_n$, the thermodynamic instability of the boundary layer has no consequences.

2—If $\Theta > \Delta T_n$, rapid nucleation in the boundary layer takes place. The occurrence of such a boundary layer is, therefore, ruled out.

For a melting point of 1000°K ≅ 700°C of the solvent metal A and a value of $K<0.3$, the value of $|dT/dN'_B|$ is of the order of 1000°. Then it follows from the condition $\Theta < \Delta T_n$ that the concentration difference across the boundary layer cannot exceed 1 atomic pct if $\Delta T_n = 10°$. The permissible concentration difference will be even less if the critical temperature difference for a significant nucleation rate is lower than 10°.

Upon equating the right-hand side of Eq. 16 for $N'_B(s) = N'_{B(b)}$ to ΔT_n, solving for $N'_B(s=0)$, and substituting in Eq. 1, a maximum value of the concentration ratio between the solid and the bulk liquid is obtained,

$$\frac{c''_B}{c'_{B(b)}} = \frac{N''_B}{N'_{B(b)}} \leqq K\left(1 + \frac{\Delta T_n}{N'_{B(b)}|dT/dN'_B|}\right). \qquad [17]$$

Eq. 17 does not invalidate equations derived above but rather limits the linear solidification rate u by an "adjustment" of the solid-liquid interface area A. Thus, according to Eq. 7, a relatively low linear solidification rate may result and accordingly the distribution ratio of a solute between solid and liquid may become much closer to the equilibrium ratio than has been estimated in the foregoing sections for special conditions.

For instance, if $K = 0.5$, and $|dT/dN'_B| = 1000°$, $\Delta T_n = 5°$, and $N'_{B(b)} \leqq 0.005$, the distribution ratio $c''_B/c'_{B(b)}$ can assume any value between $K = 0.5$ and unity.

For values of $N'_{B(b)} > 0.005$, the range of $c''_B/c'_{B(b)}$ is restricted in view of Eq. 17 as is illustrated by the following data:

$N'_{B(b)} = 0.01; 0.02; 0.05; 0.10.$
$c''_B/c'_{B(b)} \leqq 0.75; 0.625; 0.55; 0.525.$

At higher concentrations, more severe segregation is, therefore, expected.

Use of a definite value ΔT_n in Eq. 17 is, of course, only an approximation. Actually, the nucleation rate is a continuous function of temperature, i.e., the value of ΔT_n is not a constant. Olsen and Hultgren[11] have found that Cu-Ni alloys cooled at extremely high rates do not exhibit noticeable segregation. This indicates that at high solidification rates the effective ΔT_n value may be higher than at slow cooling rates. Then according to Eq. 17 the minimum value of $c''_B/c'_{B(b)}$ is raised and, eventually, $c''_B/c'_{B(b)}$ may approach unity.

Rutter and Chalmers[2] have discussed the local solidification rate at a solid-liquid interface involving protruding parts and have shown that the solidification rate at protruding points is higher if there is "constitutional supercooling" of the boundary layer shown in Fig. 3b. In other words, a solid-liquid interface will tend to "buckle." According to Rutter and Chalmers[2] even very low concentrations of alloying elements, e.g., 0.03 atomic pct, may lead to the formation of a "corrugated interface," whose area is somewhat greater than the apparent interface area.

This effect may be considered as the onset of dendrite formation, which becomes significant at higher concentrations of alloying elements.

Concluding Remarks

In view of stability limitations, the foregoing calculations can be applied directly only to the solidification of alloys involving very low concentrations of solutes, because at higher concentrations the linear solidification rate is not directly related to the mass rate of solidification. It has been shown that under most conditions no significant segregation is expected if the solute concentration is low. On the other hand, significant concentration differences between solid and liquid are expected and observed if the solute concentrations are of the order of several atomic percent, and dendrites are formed. At a given mass rate of solidification, an alloy involving 0.1 atomic pct B may, therefore, exhibit only slight segregation, whereas at a concentration of 3 atomic pct B pronounced segregation will occur. Segregation of constituent B is also expected if the concentration of B is low, e.g., 0.1 atomic pct, and another solute C is present at a concentration of several atomic percent whereby dendrites are formed and the linear solidification rate is considerably decreased in comparison to an alloy containing only 0.1 atomic pct B.

In this paper, incomplete establishment of the distribution equilibria of alloying elements between the solid and the liquid phase is not considered. Deviations from Eq. 1 as a function of the growth rate are of considerable theoretical interest. Reference is made to recent investigations on the solidification of germanium by Hall.[16]

Acknowledgment

The author is indebted to Dr. M. B. Bever for helpful comments. This work was done as a part of investigations sponsored by the Atomic Energy Commission under Contract No. AT-30-Gen-1002.

Appendix A

Concentration Distribution without Convection

When an alloy solidifies without convection and the rate of solidification is determined by heat flow into the wall of a mold according to Eq. 11, the concentration c'_B of solute B in the liquid may be calculated as follows. Fick's second law reads

$$(\partial c'_B/\partial t) = D(\partial^2 c'_B/\partial y^2) \qquad [18]$$

where y is the distance from the mold-metal interface. The initial condition is

$$c'_B = c''_{B(b)} \text{ for } y > 0,\ t = 0. \qquad [19]$$

According to Eq. 1 the equilibrium condition at the solid-liquid interface is

$$c''_B = K\,c'_B \text{ at } y = (\alpha t)^{1/2}. \qquad [20]$$

In view of Eq. 11, Eq. 2 becomes

$$\tfrac{1}{2}\alpha^{1/2}t^{-1/2}(1-K)(c'_B)_{y=(\alpha t)^{1/2}} = -D(\partial c'_B/\partial t)_{y=(\alpha t)^{1/2}}. \qquad [21]$$

Except for the end of the solidification process, solutions for a semi-infinite liquid may be used. Eqs. 18 to 21 are satisfied by

$$\frac{c'_B}{c'_{B(b)}} = 1 + \frac{(1-K)\,erfc(y/2D^{1/2}t^{1/2})}{(2D^{1/2}/\pi^{1/2}\alpha^{1/2})\exp(-\alpha/4D) - (1-K)\,erfc(\alpha^{1/2}/2D^{1/2})} \qquad [22]$$

$$\frac{c''_B}{c'_{B(b)}} = \frac{K}{1-(1-K)\dfrac{\pi^{1/2}\alpha^{1/2}}{2D^{1/2}}\dfrac{erfc(\alpha^{1/2}/2D^{1/2})}{\exp(-\alpha/4D)}}. \qquad [23]$$

For large arguments z of the complementary error function the following approximation may be used

$$erfc\,z \cong \pi^{-1/2}(e^{-z}/z)(1 - \tfrac{1}{2}z^{-2} + \ldots). \qquad [24]$$

Substitution of Eq. 24 in Eq. 23 gives Eq. 12.

Appendix B

Concentration Distribution Determined by Natural Convection

Beckmann and Schmidt[19] have derived the differential equations which determine velocity and temperature distribution in the case of heat transfer controlled by natural convection. Similar equations hold for mass transfer. According to von Kármán,[12] Goldstein,[17] Eckert,[18] and others, an approximation may be obtained by introducing appropriate polynomials for the velocity and the concentration distribution as functions of distance s in order to avoid the cumbersome numerical solution of differential equations.

According to von Kármán,[12] the shearing stress at the solid-liquid interface, given by the product of dynamic viscosity μ of the liquid and the velocity gradient $(\partial v/\partial s)_{s=0}$, is equal to the sum of the buoyancy of the boundary layer per unit interface area and the change in the flow of momentum per unit width per unit length in the flow direction. The latter term can be disregarded because for $\mu/\rho' D >> 1$ the effect of inertia is important only at large distances from the solid-liquid interface.[19] Thus

$$\mu(\partial v/\partial s)_{s=0} = g\int_0^\delta \Delta\rho\,ds \qquad [25]$$

where g is the gravitational acceleration, $\Delta\rho$ is the absolute value of the difference between the local and the bulk density of the liquid, and δ is a distance at which practically the bulk concentration is reached.

The density difference may be expressed as

$$\Delta\rho = \beta\rho'_b(c'_B - c'_{B(b)}) \qquad [26]$$

where ρ'_b is the density of the bulk liquid and

$$\beta = \frac{1}{\rho'_b}\left|\frac{\partial\rho'}{\partial c'_B}\right| \qquad [27]$$

is a constant.

Upon substituting Eq. 26 in Eq. 25 and introducing the kinematic viscosity $\nu = \mu/\rho'_b$, it follows that

$$\nu(\partial v/\partial s)_{s=0} = g\int_0^\delta \beta(c'_B - c'_{B(b)})\,ds. \qquad [28]$$

The flow velocity and the thickness of the boundary layer increase along the solid-liquid interface. Thus the mass rate also increases in the flow direction. On the other hand, the boundary layer looses the mass $\rho''u$ per unit area per unit time owing to solidification where ρ'' is the density of the solid phase. Accordingly there is an inflow of liquid into the boundary layer with a flow velocity v_n at $s = \delta$ normal to the solid-liquid interface. The equation for the conservation of mass reads

$$\frac{d}{dx}\int_0^\delta \rho' v\,dy + \rho''u = \rho'_b v_n. \qquad [29]$$

In Eq. 29, local density differences and the density difference between the liquid and the solid phase may be disregarded. Thus Eq. 29 becomes

$$v_n \cong \frac{d}{dx}\int_0^\delta v\,ds + u. \qquad [30]$$

The balance of component B in a volume element of the boundary layer of width b and thickness δ between x and $x + dx$ is calculated as follows:

1—The gain of component B per unit time due to inflow of liquid normal to the solid-liquid interface is $c'_{B(b)}v_n b\,dx$.

2—The gain of component B per unit time due to flow parallel to the solid-liquid interface at distance x is

$$b\left(\int_0^\delta c'_B v\,ds\right)_x.$$

3—The loss of component B per unit time due to flow parallel to the solid-liquid interface at distance $x + dx$ is

$$b\left(\int_0^\delta c'_s v ds\right)_x + b\left[\frac{d}{dx}\int_0^\delta c'_s v ds\right] dx.$$

4—The loss of component B per unit time due to transfer of B from the liquid to the solid phase is $c''_s u b dx$.

Thus the steady-state balance reads

$$v_x c'_{s(b)} b dx = \left[\frac{d}{dx}\int_0^\delta c'_s v ds\right] b dx + u c''_s b dx. \quad [31]$$

Upon substituting Eq. 30 in Eq. 31 and dividing Eq. 31 through by $b dx$, it follows that

$$c'_{s(b)}\frac{d}{dx}\int_0^\delta v ds + c'_{s(b)} u = \frac{d}{dx}\int_0^\delta c'_s v ds + u c''_s. \quad [32]$$

To obtain an approximate solution by means of the method suggested by von Kármán,[12] the following approximate expressions for the velocity and the concentration in the boundary layer as functions of the distance s from the solid-liquid interface are introduced

$$v = v_\delta[2(s/\delta) - (s/\delta)^2] \text{ for } 0 \leqq s \leqq \delta \quad [33]$$

$$c'_s = c'_{s(b)} + [c''_s/K - c'_{s(b)}](1 - s/\delta)^2 \text{ for } 0 \leqq s \leqq \delta \quad [34]$$

where v_δ is the flow velocity parallel to the solid-liquid interface at the outer side of the diffusion boundary layer ($s = \delta$) and c''_s/K is the concentration of B in the liquid phase at $s = 0$ according to Eq. 1. The functions assumed in Eqs. 33 and 34 are admittedly arbitrary but different functions yield the same order of magnitude for the quantities of practical interest, especially $(\partial c'_s/\partial s)_{s=0}$ and δ_{eff}.

From Eq. 34 it follows that

$$(\partial c'_s/\partial s)_{s=0} = -2[c''_s/K - c'_{s(b)}]/\delta = -2[c'_s(s=0) - c'_{s(b)}]/\delta. \quad [35]$$

The value of δ based on Eq. 34 is therefore twice the value of δ_{eff} defined by Eq. 4,

$$\delta = 2\delta_{eff}. \quad [36]$$

Substituting Eq. 36 in Eq. 5,

$$c''_s = \frac{c'_{s(b)} K}{1 - (\frac{1}{2}u\delta/D)(1 - K)}. \quad [37]$$

Substituting Eqs. 33, 34, and 37 in Eq. 28 and solving for v_δ,

$$v_\delta = \frac{g\beta c'_{s(b)} u (1 - K)\delta^2}{12\nu D[1 - (\frac{1}{2}u\delta/D)(1 - K)]}. \quad [38]$$

Substitution of Eqs. 33 and 34 in Eq. 32 yields

$$(c'_{s(b)} - c''_s)u = \frac{2}{15}\frac{d}{dx}\{[c''_s/K - c'_{s(b)}]v_\delta\delta\}. \quad [39]$$

Substituting Eqs. 37 and 38 in Eq. 39, dividing through by $u c'_{s(b)}$, and regrouping,

$$1 - \frac{K}{1 - (\frac{1}{2}u\delta/D)(1 - K)} = \frac{d}{dx}\left\{\frac{1}{180}\frac{g\beta c'_{s(b)} u (1 - K)^2\delta^3}{\nu D^2[1 - (\frac{1}{2}u\delta/D)(1 - K)]^2}\right\}. \quad [40]$$

Upon introduction of the dimensionless groups

$$\sigma = \frac{1}{2}u\delta/D = \delta_{eff}/\delta_{eff(max.)} \quad [41]$$

$$\xi = \frac{45\nu u' x}{8 g\beta c'_{s(b)} D^2}. \quad [42]$$

Eq. 40 becomes

$$1 - \frac{K}{1 - \sigma(1 - K)} = \frac{d}{d\xi}\left\{\frac{(1 - K)^2\sigma^5}{[1 - \sigma(1 - K)]^2}\right\}. \quad [43]$$

Transforming and integrating Eq. 43,

$$\xi = (1 - K)\int_0^\sigma \frac{[5\sigma^4 - 3(1 - K)\sigma^5]\, d\sigma}{(1 - \sigma)[1 - \sigma(1 - K)]^2}. \quad [44]$$

A closed solution of the integral on the right-hand side of Eq. 44 may be obtained but its numerical evaluation requires less labor.

Substitution of Eq. 41 in Eq. 37 yields

$$\frac{c''_s}{c'_{s(b)}} = \frac{K}{1 - \sigma(1 - K)}. \quad [45]$$

An auxiliary graph ξ vs σ for selected values of K according to Eq. 44 was prepared. From this graph and Eq. 45 values of $c''_s/c'_{s(b)}$ were calculated and plotted vs ξ, see Fig. 2.

The distribution of the solute between the solid and the liquid phase therefore depends on: 1—the value of the equilibrium constant K, and 2—the value of the dimensionless group ξ defined in Eq. 42, in which the solidification rate u is the most important factor.

References

[1] A. Hayes and J. Chipman: *Trans.* AIME (1939) **135**, p. 85.

[2] J. W. Rutter and B. Chalmers: *Canadian Journal of Physics* (1953) **31**, p. 15; and B. Chalmers: *Ibid.*, p. 132.

[3] W. A. Tiller, K. A. Jackson, J. W. Rutter, and B. Chalmers: *Acta Metallurgica* (1953) **1**, p. 428.

[4] A. L. Feild: *Trans.* Amer. Soc. Steel Treating (1927) **11**, p. 264.

[5] N. M. H. Lightfoot: *Journal* Iron and Steel Inst., London (1929) **119**, p. 364.

[6] C. Schwarz: *Archiv Eisenhüttenwesen* (1931) **5**, pp. 139, 177.

[7] R. W. Ruddle: The Solidification of Castings. *Monograph and Report Series No. 7*, pp. 23ff. Inst. of Metals, London (1950).

[8] J. Chipman and C. R. FonDersmith: *Trans.* AIME (1937) **125**, p. 370.

[9] H. Kelting and H. Witt: *Ztsch. Physik* (1949) **126**, p. 697.

[10] *Basic Open Hearth Steelmaking* (1951) Second edition, pp. 434ff. New York. AIME.

[11] B. Roald and W. Beck: *Journal* Electrochem. Soc. (1951) **98**, p. 278.

[12] Th. von Kármán: *Ztsch. angew. Mathematik Mechanik* (1921) **1**, p. 233. NACA Technical Memorandum No. 1092 (1946).

[13] W. G. Cochran: *Proc.* Cambridge Phil. Soc. (1934) **30**, p. 365.

[14] W. T. Olsen and R. Hultgren: *Trans.* AIME (1950) **188**, p. 1323; JOURNAL OF METALS (November 1950).

[15] R. N. Hall: *Physical Review* (1952) **88**, (2), p. 139. *Journal of Physical Chemistry* (1953) **57**, p. 836.

[16] E. Schmidt and W. Beckmann: *Techn. Mechanik u. Thermodynamik* (Forschung) (1930) **1**, pp. 541, 591.

[17] S. Goldstein: *Modern Development of Fluid Dynamics* (1938) p. 641. New York, Oxford University Press.

[18] E. R. G. Eckert: *Introduction to the Transfer of Heat and Matter* (1950) pp. 158ff. New York, McGraw-Hill Book Co.

[19] C. Wagner: *Journal* Electrochem. Soc. (1949) **95**, p. 161.

AIME OFFICERS:
President—Andrew Fletcher
Vice-Presidents—T. B. Counselman, L. E. Elkins, O. B. J. Fraser, J. L. Gillson, A. B. Kinzel, J. B. Morrow
President-Elect—L. F. Reinartz
Treasurer and Controller—G. I. Brigden
AIME STAFF:
Secretary—E. H. Robie
Ass't. Secretaries—J. B. Alford, H. N. Appleton, E. J. Kennedy, Jr., Ernest Kirkendall, R. E. O'Brien
Ass't. Treasurer—P. J. Apol

Grayson Kirk, President, Columbia University To Speak at Annual Meeting Welcoming Luncheon

LEADING off with the Welcoming Luncheon at the Hotel Statler, the Annual Meeting in New York, February 15 to 18, will present one of the most attractive lists of social functions in its history.

Prime attraction of the Welcoming Luncheon Monday will be Dr. Grayson Kirk, president of Columbia University. Dr. Kirk will speak on the

GRAYSON KIRK

Bicentennial Celebration of Columbia. Special tables have been reserved for wives of men at the head table, student paper award winners, and ladies of advanced years attending the meeting. Price for the Welcoming Luncheon is $4.50. James Boyd is Chairman of the Welcoming Luncheon committee. Members of the committee assisting him are: Mrs. Francis Cameron, Mrs. Lyman Hart, Darwin Pope, W. J. Turner, Julian W. Feiss, and Park Hodges.

The Penn Top and Sky Top rooms of the Statler will be open from 6:00 pm to 7:30 pm Monday for the pre-smoker cocktail party, free to all registrants. Annually, the cocktail party has served to help renew old friendships and strike up new ones. The party is under the sponsorship of several companies.

With the Latin Quarter show as the feature attraction, the Dinner-Smoker will begin at 8:00 pm Monday. The Latin Quarter is one of New York's most famous night clubs and its shows are always spectacular. The current edition is said to be one of the greatest in the club's history. The costuming is unusual, the talent resplendent, and the acts better than ever. Price for the Latin Quarter show and the Dinner-Smoker has been pegged at $10.00. C. DeWitt Smith is Chairman of the committee, while Louis C. Raymond serves as Vice-Chairman. Committee members are Frederick R. McIntosh, Joseph B. Terbell, and Austin Goodyear. The Michigan School of Mines will hold a cocktail party and dinner in the Penn Top North Statler Hotel, at 6:00 pm on Tuesday.

One of the most attractive events Tuesday evening will be the Informal Dance, scheduled to start at 9:00 pm. Refreshments wil be available throughout the evening. An audience participation program has been planned and door prizes will go to lucky ticket holders. Tickets for the dance are $3.50 each. C. P. Jenney is Chairman of the committee, with Mrs. Robert Rowan and David T. Steele assisting him.

The Montana School of Mines Alumni group will meet for cocktails at 6:30 pm on Tuesday, and dinner will be at 7:30 pm in Parlor A at the Statler. Ladies are invited.

Tickets for the Scotch Breakfast, slated for Tuesday morning are $5.00. The breakfast, a tradition of the Minerals Beneficiation Div., will include entertainment and will be held in the Cafe Rouge of the Statler.

The Annual Banquet will be held at 7:00 pm in the Waldorf Astoria Ballroom. Presentation of awards and honors will follow dinner and it is guaranteed that there will be no long speeches. All those attending will receive favors. The President's Reception will be held in the East Foyer following award presentations. Dancing will be from 10:00 pm to 2:00 am. Tickets for the Banquet are $12.00 each. While dress is optional, black tie is preferred. Members of the Banquet Committee are: J. T. Sherman, Chairman; John Payne, Jr., Vice-Chairman; Kenneth E. Hill; Henry W. Hitzrot; W. A. Mudge; Robert B. Fulton; Frank R. Milliken; Mrs. E. H. Robie, and Mrs. H. DeWitt Smith.

Registration for ladies who are members of WAAIME will be $1.00, and for nonmembers $2.00. The New York Section of the WAAIME will be hosts at a welcoming coffee party immediately after Monday morning registration. Monday's round of social functions will of course include the Welcoming Luncheon and evening cocktail party. The WAAIME will hold its Annual Meeting Tuesday morning. A Luncheon and Fashion Show follows on the Starlight Roof of the Waldorf Astoria, with each lady receiving a favor. Tickets are $6.00 each. The Informal Dance, Banquet, and round table discussion round out the week's activities.

Evan Just has been performing the various and many tasks of the Annual Meeting Reception Committee. Assisting him have been Alvin W. Knoerr, Rene J. Mechin, J. F. Meyers, John F. Ffolliott, James Wroth, and Clement Pollock. Robert Ramsey is Chairman of the General Committee. Alvin W. Knoerr is Secretary. Vice-Chairmen of the group are G. Howard LeFevre, and John Ffolliott, while James S. Vanick is Treasurer.

The following winners of the 1953 National Student Prize Paper Contest have been announced, and they have been invited to be guests of the Institute at the Welcoming Luncheon at the Annual Meeting. All are undergraduates, no graduate papers of sufficiently high standard having been entered this year.

Russell M. Corn, Student Associate at Montana School of Mines, for his paper *Fluorite Deposits in the Dry Creek District near Superior, Mineral County, Montana*, entered by the Montana Section.

James Milo Stewart, Student Associate at the University of Kansas, for his paper, *Calculation of Gas Reserves in a Small Kansas Gas Pool*, entered by the Kansas Section.

James Lommel, Student Associate at the Illinois Institute of Technology, for his paper, *Isothermal Grain Growth in OFHC Copper*, entered by the Chicago Section.

LEO F. REINARTZ

President, AIME, 1954

TALK to Leo F. Reinartz, the people who know him, and the men who work under him, and one transcending factor emerges—his devotion throughout his industrial career to a philosophy of teamwork and cooperation.

It has been the idea he has carried during his 44 years with Armco Steel Corp.—from chemist to vice-president in charge of mines, quarries, and special operating development. His philosophy has spilled generously over into community life. Mr. Reinartz plans to bring that feeling for teamwork and cooperation to the AIME Presidency.

Couple this attitude with a quiet confidence and Leo Reinartz begins to take form as a concrete individual with reverence for the inquisitive mind and faith in the future of the steel industry.

The day in 1909 when he came to Armco Steel was a big one for Leo Reinartz. He was a young man fresh from Carnegie Institute of Technology. The years behind him had been important ones—filled with experience and learning. The years ahead would see him become open hearth foreman, superintendent of open hearths, assistant general superintendent, manager of the Middletown Div., and assistant vice-president. He held the position of manager for 21 years.

Mr. Reinartz came from a large family. With five brothers and one sister, even the $35 per year tuition at Carnegie Tech presented problems. An odd assortment of jobs furnished the money for room, board, and books. In his freshman year Mr. Reinartz worked as conductor on a Pittsburgh streetcar. Later, he was employed as a laboratory assistant

and he also taught chemistry to nuns. Summers he worked on a farm for a dollar a day. If it rained, Mr. Reinartz recalled, he wasn't paid.

When Mr. Reinartz was a student at Carnegie Tech, practical applications were emphasized. Not enough time was devoted to theory, according to Mr. Reinartz. He feels that metallurgical engineering curriculum today is better adjusted to the needs of the student. However, Mr. Reinartz makes two reservations. He says "there is a definite need for more instruction in personal and public relations. Young engineers should be taught that every business has a personality—good, bad, or indifferent. They must learn that they have an important part to play in the shaping of that personality. There is also a need for greater emphasis on the Humanities. The engineer must be a whole man—not just a technician or scientist."

Foundation for his views stems from his years as a student in Pittsburgh and his earlier years in East Liverpool, Ohio, where he was born. Mr. Reinartz feels that bad management and lack of understanding were responsible for many of the strikes that ripped Pittsburgh during the first part of the 20th century. Conversely, his Lutheran minister father had been the arbitrator in a number of strikes in East Liverpool. Mr. Reinartz early learned the efficaciousness of common sense in labor disputes. And there were other, more personal battles fought in East Liverpool. Contracting polio at the age of three, Mr. Reinartz struggled to regain the use of weakened muscles. With his mother as an inspirational force, he endeavored to make his mind do the work his muscles could not, and at the same time he started using the gym at the YMCA under special dispensation. A measure of his success is indicated by the fact that he made his high school track team as a high jumper and competed later on in Armco industrial track meets.

It was across the river from East Liverpool at Chester, Va., that the desire to become part of the metals industry was born. Invited with his father to inspect a tin plate mill, Mr. Reinartz saw red hot sheets of metal, felt the heat, and heard the noise and decided they added up to the most glamorous thing in the world. He says, "I decided that it was the kind of work I wanted to do and I never changed my mind." Today, ask Leo Reinartz if he has a hobby and he answers, "My vocation, avocation, and continuing interest is the making of better steel."

In keeping with this absorption with his life's work, Mr. Reinartz has been one of the driving forces behind the National Open Hearth Conference of the AIME since attending its first meeting in 1925. Serving as its Chairman for 18 years, he strove mightily to make it a successful dynamic organization. He believes that the interchange of steelmaking knowledge promoted by the National Open Hearth Conference did much to make possible the tremendous increase in steel production from already existing facilities during World War II. Mr. Reinartz is now a Life Member of the National Open Hearth Conference.

All of Mr. Reinartz's 44 years with Armco have been at the Middletown works. He went there because a college professor had told him it was a company with a future. He knew little more about the corporation. A lot of Middletown residents knew even less. During his first years with Armco he set about learning all he could about open hearths. In addition to many technical improvements he has been responsible for certain other things—perhaps less tangible but of great importance. He helped convince the plant's operating and labor force that good housekeeping and good steel production go together. Mr. Reinartz started a campaign to enliven the inside and outside of the plant by use of bright colors and the planting of trees, flowers, and grass around the grounds.

Also as manager he began a newsletter to employees, telling them what was going on in the company. Today, the various works managers continue the practice. He sees Institute headquarters serving somewhat the same function of information distribution.

"Headquarters should serve as a clearing house for local sections, with its primary function the supplying of information and the giving of aid to local groups. It is the place where local sections are helped to help themselves. Institute control should be decentralized, with no group or individual exercising more than a fair share of authority."

Mr. Reinartz also feels that the office of the presidency cannot be successfully carried out by one man. The phenomenal growth of the AIME makes its imperative that the Institute's chief executive get help.

"I plan to form a voluntary group to assist in spreading the Institute gospel to colleges and local sections. Right now, AIME interest among certain faculty members and student bodies is not as intense as it could be. If the AIME story is presented properly I am sure we can look forward to the growth of strong campus student chapters."

Mr. Reinartz is a member of a long list of technical and civic groups. Among them are: American Management Assn.; Iron & Steel Engineers Assn.; National Chamber of Commerce; Board of Directors of the Hospital Care Assn., South West Ohio; Minerals and Metals Advisory Board, National Academy of Sciences; Vice President, Middletown Savings & Loan Assn.; Treasurer, Middletown Industrial Council; Board of Directors, Middletown Safety Council; Chairman, Red Cross Blood Procurement Committee, Middletown; and Board of Regents, Capital University, Columbus, Ohio.

Mr. Reinartz maintains an interest in developments in steelmaking abroad as well as in the U. S. One plan for his term as AIME President is a trip to Europe to cement already good relations with engineers in England and on the Continent.

A chat with Leo Reinartz leaves the impression that here is a man whose eyes are on the future. He has no use for the prophets of doom and feels that "the next 50 years will bring marvels to the steel industry that will literally dwarf those of the last 50."

One day in 1916 stands out in Mr. Reinartz's mind. On that day he had a new promotion, a new wife, and a new home. He married Mathilda Zix and was also named open hearth superintendent. Mr. and Mrs. Reinartz had two daughters and a son. The son, Leo Reinartz, Jr., was killed while leading a tank charge on Leyte in 1944. He is survived by a daughter born three months before her father's death. Mr. Reinartz has one interest aside from profession and community—his five grandchildren.

Mr. Reinartz served as Vice-President of the AIME from 1945 to 1948 and has been a Member of the Board of Directors. He is a Past Chairman of the Iron and Steel Div., Past Chairman of the Membership Committee, and served for many years on the Physical Chemistry of Steelmaking Committee.

Committee Plans Northwest Conference Program

AIME Members working toward making the next Pacific Northwest Conference in Portland, Ore., a success are, from left to right, Hal Seykota, Bill Wiltschko, Don W. Johnson, and Frank X. Cappa.

Four metals sessions will feature the Pacific Northwest Conference April 29 to May 1 at Portland, Ore. Headquarters for the meeting will be the Multnomah Hotel.

Francis X. Cappa is serving as General Chairman of the conference, with Harold A. Lee, G. R. Heffernan, and S. E. Maddigan, assisting in arranging the metals part of the schedule. Plant tours, luncheon and top interest speakers are slated for the program.

The Pacific Northwest Conference started eight years ago, with a one-day industrial minerals session, under the sponsorship, on a rotational basis, by the Oregon, North Pacific, and Columbia Sections. Since then, it has grown to its current three day format and includes industrial minerals, applied geology, groundwater resources, minerals industries education, extractive metallurgy, iron and steel, and physical metallurgy.

Preliminary Budget For 1954 Adopted

A preliminary budget for 1954 was adopted by the Executive and Finance Committees of the AIME at their Dec. 16, 1953 meeting. It will be reviewed and a final budget adopted next spring. Income for 1954 is set at $697,000 and expenses $678,300, leaving an expected surplus of $18,700 for further replenishment of reserve funds which were virtually exhausted to meet the deficits of 1946-50. Income from dues is expected to be $366,500, or 53 pct of the total; advertising should net $233,000, or 33 pct; sales of publications, $72,500, or 10 pct; and initiation fees, $21,000, or 3 pct.

Major expense is for publications, $374,800, or 55 pct of the total. Service of one kind or another to Branches, Divisions, Local Sections, Student Chapters, and members totals $132,000, or 19 pct. This includes the expense of the Salt Lake office, a good share of the expense of the Dallas office except that charged to publications; membership promotion and processing, Local Section appropriations and Section Delegates' travel, salaries and expenses of Division and Branch secretaries, and library service. The remaining quarter of Institute income, $171,500, is expected to cover all expenses of the Secretary's office including his travel; expenses of the business office, including office management, purchasing, accounting, filing, shipping and receiving, Addressograph, Multilithing, orders, and all expense chargeable to the Directory; pensions and related expense; insurance, and depreciation.

Branchwise, income is expected to be $314,445 for Mining, $189,435 for Metals, and $193,120 for Petroleum. Expense is divided $290,960 for Mining, $206,272 for Metals, and $181,068 for Petroleum. Present division of the AIME membership is Mining, 48.5 pct, Petroleum 26 pct, and Metals 25.5. Compared with ten years ago this represents an increase of about 10 percentage points for the Petroleum Branch and a decrease of like amount for the Mining Branch.

In considering a rough draft of the budget prepared by the staff, the Committees decided to reduce expenses by $4500 through a reduction in the number of Institute of Metals Transactions pages from 750 to 650, and by postponing the next issue of the AIME Directory to early 1955. A supplement, similar to that issued last spring, containing the names of officers and committee personnel, will, however, again be issued in the spring of 1954. An important item in the cost of the complete Directory is now some $6000 for postage, as the volume must now be sent by third class mail instead of second class as a separate section of the journals.

To Welcome Foreign Scientists and Engineers

The Cooperative Research Foundation plans to establish a number of international science centers to serve foreign scientists and engineers visiting the United States. Direct working relationships between foreign scientists and their colleagues in the regions to be served by the centers will be promoted. State or local academies of science will cooperate. The centers will provide local facilities for the visitors, especially those whose visits are sponsored by private interests. The first of these centers has been established by the Foundation at the headquarters of the California Academy of Sciences, Golden Gate Park, San Francisco, Calif. Robert L. Champion is director, the cable address "Core", and the telephone number Bayview 1-7314. A New York office will probably be established.

ASARCO Is Host To Physical Metallurgists

The American Smelting & Refining Co. was host to the Physical Metallurgy Group of the New York Section AIME on Nov. 13, 1953. In the afternoon A. J. Phillips, vice-president and director of research, and A. A. Smith, Jr., superintendent of research dept., arranged a guided tour through the new central research laboratories at South Plainfield, N. J.

Prof. Frederick Seitz of the University of Illinois spoke on *Diffusion in Metals*. W. C. Ellis, Chairman of the Physical Metallurgy Subsection, was in charge.

The name of Tenney C. DeSollar was omitted from the list of Legion of Honor previously published.

No Decision Reached On Engineering Building

New York, Pittsburgh, and Chicago continue to be in the running for the location of the proposed new building for the national engineering societies. A representative group spent December 8 in Pittsburgh, and were welcomed by the top industrial leaders of that city. Advantages of selecting Pittsburgh for a national engineering center were pointed out at a luncheon and dinner meeting and in a sightseeing trip. At least a million dollars was promised to help finance the purchase of land and erection of a suitable building. This would probably be either in the new Gateway Center in the "Golden Triangle" or in the university area some two miles east.

A small committee has been appointed to estimate as accurately as possible the relative costs of facilities in the midtown area of New York, in the suburbs of New York, in Pittsburgh, and in Chicago. Various types of buildings will be considered. The committee's report will then be presented to the boards of the Founder Societies and of the AIChE. A legal decision has been asked as to whether the proceeds from the sale of the present Engineering Societies Building in New York could be used to help finance a building outside of the city.

Pittsburgh Section And NOHC Hold Meeting

The joint meeting of the Pittsburgh Section and the National Open Hearth Committee, AIME, was held in the William Penn Hotel on Nov. 6, 1953. The morning session combined metallurgy and operations. The first metallurgical subject, *Improving Analysis in the Open Hearth*, was presented in the form of a panel discussion. The panel brought out that differences exist in the method of attacking the off-heat problem in individual plants, but it was evident that metallurgists and operators in the various plants consider the improvement of analysis performance one of their important objectives. The second topic, *Blocking Practices for Quality Killed Steels*, discussed the objective of achieving the lowest cost practice consistent with metallurgical requirements from a variety of angles.

The afternoon session combined refractories and combustion groups. The refractories part consisted of prepared papers on *Sealing Open Hearth Furnaces Against Air Infiltration* and *Survey of Handling Methods in Pittsburgh District Open Hearth Shops*. Papers on combustion were *Effect of Design Changes on the Performance of a Modern Open Hearth Furnace*, and *Combination Fuel Burners*.

Members of the Institute of Metals Div., AIME also spent the day in two technical sessions. Eight papers on such subjects as joining, titanium alloys, deposition of metals from the vapor state, notch toughness of carbon plate steels, and gas in metals were presented.

Additional Award Given To Prize Paper Contest

An additional award of $100 for graduate students in the National Student Prize Paper Contest has been authorized. Hereafter, winners in Local Section contests will have six chances instead of five to win further honors. There will be three undergraduate prizes of $100 each and three graduate prizes of the same amount. One prize in each group will be given each to students in Mining, Metals, and Petroleum, provided their papers are of a sufficiently high caliber. Junior Members will hereafter be eligible, as well as Student Associates, if they are doing at least half of their work in preparation for a Master's degree.

Powder Metallurgists Hold December Meeting

A meeting of the so-called Hobnob group of powder metallurgists was held in New York City on Dec. 9, 1953 in association with the New York Section AIME. The meeting was opened by a brief talk on the problems in the production of oilless bearings and structural parts. It was presented by Leon J. Printz, Amplex-Oilite products div., Chrysler Corp. who pointed out the difficulties which can arise as a result of nonuniformity of metal powders. A discussion period brought out the unanimous opinion that close cooperation between powder producer and fabricator is essential, and that much effort and time is being spent to maintain standards and improve quality.

A panel discussion on the practical aspects of sintering was then held. L. D. Richardson, Wright Air Development Center, presented the problem of sintered cermets and other high temperature materials. Jack Kurtz, Kulite Tungsten Co., outlined sintering methods employed in the field of refractory metals, and J. F. Kuzmick, Welded Carbide Tool Co., described hot pressing or pressure sintering of cemented carbides. Soft magnetic bodies and permanent magnets which present entirely different problems in sintering were discussed by Robert Steinitz, American Electro Metal Corp.

St. Louis Section Honors H. R. Hanley

At the Dec. 11, 1953 meeting of the St. Louis Section AIME, a resolution was adopted citing the 30 year's of service Herbert R. Hanley has given to the St. Louis Section. The citation was presented on the occasion of his departure for service as a technical advisor to the State Dept. in Formosa.

The following officers for the year 1954 were elected: Henry R. Bianco of St. Joseph Lead Co., Chairman; J. W. MacDonald of the Old Ben Coal Co., Vice-Chairman; and Carl H. Cotterill of American Zinc, Lead & Smelting Co., Secretary-Treasurer. The speaker for the meeting was C. Roger Sutton, senior metallurgist, reactor div., Argonne National Laboratory. Mr. Sutton discussed the materials used in atomic piles, both the reacting fuel and the structural members, with respect to unusual characteristics demanded of them.

L. Jaffe Addresses Boston Local Section

The Dec. 7, 1953 meeting of the Boston Section was held in the MIT Faculty Club. Leonard Jaffe of the Watertown Arsenal spoke on the work being carried out on the physical metallurgy of titanium, and Paul Allen of the National Lead Co. discussed various raw material sources of titanium. Peter Kosting, Chairman of the Section, presided at the dinner meeting.

On Jan. 11, 1954 the Boston Section had Andrew Fletcher, Past-President of the AIME, and E. H. Robie, Secretary of AIME, as speakers. Mr. Fletcher's main topic was, "The U. S. is Not a Have-Not Nation," and Mr. Robie spoke on AIME activities.

At the Chicago Section meeting on Jan. 6, 1954, W. H. Durrell, general manager, Hollinger-Hanna Ltd., spoke on the Labrador-Quebec iron ore development. Pictured from left to right are H. W. Johnson, AIME Director and vice-president of Inland Steel Co., W. H. Durrell, L. H. Timmins, president, Chromium Mining & Smelting Corp., Ltd., and C. G. Ball, vice-president, Paul Weir Co.

Personals

Anthony J. Kolk, Jr., Rudolph M. Kosar, and **Marvin A. Salovon** have joined the metallurgy dept. of Horizons, Inc., Princeton, N. J.

Roland S. Higgins is associated with Lake Erie Engineering Corp., Buffalo, N. Y.

Dave Wooster has been appointed works engineer of Basic Refractories, Inc., Gabbs, Nev.

Frederick M. Meigs has been named assistant general manager of foreign operations, General Aniline & Film Corp., New York.

Bart C. Dickey has been appointed process development engineer in the production dept. of Acheson Colloids Co., Port Huron, Mich.

N. H. Collisson and **M. F. Meissner** have been appointed vice-presidents for operations of Olin Industries, Inc., East Alton, Ill.

Frank M. Hunter has been appointed service engineer for Acheson Colloids Co., Port Huron, Mich.

Horace W. Higgs has been appointed assistant general superintendent of smelting and refining for the Cerro de Pasco Corp. He will be stationed at La Oroya, Peru.

William J. During has been elected president of the Precision Castings Co., Inc., Syracuse, N. Y.

Sam DuPree has been made general manager of all industrial products and **Herman R. Thies** has been made general manager of all chemical products, Goodyear Tire & Rubber Co.

J. D McPherson was appointed assistant manager of the manufacturers chemicals dept., industrial chemicals div., American Cyanamid Co.

Melvin B. Monson, formerly manager of the work order dept., Chicago, Joseph T. Ryerson & Son., Inc., has been named assistant manager of the company's Milwaukee steel service plant.

James H. Giles, Jr., has been appointed the Porcelain Enamel Institute's research fellow at the National Bureau of Standards, Washington, D. C.

Robert K. Beck was elected president of the Apex Smelting Co., Chicago. Mr. Beck was vice-president and general manager.

C. Burton Clark, a member of the research dept. of Harbison-Walker Refractories Co., has been named senior mineralogist.

Rush A. Lincoln has been appointed chief metallurgist by the Allegheny Ludlum Steel Corp. He is at present manager of sales development and engineering service. Dr. Lincoln joined Allegheny in 1935. In 1940 he was appointed associate director of research on stainless steel and in 1946 joined the sales development and engineering service dept. as manager.

A. J. LENA

Adolph J. Lena has been appointed associate director of research at Allegheny Ludlum Steel Corp. He will be in charge of the physical metallurgy section of the research dept. Dr. Lena was formerly research metallurgist.

L. W. Cashdollar is with the Pittsburgh Metallurgical Co., Inc., Pittsburgh. He had been associated with the Union Electric Steel Corp., Carnegie, Pa.

William Johansen, general sales manager of Magnesium Co. of America, has been elected vice-president in charge of sales.

Valentine Boise has joined the New York office of General Dyestuff Corp. as market manager, industrial dyestuffs.

Chalmer G. Kirkbridge, president and director, Houdry Process Corp., Philadelphia, has been elected president of the American Institute of Chemical Engineers for 1954. **Barnett F. Dodge,** professor of chemical engineering and head of the chemical engineering dept., Yale University, was elected vice-president.

Jan M. Krol, formerly chief metallurgist with the Sintercast Corp. of America, New York, has joined the Welded Carbide Tool Co., Clifton, N. J., as vice-president.

Joseph P[illegible]ersheim has been promoted to chief engineer, Rockwell Mfg. Co., Norwalk, Ohio. He had been project engineer at the Homewood plant.

Charles B. Elledge, General Electric Co., Schenectady, N. Y., has been elected president of the Material Handling Institute, Inc. Mr. Elledge is currently manager of materials handling industries sales for GE.

L. L. Garber, vice-president, H. K. Porter Co., Inc., Pittsburgh, has been elected a director, vice-president, and general manager of the Alloy Metal Wire Co., a newly acquired div. of the Porter Co.

Arthur C. Wilby has retired as vice-president of the U. S. Steel Corp., Chicago. He will be succeeded by **Edward C. Logelin.** Prior to becoming vice-president in 1946, Mr. Wilby was director of public relations for U. S. Steel in the Chicago district for eight years.

R. R. Williams was appointed assistant manager of the Colorado Fuel & Iron mining dept. He was superintendent of blast furnaces at the Pueblo plant for the past six years. The post of assistant manager is a newly created position in the mining dept. **John Munson** will succeed Mr. Williams as superintendent of blast furnaces.

Robert E. Byrne has been appointed chief engineer and **Charles T. Mooney** was named production superintendent of Worcester Pressed Steel Co.

William L. Healy, General Electric Co., Philadelphia, was reelected president of the Standards Engineers Society.

Samuel Katz, geophysicist at Stanford Research Institute, has won the 1953 George Frederick Kunz prize in geology and mineralogy awarded by the New York Academy of Sciences.

Kenneth H. Klipstein has been appointed general manager of the newly created research div., American Cyanamid Co.

Lewis K. Sillcox, honorary vice-chairman of the board, New York Air Brake Co., New York, N. Y., was recently elected president of the ASME.

Carl Gustafson has been appointed director of mechanical maintenance for the Colorado Fuel & Iron Corp., and will be located at Pueblo. He will continue to be superintendent of the mechanical dept. at Pueblo.

H. R. HANLEY

H. R. Hanley, professor Emeritus of of metallurgical engineering, University of Missouri, is in Formosa to organize a dept. of nonferrous metallurgy at the University of Taiwan. He is expected to remain in Formosa for a year or more. Dr. Hanley is a graduate of the School of Mines and Metallurgy, University of Missouri. For 16 years he was associated with the Bully Hill Copper Mining & Smelting Co. He joined the staff at the School of Mines in 1923.

Denis J. Bobka is a service-sales engineer for the Timken Roller Bearing Co., rock-bit div., Spokane, Wash.

Jerry Singleton has been appointed executive secretary of the Magnesium Assn., New York.

Frederick Walker, American Smelting & Refining Co., has been transferred from Los Angeles to New York.

George O. Bohrer has been named chief engineer of Magnesium Co. of America, East Chicago, Ind. For the past three years, Mr. Bohrer was an assistant plant manager for Continental Can Co., Chicago.

Obituaries

L. E. Young, An Appreciation
by M. D. Cooper

Lewis Emanuel Young was born in Topeka, Kan., on Oct. 1, 1878, and died in Pittsburgh, Pa. on Dec. 27, 1953.

A graduate of Pennsylvania State College in the Class of 1900, he went to Iowa State College, where he was an instructor in mining and a graduate student, leading to the degree of Engineer of Mines. Becoming professor of mining engineering at Colorado School of Mines, he remained at Golden from 1904 until 1907 when he was appointed director of the Missouri School of Mines. He served there for six years, until he joined the Illinois Geological Survey with which he was associated until 1917. While with the Survey, he also became assistant professor of business administration at the University of Illinois and did graduate work, earning the degree of Doctor of Philosophy. An honorary Doctor of Engineering was conferred upon him by Missouri School of Mines and by Colorado School of Mines.

In 1918, Lewis Young began his association with Union Collieries Co. of St. Louis, first as a mining engineer and later as general manager. In 1947, he became production vice-president of the Pittsburgh Coal Co.

From 1939 until his death, Dr. Young was engaged as a consulting engineer. He was especially interested in development, operation, and management of mines in coal, limestone, potash, and copper in the United States and Canada. He inspected mines in South America, Turkey, England, Scotland, and Germany.

Lewis E. Young joined the American Institute of Mining and Metallurgical Engineers in 1901 and became a Member of the Legion of

L. E. YOUNG

Honor in 1951. He served as Director from 1937 to 1941, Vice-President from 1941 to 1945, and President in 1949. Greatly devoted to the Institute, he was active in its meetings and contributed frequently to its publications. He was an Honorary Member of the Institute of Mining Engineers of England, and a member of state mining organizations and professional societies in the United States.

RESOLUTION

WHEREAS, LEWIS E. YOUNG achieved eminent success in three principal fields of activity in mining as teacher, mine official, and consulting engineer, and rendered distinguished service to the American Institute of Mining and Metallurgical Engineers as Member, Director, Vice-President, and President, therefore be it

RESOLVED, that the Directors of the Institute, convened at the meeting in January 1954, express their high regard for Lewis E. Young; their great sense of loss in his death; and enter this resolution in the minutes of the meeting, and send a copy to Mrs. Lewis E. Young.

◆◆◆◆◆◆◆◆

The year 1949, when Lewis E. Young was President of the Institute, coincided with my first year as Secretary. It was a year of major reorganization, of four-hour Board meetings, of establishment of three new journals. Dr. Young's contribution of time, talent, interest, effort, and money in this emergency was priceless. To me, especially in that year, but in earlier and later years as well, his wise counsel and friendly cooperation will never be forgotten. He was a man of great professional ability, keen and earnest interest in everything he set out to do, unsparing of himself in the things that he undertook. He was a favorite of the Institute staff, of whom he knew a large number. One of the most distinguished characteristics of a gentleman is that he does not discriminate in his interest or courtesy, and on this score Dr. Young ranked at the top.

A multitude of Institute members will sincerely and personally mourn his sudden death.—Edward H. Robie.

Louis J. Ensch (Member 1945) died Sept. 9, 1953 in Luxembourg. He was a metallurgical engineer and general director of Cia. Siderurgica Belgo-Mineira, Belo Horizonte, Brazil. Mr. Ensch was born in Luxembourg in 1895 and after finishing his university studies there in 1920 became steel plant and mill engineer for the Aciéries Réunies de Burbach.

Eero Makinen (Member 1948) died Oct. 27, 1953. He was managing director of Outokumpu Oy, Helsinki, Finland, and had been with the company since 1921. Mr. Mäkinen was born in Sortavala, Finland, in 1886 and earned his Ph.D. at the University of Helsinki, his E.M. at the Technical University of Stockholm. A geologist with the Geological Survey of Finland, he lectured for several years on mineralogy at the University and Technical University in Helsinki. Mr. Mäkinen wrote numerous technical articles and bulletins, as well as *Common Minerals and Metals,* a popular account in Finnish for the general reader.

LeRoy Gilleland Hetrick (Member 1937) died on Nov. 23, 1953. He was born in Lincoln, Neb. and attended schools at Denver, Colo. From 1909 to 1919 he was with the Mine & Smelter Supply Co., Denver. He then joined the Denver Fire Clay Co. as a price clerk and worked his way up to district manager. During World War I he was in the Army. At the time of his death he was district manager for the Denver Fire Clay Co., located in El Paso.

William B. Greenlee (Member 1920) has died, according to Institute records. Mr. Greenlee was born at Chicago in 1872 and graduated from Cornell University in 1895 (B.S.). During his career he was an officer and director of the Greenlee Bros. Co., Rockford, Ill., the Greenlee Foundry Co., Northwestern Stove Repair Co., and Northwestern Foundry Co., Chicago. He later became president of the latter three firms and was made vice-president and treasurer of Greenlee Bros. Co.

David Porter Hale, Jr., (Member 1934) formerly with the Mine & Smelter Supply Co., died on Nov. 3, 1953. Mr. Hale was a graduate of the Missouri School of Mines, graduating in 1934 with a B.S. After graduation he accepted a position with the Zulu Gold Mines at Payson, Ariz. He was also employed by the San Juan Metals, Telluride, Colo.; Kelsey Mining Co., Placerville, Calif.; Weepah Nevada Mining Co., Weepah, Nev.; Arkansas Mining Corp., Malvern, Ark.; and Cartersville Barium Corp., Cartersville, Ga., where he became manager. From 1940 to 1946 he was in the Army with the Corps of Engineers. Upon his discharge he joined the Mine & Smelter Supply Co. as a metallurgical engineer.

Necrology

Date Elected	Name	Date of Death
1919	George S. Baton	Dec. 27, 1953
1928	Frank M. Brewster	May 1953
1915	John L. Dynan	Nov. 24, 1953
1921	Ellis A. Hall	Unknown
1930	P. E. Henry	Unknown
1949	Geoffrey Jeffreys	Oct. 28, 1953
1937	R. W. Michael	Dec. 22, 1953
1949	Ralph G. Mickle, Jr.	Nov. 24, 1953
1940	William H. Nikola	Dec. 17, 1953
1952	Richard Schoof, Jr.	Dec. 4, 1953
1916	A. T. Ward	Dec. 15, 1953
1883	Pope Yeatman	Dec. 5, 1953
1901	Lewis E. Young	Dec. 27, 1953

Proposed for Membership

— Metals Branch AIME —

Total AIME membership on Dec. 31, 1953 was 19,718; in addition 2195 Student Associates were enrolled.

ADMISSIONS COMMITTEE

O. B. J. Fraser, Chairman; Philip D. Wilson, Vice-Chairman; F. A. Ayer, A. C. Brinker, R. H. Dickson, Max Gensamer, Ivan A. Given, Fred W. Hanson, T. D. Jones, G. W. Lutjen, E. A. Prentis, Sidney Rolle, J. T. Sherman, F. T. Sisco, R. L. Ziegfeld.

The Institute desires to extend its privileges to every person to whom it can be of service, but does not desire as members persons who are unqualified. Institute members are urged to review this list as soon as possible and immediately to inform the Secretary's office if names of people are found who are known to be unqualified for AIME membership.

In the following list C/S means change of status; R, reinstatement; M, Member; J, Junior Member; A, Associate Member; S, Student Associate.

California
Pasadena—Pollit, Walter M. (M)

Illinois
Alton—Lambert, Ronald F. (M)
Chicago—Ames, Richard N. (J)
Chicago—AuBuchon, Edward L. (M) (C/S—J-M)
Chicago—Ebert, Charles R. (A)
Chicago—Olsen, Willard A. (M)
Chicago—Rudin, William L. (M) (C/S—J-M)
Chicago—Straub, David R. (M)
Lansing—Boehme, Harold C. (M) (C/S—J-M)

Indiana
East Chicago—Levine, Barry H. (J)
Hammond—Alexander, John A. (J)
Hammond—Madrzyk, Edmund S. (J)

Kentucky
Lexington—Maynor, Hal W., Jr. (M) (C/S—S-M)

Massachusetts
Cambridge—King, Thomas B. (M)

Michigan
Birmingham—Grafmiller, Robert D. (S) (R. C/S)

Missouri
University City—Clauser, John M. (A)

Montana
Butte—Furgeson, Harry E. (A)

New Jersey
Bound Brook—Deily, Richard L. (M)
Fair Haven—Gagnebin, Albert P. (M)
Metuchen—Armant, David L. (M)
Metuchen—Michal, Eugene J. (M) (C/S—J-M)
West Orange—Cook, Harry C. (M) (C/S—J-M)

New York
Albany—Szymanski, Walter J. (J)
New York—Hammond, Beatrice L. (J)
New York—Perlman, Burton (J) (R. C/S—S-J)
Schenectady—Meierdirks, Joseph B., Jr. (M) (C/S—J-M)
Syracuse—Klier, Eugene P. (M) (C/S—A-M)
Tonawanda—Westfall, Edgar R. (M) (R. M)
Waterford—Aggen, George (J)

Ohio
Cleveland—Leslie, William C. (M) (C/S—J-M)
Euclid—Greenlee, Charles A. (A) (R. C/S—S-A)
Marion—Grover, Marion P. (M)
Warren—Williams, Joseph O. (M) (C/S—J-M)

Pennsylvania
Dallas—Marvel, Irvin L. (A)
Greensburg—Cameron, Joseph A. (M)) (C/S—J-M)
Pittsburgh—Doty, William D. (M) (C/S—J-M)
Pittsburgh—Pettigrew, David W., Jr. (M) (C/S—J-M)
Pittsburgh—Pierce, William B. (M)

Tennessee
Oak Ridge—Hinkle, Norman E. (J)

Texas
Bellaire—Medders, Weldon L. (M)
El Paso—Paul, Robert B. (M) (C/S—J-M)

Washington
Sunnyside—Nelson, Thomas C., Jr. (M) (C/S—J-M)
Tacoma—Krisman, Emil M. (M) (R. C/S—J-M)

Wisconsin
Waukesha—Parana, William J. (A)
Waukesha—Williams, Warren C. (M)

Argentina
Jujuy—Nicodemo, Miguel A. (M)

Canada
Ontario, Ottawa—Fisher, Henry J. (M) (C/S—J-M)

France
St. Germain-en-Laye—Crussard, Charles (M)
St. Germain-en-Laye—Husson, Louis G. (M)

Japan
Yokohama City—Shunji, Kuriyama (M)

Coming Events

Feb. 2, AIME, Chicago Section, Chicago Bar Assn., Chicago.

Feb. 6-8, Indian Institute of Metals, 31 Chowringhee Rd., Calcutta 16, India.

Feb. 15-18, AIME, annual meeting, Metals Branch, Hotel McAlpin; Mining and Petroleum Branches, Hotel Statler, New York.

Feb. 17-19, Seminar on Spectroscopy, University of Florida, Gainesville, Fla.

Mar. 3, AIME, Chicago Section, Chicago Bar Assn., Chicago.

Mar. 4-5, American Society for Metals, midwinter meeting, Hotel Statler, Boston.

Mar. 8-10, American Institute of Chemical Engineers, Statler Hotel, Washington, D. C.

Mar. 10, AIME, Connecticut Section, American Brass Co., Torrington, Conn.

Mar. 15-19, National Assn. of Corrosion Engineers, Municipal Auditorium, Kansas City.

Mar. 17, AIME, National Open Hearth Steel Committee, Western Section, Rodger Young Auditorium, Los Angeles.

Mar. 24-26, American Power Conference, annual meeting, Sherman Hotel, Chicago.

Apr. 5-7, AIME, Blast Furnace, Coke Oven, Raw Materials Conference, Palmer House, Chicago.

Apr. 5-7, AIME, National Open Hearth Conference, Palmer House, Chicago.

Apr. 5-7, American Society of Lubrication Engineers, annual meeting and exhibit, Cincinnati.

Apr. 7, AIME, Chicago Section, Chicago Bar Assn., Chicago.

Apr. 21-23, Southern Industrial Wastes Conference, Hotel Shamrock, Houston.

Apr. 26-28, Canadian Institute of Mining and Metallurgy, annual meeting, Mount Royal Hotel, Montreal.

Apr. 26-30, American Society of Tool Engineers, industrial exposition, Convention Center, Philadelphia.

Apr. 27, Assn. of Consulting Chemists and Chemical Engineers, Hotel Belmont Plaza, New York.

Apr. 29-May 1, AIME, Pacific Northwest Metals and Minerals Conference, Multnomah Hotel, Portland, Oregon.

Apr. 30-May 1, AIME, New England Regional Meeting, Bond Hotel, Hartford, Conn.

May 2-6, Electrochemical Society, La Salle Hotel, Chicago.

May 4-7, American Welding Society, national meeting, Hotel Statler, Buffalo.

May 8-14, American Foundrymen's Society, Cleveland Auditorium, Cleveland.

May 16-17, American Institute of Chemical Engineers, Kimball Hotel, Springfield, Mass.

June 20-23, Chemical Institute of Canada, Toronto, Canada.

June 20-25, American Institute of Chemical Engineers, nuclear energy meeting, University of Michigan, Ann Arbor, Mich.

July 16-21, Joint Commission on Electron Microscopy, international conference, Senate House, University of London; London School of Hygiene and Tropical Medicine, Malet St., London, W. C. 1, England.

July 19-30, International Conference, Mechanical Effects of Dislocations in Crystals, University of Birmingham, England.

July 21-28, International Union of Crystallography, general assembly and international congress, Paris.

Oct. 3-7, Electrochemical Society, Inc., Statler Hotel, Boston.

Oct. 26, Assn. of Consulting Chemists and Chemical Engineers, Inc., annual symposium and banquet, Hotel Belmont Plaza, New York.

*Lectromelt** goes to Canada on a research job...

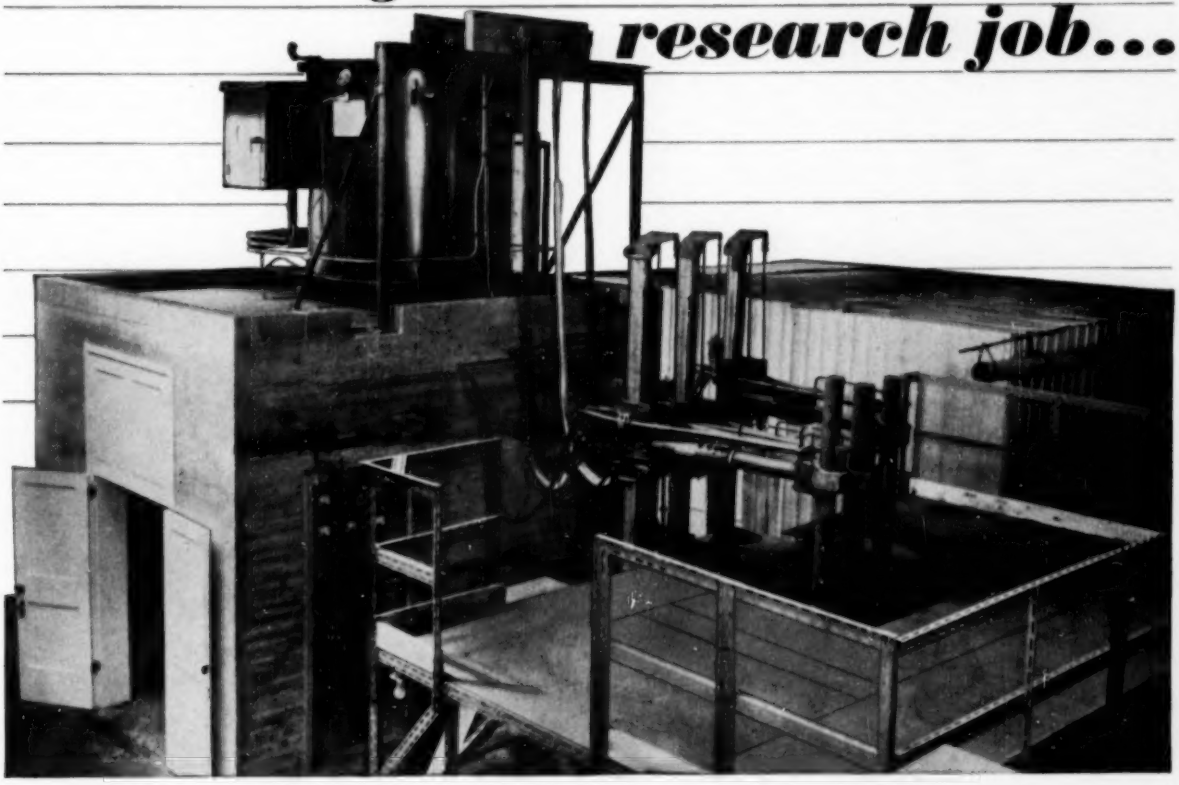

...Department of Mines & Technical Surveys installs

200KVA Lectromelt Furnace for experimentation

Cheap electric power and plentiful mineral resources have led to Canada's exploration of the economies and efficiency of electric smelting. A laboratory has been set up to test high temperature smelting and to determine whether more desirable products can be obtained more practically by using electric furnaces.

Highly satisfactory results already have been obtained in test production of ferroalloy-type material, according to the Division Chief heading the laboratory.

It is anticipated that certain ores will be smelted experimentally to obtain informative data on costs and chemical reactions encountered. Also, the smelting problems of various refractory materials will be investigated.

Expectations are that the cost of the pilot laboratory will be insignificant compared with the economies and material improvements that will result from this Canadian research. Perhaps you could benefit similarly by installing comparable research facilities.

Lectromelt Furnace engineering assistance is always available to you. Write on any problem. Also write for Catalog No. 105 which describes many types of Lectromelt Smelting and Refining Furnaces, and their versatility. Pittsburgh Lectromelt Furnace Corporation, 326 32nd Street, Pittsburgh 30, Pennsylvania.

Manufactured in . . . ENGLAND: Birlec, Ltd., Birmingham . . . FRANCE: Stein et Roubaix, Paris . . . BELGIUM: S. A. Belge Stein et Roubaix, Bressoux-Liege . . . SPAIN: General Electrica Espanola, Bilbao . . . ITALY: Forni Stein, Genoa. JAPAN: Daido Steel Co., Ltd., Nagoya

MOORE RAPID

WHEN YOU MELT... *Lectromelt*

*REG. T. M. U. S. PAT. OFF.

SAVE ALL THE WAY WITH

NATIONAL

TRADE-MARK

CARBON BLAST FURNACE LININGS

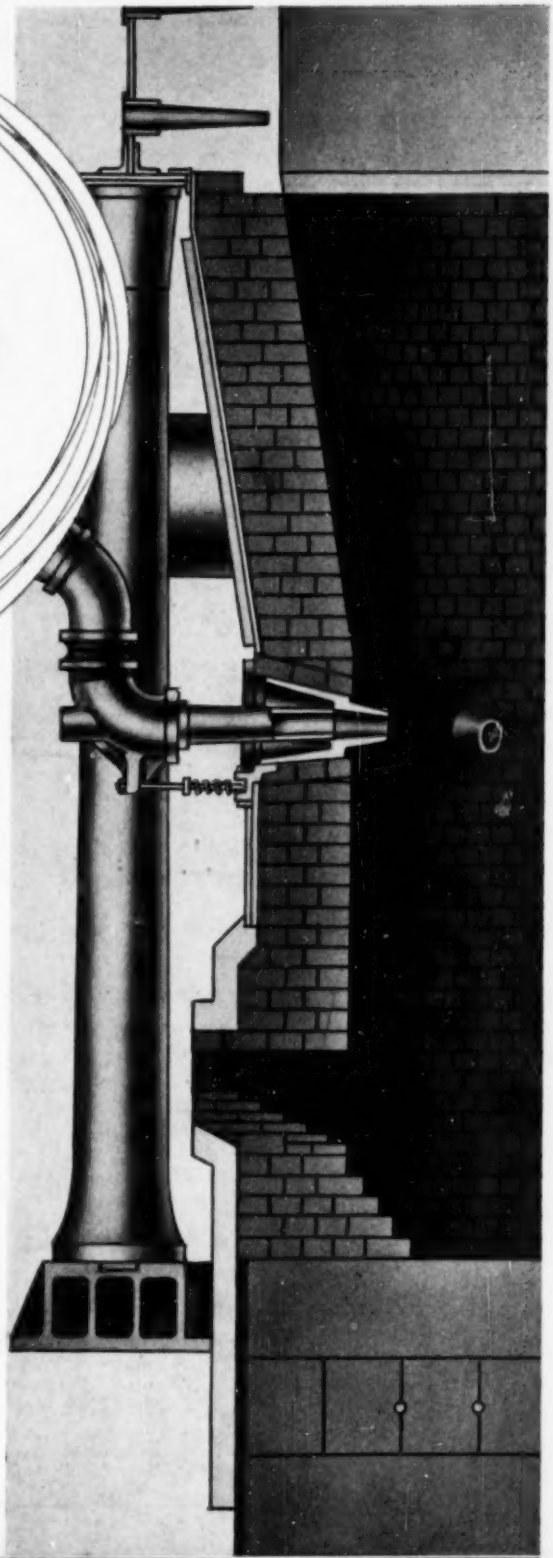

Record operating economies — so outstandingly established by "National" carbon in blast furnace hearths—*needn't stop there!* Now you can get the same advantages — longer life, lower maintenance, smoother operation—with carbon linings in blast furnace walls, in tuyere and in bosch sections.

Present day economics indicate now, more than ever, a need for carbon "all the way". Let's talk it over in terms of *your* operation!

The term "National" is a registered trade-mark of Union Carbide and Carbon Corporation

NATIONAL CARBON COMPANY
A Division of Union Carbide and Carbon Corporation
30 East 42nd Street, New York 17, N. Y.
District Sales Offices: Atlanta, Chicago, Dallas, Kansas City, New York, Pittsburgh, San Francisco

OTHER* NATIONAL CARBON *PRODUCTS:

ELECTRIC FURNACE ELECTRODES · CARBON BRICK AND RAMMING PASTE · TROUGH LINERS · MOLDS AND MOLD PLUGS · SKIMMER BLOCKS · SPLASH PLATES · TANK LININGS AND HEATERS · HEAT EXCHANGERS AND PUMPS · BRUSHES FOR MOTORS AND GENERATORS

Journal of METALS

FEBRUARY 1954

TRANSACTIONS SECTION

VOL. 6, NO. 2, IN TWO SECTIONS—SECTION TWO

High Temperature Properties, and Mechanical Properties of Ti-Mn Alloys ... F. C. Holden, H. R. Ogden, R. I. Jaffee ... 181

Constitution of Iron-Boron Alloys in the Low Boron Range ... M. E. Nicholson ... 185

Crystallographic Axides for Hexagonal Metals ... C. S. Barrett, L. Lebor ... 190

Influence of Oxygen, Nitrogen, and Carbon on the Phase Relationships in the Ti-Al System ... R. I. Jaffee, H. R. Ogden ... 196

Titanium-Chromium-Oxygen System ... C. C. Hall, R. I. Jaffee ... 200

Titanium-Manganese System ... R. C. Vilella, J. W. Bolton ... 207

Short Transverse Tensile Properties Controlled by Rolling of Beta Prime ... E. O. Hall ... 210

Aging Characteristics of Nickel-Chromium Alloys Hardened with Titanium and Aluminum ... E. Nordhorn, N. J. Grant ... 211

Primary Identification of Intermediate Phases in the Systems Ti-Zn, Ti-Cd, Zr-Zn, Zr-Cd, and Zr-Hg By X-ray Powder Diffraction Methods ... P. Pietrokowsky ... 219

Characteristics of Elevated-Temperature Tensile Deformation ... W. Geil, J. H. Keller, R. F. Miller ... 226

Sintering Titanium-Manganese-Molybdenum ... R. A. Elliott, D. W. Lawhon, W. Rostoker ... 228

Constitution and Properties of Ag-Cd-Zn Brazing Alloys ... K. M. Wolgast ... 233

System Zirconium-Oxygen ... A. S. Dworkin, D. J. McPherson ... 238

High Temperature Strength of Wrought Aluminum Powder Products ... E. Gregory, N. J. Grant ... 247

Sigma Phase in Binary Alloys ... R. Greenfield, R. A. Beck ... 253

Annealing of a Cold Rolled Aluminum Single Crystal ... A. H. Geisler, R. A. Beck ... 257

The Interrelations of the Systems Formed by Chromium, Molybdenum, and Nickel ... A. E. Bolton, N. J. Grant ... 261

Table of Contents Continued

Solid State Bonding of Aluminum to Nickel
S. Storchheim, J. L. Zambrow, H. H. Hausner **269**

Effect of Stress on the Creep Rates of Polycrystalline Aluminum Alloys Under Constant Structure
O. D. Sherby, R. Frenkel, J. Nadeau, J. E. Dorn **275**

Plasticity of Molybdenum Single Crystals at High Temperature
R. Maddin, N. K. Chen **280**

Study of the Effect of Carbon Content on the Structure and Properties of Sintered WC-Co Alloys J. Gurland **285**

Orientation Relationships in Cast Germanium W. C. Ellis, J. Fogeant **291**

Redistribution of Solutes by Formation and Solidification of a Molten Zone W. G. Pfann **294**

Hydrogen Embrittlement of Steels J. T. Brown, W. M. Baldwin, Jr. **298**

On the Temperature Range of the Martensite Transformation in the Cu-Zn System A. L. Titchener, M. B. Bever **303**

On the Torsional Deformation and Recovery of Single Crystals
S. S. Hsu, B. D. Cullity **305**

Heat Treatment, Structure, and Mechanical Properties Of Ti-Mn Alloys

by F. C. Holden, H. R. Ogden, and R. I. Jaffee

Ti-Mn alloys were studied in order to determine the factors affecting the mechanical properties of β-stabilized titanium alloys. The principal compositional factors have been found to be solid-solution strengthening, the martensitic transformation, and instability of the β phase. Structural factors, such as grain size and shape, were found to have more influence on ductility and toughness than on strength.

THE alloys of titanium with the β-stabilizing elements offer the chief hope for developing useful heat treatments. Conversely, the heat-treatment response possible with the β-stabilizing elements causes difficulties such as weld embrittlement and thermal instability during service at elevated temperature. Therefore, it is of considerable technical importance to understand the factors that govern the heat-treatment responses in these alloys, so as to be able to soften the alloys if they are embrittled by an adventitious heat treatment, to render them stable in service, or to harden them while maintaining adequate ductility and toughness.

The Ti-Mn system is a good example with which to demonstrate the factors that govern strength and heat-treatment response in a β-stabilized system. The region of the α-β transformation, after the work of Maykuth, Ogden, and Jaffee,[1] is shown in Fig. 1. The α solubilities are low. This means that, in the two-phase α-β field, partition of manganese between the two phases occurs practically only to the β phase. The solid-solution effects are therefore chiefly the result of solution in the β phase. The eutectoid occurs at 20 pct Mn and 550°C, and proceeds very sluggishly. It can be ignored in heat treatments in hypo-eutectoid alloys, except for long-time storage at low temperatures below the eutectoid temperature. Even here, there is some question that diffusion proceeds far enough to involve eutectoid decomposition.

Three compositional factors bear on the mechanical properties and structure of titanium α-β alloys. These are: 1—solid-solution strengthening, 2—martensite transformation, and 3—β instability. Combined with the purely structural factors of grain size and shape, these govern the properties of the alloys.

Perhaps the most important factor is solid-solution strengthening. The facts that manganese dissolves in α titanium to a maximum of only 0.5 pct and most of the manganese partitions to the β phase dominate

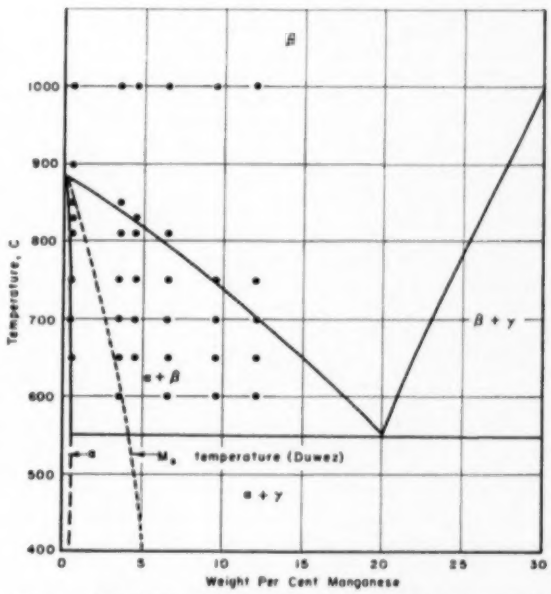

Fig. 1—Compositions and heat treating temperature in relation to phase diagram of Ti-Mn system. Phase diagram from Maykuth, Ogden, and Jaffee,[1] M_s curve from Duwez.[2]

the structure and properties of the α-β alloys. Because of the overwhelming preference of manganese for the β phase, the β phase is harder and the α phase is softer. The relative amounts of both phases may be modified by heat treatment in the α-β field as application of the lever rule in the two-phase field clearly shows.

A critical temperature in the Ti-Mn diagram is 800°C. This is the β transus temperature of the 6.4 pct Mn alloy, which has the lowest manganese content which will form all retained-β phase on quenching to room temperature. Any quench performed from below 800°C will produce a structure consisting of only α, α plus retained β, or retained β, for alloys of the compositions used in this work. For alloys containing less than 6.4 pct Mn, any quench from above 800°C will always result in structures

F. C. HOLDEN is Principal Metallurgist, H. R. OGDEN, Junior Member AIME, is Assistant Supervisor, and R. I. JAFFEE, Member AIME, is Supervisor, Nonferrous Physical Metallurgy Div., Battelle Memorial Institute, Columbus, Ohio.

Discussion on this paper, TP 3706E, may be sent, 2 copies, to AIME by April 1, 1954. Manuscript, July 22, 1953. Cleveland Meeting, October 1953.

The Transactions papers appearing in the Journal of Metals during 1954 will subsequently appear in AIME Transactions Volume 200, and may be permanently referenced to that volume.

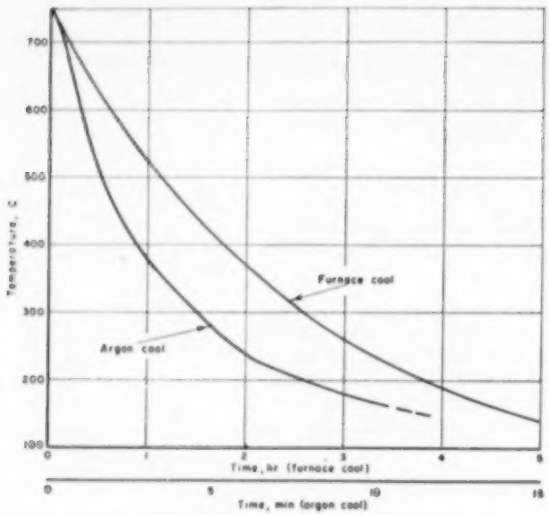

Fig. 2—Cooling rate curves from 750°C.

containing some martensite. Equilibrium or massive α will be present if the quench was performed from the α-β field. Otherwise, the structure will consist of martensite and retained β of the same composition. As Duwez[2] has shown, the amount of martensite relative to retained β will decrease as the manganese content increases. The M_s temperature decreases continuously with manganese content as shown in Fig. 1. Hardening results from undergoing the martensite reaction, and this factor must be taken into account in considering the mechanical properties possible in this system.

Instability of the β phase is a most important factor. The β phase can and does transform partially to α by nucleation and growth processes when it is heated at a temperature below its transus temperature. Such transformation should result in softening, because α is the softer phase. However, this happens only when the α transformation product is massive. If it is transformed into fine particles or as a submicroscopic array coherent with the β lattice, considerable hardening takes place. Indeed, depending on the dispersion of the α phase, softening, no change, or hardening can occur. The degree of dispersion can be modified by reheating temperature and time, cooling rate from elevated temperature, or isothermal-transformation time and temperature. Hardening resulting from instability of β phase has been termed transformation hardening, precipitation hardening, coherency hardening, or age hardening. However, no matter what term is applied to this process, the importance of β instability as a factor affecting the mechanical properties of β-stabilized titanium alloys is second only to the factor of the solid-solution effects.

So far, the respective contribution of each of these factors to the overall properties of the alloys has not been well differentiated. The objective of the work to be described was to study these factors separately and to learn their interrelationships for the case of high purity titanium alloyed with only a single β stabilizer, manganese.

Experimental Procedures

Preparation: The alloys for this work were prepared as half-pound ingots by double arc melting in an atmosphere of high purity argon. Melting stock was obtained from high purity iodide titanium,* and manganese additions were made from fused electrolytic manganese. To reduce segregation, the once-melted ingots were chipped and remelted. Irregularities in the surface of the ingots were removed by grinding. The ingots were heated in air and forged to ¾ in. diameter rods. Forging temperatures were 875°C, except for a 12.1 pct Mn alloy which was forged at 980°C. The surface scale was removed by grit-blasting and grinding operations.

* Typical analysis is presented in ref. 3.

Since it has been found that the hydrogen impurity in titanium may affect mechanical properties,[4] the more recently fabricated alloys were vacuum annealed after forging for 6 hr at 775°C at a pressure of 10^{-4} to 10^{-5} millimeters of mercury. This treatment is sufficient to remove the titanium hydride line markings from α titanium.

The forgings were next hot swaged to ¼ in. diameter rod through a series of 20 dies, with approximately 10 pct reduction in area between each die. After mechanical descaling, test and microstructure specimens were prepared from the ¼ in. diameter rod.

Heat Treatments: Heat treatments were made on the ¼ in. diameter rod sections under dry argon, 99.99 pct pure. The cooling rates used to obtain variations in structure and mechanical properties included a water quench and a furnace cool. Intermediate cooling rates were also used in the study of hardness values. These included an oil quench and an argon cool (simulated air-cooling rate under an atmosphere of argon). The cooling rates involved in the argon cool and furnace cool are indicated in Fig. 2.

Mechanical Testing: Tensile tests of these alloys were made on ⅛ in. diameter tensile specimens with

Table I. Composition and Fabrication Temperatures of Ti-Mn Alloys

Manganese, Wt Pct			Carbon, Wt Pct	Nitrogen, Wt Pct	Hydrogen, Ppm	Forging Temperature, °C	Swaging Temperature, °C	Vacuum Annealed
Nominal	Charged	Analyzed						
0.50	0.55	0.53	0.02	0.006	22	875	750	Yes
3.00	3.50	3.36	0.03	0.006	190	875	750	No
3.00	3.50	3.52	0.04	0.007	220	875	750	No
5.00	8.00	4.43	0.04	0.005	45	875	750	Yes
6.00	6.50	6.39	0.03	0.004	150	875	750	No
9.00	9.50	9.43	0.02	0.005	110	875	750	No
12.00	12.80	12.1	0.02	0.004	60	980	850	Yes
2.00*	2.13	1.99	—	—	—	875	750†	Yes
5.00*	5.12	4.59	—	—	—	875	750†	Yes
5.50*	5.50	5.01	—	—	—	875	750†	Yes

* These alloys were made in 15 gram buttons.
† These alloys were rolled to 0.040 in. sheet.

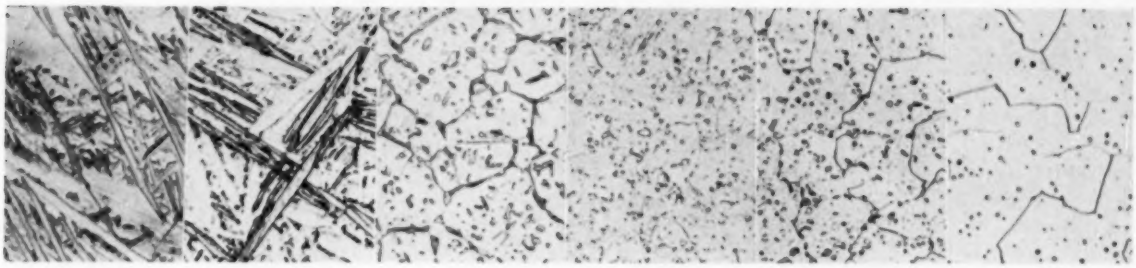

A—X250. B—X250. C—X250. D—X250. E—X250. F—X250.

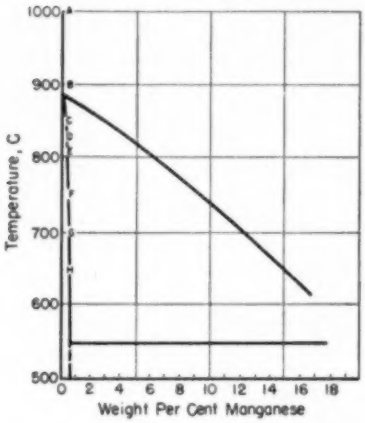

Fig. 3—Microstructures and heat treatments of a Ti-0.55 pct Mn alloy. Letters in the graph correspond to microstructures.

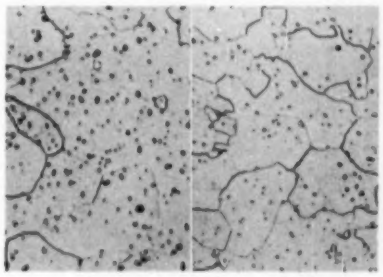

G—X250. H—X250.

a ½ in. gage length. Tests were made on Baldwin-Southwark universal testing machines, using the 2400 or 3000 lb scale at a uniform strain rate of 0.003 to 0.005 in. per min. Strain readings were taken from SR-4 resistance strain gages to about 2 pct elongation, and from a lever-type extensometer to the limit of uniform elongation.

Impact tests were made on microimpact test specimens using a Tinius Olsen testing machine with an impact velocity of 11.37 ft per sec and a maximum capacity of 200 in.-lb. Details of the test specimens and methods of testing have been presented.[8]

Metallography: The micrographs presented in this paper were taken from specimens cut from the shoulders of tensile test specimens. Sections were mounted, mechanically polished, finishing with Linde "B" on a slow-speed wheel, and etched with a 1½ HF-3½ HNO_3 solution. Phase quantities were determined by visual estimate, and grain sizes by use of a micrometer eyepiece, and a comparison chart.

Compositions: The alloys used in this study included those with manganese contents up to 12.1 pct. With the exception of three alloys prepared for hardness studies, all the alloys were made as half-pound ingots. Table I shows the composition, fabrication procedures, and fabrication temperatures for these alloys. Fig. 1 shows the compositions and heat-treating temperatures in relationship to the phase diagram of the Ti-Mn system. Base-line data for the unalloyed titanium are plotted in all curves for the hydrogen-free condition.

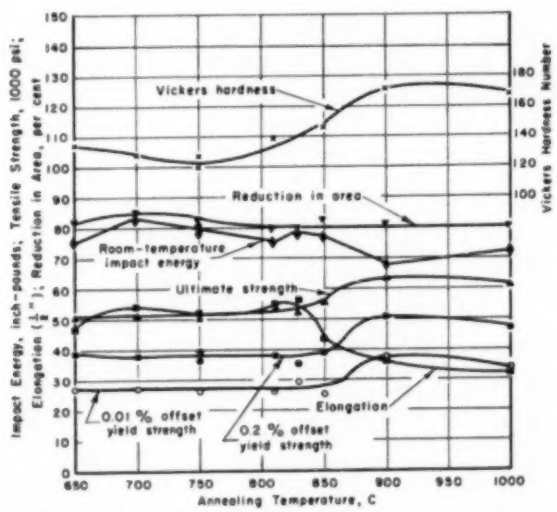
Impact Energy, inch-pounds; Tensile Strength, 1000 psi; Elongation (1/2"); Reduction in Area, per cent
Vickers Hardness Number
Vickers hardness
Reduction in area
Room-temperature impact energy
Ultimate strength
0.01 % offset yield strength
0.2 % offset yield strength
Elongation
Annealing Temperature, C
650 700 750 800 850 900 950 1000

Fig. 4—Mechanical properties of a Ti-0.55 pct Mn alloy. Specimens annealed 1 hr and water quenched.

Water-Quenched Alloys

Ti-0.55 Pct Mn Alloy: This alloy was prepared to determine the properties of the terminal α alloy. Heat treatment at the lower temperatures produces structures consisting of 95 pct α, with the balance retained β. Considerable quantities of β are formed at higher temperatures above 850°C, most of which transform to martensite during the quench.

Fig. 3 shows the microstructures produced by annealing this alloy at various temperatures, followed by water quenching, and the corresponding mechanical properties are plotted in Fig. 4. Little change in microstructure or properties is observed for quenching temperatures up to 850°C, above which considerable quantities of β exist, which on forming α' and retained β cause an increase in strength with corresponding loss of ductility. The impact-energy values are generally high for all conditions tested.

Ti-3.4 Pct Mn Alloy: Microstructures for a number of annealing and quenching heat treatments are shown in Fig. 5, and mechanical properties are plotted in Fig. 6.

Strength of this alloy increases with annealing temperature. This corresponds to the increasing quantities of the β phase in equilibrium at the quenching temperature. The highest strength and

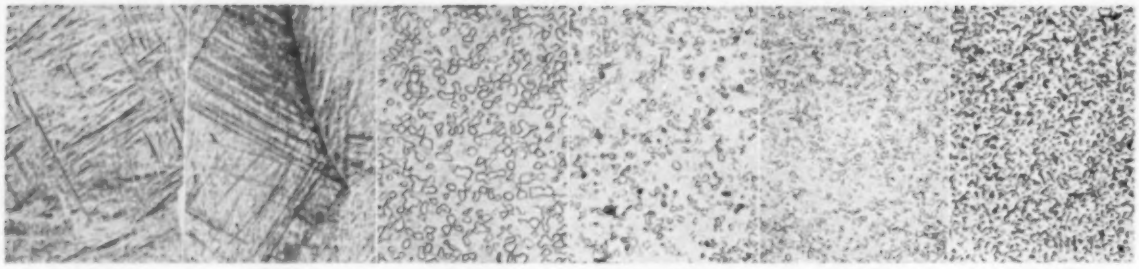

A—X250. B—X250. C—X250. D—X250. E—X250. F—X250.

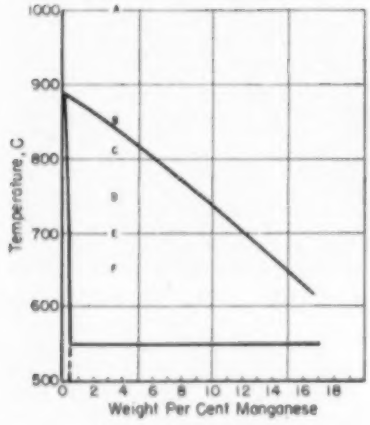

Fig. 5 — Microstructures and heat treatments of a Ti-3.4 pct Mn alloy. Letters in the graph correspond to microstructures.

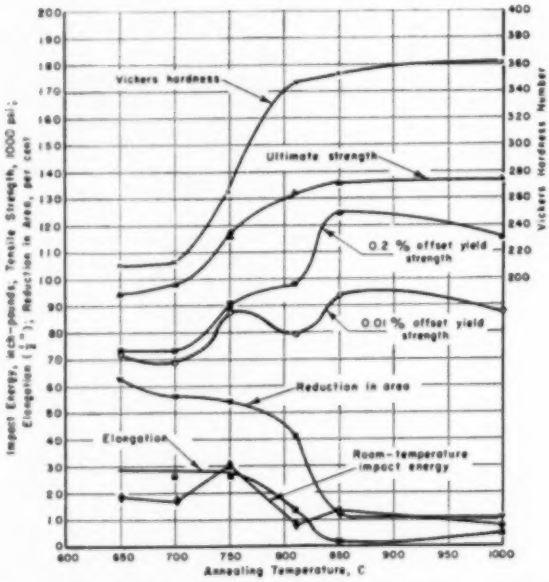

Fig. 6—Mechanical properties of a Ti-3.4 pct Mn alloy. Specimens annealed 1 hr and water quenched.

hardness for this alloy are produced by the martensitic structure formed by quenching from the β field. Ductility and impact resistance decrease with the increase in strength.

Ti-4.4 Pct Mn Alloy: This alloy is quite similar in microstructure and properties to the 3.4 pct alloy. Microstructures and mechanical properties are presented in Figs. 7 and 8.

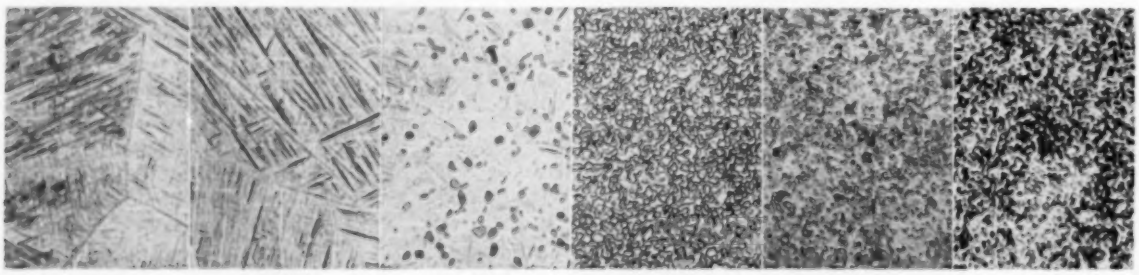

A—X250. B—X250. C—X250. D—X250. E—X250. F—X250.

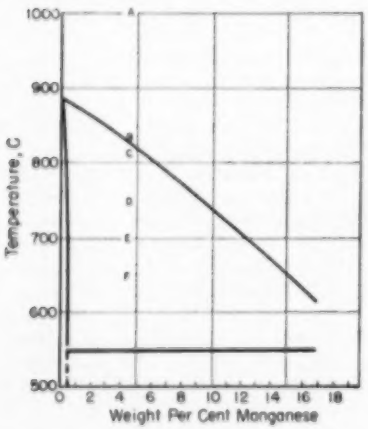

Fig. 7 — Microstructures and heat treatments of a Ti-4.4 pct Mn alloy. Letters in the graph correspond to microstructures.

Ti-6.4 Pct Mn Alloy: The composition of this alloy is close to the minimum at which β phase can be retained by a water quench. Annealing at progressively higher temperatures in the α-β field produces microstructures containing increasing quantities of β. Test specimens quenched from the β field show low ductility and low impact resistance, and tensile strengths are below the values which would be expected from hardness measurements. This embrittling of the retained β is considered to be caused by coherency hardening, which is difficult to suppress at this composition. Fig. 9 shows the microstructures produced by different annealing temperatures, and resulting mechanical properties are shown in Fig. 10.

Ti-9.4 Pct Mn Alloy: Microstructures and mechanical properties of this alloy are presented for various annealing temperatures in Figs. 11 and 12. This alloy was fabricated in the β field, and this may be

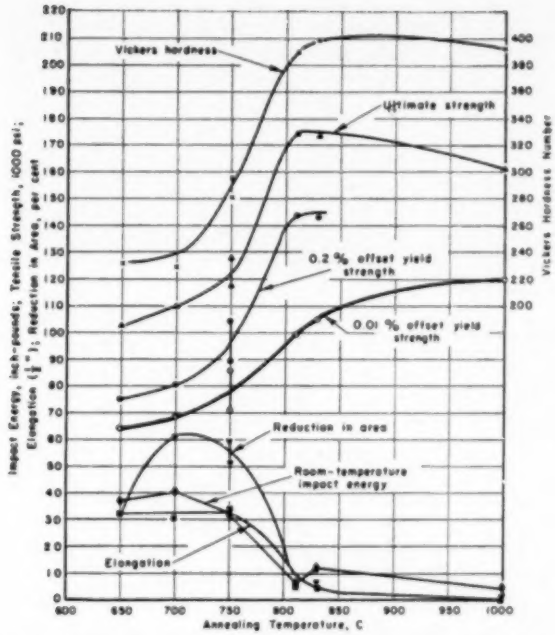

Fig. 8—Mechanical properties of a Ti-4.4 pct Mn alloy. Specimens annealed 1 hr and water quenched.

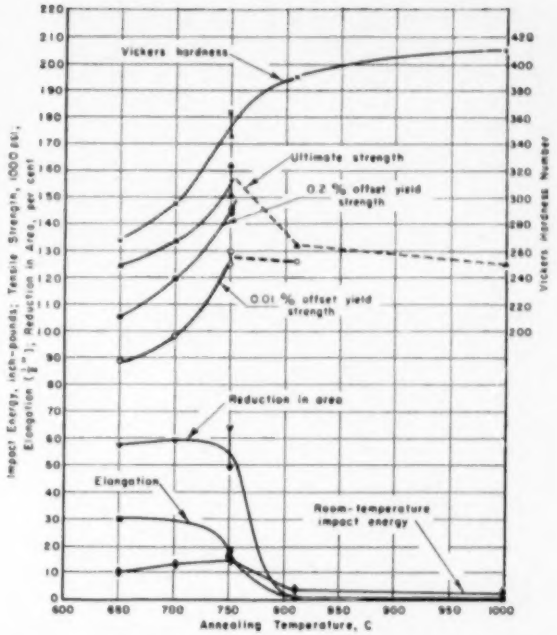

Fig. 10—Mechanical properties of a Ti-6.4 pct Mn alloy. Specimens annealed 1 hr and water quenched.

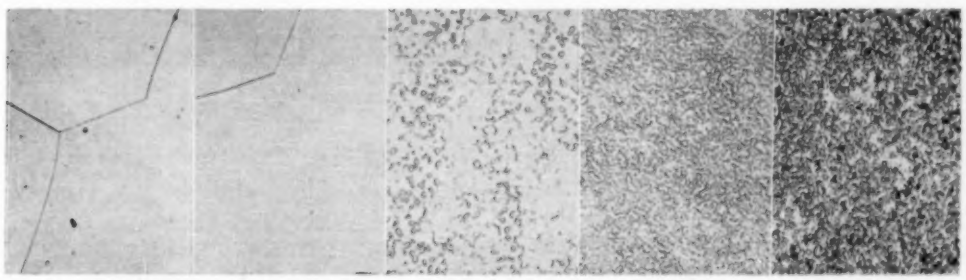

A—X250. B—X250. C—X250. D—X250. E—X250.

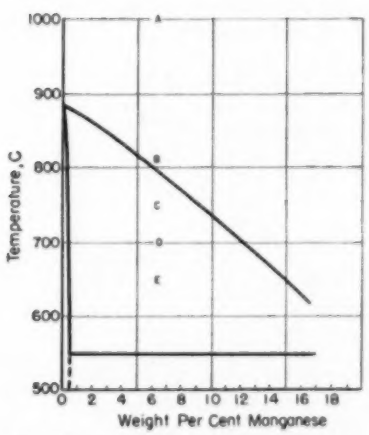

Fig. 9—Microstructures and heat treatments of a Ti-6.4 pct Mn alloy. Letters in the graph correspond to microstructures.

expected to influence the structures and properties produced by subsequent heat treatment. Annealing below the β transus produces α as an intragranular and grain-boundary precipitate, with a decrease in strength and impact resistance and an increase in ductility. Variations of mechanical properties for anneals above the β transus are slight.

Ti-12.1 Pct Mn Alloy: Microstructures produced by different heat treatments for this alloy are shown in Fig. 13, and the mechanical properties are plotted in Fig. 14. This alloy also was fabricated in the β field. Variation of properties and microstructure with heat treatment above 700°C are slight, except for a considerable decrease in the reduction in area for the 1000°C anneal. The presence of the α precipitate in the 650°C anneal increases strength slightly, with a slight loss of ductility, as measured by reduction in area.

Furnace-Cooled Alloys

In addition to the water-quenched specimens presented in the previous sections, studies were made on the structures and properties of the same alloys furnace cooled from the β field. Microstructures and mechanical properties of these conditions are presented in Figs. 15 and 16.

For compositions of 6.4 pct Mn and below, the structures are composed of coarse plates of α in a basketweave array. Above this composition, the retained-β phase predominates in the microstructures, with a much finer precipitate of intergranular and intragranular α. Strength properties increase most

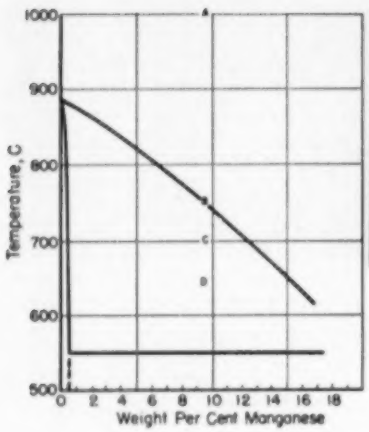

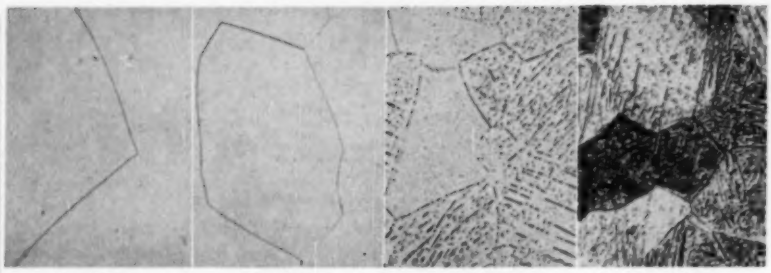

Fig. 11—Microstructures and heat treatments of a Ti-9.4 pct Mn alloy. Letters in the graph correspond to microstructures.

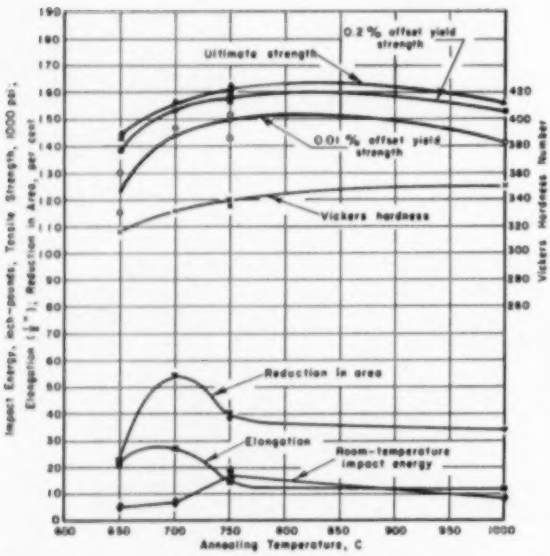

Fig. 12—Mechanical properties of a Ti-9.4 pct Mn alloy. Specimens annealed 1 hr and water quenched.

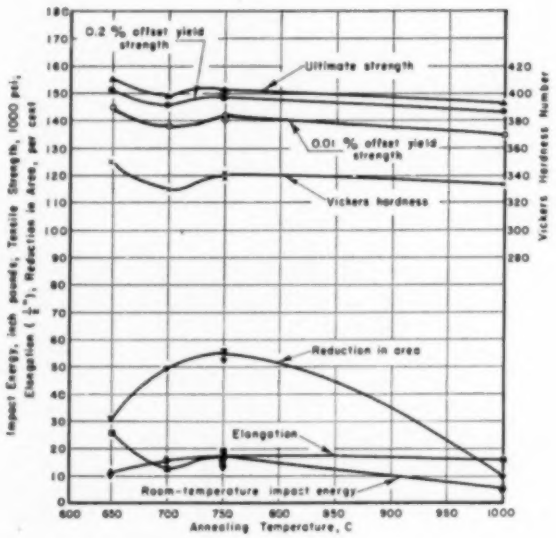

Fig. 14—Mechanical properties of a Ti-12.1 pct Mn alloy. Specimens annealed 1 hr and water quenched.

rapidly between 6.4 and 9.4 pct Mn, corresponding to the change in microstructural appearance, and the maximum precipitation hardening for this cooling rate occurs at about 9.4 pct Mn. Ductility properties decrease to a minimum at the same composition.

Solid-Solution Effects

In separating the effects of structure from those of solid solution on the strength and hardness of titanium alloys, it is helpful to consider what might be expected in the absence of structural effects. Fig. 17a is a schematic diagram for a β-stabilized tita-

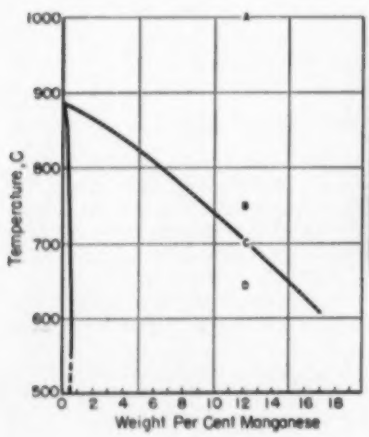

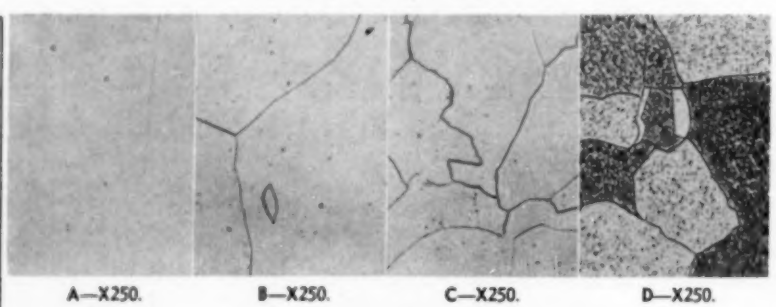

Fig. 13—Microstructures and heat treatments of a Ti-12.1 pct Mn alloy. Letters in the graph correspond to microstructures.

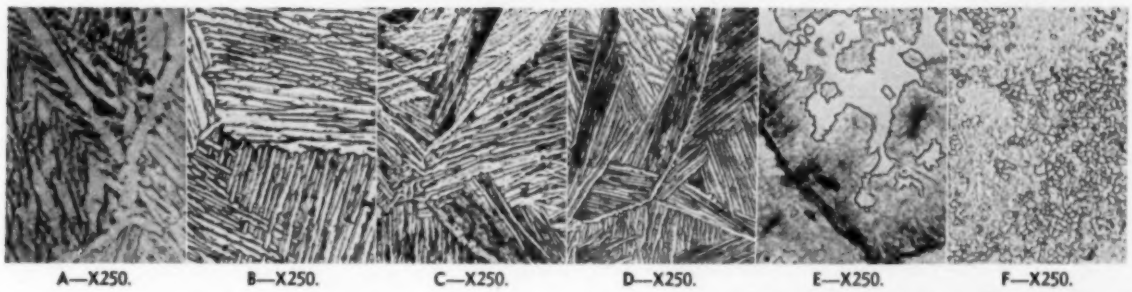

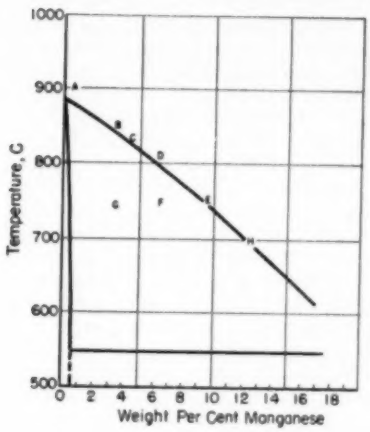

Fig. 15—Microstructures and annealing treatments of furnace-cooled Ti-Mn alloys. Letters in the graph correspond to microstructures.

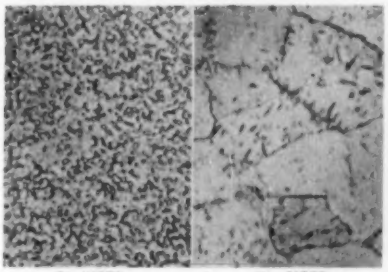

nium system. A series of temperatures from which quenches are conducted and the compositions which have constant α/β ratios in the two-phase field are shown. In Fig. 17b the expected hardnesses are indicated. The top curve is the hardness obtained by quenching from within the β field. The bottom curve shows the hardnesses obtained by quenching from within the α field. The maximum in the β-quenched curve occurs at the composition where the hardening resulting from β transformation to α (either or both by martensitic or by nucleation processes) is balanced by increasing retention of β phase. The hardnesses in the two-phase field are shown as being proportional to the quantity of β present, and to lie between the hardnesses of the two terminal compositions. The hardness curves of alloys with constant α/β ratios are seen to reflect the upper β-quench curve, but with proportionately diminished effect as the amount of β decreases.

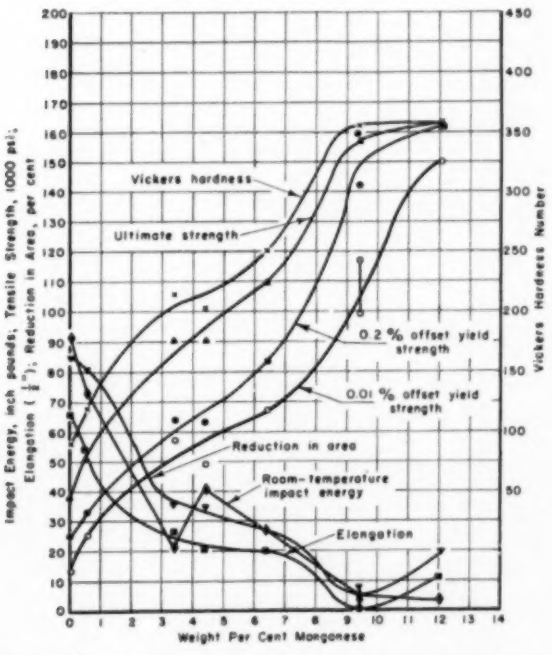
Impact Energy, inch pounds; Tensile Strength, 1000 psi; Elongation (1/2"); Reduction in Area, per cent
Vickers Hardness Number
Weight Per Cent Manganese
Vickers hardness
Ultimate strength
0.2 % offset yield strength
0.01 % offset yield strength
Reduction in area
Room-temperature impact energy
Elongation

Fig. 16—Mechanical properties of Ti-Mn alloys furnace cooled from the β field.

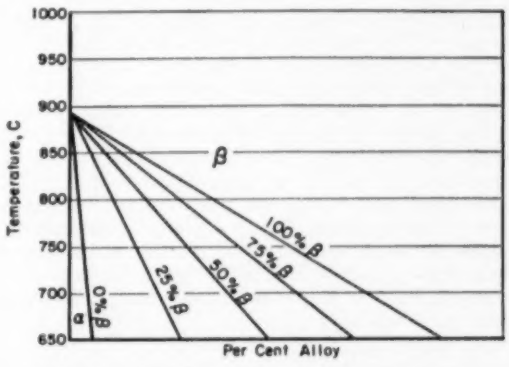

Fig. 17a—Schematic β-stabilized titanium alloy system.

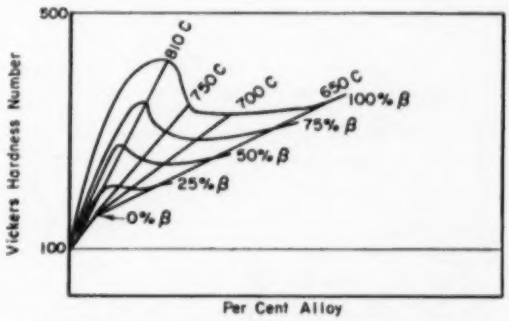

Fig. 17b—Schematic hardness-composition curves.

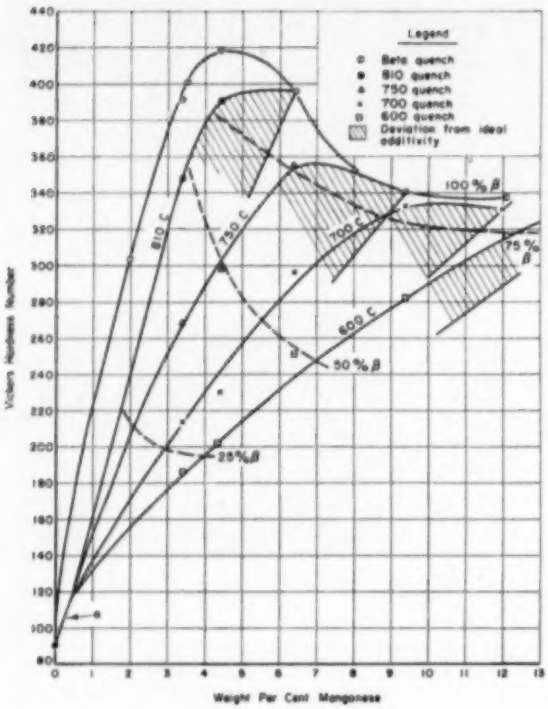

Fig. 18—Hardness of Ti-Mn alloys as a function of composition. All specimens water quenched.

The actual hardness curves determined experimentally for the Ti-Mn alloys are shown in Fig. 18. It is seen that these curves are similar in shape to the schematic curves, but with one notable difference. The α-β alloys are considerably harder than what would correspond to a linear variation between the two terminal phase hardnesses. The deviation from linearity is seen to be greatest as 100 pct β is approached. There are two possible explanations for this effect: 1—grain refinement in the α-β field, and 2—matrix effects, where the properties of the two-phase alloy tend to be closer to those of the matrix or continuous phase. At the high β contents, both of these effects would augment strength and hardness. As an example of the grain-refinement effect, the distances between grain centers were observed in 750°C annealed alloys as shown in Table II.

This shows that the grain size in the α-β alloys remains very fine until all β is approached. Then grain coarsening occurs abruptly. The β matrices in the α-β alloys were observed down to about 30 to 40 pct β in the structure. Where the matrix is β phase, the grain-refinement and matrix effects cooperate in making the alloys harder than would be expected from solid-solution hardening alone. However, it is difficult to separate the two effects. At the α end of the α-β range, the grain-refinement effect would be opposed by the matrix effect. This would account for the closer approach to linearity noted in this region.

Table II. Observed Distances Between Grain Centers

Mn, Pct	Beta, Pct	Grain Separation, Mm
0.55	<5	0.075
3.4	40	0.004
4.4	50	0.004
6.4	70	0.01
9.4	100	0.23

Fig. 18 also shows that for alloys with constant α/β ratios, hardness decreases as the annealing temperature decreases. Despite this, it is apparent that the amount of β in an α-β alloy is the major effect in governing strength and hardness. This is shown graphically in Fig. 19, in which mechanical properties are plotted against the percentage of β for annealing temperatures from 750°C and below. All results correspond to the equiaxed structural condition. The data from 810°C anneals are not included because martensite transformations were involved there. Fig. 19 shows that, within 10 to 20 thousand psi in strengths and 20 to 40 Vickers hardness numbers, strength and hardness correlate directly with the percentage of retained β irrespective of annealing temperature and alloy composition. Within these spreads, the higher strengths are, of course, associated with the higher annealing temperatures, as has been pointed out. The matrix and grain-refinement effect noted is reflected in these curves by a leveling off in strength and hardness from 70 to 100 pct retained β. The scatter in ductility and toughness values is considerably greater than in strength and hardness. Reduction in area values are particularly erratic. As will be shown later, the ductility values depend on the residual hydrogen content,

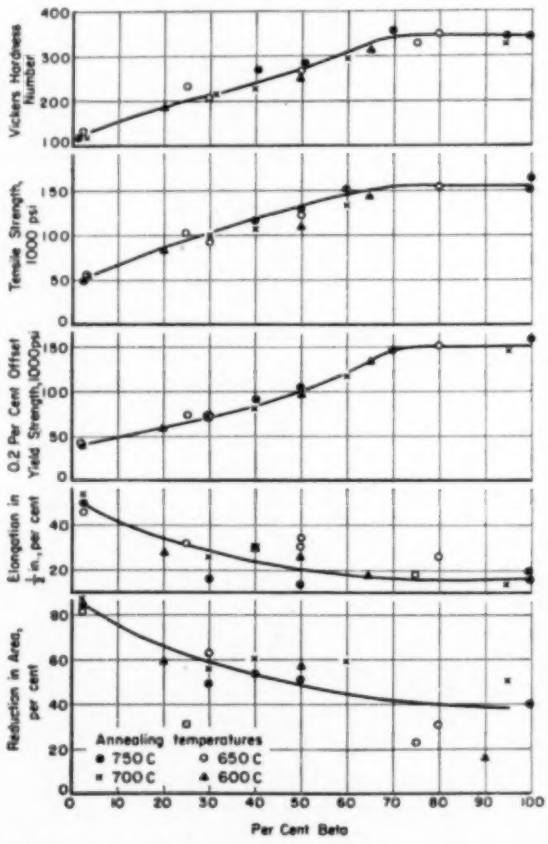

Fig. 19—Correlation of tensile properties with retained β content of Ti-Mn alloys annealed at 750°, 700°, 650°, and 600°C.

Table III. Comparison of Properties of Equilibrated Alloys with Beta Quenched Alloys

	Equilibrated (Step-Cooled to 600°C and Quenched)	Beta Quenched From 850°C	Beta Quenched From 1000°C
Tensile strength, psi	82,000	136,000	137,000
0.2 pct offset yield, psi	61,000	125,000	115,000
Elongation, pct in ½ in.	28	1	5
Reduction in area, pct	59	12	10
VHN	187	353	369
Room-temperature impact, in-lb.	18.1	12.7	7.2

which varies somewhat from alloy to alloy. There is, however, a definite trend toward lower ductility values as the percentage of β increases.

Effect of Martensitic Transformation on Properties

There are two ways in which the effect of the martensite transformation can be evaluated. The first is to compare the properties of the equilibrated alloys with those of the β-quenched alloys. This is done in Table III for the 3.4 pct Mn alloy and shows that the considerable gain in strength and hardness is obtained at the expense of almost all of the ductility.

"hard β" cannot be stated at this time. Ductility can be obtained if sufficient equiaxed α is present. Also, a comparison of the 3.4 pct Mn alloy as β quenched and as α-β quenched, with 40 pct equiaxed α present, reveals that the tensile strength and hardness resulting from the α-β quench are almost as high, but the tensile ductility is much higher. However, it is worth noting that β quenching in the martensite range is not so detrimental to impact as it is to tensile ductility.

Effect of Grain Shape in α-β Alloys

In a two-phase alloy, the effect of grain shape is a variable which may affect the mechanical properties. Grain shape is determined by the prior history of the alloy, particularly in the case of the alloys lying in the composition range where acicular structures are formed after heat treatment in the β field. In the present work, such alloys were fabricated in the α-β field such that subsequent anneals below the β transus produced equiaxed α-β structures. When the α-β heat treatment was preceded by an anneal above the β transus, the resulting structures consisted of large β grains with intergranular and intragranular plates of α.

To determine the specific effect of grain shape,

Table IV. Effect of Increasing Amounts of Martensite on Properties

Alloy Content, Pct Mn	Structure: Equiaxed α, Pct	Structure: α' Plus β, Pct	Tensile Strength, 1000 Psi: Ultimate	Tensile Strength, 1000 Psi: 0.2 Pct Offset Yield	Elongation, Pct in ½ In.	Reduction in Area, Pct	VHN	Room-Temperature Impact, In.-Lb
3.4	40	60	132	98	13	41	347	7.3
4.4	20	80	174	144	4	6	390	6.0
6.4	0	100*	132	—	0	1	396	3.2

* This structure was all retained β.

The second way to evaluate the martensite effect is to show how increasing amounts of martensite affect properties in the presence of equiaxed α. This may be done by comparing the tensile properties of alloys quenched from 810°C, as shown in Table IV. Since the 6.4 pct Mn alloy was all retained β, it must have a slightly higher alloy content than the terminal β composition at 810°C (5.5 pct Mn from Fig. 1). It is representative of what is called "hard β," and will be discussed later. It is clear from the tabulation that the β transformation products are brittle, but whether this is caused by the martensite or the

the 3.5 pct Mn alloy hot worked at 750°C was put into equilibrium at 750°C and quenched, after having approached equilibrium by four different paths: 1—α-β anneal at 750°C and quench, 2—β quench and temper at 750°C and quench, 3—isothermal transformation of β at 750°C and quench, and 4—furnace cool from β to 750°C, hold, and quench. In each case the holding time at 750°C was 32 hr, following which the alloy was quenched. Also, 750°C is above the M_s for the 3.5 pct Mn alloy. This was done both for alloys that had been vacuum annealed after hot working and those that had not.

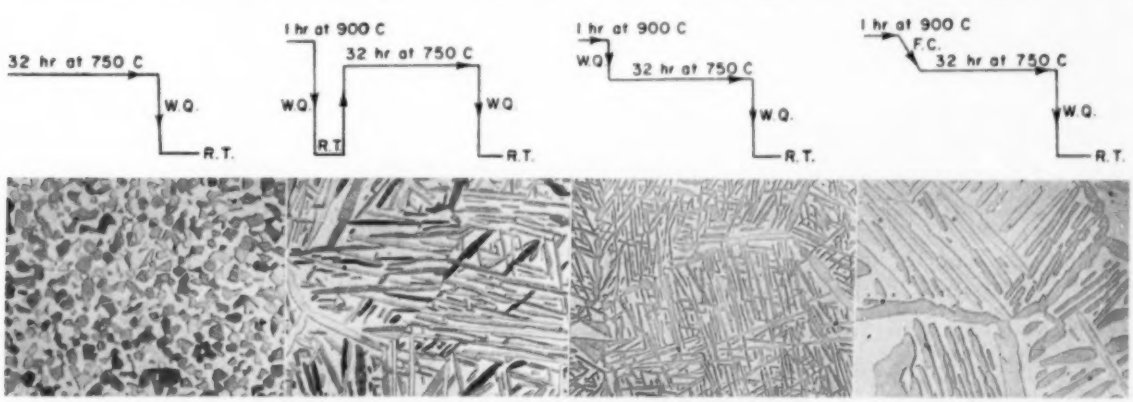

Fig. 20—Schematic heat treatments and microstructures of a Ti-3.5 pct Mn alloy. Magnification of microstructures, X250.

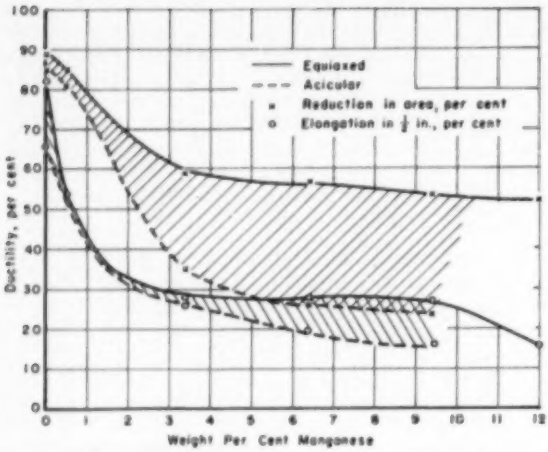

Fig. 21—Comparison of tensile ductility for α-β alloys in the equiaxed and acicular conditions.

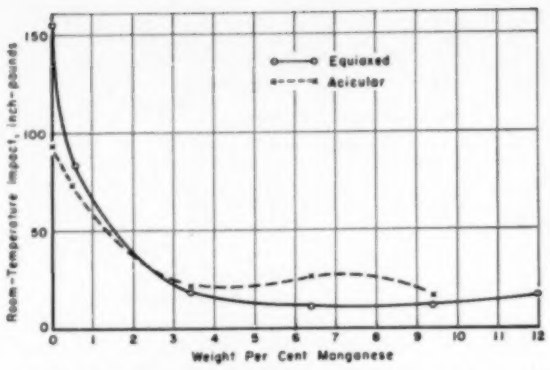

Fig. 22—Room temperature impact values for α-β alloys in the equiaxed and acicular conditions.

After the heat treatments, the alloy consisted of 60 pct α containing about 0.5 pct Mn, and 40 pct retained β containing about 9 pct Mn. Micrographs of the four structures are shown in Fig. 20. There was no difference between the structures of the vacuum-annealed specimens and those that had not been vacuum annealed. The structures of the α-β annealed and quenched specimens consisted of equiaxed α grains in a β matrix. The average distance between α grain centers was about 0.01 mm. The structure after the β-quench-and-temper treatment consisted of rather straight α platelets within the prior β grains and also α at the prior β grain boundaries. Average interplatelet distance was about 0.01 mm. The isothermal-transformation structure was quite similar to the quench-and-temper structure both in appearance and degree of fineness. Although the micrograph for the isothermally transformed alloy appears to be slightly finer than that shown for the quenched and tempered alloy, over the entire section it appeared that they were of equal fineness. The structure of the furnace-cooled specimen was much coarser, both in platelet size and interplatelet spacing. A rough estimate of the spacing from center to center of platelets would be two to three times that for the other acicular structures.

Mechanical properties for the 3.5 pct Mn alloy in the four conditions are given in Table V. Strengths and hardnesses are practically indistinguishable; this is as would be expected because the alloy consisted of the same quantities of α and β phases. When the alloy had not been vacuum annealed, it con-

Table V. Mechanical Properties of Ti-3.5 Pct Mn Alloy for Various Heat Treatments

Heat Treatment	Microstructure	VHN, 5 Kg Load	Elongation, Pct in 1/2 In.	Reduction in Area, Pct	Ultimate Tensile Strength, Psi	0.2 Pct Offset Yield Strength, Psi	Flow Constants			Room Temperature Impact Energy, In.-Lb
							B, Psi	n	$\delta_{max.}$ In. per In.	
Annealed 32 hr at 750°C and water quenched (220 ppm H)	Equiaxed α-β structure; α 0.01 mm grain size; 60 pct α	297	—	17	111,000	91,000	182,000	0.181	0.153	32.4
Same as above, but preceded by vacuum annealing treatment (about 25 to 50 ppm H)	Equiaxed α-β structure; α 0.01 mm grain size; 60 pct α	271	20	39	116,000	86,000	164,000	0.106	0.100	(18.9, 14.5)
Annealed 1 hr at 900°C, quenched to room temperature; annealed 32 hr at 750°C and water quenched (220 ppm H)	Coarse α plates in matrix of retained β; prior β grain size 0.25 mm; 60 pct α	303	13	12	114,000	90,000	183,000	0.166	0.113	28.1
Same as above, but preceded by vacuum annealing treatment (about 25 to 50 ppm H)	Coarse α plates in matrix of retained β; prior β grain size 0.25 mm; 60 pct α	286	13	28	116,000	88,000	158,000	0.093	0.094	33.0
Annealed 1 hr at 900°C, quenched to 750°C, held 32 hr, and water quenched (220 ppm H)	Coarse α plates in matrix of retained β; prior β grain size 0.25 mm; 60 pct α	285	14	15	112,000	85,000	178,000	0.160	0.127	28.2
Same as above, but preceded by vacuum annealing treatment (about 25 to 50 ppm H)	Coarse α plates in matrix of retained β; prior β grain size 0.25 mm; 60 pct α	275	16	24	118,000	83,000	170,000	0.113	0.109	36.9
Annealed 1 hr at 900°C, furnace cooled to 750°C, held 32 hr, and water quenched, (220 ppm H)	Coarse α plates in matrix of retained β; prior β grain size 0.25 mm; 60 pct α	298	7	9	101,000	87,000	160,000	0.144	0.063	21.1
Same as above, but preceded by vacuum annealing treatment (about 25 to 50 ppm H)	Coarse α plates in matrix of retained β; prior β grain size 0.25 mm; 60 pct α	275	13	17	118,000	85,000	163,000	0.094	0.089	34.7

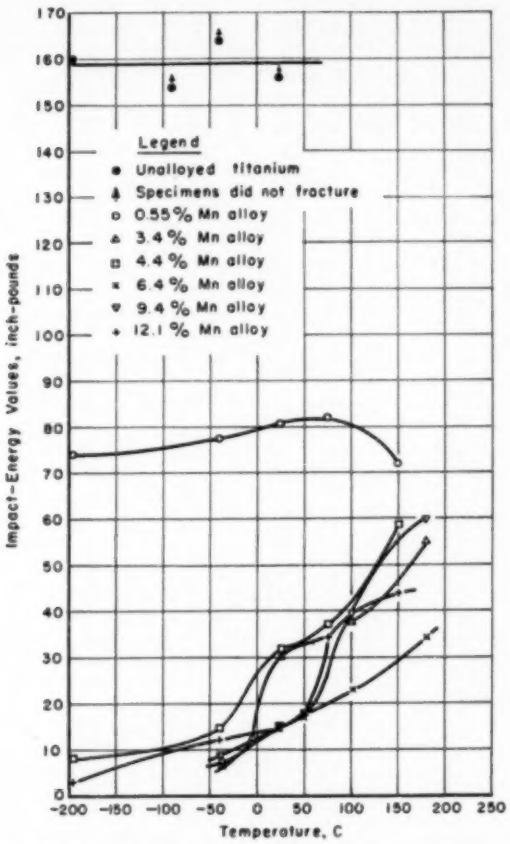

Fig. 23—Effect of testing temperature on impact-energy values for Ti-Mn alloys annealed 1 hr at 750°C and water quenched.

tained 220 ppm hydrogen, and showed lower tensile ductility than when the alloy was vacuum annealed. This will be discussed in the section on the effect of hydrogen. The tensile ductilities of the vacuum-annealed specimens that had acicular structures originating from an anneal in the β field are all quite comparable. The tensile ductility of the equiaxed vacuum-annealed specimen is higher than those of the corresponding acicular structures.

The higher tensile ductilities in the equiaxed condition are also shown in Fig. 21, which compares the tensile ductilities of Ti-Mn alloys having equiaxed structures with the tensile ductilities of the alloys having acicular structures. Up through 6.4 pct Mn, the properties in the condition step-cooled from 750° to 600°C are compared with the properties in the furnace-cooled condition. At 9.4 pct Mn, the properties in the 750°C quenched condition, which was equiaxed β, are compared with those in the 750° to 600°C step-cooled condition, which was acicular, because the β transus for this alloy is about 750°C. The 12.1 pct Mn alloy is basically an all-β alloy, which cannot be put into an acicular condition, and only the properties in the equiaxed all-β condition, as quenched from 700° to 750°C, are shown. It is apparent that there is a considerable advantage in tensile ductility, particularly in reduction in area, for the equiaxed condition.

Toughness does not appear to be so dependent on structure. The data in Table V do not show any consistent effect of equiaxed vs acicular structure on room-temperature impact value. Impact data on the alloys in the conditions described in the preceding paragraph are plotted in Fig. 22. This shows some advantage for the 6.4 pct Mn alloy in the acicular condition, but it is doubtful whether there is any clear preference for this condition so far as impact values are concerned.

Effect of Hydrogen

The presence of hydrogen in titanium and its alloys has considerable influence on their properties, and this problem is the subject of current investigations. In this work, the problem of eliminating this element as an unwanted variable has been met by vacuum-annealing processes which remove a considerable amount of the hydrogen present. The

Table VI. Effect of Vacuum Annealing on Mechanical Properties of Ti-Mn Alloys

Alloy Composition	Heat Treatment	Microstructure	VHN, 5 Kg Load	Elongation, Pct in 1/2 In.	Reduction in Area, Pct	Ultimate Tensile Strength, Psi	0.2 Pct Offset Yield Strength, Psi	Flow Constants			Room-Temperature Impact Energy, In.-Lb
								B, Psi	n	$\delta_{max.}$ In. per In.	
3.5 pct Mn (220 ppm H)	Annealed 1 hr at 750°C and water quenched	Equiaxed α-β structure; α grain size 0.004 mm; 60 pct α	284	—	21	118,000	96,000	188,000	0.161	0.152	31.0
3.5 pct Mn (about 25 to 50 ppm H)	Vacuum annealed 11½ hr at 775°C plus ½ hr at 750°C and water quenched	Equiaxed α-β structure; α grain size 0.004 mm; 60 pct α	256	26	61	117,000	90,000	166,000	0.107	0.112	31.3
6.4 pct Mn (150 ppm H)	Annealed 1 hr at 750°C and water quenched	Equiaxed α-β structure; α grain size 0.002 mm; β grain size 0.01 mm; 30 pct α	356	16	49	150,000	146,000	208,000	0.07	0.02	14.7
6.4 pct Mn (about 25 to 50 ppm H)	Vacuum annealed 11½ hr at 775°C plus ½ hr at 750°C and water quenched	Equiaxed α-β structure; α grain size 0.002 mm; β grain size 0.004 mm; 30 pct α	344	18	64	162,000	145,000	207,000	0.065	0.064	14.8
9.4 pct Mn (110 ppm H)	Annealed 1 hr at 750°C and water quenched	Equiaxed β structure; β grain size 0.25 mm	340	15	40	163,000	159,000	216,000	0.06	0.02	14.8
9.4 pct Mn (about 25 to 50 ppm H)	Vacuum annealed 11½ hr at 775°C plus ½ hr at 750°C and water quenched	Equiaxed β structure; β grain size 0.20 mm	336	—	38	160,000	156,000	—	—	—	18.9

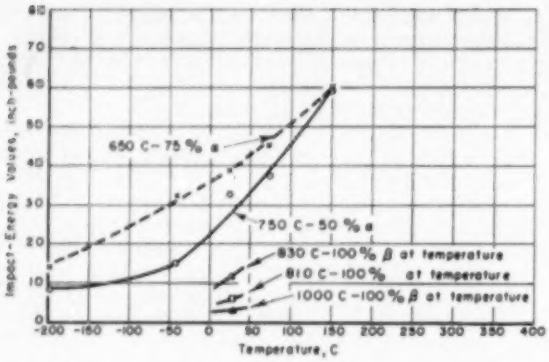
Impact-Energy Values, inch-pounds
650 C–75 % α
750 C–50 % α
830 C–100 % β at temperature
810 C–100 % β at temperature
1000 C–100 % β at temperature
Temperature, C

Fig. 24—Effect of quenching temperature and percent α on impact behavior.

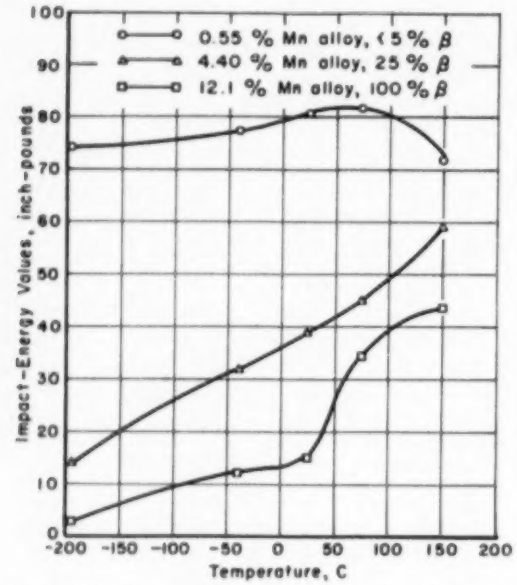

Fig. 25—Effect of α-β ratio on impact-energy temperature curves.

earlier alloys, however, were fabricated and partially tested before this procedure was adopted, and they had hydrogen contents ranging from 110 to 220 ppm. To determine the effects of hydrogen on these alloys, tensile and impact specimens were vacuum annealed and heat treated to produce structures like those already tested, but with the hydrogen content reduced by the vacuum-annealing process. From similar alloys so treated, it is estimated that the hydrogen content was reduced to 25 to 50 ppm.

It has been demonstrated that the presence of hydrogen as titanium hydride in unalloyed titanium accounts for lower levels of impact-energy values.[4] The presence of titanium hydride in unalloyed titanium and in α-stabilized titanium alloys is made evident by the appearance of line markings in the microstructure. The first α-β alloys, which had not been vacuum annealed, did not show these line markings, and since the solubility of hydrogen is greater in the β phase than in α, it is thought that the hydrogen in an α-β alloy is dissolved in the β phase. Mechanical properties of the vacuum-annealed test specimens are shown in Table VI, with corresponding values for the nonvacuum-annealed alloys. Strength and impact properties in these alloys are not significantly altered by the vacuum anneal. Tensile-ductility values appear to be lower when hydrogen is present, however, for the lower manganese content alloys. This is particularly the case for values of reduction in area. If the mechanism of tensile embrittlement of α-β alloys containing hydrogen is caused by strain aging of a hydrogen-rich precipitate from β, the lack of embrittlement in the 9.4 pct Mn alloy may simply be because the alloy contains insufficient hydrogen to become supersaturated.

Impact-Energy Values as a Function of Testing Temperature

In the testing program used in this work, each alloy and condition has been tested for impact resistance at room temperature. In addition to these tests, certain conditions were further investigated to determine the variation of impact energy with temperature. Results of these tests are tabulated in Table VII, and curves showing the variation of impact energy with temperature for Ti-Mn alloys annealed at and quenched from 750°C are shown in Fig. 23. Increasing manganese content, which corresponds to increased amounts of retained-β phase containing about 9 pct Mn, results in shifting the impact-transition curves downward and to the right—in other words, toward less tough behavior. Impact-transition curves for the alloys containing 6.4 to 12.1 pct Mn are all at about the same location, and there is no clear-cut relationship between them. The beneficial effect of high-α-phase contents on toughness is further illustrated by Fig. 24, which

Table VII. Variation of Impact Energy with Testing Temperature for Ti-Mn Alloys

Alloy Composition	Impact Energy, In.-Lb, at Various Temperatures, °C									
	−196	−80	−40	−10	25	50	75	100	150	180
Annealed 1 Hr at 750°C and Water Quenched										
0.55 pct Mn	74.1		77.5		80.7		82.0		72.1	
3.4 pct Mn			7.0	12.4	29.8			37.4		54.9
4.4 pct Mn	8.0		14.7		31.8		37.0		58.5	
6.4 pct Mn			6.5		14.7	17.1		22.9		34.1
9.4 pct Mn			8.3		14.8	17.3		39.6		59.8
12.1 pct Mn	2.8		12.1		15.0		34.4		43.7	
Annealed 1 Hr at 650°C and Water Quenched										
4.4 pct Mn	13.8		31.3		38.5		45.0		59.0	
Step-Cooled to 32 Hr at 600°C and Water Quenched										
12.1 pct Mn	1.2		4.2		9.0		18.6		38.1	
Annealed 1 Hr at 800°C and Water Quenched										
Unalloyed titanium	160.2	153.8*	164.3*		156*					

* No fracture occurred in these specimens.

Fig. 26—Fractures of impact specimens at various temperatures. X5.

shows that, for the same 4.4 pct Mn alloy, lower annealing temperatures, which correspond to higher α phase contents, result in the best impact-transition curves.

None of the alloys showed a truly sharp transition from low to high impact values, although the trend toward this increased as the amount of β increased. The compositions which were predominantly α showed no transition behavior at all down to −196°C. Supporting this, examination of the fractures of all Ti-Mn alloys showed the same kind of fracture, even when broken at low energies at −196°C. Fig. 25 shows impact curves for a predominantly all-α alloy, 0.55 pct Mn (<5 pct β); an

Table VIII. Mechanical Properties of Ti-Mn Alloys in the Solution-Annealed and Aged Conditions

Composition, Pct (Balance Ti)	Heat Treatment	Microstructure	VHN	Elongation in ½ In., Pct	Reduction in Area, Pct	Ultimate Tensile Strength, Psi	0.2 Pct Offset Yield Strength, Psi	Room Temperature Impact Energy, In.-Lb
3.4 pct Mn	1 hr at 700°C and quenched	Equiaxed α-β (30 pct β)	213	26	56	98,000	73,000	16.3
3.5 pct Mn*	1 hr at 700°C and quenched plus 1 hr at 400°C	Equiaxed α-β (30 pct β)	265	10	14	120,000	85,000	7.5
3.5 pct Mn*	1 hr at 750°C and quenched	Equiaxed α-β (40 pct β)	284	—	21	118,000	96,000	31.0
3.5 pct Mn*	1 hr at 750°C and quenched plus 4 hr at 400°C	Equiaxed α-β (40 pct β)	303	12	32	158,000	156,000	6.3
9.4 pct Mn	1 hr at 700°C and quenched	Equiaxed β grains (0.075 mm) plus 10 pct intra- and intergranular α	330	27	54	156,000	154,000	6.9
9.4 pct Mn	1 hr at 700°C and quenched plus ¼ hr at 500°C	Equiaxed β grains (0.075 mm) plus 10 pct intra- and intergranular α	412	3	4	204,000	200,000	3.0

* This alloy contained 220 ppm hydrogen which is the probable cause of the low tensile ductility in the solution-annealed condition.

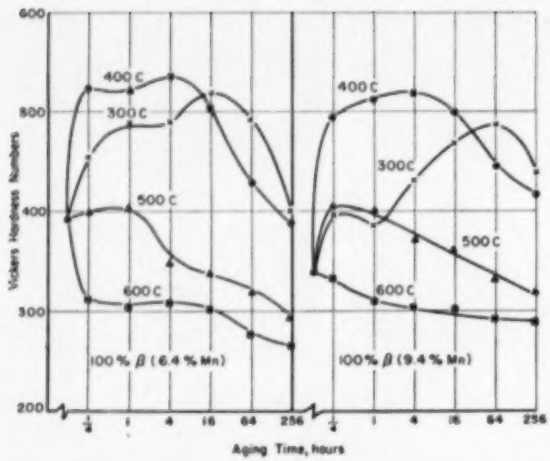

Fig. 27—Effect of aging temperature on age hardening of two Ti-Mn alloys quenched from the β field.

α-β alloy, 4.4 pct Mn quenched from 650°C (25 pct β); and an all-β alloy, 12.1 pct Mn. Photographs showing the fractures for these alloys are presented in Fig. 26.

Thermal Instability

The effect of low temperature aging on hardness of Ti-Mn alloys quenched from both the β and α-β fields was investigated. These tests were made on small samples sealed in pyrex capsules under a partial pressure of argon at temperatures of 300°, 400°, 500°, and 600°C. Aging treatments consisted of a geometric progression of ¼, 1, 4, 16, 64, and 256 hr, followed by water quenching.

In this study, the chief variables involved, in addition to aging times and temperatures, were the composition of the β phase and the microstructure of the solution-annealed condition. The effect of aging time and temperature on the β phase of two compositions is shown in Fig. 27. These curves show that the β phase age hardens to the greatest extent at 400°C, reaching a peak hardness after about 4 hr. Aging at lower temperatures is almost as effective, but longer times are required to reach the peak hardness. Aging at 500°C results in a rapid overaging with only a small hardness peak, while aging at 600°C softens the alloys, because the α precipitate is of the massive form and equilibrium is being approached. The effect of composition of the β phase on the age-hardening response is illustrated by the data for the β-quenched Ti-6.4 pct Mn and Ti-9.4 pct Mn alloys. The peak hardnesses obtained for the aging temperatures used were about the same for the two alloys with the Ti-6.4 pct Mn alloy having a slightly higher peak hardness in the 300° and 400°C aged conditions. This may be indicative that increasing the manganese content decreases the instability of the β phase, but the difference in degree of instability of the two alloys is not great enough to be significant. However, as will be discussed in the section on cooling rates, it has been found that the manganese content does have an effect on the susceptibility to hardening of the alloys.

Examination of the microstructures of aged samples showed that visible precipitates do not occur until overaging has taken place.

The effects of quantity of the β phase present in the microstructure in the solution-annealed conditions are shown in Fig. 28. These data show that, as the quantity of β phase of the same composition is decreased, the susceptibility to age hardening is decreased, or the thermal stability of the alloy is increased. Control of the quantity of β phase in the initial microstructure of the alloy has a much greater effect on reducing thermal instability than does an increase of the manganese content of the β phase.

The age hardening or instability of the β phase in α-β alloys is generally regarded as detrimental be-

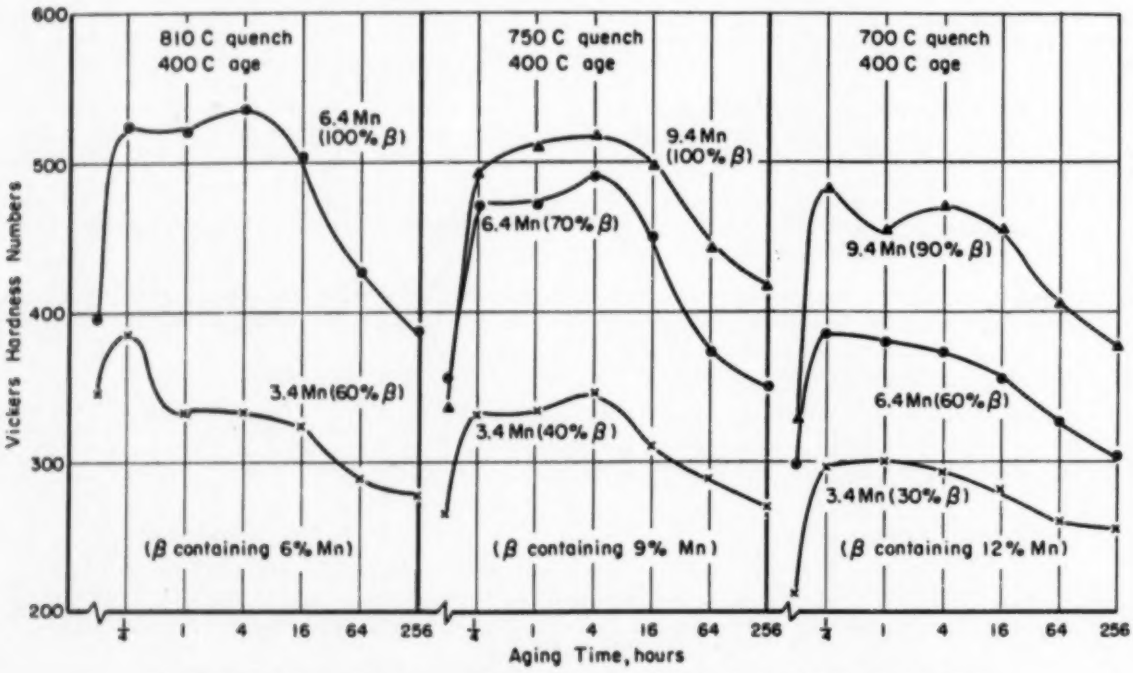

Fig. 28—Effect of quantity and composition of the β phase on age hardening of Ti-Mn alloys at 400°C.

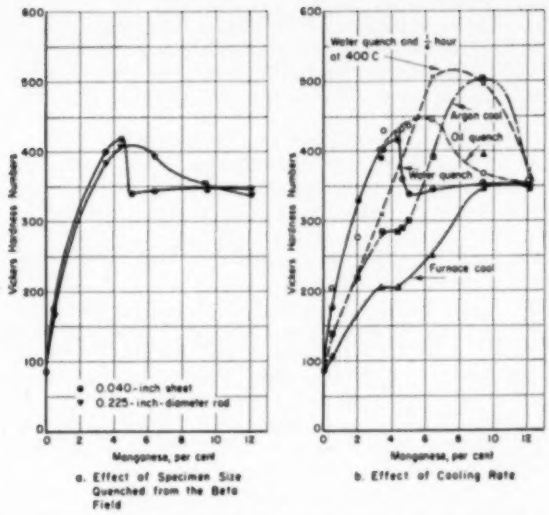

Fig. 29—Effect of specimen size and cooling rate on the hardness of β-annealed Ti-Mn alloys.

cause of the embrittlement that accompanies the age hardening. However, it is possible to produce high strengths while maintaining adequate ductility by controlling the amount of unstable β present through a solution anneal in the α-β field so that the aging response will not be too high. The data given in Table VIII illustrate how age hardening can be utilized to improve the strength of α-β alloys. In this table, the effects of aging on the properties of alloys containing 30, 40, and 90 pct β are shown. In line with the hardness data, the alloy containing the largest percentage of β phase in the solution-annealed condition has the largest increase in strength. Accompanying the increase in strength is a decrease in tensile ductility and toughness. However, good strength and ductility combinations can be obtained as illustrated by the 3.5 pct Mn alloy solution annealed at 750°C and aged for 4 hr at 400°C.

Effect of Cooling Rate and Specimen Size on Hardness of Ti-Mn Alloys

A series of specimens was cooled from annealing temperature at several cooling rates by quenching in water, quenching in oil, and cooling in argon (simulated air-cooling rate under an argon atmosphere). The effect of specimen size was also studied by the use of two specimens for each test: one, a small section of 0.040 in. sheet, and the other, a section of 0.225 in. diameter rod. Anneals were made in tube furnaces under an argon atmosphere. Specimens were prepared from the alloys previously described and, in addition, three alloys were prepared in the form of 15 gram buttons to provide data on intermediate compositions.

The cooling rate and specimen size are both important in a consideration of the hardening of these alloys. It was noted that the 6.4 pct Mn alloy is particularly sensitive to variations in cooling rate. Although all the microstructures of different-sized specimens of the 6.4 pct Mn alloy quenched from the β field show a retained-β structure, there is considerable variation in hardness. The softest retained β in this alloy was produced only by the combination of small specimen size and quenching from just above the β transus. Quenching small specimens from temperatures high in the β field results in a higher hardness. Another example of the effect of cooling rate is the 5.0 pct Mn alloy, which produces a microstructure containing about 85 pct martensite in a matrix of retained β when water quenched from just above the β transus. Water quenching from 1000°C produces a structure containing about 50 pct martensite, but with a greater

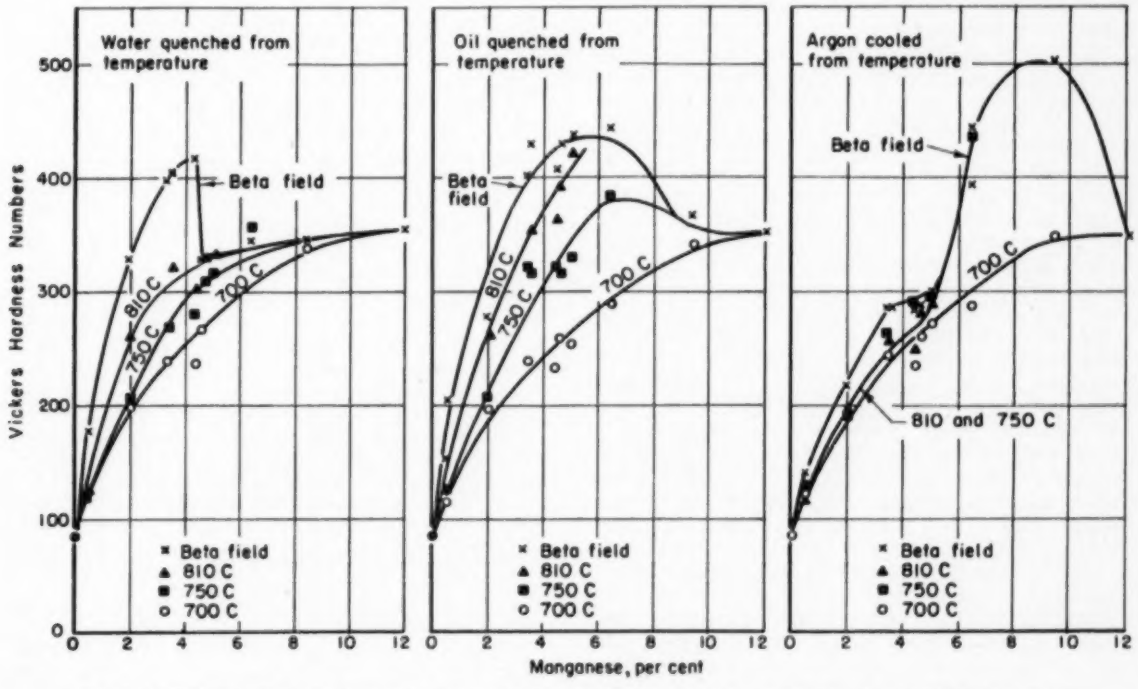

Fig. 30—Effect of cooling rates from various annealing temperatures on the hardness of Ti-Mn alloys (0.040 in. sheet).

hardness. This higher hardness is attributed to the fact that cooling from the higher temperature results in a slower cooling rate through the range at which nucleation of α takes place in the retained-β phase causing coherency hardening of the retained β.

The effect of specimen size on the hardness of β-quenched Ti-Mn alloys is shown in Fig. 29a. The difference in sample size is in reality a cooling-rate effect. The larger samples will cool at a slightly lower rate than smaller samples when quenched in the same medium. The composition range which is chiefly affected by sample size is from 5 to 7 pct Mn, where higher hardnesses are obtained in the larger samples as a result of the high degree of instability of β in this range. A more complete illustration of the effect of cooling rate on the hardness of Ti-Mn alloys annealed in the β field is shown in Fig. 29b. Here it is shown that as the cooling rate is decreased from that of a water quench to an argon cool the peak hardness obtained is increased and is shifted to higher manganese contents. It is also of interest that the alloys β quenched and aged for ¼ hr at 400°C have hardnesses similar to those obtained in the argon-cooled condition. This indicates that the hardening obtained during the cool from the β field is caused by the same nucleation-and-growth mechanism that occurs during the aging treatment.

The hardnesses of samples furnace cooled from the β field are, in general, lower than those obtained by any of the other cooling rates used. During the furnace cool, massive α is formed which does not have the hardening effect of the coherent or finely dispersed α formed during aging. Rather, there is an approach to a low temperature equilibrium. In alloys containing 6.4 pct Mn or less, the α is formed as coarse Widmanstaetten plates; while in the 9.4 and 12.1 pct Mn alloys the α is formed as fine Widmanstaetten plates. The softest condition is associated with the coarse α plates. The fine α plates precipitated in the high-manganese-content alloys did not alter the hardness significantly from the β-quenched condition.

The effect of cooling rate on the hardness of Ti-Mn alloys annealed in the α-β field is shown by the data given in Fig. 30. The effect of water quenching has been discussed earlier, where it was shown that the hardness of an α-β alloy could be related to the quantity and size of the two phases present and to the matrix effects. The differences between the curves on water-quenched alloys shown in this figure and those shown in Fig. 18 can be attributed to the difference in specimen sizes. The family of curves obtained for the oil-quenched condition also reflects the effects of amounts of phases present, grain size, and matrix. However, because the β phase in the range of 5 to 7 pct Mn is coherency hardened by the oil quench, the α-β alloys containing β phase of a composition within this range are also coherency hardened. This is shown by the 810°C oil-quenched curve in Fig. 30. Argon cooling from temperatures of 750°C and above causes a large increase in hardness in alloys containing from 6 to 9 pct Mn. Alloys containing less than 6 pct Mn are softer in the argon-cooled condition than they are in the water-quenched or oil-quenched conditions, and tend to approach the hardness values in the furnace-cooled condition. Thus hardening effects from cooling at rates approximating air cooling may be expected only in alloys within medium-high β-stabilizer contents cooled from relatively high temperature.

Summary

1—The principal compositional factors which affect mechanical properties have been found to be solid-solution strengthening, the martensitic transformation, and instability of the β phase. Structural factors (grain size and shape) have more influence on ductility and toughness than on strength.

2—Because the strength of the retained-β phase is much higher than the strength of the α phase, the α to β ratio dominates the strength of the alloys annealed in the two-phase field. Matrix and fineness effects introduce deviations from straight-line additivity. Since the strength of the β phase is relatively constant from 6.4 to 12.1 pct Mn, the strength of an α-β alloy is determined primarily by the amount of β phase present. However, because coherency hardening (formation of β') is more operative in low-manganese-content β, the higher α-β solution temperatures give slightly higher hardness, for a fixed percentage of β.

3—The martensitic transformation of β takes place when alloys containing less than 6.4 pct Mn are quenched from temperatures above 800°C. When quenched from the β field, the structure consists of plates of supersaturated α in a matrix of retained β of the same composition, with the quantity of retained β increasing with alloy content. Specimens having these structures are in a strong and brittle condition. However, the presence of equilibrium α in the structure, attained by annealing and quenching from below the β transus and above 800°C, improves the ductility considerably with some loss of strength.

4—Instability of the β phase is an important factor in the mechanical properties of these alloys. Nucleation and growth of α phase may be controlled to produce a considerable strength increase, or, if a massive α precipitate is formed, to decrease the strength of the alloy. Desired strength increases may be obtained either by a solution anneal followed by aging, or by proper choice of cooling rate from the annealing temperature. Although loss of ductility and toughness accompany this strength increase, adequate levels of these properties may be maintained by proper control of heat treatments.

5—Limited studies on the effects of hydrogen in these alloys indicate that hydrogen partitions to the β phase in an α-β alloy. The principal effect of hydrogen in the α-β alloys is a lowering of tensile ductility, without affecting toughness.

Acknowledgment

The authors wish to thank Watertown Arsenal under whose sponsorship this work was conducted for permission to publish this paper and to Mr. D. C. Buffum of that laboratory for valuable suggestions.

References

[1] D. J. Maykuth, H. R. Ogden, and R. I. Jaffee: Titanium-Manganese System. *Trans.* AIME (1953) **197**, pp. 225-230; JOURNAL OF METALS (February 1953).

[2] P. Duwez: The Martensite Transformation Temperature in Titanium Binary Alloys. *Trans.* ASM (1953) **45**, pp. 934-940.

[3] F. C. Holden, H. R. Ogden, and R. I. Jaffee: Microstructure and Mechanical Properties of Iodide Titanium. *Trans.* AIME (1953) **197**, pp. 238-242; JOURNAL OF METALS (February 1953).

[4] C. M. Craighead, G. A. Lenning, and R. I. Jaffee: Nature of the Line Markings in Titanium and Titanium Alloys. *Trans.* AIME (1952) **194**, pp. 1317-1319; JOURNAL OF METALS (December 1952).

Constitution of Iron-Boron Alloys in the Low Boron Range

by M. E. Nicholson

The solid solubility of boron in iron has been determined by saturating iron with respect to Fe_2B at several temperatures from 870° to 1135°C. In alpha iron the maximum solubility was found to be 0.002 pct B and in gamma iron the solubility varied from 0.001 pct at 915°C to 0.020 pct B at 1165°C. The eutectic and peritectoid temperatures were found to be 1165° and 911°C respectively and the gamma iron solidus was located approximately at 0.020 pct B.

RECENT investigations of boron-treated steels[1, 2] indicate that the solubility of boron in austenite is of the order of 0.003 pct at 900°C. This has led to the general belief that the solubility of boron in α and γ iron is considerably less than that indicated by Wever and Müller.[3] Therefore the solid solubilities of boron in α and γ iron have been redetermined. The eutectic and peritectoid temperatures were also remeasured and the γ-iron solidus was studied in some detail.*

* A similar investigation which yielded somewhat different results has been described recently by C. C. McBride, J. W. Spretnak, and Rudolph Speiser in American Society for Metals 1953 Preprint No. 22 entitled "A Study of the Fe-Fe_2-B System."

In 1929 Wever and Müller investigated the phase equilibria of Fe-B alloys. Fig. 1 shows the solid solubility region of the Fe-B diagram based on their investigation. They found that boron lowered the A_4 transformation temperature to 1381°C where saturated δ solid solution "which must contain about 0.15 pct B" and "γ solid solution containing about 0.10 pct B" are in equilibrium with liquid containing 1.9 pct B. At the eutectic temperature of 1174°C, γ solid solution was found to contain "about 0.15 pct B." A peritectoid relation was found to exist between α and γ iron with an invariant temperature at 915°C, where the boron solubility in γ iron was "about 0.10 pct B" and the solid solubility in α iron "did not exceed 0.15 pct B." Although most of their investigation was made using thermal analysis and metallography, the solid solubility of boron in α iron

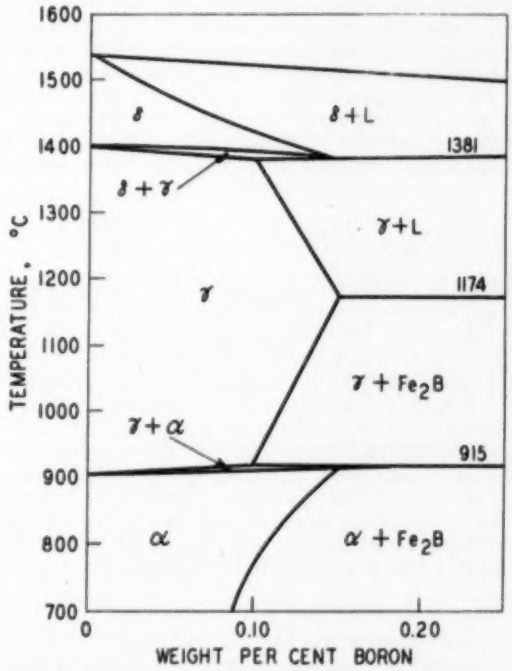

Fig. 1—Portion of Fe-B equilibrium diagram after Wever and Muller.[3]

M. E. NICHOLSON, Member AIME, is associated with the Institute for the Study of Metals, University of Chicago, Chicago.

Discussion on this paper, TP 3713E, may be sent, 2 copies, to AIME by April 1, 1954. Manuscript, Sept. 15, 1953. New York Meeting, February 1954.

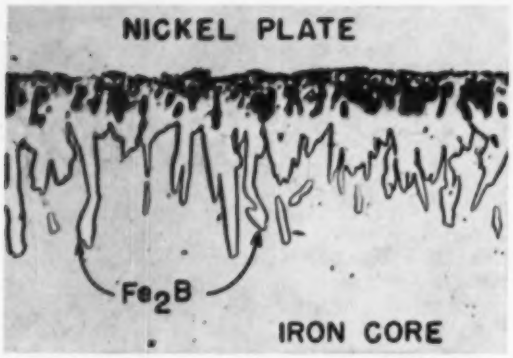

Fig. 2—Microstructure of iron boronized 3 hr at 900°C showing iron boride, Fe_2B, case. Etched with picral-nital duplex etch. X200.

was established using X-ray lattice parameter measurements.

Because of the apparent success of Wever and Müller in using the X-ray lattice parameter technique as a means of determining the limit of solid solubility in α iron, several precision lattice parameter measurements were made of a decarburized high purity iron and an Fe-0.011 pct B alloy.

The Fe-B alloy was prepared by boronizing (as will be described) a rod of decarburized iron to produce a case of iron boride, Fe_2B, and annealing it *in vacuo* at 1100°C until the core was saturated with boron. The Fe-B alloy was then annealed a second time *in vacuo* for 60 hr at 905°C and quenched into oil. The 350-mesh filings of this alloy and of the specimen of iron were then mixed with fine alundum powder to prevent sintering and grain growth during the final heat treatment. The powders were finally heated in purified helium for 15 min at 905°C and quenched into brine, after which the metal filings and alundum were separated magnetically. Lattice parameter measurements were made of the two samples, using a 50 mm back-reflection focusing camera and unfiltered cobalt and chromium characteristic radiations. The lattice parameters of the alloys were computed by using Cohen's least squares method, yielding the following values:

$$\text{Iron at } 20°C = 2.8664 \pm 0.0001\text{Å}$$
$$\text{Fe-B alloy at } 20°C = 2.8665 \pm 0.0001\text{Å}.$$

Since the difference between these values was so small, it was concluded that the X-ray method was unsatisfactory for studying the variation of the solid solubility of boron in iron with temperature.

A more suitable method for investigating the extremely limited solid solubility of boron in iron was considered to be by means of a chemical analysis of the saturated solid solution. In addition to the investigation of the solid solubility of boron in iron, the peritectoid and eutectic temperatures were measured by standard thermal analysis. Metallographic techniques were used to establish the location of the γ solidus line and to verify the eutectic temperature.

Experimental Details and Results

Determination of Solid Solubility of Boron in Alpha and Gamma Iron: In a two-component system the solid solubility of a terminal solid solution may be determined by allowing diffusion to occur between a pure metal and the intermediate phase with which it may coexist until equilibrium is reached, and then analyzing the saturated solid solution for the solute element. For determining solid solubility of boron in iron, the diffusion couple should consist of iron and iron boride, Fe_2B.

To make the couples, pieces of vacuum-melted high purity iron cut from a 3 in. diameter ingot obtained from the National Research Corp., Cambridge, Mass., were swaged into rods about ¼ in. in diameter. The iron ingot had the following analysis: 0.0035 pct C, 0.001 pct Mn, 0.008 pct Si, 0.054 pct Ni, 0.001 pct Mg, 0.001 pct Cu, 0.005 pct O, and 0.00015 pct N. The iron rods, 3 in. long, were placed in an alundum boat and surrounded with boron powder obtained from the Cooper Metallurgical Associates, Cleveland, Ohio, designated as Grade A, 325 mesh powder. This boron contained 0.22 pct C, 0.38 pct Fe, and 99.30 pct B. The specimens were heated in a dry hydrogen atmosphere at a temperature of 900°C for 2 or 3 hr. As a result of this treatment an iron boride case approximately 0.005 in. thick was produced on the surface of the iron rods.† This was sufficient to provide forty times the quantity of boron necessary to saturate the core at maximum solid solubility. Fig. 2 shows the microstructure of such a case. The iron boride was nickel-plated to prevent the porous surface layer from crumbling during polishing. The black spots are voids in the case. The specimen was etched first with 2 pct picral and then 2 pct nital. The picral etches boron-rich phases preferentially. Sometimes the etching is accompanied by a staining of adjacent ferrite. The nital removes this stain and delineates more clearly the grain boundaries.

† Previous work at this Institute by S. Harper had shown the feasibility of this method.

X-ray diffraction of the case showed it was completely Fe_2B. Thus this technique, which will be referred to as boronizing, was suitable for producing the desired couples for the solid solubility studies. The method had two advantages over the normal welding technique for producing diffusion couples. First, it produced an iron-iron boride interface which was continuous and free from contami-

Table I. Data for Solid Solubility Determination

Saturation Anneal			Analysis, Wt Pct			
Temperature, °C	Time, Hr	Specimen Diameter, In.	Boron	Oxygen	Equiv. B	"O Free" B
1135	6.0	0.06*	0.019	—	—	—
1125	48	0.25	0.015	0.0036	0.0016	0.0134
1125	48	0.25	0.015	0.0058	0.0026	0.012
1100	30	0.18	0.013	0.0043	0.002	0.010
1100	30	0.18	0.012	0.0038	0.0017	0.011
1100	30	0.18	0.011	Al treated		
1100	30	0.18	0.010	Al treated		
1075	72	0.23	0.0095	0.0036	0.0016	0.0081
1075	72	0.25	0.010	0.0053	0.0024	0.0076
1000	85	0.18	0.0044	0.0046	0.0021	0.0023
1000	85	0.18	0.0057	0.0047	0.0021	0.0036
1000	85	0.18	0.0031	Al treated		
1000	85	0.18	0.0032	Al treated		
925	165	0.18	0.0032	0.0044	0.0020	0.0012
925	165	0.18	0.0033	0.0048	0.0022	0.0012
925	165	0.18	0.0036	Al treated		
900	72	0.18	0.0043	0.0046	0.0021	0.0022
900	72	0.18	0.0039	0.0045	0.0020	0.0019
900	72	0.18	0.0020	Al treated		
900	72	0.18	0.0017	Al treated		
870	175	0.18	0.0038	0.0050	0.0022	0.0016
870	175	0.18	0.0038	0.0046	0.0021	0.0017
870	175	0.18	0.0022	Al treated		
800	D	—	0.0022	0.0017	0.0008	0.0014

* Flat specimen, thickness.

nants such as B_2O_3; second, as chemical analysis showed, the case was formed without measurable carbon pickup. Thus the contaminant which had been considered a major cause of error in earlier determinations of Fe-B phase equilibria was eliminated.

Although no detailed study has been made of the gas transfer process, several characteristics of the process were noted. It was found that virtually no boron was transferred to the iron if the treatment was carried out *in vacuo* or in helium. Even in a hydrogen atmosphere, boron transfer was negligible unless the iron was intimately surrounded with boron powder.

The iron-iron boride specimens were annealed *in vacuo* for periods listed in Table I. Calculations based on data of Wells[4] indicate all specimens were annealed for periods sufficient to saturate the iron. The sample shape and size were chosen so that: 1—after boronizing and annealing to saturation a metallographic specimen could be taken for determining the iron boride case depth, 2—the iron boride case could be easily and completely removed, and 3—samples could be prepared for chemical analysis without contamination. After the saturation anneal, a metallographic specimen from the middle of the rod was examined to determine the maximum depth of case. Generally, 0.005 in. more than the maximum case depth was removed by grinding to completely remove the iron boride case. After removing the case, an additional 0.005 in. was turned off on a lathe to remove any metal which may have had embedded Fe_2B particles. A sample of about 100 mg was then carefully turned off for chemical analysis.

Boron analyses were made using the colorimetric (quinalizarin) technique developed by the Youngstown Sheet and Tube Co. and described by Dean and Silkes.[5] However, is was modified to the extent that a photodensitometer was used for measuring densities of the final solution. The densities were measured at a wavelength of 610 millimicrons. Using boron-steel samples obtained from the National Bureau of Standards, the colorimetric method was found to have an accuracy of about 10 pct at concentrations of 0.004 pct B and about 20 pct at concentrations of 0.001 pct B. The results of saturation experiments are shown in Table I and are presented graphically in Fig. 3. The 800°C data were obtained from diffusion data of boron in iron.[6]

To determine whether the calculated annealing times were sufficient to saturate the core of the solid solubility specimens, chemical samples were taken from the outside of the core (after removing the case) and the center from several annealed rods. Analysis of these samples showed the boron content of the center was higher than that of the outside. It was suspected that an impurity such as oxygen which was more concentrated at the center than at the outside was precipitating as a boron compound.

To determine whether oxygen was affecting the boron content of the iron, several solid solubility samples of low oxygen iron were prepared from an aluminum-treated iron. To prepare this alloy, 150 grams of high purity iron was induction-melted *in vacuo* in a recrystallized alumina crucible. When the iron was molten, 5 grams of a Fe-10 pct Al alloy was added. The ingot was homogenized *in vacuo* and finally swaged to 0.180 in. diameter. Analysis of this ingot showed 0.124 pct free aluminum and 0.028 pct Al_2O_3. The boron analyses of the aluminum-treated specimens are included in Table I and

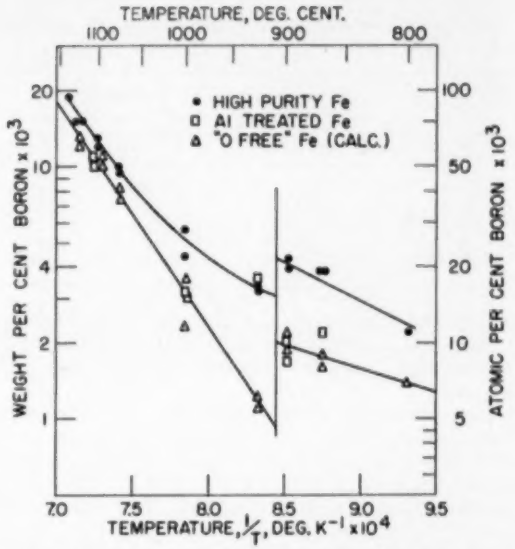

Fig. 3—Logarithm of boron content of saturated iron specimens and corrected boron content plotted as a function of reciprocal temperature.

Fig. 3 and shown graphically in Fig. 4, where the boron content of several alloys is plotted as a function of oxygen content. The uncombined oxygen of the aluminum-treated specimens was assumed to be less than 0.0005 pct. At the left a line has been drawn which has for its slope the combining ratio of oxygen to boron in B_2O_3. This slope equals 2.18 wt pct O/wt pct B. From these data which indicate that oxygen in the iron combines stoichiometrically with boron to form B_2O_3, it was apparent that to obtain the solid solubility of boron in iron, the boron contents of the iron specimens would have to be corrected for the influence of oxygen. The oxygen con-

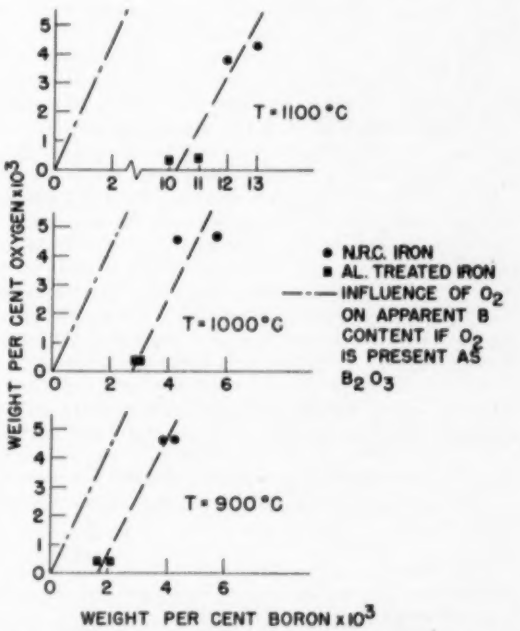
T = 1100 °C
T = 1000 °C
T = 900 °C
WEIGHT PER CENT OXYGEN x 10³
WEIGHT PER CENT BORON x 10³
• NRC. IRON
■ AL. TREATED IRON
INFLUENCE OF O₂ ON APPARENT B CONTENT IF O₂ IS PRESENT AS B₂O₃

Fig. 4—Influence of oxygen content on boron content of saturated iron specimens.

Table II. Temperature of α-γ Transformation of Iron and Iron-Boron Alloy Determined by Thermal Analysis

Specimen	Direction	Temperature, °C	
		T.C. 1	T.C. 2
Fe-B	Heating	913.2	913.5
Fe	Heating	911.7	912.6
Fe (check)	Heating	911.8	912.5
Fe-B	Cooling	910.6	911.0
Fe	Cooling	908.5	909.9
Fe (check)	Cooling	909.0	909.9

tent of the solid solubility specimens was measured by vacuum fusion analysis. These data are shown in Table I as well as the corrected or oxygen-free boron contents.

Determination of the Eutectic and Peritectoid Temperatures: The eutectic temperature was determined by thermal analysis, using a vacuum-melted Fe-3.5 pct B alloy which was remelted *in vacuo* in a recrystallized alumina crucible. The temperature was measured by means of a Pt-Pt-10 pct Rh thermocouple which was protected by an alundum protection tube. The alloy was heated to 1250°C and allowed to cool at about 0.3°C per min. Although the sample was not stirred during cooling, only a slight super-cooling occurred. At 1159°C the temperature remained invariant for 15 min.

The eutectic temperature was also checked metallographically using an Fe-0.6 pct B alloy. The alloy was first cold-worked and homogenized at 1100°C to destroy the eutectic structure of the ingot. Wafers ¼ in. in diameter and ⅛ in. thick were heated at the desired temperature in purified helium for from 10 to 30 min and then slowly cooled. Furnace temperatures were measured with a calibrated Pt-Pt-10 pct Rh thermocouple. At 1160°C no melting was observed. At 1165°C, after 10 min, some melting occurred as indicated by small areas of a eutectic in the microstructure of the sample. The sample heated for 10 min at 1170°C showed a complete eutectic network. Thus the eutectic temperature was considered to be 1165° ± 5°C.

The influence of boron on the A_3 transformation of iron was studied using a differential method of thermal analysis in which the transformation of an Fe-B alloy was compared with the transformation of iron. A sample of decarburized iron ¼ in. in diameter and ⅝ in. long was used as a reference material. The iron was decarburized by treating in wet hydrogen for 24 hr at 850°C followed by a 48 hr treatment in dry hydrogen at the same temperature. A hole 1/10 in. in diameter and 5/16 in. long was drilled on the axis of the sample to accommodate a thermocouple. The Fe-B alloy was made of a similar sample of iron which had been boronized and annealed to saturation at 1125°C, producing an alloy containing about 0.015 pct B. The samples were placed in contact with 26 gage chromel-alumel thermocouples in a cylindrical block of steel 1 in. in diameter and 3½ in. long which had been split in half longitudinally and machined to accommodate the specimens and thermocouples. The block was supported on a tripod so that it would be centered in the 3½ in. diameter quartz furnace tube. The thermal analysis was performed *in vacuo*. Instead of using a three-wire differential thermocouple arrangement, two wires were substituted for the common one so that the couples were electrically separate. Temperature measurements of the two specimens were made simultaneously, using type B Rubicon potentiometers with sensitivities of 2.5 microvolts per min. After making several heating and cooling curves, the specimens were interchanged and the measurements repeated. The heating and cooling rate of about ¼°C per min was controlled using a Wheelco program controller in conjunction with an Exactline.

Table III. Analyses of Arc-Melted Iron-Boron Alloys, Wt Pct

Boron	Oxygen	Corrected Boron
0.021	0.012	0.016
0.025	0.011	0.020
0.029	0.010	0.025
0.035	0.013	0.029

As a check of the method, an additional run was made using two specimens of the decarburized iron. Since iron was used as a reference, the couples were not calibrated. The results are shown in Table II. The temperature variation between successive runs made without changing specimen positions was 0.1°C or less; therefore, data listed are the average of several runs to the nearest 0.1°C. From these data the average temperature difference between Fe-B alloy and the reference iron was:

Heating: 1.2 ± 0.25°C
Cooling: 1.5 ± 0.4°C.

The Fe-B alloy transformed at a higher temperature than the transformation of iron both on heating and cooling.

Determination of the Solidus: The solidus line was determined metallographically at 1185°, 1250°, and 1350°C, using several arc-melted Fe-B alloys. The oxygen content and corrected boron content of these alloys are shown in Table III. The samples were treated at the desired temperature for 30 min in purified helium and quenched into brine. Fig. 5 shows the resulting microstructures of Fe-B alloys containing 0.021, 0.025, 0.029, 0.035 pct B, respectively. Fig. 5a to d shows the structures of alloys quenched from 1350°C and Fig. 5e to h shows the structures of the alloys quenched from 1185°C. In the 0.029 and 0.035 pct B alloys the grain boundary constituent indicates liquid was formed during annealing both at 1185° and 1350°C. On the other hand, the 0.021 pct B alloy shows no evidence of liquid but only a fine discontinuous grain boundary precipitate typical of Fe-B alloys quenched from high temperatures. The microstructures of the 0.025 pct B alloy are intermediate between the structures of 0.021 pct B alloy on one hand and 0.029 and 0.035 pct B on the other. The grain boundary constituent is more continuous than in the 0.021 pct B alloy, however it does not exhibit the characteristic morphology of grain boundary liquids which is evident in the 0.029 and 0.035 pct B alloys. It would therefore appear that the 0.025 pct B alloy must approximate the solidus composition both at 1185° and 1350°C. Microstructures of specimens treated at 1250°C simply served to show that no significant curvature existed in the solidus between 1185° and 1350°C. All of these specimens were etched with picral and nital.

Discussion

In Fig. 3 the logarithm of the boron content is plotted as a function of the reciprocal of the absolute temperature. All of the data presented are in reasonable agreement within the error of the analytical

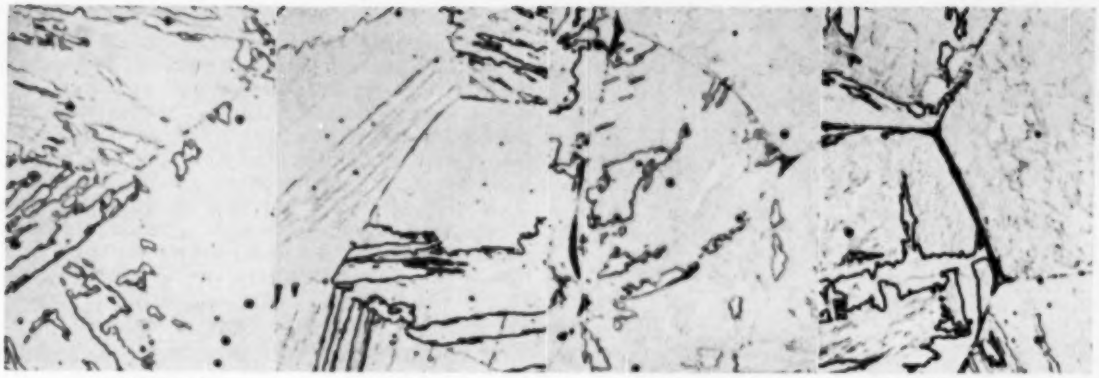

a—0.021 pct B. b—0.025 pct B. c—0.029 pct B. d—0.035 pct B.

a to d—Quenched from 1350°C.

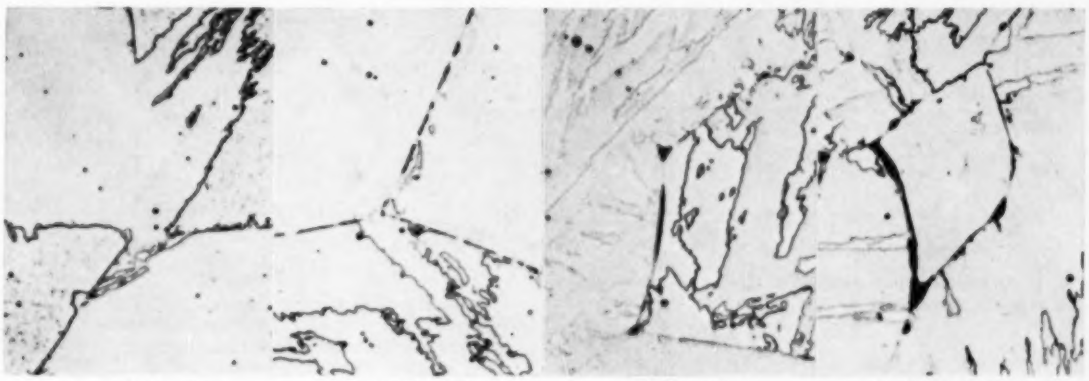

e—0.021 pct B. f—0.025 pct B. g—0.029 pct B. h—0.035 pct B.

e to h—Quenched from 1185°C.

Fig. 5—Microstructures of four Fe-B alloys heated 30 min at the temperatures indicated and quenched in brine. Etched with picral-nital duplex etch. X300.

method except that for an aluminum-treated iron saturated at 925°C. This value which is even greater than that for high purity iron at the same temperature appears to be obviously erroneous. For this reason this value was not used in establishing the location of the oxygen-free solubility line. From the figure it is clear that in γ iron a reasonably linear relation between temperature and composition exists for the oxygen-free solid solubilities, while it does not for the uncorrected ones. This would indicate that the hypothesis regarding the influence of oxygen was correct and that solid solubility of boron in γ follows the behavior of dilute solutions. The maximum solubility of boron in oxygen-free γ iron at the eutectic temperature is 0.021 pct and minimum solubility at the peritectoid temperature is 0.001 pct. In α the maximum solubility which occurs at the peritectoid temperature is 0.002 pct. The solubility of boron in α iron shows a much smaller concentration variation with temperature than in γ iron.

In considering such limited solubilities as those in the Fe-B system, the question arises whether the data represent bulk solubilities or grain boundary concentrations of solute. If the grain boundary concentration of boron is considerably higher than that of the bulk, then it would be expected that the determined concentrations should vary with the ratio of grain boundary area to volume. A measurement of this ratio using the method of Smith and Guttman[7] for all of the alloys treated below the peritectoid temperature showed the variation of this ratio was from 4.9 to 13.5 mm^{-1}. For this variation in surface-to-volume ratio there was no observed change in boron content. However, grain boundary adsorption of considerable magnitude could exist for such surface-to-volume ratios and still have any related variation in boron content obscured by the error of the analytical method. Using 0.0003 pct B as being the minimum variation which could be considered significant and the above surface-to-volume ratios, a simple calculation shows that 10 pct of the boron in the sample would have to be adsorbed at grain boundaries to be detectable. This adsorption is sufficient to form a monolayer of boron at the grain boundary.

The solubility data indicate that a peritectoid relationship exists between α and γ Fe-B solid solutions. From the solubilities which exist at the transformation, the change in the transformation temperature produced by the solid solution of boron may be calculated. Using a modification of the Van't Hoff equation,[8]

$$\Delta T = -\frac{RT^2 \Delta [B]}{\Delta H_T, 100}$$

where ΔT is the change in temperature of transformation; T, the transformation temperature of pure iron; ΔB, the difference between the boron content of γ iron and boron content of α iron in equi-

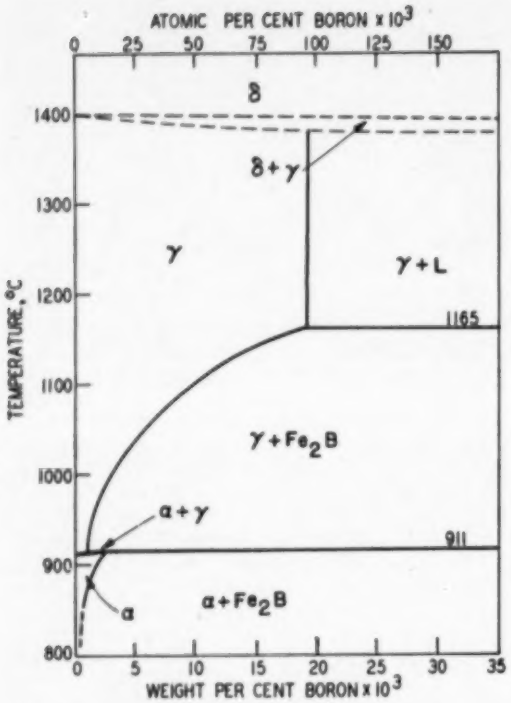

Fig. 6—Fe-B constitution diagram in the low boron range based on this investigation.

librium with it, in atomic percent; and ΔH_{Tr} the heat of transformation of iron. Using the following values, $T = 1183$, $\Delta B = 0.005 \pm 0.0015$, $\Delta H = 212 \pm 30$, the value of $\Delta T = 0.7 \pm 0.3$°C is obtained. Thus the theoretical value of ΔT agrees fairly well with the experimental one, considering the error in both of these values. The fact that in every determination both on heating and cooling (at ¼°C per min) the Fe-B alloy transformed at a temperature above that of the reference iron clearly supports the solid solubility evidence that a peritectoid relation exists between α and γ Fe-B solid solutions. With reference to the temperature of the A_3 of pure iron, 910°C, as determined by Wells et al.,[10] the peritectoid becomes 911.3 ± 0.4°C.

In connection with the location of the solidus line, as in locating the solid solubility line, it was necessary to appraise the influence of oxygen of the liquid-solid equilibrium and what fraction of the total boron was effective as a solute element. In view of the fact that the oxygen content was small in these alloys, it was assumed that it did not affect the equilibrium relations, but that it only reduced that effective boron content of the alloys by combining with boron as B_2O_3. Therefore the position of the solidus was drawn using the calculated oxygen-free boron contents of the 0.025 pct B alloy, i.e., 0.020 pct B. When the solidus was so constructed, the triple point as determined by the intersection of the solidus and the eutectic temperature falls slightly (0.001 pct B) to the left of the triple point determined by the intersection of the solid solubility line and the eutectic temperature.

The phase relations of Fe-B alloys based on this work are shown in Fig. 6.

Acknowledgments

The author appreciates very much the helpful discussions with many members of the Institute for the Study of Metals and wishes to thank those who so willingly cooperated in the preparation and analysis of these alloys. Special thanks are due Mr. Adolph A. Roman who performed the colorimetric analyses, Mr. K. K. Ikeuye who prepared some of the alloys, and Mrs. Betty Nielsen who prepared the micrographs. The work was partially supported by the Aeronautical Research Laboratory, Wright-Patterson Air Force Base, Ohio, under Contract AF 18(600)-12.

References

[1] C. Wells: Private communication.

[2] R. A. Grange and T. M. Garvey: Factors Affecting the Hardenability of Boron-Treated Steels. *Trans.* ASM (1946) **37**, pp. 136-191.

[3] F. Wever and A. Müller: The Binary System, Iron-Boron, etc. *Mitt. Kaiser-Wilhelm Inst. Eisenforsch.* (1929) **11**, pp. 193-223.

[4] P. E. Busby, M. E. Warga, and C. Wells: Diffusion and Solubility of Boron in Iron and Steel. *Trans.* AIME (1953) **197**, pp. 1463-1468; JOURNAL OF METALS (November 1953).

[5] R. S. Dean and B. Silkes: Boron in Iron and Steel. U. S. Bur. Mines *Inf. Cir.* 7363, September 1946.

[6] P. Gordon: Private communication.

[7] C. S. Smith and L. Guttman: Measurement of Internal Boundaries in Three-Dimensional Structures by Random Sectioning. *Trans.* AIME (1953) **197**, pp. 81-87, JOURNAL OF METALS (January 1953).

[8] O. Kubaschewski: The Atomic Heats of Several Metals. *Ztsch. Metallkunde* (1950) **41**, p. 445.

[9] G. N. Lewis and M. Randall: *Thermodynamics* (1923) p. 238, New York. McGraw-Hill Book Co.

[10] C. Wells, R. A. Ackley and R. F. Mehl: A Dilatometric Study of the Alpha-Gamma Transformation in High Purity Iron. *Trans.* ASM (1936) **24**, pp. 46-66.

Technical Note

Crystallographic Angles for Hexagonal Metals

by A. Taylor and Sam Leber

WHEN studies of deformation texture, lattice stress, and crystal orientation are made, it is frequently required to know the interplanar angles and subsequently to embody the results of the investigation in a stereographic projection. Tables of

A. TAYLOR is Head, Structural Physics Section, and S. LEBER, Junior Member AIME, is Senior Research Associate, Horizons Inc., Cleveland.

TN 207E. Manuscript, Nov. 9, 1953.

Table I. Errors in Interplanar Angles in Published Tables

Element	Plane *hkil*	Angle Between (0001) and (*hkil*) Planes: Taylor and Leber	Angle Between (0001) and (*hkil*) Planes: Published	Author
Zr	$20\bar{2}1$	74.76	74.78	McHargue
Zn	$21\bar{3}2$	70.57	70.62	Salkovitz
Cd	$20\bar{2}3$	35.44	36.21	Salkovitz
Zn	$20\bar{2}5$	40.61	41.41	Salkovitz
Ti	$20\bar{2}7$	27.64	25.45	McHargue
Ti	$11\bar{2}8$	21.64	21.60	McHargue
Zr	$10\bar{1}5$	20.15	20.52	McHargue
Mg	$10\bar{1}6$	17.35	17.56	Salkovitz

interplanar angles for hexagonal crystals and standard stereonets have so far been obtained for the special cases of the unalloyed elements. A set of interplanar angles for magnesium, zinc, and cadmium has been compiled by Salkovitz[1] along with a pole figure for zinc. A similar table for titanium and zirconium together with a pole figure for titanium has been published by McHargue,[2] while a pole figure containing only a limited number of poles has been drawn for magnesium.[3]

The extension of orientation and plastic deformation studies to alloys of the hexagonal metals has made it necessary to widen the scope of the existing tables. To a first approximation, interplanar angles within the range given by the existing tables, could have been obtained by graphical interpolation. When this was attempted, it was immediately evident that several of the published angles were in error by significant amounts. These values and the corrected ones are listed in Table I.

Since the interplanar angles, ϕ, are a function only of the axial ratio c/a, it is possible to calculate them from the well-known formula

$$\cos\phi = \frac{Hh + Kk + \frac{1}{2}(Hk + hK) + \frac{3}{4}\left(\frac{a}{c}\right)^2 Ll}{\left\{\left[H^2 + HK + K^2 + \frac{3}{4}\left(\frac{a}{c}\right)^2 L^2\right]\left[h^2 + hk + k^2 + \frac{3}{4}\left(\frac{a}{c}\right)^2 l^2\right]\right\}^{1/2}} \quad [1]$$

where $(HKiL)$ and $(hkil)$ are the indices of the intersecting planes. The most frequently required angle is that between the basal plane (0001) and the general plane $(hkil)$. In this case, the formula reduces to

$$\cos\phi = \frac{\sqrt{\frac{3}{4}}\cdot\left(\frac{a}{c}\right)l}{\left\{h^2 + hk + k^2 + \frac{3}{4}\left(\frac{a}{c}\right)^2 l^2\right\}^{1/2}}. \quad [2]$$

$\bar{1}010$
$3\bar{1}20$
$2\bar{1}10$
$3\bar{2}10$
$1\bar{1}00$
$2\bar{3}10$
$1\bar{2}10$
$1\bar{3}20$
$2\bar{3}11$
$1\bar{3}21$
$2\bar{3}12$
$1\bar{3}22$
$2\bar{3}01$
$1\bar{3}02$
$2\bar{3}03$
$1\bar{3}01$
$2\bar{3}02$
$1\bar{3}00$
$2\bar{3}00$
$1\bar{3}10$
$2\bar{3}01$
$1\bar{3}11$
$2\bar{3}02$
$1\bar{3}12$
$2\bar{3}03$
$1\bar{3}13$
$2\bar{3}04$
$1\bar{3}14$
$2\bar{3}05$
$1\bar{3}15$
$2\bar{3}06$
$1\bar{3}16$
$2\bar{3}07$
$1\bar{3}17$
$2\bar{3}08$
$1\bar{3}18$
$2\bar{3}09$
$1\bar{3}19$
$2\bar{3}10$
$1\bar{3}20$
$2\bar{3}11$
$1\bar{3}21$
$2\bar{3}12$
$1\bar{3}22$
$2\bar{3}13$
$1\bar{3}23$
$2\bar{3}14$
$1\bar{3}24$
$2\bar{3}15$
$1\bar{3}25$
$2\bar{3}16$
$1\bar{3}26$
$2\bar{3}17$
$1\bar{3}27$
$2\bar{3}18$
$1\bar{3}28$
$2\bar{3}19$
$1\bar{3}29$
$2\bar{3}20$
$1\bar{3}30$
$2\bar{3}21$
$1\bar{3}31$
$2\bar{3}22$
$1\bar{3}32$
$2\bar{3}23$
$1\bar{3}33$
$2\bar{3}24$
$1\bar{3}34$
$2\bar{3}25$
$1\bar{3}35$
$2\bar{3}26$
$1\bar{3}36$
$2\bar{3}27$
$1\bar{3}37$
$2\bar{3}28$
$1\bar{3}38$
$2\bar{3}29$
$1\bar{3}39$
$2\bar{3}30$
$1\bar{3}40$
$2\bar{3}31$
$1\bar{3}41$
$2\bar{3}32$
$1\bar{3}42$
$2\bar{3}33$
$1\bar{3}43$
$2\bar{3}34$
$1\bar{3}44$
$2\bar{3}35$
$1\bar{3}45$
$2\bar{3}36$
$1\bar{3}46$
$2\bar{3}37$
$1\bar{3}47$
$2\bar{3}38$
$1\bar{3}48$
$2\bar{3}39$
$1\bar{3}49$
$2\bar{3}40$
$1\bar{3}50$
$2\bar{3}41$
$1\bar{3}51$
$2\bar{3}42$
$1\bar{3}52$
$2\bar{3}43$
$1\bar{3}53$
$2\bar{3}44$
$1\bar{3}54$
$2\bar{3}45$
$1\bar{3}55$
$2\bar{3}46$
$1\bar{3}56$
$2\bar{3}47$
$1\bar{3}57$
$2\bar{3}48$
$1\bar{3}58$
$2\bar{3}49$
$1\bar{3}59$
$2\bar{3}50$
$1\bar{3}60$
$2\bar{3}51$
$1\bar{3}61$
$2\bar{3}52$
$1\bar{3}62$
$2\bar{3}53$
$1\bar{3}63$
$2\bar{3}54$
$1\bar{3}64$
$2\bar{3}55$
$1\bar{3}65$
$2\bar{3}56$
$1\bar{3}66$
$2\bar{3}57$
$1\bar{3}67$
$2\bar{3}58$
$1\bar{3}68$
$2\bar{3}59$
$1\bar{3}69$
$2\bar{3}60$
$1\bar{3}70$
$2\bar{3}61$
$1\bar{3}71$
$2\bar{3}62$
$1\bar{3}72$
$2\bar{3}63$
$1\bar{3}73$
$2\bar{3}64$
$1\bar{3}74$
$2\bar{3}65$
$1\bar{3}75$
$2\bar{3}66$
$1\bar{3}76$
$2\bar{3}67$
$1\bar{3}77$
$2\bar{3}68$
$1\bar{3}78$
$2\bar{3}69$
$1\bar{3}79$
$2\bar{3}70$
$1\bar{3}80$
$2\bar{3}71$
$1\bar{3}81$
$2\bar{3}72$
$1\bar{3}82$
$2\bar{3}73$
$1\bar{3}83$
$2\bar{3}74$
$1\bar{3}84$
$2\bar{3}75$
$1\bar{3}85$
$2\bar{3}76$
$1\bar{3}86$
$2\bar{3}77$
$1\bar{3}87$
$2\bar{3}78$
$1\bar{3}88$
$2\bar{3}79$
$1\bar{3}89$
$2\bar{3}80$
$1\bar{3}90$
$2\bar{3}81$
$1\bar{3}91$
$2\bar{3}82$
$1\bar{3}92$
$2\bar{3}83$
$1\bar{3}93$
$2\bar{3}84$
$1\bar{3}94$
$2\bar{3}85$
$1\bar{3}95$
$2\bar{3}86$
$1\bar{3}96$
$2\bar{3}87$
$1\bar{3}97$
$2\bar{3}88$
$1\bar{3}98$
$2\bar{3}89$
$1\bar{3}99$
$2\bar{3}90$
$1\bar{3}00$
$2\bar{3}91$
$1\bar{3}01$
$2\bar{3}92$
$1\bar{3}02$
$2\bar{3}93$
$1\bar{3}03$
$2\bar{3}94$
$1\bar{3}04$
$2\bar{3}95$
$1\bar{3}05$
$2\bar{3}96$
$1\bar{3}06$
$2\bar{3}97$
$1\bar{3}07$
$2\bar{3}98$
$1\bar{3}08$
$2\bar{3}99$
$1\bar{3}09

Table II. Angles Between Crystallographic Planes for the Hexagonal System

HKiL	*hkil*	*c/a* = 1.500	1.550	1.600	1.650	1.700	1.750	1.800	1.850	1.900	1.950	2.000
0001	$10\bar{1}8$	12.23	12.61	13.00	13.40	13.79	14.18	14.57	14.95	15.34	15.72	16.10
	$10\bar{1}7$	13.90	14.34	14.78	15.23	15.66	16.10	16.54	16.97	17.40	17.83	18.26
	$10\bar{1}6$	16.10	16.61	17.12	17.62	18.12	18.61	19.11	19.60	20.08	20.57	21.05
	$10\bar{1}5$	19.10	19.70	20.28	20.86	21.44	22.00	22.57	23.14	23.69	24.24	24.79
	$10\bar{1}4$	23.41	24.11	24.79	25.47	26.14	26.80	27.46	28.10	28.74	29.38	30.00
	$20\bar{2}7$	26.33	27.08	27.83	28.56	29.29	30.00	30.70	31.40	32.08	32.76	33.42
	$10\bar{1}3$	30.00	30.82	31.63	32.42	33.20	33.96	34.71	35.45	36.18	36.89	37.59
	$20\bar{2}5$	34.72	35.60	36.46	37.31	38.14	38.95	39.74	40.48	41.27	42.01	42.73
	$10\bar{1}2$	40.89	41.82	42.73	43.61	44.46	45.30	46.10	46.89	47.65	48.39	49.11
	$20\bar{2}3$	49.11	50.03	50.93	51.79	52.62	53.41	54.18	54.92	55.64	56.33	57.00
	$10\bar{1}1$	60.00	60.81	61.58	62.31	63.01	63.67	64.31	64.91	65.50	66.05	66.59
	$20\bar{2}1$	73.90	74.39	74.86	75.30	75.71	76.10	76.47	76.83	77.16	77.48	77.78
	$10\bar{1}0$	90.00	90.00	90.00	90.00	90.00	90.00	90.00	90.00	90.00	90.00	90.00
	$21\bar{3}2$	66.42	67.10	67.75	68.36	68.94	69.49	70.01	70.51	70.99	71.44	71.88
	$21\bar{3}1$	77.69	78.08	78.44	78.78	79.10	79.41	79.69	79.97	80.22	80.47	80.70
	$21\bar{3}0$	90.00	90.00	90.00	90.00	90.00	90.00	90.00	90.00	90.00	90.00	90.00
	$11\bar{2}8$	20.56	21.18	21.80	22.42	23.02	23.63	24.23	24.82	25.41	25.99	26.56
	$11\bar{2}6$	26.56	27.32	28.07	28.81	29.54	30.26	30.96	31.66	32.35	33.02	33.69
	$11\bar{2}4$	36.87	37.78	38.66	39.52	40.36	41.19	41.99	42.77	43.53	44.28	45.00
	$11\bar{2}2$	56.31	57.17	58.00	58.78	59.53	60.26	60.94	61.61	62.24	62.85	63.44
	$11\bar{2}0$	90.00	90.00	90.00	90.00	90.00	90.00	90.00	90.00	90.00	90.00	90.00
$10\bar{1}0$	$21\bar{3}0$	19.11	19.11	19.11	19.11	19.11	19.11	19.11	19.11	19.11	19.11	19.11
	$11\bar{2}0$	30.00	30.00	30.00	30.00	30.00	30.00	30.00	30.00	30.00	30.00	30.00
	$01\bar{1}0$	60.00	60.00	60.00	60.00	60.00	60.00	60.00	60.00	60.00	60.00	60.00

A further computational simplification may be made by working in angles of 2ϕ. Since $\cos 2\phi = 2\cos^2\phi - 1$, then

$$\cos 2\phi = \left[\frac{2}{1 + \frac{4}{3}\left(\frac{c}{a}\right)^2 \frac{h^2 + hk + k^2}{l^2}}\right] - 1. \quad [3]$$

The more important interplanar angles have been computed by means of Eq. 3 for axial ratios ranging from 1.500 to 2.000 at c/a intervals of 0.050 and are given in Table II. All the angles were computed by means of Peters' tables[4] to 0.001 of a degree and rounded off to the second decimal place, this being considered more than ample for most goniometric work. The angles are also presented in decimal notation since the modern trend is away from the system using minutes and seconds to represent fractions of a degree.

Table III. Angles Between Crystallographic Planes for Hexagonal Elements

		Be	Ti	Zr	Mg	Zn	Cd
HKiL	*hkil*	*c/a* = 1.5847	1.5873	1.5893	1.6235	1.8563	1.8859
0001	$10\bar{1}8$	12.88	12.90	12.92	13.19	15.00	15.23
	$10\bar{1}7$	14.65	14.67	14.69	14.99	17.03	17.28
	$10\bar{1}6$	16.96	16.99	17.01	17.35	19.66	19.95
	$10\bar{1}5$	20.10	20.13	20.15	20.55	23.21	23.53
	$10\bar{1}4$	24.58	24.62	24.65	25.11	28.19	28.56
	$20\bar{2}7$	27.60	27.64	27.67	28.17	31.48	31.89
	$10\bar{1}3$	31.38	31.42	31.45	32.00	35.55	35.98
	$20\bar{2}5$	36.20	36.25	36.29	36.87	40.61	41.06
	$10\bar{1}2$	42.46	42.50	42.54	43.15	46.98	47.43
	$20\bar{2}3$	50.66	50.70	50.74	51.31	55.02	55.44
	$10\bar{1}1$	61.34	61.38	61.41	61.92	64.99	65.33
	$20\bar{2}1$	74.72	74.74	74.76	75.07	76.87	77.07
	$10\bar{1}0$	90.90	90.00	90.00	90.00	90.00	90.00
	$21\bar{3}2$	67.55	67.59	67.61	68.04	70.57	70.86
	$21\bar{3}1$	78.33	78.35	78.36	78.60	80.00	80.15
	$21\bar{3}0$	90.00	90.00	90.00	90.00	90.00	90.00
	$11\bar{2}8$	21.61	21.64	21.71	22.09	24.89	25.24
	$11\bar{2}6$	27.85	27.88	27.91	28.42	31.75	32.16
	$11\bar{2}4$	38.39	38.44	38.47	39.07	42.87	43.32
	$11\bar{2}2$	57.75	57.79	57.82	58.37	61.69	62.07
	$11\bar{2}0$	90.00	90.00	90.00	90.00	90.00	90.00
$10\bar{1}0$	$21\bar{3}0$	19.11	19.11	19.11	19.11	19.11	19.11
	$11\bar{2}0$	30.00	30.00	30.00	30.00	30.00	30.00
	$01\bar{1}0$	60.00	60.00	60.00	60.00	60.00	60.00

Table III gives interplanar angles calculated for the hexagonal elements using the most recently available data for the axial ratios. They were cross-checked by plotting curves relating interplanar angle with (c/a), using values listed in Table II, and interpolating. Finally, a new pole figure for magnesium is presented in Fig. 1 which is much more complete than the one originally given by Schmidt and Boas. Its principal value lies in the fact that it corresponds very closely to the pole figure for a hexagonal close-packed structure consisting of theoretically perfectly spherical atoms and with an axial ratio of 1.633.

Table II may be used to interpolate interplanar angles for hexagonal crystals with a high degree of accuracy for intermediate values of c/a. A similar set of tables could have been constructed to cover tetragonal crystals.

Acknowledgment

The authors wish to thank Horizons Incorporated for their kind permission to publish this note, and Dr. Eugene Wainer, Director of Research, for his very helpful interest.

References

[1] E. I. Salkovitz: *Trans.* AIME (1951) **191**, p. 64; JOURNAL OF METALS (January 1951).

[2] C. J. McHargue: *Trans.* AIME (1952) **194**, p. 660; JOURNAL OF METALS (June 1952).

[3] E. Schmidt and W. Boas: *Plasticity of Crystals* (English translation of *Kristallplastizität*). (1950) London. F. A. Hughes and Co.

[4] J. Peters: *Seven Place Values of Trigonometric Functions for Every Thousandth of a Degree.* (1942) New York. D. Van Nostrand Co.

Influence of Oxygen, Nitrogen, and Carbon on The Phase Relationships of the Ti-Al System

by R. J. Van Thyne and H. D. Kessler

Phase diagrams of the titanium-rich portion of the ternary systems from 0 to 10 wt pct Al and 0 to 1 wt pct O, N, and C were determined. Micrographic analysis of annealed high purity arc melted alloys was the principal method of investigation and was supplemented by X-ray diffraction.

TITANIUM-ALUMINUM alloys exhibit excellent properties, particularly for elevated temperature use. For this reason, the Materials Laboratory, Wright Air Development Center, sponsored an investigation of the effect of the interstitially soluble contaminants, oxygen, nitrogen, and carbon, on the Ti-Al system. Using high purity arc melted alloys and micrographic analysis of annealed samples as the chief method of investigation, titanium-rich partial phase diagrams were determined for the ternary systems.

Experimental Procedure

Materials: The titanium used in the preparation of the alloys was iodide crystal bar (99.9+ pct pure) produced by the New Jersey Zinc Co. and Foote Mineral Co.

The aluminum was obtained from the Aluminum Co. of America in the form of sheet. The given analysis was: Si, 0.0006 pct; Fe, 0.0005; Cu, 0.0022; Mg, 0.0003; Ca, <0.0006; Na, <0.0005; and Al, 99.99.

High purity titanium dioxide purchased from the National Lead Co. was used in the preparation of the oxygen-bearing alloys. The spectrographic analysis of this material was as follows: SiO_2, 0.07 pct; Fe_2O_3, 0.002; Al_2O_3, <0.001; Sb_2O_3, <0.002; SnO_2, <0.001; Mg, <0.001; Cb, <0.01; Cu, 0.0004; Pb, 0.002; Mn, <0.00005; W, <0.01; V, <0.002; Cr, <0.002; Ni, <0.001; and Mo, <0.002.

Special spectroscopic graphite rod purchased from the National Carbon Co. was used in the preparation of the Ti-Al-C alloys.

Alloy Preparation: Alloy ingots weighing 10 grams were melted in a nonconsumable tungsten electrode arc melting furnace using water-cooled copper hearths and a helium atmosphere. The arc was struck on a tungsten stud in the copper block to minimize contamination from the electrode. Details of the techniques have been reported.[1, 2] Each ingot was inverted and remelted a minimum of four times to insure homogeneity, without opening the furnace. Remelting small control ingots of iodide titanium under similar conditions resulted in no measurable hardness increase, indicating contamination-free melting conditions were used.

The alloy charges and resultant ingots were weighed to the nearest milligram. Only small weight losses were obtained upon melting, indicating that the actual compositions were very close to the nominal compositions. Check analyses substantiated this.

Oxygen and nitrogen were added during ingot preparation as master alloys. An oxygen master alloy containing 25 wt pct O was prepared by melting iodide titanium and pressed titanium dioxide (40 pct O) powder. The Ti-25 pct O alloy is more easily handled during weighing and charging than the pressed TiO_2 powder. Chemical analysis indicated that titanium-nitride received from an outside source contained large amounts of impurities (2.7 pct Ca). Therefore, a master alloy containing approximately 12 pct N was prepared by melting nitrided sponge titanium. As the sponge melted with difficulty, the alloy was diluted by addition of titanium to lower the melting point. The chemical analysis of the final alloy was 6.69 pct N. Both master alloys are friable and were used as −8 +16 mesh lumps resulting from crushing the ingots. Melting the Ti-Al-O and Ti-Al-N compositions five times produced homogeneous ingots.

The preparation of homogeneous carbon-bearing alloys caused considerable difficulty. Alloys containing less than 1 pct C were prepared using spectrographic graphite rod, ⅛ in. diameter by ⅛ in. long. However, the graphite did not dissolve even with long melting times and many remelts. The ⅛ in. pieces of graphite were used rather than powder because the low density powder is troublesome in arc melting.

R. J. VAN THYNE is Associate Metallurgist and H. D. KESSLER, Junior Member AIME, is Supervisor of Nonferrous Metallurgy Research Section, Armour Research Foundation of Illinois Institute of Technology, Chicago.

Discussion on this paper, TP 3715E, may be sent, 2 copies, to AIME by April 1, 1954. Manuscript, Sept. 14, 1953. New York Meeting, February 1954.

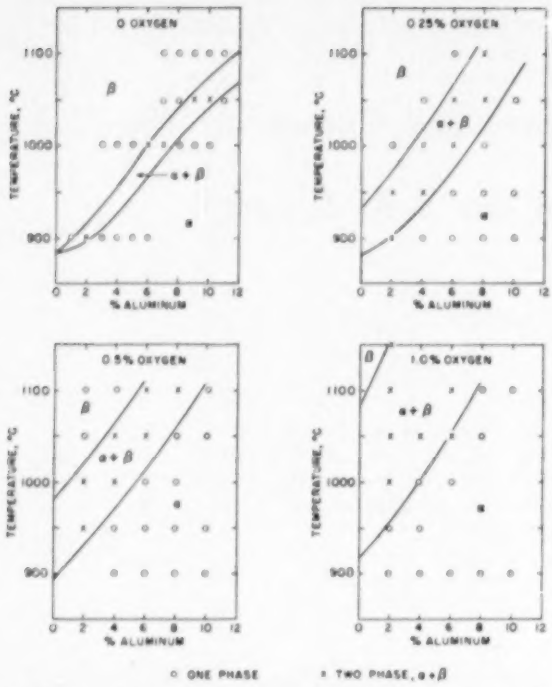

Fig. 1—Vertical sections at constant oxygen content of the partial Ti-Al-O system.

Efforts were then turned to producing a good master alloy. When a tungsten-tipped electrode was used, tungsten contamination would result from the high current and long melting times required; therefore, a carbon tip was employed. The amount of carbon pick-up from the tip during melting was rather erratic. Homogeneous ingots containing a few percent carbon were difficult to melt and were not frangible. A 13 pct alloy had a very high melting point; consequently, this composition was discarded. As a 30 pct master alloy was melted more easily than those of lower composition and was friable, this composition was used. Often the master alloy consisted of an inner core of compound surrounded by a case of apparently lower melting alloy. This difficulty was circumvented by crushing the ingot to powder and remelting.

Ti-Al-C ingots were prepared using pieces of the 30 pct alloy (chemical analysis, 30.0 pct C) approximately ⅛ in. in size and melting five times. It was found necessary to keep the ingots molten for longer times than are usually employed. A tungsten-tipped electrode was employed as the melting currents and times were not excessive.

Annealing Treatments: As-cast samples were annealed in quartz (above 1100°C) or Vycor bulbs. At lower temperatures, the bulbs were sealed under high vacuum but above 1000°C a partial pressure of argon was used to prevent their collapse. Table I gives information on the annealing times used for various temperatures. The specimens that were heat treated at 750° and 600°C were first annealed

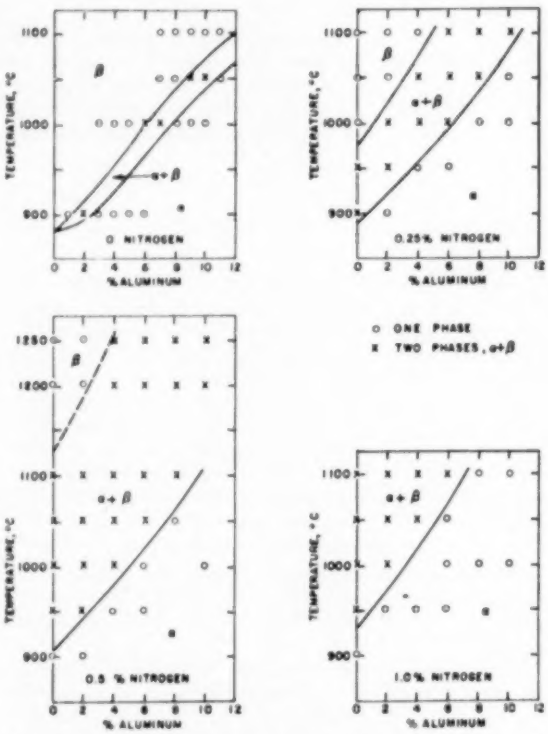

Fig. 2—Vertical sections at constant nitrogen content of the partial Ti-Al-N system.

Fig. 3—2 pct Al-0.25 pct N alloy water quenched after annealing at 1000°C for 24 hr. Transformed β. Etchant: HNO_3-HF-glycerine. X200.

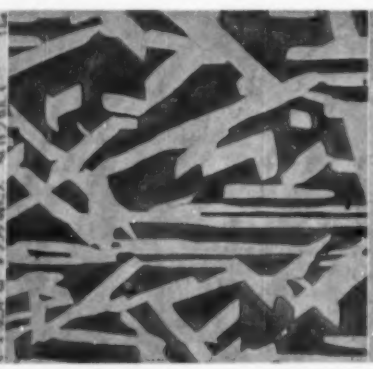

Fig. 4—6 pct Al-0.25 pct N alloy treated the same as the sample of Fig. 3. $\alpha + \beta$. Etchant: HNO_3-HF-glycerine. X200.

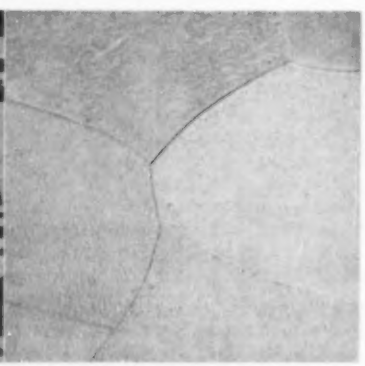

Fig. 5—10 pct Al-0.25 pct N alloy treated the same as the sample of Fig. 3. Large grained isothermal α. Etchant: HNO_3-HF-glycerine. X200.

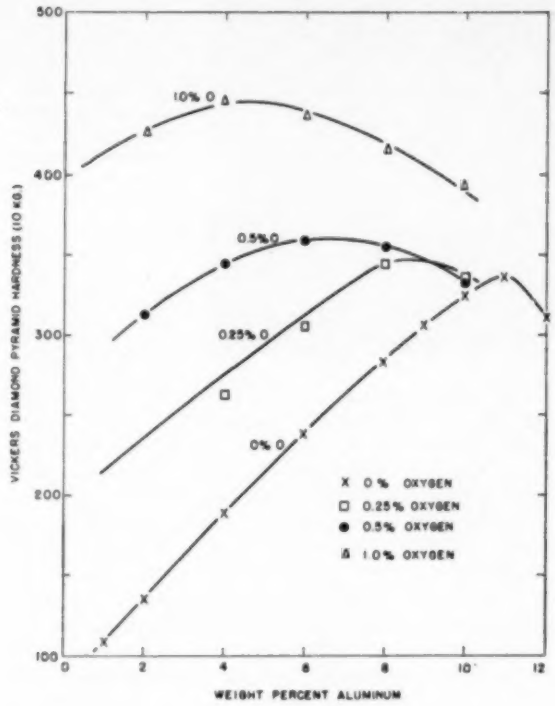

Fig. 6—Average Vickers hardness of Ti-Al-O alloys annealed in the α phase space at temperatures between 700° and 1100°C.

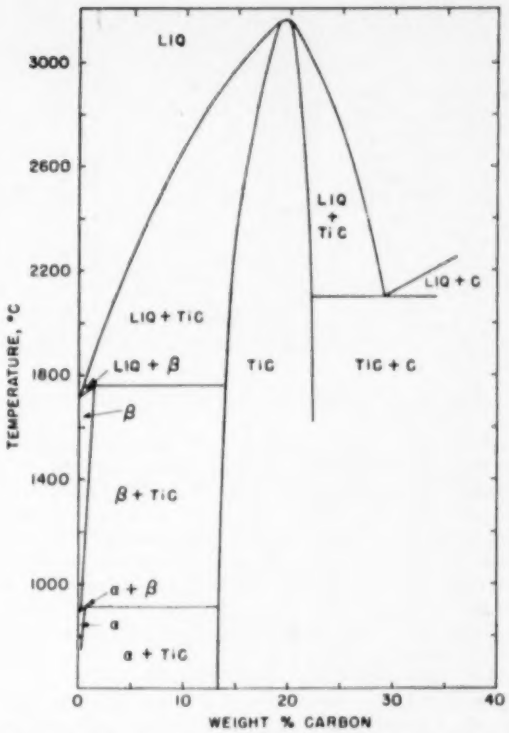

Fig. 8—Probable type of phase diagram for the partial system Ti-C.

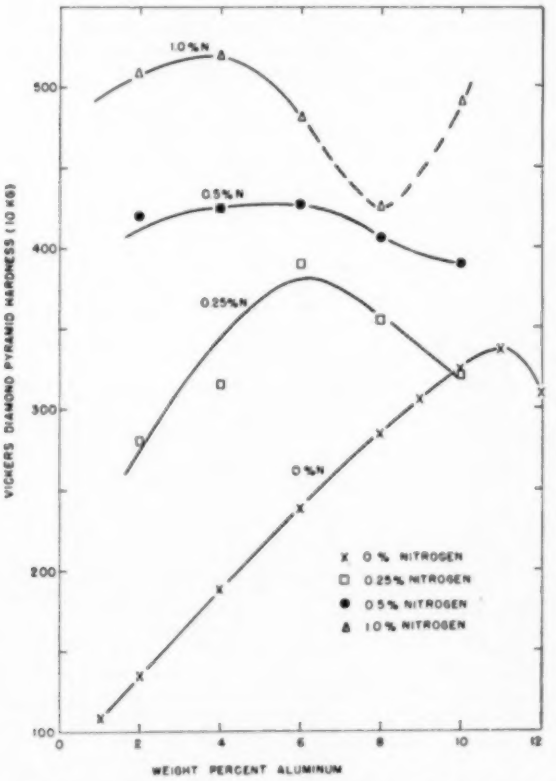

Fig. 7—Average Vickers hardness of Ti-Al-N alloys annealed in the α phase space at temperatures between 700° and 1100°C.

at 950°C for 48 hr and then furnace cooled to the temperature of final annealing. The furnace temperature control was ± 3°C below 1100°C, and about ±10°C for high temperatures.

Discussion of Results

Systems Ti-Al-O and Ti-Al-N

Phase Diagrams: Figs. 1 and 2 illustrate partial vertical sections through the Ti-Al-O and Ti-Al-N space models, respectively. The phase diagrams were constructed placing emphasis on the binary intercepts of the previously determined Ti-Al[3] and Ti-O[4] systems. As can be seen, both oxygen and nitrogen raise the $\beta/\alpha + \beta$ space boundary and widen the $\alpha + \beta$ field of the Ti-Al system. Nitrogen raises the $\beta/\alpha + \beta$ boundary appreciably more than oxygen. No attempt was made to locate the $\beta/\alpha + \beta$ boundary for alloys containing 1 wt pct N.

Microstructures of Ti-Al-N alloys containing 0.25 pct N are presented in Figs. 3 to 5, which depict the β, $\alpha + \beta$, and α fields, respectively. The β phase is not retained upon water quenching the Ti-Al-O or Ti-Al-N alloys but transforms to a serrated or acicular α' structure. The addition of the interstitially

Table I. Annealing Data

Temperature, °C	Time, Hr	Temperature, °C	Time, Hr
1250	6	950	48
1200	8	900	72
1150	16	850	118
1100	18	750	240
1050	24-30	609	576
1000	36-40		

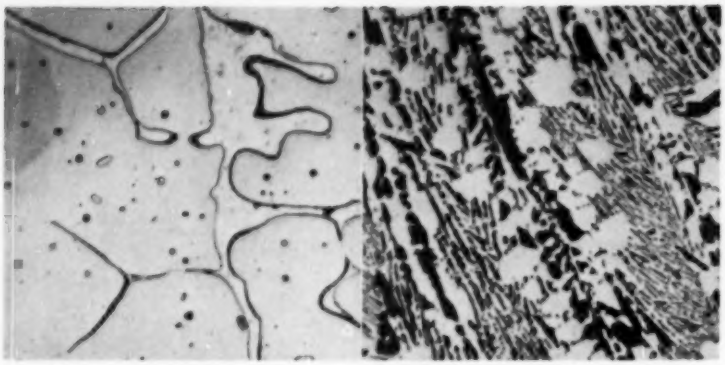

Fig. 9—13 pct C alloy arc melted and chill cast. TiC plus transformed β at the grain boundaries. Etchant: HNO_3-HF-glycerine. X250.

Fig. 10—30 pct C alloy arc melted and chill cast. Eutectic structure. Unetched. X250.

soluble elements appears to refine the transformation structure.

Hardness: Vickers hardness data obtained for Ti-Al-O and Ti-Al-N alloys, annealed in the α field, are presented graphically in Figs. 6 and 7, respectively. Considerable difficulty was encountered in obtaining reproducible values. Large differences in average values were produced by successively grinding out the old impressions and making new ones. For example, a series of values obtained by the latter method on a Ti-8 pct Al-1 pct O sample annealed at 900°C were 394, 435, 470, and 496 DPH. The reasons behind these hardness variations are not known but upon averaging the values for several temperature levels, correlatable data were obtained as illustrated in Figs. 6 and 7.

The results show that for a given aluminum level, the hardness generally increases with increasing oxygen and nitrogen content; nitrogen has the greater hardening effect. Although not conclusive, previously determined data of the Ti-Al system indicated a peak hardness at about 11 pct Al for alloys annealed in the α field.[3] The average hardness data of Ti-Al alloys annealed at 700° and 800°C are reproduced in the figures for comparison.

A hardness peak is apparent for all the curves in Figs. 6 and 7. The composition of maximum hardness moves to lower aluminum contents with increasing amounts of the interstitial elements. The greatest effect was found with 1 pct N; the maximum hardness of over 500 Vickers occurs at about 3 to 4 pct Al. A minimum in the curve for 1 pct N has been shown as a dashed line because only a few data points are available at these compositions and only this one curve exhibits the minimum. The curve may very likely be correct as it is expected that with increasing aluminum content the hardness curve for ternary alloys has a minimum similar to that obtained for the Ti-Al alloys. Data for the latter alloys indicate a minimum hardness at 16 pct Al. As the α field of the Ti-Al system extends to 25 pct Al at the temperature involved, and no phase changes are known to occur at lower temperatures, the reason for the indicated hardness minimum in the binary or ternary alloys is not known.

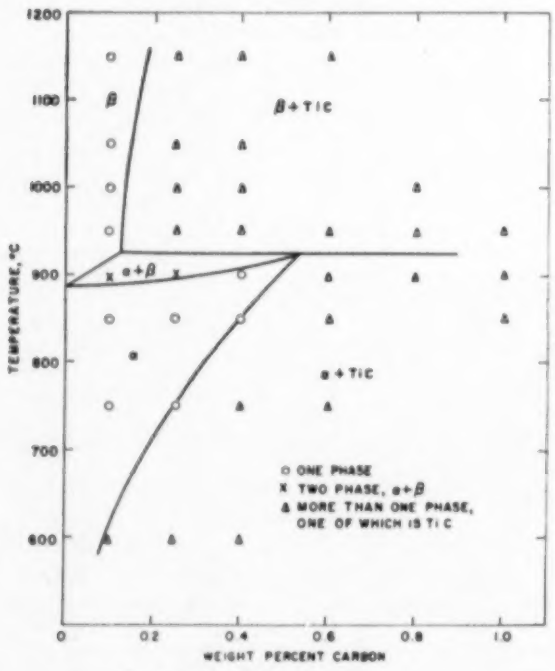

Fig. 11—Partial Ti-C phase diagram.

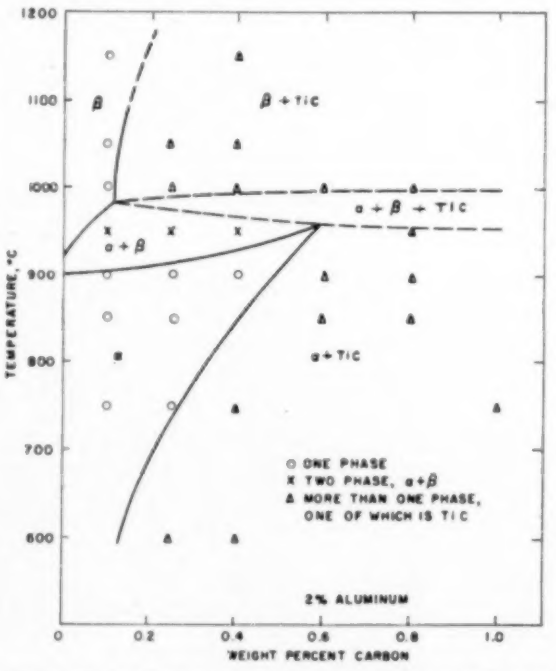

Fig. 12—Vertical section at 2 pct Al content of the partial Ti-Al-C system.

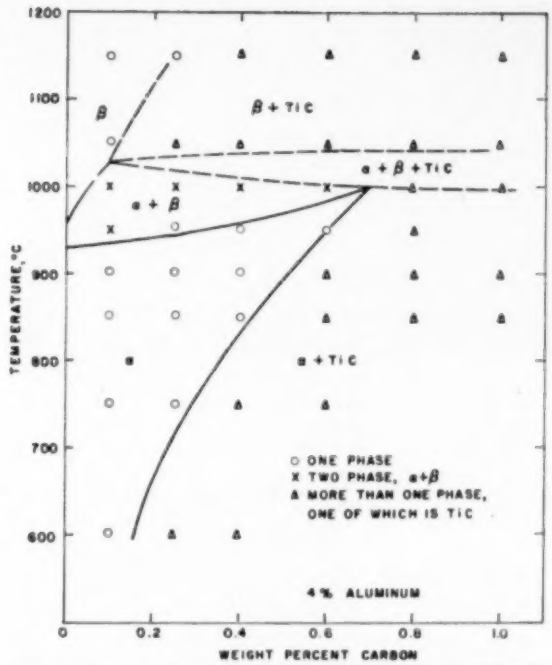

Fig. 13—Vertical section at 4 pct Al content of the partial Ti-Al-C system.

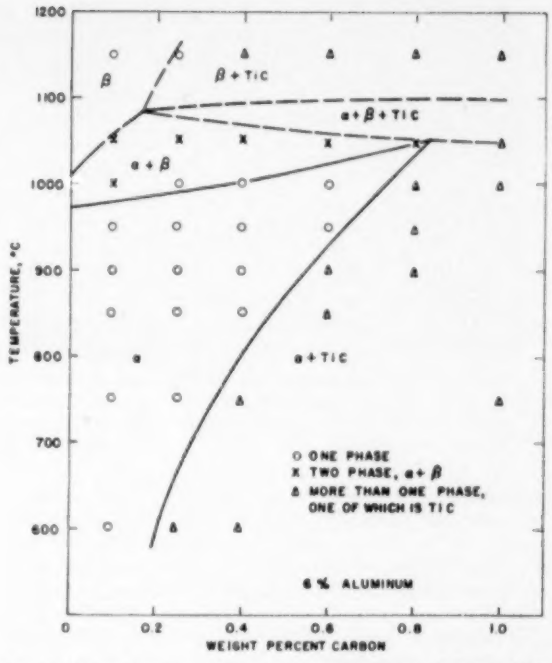

Fig. 14—Vertical section at 6 pct Al content of the partial Ti-Al-C system.

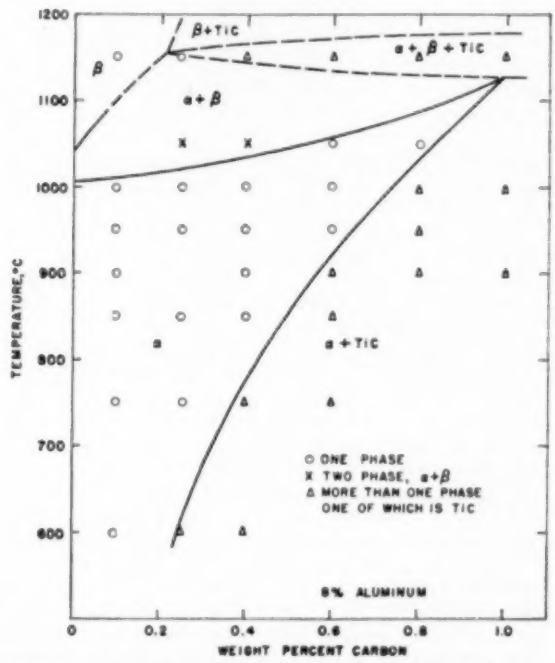

Fig. 15—Vertical section at 8 pct Al content of the partial Ti-Al-C system.

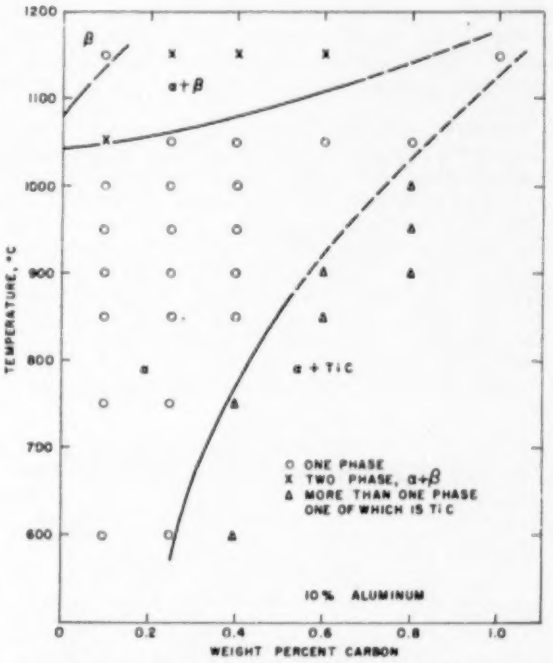

Fig. 16—Vertical section at 10 pct Al content of the partial Ti-Al-C system.

System Ti-Al-C

Ti-C Diagram: Data obtained from as-cast microstructures of the various master alloys containing up to 30 pct C permitted an outline of the Ti-C system to be constructed. The probable diagram is presented in Fig. 8.

Extremely high melting alloys in the compound region indicated an open maximum for TiC. Fig. 9 illustrates the duplex β + TiC microstructure of a 13 pct C alloy. A nominal 15 pct C master alloy was entirely TiC. Therefore, the lower limit of the TiC phase field is near 15 pct C. The compound appears to exist over a range of compositions; the lower limit of TiC lies close to 15 pct C and the stoichiometric composition is 20 pct.

The eutectic shown in Fig. 8 was based on the

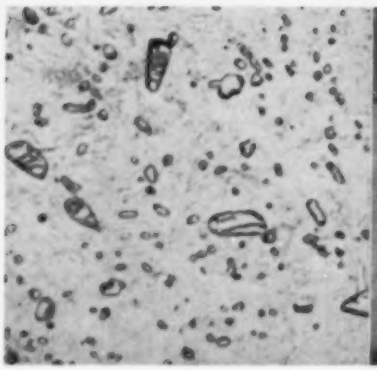

Fig. 17—0.6 pct C alloy annealed at 950°C for 48 hr and water quenched. TiC in a matrix of transformed β. Etchant: HNO_3-HF-glycerine. X200.

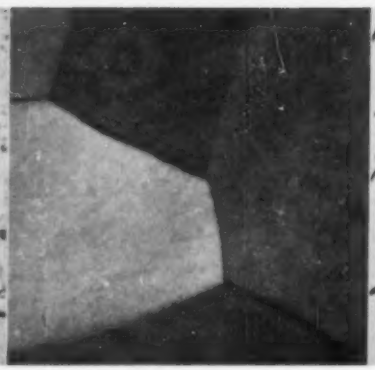

Fig. 18—4 pct Al-0.6 pct C alloy annealed at 950°C and water quenched. Large equiaxed grains of α. Etchant: HNO_3-HF-glycerine. Polarized light. X200.

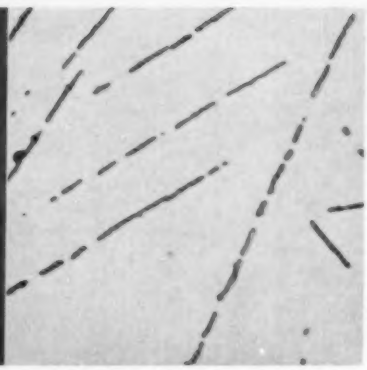

Fig. 19—8 pct Al-0.8 pct C alloy water quenched after annealing at 900°C for 72 hr. α + TiC. Etchant: HNO_3-HF-glycerine. X750.

structural appearance of a 30 pct alloy, Fig. 10. This sample also seemed to melt at a lower temperature than the 15 pct C alloy. Collaborative X-ray diffraction studies of this eutectic alloy indicated only TiC; therefore, the other phase is apparently graphite. The fact that black material can be rubbed off the alloys of high carbon content corroborates the presence of graphite.

As part of the Ti-Al-C investigation, the Ti-C diagram to 1 pct C was studied and the results are presented in Fig. 11. The diagram agrees closely with previous investigations.[5, 6] A more detailed study of the binary system indicates that the peritectoid reaction occurs at 920°C ± 3°C and that the probable diagram presented in Fig. 8 is correct to 20 pct C.[6]

Ti-Al-C Diagram: The Ti-Al-C diagram is presented by a series of vertical sections through the space model at constant aluminum contents. Although isotherms were constructed for each of the eight annealing temperatures, no isothermal sections are given as the equilibria involved are best illustrated by the vertical sections. The phase boundaries were not drawn based on data of any one vertical cut alone. Graphical interpolation, using all of the vertical and isothermal sections, was used to obtain the phase boundaries.

Emphasis was placed on the binary intercepts of

Table II. X-Ray Diffraction Data for a Ti-10 Pct Al-1 Pct C Alloy*

hkl	Intensity Observed†	d (Observed), kX	d (Calculated),‡ kX
400	ft	2.789	2.800
331	ft	2.569	2.569
421	wm	2.457	2.444
332	ft	2.394	2.388
511	vvft	2.147	2.155
520	ft	2.075	2.080
531	ft	1.892	1.893
610	vft	1.845	1.841
444	ft	1.614	1.616
800	vvft	1.399	1.400
733	vw	1.367	1.368
821	ft	1.351	1.348
662	vvft	1.286	1.285
840	vvft	1.249	1.252
664	vvft	1.196	1.194
852	ft	1.165	1.161

* Alloy annealed at 750°C for 240 hr and water quenched. Indexed on a cubic lattice, a = 11.20 kX.
† m, medium; wm, weak medium; w, weak; vw, very weak; ft, faint; vft, very faint; vvft, very very faint.
‡ Calculated from a = 11.20 kX.

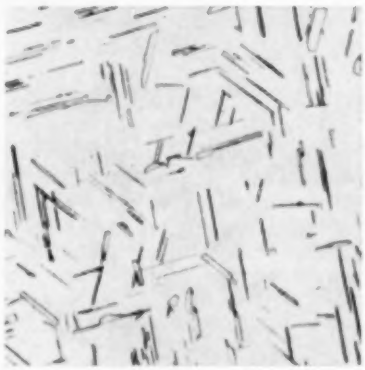

Fig. 20—10 pct Al-0.8 pct C alloy treated the same as the sample of Fig. 19. α + unidentified phase and probably TiC. Etchant: HNO_3-HF-glycerine. X750.

the Ti-Al system and the phase boundaries of the drawings agree with the Ti-Al diagram previously published.[6] Principle features of the Ti-Al diagram include extensive solubility of aluminum in both α and β and a peritectoid reaction, β (29 pct Al) + TiAl (35 pct Al) $\rightleftharpoons$ α (31 pct Al) at 1240°C. The phase relationships were drawn assuming that there is little solubility of aluminum in TiC.

An outstanding feature of the vertical sections presented in Figs. 11 to 16 is the increase in the extent of the α field to higher temperatures and higher carbon compositions with greater aluminum contents. Whereas the maximum solubility of carbon in α is near 0.5 pct in the binary system, it is increased to over 1 pct with 10 pct Al in the alloy.

It can be seen in the succeeding diagrams (Figs. 12 to 16) that in the ternary system the peritectoid reaction, β + TiC $\rightleftharpoons$ α, occurs over a range of temperatures and moves to higher temperatures with greater aluminum contents. The effect of aluminum on increasing the solubility of carbon in α and raising the temperature of the peritectoid reaction is illustrated by Figs. 17 and 18. Both alloys were annealed at 950°C; they were located in the β + TiC and α spaces, respectively. Boundaries of the α + β + TiC space have been shown as dashed lines as it is difficult to differentiate between α and α' in the microstructures containing large amounts of TiC. X-ray diffraction was not useful for this determination as the β phase transforms to α' upon water quenching.

Certain identification of the indicated α + TiC microstructures could be made for alloys with alu-

minum contents of 0 to 8 pct for all carbon compositions (0 to 1 pct). TiC was also definitely observed in the Ti-10 pct Al-0.4 pct C sample. However, microstructures unlike those for the other alloys were observed for the following: Ti-10 pct Al-0.6 pct C, Ti-10 pct Al-0.8 pct C, and Ti-10 pct Al-1.0 pct C.

Micrographs of Ti-8 pct Al-0.8 pct C and Ti-10 pct Al-0.8 pct C alloys, annealed at 900°C for 72 hr and water quenched, are presented in Figs. 19 and 20, respectively. The former consists of α + TiC and the latter is apparently α plus a different phase and probably TiC. An X-ray diffraction pattern was obtained for a Ti-10 pct Al-1.0 pct C alloy annealed at 750°C for 10 days and was identified as α plus a new phase. The lines of the new phase (Table II) could not be indexed as TiC, TiAl, or $TiAl_3$ but were indexed as belonging to a cubic structure. As seen in Table II, close correlation was obtained between the experimental and calculated lattice parameter values; therefore, the phase apparently has a cubic structure with a = 11.20 kX. Using X-ray diffraction, the new phase was not observed in the Ti-1.0 pct C or Ti-8 pct Al-1 pct C samples.

Because of the uncertain identification of the Ti-10 pct Al-(0.6, 0.8, 1.0) pct C alloys, the α/α + TiC boundary in Fig. 16 has been dashed above 0.5 pct C. A reaction could occur that would bring a new phase into equilibrium in the section illustrated by Fig. 16. A series of ternary phases having the compositions Ti_4X_2O and Ti_5X_2O has been studied.[7] It is possible that a similar ternary intermediate phase is formed in the Ti-Al-C system.

Hardness: Vickers hardness data were obtained for the Ti-Al-C alloys used for the phase diagram study. At any given aluminum content, the most pronounced hardening occurs when the carbon is taken into solution in α titanium. Increasing amounts of carbon beyond the solubility limit result in a relatively small increase in hardness.

Fig. 21 illustrates the effect of increasing aluminum and carbon content on the hardness of α alloys. The data represent average hardness values obtained for one or more heat treatments in the α field. The curve for 8 pct Al lies above that for 10 pct; however, this is within experimental accuracy. Above 0.6 pct C, the data indicate a hardness peak or plateau; however, the curves have been shown as dashed lines as only a few data points are available at these higher alloy contents.

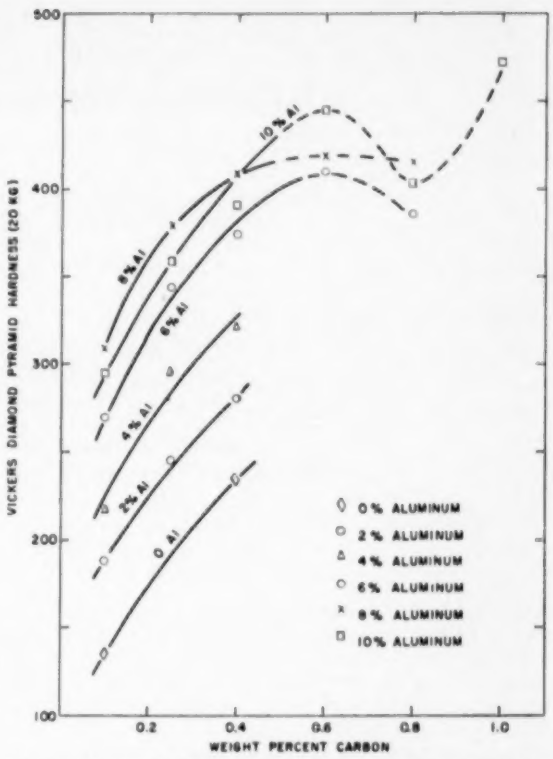

Fig. 21—Average Vickers hardness of Ti-Al-C alloys annealed in the α phase space at temperatures between 600° and 1150°C.

Summary of Results

Ti-Al-(O and N) Systems: Both oxygen and nitrogen raise the $\beta/\alpha + \beta$ space boundary and widen the $\alpha + \beta$ field of the Ti-Al system. The β phase transforms to α' upon water quenching. The hardness of ternary alloys is increased by the addition of oxygen or nitrogen. A hardness peak, which was found to occur at about 11 pct Al in the Ti-Al system, moves to lower aluminum contents and higher hardnesses with increasing amounts of oxygen or nitrogen for alloys annealed in the α space.

Ti-Al-C System: A probable Ti-C diagram to 30 pct C is presented. The lower composition limit of a very high melting compound, TiC, occurs near 15 pct C. A eutectic between TiC and carbon exists at about 30 pct C.

Vertical sections of the Ti-Al-C system illustrate the solubility of carbon in α increases with greater aluminum contents. The solubility is increased to over 1 pct C at 10 pct Al. The peritectoid reaction of the Ti-C system occurs at successively higher temperatures in the ternary system. An unidentified phase was observed in samples of high alloy content. For a given aluminum content, the hardness of α titanium increases with greater carbon contents.

Acknowledgments

The authors are grateful to the Materials Laboratory, Wright Air Development Center, who sponsored the work under Contract AF 33(038)-8708 for permission to publish this paper. Thanks are due to W. Rostoker for the X-ray diffraction data and C. A. Johnson who was responsible for the metallographic work.

References

[1] M. Hansen, H. D. Kessler, and D. J. McPherson: The System Titanium-Silicon. *Trans.* ASM (1952) **44**, p. 518.

[2] M. Hansen, E. L. Kamen, H. D. Kessler, and D. J. McPherson: The Systems Titanium-Molybdenum and Titanium-Columbium. *Trans.* AIME (1951) **191**, p. 881; JOURNAL OF METALS (October (1951).

[3] E. S. Bumps, H. D. Kessler, and M. Hansen: Titanium-Aluminum System. *Trans.* AIME (1952) **194**, p. 609; JOURNAL OF METALS (June 1952).

[4] E. S. Bumps, H. D. Kessler, and M. Hansen: The Titanium-Oxygen System. *Trans.* ASM (1953) **45**, p. 1008.

[5] R. I. Jaffee, H. R. Ogden, and D. J. Maykuth: Alloys of Titanium with Carbon, Oxygen, and Nitrogen. *Trans.* AIME (1950) **188**, p. 1261; JOURNAL OF METALS (August 1950).

[6] I. Cadoff and J. P. Nielsen: Titanium-Carbon Phase Diagram: *Trans.* AIME (1953) **197**, p. 248; JOURNAL OF METALS (February 1953).

[7] W. Rostoker: Observations on the Occurrence of the Ti_2X Phases. *Trans.* AIME (1952) **194**, p. 209; JOURNAL OF METALS (February 1952).

Titanium-Chromium-Oxygen System

by Chih-Chung Wang and Nicholas J. Grant

The Ti-Cr-O ternary system has been studied in detail near the titanium-rich corner within the limits of 10 wt pct O_2 and 20 wt pct Cr. Studies were extended, but not in detail, to the region beyond 25 wt pct O_2 (50 atomic pct) and 62 wt pct Cr (60 atomic pct). Four isothermal sections at 1400°, 1200°, 1000°, and 800°C are presented as well as two vertical sections at 1 and 2 wt pct O_2.

DURING the last decade much interest has been shown in the development of high strength titanium alloys for high temperature and corrosion resistant applications. Extensive research is being carried out at present, as the current literature indicates, in order to study the properties of titanium and to develop improved alloys. Two of the important alloying elements in commercial titanium alloys are chromium and oxygen and it would be desirable to know their combined influence upon titanium. For this purpose the present work was carried out to investigate the titanium-rich corner of the ternary system Ti-Cr-O.

The binary systems Ti-Cr and Ti-O have been published recently. The Ti-Cr system was studied by several investigators[1-5] and their results are in close agreement. The eutectoid decomposition of the β phase has been shown to be extremely sluggish. $TiCr_2$ was the only intermetallic compound found in this binary system and was formed at 1350°C by a transformation from the β phase. $TiCr_2$ was established as the cubic C 15 ($MgCu_2$) type of structure with 24 atoms per unit cell and was designated as the γ phase.[5] This terminology will be adopted in the present work. There was disagreement about the actual composition of this compound among the several investigators, although it is evident from their data that the compound probably has a solubility range of about 2 to 3 pct and is in the vicinity of 65 pct Cr. It has been indicated recently that a high temperature modification of this γ phase ($TiCr_2$) existed at a temperature above 1300°C.[6, 7] This high temperature modification was identified as a hexagonal C 14 ($MgZn_2$) type of structure with 12 atoms per unit cell. The exact transformation temperature from the high temperature phase to the low temperature phase has not been established. A considerable hysteresis was observed and, due to the sluggishness of this transformation, the high temperature phase often co-existed with the low temperature phase at temperatures below 1300°C.

A preliminary study of several Ti-O compounds and the Ti-O system had been carried out by Ehrlich.[8-10] The most complete binary Ti-O system was the one reported recently by Bumps, Kessler, and Hansen.[11] The first intermediate phase found in the system was the δ phase which formed by a peritectoid reaction of the phases α and TiO at temperatures below 925°C. This reaction is extremely sluggish. The structure of this δ phase was tentatively identified by these authors as being tetragonal and the lattice constants were found as $c_o = 6.645$Å, $a_o = 5.333$Å and $c/a = 1.246$Å.

Experimental Procedure

The raw materials used for this investigation were TiO_2, electrolytic chromium, iodide titanium, and sponge titanium. The TiO_2 was in the form of powder of chemically pure grade (99.8 pct pure). The chemical analysis of the electrolytic chromium was: O, 0.50 pct; Fe, 0.07; Cu, N, and C, 0.01; and Pb, 0.001. The oxygen in the chromium was calculated as part of the final oxygen content of the alloys.

The alloys were prepared by the cold crucible method using a tungsten arc. The entire system was evacuated and flushed with purified helium three times and then filled with helium. Each alloy was melted, turned over, and remelted at least four times to insure homogeneity. The total melting time was generally from 6 to 10 min.

A master alloy of 25 pct O_2-75 pct Ti was prepared to facilitate alloying by melting compacts of TiO_2 powder with either iodide or sponge titanium, yielding the compound TiO. It was found necessary to bake the TiO_2 powder compact at about 150°C to remove adsorbed moisture. This was done to prevent the disintegration and spattering of the compact when the arc was struck. TiO_2 powder dissolved quite readily into the melt and no other trouble was encountered.

C. C. WANG, Associate Member AIME, formerly Research Assistant, Dept. of Metallurgy, M.I.T., is now associated with engineering group, Sylvania Electric Products, Inc., Ipswich, Mass., and N. J. GRANT, Member AIME, is Associate Professor of Metallurgy, Massachusetts Institute of Technology, Cambridge, Mass.

Discussion on this paper, TP 3699E, may be sent, 2 copies, to AIME by April 1, 1954. Manuscript, Sept. 15, 1953. New York Meeting, February 1954.

This paper is based on a thesis by C. C. Wang submitted in partial fulfillment of requirements for the degree of Doctor of Science to the Dept. of Metallurgy, Massachusetts Institute of Technology.

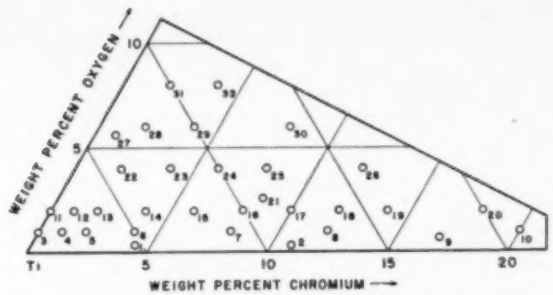

Fig. 1—Alloys prepared with iodide titanium for the study of the titanium-rich corner of the Ti-Cr-O system, weight percent.

The experimental alloys were made by melting the master alloy with the correct amount of titanium and chromium. Each alloy was weighed accurately before and after melting except some alloys in the extended regions of the ternary. The study of weight loss was intended to give an approximate check as to whether there was excessive loss of alloying constituents during melting. Comparison of the weight loss with the results of chemical analysis for chromium on several alloys showed that when the weight loss was high it was usually due to a greater loss of chromium. Loss of oxygen was also indicated at times in these alloys; accordingly, alloys with weight losses over 1 pct for the alloys in the titanium-rich corner, and over 2 pct for the alloys with higher chromium and oxygen content were discarded and new alloys prepared. The nominal composition of the alloys was used in this work; however, it is estimated that the actual composition of chromium and oxygen in the alloys used differed by considerably less than 1 wt pct in the titanium-rich corner, and by less than 2 wt pct in the extended region.

Thirty-two alloys made of iodide titanium were prepared for the investigation of the titanium-rich corner and are shown in Fig. 1. For practical purposes, the compositions are plotted as weight percent. Thirty-three alloys, numbers 33 to 65, were prepared for the study of the extended region and their compositions are shown as atomic percent in Fig. 2. These latter alloys were made by using sponge titanium except the alloys 37 (14.3 O_2-42.9 Cr), 50 (12.0 O_2-42.0 Cr), and 64 (50.0 O_2-0 Cr), which were made from iodide titanium. The use of atomic percent permits an expansion of the oxygen axis in several of the subsequent figures without severe crowding of the various phase fields.

The alloys became increasingly brittle as their oxygen and chromium contents increased. Most of the alloys having compositions lying in the extended region, and especially those with higher oxygen content, cracked into several pieces on cooling in the copper crucible after solidification. All the alloys had a metallic, silvery luster except numbers 40 (43.0 O_2-9.6 Cr), 63 (46.5 O_2), 64 (50.0 O_2), and 65 (53.7 O_2), which had a yellowish-golden color, the characteristic color of the TiO phase.

Although coring (microsegregation) was present in most of the alloys, especially in those of high oxygen and chromium contents, no evidence of ingot segregation (macrosegregation) was observed. This was verified by analyzing for chromium from three different portions of each of a number of alloys.

The as-cast ingots of the highly alloyed heats 55 (20.0 O_2-46.0 Cr), 56 (20.0 O_2-60.0 Cr), and 60 (30.0 O_2-30.0 Cr) clearly showed two layers. This could not be prevented simply by increasing the melting time or power setting. Metallographic examination did not reveal any ingot segregation within each layer.

Specimens to be heat treated were sealed under purified argon in Vycor, however for temperatures above 1300°C, quartz tubing was used instead. Prior to the final annealing treatments all the alloys were homogenized at 1300°C for 6 to 8 hr. Metallographic examination showed that coring and the as-cast structure were completely removed, except for a few of the alloys with the highest chromium and oxygen contents.

Since the phase transformations in this ternary system were generally very sluggish, it was necessary to determine the annealing time required to attain equilibrium at each temperature. This was done by studying the microstructures of several specimens after they had been annealed at different temperatures for increasing periods of time. Table I lists the range of annealing times selected. At each temperature the longer annealing time was used for alloys of higher oxygen and chromium contents.

The quenching of alloys annealed at, or below, 1200°C was done by quickly withdrawing the sealed Vycor capsule from the furnace and breaking it under water. For homogenization treatment specimens were quenched without breaking the Vycor

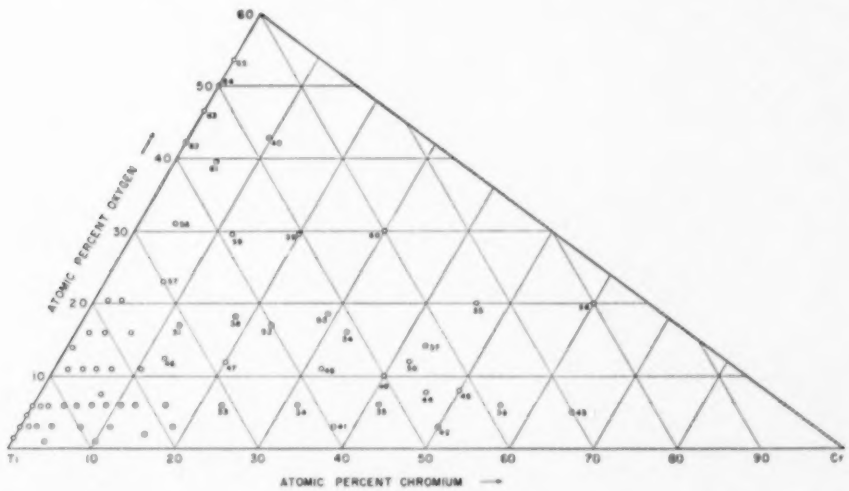

Fig. 2—Alloys Nos. 33 to 65 prepared for the study of the extended region of the Ti-Cr-O system, atomic percent. Location of alloys Nos. 1 to 32 also included.

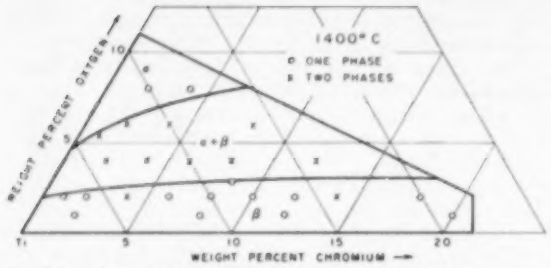

Fig. 3 (a, above; b, below)—1400° and 1200°C isothermal sections of titanium-rich corner of the Ti-Cr-O system.

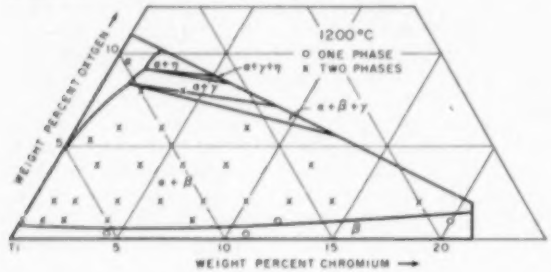

tube. Water quenching of specimens annealed at 1400°C resulted, in several cases, in an attack of the grain boundaries, causing the specimens to disintegrate. Accordingly, all the specimens annealed at 1400°C were quenched in liquid argon.

Metallographic and X-ray diffraction methods were the main methods used in this work. Metallographic specimens were prepared by using the standard polishing techniques. The usual etching reagent was a solution of one part hydrofluoric acid, one part nitric acid, and two parts glycerin. A second etching reagent, an aqueous solution containing 3 pct hydrofluoric acid and 2 pct nitric acid, was sometimes used with about equal results.

The X-ray diffraction patterns were made on a Norelco recording X-ray Spectrometer, using copper Kα radiation with a nickel filter. X-ray specimens were prepared by crushing and grinding the central

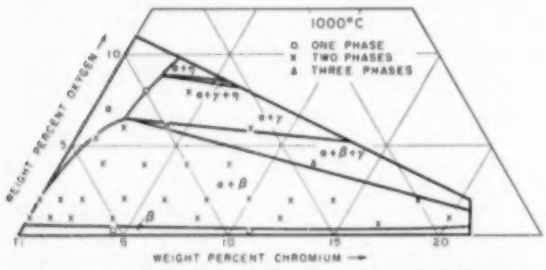

Fig. 4 (a, above; b, below)—1000° and 800°C isothermal sections of titanium-rich corner of the Ti-Cr-O system.

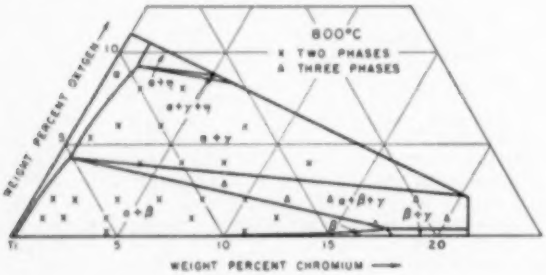

Table I. Annealing Times for Ternary Ti-Cr-O Alloys

Annealing Temperature, °C	Annealing Time, Hr
1400	½ – 3
1300	6 – 14
1200	10 – 20
1000	25 – 80
800	200

parts of the annealed specimens to minus 200 mesh. The lines of the X-ray patterns obtained from these powders were sharp, hence a stress relieving anneal was not necessary.

Experimental Results and Discussion

Titanium-Rich Corner of the Ti-Cr-O System: This region includes up to about 10 wt pct O_2 and 20 wt pct Cr. The alloys used are shown in Fig. 1. Four isothermal sections, namely those at 1400°, 1200°, 1000°, and 800°C, were completed in this region and are presented in Figs. 3 and 4, using weight percent values. These four sections were determined mainly from metallographic examination, while X-ray investigations were undertaken only to confirm the phases present. All the alloys used were made from iodide titanium.

Table II. X-Ray Diffraction Data of Epsilon and Eta Phases

Observed Intensity*	hkl	d, A (Obs.)	d, A (Calc.)
Epsilon Phase			
w	331	2.583	2.592
	420	—	2.527
m	422	2.301	2.307
s	511;333	2.169	2.175
m	440	1.991	1.998
vw	531	1.904	1.910
mw	600;442	1.878	1.883
	620	—	1.787
vw	533	1.720	1.723
w	622	1.702	1.704
vw	444	1.629	1.631
w	711;551	1.578	1.582
	640	—	1.567
vw	642	1.510	1.510
vw	731;553	1.473	1.471
vw	733	1.380	1.381
m	822;660	1.331	1.332
w	751;555	1.304	1.305
vw	662	1.294	1.290
w	842	1.234	1.233
mw	933;771;755	1.1336	1.1357
w	10,22;666	1.0855	1.0873
w	12,00;884	0.9414	0.9417
vw	11,50;11,51;11,43	0.9318	0.9320
	951;777		
vw	12,22;10,64	0.9158	0.9166
mw	13,11;11,71;11,55;993	0.8637	0.8641
vw	10,66	0.8614	0.8616
w	13,31;11,73;977	0.8441	0.8446
vw	12,60;10,84	0.8418	0.8423
vw	12,62	0.8331	0.8330
vw	13,51;1175	0.8085	0.8092
w	14,20;10,10,0;10,86	0.7987	0.7990
vw	14,22;10,10,2	0.7987	0.7912
Eta Phase			
vvw	222	3.559	3.575
vw	400	3.297	3.286
	331	—	2.985
vvw	004	2.801	2.800
	242	—	2.600
vw	151	2.520	2.510
vvw	333	2.366	2.385
vw	440	2.327	2.325
	351	—	2.210
mw	600	2.190	2.191
s	404	2.131	2.132
	153	—	2.120
mw	260	2.079	2.078
vvw	244	2.030	2.028
w	262	1.938	1.948
	353	—	1.928
w	006	1.859	1.867
w	460	1.823	1.823
	335	—	1.815
vw	462	1.727	1.733
w	266	1.386	1.388

* s indicates strong; m, medium; mw, medium weak; w, weak; vw, very weak; and vvw, very, very weak.

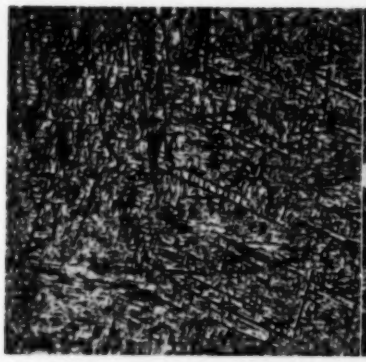

Fig. 5—Alloy 5, 1 wt pct O_2, 2 wt pct Cr. Quenched from 1400°C. Acicular α. X500.

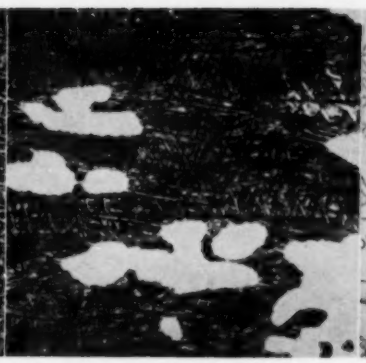

Fig. 6—Same alloy as Fig. 5. Quenched from 1200°C. α (white) plus acicular α. X150.

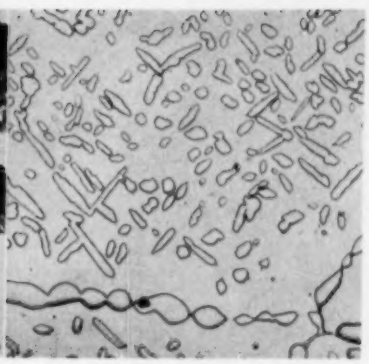

Fig. 7—Alloy 18, 2 wt pct O_2, 14 wt pct Cr. Quenched from 1200°C. α particles in β matrix. X150.

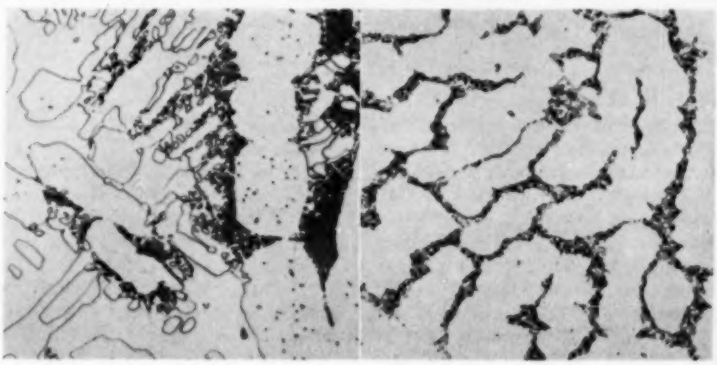

Fig. 8—Same as Fig. 7 except the alloy was quenched from 800°C. The presence of precipitated γ phase (dark) is noted. X500.

Fig. 9—Alloy 24, 4 wt pct O_2, 8 wt pct Cr. Quenched from 800°C. Phases present are α (white areas) and a mixture of α and γ phases (dark). X500.

Fig. 5 is an example of the acicular α structure for an alloy of 1 pct O_2 and 2 pct Cr. This alloy was quenched from the β field at 1400°C (Fig. 3). Fig. 6, obtained from the same alloy but quenched from the $\alpha + \beta$ field at 1200°C (Fig. 3), now shows the acicular α structure as well as the primary α phase. This transformation of β phase to the acicular α during quenching was found to occur in alloys close to the titanium corner (in the 1400°C section, alloys 5, 12 to 16, and 21; in the 1200°C section, alloys 3 to 6 and 12 to 16; in the 1000°C section, alloys 3 to 5; in the 800°C section, none). A similar behavior was found for high titanium alloys in the binary Ti-Cr and binary Ti-O systems. This acicular α phase was designated as α', and is believed to be transformed from the β phase by a mechanism similar to the martensitic type transformation.[5, 12-14]

Fig. 7 is the microstructure of alloy 18 (2.0 O_2-12.0 Cr) quenched from 1200°C. It is a typical example of the structure of the alloys in the $\alpha + \beta$ field showing a retained β phase. Fig. 8 shows the $\alpha + \beta + \gamma$ phases, and was obtained from alloy 18 treated at 800°C in the three-phase field. The existence of the γ phase was also confirmed by X-ray results.

Fig. 9 shows the $\alpha + \gamma$ phases and was obtained from alloy 25 (4.0 O_2-8.0 Cr) quenched from 800°C. The white areas are primary α while the dark regions are mixtures of $\alpha + \gamma$ resulting from the decomposition of the original β grains. These β grains existed originally at the homogenization temperature of 1300°C. X-ray diffraction patterns verified that only α and γ phases were present in these alloys.

As can be seen from Figs. 3 and 4, the β field decreases as the temperature decreases. The precipitation of the α phase from the β was not sluggish. In fact, in some alloys quenched from 1400°C at relatively slow quenching rates, some α precipitated from the β during quenching. This was especially so when there was some primary α present.

Alloys 27, 28, 29, 31, and 32, close to the Ti-O side, were extremely brittle. They often cracked extensively during mounting in bakelite for microscopic examination, suggesting that alloys near the Ti-Cr side might be embrittled if this α phase precipitated at the grain boundaries.

Extended Region of the Ti-Cr-O System: To extend the above results and fix the various phase boundaries, the study was extended, in a more limited way, to alloys containing up to 50 atomic pct O_2 (25 wt pct) and 60 atomic pct Cr (62 wt pct). Fig. 10 shows the 1200°C isothermal section, which includes the phase boundaries determined in Fig. 3. Atomic percents are used in this figure and in micro-

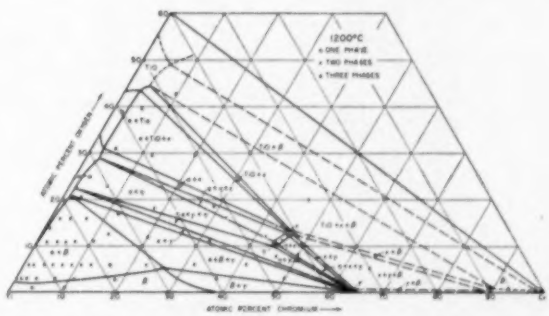

Fig. 10—1200°C isothermal section of the extended region of the Ti-Cr-O system.

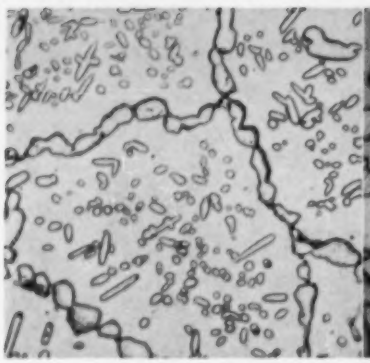

Fig. 11—Alloy 33, 5.9 atomic pct O_2, 22.5 atomic pct Cr. Quenched from 1200°C. α in a β matrix. X150.

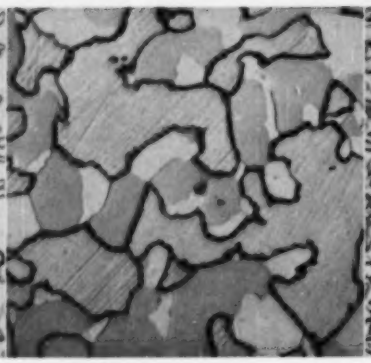

Fig. 12—Alloy 34, 5.9 atomic pct O_2, 31.9 atomic pct Cr. Quenched from 1200°C. Phases present are α, β, and γ. The smooth darker gray phase is α, the phase with scratches is β, and the white phase is γ. Note that β grains are clearly delineated by a dark-etching grain boundary. X500.

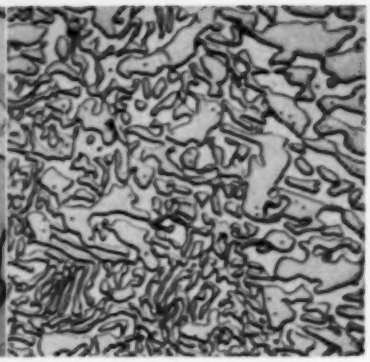

Fig. 13—Alloy 48, 11 atomic pct O_2, 32 atomic pct Cr. Quenched from 1200°C. Phases present are α and γ (white areas). X750.

graphs representing alloys from the extended region since this method expands the oxygen axis. Dashed lines are utilized in the extended ternary regions since the accuracy in drawing the positions of the phase boundaries is not exact.

Ternary Phase—Epsilon: The results of X-ray analysis revealed the existence of a ternary phase, Ti_3Cr_3O, and was named the ϵ phase. The structure is of the same type as a group of titanium compounds reported by Karlsson[15] and Rostoker,[16] being of the type Ti_3X_3O, or Ti_4X_2O, X being one of the transition elements Cu, Ni, Co, Fe, and Mn. The structure of this group of compounds is of the type Fe_3W_3C found in high speed steel. Ti_3Cr_3O has a face-centered cubic lattice with 112 atoms per unit cell, based on a measured density of 5.82 grams per cc (alloy 37, 14.3 O_2-42.9 Cr). Table II lists the diffraction data for this compound, whose lattice constant a_o was calculated to be 11.30Å.

Alloys containing the ϵ phase at lower temperatures were free of it after a 1400°C treatment. In addition, since the as-cast alloy did not show the ϵ phase, it appears that ϵ phase is stable only up to about 1300°C.

Ternary Phase—Eta: Another ternary phase was found and was named the η phase. Table II lists the lines from the X-ray pattern of this phase. These lines could not be fitted to a cubic or hexagonal lattice; however, it was possible to index them on a Hull-Davey chart for the tetragonal system. The lattice parameter thus calculated was: $a_o = 13.14$Å, $c_o = 11.20$Å, $c/a = 0.852$. The observed and calculated d values are also listed in Table II and they are in fairly good agreement. No further studies of the intensities of the X-ray lines and the possible atomic arrangements were made. From the phase diagram the stoichiometric composition of the η phase should be in the vicinity of Ti_4Cr_2O. Calculations were made for a number of possible ternary compounds in this vicinity. Their densities were obtained by extrapolating the values of density measurements of alloys 44, 45, 49, 50, and 51. The most probable composition calculated for this compound was Ti_4Cr_2O. The calculation gave a unit cell

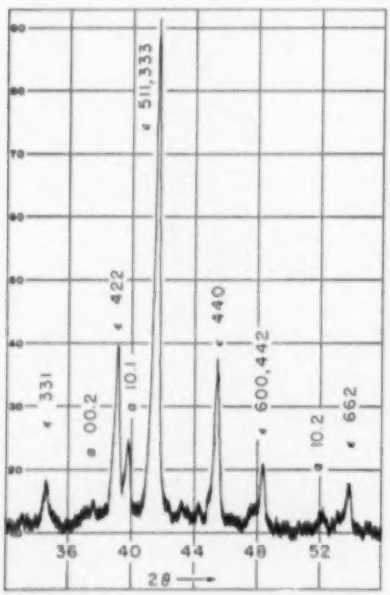

Fig. 14a (left)—X-ray spectrometer pattern of alloy 37 (14.3 atomic pct O_2, 42.9 atomic pct Cr) quenched from 1200°C. $\alpha + \epsilon$.

Fig. 14b (right)—X-ray spectrometer pattern of alloy 54 (16 atomic pct O_2, 32.5 atomic pct Cr) quenched from 1200°C. $\alpha + \eta$.

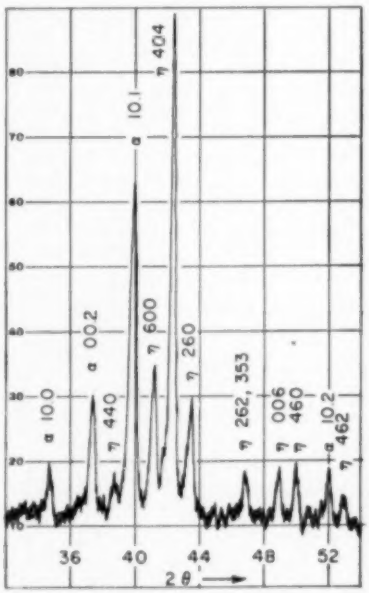

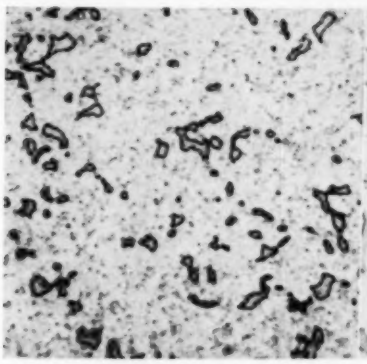

Fig. 15—Alloy 37, 14.3 atomic pct O_2, 42.9 atomic pct Cr. Quenched from 1200°C. α particles in ϵ matrix. X500.

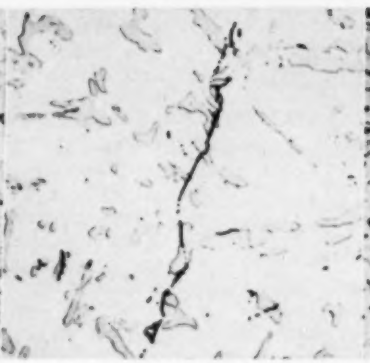

Fig. 16—Alloy 54, 16 atomic pct O_2, 32.5 atomic pct Cr. Quenched from 1200°C. α particles in matrix of η phase. X500.

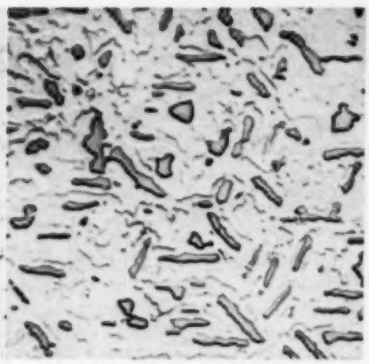

Fig. 17—Alloy 49, 10 atomic pct O_2, 40 atomic pct Cr. Quenched from 1200°C. Three phases present, identified by X-ray as being $\alpha + \gamma + \eta$. X500.

of 144 atoms and a calculated density of 5.71 grams per cc, whereas the density extrapolated for this composition was 5.74 grams per cc. Although this tentatively identified structure appeared correct, further work needs to be done for the complete determination of this structure. While the η phase, like the ϵ phase, was not formed directly from the liquid, it was found to be stable at 1400°C.

1200°C Isothermal Section of Extended Region: The isothermal section at 1200°C is shown in Fig. 10. Fig. 11 shows the microstructure of alloy 33 (5.9 O_2-22.5 Cr) in the two-phase field $\alpha + \beta$. Next to this two-phase field there exists a large three-phase field, $\alpha + \beta + \gamma$. Fig. 12 is an example of alloy 34 (5.9 O_2-31.9 Cr) in this three-phase field. This particular specimen was polished only through the No. 1 wheel (canvas cloth and 600 mesh alundum powder) to leave scratches on the surfaces of the β phase in order to differentiate it from α. Fig. 13 shows the microstructure of alloy 48 (11.0 O_2-32.0 Cr) in the long and narrow $\alpha + \gamma$ field.

Recently, the existence of a high temperature γ phase above 1300°C in the binary Ti-Cr system was reported.[6, 7] The transformation rate from one phase to the other was found to be sluggish and alloys annealed at temperatures below 1300°C still showed the existence of the high temperature γ phase in the X-ray pattern. This was also observed in the ternary system. Alloys containing the γ phase in this region often showed the high temperature phase together with the low temperature phase; however, the former gradually decreased in amount with increasing time of annealing.

It is interesting that though the ϵ and η phases are the only two ternary phases found in the region of study, they are very close together. Fig. 14a is the X-ray spectrometer pattern of alloy 37 (14.3 O_2-42.9 Cr). It shows weak α lines and the alloy was actually in the $\alpha + \epsilon$ two-phase field. Fig. 15 shows its microstructure, which consists of small particles of α in a matrix of the ϵ phase. The α looks bluish gray while the ϵ phase always etches rough. The α particles can be identified also with polarized light. Although alloy 37 had the stoichiometric composition of Ti_3Cr_3O, it did not show a single phase. This could be attributed either to a lack of equilibrium or to a defect lattice structure.

Fig. 14b is the X-ray spectrometer pattern of alloy 54 (16.0 O_2-32.5 Cr) in the two-phase region of $\alpha + \eta$. The microstructure of alloy 54 is shown in Fig. 16. The α phase again shows a dark bluish-gray color, but the η phase, unlike the ϵ phase, etches clean. Fig. 17 shows the microstructure of alloy 49 (10.0 O_2-40.0 Cr) which is in the three-phase field $\alpha + \gamma + \eta$.

The microstructure of alloy 39 (29.5 O_2-20.0 Cr) in the three-phase field $\alpha + TiO + \epsilon$ is shown in Fig. 18. The banded structure looks very much like twins but is actually composed of two phases, α and TiO. This same type of structure was also observed in the binary Ti-O system.[11] It did not spherodize on long time annealing but only coarsened. This type of structure was first found by Smith[17] in the Cu-Si system where the two phases involved are also of face-centered cubic and hexagonal close-packed structures. The existence of this banded structure in these two binary systems was explained by Smith[17] and Bumps et al.[11] as being due to the good match of the octahedral plane of the face-centered cubic phase with the basal plane of the hexagonal close-packed phase. The low interfacial energy between these two phases undoubtedly contributes to the unusual stability of this banded structure.

The three-phase fields, $\epsilon + \gamma + \beta$, and $TiO + \epsilon + \beta$, were roughly outlined by means of X-ray data from the alloys available. Dotted lines were drawn for these phase fields, and further work was not attempted since the study of this region was beyond the planned scope.

As mentioned before in the section on alloy preparation, two distinct layers were found in the ingots of alloys 55 (20.0 O_2 — 46.0 Cr), 56 (20.0 O_2 — 60.0 Cr), and 60 (30.0 O_2 — 30.0 Cr) and could not be eliminated by remelting or heat treatment. The upper layer was golden in color and was identified

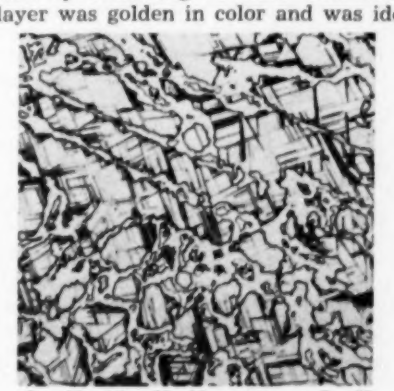

Fig. 18—Alloy 39, 30 atomic pct O_2, 20 atomic pct Cr. Quenched from 1200°C. ϵ and banded structure of $\alpha + TiO$. X500.

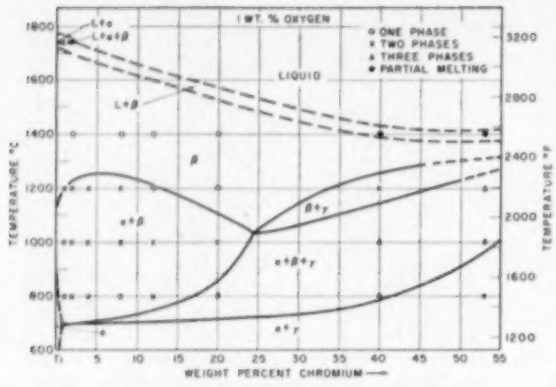

Fig. 19—Vertical section at 1 wt pct O_2 in the Ti-Cr-O system.

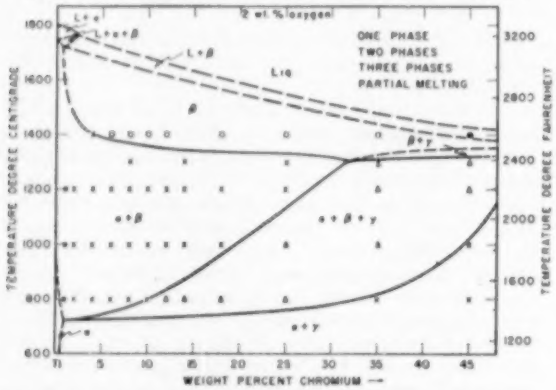

Fig. 20—Vertical section at 2 wt pct O_2 in the Ti-Cr-O system.

by X-ray investigation to be the TiO phase. The lower layer contained the β phase. This leads to the belief that there must be liquid immiscibility in the region containing these alloys. If this is true, then some method other than the arc melting method will be needed to avoid layering.

Vertical Sections of 1 and 2 Wt Pct O_2: With the data from the available alloys and the phase boundaries extrapolated from the isothermal sections, two vertical sections were drawn and are shown in Figs. 19 and 20.

From these two diagrams it is evident that a small amount of oxygen has a great influence upon binary Ti-Cr alloys. The β, and $\alpha + \beta$, phase boundary rises rapidly with the addition of oxygen. The solidus rises only gradually as the oxygen content increases. Both of these two vertical sections show a large area of the three-phase field $\alpha + \beta + \gamma$.

Summary

The titanium-rich corner of the Ti-Cr-O system has been studied in detail within the limits of 10 wt pct O_2 and 20 wt pct Cr. Four isothermal sections at 1400°, 1200°, 1000°, and 800°C were completed.

The α phase at the Ti-O side was found to be extremely brittle. The β phase near the titanium corner was not retained by quenching and instead an acicular α structure was formed. The β phase field decreases rapidly with decreasing temperature.

The region extending to about 25 wt pct O_2 (50 atomic pct) and 62 wt pct Cr (60 atomic pct) has also been studied. An isothermal section at 1200°C is presented.

Two ternary phases were found. The first one, designated ϵ phase, corresponds to Ti_4Cr_2O and had a face-centered cubic structure of the Fe_3W_3C type. The lattice constant was found to be $a_o = 11.30$Å, and the unit cell contains 112 atoms. The second ternary phase, designated η phase, had a more complicated structure. It was tentatively identified as tetragonal. The lattice constants measured were $a_o = 13.14$Å, $c_o = 11.20$Å, and $c/a = 0.852$. The suggested formula was Ti_4Cr_4O and on the basis of density measurements it contains 144 atoms per unit cell. Neither of the ternary phases formed directly from the liquid phase. The ϵ phase was stable only below a temperature which is between 1300° and 1400°C, while the η phase existed up to about 1400°C.

Two vertical sections of 1 and 2 wt pct O_2 were constructed. They showed that a small amount of oxygen has a great influence upon the binary Ti-Cr alloys.

Acknowledgments

The authors wish to express their appreciation for the assistance of Mrs. Gloria Johnson, Dr. Arup Chaudhuri, and Dr. Hsing Chang. This work was initiated under the sponsorship of Army Air Forces, under contract number AF 33 (038)-8754, and was completed through support of the Office of Naval Research under contract number N5-ori-07881. The support of both groups is deeply appreciated.

References

[1] D. J. McPherson and M. G. Fontana: Preparation and Properties of Titanium-Chromium Binary Alloys. *Trans.* ASM (1951) **43**, p. 1098.

[2] F. B. Cuff, Jr., N. J. Grant, and C. F. Floe: The Titanium-Chromium Phase Diagram. *Trans.* AIME (1952) **194**, p. 848; JOURNAL OF METALS (August 1952).

[3] M. K. McQuillan: A Provisional Constitutional Diagram of the Chromium-Titanium System. *Journal* Inst. Metals (1951) **79**, p. 379.

[4] R. J. Van Thyne, H. D. Kessler, and M. Hansen: The System Titanium-Chromium and Titanium-Iron. *Trans.* ASM (1952) **44**, p. 974.

[5] P. Duwez and J. L. Taylor: A Partial Titanium-Chromium Phase Diagram and the Crystal Structure of $TiCr_2$. *Trans.* ASM (1952) **44**, p. 495.

[6] B. Levinger: A High Temperature Modification of $TiCr_2$. *Trans.* AIME (1953) **197**, p. 196; JOURNAL OF METALS (February 1953).

[7] R. J. Van Thyne and H. D. Kessler: Discussion to ref. 2. *Trans.* AIME (1953) **197**, p. 744; JOURNAL OF METALS (May 1953).

[8] P. Ehrlich: *Elektrochemie* (1939) **45**, p. 362.

[9] P. Ehrlich: *Ztsch. anorg. allgem. Chemie* (1941) **247**, p. 53.

[10] P. Ehrlich: *Ztsch. anorg. allgem. Chemie* (1949) **259**, p. 1.

[11] E. S. Bumps, H. D. Kessler, and M. Hansen: The Titanium-Oxygen System. *Trans.* ASM (1953) **45**, p. 1008.

[12] P. Duwez: Effect of Rate of Cooling on the Alpha-Beta Transformation in Titanium and Titanium-Molybdenum Alloys. *Trans.* AIME (1951) **191**, p. 765; JOURNAL OF METALS (September 1951).

[13] D. J. Delazaro, M. Hansen, R. E. Riley, and W. Rostoker: Time-Temperature Transformation Characteristics of Titanium-Molybdenum Alloys. *Trans.* AIME (1952) **194**, p. 265; JOURNAL OF METALS (March 1952).

[14] P. Duwez: The Martensite Transformation Temperature in Titanium Binary Alloys. *Trans.* ASM (1953) **45**, p. 934.

[15] N. Karlsson: *Nature* (1951) **168**, p. 558.

[16] W. Rostoker: Observation on the Occurrence of Ti_2X Phases. *Trans.* AIME (1952) **194**, p. 209; JOURNAL OF METALS (February 1952).

[17] C. S. Smith: Constitution and Microstructure of Copper-Rich Silicon-Copper Alloys. *Trans.* AIME (1940) **137**, p. 313.

Uranium-Titanium Alloy System

by Murray C. Udy and Francis W. Boulger

AN incomplete phase diagram for the U-Ti system was determined earlier,[1] and more recently, a tentative diagram was presented for the uranium-rich end of the system.[2] In the present re-examination of the whole system of U-Ti alloys, high purity materials were used.

Melting stock for the alloys was high purity uranium, containing about 0.09 pct C as the only appreciable impurity, and high purity iodide-process titanium purchased from New Jersey Zinc Co. Both metals were cold rolled to about 1/6 in. thickness, sheared to about ¼ in. squares, and cleaned by pickling. The alloys were arc melted under a helium atmosphere in a water-cooled copper crucible. A thoriated-tungsten electrode was used. The furnace chamber was evacuated, then flushed with helium, prior to each melting. It was finally filled with stagnant helium at one atmosphere pressure.

Each alloy was remelted three times after the original melting, to insure homogeneity. The alloy button was turned bottom side up before each remelting operation. Some 22 alloys were examined. Their compositions were spaced at appropriate intervals between 100 pct Ti and 100 pct U. Analyses were made on chips taken after fabrication. The major contaminant was carbon, which varied from 0.03 to 0.08 pct. It appeared in the microstructure as titanium carbide. Alloy compositions were calculated to a carbon-free basis for consideration on the diagram.

Tungsten and copper, possible contaminants from the melting operation, were generally less than 100 parts per million each.

Fabrication

All alloys were forged and rolled to bars approximately ⅛ in. square. They were clad either in SAE 1020 steel or in a 5 pct Cr-3 pct Al-Ti-base alloy, depending on the fabrication temperature. A temperature of 1800°F (980°C) was used for alloys near the compound composition. This necessitated using the titanium-base alloy, since iron reacts with titanium at this temperature, producing a low melting alloy. Other alloys were fabricated at 1450°F (790°C), using steel jackets. No iron-titanium reaction occurred at this temperature. The jackets were welded in place in an argon atmosphere. Those alloys sheathed in steel were declad and then reclad between rolling and forging operations. On the other hand, those clad with the titanium alloy were cut to a roughly rectangular shape prior to clading and were then carried through both the forging and rolling operations without opening. Those alloys near the compound composition were found to be cracked when the clading was removed. The cracked materials had been plastically deformed, however, and at least some of the cracking had occurred during cooling.

M. C. UDY and F. W. BOULGER, Members AIME, are Assistant Division Chief and Division Chief, respectively, Metallurgy Dept., Battelle Memorial Institute, Columbus, Ohio.

Discussion on this paper, TP 3686E, may be sent, 2 copies, to AIME by April 1, 1954. Manuscript, July 3, 1953. New York Meeting, February 1954.

Heat Treatment

The rolled bars, after being declad and shaped to remove surface contamination, were all given an homogenizing treatment of 160 hr at 2000°F. (Samples were taken for analysis following the declading and shaping operations.) All were heat treated at the same time in one furnace, but each was sealed in a purified argon atmosphere in an individual Vycor glass tube. Argon pressure was such that it was approximately atmospheric at temperature. One end of each tube contained titanium chips and this end was heated to 1200°F (650°C) for 10 min prior to the heat treatment. This purged the atmosphere of residual reactive gases. The balance of the tube was warmed during the purge to liberate adsorbed moisture and gases, which also reacted with the hot chips. The bars were furnace cooled from the homogenization treatment.

Specimens of each alloy were water quenched after 2 hr heating at 1000°, 1200°, 1400°, 1600°, 1800°, and 2000°F (540°, 650°, 760°, 870°, 980°, and 1095°C). In addition, some were treated at intermediate temperatures of 1300°, 1500°, and 1700°F (705°, 815°, and 925°C) and at 2150°F (1175°C). Specimens, about ⅛ in. cubes, were cut from the bars, sealed in individual Vycor tubes, and heat treated as described. All specimens heat treated at the same temperature were processed together. Samples were quenched by breaking the Vycor tube rapidly under water.

Metallographic Examination

Specimens were mounted in bakelite and ground wet on 180 grit paper held on a 1750 rpm disk. They were then ground wet by hand, using 240, 400, and 600 grit papers. The rough grinding was continued long enough to get well below the surface. Specimens were mounted separately because of the variation in the rate of etching between alloys. The specimens were polished with rouge on a 4 in., 1725 rpm wheel covered with Miracloth.

Alloys on the titanium side of the compound composition were etched with a solution of 2 pct hydrofluoric acid in water saturated with oxalic acid. A few crystals of ferric nitrate were added as a brightener. Specimens were immersed 5 sec, polished to remove the etch, then re-etched. With the higher titanium alloys, it was often necessary to start the etch on the polishing wheel, because of the formation of a passive film. In some instances, a plain 2 pct hydrofluoric etch was satisfactory.

For the alloys on the uranium side of the compound, a distinction between the compound and the uranium phase developed after standing a short time in air. This could be hastened by the application of heat, such as obtained by placing the specimen on a radiator. A deep etch was necessary to develop details in the uranium-rich phase, such as the Widmanstaetten pattern sometimes obtained by quenching γ uranium. A 2 pct hydrofluoric acid solution was used for this deep etching.

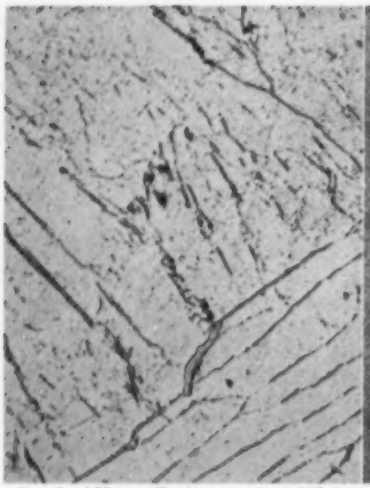

Fig. 1—100 pct Ti, homogenized 160 hr at 2000°F (1095°C) and slow cooled. Large grained α titanium. X500.

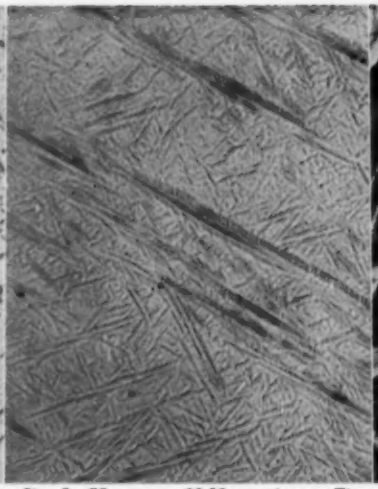

Fig. 2—70 wt pct, 92.05 atomic pct Ti, quenched after 2 hr at 1600°F (870°C). Widmanstaetten α titanium which had been β titanium at temperature. X500.

Fig. 3—51.4 wt pct, 84 atomic pct Ti, homogenized 160 hr at 2000°F (1095°C) and slow cooled. Primary α titanium plus α-titanium-compound eutectoid. X500.

Fig. 4—51.4 wt pct, 84 atomic pct Ti, quenched after 2 hr at 2000°F (1095°C). β titanium deep etched to show grain boundaries. X500.

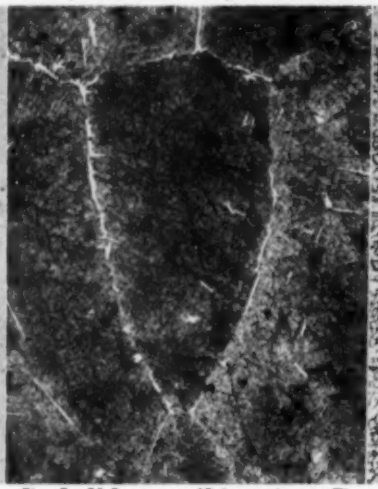

Fig. 5—31.5 wt pct, 69.4 atomic pct Ti, quenched after 2 hr at 1400°F (760°C). β titanium with residual compound in grain boundaries and some in the remnants of the eutectoid. This is close to the eutectoid composition. X100.

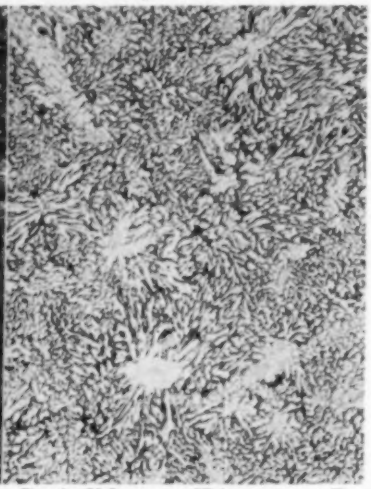

Fig. 6—21.3 wt pct, 57.4 atomic pct Ti, homogenized 160 hr at 2000°F (1095°C) and slow cooled. Compound plus compound-α-titanium eutectoid. X500.

Specimens were examined at 100, 500, and sometimes 2000, magnifications. In most instances, pictures were taken for record purposes. Figs. 1 through 9 show typical structures.

X-Ray Examination

To aid in the interpretation of microstructure, X-ray diffraction methods were used to identify phases. The best diffraction data were obtained with an X-ray spectrometer, using filtered copper radiation. The majority of the X-ray data were obtained from the polished and etched samples used for metallographic study. Because many of the samples were very coarse grained, it was necessary to mount the specimen on a goniometer and oscillate the angle of incidence of the X-ray beam upon the sample in order to obtain all the reflections possible from the various phases.

The following phases were identified:

1—α titanium—low temperature hexagonal phase.

2—β titanium—high temperature body-centered phase.

3—Compound based on U_2Ti—hexagonal phase, $a_o = 4.817$Å, $c_o = 2.844$Å.

4—α uranium—low temperature phase.

Table I. Liquidus Temperatures of U-Ti Alloys

Specimen	Uranium, Pct		Liquidus, °C (Corrected)
	Wt	Atomic	
Uranium	100	100	1132 ± 10
11	98	90.8	1210 ± 20
22	96.4	84.3	1230 ± 20
21	94.8	78.4	1350 ± 20
3	92.5	71.3	1370 ± 20
9	89.2	62.4	1435 ± 20
1	86.4	56.1	1465 ± 20
6	75.7	42.6	1535 ± 20
20	68.5	30.6	1555 ± 20
23	60.6	23.7	1615 ± 20
19	48.6	16.0	1625 ± 20
18	30.0	7.95	1645 ± 20
16	0.9	0.2	1685 ± 25
Iodide Ti	0	0	1725 ± 25

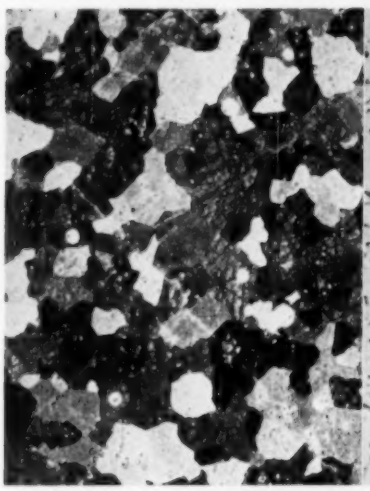

Fig. 7—10.8 wt pct, 37.6 atomic pct Ti, quenched after 2 hr at 1200°F (650°C). Essentially all compound. X100.

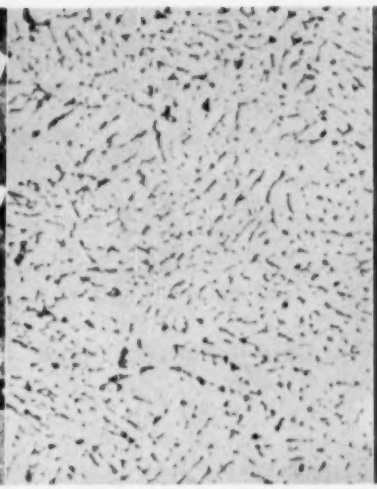

Fig. 8—7.5 wt pct, 28.7 atomic pct Ti, homogenized at 2000°F (1095°C) and slow cooled. Compound and α uranium. X500.

Fig. 9—2.0 wt pct, 9.2 atomic pct Ti, quenched after 2 hr at 1400°F (760°C). Widmanstaetten α uranium and compound. X500.

5—γ uranium—high temperature phase.

In no case was β uranium identified.

Determination of Liquidus Temperatures

Liquidus temperatures, for 12 of the alloys, were determined optically by observing the temperature at which the center of a $\frac{1}{8}$x$\frac{1}{8}$x$\frac{1}{2}$ in. specimen melted. An attempt was also made to determine the solidus, but in most cases accuracy was impossible. The specimens were supported on the edge of a strip of thin tantalum sheet bent to triangular shape. The determinations were conducted in an induction-heated, argon-atmosphere furnace. The readings were corrected by observing the melting temperatures of substances of known melting point. Results are given in Table I.

Uranium-Titanium Diagram

Fig. 10 is the phase diagram of the U-Ti system, based principally on the present work. The points indicate the phases believed to exist at temperatures based on the metallographic and X-ray examinations.

Since no specimens were examined in the region where α and β uranium should be stable, the results of Buzzard, Liss, and Fickle[2] were used for the composition of the eutectoid between β uranium and the compound and for the composition of the peritectoid involving α uranium and the compound. No solid-solution phase, such as labeled "delta" by Buzzard et al.,[2] was identified metallographically or by X-ray. Instead, complete solid solubility between β titanium and γ uranium is indicated. At about 1635°F (890°C), the compound U_2Ti decomposes into β titanium plus γ uranium solid solution. This temperature has been established by thermal as well as metallographic means.

The higher melting points observed in the uranium-rich end of the system in the previous study[1] and in the work by Buzzard et al.[2] were not verified. It is believed that the high values observed earlier on samples melted in beryllia may have resulted from the same type of film that obscured the true melting point of uranium for so long.

On the titanium side of the diagram, liquidus and solidus determinations of the previous work[1] with less pure material are in good agreement with present observations. They are shown in Fig. 10 as triangles.

The temperatures of the eutectoids between α uranium and the compound, and between β uranium and the compound and the temperature of the peritectoid involving α uranium and the compound are those determined in the earlier work by dilatometric and thermal means.[1] The structure of the compound confirms that determined by X-ray in the earlier work by W. J. Tucker, of Knolls Atomic Power Laboratory.[1]

The complete solid solubility between γ uranium and β titanium is not unique. A similar condition exists in the Ti-Cr, Ti-Mo, and Ti-Cb systems. In the case of uranium, 50 wt pct or 18 atomic pct is needed to stabilize β titanium on quenching. Otherwise, a Widmanstaetten α titanium structure is obtained. On the uranium side, 3 wt pct Ti, or 14 atomic pct is needed to stabilize γ uranium on quenching. Otherwise, a Widmanstaetten α uranium structure is obtained.

The intermediate β uranium phase was not observed in any of the structures. This seems to indicate that titanium does not stabilize this structure. However, no concentrated effort was made to study this region of the diagram. One specimen quenched from the supposed β titanium plus compound field showed a Widmanstaetten α uranium structure.

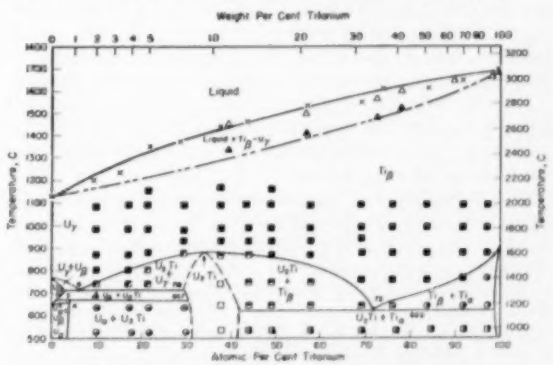

Fig. 10—Uranium-titanium constitution diagram.

Acknowledgments

The help of various staff members of Battelle Memorial Institute in specimen preparation and in experimental determinations is gratefully acknowledged. Discussion with F. A. Rough and H. A. Saller of recent thermal studies by them has been of great assistance in interpreting the data in the region of the compound. This help is greatly appreciated. The work was performed under Atomic Energy Commission Contract W-7405-Eng-92.

References

[1] A. W. Seybolt, D. E. White, F. W. Boulger, and M. C. Udy: Tentative Uranium-Titanium Phase Diagram. *Reactor Science and Technology* (April 1951) **1**, No. 1, pp. 118-119.

[2] R. W. Buzzard, R. B. Liss, and D. P. Fickle: The Uranium-Titanium Binary System. *Reactor Science and Technology* (April 1952) **2**, No. 1, pp. 97-103. Also Nat. Bur. of Standards, *Journal of Researches* (April 1953) **50**, pp. 209-214.

Technical Note

Heat Treatment of Titanium Generalized in Terms of Beta Prime

by Leonard D. Jaffe

THE data recently published[1-9] on heat treatment of titanium alloys have not been readily systematized into an overall picture. When the β titanium phase transforms isothermally at low temperatures, the hardness follows a typical age-hardening pattern, going through a peak as schematized by the "hardness" vs "time of isothermal transformation" coordinates of Fig. 1. As the temperature is raised, the peak will decrease in height and occur at shorter times; slowing must however take place as the β transus is approached.

The brittle microconstituent in the region of peak hardness has been termed β'. Its structure is still undetermined but it is clearly a transition stage from soft β to the $\beta + \alpha$ that is found at the right of the peak.

On continuous cooling, high cooling rates correspond to short times on Fig. 1; abscissa labeling has been added accordingly. Extremely rapid cooling will retain soft β; very slow cooling will precipitate soft α; intermediate rates give hard β'. Increasing distance from the water-quenched end of a Jominy hardenability bar corresponds to slower cooling (right on Fig. 1), but the range of cooling rates covered by a Jominy bar is only a small portion of that shown in the figure.

The β-stabilizing alloying elements retard the transformation process, moving the material to the left on Fig. 1. A lean alloy is harder water-quenched (β') than air-cooled ($\beta + \alpha$); a rich alloy is harder air-cooled (β') than water-quenched (β). Examples of the position of various compositions with respect to the curve, based on limited data in the literature, are given at the top of the figure.

Oxygen and carbon accelerate the transformation process, moving the material to the right on Fig. 1.

If an alloy quenched quickly enough to retain soft β is reheated below the β transus (tempered), it ages, going through a hardness maximum as time increases (moving right on Fig. 1). Material which after cooling from the β range lies on or right of the hardness peak, will move still further right on tempering, and so soften.

Since the rate of the tempering (aging) reaction increases with temperature, the figure also may be used to represent the variation in properties with tempering temperature, at short tempering times.

The simple picture given here neglects martensite transformation, as well as differences between decomposition products of β formed by direct isothermal transformation and those formed by quenching and tempering. It may nevertheless be of use as a guide for practical heat treatment and for further research.

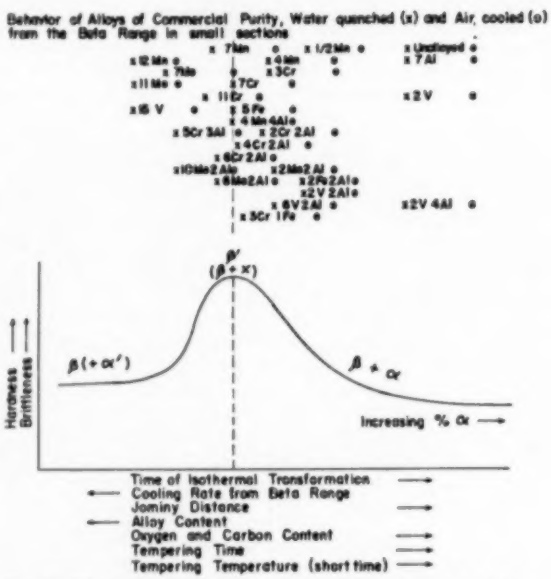

Fig. 1—Effect of variables upon properties of alloys first held in β range, schematic.

References

[1] H. W. Worner: *Journal* Inst. Metals (1951-1952) **80**, pp. 213-216.

[2] H. K. Adenstedt, J. R. Pequignot, and J. M. Raymer: *Trans.* ASM (1952) **44**, pp. 990-1003.

[3] D. J. Delazaro, M. Hansen, R. E. Riley, and W. Rostoker: *Trans.* AIME (1952) **194**, pp. 265-269; JOURNAL OF METALS (March 1952).

[4] C. W. Phillips and D. N. Frey: *Trans.* AIME (1952) **194**, pp. 381-386; JOURNAL OF METALS (April 1952).

[5] L. S. Busch: JOURNAL OF METALS (February 1953) **5**, pp. 146-149.

[6] M. W. Parris, L. L. Hirsch, P. D. Frost, and J. H. Jackson: ASM Preprint No. 4, 1953.

[7] H. D. Kessler and M. Hansen: ASM Preprints No. 5 and No. 6, 1953.

[8] P. D. Frost, W. M. Parris, L. L. Hirsch, J. R. Doig, and C. M. Schwartz: ASM Preprint No. 7, 1953.

[9] D. J. Delazaro and W. Rostoker: ASM Preprint No. 8, 1953.

L. D. JAFFE, Member AIME, is associated with the Watertown Arsenal Laboratory, Watertown, Mass.

TN 204E. Manuscript, Oct. 8, 1953.

Aging Characteristics of Nickel-Chromium Alloys Hardened with Titanium and Aluminum

by Rolf Nordheim and Nicholas J. Grant

An extensive study was made of the aging characteristics of alloys based on the 80 pct Ni-20 pct Cr composition hardened with aluminum and/or titanium, each up to 4 pct. Aging was followed by means of hardness and hot electrical resistance measurements as well as by X-ray and microscopy. Stress rupture tests at 1500°F were utilized as a check on the predicted behavior.

THE titanium and aluminum hardened Ni-Cr alloys, exemplified by Nimonic 80 and Inconel X, constitute one of the more important groups of alloys developed to meet the demand for materials retaining their strength at elevated temperatures. For service in the temperature range 1200° to 1500°F, these alloys offer high creep resistance. With increasing service temperature, however, the strength of the simpler Ni-Cr base alloys falls off rapidly so that above 1500°F there is a significant loss of strength.

The present investigation was undertaken with the hope that a better understanding of the factors controlling the precipitation hardening of these alloys would make it possible to increase the useful service temperature range. Primarily this investigation involved the study of the effects of titanium and aluminum on the hardening and the subsequent softening at elevated temperatures. The titanium and aluminum contents were each varied between 0 and 4 pct by weight at a constant nickel to chromium weight ratio of about 4:1. (Except when otherwise stated, all compositions are expressed on a weight basis.) The major part of the investigation was confined to alloys with less than 0.06 pct C.

Recently several papers dealing with the identity of the microconstituents in the titanium and aluminum hardened Ni-Cr alloys have been published. Using X-ray analysis of the residues from anodic dissolution, Rosenbaum[1] was only able to identify carbides and nitrides in Nimonic 80 and Inconel X. However, since Rosenbaum worked with alloys in the hot rolled rather than in the aged condition, his results are inconclusive. Recently Hignett[2] reported that the hardening of Nimonic 80 was due to the controlled precipitation of $Ni_3(TiAl)$ having the cubic Ni_3Al structure. Taylor and Floyd[3-5] published the results of an investigation of the nickel-rich corner of the Ni-Cr-Ti, Ni-Cr-Al, and Ni-Ti-Al systems. In the Ni-Ti and the Ni-Al systems the hexagonal Ni_3Ti phase, η, and the cubic Ni_3Al phase, γ', respectively, exist in equilibrium with the nickel-rich solid solution. The interatomic distances in the basal plane of Ni_3Ti and the octahedral planes of the matrix are almost equal, thus explaining the Widmanstaetten type structure formed when Ni_3Ti precipitates from solid solution. When Ni_3Al precipitates from solid solution, it appears usually in globular form, often dispersed along rows corresponding to definite crystallographic directions. The η and γ' phases are also the only intermetallic compounds which occur in the nickel ternary alloys with up to 25 pct Cr and 10 pct Ti or Al. Taylor and Floyd found that Ni_3Ti takes practically no nickel, chromium, or aluminum into solution. Ni_3Al, on the other hand, dissolves a considerable amount of chromium and titanium and some nickel. Up to three out of every five aluminum atoms could be replaced by titanium in Ni_3Al. This substitution caused a slight increase (less than 1 pct) in the lattice parameter.

With respect to the effect of variation in the titanium and aluminum contents on the high temperature strength of Nimonic 80 type alloys, Pfeil, Allen, and Conway[6] reported that an 80 pct Ni-20 pct Cr alloy containing 0.20 to 0.30 pct Al had the highest creep resistance when the titanium content was kept between 1.65 and 2.75 pct.

Experimental Procedure

The materials used for this investigation were electrolytic nickel, electrolytic or low carbon chromium, sponge titanium and 2S aluminum. The alloys were melted in an indirect carbon arc furnace under

R. NORDHEIM, Junior Member AIME, formerly Research Assistant, Dept. of Metallurgy, Massachusetts Institute of Technology, is in Cambridge, Mass., and N. J. GRANT, Member AIME, is Associate Professor, Dept. of Metallurgy, Massachusetts Institute of Technology, Cambridge, Mass.

Discussion on this paper, TP 3692E, may be sent, 2 copies, to AIME by April 1, 1954. Manuscript, Sept. 15, 1953. New York Meeting, February 1954.

This paper is based on a thesis by R. Nordheim submitted in partial fulfillment of requirements for the Doctor of Science degree to the Department of Metallurgy, M.I.T.

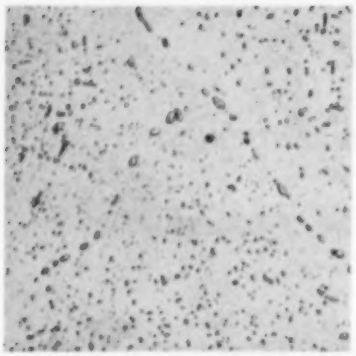

Fig. 1—Alloy 684. 3.2 pct Al, aged 430 hr at 1650°F. Etchant A. X500.

a slightly oxidizing atmosphere, the weight of the heats being approximately 2 lb.

The results of chemical analysis for titanium, aluminum, and carbon are given in Table I. It was found that the chromium recovery was 98 to 99 pct. One alloy was analyzed for iron, manganese, and silicon with the following results: 0.67 pct Fe, 0.04 pct Mn, and 0.31 pct Si.

All the heats used for the study of the precipitation processes were poured into silica precision casting investment molds giving bars of ⅜ and ¼ in. diameter. These bars were homogenized for 45 hr at 2170°F, which resulted in an average grain size of about 1/16 in. The subsequent heat treatments included a 4 hr solution treatment at 2000°F, followed by water quenching and then aging at temperatures ranging from 1250° to 1800°F. The atmosphere was purified helium for all the heat treatments at and above 1650°F and at 1450° and 1550°F for periods of time longer than 20 hr.

The precipitation processes were followed by metallographic techniques, Rockwell hardness measurements, and electrical resistance measurements at temperature. Disks 3/16 in. thick were cut from the ⅜ in. diameter bars and used for both the hardness readings and the metallographic examinations. These samples were water quenched from the aging temperature. The reported hardness values represent the average of three or four readings and in practically no case differed by more than three units.

Table I. Titanium, Aluminum, and Carbon Contents of the Experimental Alloys

Alloy No.	Weight Percent Ti	Al	C	Atomic Percent Ti	Al
Alloys for Precipitation Studies					
649	2.1	0.5	0.03	3.4	1.0
653	0	0.9	0.024	0	1.9
654	0.9	0.5	0.034	1.0	1.0
661	2.2	0.9	0.03	2.6	1.9
662	2.2	0	0.06	2.6	0
684	0.05	3.2	0.03	0.05	6.5
688	3.2	0.8	0.02	3.7	1.8
689	2.2	1.4	0.025	2.6	2.8
690	2.3	2.1	0.068	2.7	4.3
692	3.7	0	0.066	4.4	0
854	1.0	0.7	0.027	1.2	1.5
855	3.0	0.5	0.022	3.5	1.0
982	0	2.8	0.01	0	5.7
Alloys for Stress Rupture Tests					
930	2.0	0.9	0.012	2.4	1.9
932	2.3	1.5	0.011	2.7	3.1
934	3.2	0	0.016	3.7	0
1027*	0	3.8	0.04	0	7.8
1028*	0	3.9	0.027	0	8.0
1043*	3.3	1.0	0.037	3.8	2.1

* Alloys deoxidized with 0.2 pct Ca-Si.

For metallographic examination the samples were mechanically polished and etched anodically (3 to 4 volts) in one of the following reagents: etchant A—aqueous solution of 10 pct glycerine and 5 pct hydrofluoric acid for 5 to 10 sec, etchant B—aqueous solution of 10 pct oxalic acid for 5 sec, etchant C—aqueous solution of 5 pct sodium hydroxide for 15 to 30 sec.

Etchant A was generally used to reveal the structure of the aged samples. The effect of this etchant was to dissolve the matrix around the precipitated particles. No staining was observed when the etching period was limited to 10 sec. Since etchant A did not successfully develop the grain boundaries of alloys quenched from above the saturation temperature, etchant B was used to reveal the structure after solution treatment. Etchant C was occasionally used for Ni-Cr-Ti alloys. Etching with this reagent stained the matrix, but left the precipitated particles unattacked.

The 3/16 in. diameter bars were used for the electrical resistance measurements. Nickel wire, spot-welded to the specimen, served as current and potential leads. With a Kelvin double bridge, changes corresponding to 0.1 pct of the gage resistance could be detected. The temperature was measured with a chromel-alumel thermocouple attached to the specimen. The heat treatments were done in furnaces having a temperature fluctuation not exceeding ±2°F. The temperature variation along the specimen was less than 2°F. After the specimen had been placed in the furnace, the aging period was timed from the moment the thermocouple reached the temperature chosen for the heat treatment. This usually occurred within 3 or 4 min.

For each alloy the same specimen was used for all the aging treatments. After each run the specimens were given a 4 hr solution treatment at 2000°F and water quenched. Since the room temperature resistance after such a 2000°F water quench remained constant within ±0.3 pct during the course of the runs, it was concluded that an insignificant amount of chromium had been lost during the repeated solution and aging treatments.

Identification of the phases which precipitated during aging was done by X-ray analysis of solid samples. Disks used for this examination were cold worked after solution treatment, recrystallized at 2000°F, and aged for 500 hr at 1450°F. These aged samples were mechanically polished and etched anodically with etchant A for 5 to 10 sec. This left the precipitated particles standing out in relief.

On the basis of the precipitation studies some alloys were prepared for stress rupture tests. The heats for these tests were poured in 1 in. diameter graphite molds. A Ca-Si alloy of 0.2 pct was added to some of the heats to facilitate the forging operation. For the same purpose all the ingots were homogenized for 24 hr at 2170°F. The ingots were forged at 2200° to 2000°F to bars of ⅜ in. diameter. From these, ¼ in. diameter, 1 in. gage length test bars were machined. The bars were solution treated at 2000°F and aged at temperatures ranging from 1300° to 1500°F. They were tested at 1500°F.

Results and Discussion

Structural Characteristics of the Microconstituents: In alloys having additions of aluminum only, aging resulted in the precipitation of a finely dispersed

phase. Fig. 1 shows that this phase occurred to a great extent as globular particles, but there was also evidence of preferential growth of some of the precipitate along certain lattice planes in the matrix. It was determined from observations of aged structures that about two-thirds of the aluminum atoms could be replaced by titanium without any appreciable change in the microstructure, confirming the observations of Floyd and Taylor.[5]

In Fig. 2 are shown, using atomic percentages, the compositions of the alloys used for the aging studies. For all the quaternary alloys represented by this chart, precipitation produced a microstructure similar to that of Fig. 1. (Alloy 855, having a titanium to aluminum atomic ratio of about 4:1, also contained a small amount of the acicular phase which precipitated in Ni-Cr-Ti alloys; see below.) The X-ray patterns of the alloys for which the microstructure showed the precipitation of the finely dispersed phase were all similar and revealed in addition to the pattern of the matrix, the presence of a second constituent which was identified as Ni_3Al. The Bravais lattice of this constituent is face-centered cubic,[7] with the aluminum and nickel atoms occupying the cube corners and faces, respectively. It was found that the lattice parameter of this second phase increased with the titanium to aluminum ratio of the alloys as shown in Table II. This indicates that in the alloys containing both aluminum and titanium, titanium, which has a larger atomic radius than aluminum, had replaced some of the aluminum atoms in Ni_3Al.

In alloys containing titanium only, aging resulted in the precipitation of a needle-like phase which formed a well-defined Widmanstaetten type structure, Fig. 3. This phase was identified as being the hexagonal close-packed Ni_3Ti compound. Comparison of Figs. 1 and 3 shows that for similar heat treatments the Ni_3Ti particles grew to a larger size than the Ni_3Al particles.

These results agree well with those of Taylor and Floyd, particularly with respect to the existence of the intermetallic compounds Ni_3Al and Ni_3Ti and their respective homogeneity ranges. However, the solubilities for titanium and aluminum in an 80 pct Ni-20 pct Cr alloy, as observed in the present work, were lower than those reported by Taylor and Floyd. The higher solubilities found by these investigators may be due to the higher purity of their alloys. Included in Fig. 2 are the tentative saturation temperatures based on metallographic examinations.

In the following presentation the two phases Ni_3Al and Ni_3Ti will be referred to as γ' and η, respectively, in conformity with the notation used by Taylor and Floyd.

Precipitation of γ': Figs. 4 to 6 show the microstructural changes during aging of an alloy with 2.2 pct Ti and 0.9 pct Al (alloy 661). The composition of this alloy is close to that of the early variation of Nimonic 80. (For comparison, for each micrograph the corresponding Rockwell B hardness is listed.)

After aging for 1 and 20 hr at 1250°F, Fig. 5a and b, there was evidence of recrystallization along the grain boundaries, probably as a consequence of the plastic strains caused by the precipitation stresses, resulting in what appears to be grain boundary migration. This kind of recrystallization was observed quite frequently in the alloys containing titanium, but never in alloys without titanium additions. This observation supports the other data that the stresses associated with the precipitation of γ'

Fig. 2—Composition of low carbon alloys used for aging studies. Numbers appearing above the circles indicate the respective alloy numbers. The dotted lines are tentative saturation temperatures based on the microstructural appearances after aging.

are increased by substitution of titanium for aluminum in Ni_3Al, as shown by the lattice parameter data presented in Table II. The difference between the lattice parameter of the matrix and the γ' phase, and thus the misfit between the lattices of the two phases, increased with the substitution of titanium for aluminum. After aging 480 hr at 1250°F there was evidence of heavy, although submicroscopic, precipitation along the grain boundaries and within the grains, Fig. 5c. The finely dispersed dark spots in the grains are due to the etch attack, around each precipitated particle. During aging at 1450°F for 540 hr, growth to particles visible at X500 had occurred along the grain boundaries but growth of the particles within the grains was limited, see Fig. 6d. Aging at 1650°F for increasing periods of time caused no significant changes in the microstructure, indicating that the saturation temperature had been exceeded almost immediately.

Comparison of the microstructural changes during aging of alloys 684 (3.2 pct Al) and 688 (3.2 pct Ti, 0.8 pct Al) showed that by replacing aluminum with titanium the rate of growth of the precipitate was decreased.

Although the hardness and electrical resistance changes during aging were qualitatively similar irrespective of the titanium to aluminum ratio of the alloys, Figs. 7 and 8 show that the substitution of titanium for aluminum did modify the time-temperature relationships for the changes noticeably: the hardness for a given time at temperature was higher and the initial increase in electrical resistance was more marked in the alloys containing both titanium and aluminum as compared to the

Table II. Lattice Parameter of the Phases in Alloys Containing Aluminum With or Without Titanium. Alloys Aged 500 Hr at 1450°F

Alloy No.	Composition	Lattice Parameter	
		Matrix	Second Phase
684	3.2% Al	3.57 kX	3.575 kX
690	2.3% Ti; 2.1% Al	3.57 kX	3.59 kX
688	3.2% Ti; 0.8% Al	3.57 kX	3.60 kX

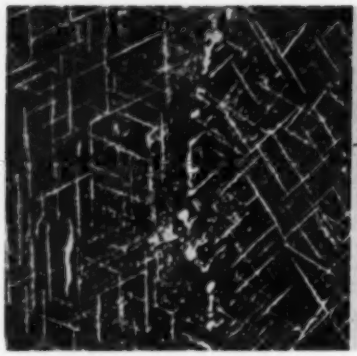

Fig. 3—Alloy 692. 3.7 pct Ti, aged 430 hr at 1650°F. Etchant C. X500.

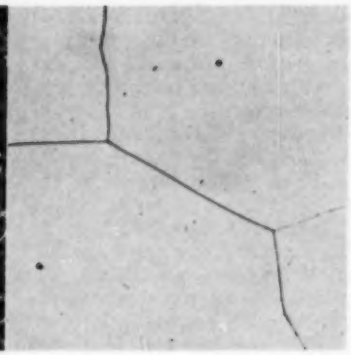

Fig. 4—Alloy 661. 2.2 pct Ti, 0.9 pct Al, solution treated at 2000°F. Etchant B. 65 R_B. X500.

a—Aged 1 hr at 1250°F. R_B, 80. b—Aged 20 hr at 1250°F. R_B, 90. c—Aged 480 hr at 1250°F. R_B, 102.

Fig. 5—Alloy 661. 2.2 pct Ti, 0.9 pct Al. Etchant A. X500.

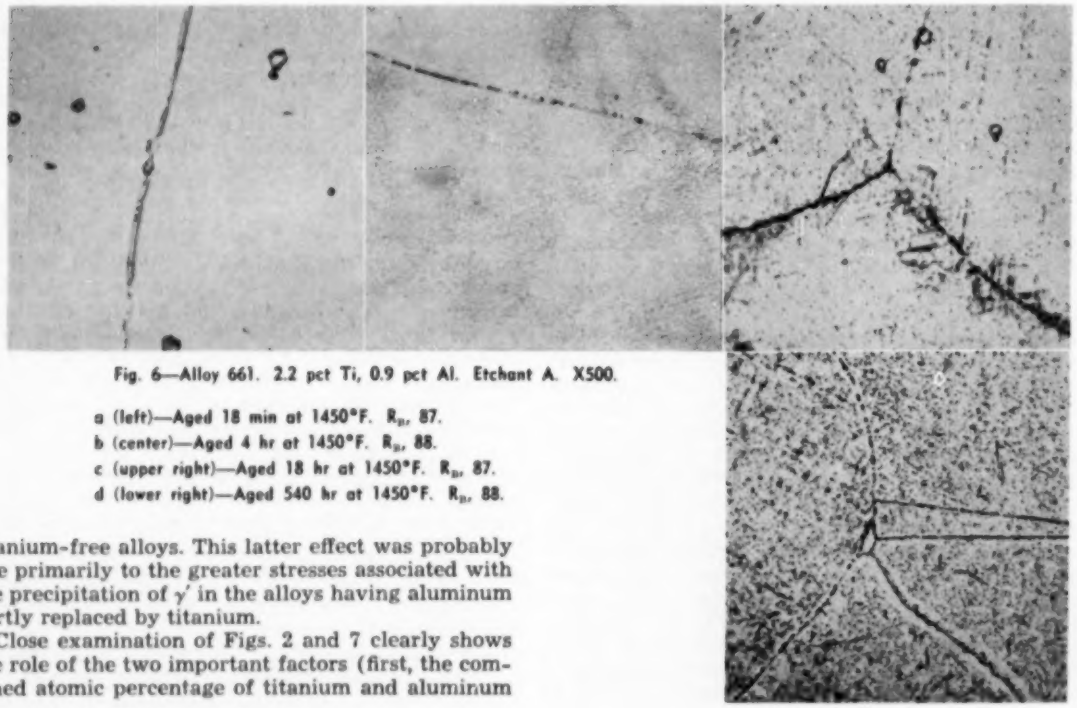

Fig. 6—Alloy 661. 2.2 pct Ti, 0.9 pct Al. Etchant A. X500.

a (left)—Aged 18 min at 1450°F. R_B, 87.
b (center)—Aged 4 hr at 1450°F. R_B, 88.
c (upper right)—Aged 18 hr at 1450°F. R_B, 87.
d (lower right)—Aged 540 hr at 1450°F. R_B, 88.

titanium-free alloys. This latter effect was probably due primarily to the greater stresses associated with the precipitation of γ' in the alloys having aluminum partly replaced by titanium.

Close examination of Figs. 2 and 7 clearly shows the role of the two important factors (first, the combined atomic percentage of titanium and aluminum

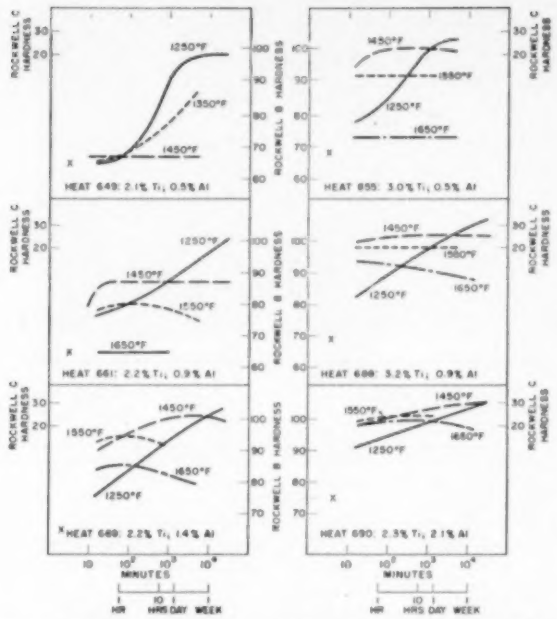

Fig. 7—Change in the hardness of alloys 649, 661, 689, 855, 633, and 690 during aging at 1250° to 1650°F. X represents the hardness for solution treated structure.

on the saturation temperature, and second, the substitution of titanium for aluminum on the rate of overaging) on the hardness curves of the various alloys as a function of time at temperature. As the total aluminum plus titanium content increases, in the order of alloys 649, 661, 855, 689, 688, and 690, the hardness at each temperature is higher and overaging (as measured by hardness) occurs progressively more slowly. The curves in Fig. 7 are based on many points at each temperature; the points were omitted for the sake of clarity. The deviation of points (average of at least three readings) was less than 2 hardness numbers from the curves shown.

Alloys 661 (2.2 pct Ti, 0.9 pct Al) and 855 (3.0 pct Ti, 0.5 pct Al) have about the same total atomic percentage of the two elements and have about the same saturation temperatures (see Fig. 2). Fig. 7 shows, however, that the increased titanium content is more significant in imparting hardness at the higher temperatures than is aluminum. This is probably due to the decreased rate of growth of the precipitate caused by the replacement of some of the aluminum by titanium.

Typical electrical resistance curves (at temperature) are shown in Fig. 8. They indicate a similar behavior to that shown by the hardness curves but were more difficult to interpret. Such resistance curves were used to confirm the hardness data for all the alloys and served as a simple check; however, they were not entirely useful by themselves, without supporting data of other types.

Reference to Fig. 7 shows that the hardness of alloy 661 (2.2 pct Ti, 0.9 pct Al) did not change during aging at 1650°F. This is in agreement with the results of the microstructural examinations, discussed previously, which indicated that 1650°F is above the saturation temperature for alloy 661.

On the basis of the hardness curves for alloy 661 and the tentative saturation temperatures shown in Fig. 2, it can be seen why the strength of the early Nimonic 80 variation (2.0 to 2.5 pct Ti, 0.7 to 1.0 pct Al) dropped so sharply when the service temperature was increased to 1500°F, or higher. To increase the useful service temperature of the Nimonic 80 type alloys the total solute content should be increased according to the increase in solubility with temperature.

Precipitation of η: Fig. 9 shows the course of precipitation of η from alloy 692 (3.7 pct Ti) at 1450°F. After aging 540 hr, the needlelike particles could clearly be resolved at a magnification of X500. During aging at 1650°F, however, the particles grew within a few hours to a size visible under an optical microscope. Fig. 3 shows the microstructure after aging 430 hr at 1650°F.

Precipitation of η in alloy 692 was characterized by a noticeable incubation period for the changes in hardness and electrical resistance, Fig. 10. (At 1650°F the hardness readings were scattered randomly around 75 Rockwell B.) Such an incubation period was not observed during precipitation of γ' from alloys having a saturation temperature approximately equal to that for alloy 692. (Compare, for example, Fig. 10 with the hardness and electrical resistance curves for alloy 661, Figs. 7 and 8.) This difference in the hardness and resistivity changes of the two types of alloys might be explained by consideration of the precipitation processes for the γ' and the η phases. Whereas the nucleation of γ' involves only a segregation and an ordering of the titanium and aluminum atoms, the formation of a nucleus of η requires in addition a restacking of the close-packed layers from the face-centered cubic to the hexagonal arrangement. Furthermore, as was shown by Taylor and Floyd,[6, 4] η dissolves practically no chromium and nickel, whereas γ' dissolves a considerable portion of chromium and some nickel.

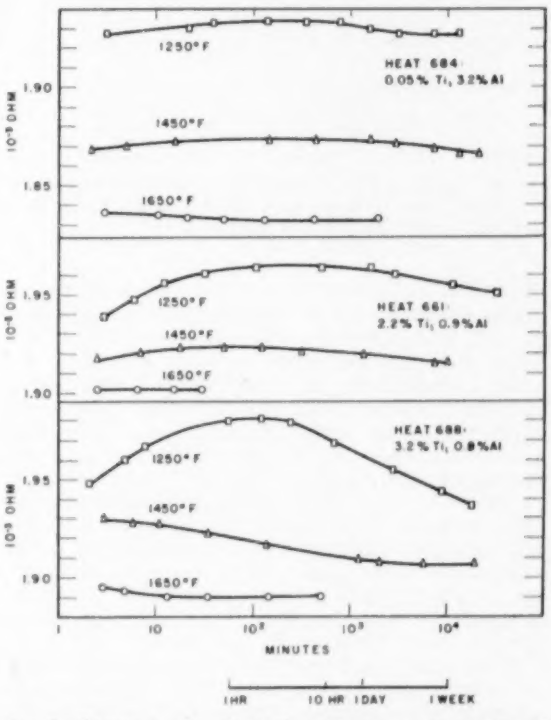

Fig. 8—Change in the electrical resistance at temperature of alloys 661, 684, and 688 during aging at 1250° to 1650°F.

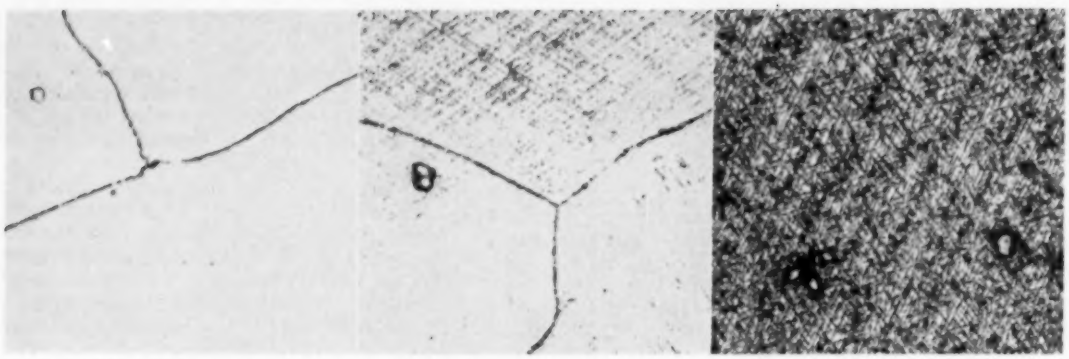

a—Aged 1 hr at 1450°F. R_B, 72. b—Aged 4 hr at 1450°F. R_B, 76. c—Aged 540 hr at 1450°F. R_B, 104 (R_C, 28).

Fig. 9—Alloy 692. 3.7 pct Ti. Etchant A. X500.

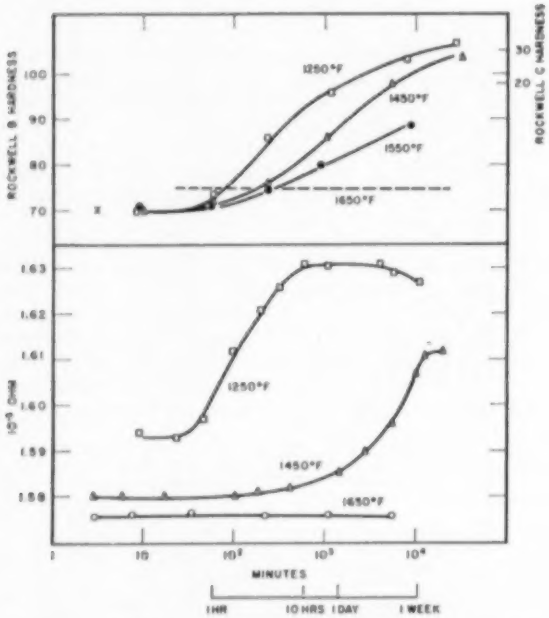

Fig. 10—Change in the hardness and the electrical resistance of alloy 692 (3.7 pct Ti) during aging at 1250° to 1650°F. X represents the hardness after solution treatment.

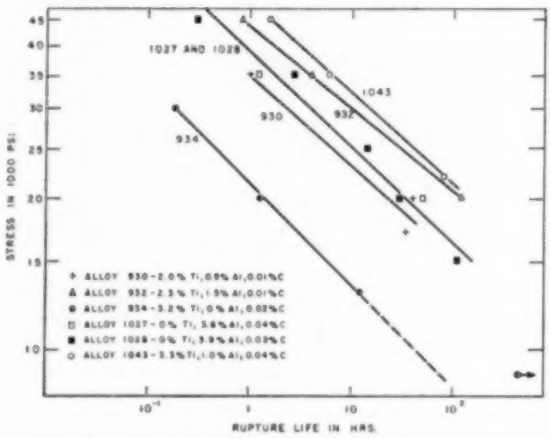
1027 AND 1028
1043
932
930
934
STRESS IN 1000 PSI
RUPTURE LIFE IN HRS.
ALLOY 930 - 2.0% Ti, 0.9% Al, 0.01%C
ALLOY 932 - 2.3% Ti, 1.5% Al, 0.01%C
ALLOY 934 - 3.2% Ti, 0% Al, 0.02%C
ALLOY 1027 - 0% Ti, 3.8% Al, 0.04%C
ALLOY 1028 - 0% Ti, 3.9% Al, 0.02%C
ALLOY 1043 - 3.3% Ti, 1.0% Al, 0.04%C

Fig. 11—Stress vs rupture life for alloys solution treated 8 hr at 2000°F (air cooled) and aged 16 hr at 1300°F. Test temperature 1500°F.

Thus, for the formation of η the composition requirements are more strict than for the precipitation of γ'. It is expected therefore that the nucleation of η is a slow process compared with that of γ', and when a nucleus of η is formed, further depletion of the neighborhood matrix will take place more easily by growth of this nucleus than by formation of new ones. As a result, the number of η particles formed during the early part of the aging treatment was relatively small, and the interparticle distance large. Consequently, the associated changes in hardness and electrical resistance were small, or not at all noticeable. As the aging period increased, the number of precipitated particles increased, which decreased their spacing. Ultimately, increases in both hardness and resistance were observed.

Stress Rupture Tests: Fig. 11 is a log-log plot of stress vs rupture life at 1500°F for some wrought alloys with compositions similar to those alloys discussed in the previous sections. Before testing, the rupture bars were solution treated for 8 hr at 2000°F, air cooled, and aged for 16 hr at 1300°F. This heat treatment is close to that recommended for Nimonic 80 by Mond Nickel Co.[9]

For the alloys hardened by precipitation of γ' the fracture was a combination of transcrystalline and intercrystalline at the higher stress levels and

Table III. Elongation at Rupture for Alloys Tested at 1500°F

Stress	Alloy 930 2.0% Ti, 0.9% Al	Alloy 932 2.3% Ti, 1.5% Al	Alloy 934 3.2% Ti	Alloy 1027 3.8% Al	Alloy 1028 3.9% Al	Alloy 1043 3.3% Ti, 1.0% Al
Solution Treated 8 Hr at 2000°F and Aged 16 Hr at 1300°F						
45,000		4.0			18.0	1.0
35,000	6.0	2.0		17.5	9.5	1.0
30,000			35.0			
25,000					9.0	
22,000						1.0
20,000	6.0	3.0	23.5	2.0	3.0	
13,000			25.0			
Solution Treated 4 Hr at 2000°F and Aged 20 Hr at 1450°F						
60,000						3.5
45,000				15.5		5.0
35,000				8.5		1.0
22,500						1.0
20,000				2.0		2.0
Solution Treated 4 Hr at 2000°F and Aged 20 Hr at 1560°F						
60,000						7.5
45,000						5.0
35,000						2.0
20,000						3.0

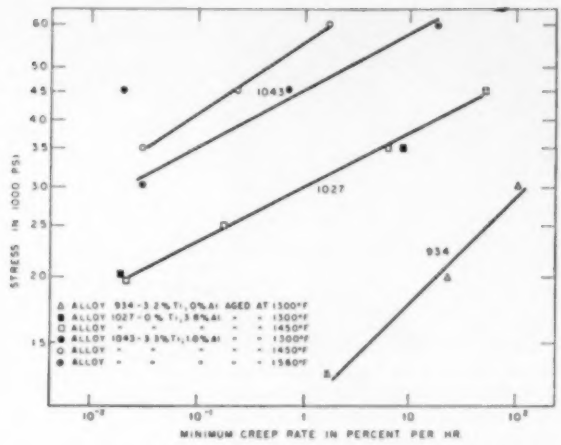

Fig. 12—Stress vs minimum creep rate for alloys with the following combinations of solution and aging treatments: Solution treated 8 hr at 2000°F (air cooled) and aged 16 hr at 1300°F; solution treated 4 hr at 2000°F (water quenched) and aged 20 hr at 1450°F; solution treated 4 hr at 2000°F (water quenched) and aged 20 hr at 1560°F. Test temperature 1500°F.

mainly intercrystalline at 20,000 psi or lower. The curves for alloys 1027 (3.8 pct Al), 1028 (3.9 pct Al), and 1043 (3.3 pct Ti, 1.0 pct Al) confirm the observations that were made regarding the increased strengthening effect obtained by replacing aluminum in part by titanium. Such substitution also decreased the creep rate (Fig. 12), the elongation at rupture (Table III), and the tendency to transcrystalline fracture. Fig. 11 also demonstrates the effect of an increase in the solute content of the alloys. Compare the progressively improved rupture strengths of alloys 930 (2.0 pct Ti, 0.9 pct Al), 932 (2.3 pct Ti, 1.5 pct Al), and 1043 (3.3 pct Ti, 1.0 pct Al).

The rupture lives obtained during these tests are somewhat lower than expected from data published for commercial alloys. For a Nimonic 80 alloy with 2.5 pct Ti and 0.8 pct Al, the 100 hr rupture strength at 1500°F was 21,000 psi,[10] and higher values have been reported for alloys with higher solute content. It was thought that the lower strength observed during the present investigations was in part due to the large grains which occasionally occurred in the structure, Fig. 13. In an attempt to reduce the amount of abnormal grain growth taking place during the solution treatment, a series of test bars were solution treated for only 4 hr. These bars were water quenched from the solution temperature (2000°F). Furthermore, to produce, if possible, a more stable structure the aging temperature was increased to 1450°F, the aging period being 20 hr. The results of stress rupture tests of alloys 1027 (3.8 pct Al) and 1043 (3.3 pct Ti, 1.0 pct Al) heat treated in this manner, are reproduced in Figs. 12 and 14. Whereas the change in heat treatment had no effect on the rupture and creep strengths of alloy 1027, which contains only aluminum, it increased significantly the rupture strength from 21,000 to 25,000 psi for 100 hr at 1500°F, and decreased the creep rate of alloy 1043. For alloy 1043 the 4 hr-2000°F solution treatment, 20 hr-1450°F aging treatment also resulted in greater rupture elongation at the higher stress levels, Table III. Similar changes were observed for alloy 661 (2.0 pct Ti, 0.9 pct Al).

This change in the rupture characteristics of alloy 661 and 1043 cannot be a grain size effect because the grain size range and the grain size distributions after the two different combinations of solution and aging treatments were practically the same. Most probably the improvement in rupture strength is related to the increased aging temperature. The 1300°F aging treatment might have strengthened the grains to such an extent that stress concentrations could not be released by local deformation within the grains. This would cause early rupture with little elongation. On the other hand, aging at 1450°F might probably result in a somewhat softer (see Fig. 7), less critically strained structure capable of some deformation, as evidenced by the higher creep rate in spite of the longer rupture life.

To determine the effect of a further increase in the aging temperature for alloy 1043, one series of test bars was aged at 1560°F for 20 hr after a 4 hr solution treatment. Compared with the 1450°F aging treatment, the 1560°F treatment gave the same high rupture strength, but a higher creep rate and rupture elongation (see Fig. 12 and Table III). This again is in line with the concept of a less critically strained structure.

In Figs. 11 and 12 are also plotted the rupture and creep strengths of alloy 934 (3.2 pct Ti) which was

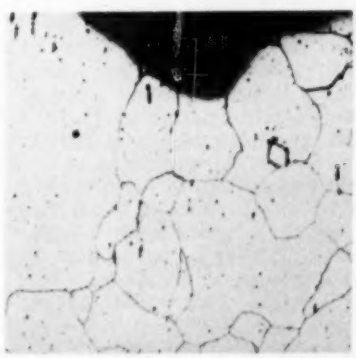

Fig. 13—Alloy 1043. 3.3 pct Ti, 1.0 pct Al. Solution treated 8 hr at 2000°F (air cooled) and aged 16 hr at 1300°F (air cooled). Fracture zone of rupture bar tested at 1500°F and 45,000 psi. Etchant A. X75.

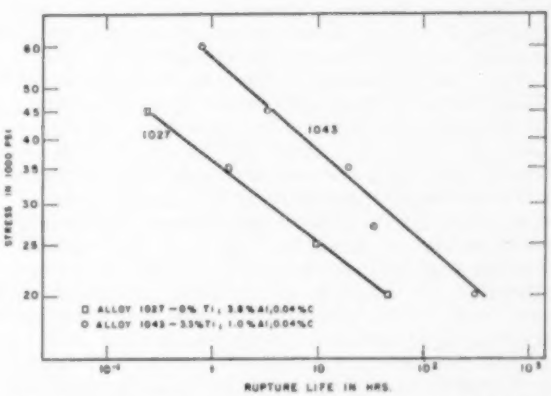

Fig. 14—Stress vs rupture life for alloys solution treated 4 hr at 2000°F (water quenched) and aged 20 hr at 1450°F. Test temperature 1500°F.

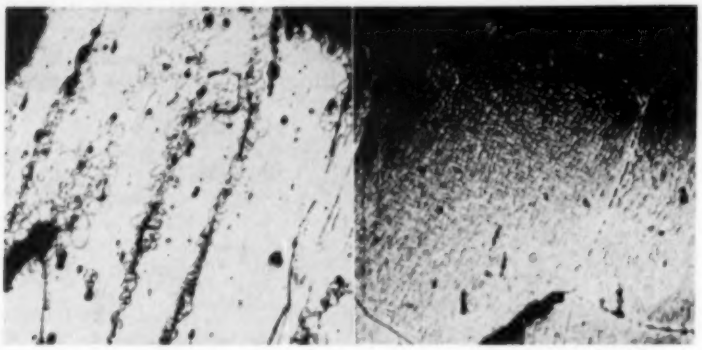

a—Fracture zone of rupture bar tested directly at 1500°F and 20,000 psi. 1.2 hr rupture life and 23.5 pct elongation. X150.

b—Fracture zone of rupture bar tested at 1500°F and 9000 psi for 431 hr without fracture. 1.1 hr at 20,000 psi to fracture. Total elongation, 6.5 pct. X250.

Fig. 15—Alloy 934. 3.2 pct Ti. Solution treated 8 hr at 2000°F (air cooled) and aged 16 hr at 1300°F (air cooled). Etchant A.

hardened by precipitation of η. The high temperature short time strength of this alloy was much lower than that for any of the alloys hardened by γ', probably because of the lower rate of nucleation of η.

Fig. 11 shows, however, that a specimen tested at 9000 psi lasted considerably longer than that expected from the extrapolation of the short time data. Presumably appreciable further precipitation occurred during the rupture test and resulted in an increase in the strength of this alloy (cf., Fig. 10 which shows that the hardness of alloy 692, 3.7 pct Ti, was still increasing even after 540 hr at 1450°F). After 431 hr at 9000 psi (the specimen was unbroken) with a total creep strain of 6 pct, the stress was increased to 20,000 psi. Without much further elongation, the specimen broke after 1.1 hr. The total elongation was 6.5 pct compared with 23.5 pct for a bar stressed directly at 20,000 psi. Fig. 15a and b shows the fracture zones for these two test bars. The heavy precipitation which had occurred during the 431 hr exposure at 9000 psi was evidently sufficient to prevent any marked deformation when the stress later was raised to 20,000 psi. Note the presence of the intergranular cracking in Fig. 15b.

Conclusions

The present investigation has confirmed the statement by Hignett[2] that the titanium and aluminum hardened Ni-Cr alloys of the Nimonic 80 type owe their high strength to the precipitation of an intermetallic compound based on the cubic Ni_3Al phase, γ', but with aluminum partly replaced by titanium. This substitution, which increases the misfit between the lattices of the γ' phase and the matrix, raises the creep and rupture strength of the alloys. This increase in strength was accompanied by a relatively large decrease in ductility. It was found, however, that by raising the aging temperature of the high titanium alloys their ductility can be improved without any loss or even with a gain in rupture strength. Substitution of titanium for aluminum appears to decrease the rate of growth and coalescense of γ', resulting in stronger alloys.

When the titanium to aluminum ratio of the alloys is increased beyond the solubility limit for titanium in Ni_3Al, the hexagonal Ni_3Ti phase, η, starts to precipitate. The precipitation rate of η is slow, as indicated by hardness; therefore the increase in strength due to precipitation of this phase occurs very slowly and may not be achieved at all in short time or intermediate length tests.

To raise the useful service temperature for the Ni-Cr type alloys, it is suggested that the titanium to aluminum ratio be increased toward the end of the homogeneity range for γ', and the sum of the titanium and aluminum contents should be increased within the limits permitted by fabrication or processing.

Acknowledgments

The authors express their thanks to Mrs. Gloria Johnson and Mr. Philip Manganaro for extensive assistance. The authors deeply appreciate the initial support of the Bureau of Ships and the support of the Office of Naval Research, which permitted the completion of the work.

References

[1] B. M. Rosenbaum: Nat. Advisory Comm., Aeronaut., Tech. Note 1580, (July 1948).

[2] H. W. G. Hignett: High Temperature Alloys in British Jet Engines. Lecture presented before the Detroit Chapter of ASM on Nov. 12, 1951, (reprinted by the International Nickel Co., Inc.).

[3] A. Taylor and R. W. Floyd: The Constitution of Nickel-rich Alloys of the Nickel-Chromium-Titanium System. *Journal* Inst. Metals (1951-1952) **80**, p. 577.

[4] A. Taylor and R. W. Floyd: The Constitution of Nickel-rich Alloys of the Nickel-Chromium-Aluminum System. *Journal* Inst. Metals (1952-1953) **81**, p. 451.

[5] A. Taylor and R. W. Floyd: The Constitution of Nickel-rich Alloys of the Nickel-Titanium-Aluminum System. *Journal* Inst. Metals (1952-1953) **81**, p. 25.

[6] L. B. Pfeil, H. P. Allen, and C. G. Conway: Nickel-Chromium-Titanium Alloys of the Nimonic 80 Type. Paper in *High Temperature Steels and Alloys for Gas Turbines*. Iron Steel Inst. (London), Special Report No. 43 (1951).

[7] A. J. Bradley and A. Taylor: An X-ray Analysis of the Nickel Aluminum System. *Proc.* Royal Soc., London (1937) **159A**, p. 56.

[8] L. Pauling: Atomic Radii and Interatomic Distances in Metals. *Journal* ACS (1947) **69**, p. 542.

[9] The Nimonic Series of Alloys—Their Application to Gas Turbine Design. Mond Nickel Co., Ltd., London (1948).

[10] G. H. Boss: Approximate Strength of Important Jet Engine Alloys. *Metals Progress* (November 1951) **60**, p. 80B.

A Cursory Investigation of Intermediate Phases in the Systems Ti-Zn, Ti-Hg, Zr-Zn, Zr-Cd, and Zr-Hg by X-Ray Powder Diffraction Methods

by Paul Pietrokowsky

Intermediate phases in the binary metal alloy systems Ti-Zn, Ti-Hg, Zr-Zn, Zr-Cd, and Zr-Hg have been investigated by X-ray powder diffraction methods. Gamma-Ti_3Hg and Zr_3Hg have a beta tungsten structure; TiHg and ZrHg are analogous to ordered AuCu (L 1_0 type); delta-Ti_3Hg and $ZrHg_3$ are isomorphous with ordered $AuCu_3$ (L 1_2 type); $ZrZn_2$ is face-centered cubic (C 15 type); $TiZn_2$ crystallizes in a C 14 type structure; and $Zr_{(1-x)}Cd_{(x)}$ occurs in cubic and tetragonal modifications in which a random distribution of atoms exists. Additional information for the intermediate phase $TiZn_3$ is presented.

THE physical metallurgy of titanium and zirconium when alloyed with elements in subgroup II-B of the periodic table has received comparatively little attention in the literature. Laves and Wallbaum[1] reported the existence of several intermediate phases in the system Ti-Zn. They identified TiZn as a CsCl (B 2) structure and described $TiZn_3$ as an ordered Cu_3Au (L 1_2 type) crystal structure. Gebhardt[2] investigated very limited zinc-rich regions in the systems Ti-Zn and Zr-Zn. Phase relationships in these partial constitution diagrams were deduced from the results of thermal analysis and metallography, X-ray results being inconclusive. The first zinc-rich intermediate phase in either system was not identified. More recently, Anderson, Boyle, and Ramsey[3] have had occasion to refer to a partial Ti-Zn phase diagram (unpublished data) covering the region 0 to 10 atomic pct Ti, wherein two intermediate phases corresponding approximately to $TiZn_{15}$ and $TiZn_{10}$ were indicated.

The metals used in this investigation and typical analyses as determined by the suppliers are given in Table I. The iodide-process zirconium which was used was not hafnium free.

Table I. Materials Used

Metal	Supplier	Analysis	
Zn	J. T. Baker Chemical Co.	As	1×10^{-4} pct
		Pb	3×10^{-4} pct
		Fe	3×10^{-5} pct
Cd	J. T. Baker Chemical Co.	Cu	8×10^{-5} pct
		Pb	1×10^{-2} pct
		Fe	2×10^{-5} pct
Hg	Braun Corp.	Triple distilled	
Ti	New Jersey Zinc Co.	Mn	6.5×10^{-4} pct
		Fe	2.2×10^{-3} pct
		Cu	1.5×10^{-3} pct
		Pb	4.2×10^{-4} pct

Experimental Methods

Alloy Preparation: The relative ease with which titanium and zirconium combine with other elements places extensive restrictions on the methods by which alloying can be achieved. The direct current electric arc melting procedure was found to be unsatisfactory for preparing these binary alloys and for this reason solid state diffusion methods were utilized.

The iodide process titanium and zirconium rods were filed by hand. Fines were subjected to a magnetic separation and classified as to size as either finer than 200 mesh or coarser than 200 but finer than 80 mesh. Powder mixtures of various binary combinations of titanium and zirconium with zinc and cadmium were compacted in a 12 mm diameter die and then placed in Vycor or quartz vials which were evacuated and sealed. The mercury alloys were prepared in a similar manner; the proper weight of liquid mercury being placed in a vial with minus 200 mesh titanium or zirconium. These ampoules were then heat treated at various temperatures and times depending on the characteristics of the particular alloy system. Upon completion of the heat treatment the ampoules were cooled rapidly and the specimens weighed. The loss in weight varied from 1 to 3 pct (except as noted in the text) and for this reason the calculated compositions were accepted as a fair measure of the actual alloy compositions.

X-Ray Diffraction Techniques: Powder diffraction experiments were conducted at room temperature with a 143.2 mm Debye-Scherrer X-ray camera in which the film was placed in the Straumanis arrangement. When copper radiation was used, a nickel filter was employed, and for the cobalt target a filter of iron oxide was used. In both cases, the β filter was placed between the X-ray target and the powder specimen which was mounted on a glass fiber.

The lack of information based on optical metallography placed reliance on the results obtained from the X-ray experiments for determination of

P. PIETROKOWSKY, Junior Member AIME, is Research Engineer, Jet Propulsion Laboratory, California Institute of Technology, Pasadena, Calif.

Discussion on this paper, TP 3716E, may be sent, 2 copies, to AIME by April 1, 1954. Manuscript, July 17, 1953. New York Meeting, February 1954.

Table II. Lattice Constants, Interatomic Distances, and Atomic Volumes for Titanium, Zirconium, Zinc, Cadmium, and Mercury

Element	Lattice Constants, A	Interatomic Distances, A	Atomic Volume, A³	Reference
Ti	$a = 2.9503$ $c = 4.6832$ $c/a = 1.587$	2.8935 2.9503	17.65	12
Zr	$a = 3.2321 \pm 0.0001$ $c = 5.1475 \pm 0.0004$ $c/a = 1.592$	3.1790 3.2321	23.29	13
Zn	$a = 2.6595 \pm 0.0001$ $c = 4.9369 \pm 0.0001$ $c/a = 1.856$	2.6595 2.9070	15.12	14
Cd	$a = 2.9731 \pm 0.0001$ $c = 5.6069 \pm 0.0005$ $c/a = 1.886$	2.9731 3.287	21.46	14
Hg	$a = 2.999$ (227° Abs.) $\alpha = 70° 31.7'$	2.999	22.53*	8, 15

* Explanation in text.

Table III. X-Ray Powder Diffraction Data for $ZrZn_2$. Copper Radiation.

d, A	hkl	I (Obs.)*	I (Calc.)†
2.63	220	s	390
2.23	311	vs	1000
2.13	222	ms	291
1.85	400	w	13
1.51	422	m	133
1.428	511–333	s	297
1.306	440	s	238
1.168	620	m_{α_1}	56
1.127	533	s_{α_1}	103
1.115	622	s_{α_1}	101
0.9883	642	m_{α_1}	83
0.9624	731–553	vs_{α_1}	243
0.9244	800	w_{α_1}	60
0.8718	822–660	m_{α_1}	54
0.8541	555–751	s_{α_1}	188
0.8482	662	m_{α_1}	98
0.7885	664	s_{α_1}	100
0.7752	931	vs_{α_1}	755

* vs, very strong; s, strong; ms, medium strong; m, medium; wm, weak medium; w, weak; and vw, very weak. Miller and Miller-Bravais indices without a subscript refer to unresolved $K\alpha_1$, $K\alpha_2$ doublets; subscript α_1 represents the coincidence of a $K\alpha_1$ reflection with the $K\alpha_2$ from a plane of larger interplanar spacing. Letter "A" was used to indicate that an absorption correction would be necessary before the particular calculated intensity could be compared with adjacent maxima.

† To conserve space, calculated intensities too weak to be observed were omitted, except as discussed in the text.

the intermediate phases. When the Debye-Scherrer X-ray powder technique is employed only a relatively small volume of diffracting material is irradiated, hence questions may arise as to whether the small sample which has been examined is representative of the alloy in bulk. For this reason, whenever possible, a Geiger counter spectrometer employing a divergent beam was used in conjunction with the powder rod method. The source of X-rays for the spectrometer was a line focus which, together with the slit system, resulted in an irradiated area, dependent upon the Bragg angle, approximately 11 by 6 mm.

Calculations

Lattice Parameters: In this investigation, the least-squares method was used to determine unit cell dimensions, since it yields less biased values for the parameters and in addition permits the probable error in these measurements to be calculated. The weighted observational equation for the i^{th} reflection of a tetragonal crystal can be written

$$\sqrt{w_i}\sin^2\theta_i = \sqrt{w_i}\,A_o\,\alpha_i + \sqrt{w_i}\,B_o\,\beta_i + \sqrt{w_i}\,D\,\delta_i \ldots \quad [1]$$

where $A_o = (\lambda/2a)^2$; $B_o = (\lambda/2c)^2$; $\alpha_i = h_i^2 + k_i^2 + h_i k_i$; $\beta_i = l_i^2$; λ is the wavelength of the characteristic radiation; D is a proportionality constant; $\delta_i = \delta_i(\theta)$; $w_i = w_i'/\cos^2\theta_i$ = weight function.

The function $\delta_i(\theta)$, which was used, is that suggested by the investigation of Nelson and Riley[4] for cubic crystals; this graphical method of analysis was extended to nonisometric systems of crystals by Taylor and Floyd.[5] An auxiliary weight function, w_i', was assigned integral values, 1, 2, 3, or 4, depending upon the quality of the diffracted maxima. Factors which would influence the reliability of the measurements, such as very low intensity, line broadening produced by a near coincidence of reflections, and line broadening prior to $K\alpha_1$, $K\alpha_2$ doublet resolution, were considered in assigning values to this function. Normal equations were written in the usual manner. Methods for solving these equations are discussed by Whittaker and Robinson.[6] When the determinant form is used the standard errors may be calculated from the residuals and coefficients of the determinant. Errors so determined reflect upon the accuracy of the data and do not include those uncertainties which are imposed by the variation in specimen temperature during an X-ray exposure and chemical impurities. The accuracy obtained from the least-squares analysis varied from approximately 1 part in 50,000 to 1 part in 300. The high precision which was obtained may not be too significant although it does indicate that the experimental and analytical procedures used are capable of accurate results.

Wavelengths which were used for calculations are those suggested by Lonsdale.[7]

Intensities: Calculated intensities for the diffraction maxima corresponding to the crystal structures were obtained by application of the following expression for the intensity of a Debye-Scherrer powder photograph maxima:

$$\text{Intensity } (hkl) = \text{constant } |F\,(hkl)|^2 p\,\frac{1+\cos^2 2\theta}{\sin^2\theta\cos\theta} \quad [2]$$

where $F\,(hkl)$ is the structure factor; p is the multiplicity of (hkl); and $(1 + \cos^2 2\theta)/(\sin^2\theta\cos\theta)$ is the Lorentz and polarization factor.

Temperature and absorption factors have been omitted from Eq. 2. The former is a decreasing exponential function and the latter an increasing exponential function. For the structures which were considered in this paper, these factors would tend to nullify one another, although the absorption would exert more influence upon the intensity.

Unit Cell Content: For unit cells of moderate size, with which this investigation was concerned, an approximate value for the density of an alloy is sufficient to establish the number of atoms which are present in the unit cell. Values of atomic volumes which were used for calculations are given in Table II. The volume per atom given for mercury represents an approximate volume based on the

Table IV. Interatomic Distances for $ZrZn_2$

Atom	Neighbors	Distance, A
Zn (d)	6 Zn (d)	2.61
Zr (a)	12 Zr (a)	3.07
Zn (d)	4 Zr (d)	3.20

extrapolation of unit cell volumes in the system Cd-Hg which have been summarized.[4] It is the average of atomic volumes of the cadmium-rich hexagonal phase and mercury-rich tetragonal phase when extrapolated to 100 pct Hg.

Results

System Zr-Zn: An intermediate phase in this binary system was found close (65 atomic pct Zn) to the stoichiometric ratio expressed by the formula $ZrZn_2$. X-ray diffraction maxima of powder samples of this phase were indexed as a face-centered cubic lattice; $a = 7.3958 \pm 0.0003$Å.

A survey of the indexing presented in Table III indicates the following systematic reflections:

$$(hkl) \text{ with } (h + k), (k + l) = 2n$$
$$(hkO) \text{ with } (h + k) = 4n.$$

From these observations, one is led to the space group $O^7_h - Fd3m$, which has all the symmetry elements required by the data. The number of atoms in the unit cell is 8 zirconium and 16 zinc. The zirconium atoms can be placed in the eight-fold positions (*a*) or (*b*) of space group *Fd3m*. Similarly, the 16 zinc atoms may be placed in either (*c*) or (*d*). A solution based on 8 zirconium in (*a*) and 16 zinc in (*c*) or 8 zirconium in (*b*) and 16 zinc in (*d*) cannot be accepted, because the zirconium to zinc interatomic distances would be unreasonably small. A packing of atoms involving either 8 zirconium in (*a*) and 16 zinc in (*d*) or 8 zirconium in (*b*) and 16 zinc in (*c*) is acceptable. The former mode of packing differs from the latter by a translation of the origin from (000) to ($\frac{1}{2}\frac{1}{2}\frac{1}{2}$). Intensities were calculated with the unit cell content distributed as follows:

000; $0\frac{1}{2}\frac{1}{2}$; $\frac{1}{2}0\frac{1}{2}$; $\frac{1}{2}\frac{1}{2}0$; +

8 Zr in (*a*): 000; $\frac{1}{4}\frac{1}{4}\frac{1}{4}$;

16 Zn in (*d*): $\frac{5}{8}\frac{5}{8}\frac{5}{8}$; $\frac{5}{8}\frac{7}{8}\frac{7}{8}$; $\frac{7}{8}\frac{5}{8}\frac{7}{8}$; $\frac{7}{8}\frac{7}{8}\frac{5}{8}$.

Results of the intensity calculations are in order except for the single reflection from (800) and the coincidence of reflections from (822) and (660). It is apparent that the effect of absorption must be considered in comparing these intensities since an appreciable difference in sin θ/λ for these spectra does exist. Table IV gives the interatomic distances for $ZrZn_2$.

System Ti-Zn: Although the crystal structure of the zinc-rich compound, $TiZn_3$, of this system has been reported,[1] no data concerning this structure are given except the lattice dimensions, and packing considerations indicate that it is not possible to place one titanium atom and three zinc atoms into the reported unit cell. For these reasons, a brief description of $TiZn_3$ is included here. The indexing for the phase is given in Table V. Observed X-ray reflections may be indexed on a primitive cubic lattice; $a = 3.9322 \pm 0.0003$Å.

If it is assumed that this intermediate phase possesses the crystal structure of ordered $AuCu_3$ (L 1_2 type), then the atoms occupy the following positions of $O^1_h - Pm3m$:

1 Ti in (*a*): 000;
3 Zn in (*c*): $0\frac{1}{2}\frac{1}{2}$; $\frac{1}{2}0\frac{1}{2}$; $\frac{1}{2}\frac{1}{2}0$.

The interatomic distances for $TiZn_3$ are given in Table VI.

A second phase, $TiZn_2$, was found to exist at its ideal composition. An X-ray diffraction photograph made with cobalt radiation was indexed on a hexagonal lattice: $a = 5.064 \pm 0.002$Å; $c = 8.210 \pm 0.002$Å.

The unit cell was calculated to contain 11.9 (i.e., 12) metal atoms, assuming additivity of atomic volumes. The indexing for this intermediate phase, which is given in Table VII, suggests the following systematic reflections are present: (*hhl*) with $l = 2n$.

In the hexagonal system, the space group of highest symmetry consistent with these data is $D^4_{6h} - P6_3/mmc$. Since it had already been determined that $ZrZn_2$ formed an $MgCu_2$ (C 15 type) structure, the possibility that $TiZn_2$ might be similar to $MgZn_2$ or $MgNi_2$ was considered. Friauf[5] regarded D^4_{6h} as the most probable space group for the crystal structure of $MgZn_2$. Intensity calculations for this two

Table V. X-Ray Powder Diffraction Data for $TiZn_3$. Copper Radiation.

d, A	*hkl*	I (Obs.)*
3.93	100	w
2.79	110	w
2.26	111	vs
1.96	200	s
1.75	210	w
1.60	211	w
1.388	220	s
1.312	300-221	w
1.235	310	w
1.184	311	s
1.134	222	ma
0.9823	400	ma
0.9024	331	vsa
0.8790	420	sa
0.8026	422	vsa

* See footnote to Table III.

Table VI. Interatomic Distances for $TiZn_3$

Atom	Neighbors	Distance, A
Zn (c)	8 Zn (c)	2.78
Zn (c)	4 Ti (a)	2.78
Ti (a)	6 Ti (a)	3.93

Table VII. X-Ray Powder Diffraction Data for $TiZn_2$. Cobalt Radiation.

d, A	*hk.l*	I (Obs.)*	I (Calc.)†
4.38	10.0	m	255
4.08	00.2	w	119
3.85	10.1	w	136
2.54	11.0	w	189
2.31	10.3	ms	556
2.19	20.0	vw	89
2.15	11.2	vs	996
2.12	20.1	vs	1000
2.04	00.4	w	225
1.93	20.2	m	321
1.85	10.4	w	152
1.71	20.3	w	111
1.66	21.0	vw	29
—	30.0	—	29
1.419	21.3	m	206
1.379	30.2	m	218
—	00.6	—	37
1.312	20.5	ms	280
1.291	21.4	wm	86
1.270	22.0	ms	263
1.159	20.6	ma	123
1.115	31.3	ma	95
1.090	40.1	ma	111
1.079	22.4	msa	189
1.061	40.2	wa	45
1.045	31.4	wa	49
0.9464	32.3	ma	78
0.9347	41.2	vsa	177
0.9300	22.6	msa	91
0.9131	40.5	sa	140

*† See footnotes to Table III.

Table VIII. Interatomic Distances for $TiZn_2$

Atom	Neighbors	Distance, A
Zn_{II} (h)	2 Zn_{II} (h)	2.48
Zn_I (a)	6 Zn_{II} (h)	2.53
Ti (f)	3 Zn_I (a)	2.96
Ti (f)	3 Ti (f)	3.10

parameter structure were made with atoms being located as follows:

4 Ti in (f): 1/3 2/3 z; 2/3 1/3 $\bar{z}$; 2/3 1/3 ½ + z; 1/3 2/3 ½ − z; z = 1/16

2 Zn_I in (a): 000; 00½

6 Zn_{II} in (h): $x\ 2x\ ¼$; $2\bar{x}\ \bar{x}\ ¼$; $x\ \bar{x}\ ¼$; $\bar{x}\ 2\bar{x}\ ¾$; $2x\ x\ ¾$; $\bar{x}\ x\ ¾$; x = 5/6.

The ideal parameters which have been used constitute a good trial structure as the calculated relative intensities indicate (see Table VII). The absence of (30.0) and (00.6), which calculate to be very weak reflections, suggests that parameter refinement may be necessary for this structure. Calculated intensity for the (00.6) decreases if z is reduced; the intensity of (30.0), however, will decrease in value with either a positive or negative displacement of x from the trial position. What is necessary here is a refinement that will include all the observed data and ($hk.l$) which are susceptible to small variations in z and x. The interatomic distances for $TiZn_2$ are given in Table VIII.

System Zr-Cd: Subsequent to heat treatment at 700°F (371°C) for four days, the zirconium-rich alloys indicated that mixtures of α or α' zirconium (A 3 type) and a cubic phase were present. With increasing cadmium content, but not more than 67 atomic pct Cd, an increase in the relative proportion of the cubic phase resulted. An alloy containing 60 atomic pct Cd gave very strong diffraction lines corresponding to the Cu (A 1 type) structure. There was only one diffraction maximum which could be related to hexagonal close-packed zirconium and that was a very weak reflection from (10.1). Indexed reflections corresponded to a face-centered cubic lattice: a = 4.3768 ± 0.0006Å.

Table IX. X-Ray Powder Diffraction Data for Cadmium-Rich Zr-Cd Intermediate Phases. Copper Radiation.

	Cubic Phase	Tetragonal Phase		
d, A	*hkl*	*hkl*	*HKL*	*I* (Obs.)*
2.52	111	111	101	vs
2.19	200	200	110	s
2.14		002	002	w
1.56		202	112	w
1.54	220	220	200	s
1.326		131	211	vs
1.317	113			s
1.301		113	103	m
1.262	222	222	202	vs
1.102		400	220	w
1.093	400			w
1.074		004	004	vw
1.011		331	301	wm
1.004	331			sm
1.000		313	213	wm
0.9872		420	310	mm
0.9629		402	222	wm
0.9791	420			mm
0.9685		204	114	mm
0.8982		422	312	mm
0.8913	422			sm
0.8859		224	204	wm
0.8493		151	321	mm
0.8421	115–333	333	303	sm
0.8291		115	105	wm
0.7812		440	400	wm

* See footnote to Table III.

Table X. Interatomic Distances for $Zr_{(1-x)}Cd_{(x)}$

Atom	Neighbors	Distance, A
Cubic		
Zr, Cd (a)	12 Zr, Cd (a)	3.10
Zr, Cd (a)	6 Zr, Cd (a)	4.38
Tetragonal		
Zr, Cd (a)	8 Zr, Cd (a)	3.08
Zr, Cd (a)	4 Zr, Cd (a)	3.12

Data obtained from alloys containing 67, 75, and 80 atomic pct Cd indicated that two phases were present, the cubic phase described in the previous paragraph and a second phase whose lines appeared to be split from this cubic phase. Diffraction patterns of the second phase could be fitted to a tetragonal unit cell. Choice of the axial ratio was made by consideration of the intensities of the split lines relative to the index of the corresponding cubic line. Calculated values of $(1/d)^2$ were in good agreement with the observed data. In Table IX the indices *hkl* refer to a four atom tetragonal unit cell, for comparison with the four atom cubic unit cell. The indices *HKL* which were obtained by the lattice transformation described in the next section on Ti-Hg refer to a body-centered tetragonal unit cell containing two atoms: a = 4.4184 ± 0.0004Å; c = 4.3008 ± 0.0006Å.

After 47 days of heat treatment at 700°F (371°C), there was no evidence of the tetragonal intermediate phase in the 67 atomic pct Cd alloy. Binary mixtures containing more than 67 atomic pct Cd lost considerable quantities of cadmium during heat treatment. Lattice constant measurements of the cubic phase showed no change.

The cubic and tetragonal unit cells which have been described each contain four atoms. Intensity data which are given in Table IX may arise from either of two situations: 1—a random distribution of zirconium and cadmium among all available sites, or 2—the location of each chemical species of atoms

Table XI. X-Ray Powder Diffraction Data for TiHg. Copper Radiation.

d, A	*hkl*	*HKL*	*I* (Obs.)*	*I* (Calc.)†
4.04	001	001	s	380
3.00	110	100	s	372
2.41	111	101	vs	1000
2.12	200	110	s	311
2.021	002	002	ms	153
1.879	201	111	s	201
1.676	112	102	ms	137
1.503	220	200	ms	121
1.463	202	112	s	218
1.419	221	201	m	80
1.346	310–003	210–003	m	84
1.276	311	211	s	275
1.227	113	103	ms	120
1.206	222	202	ms	115
1.138	203	113	m	57
1.119	312	212	ms	76
1.062	400	220	m	42
1.028	401	221	m	33
1.004	223–330	203–300	m	47
0.9728	331	301	msm	77
0.9516	313–420	213–310	sm	234
0.9408	402	222	msm	76
0.9257	421	311	mm	67
0.9126	204	114	msm	78
0.8978	332	302	wm	35
0.8611	422	312	sm	180
0.8393	224	204	mm	102
0.8348	510–403	320–223	mm	90
0.8172	511	321	sm	236
0.8079	005–314	005–214	msm	139
0.8046	333	303	msm	142
0.7807	115	105	vsm	354
0.7775	423	313	vsm	415

*† See footnotes to Table III.

Table XII. Interatomic Distances for TiHg

Atom	Neighbors	Distance, A
Ti (d)	8 Hg (a)	2.93
Ti (d)	4 Ti (d)	3.01
Hg (a)	4 Hg (a)	3.01

in a set of crystallographically equivalent positions. The latter configuration of atoms is possible if the reflections from planes of mixed indices are too weak to be detected by the X-ray methods employed. In the case of $TiZn_3$ weak lines are observed from planes with mixed indices; these intensities are proportional to $|f_{Ti} - f_{Zn}|^2$. The choice between the two situations rests on the absolute value of the difference in scattering factors of zirconium and cadmium as compared to titanium and zinc. Tabulated values of the Thomas-Fermi scattering factors,[10] in the direction of the incident beam, indicate a difference in scattering of eight electrons for the elements in each pair of binary systems being considered. As sin θ/λ increases this difference decreases, and at sin θ/λ equal to 0.3, the absolute value of the difference in scattering of zirconium and cadmium atoms is 0.4 electron greater than the corresponding difference for zinc and titanium. A further correction is necessary when the incident radiation λ is in the neighborhood of an absorption edge, λ_K, of an element being irradiated. Corrections for dispersion by K electrons were calculated with the formulae of Hönl.[11] The general expression for a dispersion correction is a complex quantity which is independent of sin θ/λ. For specimens containing zinc, zirconium, and cadmium which are examined with copper X-radiation, λ/λ_K is greater than unity and therefore the imaginary component of this correction is zero. The imaginary component calculated for titanium was so small that it was neglected. The real components of this correction were calculated and indicated that zirconium and cadmium showed a greater difference in scattering factors for all values of sin θ/λ. It is for these reasons that the cadmium-rich Zr-Cd crystal structures which have been reported are considered a random mixture of atoms in all available crystallographic sites. It is not possible, from available evidence, to assign a chemical formula of simple stoichiometric ratio to these intermediate phases. Until this point becomes clarified, the notation $Zr_{(1-x)}Cd_{(x)}$ with $x>0.60$ is suggested. The interatomic distances are given in Table X.

System Ti-Hg: Mercury-rich alloys of titanium were in either a liquid or mushy state. A 60 atomic pct Ti alloy, which had been heat treated at 1200°F (649°C), was solid and stable when in the evacuated ampoule. Immediately after the ampoule was opened, Debye-Scherrer photographs and X-ray spectrometer recordings were made and the diffraction data indexed in the tetragonal system. After several days, liquid mercury began to separate from this alloy; this was accompanied by a pronounced decrease in the resolution of spectrometer lines: $a = 4.256 \pm 0.001$Å; $c = 4.041 \pm 0.001$Å; $c/a = 0.949$.

Atomic volume and packing considerations indicate that four atoms are present in the unit cell which has been described. Under these circumstances, it is not unreasonable to assume an ideal composition of this intermediate phase to be TiHg for purposes of calculation and discussion. The unit cell contents were placed in the special positions of space group D^1_{4h} — C4/*mmm* as indicated:

1 Hg_I in (*a*): 000
1 Hg_{II} in (*c*): ½½0
2 Ti in (*e*): 0½½; ½0½.

Calculated intensities for this crystal structure are given in Table XI. If the vector triple $\mathbf{a}_1\mathbf{a}_2\mathbf{a}_3$, which defines the four atom unit cell, is associated with the indices *hkl*, it is possible, by a simple transformation, to select a two-atom unit cell with a vector triple $\mathbf{A}_1\mathbf{A}_2\mathbf{A}_3$ and indices *HKL*.

$$H = (h + k)/2 \quad K = (h - k)/2 \quad L = l.$$

The transformed cell can be described formally with the notation for space group D^1_{4h} — *P*4/*mmm*:

1 Hg in (*a*): 000
1 Ti in (*d*): ½½½

$a = 3.009 \pm 0.001$Å $c = 4.041 \pm 0.001$Å $c/a = 1.343$.

The interatomic distances for TiHg are given in Table XII.

In the titanium-rich region of this binary system, two intermediate phases, each containing approximately 75 atomic pct Ti, were found to exist. The phase which was stable between 1000° and 1400°F (538° and 760°C) has been designated γ Ti_3Hg. At 1500°F (816°C), the stable phase is δ Ti_3Hg. Powder diffraction lines of the phase δ Ti_3Hg were indexed in the cubic system: $a = 4.1654 \pm 0.0004$Å.

The unit cell so defined must contain four atoms. Experimental measurements yield an atomic volume of 18.07Å³ per atom, as compared to 18.84Å³ per atom when an additive density relationship is assumed. Indexed reflections presented in Table XIII indicate that the lattice is primitive and no systematic extinctions are present. Contents of the

Table XIII. X-Ray Powder Diffraction Data for Delta-Ti_3Hg. Copper Radiation.

d, A	*hkl*	*I* (Obs.)*	*I* (Calc.)†
4.16	100	s	594
2.95	110	s	517
2.40	111	vs	1000
2.07	200	s	470
1.85	210	ms	283
1.69	211	ms	213
1.470	220	s	301
1.386	300–221	m	141
1.317	310	wm	94
1.255	311	s	360
1.199	222	wm	103
1.153	320	w	63
1.112	321	m	114
1.041	400	$w\alpha_1$	54
1.009	410–322	$wm\alpha_1$	96
0.9807	411–330	$wm\alpha_1$	72
0.9550	331	$s\alpha_1$	205
0.9309	420	$s\alpha_1$	208
0.9086	421	$wm\alpha_1$	99
0.8880	332	$w\alpha_1$	52
0.8504	422	$s\alpha_1$	254
0.8331	500–430	$w\alpha_1$	84
0.8172	510–431	$ms\alpha_1$	227
0.8016	511–333	$vs\alpha_1$	519

*† See footnotes to Table III.

Table XIV. Interatomic Distances for Delta-Ti_3Hg

Atom	Neighbors	Distance, A
Ti (c)	8 Ti (c)	2.95
Ti (c)	4 Hg (a)	2.95
Hg (a)	6 Hg (a)	4.17

Table XV. X-Ray Powder Diffraction Data for Gamma-Ti_3Hg. Copper Radiation.

d, A	hkl	I (Obs.)*	I (Calc.)†
3.645	110	s	844
2.576	200	ms	476
2.310	210	m	207
2.111	211	vs	1000
1.825	220	wm	131
1.634	310	m	185
1.434	330	wm	38
1.383	321	vsm	517
1.296	400	mm	96
1.222	411–330	msm	106
1.158	420	sm	148
1.132	421	mm	35
1.105	332	sm	132
1.058	422	mm	49
1.017	510–431	sm	142
0.9629	520–432	wm	39
0.9464	521	vsm	218
0.9167	440	mm	102
0.8894	530–433	msm	98
0.8644	600–442	sm	148
0.8527	610	vwm	16
0.8416	611–532	vsm	430
0.8204	620	mm	71
0.8006	541	sm	188
0.7823	622	wmm	38
0.7736	542–630	vsm	317

*† See footnotes to Table III.

unit cell were placed in the following positions of $O^1_h - Pm3m$:

3 Ti in (c): $0\frac{1}{2}\frac{1}{2}$; $\frac{1}{2}0\frac{1}{2}$; $\frac{1}{2}\frac{1}{2}0$
1 Hg in (a): 000

The interatomic distances for δ Ti_3Hg are given in Table XIV.

Powder patterns of γ Ti_3Hg, made with filtered copper radiation, were also indexed in the cubic system: $a = 5.1888 \pm 0.0001$Å.

A comparison of the relative volumes of δ Ti_3Hg and γ Ti_3Hg indicates that the larger unit cell of γ Ti_3Hg contains six titanium atoms and two mercury atoms. Indices assigned to diffraction maxima from this phase (Table XV) show that reflections from (hhl) occur only if $l = 2n$. Two space groups which would explain this systematic reflection are $O^3_h - Pm3n$ and $T^4_d - P\bar{4}3n$. Since the present study is concerned with two-fold and six-fold equivalent positions, it is necessary to consider only one of these space groups, the other being identical for these positions. Mercury atoms, of which there are two, must be in (a). If the six titanium atoms were placed in (b), general reflections with one index odd would be extinct and this is not consistent with the data. The titanium atoms could be placed in either 6(c) or 6(d), since these positions differ only by a translation of the origin.

2 Hg in (a): 000; $\frac{1}{2}\frac{1}{2}\frac{1}{2}$
6 Ti in (d):
$\frac{1}{4}0\frac{1}{2}$; $\frac{1}{2}\frac{1}{4}0$; $0\frac{1}{2}\frac{1}{4}$; $\frac{3}{4}0\frac{1}{2}$; $\frac{1}{2}\frac{3}{4}0$; $0\frac{1}{2}\frac{3}{4}$.

Special conditions of extinction for (d) would explain the absence of reflections from (410), (430), and (531), since the mercury atoms do not contribute to maxima for which $h + k + l \neq 2n$. Although the unit cell content might be placed into the space group of highest symmetry, $O^3_h - Pm3n$ in this particular case, the observed intensities could be equally well explained if the eight atoms were arranged in $T^1_h - Pm3$ as follows:

1 Hg in (a): 000
1 Hg in (b): $\frac{1}{2}\frac{1}{2}\frac{1}{2}$
6 Ti in (g): $x\frac{1}{2}0$; $0x\frac{1}{2}$; $\frac{1}{2}0x$; $\bar{x}\frac{1}{2}0$; $0\bar{x}\frac{1}{2}$; $\frac{1}{2}0\bar{x}$
with $0.235 < x < 0.250$.

Table XVI. Interatomic Distances for Gamma-Ti_3Hg

Atom	Neighbors	Distance, A
Ti (d)	2 Ti (d)	2.59
Ti (d)	2 Hg (a)	2.90
Ti (d)	8 Ti (d)	3.18

Table XVII. X-Ray Powder Diffraction Data for Zr_3Hg. Copper Radiation.

d, A	hkl	I (Obs.)*	I (Calc.)†
3.95	110	m	275
2.79	200	ms	443
2.50	210	s	528
2.27	211	vs	1000
1.96	220	w	43
1.76	310	w	63
1.54	320	m	110
1.485	321	s	511
1.391	400	m	134
1.311	330–411	w	38
1.243	420	ms	142
1.213	421	ms	99
1.185	332	ms	122
1.133	422	vw	16
1.089	431–510	wm	44
1.033	432–520	mm	102
1.015	521	sm	175
0.9829	440	msm	111
0.9540	530–433	wm	26
0.9270	442–600	msm	109
0.9143	610	wm	33
0.9020	532–611	vsm	270
0.8790	620	vwm	14
0.8581	541	wm	31
0.8291	630–542	mm	133
0.8199	631	vsm	259
0.8024	444	sm	141
0.7868	710–550–543	sm	124

*† See footnotes to Table III.

Table XVIII. Interatomic Distances for Zr_3Hg

Atom	Neighbors	Distance, A
Zr (d)	2 Zr (d)	2.78
Zr (d)	2 Hg (a)	3.11
Zr (d)	8 Zr (d)	3.40

Table XIX. X-Ray Powder Diffraction Data for ZrHg. Copper Radiation.

d, A	hkl	HKL	I (Obs.)*	I (Calc.)†
4.19	001	001	vw	A
3.15	110	100	w	104
2.52	111	101	vs	1000
2.22	200	110	s	344
2.08	002	002	m	142
1.96	201	111	w	66
1.74	112	102	w	45
1.57	220	200	w	111
1.52	202	112	m	201
1.331	311	211	s	280
1.271	113	103	ms	111
1.254	222	202	msB	108
1.110	400	220	wB	38
1.044	004–223	004–203	wB	31
1.013	331	301	wB	62
0.9895	114–313	104–213	sB	135
0.9812	402	222	mB	62
0.9449	204	114	mB	62
0.8975	422	312	msB	62
0.8901	224	204	msB	69
0.8541	511	321	sB	149
0.8373	314–333	214–303	sB	108
0.8079	115–423	105–313	sB	142

*† See footnotes to Table III.

Table XX. Interatomic Distances for ZrHg

Atom	Neighbors	Distance, A
Zr (d)	8 Hg (a)	3.05
Zr (d)	4 Zr (d)	3.15
Hg (a)	4 Hg (a)	3.15

Table XXI. X-Ray Powder Diffraction Data for $ZrHg_3$, Copper Radiation

d, A	hkl	I (Obs.)*
4.42	100	m
3.10	110	m
2.53	111	vs
2.18	200	s
1.95	210	wm
1.78	211	wm
1.54	220	s
1.457	300–221	w
1.381	310	w
1.316	311	vs
1.261	222	s
1.209	320	vw
1.167	321	wαι
1.091	400	mαι
1.059	410–322	wαι
1.030	411–330	wαι
1.001	331	sαι
0.9764	420	sαι
0.9310	332	vwαι
0.8916	422	sαι
0.8727	500–430	wαι
0.8567	510–431	wαι
0.8403	511–333	vsαι
0.8106	432–520	wαι
0.7971	521	sαι

* See footnote to Table III.

Table XXII. Interatomic Distances for $ZrHg_3$

Atom	Neighbors	Distance, A
Hg (c)	8 Hg (c)	3.09
Hg (c)	4 Zr (a)	3.09
Zr (a)	6 Zr (a)	4.37

It is clear that additional experimental evidence such as the Laue symmetry or diffraction spectra from planes in which $\Sigma(h^2 + k^2 + l^2) > 45$ are necessary before a choice of space groups can be made. Intensity calculations in Table XV were made with $x = 0.250$. The interatomic distances for γ Ti_3Hg are given in Table XVI.

System Zr-Hg: Several of the intermediate phases which occur in the system Zr-Hg are isomorphous with Ti-Hg alloys which have been described. The zirconium-rich phase, Zr_3Hg, is related to γ Ti_3Hg. Since the method of deducing this structure and the uncertainty in the choice of space group has already been discussed, a description of Zr_3Hg will be given without further comment. $a = 5.5581 \pm 0.0002$Å.

The eight atoms in the unit cell are located as follows:

2 Hg in : 000; ½½½

6 Zr in : x½0; 0x½; ½0x; $\bar{x}$½0; 0$\bar{x}$½; ½0$\bar{x}$.

The arrangement of atoms, with $x = 0.250$, was used to calculate the intensities which are displayed in Table XVII. The interatomic distances for Zr_3Hg are given in Table XVIII.

Alloys containing 50 atomic pct Hg gave relatively poor diffraction photographs, especially in the region of small interplanar spacings. There were, however, sufficient data to relate ZrHg (see Table XIX) to isomorphous TiHg. In computing the lattice parameters, the weight functions were set equal to unity for all reflections and the function $\delta_i(\theta)$ placed equal to zero. $a = 3.15 \pm 0.01$Å; $c = 4.17 \pm 0.01$Å; $c/a = 1.32$.

The interatomic distances for ZrHg are given in Table XX.

Mercury-rich alloys in this system decomposed within several hours after the evacuated ampoules had been opened. Diffraction photographs which were made immediately after the alloys were exposed to atmospheric pressure showed only one intermediate phase between ZrHg and mercury. Maxima from a cubic mercury-rich phase were readily indexed (see Table XXI). $a = 4.3652 \pm 0.0008$Å.

The ideal composition for this phase is represented by the chemical formula $ZrHg_3$. The following positions of space group O^1_h — $Pm3m$ were utilized:

1 Zr in (a): 000

3 Hg in (c): 0½½; ½0½; ½½0.

The interatomic distances for $ZrHg_3$ are given in Table XXII.

Conclusions

Phase relationships in the systems Ti-Zn, Ti-Hg, Zr-Zn, Zr-Cd, and Zr-Hg have been studied. Several intermediate phases have been established and their crystal structures determined by X-ray powder diffraction methods. Table XXIII gives a summary of the structures and atomic volumes.

$ZrZn_2$ is a face-centered cubic C 15 type structure. The previously reported structure for $TiZn_3$ has been confirmed. Intensity calculations indicate that the ideal position parameters for $MgZn_2$ (C 14 type) present a reasonable trial structure for $TiZn_2$. A random distribution of atoms characterizes the face-centered cubic and body-centered tetragonal phases which have been designated $Zr_{(1-x)}Cd_{(x)}$. TiHg and ZrHg crystallize in the ordered AuCu (L 1_0) structure. Gamma-Ti_3Hg and Zr_3Hg are isomorphous with β tungsten. At high temperatures the stable titanium-rich Ti-Hg intermediate phase is δ Ti_3Hg, which is analogous to the ordered $AuCu_3$ (L 1_2)

Table XXIII. Summary of Crystal Structures and Atomic Volumes

Phase	Unit Cell Parameters, A	Atomic Volume, A³	Space Group	Structure Type
$ZrZn_2$	$a = 7.3958 \pm 0.0003$	16.856 ± 0.002	O^7_h – $Fd3m$	$MgCu_2$ (C 15)
$TiZn_3$	$a = 3.9322 \pm 0.0003$	15.200 ± 0.005	O^1_h – $Pm3m$	$AuCu_3$ (L 1_2)
$TiZn_2$	$a = 5.064 \pm 0.002$ $c = 8.210 \pm 0.002$	15.20 ± 0.02	D^4_{6h} – $P6_3/mmc$	$MgZn_2$ (C 14)
$Zr_{(1-x)}Cd_{(x)}$	$a = 4.3768 \pm 0.0006$	20.961 ± 0.009	O^5_h – $Fm3m$	Random distribution of atoms
$Zr_{(1-x)}Cd_{(x)}$	$a = 3.1243 \pm 0.0004$ $c = 4.3008 \pm 0.0006$	20.990 ± 0.009	D^{17}_{4h} – $I4/mmm$	Random distribution of atoms
TiHg	$a = 3.009 \pm 0.001$ $c = 4.041 \pm 0.001$	18.30 ± 0.01	D^1_{4h} – $P4/mmm$	AuCu (L 1_0)
Delta-Ti_3Hg	$a = 4.1654 \pm 0.0004$	18.068 ± 0.005	O^1_h – $Pm3m$	$AuCu_3$ (L 1_2)
Gamma-Ti_3Hg	$a = 5.1888 \pm 0.0001$	17.463 ± 0.001	O^9_h or T^1_h	Beta tungsten
Zr_3Hg	$a = 5.5583 \pm 0.0002$	21.465 ± 0.002	O^9_h or T^1_h	Beta tungsten
ZrHg	$a = 3.15 \pm 0.01$ $c = 4.17 \pm 0.01$	20.6 ± 0.1	D^1_{4h} – $P4/mmm$	AuCu (L 1_0)
$ZrHg_3$	$a = 4.3652 \pm 0.0008$	20.79 ± 0.01	O^1_h – $Pm3m$	$AuCu_3$ (L 1_2)

crystal structure. $ZrHg_3$ is isomorphous with δ Ti_3Hg.

Acknowledgment

This work was done at the Jet Propulsion Laboratory, California Institute of Technology, under contract number DA-04-495-ORD-18 with the Army Ordnance Corps, Washington, D. C. The author wishes to thank this agency for permission to publish the results of this investigation.

References

[1] F. Laves and H. Wallbaum: The Crystal Chemistry of Titanium Alloys. *Naturwissenschaften* (1939) **27**, pp. 674-675.

[2] E. Gebhardt: Partial Phase Diagrams of Zinc-Titanium and Zinc-Zirconium. *Ztsch. Metallkunde* (1941) **33**, pp. 355-357.

[3] E. A. Anderson, E. J. Boyle, and P. W. Ramsey: Rolled Zinc-Titanium Alloys. *Trans.* AIME (1944) **156**, pp. 278-286.

[4] J. B. Nelson and D. P. Riley: An Experimental Investigation of Extrapolation Methods in the Derivation of Accurate Unit-Cell Dimensions of Crystals. *Proc.* Physical Soc. (1945) **57**, pp. 160-177.

[5] A. Taylor and R. W. Floyd: Precision Measurements of Lattice Parameters of Non-cubic Crystals. *Acta Crystallographica* (1950) **3**, pp. 285-289.

[6] E. Whittaker and G. Robinson: *The Calculus of Observations* (1937) London. Blackie and Sons Ltd.

[7] K. Lonsdale: X-Ray Wave Length Values. *Acta Crystallographica* (1950) **3**, pp. 400-401.

[8] A. J. C. Wilson (Editor): *Structure Reports for 1947-1948* (1951) Vol. 11, pp. 58-59. Utrecht. N.V.A. Oosthoek's Uitgevers Mij.

[9] J. Friauf: The Crystal Structure of Magnesium Dizincide. *Physical Review* (1927) **29**, pp. 35-40.

[10] *International Tables for Crystal Structure Determination* (1935) Vol. II. Berlin. Gebrüder Borntraeger.

[11] H. Hönl: Dispersion Theory of X-Rays. *Ztsch. Physik* (1933) **84**, pp. 1-16.

[12] Private communication from Dr. Pol Duwez, California Institute of Technology, Pasadena, Calif.

[13] R. M. Treco: Effect of Small Additions of Oxygen on the Lattice Constants and Hardness of Zirconium. *Trans.* AIME (1953) **197**, pp. 344-348; JOURNAL OF METALS (February 1953).

[14] E. R. Jette and F. Foote: Precision Determination of Lattice Constants. *Journal of Chemical Physics* (1935) **3**, pp. 605-616.

[15] M. C. Neuburger: Lattice Constants for the Year 1936. *Ztsch. Kristallographie* (1936) **93**, pp. 1-36.

Technical Note

Observations on Elevated-Temperature Tensile Deformation

by R. W. Guard, J. H. Keeler, and S. F. Reiter

DURING the last several years the authors have been conducting tests on a tensile machine that autographically records load-elongation data. In certain tests at elevated temperatures on face-centered cubic, hexagonal close-packed, and body-centered cubic materials (binary alloys of nickel, zirconium, and iron), the load-elongation curve as shown in Fig. 1 reaches a maximum load ($P_{max.}$) at relatively small amounts of strain and a large amount of elongation occurs subsequently with a continuously decreasing load, until finally localized necking and fracture take place. This early maximum load behavior has been found without the accompanying evidence of localized necking as has been assumed by some, or of evidence of cracking as observed by others.[1] This behavior has also been observed by Nadai and Manjoine[2] whose results are in good agreement with ours. The prior strain, strain rate, test temperature, and crystal structure affect the observations.

The influence of prior strain was observed in tests on unalloyed zirconium at 300°C in which specimens containing large amounts of prior strain (cold work) exhibited the type of curve shown in Fig. 1. No localized necking was observed after strain as much as that of point *B*. Annealed and recrystallized specimens of the same material showed a load-elongation curve with maximum load occurring after considerable strain hardening and at the beginning of localized necking. Interrupted tests (Fig. 2) show no loss in strength because of recovery or recrystallization during an interval at temperature without load. Recovery under stress such as found by

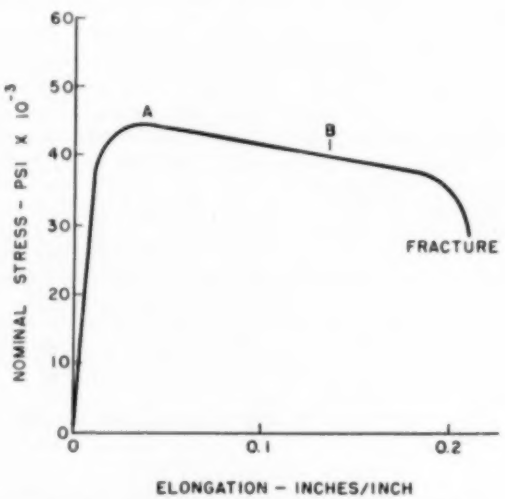

Fig. 1—Characteristic early $P_{max.}$ tensile curve. (Test at 300°C on severely cold worked zirconium.)

Wood and Suiter[3] in aluminum is now being investigated as one possible explanation.

The strain rate is a contributing variable as shown in Fig. 3, a test on high purity nickel. Here the strain rate was decreased by a factor of ten during a test in which the maximum load was reached at a small strain. The slope of the true stress-true strain curve was positive with the more rapid strain rate and negative with the slower strain rate.

In many binary ferrites an added effect of temperature has been observed. Fig. 4 shows the load-elongation plots for a binary ferritic alloy containing 2 pct Mo. The slope of the small portion of the stress-strain curve obtained at a strain rate of 0.01 min^{-1} changes sign from negative to positive on going

R. W. GUARD, Junior Member AIME, and J. H. KEELER, Member AIME, are associated with the Research Laboratory, General Electric Co., Schenectady, and S. F. REITER, Junior Member AIME, formerly with General Electric Co., is now Technical Manager, Rome Fastener Corp., New Haven, Conn.

TN 205E. Manuscript, October 23, 1953.

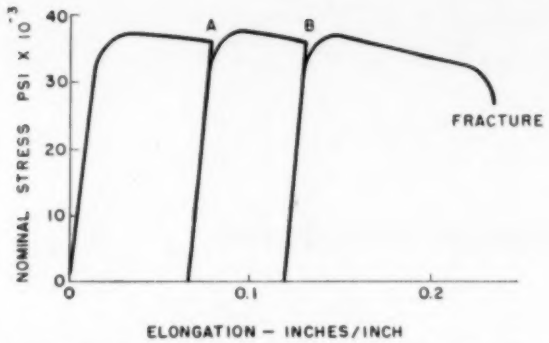

Fig. 2—Test showing absence of recovery in early $P_{max.}$ test. (Test at 300°C on severely cold worked zirconium at a strain rate of 0.09 min^{-1}.)

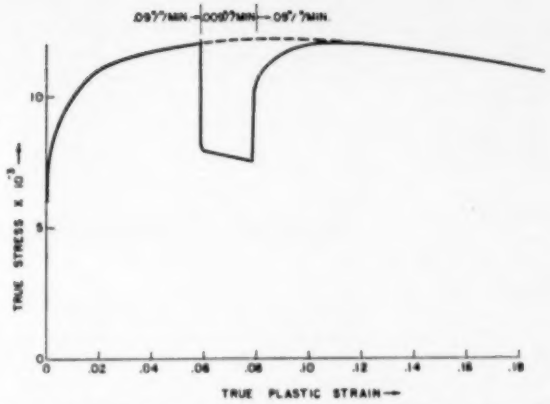

Fig. 3—High purity nickel annealed 1 hr at 500°C. Test at 650°C showing effect of change in strain rate on slope of flow curve.

from 650° to 870°C, whereas the slope of the major part of the curve obtained at a strain rate of 0.1 min^{-1} remained negative throughout. The reasons for this behavior have not been clarified at present.

The effect of crystal structure on the characteristics of the tensile curve is illustrated in Fig. 5. At 870°C, both the 1 and 2 pct molybdenum ferrites are body-centered cubic, while at 980°C, the 2 pct alloy is body-centered cubic and the 1 pct alloy is within the γ loop and face-centered cubic. The shapes of the load-elongation curves for the three body-centered cubic materials are quite similar. However,

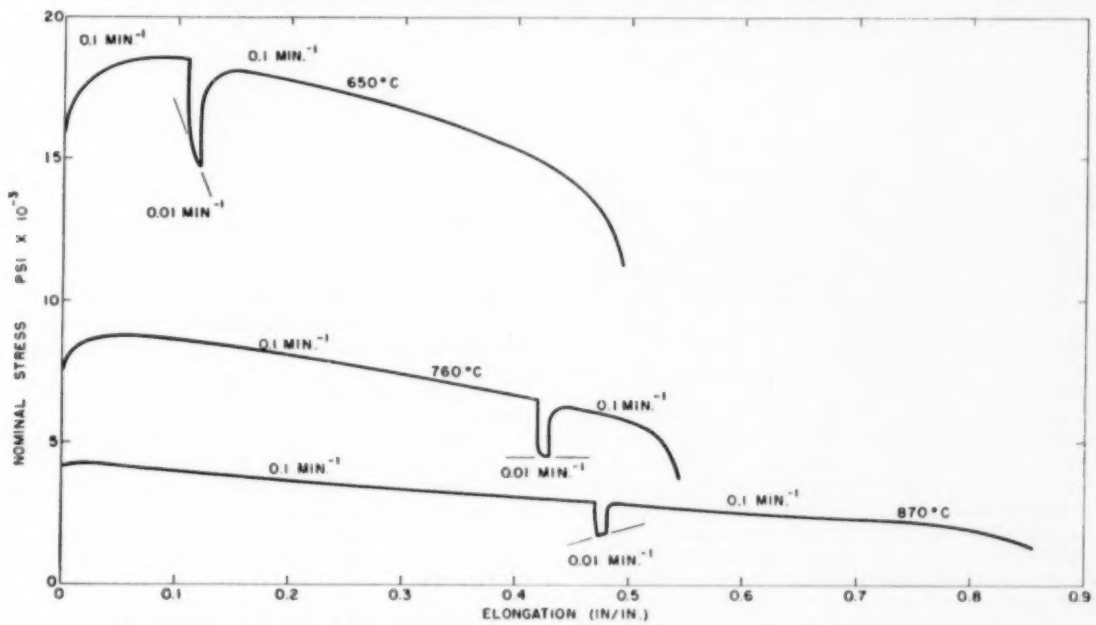

Fig. 4—Effect of strain rate and temperature on the slope of the load-elongation curve in a 2 pct Mo-98 pct Fe alloy.

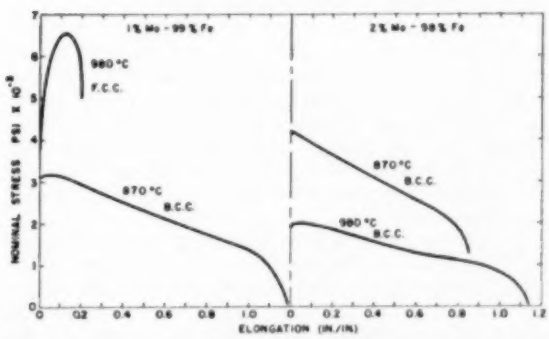

Fig. 5—Effect of composition and crystal structure on the shape of load-elongation curves. Samples elongated at 0.1 min^{-1}.

the face-centered cubic material displays a distinctly different type curve.

The characteristics of the "early $P_{max.}$" tensile curve are dependent upon the strain rate, the test temperature, and the material under consideration. The general features of the behavior are similar in the materials so far investigated, but the details are dependent upon the material.

References

[1] R. F. Miller, G. V. Smith, and G. L. Kehl: *Trans.* ASM (1943) **31**, pp. 817-848.

[2] M. J. Manjoine and A. Nadai: High Speed Tension Tests at Elevated Temperatures. Parts II and III. *Journal of Applied Mechanics* (1941) **8**, p. A-77.

[3] W. A. Wood and J. W. Suiter: *Journal* Inst. Metals (May 1952) **80**, pp. 501-506.

System Titanium-Manganese-Molybdenum

by R. P. Elliott, B. W. Levinger, and W. Rostoker

Phase equilibria in the Ti-Mn-Mo system have been investigated in the composition range 100 to 60 pct Ti and in the temperature range 550° to 1150°C. Three out of ten isothermal sections are presented as well as seven vertical sections, projections of the beta space and the surface of incipient melting.

A STUDY of the system Ti-Mn-Mo was undertaken as part of a program to aid in the development of titanium-base phase equilibrium diagrams of potential technical importance to alloy development. The scope of the investigation included the composition range 100 to 60 wt pct Ti (all compositions refer to weight percentages) and the temperature range 550° to 1150°C. A surface of incipient melting was constructed from measurements of a large number of alloys.

In the binary system Ti-Mo,[1] the high temperature modification of titanium generally spoken of as the β phase is stabilized to successively lower temperatures with increasing alloy content. There are no known intermediate phases, and complete miscibility exists between body-centered cubic titanium and molybdenum. The α solid solution is limited to less than 0.8 pct Mo at temperatures between 885° and 600°C.

An equilibrium diagram for the binary system Ti-Mn has been published.[2] Manganese behaves as a β stabilizer but undergoes a eutectoid transformation at about 20 pct Mn and 550°C to α plus an intermediate phase. The structure of this phase has been found to be isomorphous with the σ phase FeCr.[3] Accordingly, the phase is assigned the formula TiMn, although its actual location on the composition scale has not been determined and may well be not exactly at the equiatomic composition. In disagreement with ref. 2, the origin of the TiMn phase has been shown[4] to be a peritectoid transformation at a temperature between 900° and 1000°C. A second intermediate phase occurs at the atomic proportions $TiMn_2$. The structure of this phase was originally established by Wallbaum[5] as having a hexagonal lattice (C 14 type, 12 atoms per unit cell) isomorphous with $MgZn_2$. In this work, the structure determination was confirmed and lattice parameters determined to be: $a = 4.815$ kX, $c = 7.901$ kX.

Because of the extensive range of the β phase, the ternary system was suited to the determination of the phase boundaries by the parametric method of Andersen and Jette.[6] During the course of the investigation, this method was found applicable only to the $\beta/\alpha+\beta$ boundaries but not to $\beta/\beta+$ compound boundaries. Metallographic methods were used alternatively for delineating these phase boundaries.

Preparation and Treatment of Alloys

Over 70 alloys were prepared for the study of this system. Ten gram alloy buttons were arc melted in a nonconsumable electrode furnace using inert atmosphere protection, and a water cooled copper crucible. The construction and operation of this type of melting unit has been described.[7] To insure complete solution of alloy additions, especially molybdenum, the buttons were remelted alternately on top or bottom as many as five times. This was accomplished by a suitable mechanism for "flipping" the ingots over.

It was very difficult to obtain homogeneous melts in the region of less than 75 pct Ti because of the very high melting point of molybdenum and Ti-Mo master alloys and the comparatively low boiling point of manganese. Thus, the arc conditions for insuring complete solution of molybdenum were incompatible with the prevention of heavy losses of

R. P. ELLIOTT, Student Associate AIME, is Assistant Metallurgist, and W. ROSTOKER is Senior Metallurgist, Metals Research Dept., Armour Research Foundation of Illinois Institute of Technology, Chicago, and B. W. LEVINGER, Junior Member AIME, is Research Metallurgist, Tung-Sol Electric Inc., Bloomfield, N. J.

Discussion on this paper, TP 3700E, may be sent, 2 copies, to AIME by April 1, 1954. Manuscript, Aug. 20, 1953. New York Meeting, February 1954.

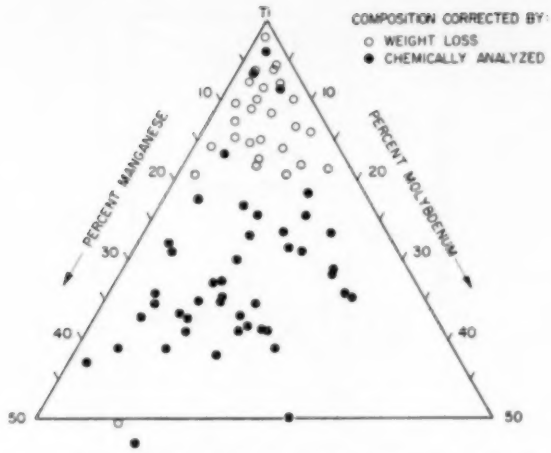

Fig. 1—Compositions of alloys for study of the system Ti-Mn-Mo.

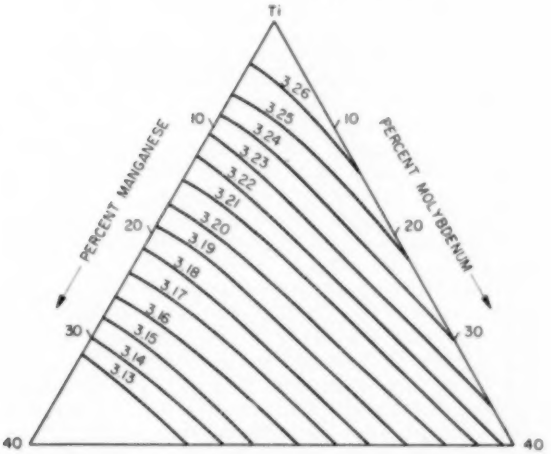

Fig. 2—Isoparametric projection of the parametric surface for the β phase.

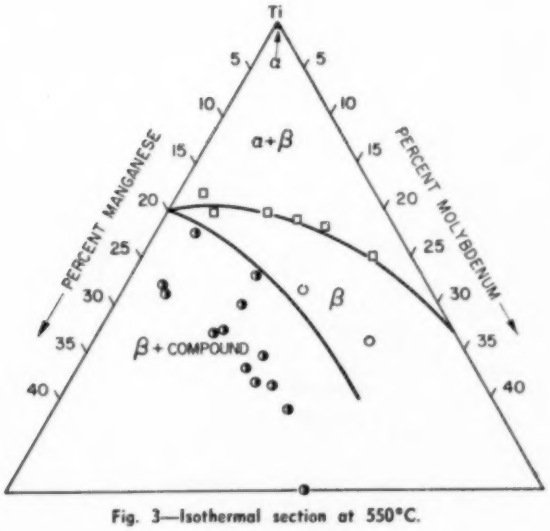

Fig. 3—Isothermal section at 550°C.

manganese by volatilization. Accordingly, it was not possible to prepare alloys to predetermined compositions, the approximate uncertainty being directly related to the molybdenum content.

Iodide titanium (~99.97 pct Ti) was used as an alloy base. An especially high quality manganese (~99.9 pct Mn) was obtained from the National Research Corp. Molybdenum sheet (0.003 in.) of 99.9 pct purity was used.

Charges were weighed to the nearest milligram and the resultant ingot reweighed to the same accuracy. Average weight losses for iodide titanium melts were of the order of 0.02 grams. By careful standardization with chemical analyses, it was found possible for alloys containing less than 20 pct total alloy content to use weight losses to correct nominal analyses by assigning all weight losses above 0.02 grams to manganese. Above 20 pct alloy content all

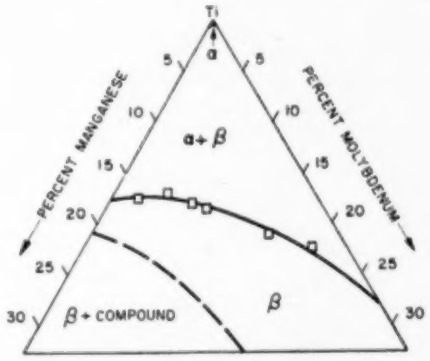

Fig. 4—Isothermal section at 600°C.

alloys were chemically analyzed. Adjusted chemical compositions of all alloys are shown in Fig. 1.

Specimens heat treated below 1100°C were enclosed in Vycor bulbs. For temperatures in excess of 1100°C, quartz bulbs were used. Partial pressures of argon prevented collapse of the bulbs at temperatures above 950°C. Bulbs were simply evacuated at lower temperatures. Heat treatments were conducted in resistance element tube furnaces with temperature control of ± 3°C.

All as-melted alloys were given a preliminary homogenization anneal at 1000°C for 24 hr. Homogenized buttons were broken or cut to provide sufficient specimens for subsequent equilibrium anneals. Time schedules for equilibrium anneals are given in Table I.

Examination of Alloys and Analyses of Data

Lattice parameters of the β phase were obtained from back-reflection patterns using filtered characteristic copper radiation (Cu $K\alpha_1 = 1.5374$ kX units). Suitable powder specimens were prepared by filing or crushing annealed alloys and screening through

Table I. Annealing Schedules for Attainment of Equilibrium

Temperature, °C	Time, Hr
550	720
650	260
750	110
850	56
950	33
1050	19
1150	13

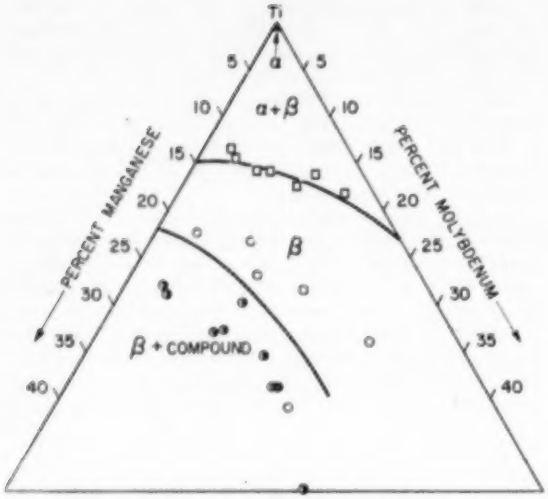

Fig. 5—Isothermal section at 650°C.

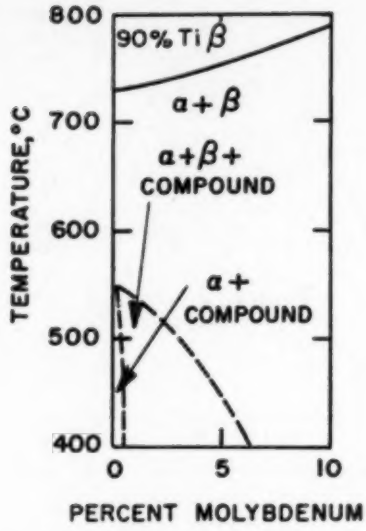

Fig. 8—Vertical section at 90 pct Ti.

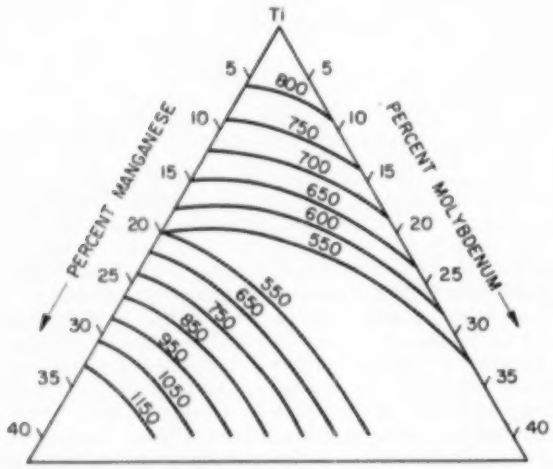

Fig. 6—Projection of the $\beta/\alpha+\beta$ and $\beta/\beta+$ compound surfaces.

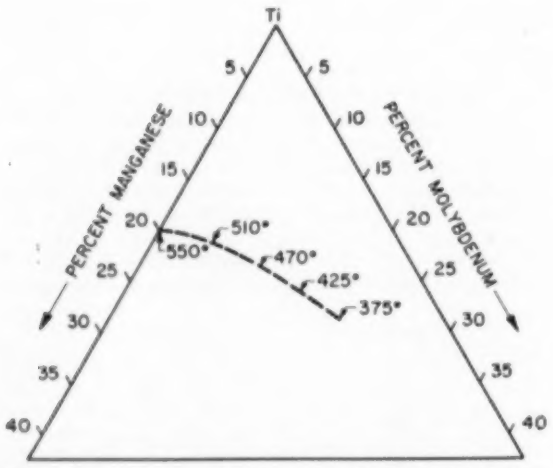

Fig. 7—Locus of the eutectoid temperature, based on extrapolations.

200 mesh. Annealing was performed by sealing in small Vycor tubes and heat treating for about 10 min at the temperature at which the original specimen was annealed. The powder capsule was then vigorously quenched but not broken. Lattice parameters of samples quenched from a 300° range of temperature in the β field were identical. From this, it could be concluded that this method of quenching was sufficiently rapid to prevent detectable anisothermal transformation.

In conjunction with published data for parameters of the Ti-Mo[1] and Ti-Mn[2] binary systems, lattice parameters of the β phase as-quenched from the single-phase field were used to construct the parametric surface shown in Fig. 2. The graphical method of Andersen and Jette[6] for the construction of the projection of the parametric surface is particularly adaptable to selections of alloy compositions wherein the proportion of one component is held constant. Much of the convenience of construction is lost if it is not possible to prepare alloys along predetermined directions within the composition triangle. Because of the volatility of manganese, this proved to be the case for the system under discussion. The projection of the parametric surface can, however, be constructed by somewhat more laborious means.

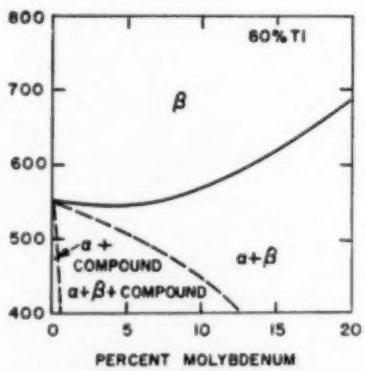

Fig. 9—Vertical section at 80 pct Ti.

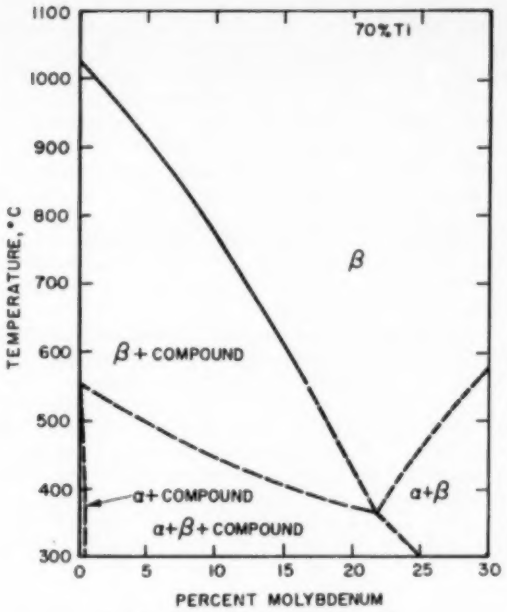

Fig. 10—Vertical section at 70 pct Ti.

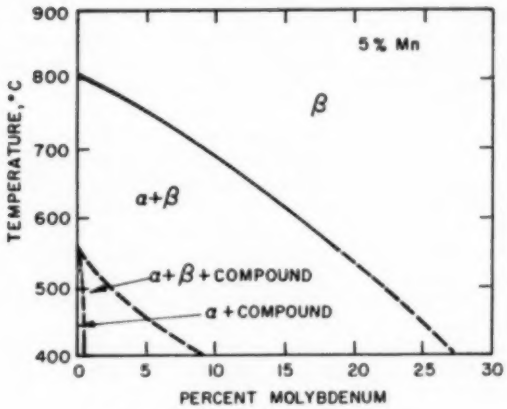

Fig. 11—Vertical section at 5 pct Mn.

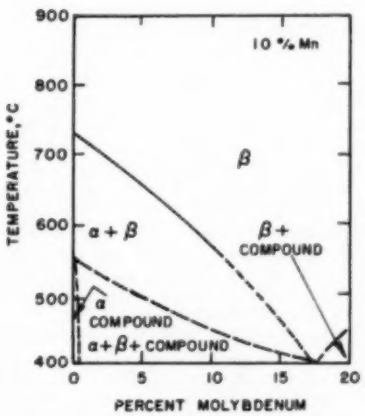

Fig. 12—Vertical section at 10 pct Mn.

If the resultant compositions of the alloys prepared are plotted, then by inspection, straight lines can be drawn to intersect three or more compositions. If the parametric surface is continuous, then the trace of the surface on a vertical plane whose abscissa is colinear with the composition line will be a smooth curve. This curve will permit interpolation of the compositions, giving equal parameter values for the isoparametric plot. In practice, one of two intersecting traces of the parametric surface may be used to improve the accuracy of construction of the other. By repeated use of such constructions, a satisfactory projection of the parametric surface can be obtained.

The $\beta/\alpha+\beta$ boundaries were established by the use of the parametric surface and by directing the tie-lines from the titanium corner of the composition triangle. Since the solubility range of α is extremely small, this approximation introduces no significant error.

For a number of reasons it was not possible to use the parametric method to establish the $\beta/\beta+$ compound boundary. In the first place, with increasing manganese content, the diffuse background of diffraction patterns increased. This made the distinction between TiMn and $TiMn_x$ as the compound extremely difficult. Secondly, since the actual composition location of TiMn was unknown, it was not possible to establish the direction of the tie-lines. The $\beta/\beta+$ compound boundaries were constructed from metallographic studies. Again, by this method, it was not possible to distinguish consistently between TiMn and $TiMn_x$. Accordingly, it is felt that the definition of more than the boundary of the β field was likely to be inaccurate.

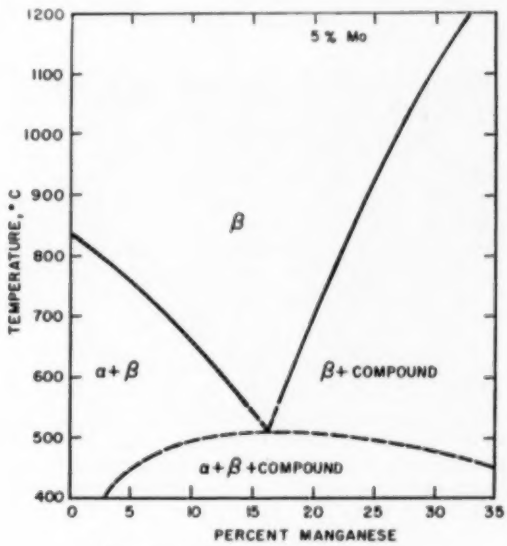

Fig. 13—Vertical section at 5 pct Mo.

It is generally very difficult to measure the liquidus and solidus temperatures of refractory metal systems by thermal arrest methods. An approximation of the solidus temperature is achieved by the use of incipient melting techniques. In principle, sharp corners of small specimens are observed to round or collapse on heating to a temperature above the solidus at which sufficient liquid has formed to destroy the ability of the specimen to retain its external shape. When this observation is made with

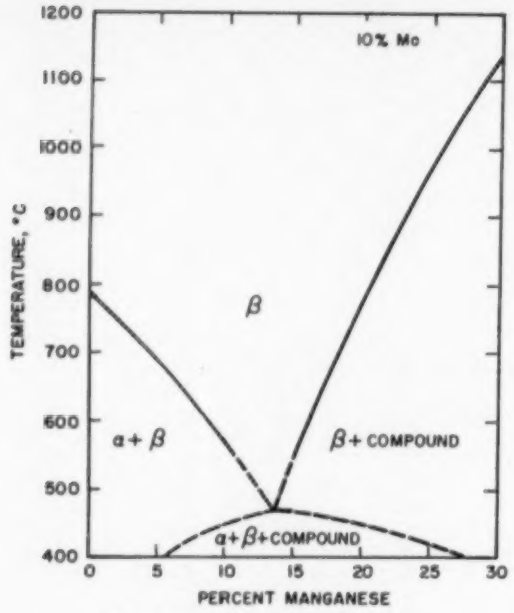

Fig. 14—Vertical section at 10 pct Mo.

an optical pyrometer, the temperature at which incipient melting occurs can be measured concurrently. Specimens are suspended on a tungsten wire in a high temperature vacuum induction furnace. The design and operation of this unit have been described.[7] The incipient melting procedure was calibrated against a selection of pure metals with sufficiently diverse melting points that the correction curve covered the whole range encountered in the alloys under study. Thus, all corrections were based on interpolations.

Discussion of Phase Equilibria

Between 550° and 1150°C the ternary equilibria is dominated by the β space. Since the eutectoid transformation in the binary Ti-Mn system occurs below 550°C, it cannot be expected to appear in the ternary system in the temperature range under study.

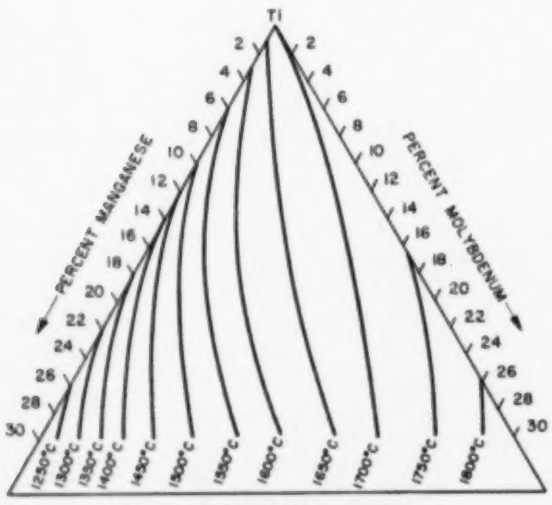

Fig. 15—Surface of incipient melting.

Isothermal sections were constructed at 50°C intervals between 550° and 850°C, inclusive, and at 100°C intervals between 850° and 1150°C, inclusive. Because of the insuppressible transformation $\beta \rightarrow \alpha'$ on quenching alloys of low manganese and molybdenum content, it was necessary to determine the $\beta/\alpha+\beta$ boundaries at 800° and 850°C by metallographic methods. Isothermal sections with supporting data for the 550°, 600°, and 650°C levels are shown in Figs. 3, 4, and 5. Fig. 6 presents a contour plan of the $\beta/\alpha+\beta$ and $\beta/\beta+$ compound surfaces. Based on extrapolations of vertical section constructions the probable course of the eutectoid depression is presented in Fig. 7.

Experimentally determined isothermal sections have been used to construct vertical sections along selected directions in the composition triangle. These in turn have been used to adjust the boundaries in the isothermal sections within the latitude permitted by the data. By such repeated constructions all of the experimental data are used to define the phase boundary surfaces. Phase boundaries in Figs. 3, 4, and 5 have been adjusted in this fashion. Vertical sections at 90, 80, and 70 pct Ti; 5 and 10 pct Mn; and 5 and 10 pct Mo are shown in Figs. 8 to 14, inclusive.

The incipient melting measurements for 30 alloys were used to construct the projection of the surface of incipient melting shown in Fig. 15. The method of construction was exactly the same as used to construct the parametric surface. It is likely that alloys on the high manganese side gave somewhat higher melting points because manganese was observed to be volatilizing from the surface of these specimens during the incipient melting experiments.

Summary

1—The ternary equilibria of the Ti-Mn-Mo system have been investigated in the composition range 100 to 60 pct Ti and over the temperature range 550° to 1150°C.

2—The bounding surfaces $\beta/\alpha+\beta$ and $\beta/\beta+$ compound have been determined in this region.

3—A surface of incipient melting has been constructed.

4—The lattice parameters of the β phase have been used to construct a parametric surface.

Acknowledgments

The authors wish to express their appreciation of the sponsorship of this work by the Ordnance Corps, U. S. Army, Watertown Arsenal, Watertown, Mass., under Contract DA-11-022-ORD-272, and for their permission to publish this paper.

References

[1] M. Hansen, E. L. Kamen, H. D. Kessler, and D. J. McPherson: *Trans.* AIME (1951) **191**, p. 881; JOURNAL OF METALS (October 1951).

[2] D. J. Maykuth, H. R. Ogden, and R. I. Jaffee: *Trans.* AIME (1953) **197**, p. 225; JOURNAL OF METALS (February 1953).

[3] R. P. Elliott and W. Rostoker: *Trans.* AIME (1953) **197**, p. 1203; JOURNAL OF METALS (September 1953).

[4] W. Rostoker, R. P. Elliott, and D. J. McPherson: Discussion to ref. 2. *Trans.* AIME (1953) **197**, p. 1566; JOURNAL OF METALS (November 1953).

[5] H. Wallbaum: *Ztsch. Kristallographie* (1941) **103**, p. 391.

[6] A. G. H. Andersen and E. R. Jette: *Trans.* ASM (1936) **24**, pp. 375, 519.

[7] M. Hansen, H. D. Kessler, and D. J. McPherson: *Trans.* ASM (1952) **44**, p. 518.

Constitution and Properties of Ag-Cu-Zn Brazing Alloys

by Karl M. Weigert

The position of the three-phase field between the alpha and the beta phases was established. The exact location differs from previous assumptions. The extremely high strength and hardness values were found near the phase boundaries of the ternary compositions.

IN 1929, Ueno[1] investigated vertical sections of the Ag-Cu-Zn diagram at constant silver and zinc values. From the evaluation of cooling curves and microscopic studies, he concluded that there was no evidence of a three-phase field in the solid state between the α and β fields. The failure to find evidence for this field was due to the fact that it exists only in a very narrow range of compositions and requires special methods of heat treatment to establish phase equilibrium.

In a later publication on the same subject Keinert[2] rearranged Ueno's diagrams to conform with the basic phase rules. The existence of a three-phase field was postulated in the solid state between the α phases and the homogeneous β phase between the Cu-Zn and the Ag-Zn binary border systems. The approximate location was based on a few microscopic observations of the structure and it was pointed out that the exact position could be determined only by a larger number of experiments.

In the twenty years following these investigations alloys of Ag-Cu-Zn have become of general interest due to various technical applications, principally for brazing. In the course of an overall investigation of the physical properties of ternary Ag-Cu-Zn alloys the author found extremely high values of hardness and strength in alloys of compositions between the α and the β fields. The exact location of the intermediate phase fields was established by the evaluation of more than a hundred cooling curves and microscopic mountings.

Experimental Procedures

Preparation of Test Samples: At the beginning of the investigation samples were chillcast into ¼ in. diameter iron molds to determine hardness, strength, and the mechanism of primary crystallization. These

K. M. WEIGERT, Member AIME, is associated with Goldsmith Bros. Smelting and Refining Co., Chicago.

Discussion on this paper, TP 3717E, may be sent, 2 copies, to AIME by April 1, 1954. Manuscript, Nov. 21, 1952. New York Meeting, February 1954.

Fig. 1—30 pct Ag-40 pct Cu-30 pct Zn alloy heat treated at 600°C for 10 hr. X300.

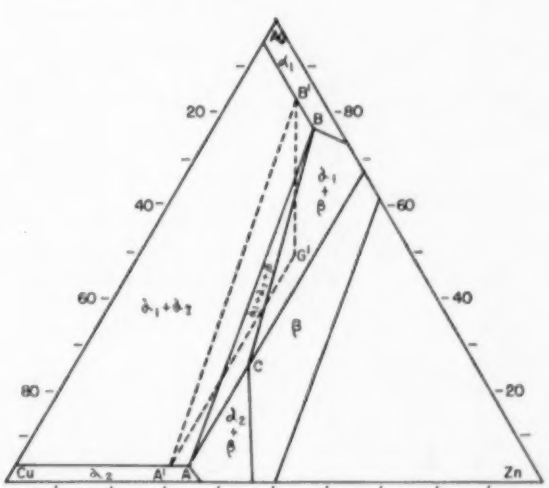

Fig. 2—Horizontal section through the Ag-Cu-Zn diagram at 600°F.

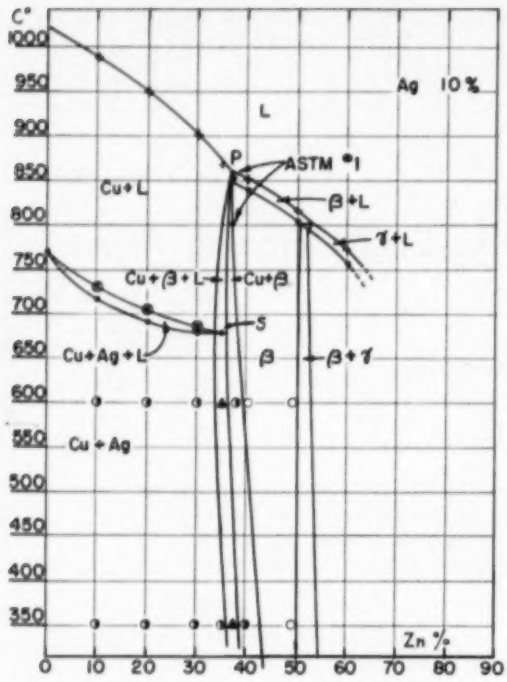

Fig. 3a—Vertical section through the Ag-Cu-Zn diagram at 10 wt pct Ag.

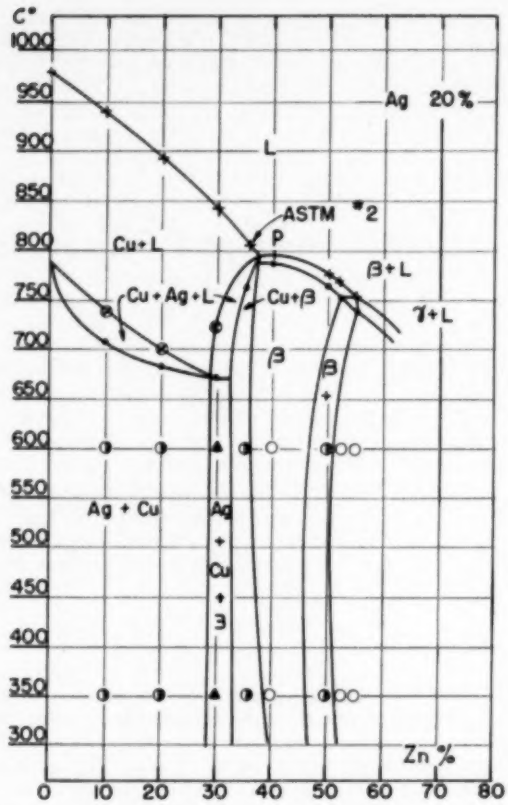

Fig 3b—Vertical section through the Ag-Cu-Zn diagram at 20 wt pct Ag.

samples were not particularly suited for microscopic studies of the solid transformations.

The preparation of test samples for studies at different temperatures in the solid state was done in

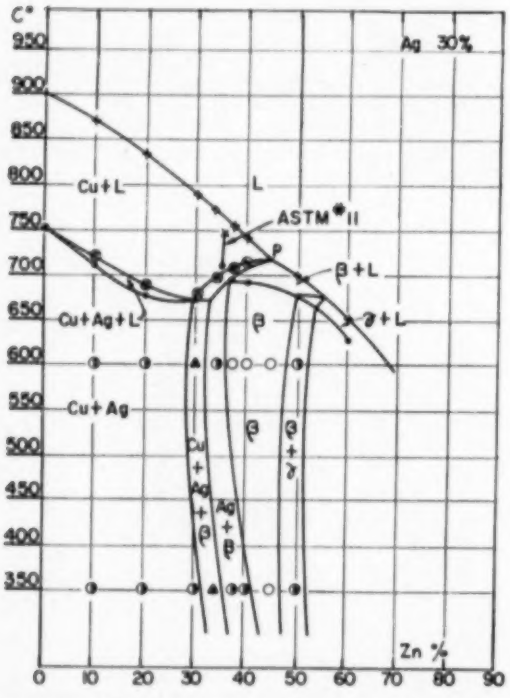

Fig. 3c—Vertical section through the Ag-Cu-Zn diagram at 30 wt pct Ag.

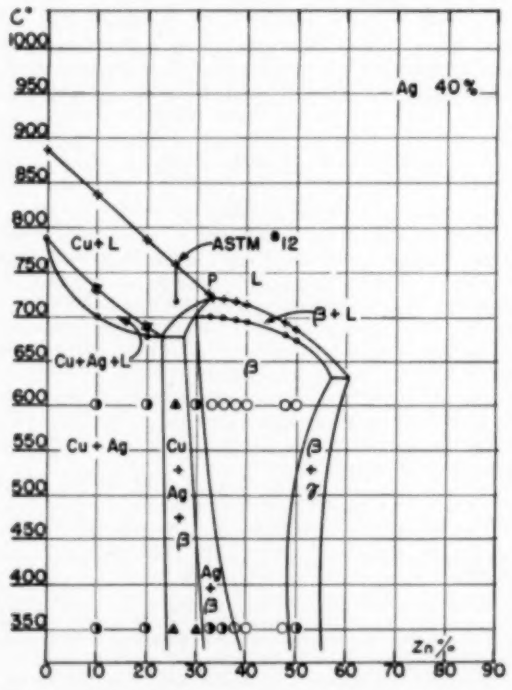

Fig. 3d—Vertical section through the Ag-Cu-Zn diagram at 40 wt pct Ag.

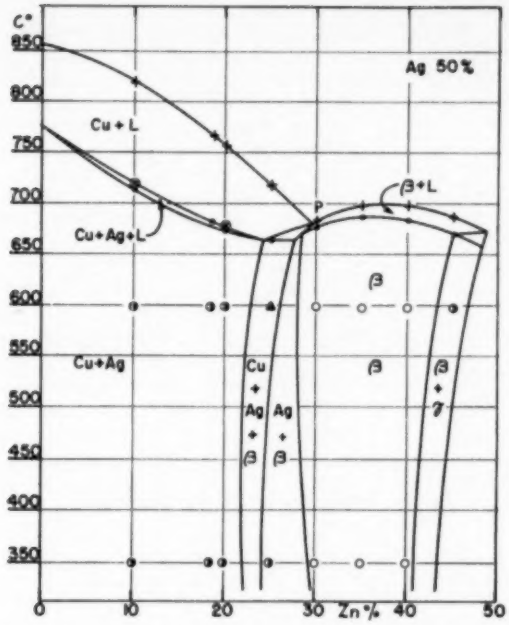

Fig. 3e—Vertical section through the Ag-Cu-Zn diagram at 50 wt pct Ag.

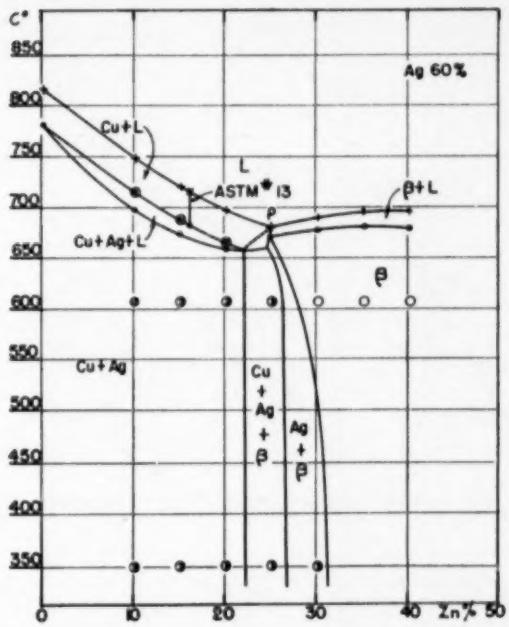

Fig. 3f—Vertical section through the Ag-Cu-Zn diagram at 60 wt pct Ag.

the following manner: In cylindrical brass pieces 1 in. diameter and 1½ in. high, up to 15 holes were drilled lengthwise down to within ⅛ in. of the bottom. Precast sample pieces of varying compositions were inserted into the holes, reaching almost to the top. After applying flux, the whole block was heated until the samples were melted down and then was air cooled slowly so that large crystals would form. Then sections of the block were cut off, after polishing and examining the structure. The remainder could be heat treated at various temperatures and eventually more sections could be put aside. Among the advantages of this procedure are the following:

No special mounting equipment is required. Many samples, representing a whole section of a diagram can be processed simultaneously, assuring the same kind of heat treatment. Changes in the structure can be examined from time to time, and the heat treatment can be interrupted when equilibrium has been established. The etching of alloys mounted in metals is much faster, due to local potentials. Reliable hardness tests can be conducted on the surface.

Identification of Phases: Conventional etching solutions were used, e.g., 10 pct ammonium persulphate with occasional additions of potassium cyanide, ammonia and hydrogen peroxide. The identification of the α phase near the copper side was very easy. Good phase contrast for the β phase against the primary copper crystallization and the silver-rich eutectic could be achieved by the use of ferric chloride and cuprous ammonium chloride solutions. The primary β crystals on the silver-rich side were somewhat difficult to etch. The grain boundaries could be brought out with nital solutions. The structures of the α and β fields have been reported. Therefore only a typical example of the structure of the three-phase field is shown, Fig. 1. At a composition of 30 pct Ag-40 pct Cu-30 pct Zn, the primary crystallization consists of large copper dendrides. At 1235°F the melt reacts with the copper-rich α crystals in a peritectic four-phase reaction to form a silver-rich phase and some β crystals. The color of the copper crystals is light brown and the silver-rich phase remains white. The β phase varies considerably in color from yellow to very dark brown. The elongated β crystals can be easily distinguished from the rather round α copper dendrides.

All the alloys were reheated for 5 hr at 1200°F and quenched in water. In order to observe the phase formation at lower temperatures the samples were aged up to 100 hr at 600°F, until phase equilibrium was established.

Location of Phase Fields—Horizontal Sections: The horizontal section at 600°F is comparable to the one proposed by Keinert[2] at a low temperature, Fig. 2. The positions of the corner points of the three-phase triangle are given in Table I.

The relocation of the three-phase field toward higher zinc values conforms with the findings of high values of strength and hardness of alloys with compositions located in the range of the intermediate phases between the α and β fields. This will be shown in the investigation of physical properties.

Vertical Sections: The vertical sections of the ternary diagram were re-examined and the boundaries of the liquid and partly liquid phases located

Table I. Position of Corner Points in Three-Phase Triangle

		Copper Side, A, Wt Pct	Silver Side, B, Wt Pct	Beta Side, C, Wt Pct
Author				
	Ag	3	77	20
	Cu	65	3	46
	Zn	32	20	34
Keinert				
	Ag	3	80	49
	Cu	68	3	22
	Zn	29	17	29

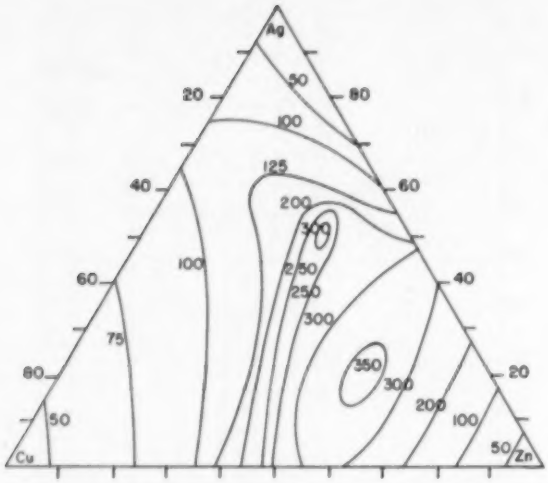

Fig. 4a—Brinell hardness number of the as-cast alloys.

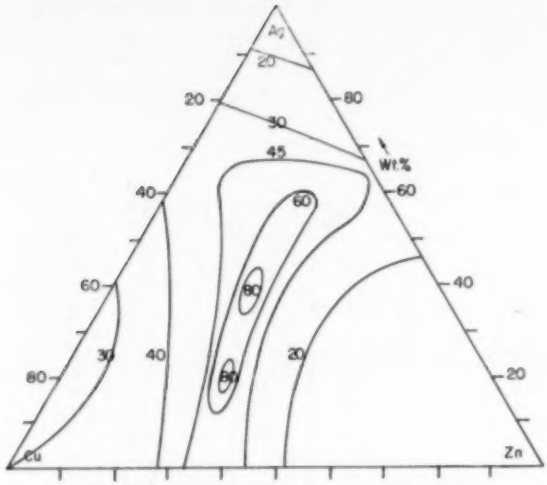

Fig. 4b—Tensile strength of the as-cast alloys.

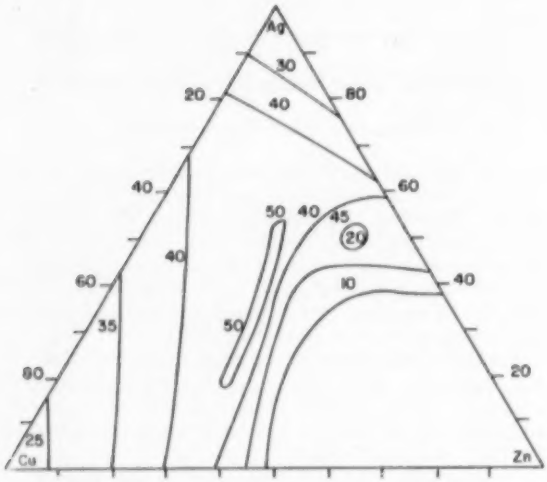

Fig. 4c—Shear strength of the as-cast alloys.

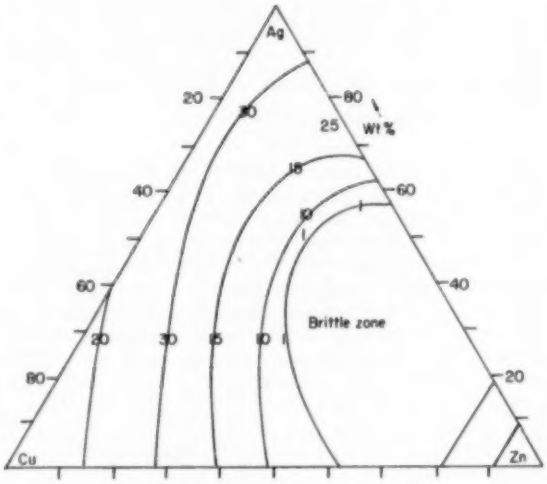

Fig. 4d—Elongation of the as-cast alloys.

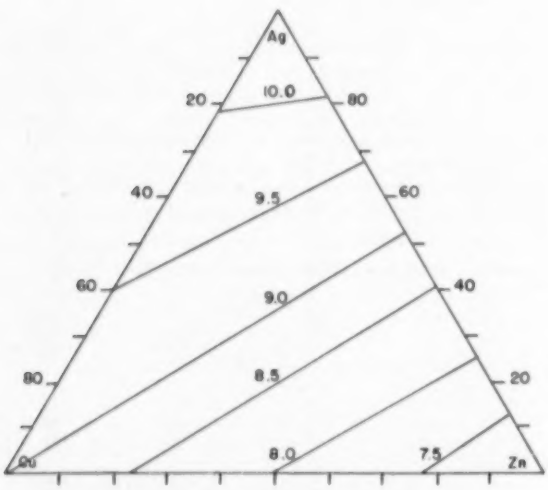

Fig. 4e—Density of the as-cast alloys.

by evaluating conventional cooling curves taken with a Leeds and Northrup micromax recorder. The location of the solid phase boundaries was found from microscopical structure determinations. The results have been compiled in Fig. 3a to f.

10 pct Silver Section, Fig. 3a: The liquidus resembles the Cu-Zn diagram at slightly lower temperatures. Three narrow three-phase fields were identified:

1—The Cu + Ag + L field extending from the eutectic point "E" at 0.0 wt pct Zn (779°C) to the solidus four-phase plane "S" at 36 wt pct Zn (680°C).

2—The Cu + β + L field extending from the peritectic point "P" at 40 wt pct Zn (850°C) to the solidus four-phase plane at 36 wt pct Zn (680°C).

3—The Cu + Ag + β field extending from the four-phase plane at 36 wt pct Zn (680°C) to lower temperatures.

The locations of the solid and liquid two-phase fields were corrected and details worked out near the peritectic point "P." The melting range ASTM grade No. 1 (ref. 3) checks with the diagram.

20 Pct Silver Section, Fig. 3b: The diagram is similar to the 10 pct section. It can be seen that "P," the origin of the peritectic reaction, shifts to the higher zinc values. The melting range data of the alloy ASTM grade No. 2 (ref. 3) are also in good agreement with the diagram.

30, 40, and 50 Pct Silver Sections, Fig. 3c, d, and e: Details of the shifting of the peritectic point "P" and the narrowing of the distance between this point and the four-phase plane can be seen in the diagrams. This is also in agreement with the ASTM grade alloys No. 11, 12, 4, and 5.

60 Pct Silver Section, Fig. 3f: The four-phase plane reaches a temperature as low as 650°C and the distance between this plane and the peritectic point "P" is only 10°C. The fact that the liquidus goes through a minimum has sometimes been misinterpreted as the existence of a ternary eutectic point.[4]

Selection of ASTM Grade Brazing Alloys: A glance at the position of the ASTM grade alloys in the phase diagrams reveals common features which are too obvious to be accidental. Grades 1, 2, 4, 5, 11, and 12 show high strength and a narrow melting range. The grades 5, 6, 7, 8, and 13 offer high ductility combined with limited fluidity, desirable features in certain brazing operations. A description of the brazing properties of the alloys will be published elsewhere.[5]

Physical Properties of the Ternary Alloys

Brinell Hardness of Cast Samples, Fig. 4a: Hardness values were determined on the chill-cast samples on a superficial Rockwell tester and converted by a conventional scale to Brinell hardness numbers. Superficial hardness measurements are preferably used on small precious metal pieces to simulate casting conditions prevailing in joints of 0.005 to 0.010 in. thickness. No difference in hardness values could be found on the outside or inside of castings up to 1 in. in diameter.

It would be out of the scope of the investigation to explain the small discrepancies in the conversion of Rockwell to BHN values. It simply amounts to the question of whether or not the increase in depth corresponds to the increase of the diameter of the indentation. Also the BHN values of different cast samples might vary from 5 to 10 points. The Rockwell readings were checked against a calibration curve measuring the diameter of the indentation on a microscope scale corresponding to the evaluation of the Brinell method. There were no disturbing embossing or springback effects noticeable.

The hardness of the alloys in the α field varies between 100 to 150 BHN, increasing with the zinc content. The β phase reaches hardness values of 200 to 300 BHN. A maximum of hardness at high silver content occurs at the composition 55 wt pct Ag-30 wt pct Zn-15 wt pct Cu. Another maximum in the brittle γ field lies outside of the scope of this investigation.

Tensile Strength of the Alloys, Fig. 4b: Rods of 5 in. length and 0.25 in. diameter were used to determine the tensile strength of the alloys. Some difficulty was encountered in the vicinity of the ternary compositions due to slipping and mashing of the ends of the extremely hard rods. The tensile strength of 30,000 to 60,000 psi in the α field is in agreement with data previously reported.[6] For the compositions of 25 to 30 wt pct Ag, 35 to 45 wt pct Cu, and 32 to 35 wt pct Zn, the tensile strength reaches its maximum and was found to vary between 80,000 to 100,000 psi. The average accuracy of the test was of the order of 10 to 20 pct.

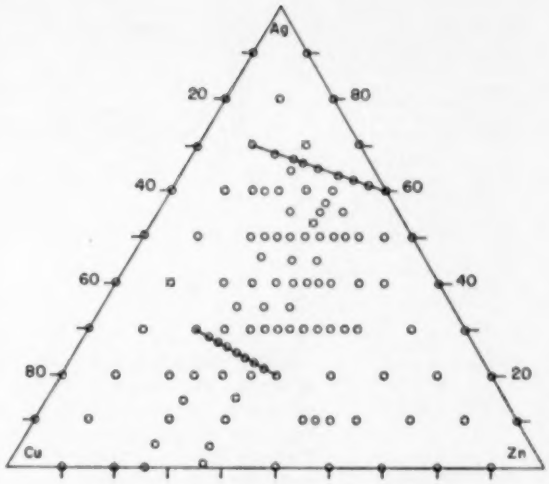

Fig. 5—Compositions of samples investigated.

Shear Strength Tests on the 0.25 In. Rods, Fig. 4c: The distribution of shear strength values over the ternary system was found to be similar to the one of the tensile strength. The shear strength is in most cases about one-half of the tensile strength. The rods were sheared off by the motion of a plate sliding between two plates on the outside, moving in opposite directions, a method used for testing rivets.

Elongation of Rods, Fig. 4d: The high elongation values in the α field are an indication for good cold workability. Elongation (2 in. gage length) and cold workability decrease rapidly toward the β phase field.

Density of the Ternary System, Fig. 4e: A density diagram ends the list of physical properties. Sufficient literature information was available to plot this chart.

Compositions of the samples investigated are plotted in Fig. 5.

Acknowledgments

The author wishes to thank Dr. Max Hansen for the valuable help extended to him in the discussion of the experimental data and for providing the theoretical framework for the phase diagrams. The experimental work was carried out in the Metallurgical Dept. of Goldsmith Bros. Smelting and Refining Co. Thanks are due to Mr. Andrew R. Devereux for his interest and support of the investigation and the company for their permission to publish the paper.

References

[1] Shuzo Ueno: The System Ag-Cu-Zn. *Mem. Kyoto Univ. Ser. 12A* (1929) pp. 347-373.

[2] M. Keinert: The System Ag-Cu-Zn. *Ztsch. Phys. Chem. A* (1932) **160**, pp. 15-33.

[3] A.S.T.M. Spec. B260-52 T (1952) and B73-29. (1929).

[4] *Metals Handbook* (1948) p. 1242. Cleveland. ASM.

[5] *Welding Engineer*, to be published in March 1954.

[6] R. H. Leach: Silver Solders. *Proc.* A.S.T.M. (1930) **30**, p. 11.

System Zirconium-Oxygen

by R. F. Domagala and D. J. McPherson

Iodide zirconium was combined with calculated amounts of ZrO_2 or master alloys and arc-melted. Annealing treatments were carried out at 21 temperature levels. Metallographic examination of the heat treated specimens permitted construction of the binary phase diagram from zirconium to ZrO_2. Oxygen additions to zirconium raise the transformation temperature as well as the melting point. Features of the diagram include the peritectic formation of beta, the formation of alpha directly from the melt, an intermediate phase ZrO_2 with a range of homogeneity, and a eutectic between alpha and ZrO_2.

PHASE relationships in the Zr-O system were determined in the range 0 to 66.7 atomic pct O (ZrO_2). Arc-melted alloys were annealed at temperature levels between 600° and 2000°C. Determination of the phase boundaries was accomplished by metallographic evaluation of specimens quenched from the various temperatures. Incipient melting techniques were used to determine solidus curves, and X-ray diffraction work was employed to study the lattice parameters of the α solid solution and the phase ZrO_2.

Experimental Procedures

Westinghouse "Grade 1" iodide zirconium crystal bar (approximately 99.8 pct pure) was employed for the investigation. This material is substantially free of the impurity inclusions characteristic of most zirconium metal. Previous work has shown it to be the most satisfactory grade for phase diagram studies.

The zirconium crystal bar, as-received, was coated with corrosion product from autoclave tests by which its grade designation is determined. The bars were sand blasted lightly, pickled for 1 min in a 20 pct HNO_3-5 pct HF aqueous solution, rinsed in water and acetone, and dried. The bars were rolled to about 1/32 in. strip, cut into 10 in. lengths, and pickled again. The material was sheared to approximately ¼ in. squares, cleaned with acetone, and stored for use.

Two pounds of specially prepared "chemically pure," and 100 grams of spectrographic grade ZrO_2 were obtained for the preparation of alloys. The "Specpure" ZrO_2 was obtained from Johnson, Matthey Co., Ltd., and Titanium Alloy Manufacturing Div. of National Lead Co. supplied the other grade of oxide. The "chemically pure" material (henceforth referred to as C.P. ZrO_2) was used for the preparation of all alloys employed in the determination of phase relationships. A limited number of alloys were prepared with the "Specpure" oxide to recheck certain phase boundaries. Analyses of the two grades of oxide are given in Table I.

Table I. Analyses of Zirconium Dioxide

Impurity	Specially Prepared C.P. (Powder), PPM	Impurity	Specially Prepared C.P. (Powder), PPM
Al_2O_3	40	MgO	500
B_2O_3	3	MnO_2	0.2
BaO	10	Na_2O	10
CaO	150	Ni_2O_3	100
Cr_2O_3	0.5	PbO	5
CuO	30	SiO_2	25
Fe_2O_3	200	SnO_2	5
HfO_2	20,000	SrO	10
K_2O	2	TiO_2	100

The spectrographic analysis of the "Specpure" ZrO_2 showed the sensitive lines of hafnium, silicon, calcium, copper, and iron to be faintly or barely visible with no other lines observed.

The C.P. ZrO_2 was received in powder form, not suitable for arc melting. Therefore, this material was compressed to wafers 1 in. in diameter and about ¼ in. thick. These were segmented and stored for use. The "Specpure" material, in the form of small granules, was suitable for use in the as-received condition.

A nonconsumable electrode arc-melting furnace was used to prepare alloys. A water-cooled copper crucible and tungsten-tipped electrode were employed. The material was placed in the crucible and rapidly melted under a protective atmosphere of helium gas by striking the arc on a tungsten stud and directing it upon the charge material. Details of operation, including drawings of this type furnace, have been published.[1]

R. F. DOMAGALA and D. J. McPHERSON, Junior Members AIME, are Associate Metallurgist and Supervisor, respectively, Physical Metallurgy Research, Metals Research Dept., Armour Research Foundation of Illinois Institute of Technology, Chicago.

Discussion on this paper, TP 3707E, may be sent, 2 copies, to AIME by April 1, 1954. Manuscript, Aug. 10, 1953. New York Meeting, February 1954.

Two 75 gram master alloy ingots containing 15 pct O and three containing 20 pct O were prepared by arc melting calculated amounts of compressed, C.P. ZrO_2 powder with zirconium. The ingots were melted, inverted, and remelted twice without opening the furnace. The ingots having a given oxygen content were then broken, combined, divided into 75 gram lots, and remelted. This process of breaking and combining ingots was repeated once more. After the third melting operation, macroexamination and microexamination of the ingots showed them to be completely homogeneous. The ingots were then crushed and screened; particles of −4 +20 mesh were reserved for alloy charging. The reason for using master alloys was twofold. First, the necessity of handling fragile compacts of ZrO_2 powder for every alloy was precluded. Second, the melting times and power levels necessary to produce completely homogeneous ingots were reduced.

For the phase diagram study, 20 gram ingots were made by combining carefully weighed amounts of master alloy with zirconium and arc melting. Alloys containing up to 5.5 pct O were prepared using the 15 pct master alloy, while the 20 pct master alloy was employed for alloys containing from 6.0 to 12.5 pct O. Alloys of higher oxygen content were made directly from compressed ZrO_2 powder and zirconium. All of the alloys were melted a total of four or five times.

A set of alloys was also made utilizing "Specpure" ZrO_2. For this work a master alloy containing 5 pct O was first prepared following the technique outlined above.

Before the regular isothermal annealing treatments were carried out, certain alloys were homogenized and cold worked to hasten the approach to equilibrium during the anneals. Specimens suitable for use were then prepared by sawing (for only the very dilute oxygen alloys), or breaking the ingots.

Samples were sealed in either Vycor or quartz bulbs for isothermal annealing treatments up to 1500°C. Anneals up to this temperature were carried out in resistance-type, porcelain tube furnaces having a temperature control of ±3°C. Specimens were quenched at the conclusion of an anneal by rapidly withdrawing the bulb from the furnace and breaking it under water.

Inasmuch as oxygen additions to zirconium raise its melting point as well as its transformation point, important phase boundaries had to be delineated at temperatures well above the maximum operating temperatures of the porcelain tube furnaces. The vacuum resistance furnace constructed for these anneals is shown in cross section in Fig. 1. Fundamentally, the furnace is a modification of a unit designed by McRitchie and Ault.[5] The heater element is a split cylinder of 0.005 in. thick molybdenum sheet, held in place by removable copper contacts (Items No. 6, 12 and 18 in Fig. 1). The top and bottom of the furnace are at different electrical potentials, and are insulated by an "O" ring (No. 17, Fig. 1). This ring also serves as a vacuum seal. The top and bottom covers are held in place by an interrupted thread arrangement and clamping device, respectively. "O" rings are provided to make these seals vacuum tight.

Four cylindrical radiation shields within the furnace increase the maximum operating temperature. The shields are formed from 0.005 in. thick sheet; the innermost being tantalum, while the remaining three are molybdenum. Specimen-supporting tungsten wires are hung axially in the furnace from a fork attached to a horizontal, off-center shaft (No. 4, Fig. 1). Quenching is accomplished by rotating the shaft, thus allowing the specimens and wire to fall into the bottom chamber. The brass shell and the copper contacts are cooled by water flowing through ¼ in. copper tubing and water chambers, respectively. Sight ports at the top and side of the furnace permit observation of the specimen temperature during heating.

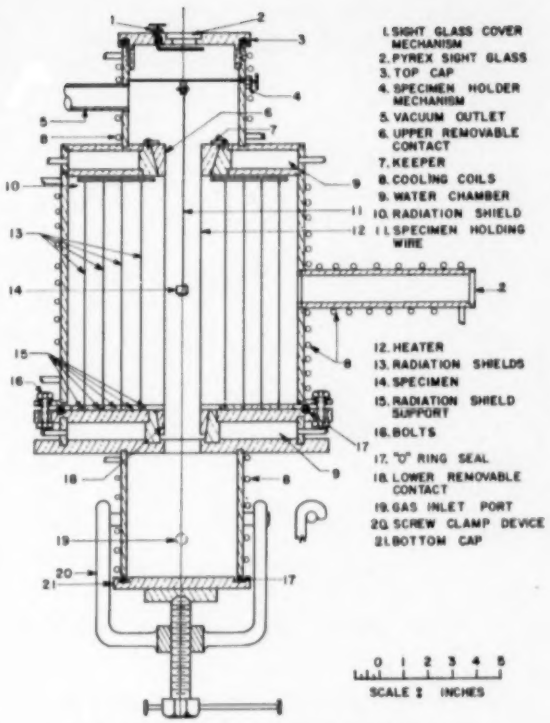

Fig. 1—High temperature vacuum resistance furnace.

Power is supplied to the heater through bus bars attached to the top and bottom portions of the furnace. A 13 kw Powerstat, operating off a 220 v line, controls the power supplied to a 15 kw step-down transformer. The transformer transmits current to the furnace at 0 to 10 v. The furnace is evacuated to a pressure below 0.1 micron, (1×10^{-4} mm of Hg). Prior to annealing runs, a correlation of optically measured vs true temperatures was made. The optically measured melting points of nickel and platinum were plotted against the accepted values. The melting point of zirconium was then determined on a basis of the calibration curve and was found to average 1845°C, about 7°C lower than the average value previously determined in a vacuum induction furnace, but within the estimated range of experimental accuracy.

Anneals were conducted by suspending the samples in the center of the furnace and slowly heating to temperature. Although very rapid heating rates were possible, the specimens were brought to temperature in about 15 min. The desired annealing temperature was maintained for 5 to 10 min, and then the specimens were dropped to the bottom of the furnace and the power was shut off simultaneously. Temperature control during annealing treatments was ± 10°C.

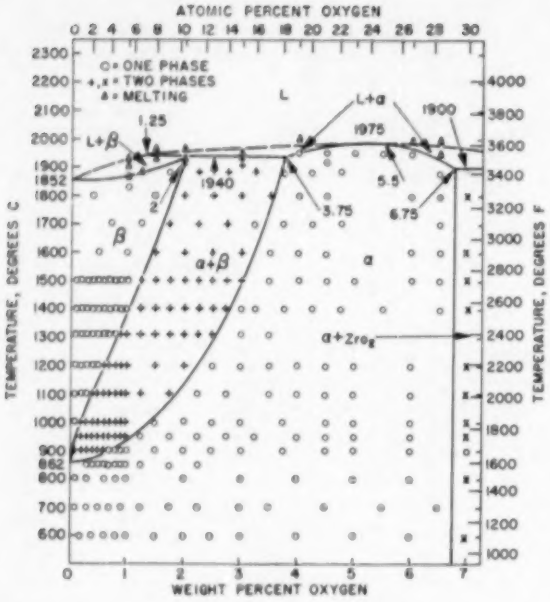

Fig. 2—Expanded diagram of the zirconium-rich region of the Zr-O system.

The vacuum induction furnace used to aid in outlining the solidus curves for this system has been described.[1] Specimens supported on tungsten wires are rapidly heated until visible melting occurs; then samples of the same alloy content are quenched from successively lower temperatures. By metallographic evaluation of the resulting structures, the solidus curve is determined.

The method employed for determination of oxygen in zirconium was substantially that of Read and Zopatti.[5] Hydrogen chloride gas freshly generated by reacting sulphuric acid and sodium chloride is dried, purified, and passed over the alloy. The zirconium is volatilized as a chloride and carried away in a stream of helium gas. The oxygen in the alloy remains, combined with zirconium as ZrO_2. The reaction is carried out at 400° to 600°C in platinum crucibles.

The accuracy of analysis by this method is believed to be good. Checks made on an alloy of a given oxygen content always yielded the same results, and in every case agreement with nominal compositions was excellent.

Results and Discussion

Fifty-six alloys based on C.P. ZrO_2 were prepared for the study of phase relationships in this system. A complete tabulation of these alloys, with analyses, is given in Table II. Similar data for alloys based on "Specpure" ZrO_2 are presented in Table III. All compositions were not prepared with the higher purity oxide due to the limited quantity available. Alloys containing 0 to 7.5 pct O were homogenized at 1200°C for 48 hr prior to annealing treatments. Alloys were cold rolled before annealing when possible. The amount of reduction accomplished decreased from 70 pct for the 0.1 pct O alloy to 3 pct for the 0.8 pct O alloy. It was not possible to cold work alloys containing more than 0.8 pct O.

The results of analyses illustrate that the analyzed compositions were in excellent agreement with the intended compositions. Within the accuracy of the analytical techniques employed, it can be said that the nominal compositions are correct to within ± 0.1 pct O in the dilute alloy region and well within ±0.5 pct O in the oxygen-rich alloys. Weight loss measurements made on many of the ingots after arc melting also indicated that the true compositions must be very close to the intended compositions.

The phase diagram has been constructed on a basis of the intended oxygen contents of the alloys. The accuracy of phase boundary delineations, therefore, is at least as good as the accuracy of compositions given in Tables II and III.

In order to determine times necessary to approach equilibrium during isothermal annealing, preliminary treatments were made. Alloys containing 0.3, 2, 4, 7, and 10 wt pct O were annealed for three different times at 800°, 1000°, and 1200°C. Metallographic examination of these samples showed no change in the relative amounts of phases after 150, 75, and 15 hr at 800°, 1000°, and 1200°C, respectively. These data were extrapolated to determine appropriate annealing times at all temperature levels employed for this study.

Anneals of alloys based on C.P. ZrO_2 were carried out at 21 temperature levels between 605° and 2000°C. Table IV presents a tabulation of the temperatures and times of annealing together with the number of specimen compositions treated at each temperature. A control sample of unalloyed zirconium was included with each annealing treatment from 605° to 1800°C.

Table II. Summary of C.P. Zr-O Alloys

Intended Oxygen, Wt Pct	Analyzed Oxygen, Wt Pct	Intended Oxygen, Wt Pct	Analyzed Oxygen, Wt Pct
Zr	0.027	6.5	
0.1		7.0	7.0
0.2	0.31	7.5	
0.3		8.0	8.0
0.4	0.47	8.5	
0.5		9.0	9.0
0.6	0.62	9.5	
0.7		10.0	9.9
0.8	0.89	10.5	
0.9		11.0	10.9
1.0	1.0	11.5	
1.25		12.0	12.0
1.5		12.5	
1.75		13.0	13.2
2.0	2.1	13.5	
2.25		14.0	14.2
2.5		14.5	
2.75		15	15.2
3.0	3.2	16	16.4
3.25		17	
3.5		18	18.1
3.75		19	
4.0	4.2	20	20.3
4.25		21	
4.5		22	22.6
4.75		23	
5.0	5.4	24	
5.5		25	
6.0	6.2	ZrO_2	25.9

Table III. Summary of "Specpure" Zr-O Alloys

Intended Oxygen, Wt Pct	Analyzed Oxygen, Wt Pct	Intended Oxygen, Wt Pct	Analyzed Oxygen, Wt Pct
0.1		0.8	0.80
0.2	0.26	0.9	
0.3		1.0	1.0
0.4	0.44	1.5	
0.5		2.0	2.0
0.6	0.67	2.5	
0.7		3.0	3.0
		ZrO_2	25.8

Partial diagrams of the Zr-O binary system, based on weight percent, are presented in Figs. 2 and 3. The former figure is an expanded diagram of the zirconium-rich region, while the latter presents the phase relationships up to ZrO_2. These are documented with most of the metallographic data points necessary for construction of the diagram.

Metallographic evidence substantiating the placement of various phase boundaries and temperature horizontals is presented in the following micrographs.* Figs. 4 and 5 show a transformed β and an α + transformed β structure observed in 0.3 and 0.4 pct O alloys, respectively, quenched from 1100°C. The positioning of the $\alpha + \beta/\alpha$ boundary at the same level was based on the $\alpha + \beta$ and α structures found in alloys containing 1.75 and 2.25 pct O, Figs. 6 and 7, respectively, also quenched from 1100°C. Figs. 8 and 9 show 100 pct α and $\alpha + ZrO_2$ structures of specimens containing 6.0 and 7.0 pct O, respectively, quenched from the same temperature.

* The composition values given in the discussion of structures refer to weight percent. The etchant employed was 20 pct HF, 20 pct HNO_3 in glycerine.

Micrographs of specimens quenched from 1600°C are presented next. An alloy containing 1.0 pct O (Fig. 10) is seen to be transformed β, while at 1.5 pct O (Fig. 11) an α + transformed β structure is observed. Samples containing 3.0 and 3.5 pct O are shown in Figs. 12 and 13. The 3 pct composition is mostly α phase with "bars" of residual transformed β, while at 3.5 pct O the structure is 100 pct α. The $\alpha/\alpha + ZrO_2$ boundary is positioned at 1600°C by the micrographs of Figs. 14 and 15, 6.5 and 7.0 pct O alloys, respectively. The former is all α while the latter is two phase, $\alpha + ZrO_2$.

It was interesting to note that the retained β structure was not observed in any alloy, regardless of its thermal history.

Due to the slightly slower cooling rate of samples quenched from very high temperatures in the vacuum resistance furnace, some difficulty was encountered in the interpretation of microstructures across the $\beta/\alpha + \beta$ boundary. The resulting coarseness of the β transformation product made it difficult to distinguish all-β structures from those containing some isothermal α. The difficulty was limited to this single high temperature region, and with the help of other data, the boundary placement is believed accurate to at least ± 0.25 pct O.

Table IV. Annealing Schedule of C.P. Zr-O Alloys

Temperature, °C	Time, Hr	No. of Compositions Treated
2000	*	9
1950	*	6
1930	*	3
1920	0.1	1
1910	*	3
1885	0.1	20
1800	0.1	18
1700	0.1	20
1600	0.1	21
1500	0.25	40
1398	1	44
1308	5	19
1204	16	33
1100	40	32
1003	70	30
947	90	32
898	100	30
849	125	33
800	130	24
700	305	28
605	500	25

* Held at temperature until visible melting was observed.

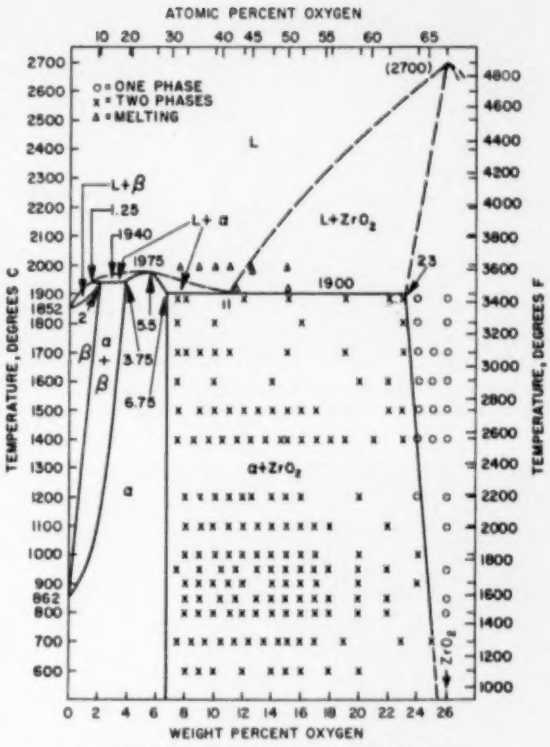

Fig. 3—Partial diagram of the Zr-O system.

The $\beta/\alpha + \beta$ and $\alpha + \beta/\alpha$ boundaries were checked by examining "Specpure" alloys annealed and quenched from 1000°, 1200°, and 1400°C. Structures identical to those found in the C.P. alloys were observed in every case. Because of this agreement, no additional checks were made on boundaries delineated with alloys based on C.P. ZrO_2.

The location of boundaries in the dilute alloy region in the vicinity of the solidus is shown by the microstructures of the next series of samples. Fig. 16 shows a 1.25 pct O sample quenched from 1885°C. Transformed β phase plus signs of melting are evident here. A 1.75 pct O alloy, annealed at the same level, is 100 pct transformed β with no signs of melting, Fig. 17. A 2.25 pct O alloy also annealed at 1885°C, Fig. 18, consists of two phases, α + transformed β.

The placement of the peritectic temperature is supported by the structures of Figs. 19 and 20. In both figures a 3 pct alloy is shown. Fig. 19 illustrates the $\alpha + \beta$ structures found at this composition when quenched from 1930°C, while the following figure shows the indications of melting observed when the specimen is quenched from 1950°C.

Figs. 21 and 22 show structures observed in alloys containing 1.0 and 1.5 pct O, respectively. The former sample was quenched from 1930°C; β plus signs of melting are evident. The latter alloy was quenched from 1960°C; here primary dendrites of α have appeared on re-solidification. These structures position the composition of the peritectic liquid between 1.0 and 1.5 pct O and also add supporting evidence to the placement of the temperature of the peritectic reaction.

The maximum extent of the $\alpha + \beta$ field and the composition of α solid solution which enters into the peritectic reaction are confirmed by the microstruc-

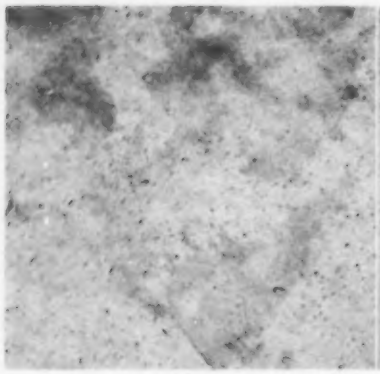

Fig. 4—0.3 pct O alloy quenched from 1100°C. Transformed β solid solution. Etched. X250.

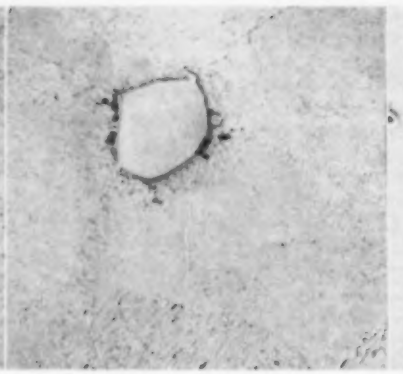

Fig. 5—0.4 pct O alloy quenched from 1100°C. Isothermal α plus transformed β. Etched. X250.

Fig. 6—1.75 pct O alloy quenched from 1100°C. α plus last traces of transformed β. Etched. X250.

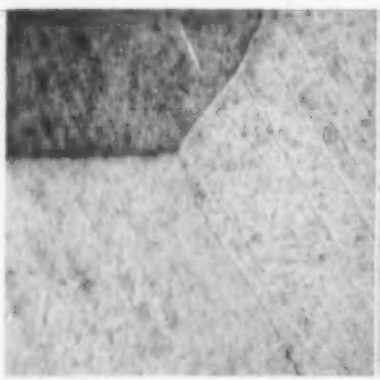

Fig. 7—2.25 pct O alloy quenched from 1100°C. A veined all α structure. Etched. Polarized light. X250.

Fig. 8—6.0 pct O alloy quenched from 1100°C. An all α structure. Etched. X500.

Fig. 9—7.0 pct O alloy quenched from 1100°C. A two-phase, $\alpha + ZrO_2$ structure. Unetched. X500.

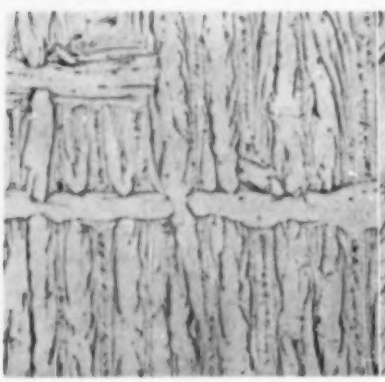

Fig. 10—1.0 pct O alloy quenched from 1600°C. Coarse transformed β. Etched. X250.

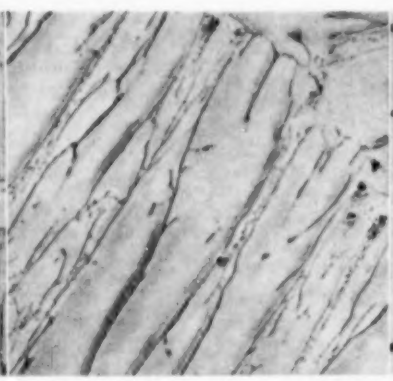

Fig. 11—1.5 pct O alloy quenched from 1600°C. Transformed β plus isothermal α. Etched. X250.

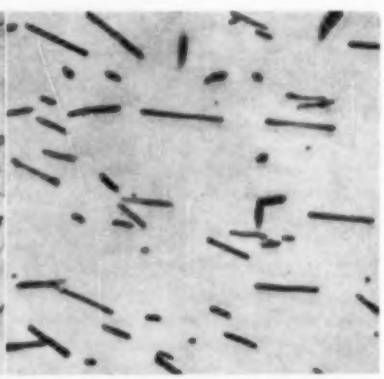

Fig. 12—3.0 pct O alloy quenched from 1600°C. α plus "bars" of transformed β. Etched. X200.

tures of a 4.0 pct O alloy shown in Figs. 23 and 24. Fig. 23 is the microstructure of this alloy quenched from 1950°C; an α structure is present. Signs of melting in the α are seen in this alloy when quenched from 2000°C, Fig. 24.

The maximum at 5.5 pct O and 1975°C is verified by the sequence of structures in Figs. 25 to 28. Fig. 25 is a 5 pct O alloy quenched from 1950°C, while Fig. 26 shows the same alloy quenched from 2000°C. The former is 100 pct α, while the latter has signs of melting in addition to the α phase. The structures of Figs. 27 and 28 show a 6.5 pct O alloy quenched from 1885° and 1950°C, respectively. The presence of all α and α plus signs of melting, respectively, serves to position the solidus curve at another composition.

Fig. 29 shows the eutectic structure of an as-cast alloy containing 11.0 pct O. The structures of Figs. 30 and 31 show a 15.0 pct O alloy quenched from 1885° and 1990°C, respectively. The latter shows the appearance of melting characterized by the spheroidization of the α entrapped in the ZrO_2 dendrites,

Fig. 13—3.5 pct O alloy quenched from 1600°C. 100 pct α. Unetched. Polarized light. X250.

Fig. 14—6.5 pct O alloy quenched from 1600°C. 100 pct α. Unetched. Polarized light. X250.

Fig. 15—7.0 pct O alloy quenched from 1600°C. α plus particles of ZrO_2. Unetched. X250.

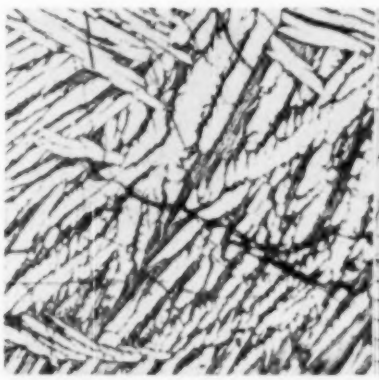

Fig. 16—1.25 pct O alloy quenched from 1885°C. Transformed β plus signs of melting. Compare with the normal transformed β structure of Fig. 17. Etched. X250.

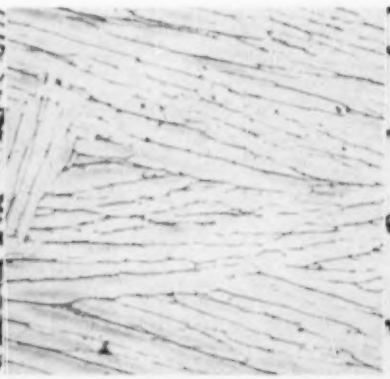

Fig. 17—1.75 pct O alloy quenched from 1885°C. 100 pct transformed β. No melting. Etched. X250.

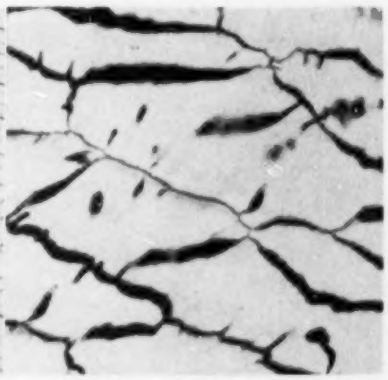

Fig. 18—2.25 pct O alloy quenched from 1885°C. Two phases, α plus transformed β. Etched. X250.

and the general loss of shape of the dendrites. The former structure characterizes the appearance of unmelted, hypereutectic alloys.

The nonexistence of a phase ZrO (14.9 wt pct, 50 atomic pct O) is confirmed by the micrographs of the 15 pct O alloys described above at high temperatures and at lower levels by Fig. 32. A 15 pct O alloy is shown quenched from 700°C. Only the phases α and ZrO_2 are seen, which refutes the possible peritectoid formation of ZrO. In the course of the investigation, no single piece of evidence was found which could be construed as evidence for the existence of ZrO.

A series of four micrographs illustrating the miscibility range of ZrO_2 is shown in Figs. 33 to 36. Fig. 33 is a 23 pct O alloy annealed and quenched from 1885°C. At this composition, a two phase α + ZrO_2 structure is seen. The α at the grain boundaries is isothermal, while the α striations within the grains appear to be the result of an unsuppressible rejection on cooling. At 24 pct O, and 1885°C (Fig. 34), ZrO_2 may be seen with only anisothermal α striations as before. The decrease in the miscibility range with decreasing temperature is illustrated in the structure of Fig. 35, a 25 pct O alloy quenched from 700°C. The two phases α +ZrO_2 are present, as in the 23 pct O alloy quenched from 1885°C. There is a notable decrease in the number of striations at this composition. Fig. 36 is a 26 pct O alloy (stoichiometric ZrO_2). This sample had been treated at 1885°C and the striation-free single-phase ZrO_2 is present. The absence of markings in stoichiometric ZrO_2, quenched from all temperatures, further supports the decreasing miscibility range of the phase and precludes the possible association of the markings with polymorphy in ZrO_2.

In addition to the data points obtained from the high temperature heat treatments for positioning the solidus line, limited additional data from quenches in the incipient melting furnace generally confirmed the curve. Table V is a summary of the data obtained in this way. Most of the information given here was plotted on the diagrams.

To investigate the possible change in composition of alloys treated at high temperatures in the vacuum

Table V. Incipient Melting Data

Alloy Compositions, Wt Pct O	Melting Observed, °C	No Melting, °C
Zr	1850	
1.0	1855	1830
1.5	1960	
2.0	1930	1900
3.0	1950	
3.5	1930	1855
4.5	1955	1885
11.5	1990	
15	1920	
18	2310 (visible melting)	
21	2390 (visible melting)	

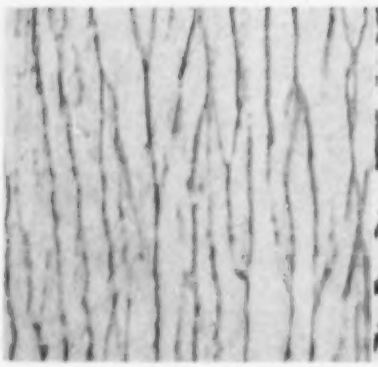

Fig. 19—3.0 pct O alloy quenched from 1930°C. An α plus transformed β structure. Compare with Fig. 20. Etched. X250.

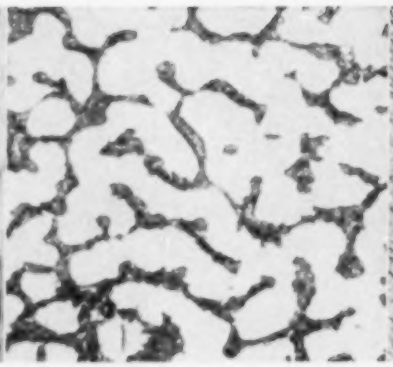

Fig. 20—3.0 pct O alloy quenched from 1950°C in the incipient melting furnace. Signs of melting in the $\alpha + \beta$ structure. Etched. X250.

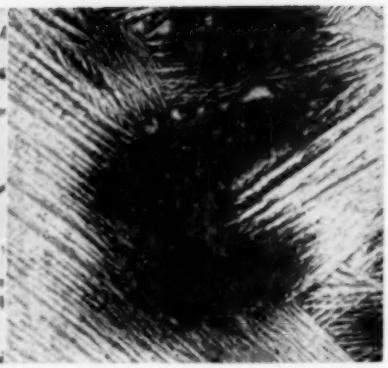

Fig. 21—1.0 pct O alloy quenched from 1930°C. β plus signs of melting. No α dendrites formed in the melted regions. Compare with Fig. 22. Etched. X150.

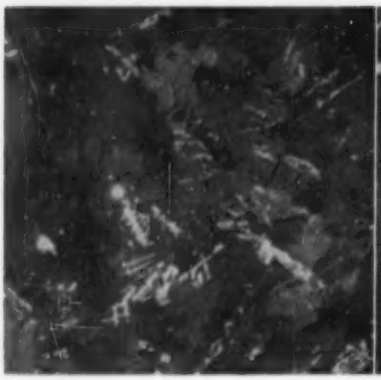

Fig. 22—1.5 pct O alloy quenched from 1960°C in the incipient melting furnace. β plus signs of melting. At this composition α dendrites formed on solidification of the melted regions. Unetched. Polarized light. X250.

Fig. 23—4.0 pct O alloy quenched from 1950°C. An all α structure with no signs of melting. Compare with Fig. 24. Unetched. Polarized light. X150.

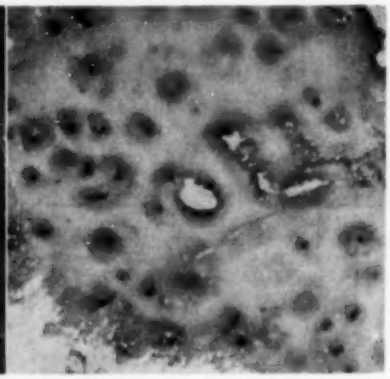

Fig. 24—4.0 pct O alloy quenched from 2000°C. α plus signs of melting. Etched. X150.

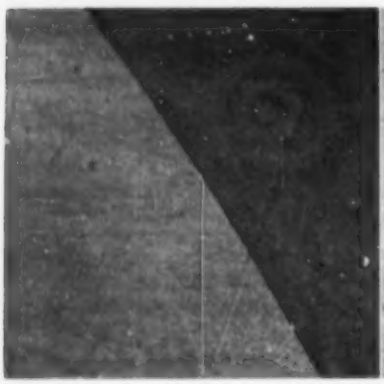

Fig. 25—5.0 pct O alloy quenched from 1950°C. An all α structure. Unetched. Polarized light. X250.

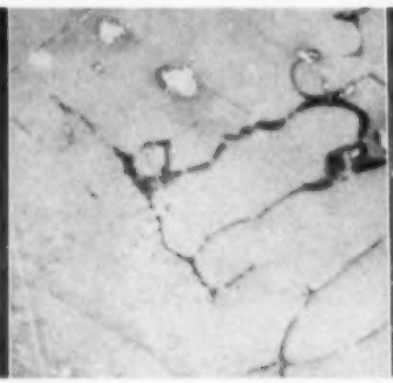

Fig. 26—5.0 pct O alloy quenched from 2000°C. α plus signs of melting. Unetched. Polarized light. X200.

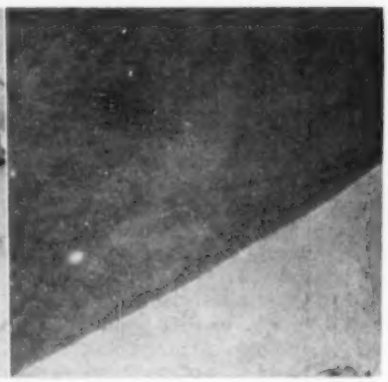

Fig. 27—6.5 pct O alloy quenched from 1885°C. 100 pct α. Unetched. Polarized light. X250.

furnaces, four samples were selected, heated to just below the solidus, and quenched. Analyses were obtained for the oxygen concentration and the values were found to fall within ± 0.1 pct O of the original analyses. The samples chosen for this study nominally contained 3.0, 5.0, 8.0, and 15.0 pct O.

The variation of lattice parameters of the α phase with oxygen content was determined from 16 alloys containing 0 to 33 atomic pct O (0 to 8 wt pct). Alloys for the study were annealed at and quenched from 1000°C. The unit cell is expanded by an average value of 0.0016 kX per atomic pct oxygen in the "*C*" direction and by only about 0.0004 kX per atomic pct oxygen in the "*a*" direction. The expansion in the "*C*" direction compares to 0.0043 kX in the analogous α solid solution of the Ti-O system,[4] so it is evident that of the two, the zirconium lattice can much more easily accommodate the interstitial

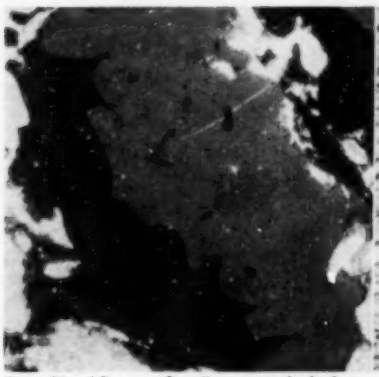

Fig. 28—6.5 pct O alloy quenched from 1950°C. α plus signs of melting. White areas are voids in this very brittle alloy. Unetched. Polarized light. X200.

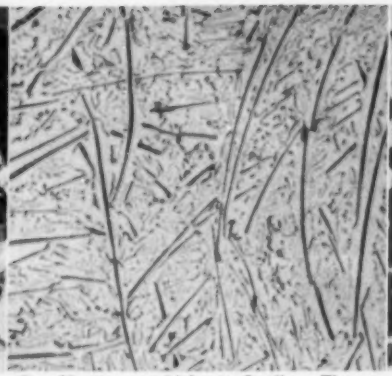

Fig. 29—As-cast 11.0 pct O alloy. The α-ZrO_2 eutectic. Unetched. X250.

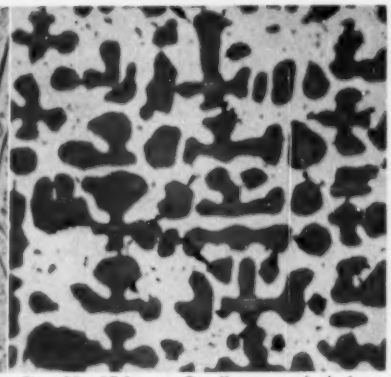

Fig. 30—15.0 pct O alloy quenched from 1885°C. At this temperature there is no indication of melting in the α + ZrO_2 structure. Unetched. X250.

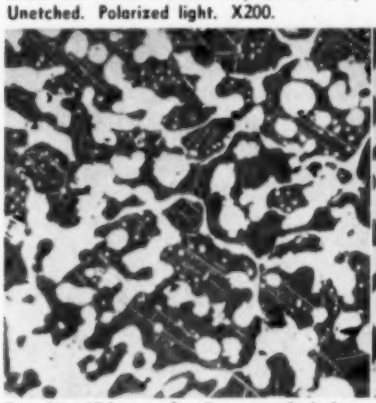

Fig. 31—15.0 pct O alloy quenched from 1920°C. The same phases as in the previous figure, but the change in appearence is characteristic of the slightly melted structure. Unetched. X250.

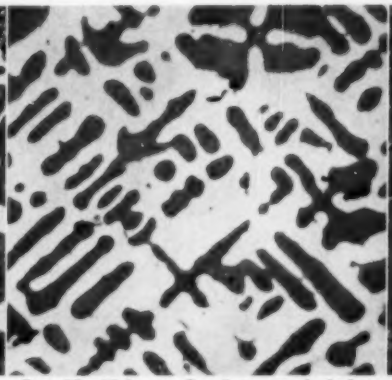

Fig. 32—15.0 pct O alloy quenched from 700°C. α + ZrO_2. This figure as well as Figs. 30 and 31 deny the existence of a phase ZrO. Unetched. X250.

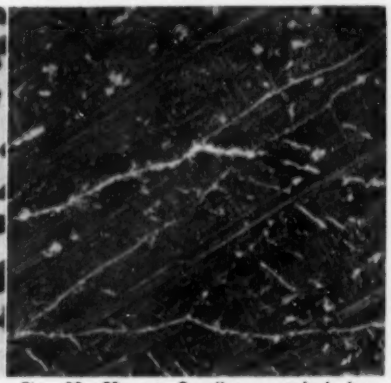

Fig. 33—23 pct O alloy quenched from 1885°C. Striated ZrO_2 plus a small amount of isothermal α. The striations are rejected α. Unetched. X250.

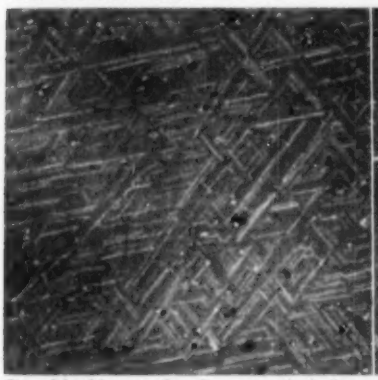

Fig. 34—24 pct O alloy quenched from 1885°C. Only striated ZrO_2 is present here. There is no isothermal α. Unetched. X250.

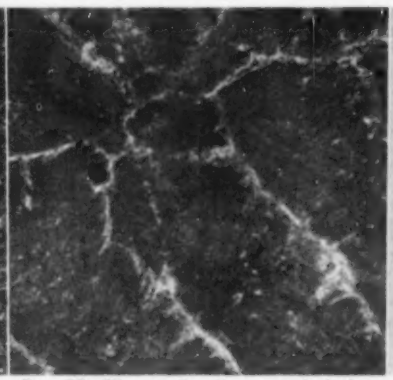

Fig. 35—25 pct O alloy quenched from 700°C. The two-phase α + ZrO_2 structure as in Fig. 33. Notice the lesser number of striations in the ZrO_2 grains. Unetched. X250.

Fig. 36—26 pct O alloy (stoichiometric ZrO_2) quenched from 1885°C. The single-phase ZrO_2 structure is seen with no striations as in Figs. 33, 34, and 35. Unetched. X250.

solution of oxygen. Complete results and details of the lattice parameter study are available in ref. 5.

Comparisons with Former Results

The data available in unclassified literature for comparison with the present work were limited. De Boer and Fast[6] proved that the $\alpha \rightarrow \beta$ transformation temperature is raised by the addition of oxygen. Cubicciotti[7] presented a "melting point-composition diagram" for the system which is in disagreement with the present work. Cubicciotti's data were obtained by optically measuring the temperature at which wire samples visibly melted. His alloys were prepared by allowing oxygen to react with iodide zirconium wire, followed in some cases by an annealing treatment to allow diffusion and homogenization. The curve presented showed a steady increase in visual melting temperature with the addition of oxygen, from zircorium to ZrO_2. The existence of the α-ZrO_2 eutectic immediately refutes this type of relationship. A slight leveling off in the curve was found by Cubicciotti at about

2475°C and approximately 18 to 23 wt pct O (55 to 63 atomic pct).

Due to the technique of alloy formation it is unfortunate that alloy homogeneity, over the composition range studied, was not documented by metallographic evidence in Cubiccotti's work. The visual method of melting point determination can also produce spurious results. In the present investigation it was found that an alloy rich in oxygen (greater than about 6 pct) could be heated considerably above the solidus before any outward visible signs of melting were detected. These factors indicate that if a thin oxide coat or an oxygen-rich layer were present on the wire specimens, Cubicciotti's melting point data would tend to be quite high, as was the case when compared with the present work.

Although disagreement on the solidus curve exists, several points of agreement were found. The maximum solubility of zirconium in ZrO_2 found in the present investigation coincides with that reported by Cubicciotti, and further, no evidence for the existence of a phase ZrO was found in either work.

The maximum solubility of oxygen in α zirconium was found to agree with semiquantitative data presented by several authors.[6, 9]

The presence of a eutectic in the system has never been reported by previous investigators.

One important feature of the diagram, the melting point of ZrO_2, was not determined in the present work. The value presented, 2700°C, is an average of the values found in the literature.[10-14]

According to the literature[12, 15-17] there are two or more polymorphic forms of ZrO_2; there is, however, considerable disagreement on the number of transformations and the temperatures at which they occur. It was considered of interest in the present investigation to determine whether or not any high temperature modification of ZrO_2 could be retained by quenching to room temperature. X-ray powder patterns were made with as-received and arc-cast C.P. and "Specpure" ZrO_2. In addition, samples of "Specpure" ZrO_2 were heated and quenched from 900°, 1210°, 1745°, and 2315°C. The monoclinic modification, corresponding to that listed in the Hanawalt Tables,[18] was invariably found. The results of this brief study do not preclude the possible existence of allotropes of ZrO_2, but indicate that the problem must be resolved by dynamic techniques.

Summary

Metallographic analysis of as-cast and annealed samples of arc-melted alloys yielded the partial Zr-O binary phase diagram.

Important features of the diagram include:

1—β solid solution forms by the peritectic reaction liquid (1.25 wt pct, 7 atomic pct O) + α (3.75 wt pct, 18 atomic pct O) → β solid solution (2 wt pct, 10.5 atomic pct O), at 1940° ± 20°C.

2—Oxygen stabilizes α zirconium, raising the transformation temperature and yielding an open maximum melting point for the α solid solution. The maximum occurs at 1975° ± 25°C and 5.5 wt pct O (25 atomic pct).

3—The maximum solubility of oxygen in β zirconium is 2 wt pct (10.5 atomic pct) at the temperature of the peritectic reaction, decreasing to zero at the transformation temperature, 862°C.

4—The α modification of zirconium can dissolve up to 6.75 wt pct O (29 atomic pct) and the α/α + ZrO_2 solubility boundary is a vertical line at that composition.

5—A eutectic occurs at 1900° ± 20°C and 11 wt pct O (43.5 atomic pct), whereby liquid (11 wt pct, 43.5 atomic pct O) → α solid solution (6.75 wt pct, 29 atomic pct O) + ZrO_2 solid solution (23 wt pct, 63 atomic pct O).

6—The intermediate phase ZrO_2 which melts with an open maximum at 2700°C has a range of homogeneity on the zirconium side of the stoichiometric composition (25.97 wt pct, 66.67 atomic pct O), changing from 23 wt pct O (63 atomic pct) at the eutectic temperature, 1900°C, to 25 wt pct O (65.5 atomic pct) at 700°C.

7—There are no additional singular phases between zirconium and ZrO_2.

The characteristic compositions presented above are believed to be accurate to ± 0.25 wt pct O except for the α/α + ZrO_2 boundary and the solubility range of ZrO_2, which are within ± 0.5 wt pct O of the equilibrium value.

Acknowledgments

The authors wish to thank the Atomic Energy Commission, sponsors of this work under Supplement No. I of Contract No. AT(11-1)-149, "Phase Diagrams of Zirconium Base Alloys," for permission to publish this paper. Special thanks are due to C. A. Johnson who was responsible for the metallographic work, W. Rostoker for interpretation of the X-ray patterns, W. A. Dupraw and H. M. Manasevit for chemical analyses, and to H. L. Nurnberg, project technician.

References

[1] M. Hansen, H. D. Kessler, and D. J. McPherson: *Trans.* ASM (1952) **44**, p. 518.

[2] F. H. McRitchie and N. N. Ault: *Journal* Amer. Ceramic Soc. (1950) **33**, p. 25.

[3] E. B. Read and L. P. Zopatti: Presented at Conference on Analytical Chemistry and Applied Spectroscopy, Pittsburgh, Feb. 15-17, 1950. AECD 2798.

[4] W. Rostoker: *Trans.* AIME (1952) **194**, p. 981; JOURNAL OF METALS (September 1952).

[5] R. F. Domagala and D. J. McPherson: Summary Report (COO-181) on USAEC Contract No. AT(11-1)-149, March 1953.

[6] J. H. DeBoer and J. D. Fast: *Rec. Trav. Chim.* (1935) **55**, p. 459.

[7] D. Cubicciotti: Tech. Report No. 6, U.S. Navy, Office of Naval Research, Research Contract N7-ONR-329, Task Order II, May 1950.

[8] C. F. P. Bevington, S. L. Martin, and D. H. Mathews: *Proc.* Intern. Congr. Pure Applied Chem. (London) (1947) **11**, p. 3.

[9] W. G. Guldner and L. A. Wooten: *Journal* Electrochem. Soc. (1948) **93**, p. 223.

[10] N. Zirnowa: *Ztsch. anorg. allgem. Chemie* (1934) **218**, p. 193.

[11] F. Henning: *Naturwiss* (1925) **13**, p. 161.

[12] I. E. Campbell, C. F. Powell, D. H. Nowicki, and B. W. Gonser: *Journal* Electrochem. Soc. (1949) **96**, p. 318.

[13] E. A. Gulbransen and K. Andrew: *Trans.* AIME (1949) **185**, p. 515; JOURNAL OF METALS (August 1949).

[14] W. A. Lambertson and F. H. Gunzel, Jr.: AECD-3465, Oct. 22, 1952.

[15] W. M. Cohn: *Trans.* Electrochem. Soc. (1935) **68**, p. 65.

[16] P. Duwez and F. Odell: *Journal* Amer. Ceramic Soc. (1950) **33**, p. 274.

[17] W. E. Hauth, Jr.: *Bull.* Amer. Ceramic Soc. (1951) **30**, p. 165.

[18] Hanawalt Card gave following reference: Ruff and Ebert: *Ztsch. anorg. allgem. Chemie* (1929) **24**, p. 180.

High Temperature Strength of Wrought Aluminum Powder Products

by Eric Gregory and Nicholas J. Grant

The creep rupture properties of wrought aluminum powder products made from five grades of sintered aluminum powder were investigated at temperatures from 400° to 900°F for rupture times up to 1000 hr. The effect of stress concentrations on materials of this type was investigated by means of notched creep rupture tests. A tentative correlation was obtained between the creep rupture properties and the structure as revealed by electron microg.aphs.

SEVERAL papers have been published recently concerning the production and properties of wrought aluminum powder products and their possible high temperature applications. Most of the published work in this field has come from abroad, notably Switzerland, and articles by Irmann and his colleagues were summarized in English recently.[1,2]

Most of the papers published by Dr. Irmann are principally concerned with the retention of properties (by a product which is produced from extremely fine flake powder and is subsequently hot extruded) after heating to high temperature for prolonged times. The powder may be in atomized or flake form, and during hot working the applied pressure is reported to plastically deform the aluminum powder, thus breaking the oxide skin and welding the particles together. Irmann attributes the remarkable properties to the dispersion of oxide inclusions. Specifically, the product described by Irmann is one labeled SAP (Sintered Aluminum Powder) in which the initial flake powder is so fine that at least 50 pct of the flakes have one dimension of 2 microns or less. The composition of the starting aluminum shows in percent, Fe, 0.18; Si, 0.19; Zn, 0.06; Ti, 0.03; Cu, Mn, Mg, all nil; balance Al, approximately 99.5 pct.

Aluminum is not the only material that has been found to have increased resistance to deformation at elevated temperatures when produced by powder metallurgy. It has been reported by Middleton, Pfeil, and Rhodes[3] that platinum has a higher recrystallization temperature when produced by powder metallurgy and exhibits peculiar properties, many of which are similar to those of the aluminum powder products. Difficulties were encountered in explaining the reason for the strengthening in the case of platinum since the existence of the oxide is doubtful. The authors attributed the special properties to "a small amount of suitably dispersed porosity." This theory was supported by von Zeerleder[4] in the discussion to the paper, and the similarity between this method of hardening and that suggested by Röhner in his theory of age hardening was pointed out.

R. de Fleury[5] attempted to explain some of the properties in terms of the modulus of elasticity and elastic limit of alumina and aluminum while von Zeerleder examined the relationship between the yield strength and the reciprocal of the powder particle size.

Boenisch and Widerholt[6] dealt mainly with the corrosion resistance of the powder aluminum material and compared it with other aluminum alloys. The diffusion rates of other metals in SAP and pure aluminum have been compared by Seith and Löpmann.[7] They showed that the alloying metals diffuse particularly quickly in SAP possibly due to the very fine grain size. The properties of the Alcoa products were given by Lyle.[8] The creep rupture properties of SAP and two of the Alcoa experimental powder products were compared by Gregory and Grant[9] and it was shown that these products are vastly stronger at 900°F than are the best cast and wrought alloys at 600°F. Since the publication of these data, the authors have investigated two further aluminum powder products and it is the object of this paper to show how the high temperature creep rupture properties of the five materials vary with oxide content and with the structure as revealed by electron microscopy.

Table I. Room Temperature Properties

Material	Oxide Content, Wt Pct	Tensile Strength, Psi	Yield Strength, Psi	Elongation, Pct	Distance Between Particles**	
					Center to Center, Microns	Surface to Surface, Microns
M255*	0.5- 1	22,600	17,600	22	2.77	2.17
M293*	1- 3	27,200	17,400	25	1.35	1.07
M257*	6- 8	35,800	24,600	16	0.85	0.71
M276*	15-17	53,300	35,800	4	0.65	0.39
SAP	10-14	50,000	32,800	8	0.54	0.35

* Mechanical data from Alcoa.
** See section on electron microscopy.

Materials

One of the five products, SAP, a sintered aluminum product, was supplied by the Societe Anonyme pour l'Industrie de l'Aluminium, Neuhausen a/RHF, Switzerland, through Dr. R. Irmann, while the others, M276, M257, M293, and M255 were supplied by the Aluminum Company of America as experimental powder metallurgical products. M255 and M293 were made from coarse and fine atomized powders, respectively. The other materials were made from flake powders with significant differences in oxide content. The details of the type of powders used in the manufacture of these materials

E. GREGORY, Junior Member AIME, is Staff Member, and N. J. GRANT, Member AIME, is Associate Professor, Dept. of Metallurgy, Massachusetts Institute of Technology, Cambridge, Mass.

Discussion on this paper, TP 3664E, may be sent, 2 copies, to AIME by April 1, 1954. Manuscript, July 28, 1953. New York Meeting, February 1954.

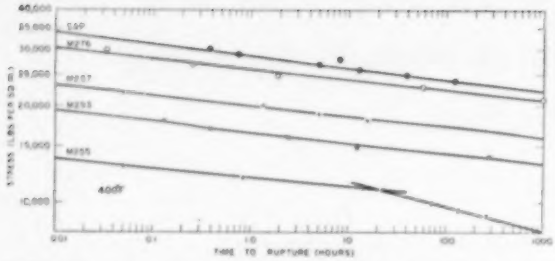

Fig. 1—Log stress vs log rupture time plots for the five alloys at 400°F. Note instability break in curve for alloy M255.

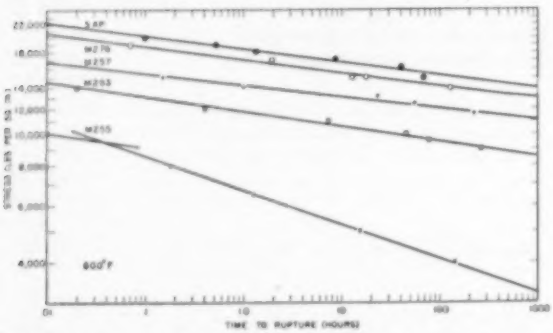

Fig. 2—Log stress vs log rupture time plot for the five alloys at 600°F. Note instability break in curve for alloy M255.

together with the room temperature, short time tensile data are given in Table I.

Stress Rupture Data

These different materials gave a wide range of high temperature strength and ductility values and the stress rupture curves at 400°, 600°, and 900°F are shown in Figs. 1, 2, and 3, respectively. The small slopes and absence of breaks up to 900°F in the log stress vs log rupture life curves for SAP, M276, and M257 indicate their structural stability by retention of their properties with time at temperature. Fig. 3 shows for comparison the stress rupture properties at 600°F of alloy XF 18S-T61, possibly the strongest of the wrought aluminum high temperature alloys. In order to illustrate the data collectively, stress to rupture was plotted[10] in Fig. 4 against the parameter $T(20 + \log t)$ where T is the temperature in degrees absolute; t, is the rupture time in hours; and 20 was selected arbitrarily as the constant. The curves for M255 and M293 show a downward break, confirming the existence of the instabilities in Figs. 1 to 3, due possibly to change in grain size or to stress relief.

The curve for SAP is unusual since there is an upward break based on the 900°F data, which is not predicted by the 400° and 600°F data. Accordingly, the curve beyond 600°F is drawn dotted since there is a possibility that there may have been a change in the oxide content or oxide particle spacing of the bar stock used for the tests at 600° compared to 900°F.

Interestingly, the curve for M276 has a much steeper gradient than M257, and appears to become weaker at longer times and higher temperatures, a result which is in agreement with data on the variation of tensile and yield strengths with temperature as reported by Lyle.[8]

In studying Figs. 1 to 4 it should be kept in mind that these data are not presented merely to show which of these products is the strongest at high temperatures. Of greater significance is the fact that they represent a series of aluminum-aluminum oxide alloys in which the strength is increased as a function of the oxide content, and in which the ductility (see Table I), the impact and fatigue properties, the conductivity, and other properties vary accordingly.[1, 2, 8, 9] Such combinations of metal and oxide, therefore, provide a continuous series of alloys useful for a wide range of applications both at high and low temperatures.

Notched Stress Rupture Results

In order to determine the effect of stress concentrations on these materials, notched creep rupture specimens were made of alloys M293 and M276, selected as being representative of low strength-high ductility and high strength-low ductility materials, respectively.

As the amount of these materials did not permit an investigation of the effects of notch geometry, it was decided to standardize the tests using a specimen of the type shown in Fig. 5. The dimensions of this specimen were based on the data and suggestions put forward by Hull, Humm, and Scott.[11]

The stress-rupture curves obtained from the notched alloys are compared with those from the normal unnotched rupture specimens in Figs. 6 and 7.

The introduction of a notch into a material can, by causing a system of triaxial stress in its neighborhood, increase the apparent strength. For this to

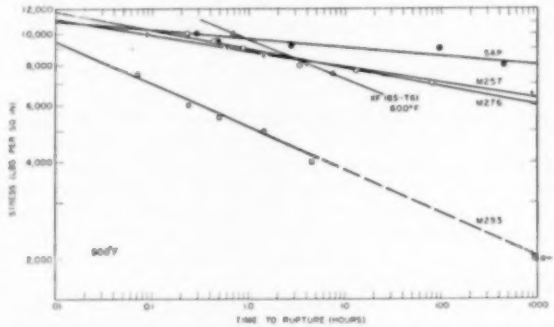

Fig. 3—Log stress vs log rupture time plot for the four stronger alloys at 900°F. Note sharp decrease in strength for alloy M293. Alloy XF 18S-T61 at 600°F is shown for comparison with the wrought powder products.

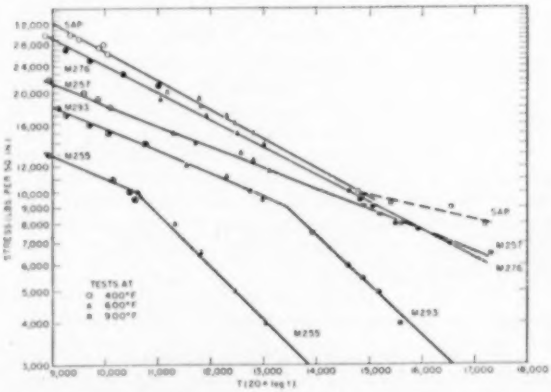

Fig. 4—Stress vs T $(20 + \log t)$ plot for all five alloys. Points are listed according to test temperatures. Note downward breaks in curves for alloys M255 and M293, upward break for SAP, and crossover of curves for M257 and M276.

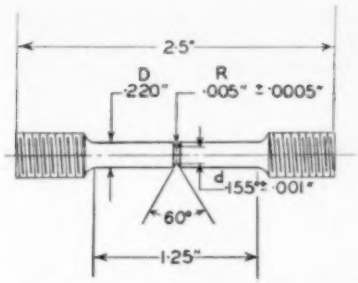

Fig. 5—Dimensions of notched creep-rupture specimen tested at 400° and 600°F.

happen, however, the material must have sufficient ductility to accommodate the stress concentration caused by the presence of the notch. The amount of ductility required in the normal stress rupture bar varies according to the notch geometry. The ductility of the M293 was far greater under the same conditions of stress and temperature than that of M276. In both these materials the elongation decreased with increasing temperature and with increasing time at a given temperature, as is shown by the percentage of elongation values noted next to each unnotched creep rupture test point in Figs. 6 and 7. As expected, the effect of a notch of the type shown in Fig. 5 was far less deleterious to alloy M293 than to M276. At 400°F, M293 sustained higher stresses for a given rupture life in the notched condition up to about 500 hr, whereas in M276 this was only true up to about 3 hr. The corresponding figures at 600°F were 1 hr and 0.1 hr. It will be seen that when the elongation of the normal rupture specimen of M293 falls below about 10 pct at both 400° and 600°F, the apparent increase in strength no longer occurred. The corresponding elongation value for M276 was somewhat lower, about 5 pct.

The scatter of the rupture life values among those specimens having sufficient ductility to result in an increased rupture life in the presence of a notch appears to be far less than that when notch embrittlement occurred.

Identification of the Disperse Phase

Since examination of an electropolished and etched specimen of these materials with X-rays did not reveal the lines of the disperse phase clearly, extraction of the particles was carried out using an HCl solution. X-ray examination of this extract showed the phase to be γ Al_2O_3. This was later confirmed by careful electron diffraction of the electropolished and etched solid material. Control experiments were carried out on pure aluminum to make certain that the pattern observed by electron diffraction was not oxide formed on the samples due to the polishing and etching treatment.

The γ aluminum pattern was observed on the wrought powder specimens both after electropolishing and electropolishing and etching in dry gaseous HCl.

Metallographic Examination and Structure Relationships

In determining the metallography of the materials, difficulties were encountered due to the very fine dispersion of the hard oxide phase which, during polishing, tended to be removed or covered up with flowed matrix metal. The method finally adopted was to put the alloys through the usual stages of polishing and to follow the finest wheel with a brief electropolish in a perchloric acid-acetic anhydride mixture. The function of the electropolish was to remove a very thin layer of distorted metal and the fine scratches probably caused by the tearing out of oxide. The electropolishing was not carried on for a time sufficient to cause pitting. Etching of the alloys, on the other hand, generally led to pitting, however for most purposes a structure was revealed sufficiently clearly after electropolishing. Figs. 8a, b, c, show micrographs of unetched transverse sections of three of the materials in the as-received state, at X2000. Owing to the extreme fineness of the structures of these alloys this magnification was not sufficient to give useful information. Electron micrographs, however, did reveal a more clearly defined structure. Paralodion negative replicas of the unetched material were rotary shadowed with chromium to increase the contrast and still maintain a fairly accurate representation of the size and shape of the particles revealed.

Owing to the difficulty of etching without pitting it is, as yet, not possible to outline clearly the grain boundaries in the as-received material and the micrographs and electron micrographs are on the unetched material. The grain size is presumed to be exceedingly small.

Electron micrographs at X20,000 are shown in Figs. 9 to 13 for the five alloys. There is, as yet, some doubt concerning the interpretation of these structures and the ideas expressed here must therefore be considered to be tentative.

The white areas in the electron photographs are thought to be oxide platelets, and as can be seen in the micrographs they increase in number as the oxide content increases. The area of the white regions is in all cases in excess of that predicted by the chemical analysis of the oxide (Table I). There are two possible reasons for this. First, because the oxide exists in thin flakes, those particles not on

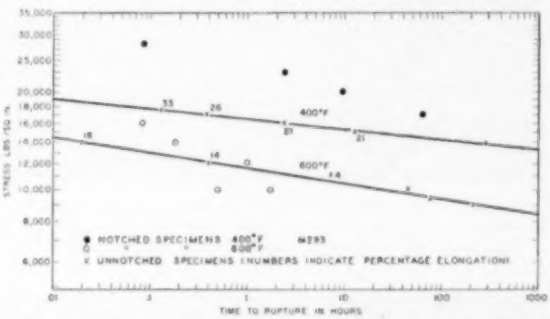

Fig. 6—Notch stress-rupture tests for alloy M293 at 400° and 600°F compared with unnotched tests.

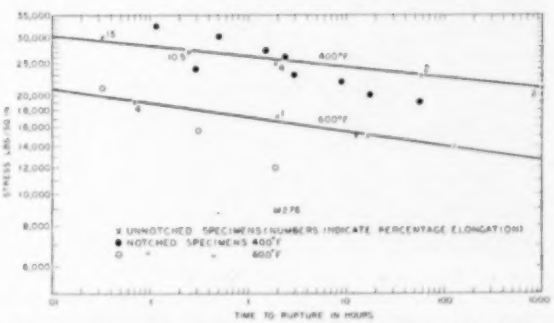

Fig. 7—Notch stress-rupture tests for alloy M276 at 400° and 600°F compared with unnotched tests.

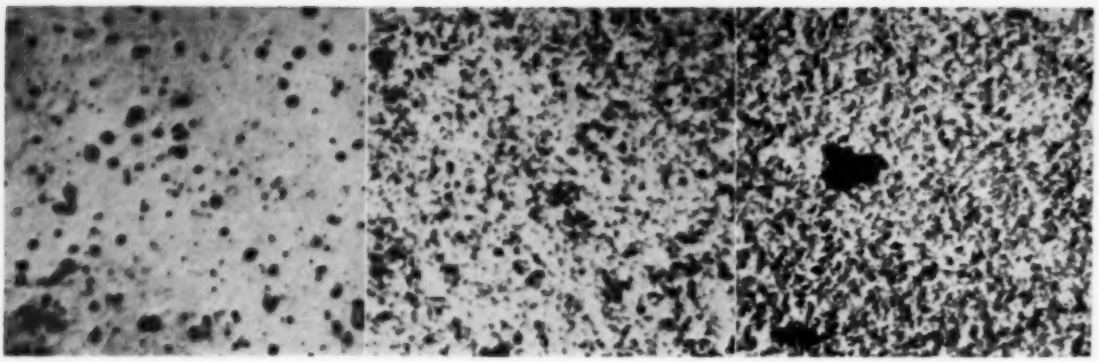

a—M255. b—M257. c—SAP.

Fig. 8—Optical microscopic micrographs of unetched specimens. X2000. Area reduced approximately 50 pct for reproduction.

edge to the cross section yield a fictitiously high area. Second, the electropolished surface is not perfectly plane, and, owing to a relief effect during polishing, a volume of the specimen is represented instead of a plane cross section. Theoretical predictions of the thickness of the oxide films suggest a value from 50 to 100Å units in some cases. Such a dimension would not be revealed by the techniques employed here if the oxide were on-edge to the cross section. However, other orientations would be expected to be revealed in view of the considerably larger area of the flakes.

Because of the uncertainty in the interpretation of these structures, the proposed relationships, below, must be somewhat tentative. The rather good relationship observed between the measured spacing between these white areas and the tensile strength and rupture life, on the other hand, lend confidence in the observations and assumptions.

Recently there have been several studies of the effect of hard phase dispersions on the plastic properties of alloys. Gensamer and his colleagues[12] reported the effect of carbide spacing in pearlite on the plastic properties of steels. Their data showed a

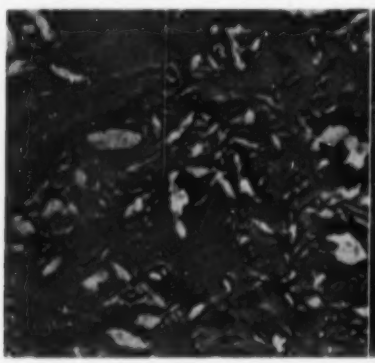

Fig. 9—Electron micrograph of SAP. White areas are oxide particles. X20,000. Area reduced approximately 50 pct for reproduction.

Fig. 10—Electron micrograph of M276. X20,000. Area reduced approximately 50 pct for reproduction.

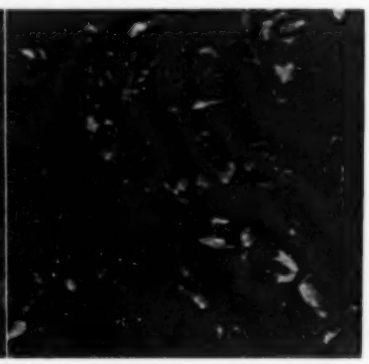

Fig. 11—Electron micrograph of M257. X20,000. Area reduced approximately 50 pct for reproduction.

Fig. 12—Electron micrograph of M293. Note pitting around oxide particles. X20,000. Area reduced approximately 50 pct for reproduction.

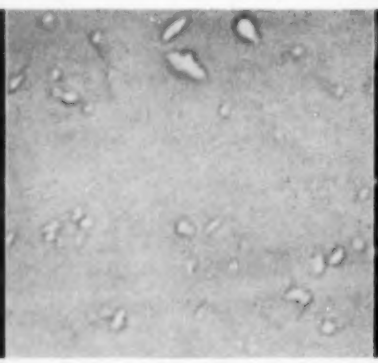

Fig. 13—Electron micrograph of M255. X20,000. Area reduced approximately 50 pct for reproduction.

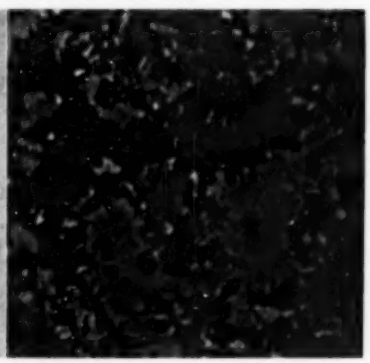

Fig. 14—Electron micrograph of M276 showing large oxide particles and segregation. Compare with Fig. 10. X20,000. Area reduced approximately 50 pct for reproduction.

linear relationship between the logarithm of the mean ferrite path and the stress at definite strain.

Orowan[10] has considered the particles as barriers preventing the movement of dislocations and predicted that the yield strength of a material containing uniformly distributed particles should be inversely proportional to the mean free path in the matrix.

Other relationships between strength and structure have been proposed and discussed by Unkel,[11] by Shaw et al.,[12] and by Fisher, Hart, and Pry.[13]

The present data on the wrought aluminum powder products do not allow a strict choice to be made among the several different theories for several reasons in addition to the question regarding interpretation of the electron micrographs. Specifically, values of the stress for a fixed strain were not obtained since these tests were creep rupture rather than tensile tests. Furthermore, in any search for a relationship between strength and structure, it is necessary that the materials undergo deformation according to a fixed mechanism. In these tests where the temperature varied from room temperature to 900°F, it is unlikely that a common deformation mechanism was prevalent as is evidenced by the breaks in the log-log plots of stress vs rupture life in Figs. 1 to 3 and by the changes in slope noted in Fig. 4.

To attain the best possible relationship, however, a rupture time of 0.01 hr was selected and the stress for fracture in this time was then the strength variable. This 0.01 hr rupture time is not significantly different from the short time hot tensile strength.

Finally, as will be noted below, there is some evidence that the matrix is likely to be in a strained state of variable magnitude because of the finely dispersed second phase which interferes with recovery and recrystallization.

By selecting a number of representative electron micrographs it was possible to determine a figure for the average separation among the particles of the second phase.

In this way surface to surface spacings and center to center spacings were measured and are shown in Table I. A large number of micrographs were not utilized for these determinations when it was noted that the difference between two micrographs was very small. Possibly the largest error would be due to areas in which oxide segregation or depletion may have occurred, and which may have had an effect on the rupture life. The fact that certain of the materials have a wider range of particle sizes also influences the results. Such a nonuniform structure is clearly shown in alloy M276 at X20,000 in Fig. 14. Large segregated areas are noted and are probably instrumental in the apparent anomalies in the behavior of this alloy (see Figs. 1 to 4).

Both surface to surface and center to center spacings were plotted against strength but it is believed that the former is the more significant value barring a condition where fracture may originate in an oxide plate due to its size. The surface to surface plots appeared to give less scatter of values and were alone used in the relationships shown below.

The room temperature tensile strength and the stress to rupture in 0.01 hr at 400° to 900°F were plotted against oxide content in Fig. 15. The values of oxide are only aproximate and were obtained by averaging the chemical values in Table I. On theoretical grounds it seems improbable that there is a simple relationship between total oxide content and strength unless the size of the oxide platelets can be

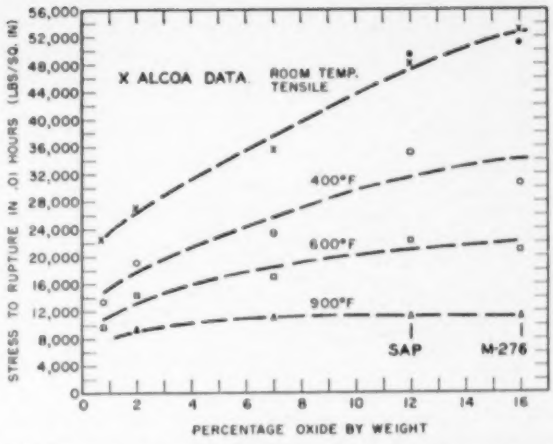

Fig. 15—Stress vs weight percent of oxide (by chemical analyses) for room temperature tensile strength and 0.01 hr rupture life at 400°, 600°, and 900°F.

presumed to be the same in all materials, which it is not. The values of strength for M276 appear to be low at 400° and 600°F, but this is probably due to deviations caused by coarse oxide areas and segregation.

A plot of stress vs $1/d$, Fig. 16, shows that the strengthening effect of the oxide phase is greatest at the lower temperatures, for short time tests, and has little effect at 900°F. However, it must be remembered that the comparison is made for a 0.01 hr rupture time, a time which is for all the alloys prior to the break in the strength curves of Figs. 1 to 4. If longer rupture times are selected, 1000 hr, for example, then the relationship shown in Figs. 16 to 18 would no longer be valid because of more than one operative deformation mechanism, but the value of the oxide strengthening would be noted in a more realistic manner (see Figs. 1 to 3). Fig. 16 shows good straight line relationships for all test temperatures.

A plot of log stress vs log spacing, Fig. 17, yields relatively good straight lines at the higher temperatures but is not straight at room temperature.

Fig. 18 shows the relationship between stress and log spacing, straight lines being achieved essentially

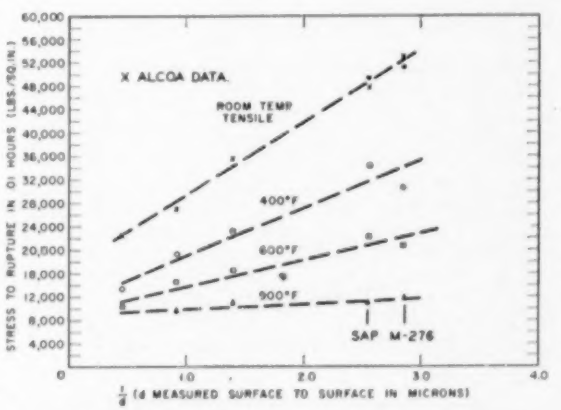

Fig. 16—Stress vs reciprocal of average spacing between oxide particles for room temperature tensile strength and 0.01 hr rupture life at 400°, 600°, and 900°F.

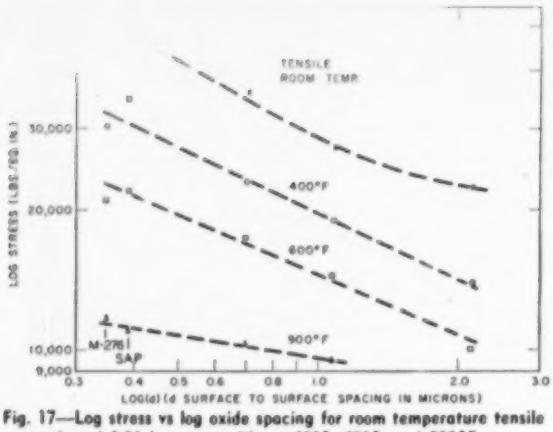

Fig. 17—Log stress vs log oxide spacing for room temperature tensile strength and 0.01 hr rupture life at 400°, 600°, and 900°F.

at 600° and 900°F but not at room temperature and 400°F.

The validity of extrapolation is somewhat doubtful, but it would appear that the room temperature tensile data predict a strength for the pure matrix material equal to that of hardened aluminum. This may not be unexpected since the wrought powder materials have an excess phase dispersion which hinders recovery and recrystallization in the matrix. The 600° and 900°F curves predict a value for the 0.01 hr rupture life of the pure material which is more nearly equal to that of the fully annealed matrix material tested at room temperature rather than for the same material tested at 600° and 900°F.

While no attempt will be made to make a choice among the structure-stress relationships illustrated, it will be seen that for approximate practical predictions of strength at a given temperature and short time rupture life, the $1/d$ plot may be most convenient.

Aside from efforts to obtain a fundamental relationship between structure and strength properties, a more realistic measure of the high temperature creep rupture strength contribution of the finely dispersed insoluble oxide phase can be obtained by comparing the various alloys at 100, 1000, or 10,000 hr rupture life.

Summary

It is shown that a super-fine dispersion of an oxide phase in a pure aluminum matrix, where the particle spacing is of the order 0.35 to 2 microns, results in extreme strengthening. The largest benefits are derived at long times at high temperatures since the alloys with the higher oxide content are extremely stable and do not lose strength due to a change in the structure.

An effort has been made to see if the strengthening can be related to one or more of the current theories on strengthening by a disperse phase, the best relationship being shown, for short time tests, by a plot of stress (for 0.01 hr rupture time) vs the reciprocal of the particle spacing.

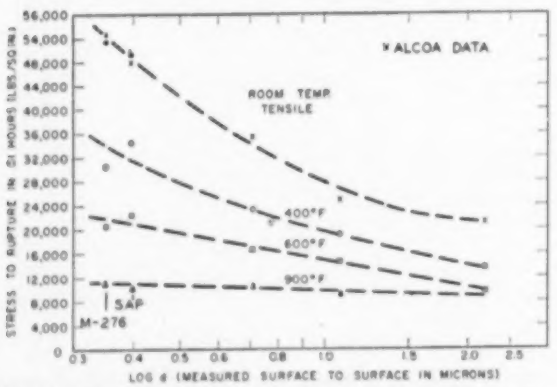

Fig. 18—Stress vs log oxide spacing for room temperature tensile strength and 0.01 hr rupture life at 400°, 600°, and 900°F.

Acknowledgments

The authors are indebted for cooperation, samples, and data from Dr. R. Irmann, of Societe Anonyme pour l'Industrie de l'Aluminium, Switzerland, and Mr. W. T. Ennor of the Aluminum Company of America. Thanks are extended to Dr. L. O. Brockway of the University of Michigan for the electron diffraction work, and Dr. B. S. Lement of the Massachusetts Institute of Technology for the electron microscopy. The work was done under the sponsorship of the Wright Air Development Center, Contract No. AF 33 (616)-284, whose support is appreciated and acknowledged.

References

[1] Sintered Aluminum Powder: *Metal Industry* (Aug. 22, 1952) pp. 143-146.

[2] R. Irmann: Sintered Aluminium with High Strength at Elevated Temperatures. *Metallurgia* (September 1952) **46**, No. 275, pp. 125-133.

[3] A. B. Middleton, L. B. Pfeil, and E. C. Rhodes: Pure Platinum of High Recrystallization Temperature Produced by Powder Metallurgy. *Journal* Inst. Metals (1949) **75**, pp. 595-608.

[4] A. von Zeerleder: Uber Sintern von Aluminium Legierungen. *Ztsch. Metallkunde* (1950) **41**, pp. 228-231.

[5] R. de Fleury: Considerations sur le Module d'Elasticite et la Limite Elastique du Complex Alumine-Aluminium. *Revue de l'Aluminium* (May 1952) **29**, pp. 183-185.

[6] E. Boenisch and W. Wiederholt: Untersuchungen an Gesintertem Aluminium. *Ztsch. Metallkunde* (1951) **42**, pp. 344-349.

[7] W. Seith and G. Löpmann: Diffusion of Metals in Samples of Sintered Aluminium. *Ztsch. Elecktrochem* (1952) **36**, No. 4, pp. 373-379.

[8] J. P. Lyle: Excellent Products of Aluminum Powder Metallurgy. *Metal Progress* (December 1952) **62**, No. 6, pp. 109-112.

[9] E. Gregory and N. J. Grant: Aluminum Powder Products Compared. *Iron Age* (Dec. 25, 1952) **170**, No. 21, pp. 69-73.

[10] F. R. Larson and J. Miller: A Time Temperature Relationship for Rupture and Creep Stresses. *Trans.* ASME (July 1952) **74**, No. 5, p. 765.

[11] F. C. Hull, E. K. Humm, and H. Scott: Effect of a Notch and of Hardness on the Rupture Strength of "Discaloy". ASTM 1952 Preprint No. 75.

[12] M. Gensemer, E. B. Pearsall, W. S. Pellini, and J. R. Low, Jr.: The Tensile Properties of Pearlite, Bainite, and Spherodite. *Trans.* ASM (1942) **30**, p. 983.

[13] E. Orowan: Discussion of paper by Sir Lawrence Bragg, "Effects Associated with Stresses on a Microscopic Scale." Inst. of Metals, Symposium on Internal Stresses in Metals and Alloys, 1948. Monograph and Report Series No. 5.

[14] H. A. Unkel: The Dependence of Mechanical Properties upon the Structure of Two Phase Alloys. *Metall* (1951) **5**, p. 146.

[15] R. B. Shaw, L. A. Shepard, C. D. Starr and J. E. Dorn: The Effect of Dispersions on the Tensile Properties of Aluminum-Copper Alloys. *Trans.* ASM (1953) **45**, pp. 249-271.

[16] J. C. Fisher, E. W. Hart, and R. H. Pry: General Electric Research Reports.

The Sigma Phase in Binary Alloys

by Peter Greenfield and Paul A. Beck

THE σ phase is a hard and extremely brittle material with a tetragonal crystal structure, containing 30 atoms per unit cell.[1] It occurs in many binary and ternary alloys of the transition elements. The existence of twelve σ phases has been reported in binary alloys of metals from the group vanadium, chromium, molybdenum, and tungsten with metals from the group manganese, iron, cobalt, and nickel. It is a characteristic fact that the composition of the σ phases in the various binary systems is not the same. Rather, there is a gradual shift in composition, for instance in the series of chromium σ phases, approximately as follows: $CrMn_2$, FeCr, Cr_2Co_3. In recent years several ideas have been put forward to account for this variability of composition.

Sully[2] proposed that σ was a type of electron compound, characterized by 1.7 electrons per atom in excess of the number required to fill the Pauling atomic orbitals. These excess electrons were supposed to just fill the first Brillouin zone of the σ structure. However, later work indicated that the phase is ferromagnetic at low temperatures, so that σ is unlikely to be a full zone compound.[3]

Another proposal,[4] which is also based on the structure of the transition elements advanced by Pauling, and in fact leads to essentially the same σ compositions as Sully's theory, suggests that the σ phase is characterized by a constant number of electron vacancies per atom. The electron vacancy numbers N_v used were originally the same as those in the Pauling theory, but were later modified empirically[5] in order to bring about better agreement with data for the μ phase in certain ternary systems. For alloys, N_v was calculated on the assumption of simple additivity from the electron vacancy numbers of the components, as follows: $N_v = 4.66$ (Mo + Cr + V) + 3.2 (Mn) + 2.2 (Fe) + 1.71 (Co) + 1.6 (Ni). On this basis a reasonably constant value of $N_v = 3.4$ was obtained for all of the binary σ phases and a fairly constant value of $N_v = 3.1$ for the various μ phases.

P. GREENFIELD is associated with the Dept. of Metallurgical Engineering, and P. A. BECK, Member AIME, is Research Professor of Physical Metallurgy, College of Engineering, University of Illinois, Urbana, Ill.

Discussion on this paper, TP 3658E, may be sent, 2 copies, to AIME by April 1, 1954. Manuscript, July 27, 1953. New York Meeting, February 1954.

More recently, Bloom and Grant[6] pointed out that a similar correlation with the total number of 3*d* and 4*s* electrons per atom is also fairly well fulfilled and concluded that no reference need be made to the Pauling theory. This proposal does not lead to the same binary σ compositions as the one described above, so that the relative merits of the two proposals may be determined on the basis of direct comparison with experimental composition data. The purpose of the present paper is to provide such a comparison. Since the experimental data for the composition ranges of several of the known σ phases were rather incomplete, it was decided to carry out new experimental determinations for many of the binary systems.

Experimental Procedure

The alloys were prepared by induction melting in recrystallized alumina crucibles, either in vacuum or in helium atmospheres. Some aluminum was picked up from the crucibles in the alloys of high vanadium content, but this was minimized by keeping the alloys in the molten state for as short a time as possible. The maximum aluminum impurity was 0.13 wt pct by chemical analysis, in an alloy containing over 50 wt pct V. In general, the as-melted compositions agreed accurately with those obtained by chemical analysis. In the case of manganese, however, losses inevitably occurred; consequently all manganese alloys were analyzed.

Specimens of all alloys were annealed at temperatures ranging from 1000° to 1300°C in an atmosphere of purified 92 pct helium and 8 pct hydrogen mixture. All manganese alloys were sealed in quartz tubes under vacuum before annealing. The specimens were held at temperature for between four and eight days before being quenched into cold water. Alloys were prepared for microscopic examination by mechanical polishing, usually followed by electrolytic etching.

X-ray diffraction specimens were prepared by crushing the homogenized alloys, and by reannealing the obtained powders in evacuated quartz tubes for a few hours at the temperature of the lump anneal. X-ray diffraction patterns were made with unfiltered chromium radiation, using an asymmetrical focusing camera of high dispersion. Using microscopic and X-ray techniques jointly, the accuracy

Table I. Composition Range and Mean Composition of Various Binary Sigma Phases

System	Temperature, °C	Range, Atomic Pct	Mean Composition, Atomic Pct
V-Ni	1200	55-68.5 V	61.5 V
V-Co	1200	44.4-53.1 V	48.8 V
V-Fe	1075	39-54.5 V	47 V
V-Mn	1000	13.4-24.5 V	19 V
Cr-Fe	600	43-49 Cr	46 Cr
Cr-Co	1200	58.6-63 Cr	60.8 Cr
Cr-Mn	1000	16-24 Cr	20 Cr
Mo-Fe	1300	50 Mo (less than ½ pct wide)	50 Mo
Mo-Co	1300	60.5 Mo (less than ½ pct wide)	60.5 Mo

of location of the phase boundaries is estimated at better than ±1 pct of any component.

Results

Vanadium-Nickel: This system has been investigated by Pearson and Hume-Rothery[7] in the region 0 to 60 atomic pct V and they found that the σ field extended from 55 to more than 65 atomic pct V, at 1200°C. The vanadium-rich boundary was not located.

As the nickel-rich boundary had already been accurately determined, the present work was concentrated on the vanadium-rich end. This boundary was located at 1200°C by an alloy containing 68.2 atomic pct V, which was homogeneous σ, and an alloy containing 69.3 atomic pct V, which was two-phase. As this latter alloy contained an appreciable amount of a second phase, it is estimated that the σ range is between 55 and 68.5 atomic pct V at 1200°C.

Vanadium-Cobalt: There is no published work on the precise limits of the σ phase region in this system. Duwez and Baen[8] have shown that an alloy of the equiatomic composition lies in the homogeneous σ field, but little else is known.

Examination of a series of alloys at 1200°C shows that the σ field boundaries are located between 52.6 and 53.6 atomic pct V at the vanadium-rich end, and between 43.6 and 44.7 atomic pct V at the cobalt-rich end. The estimated σ range is therefore between 44.4 and 53.1 atomic pct V at 1200°C.

Vanadium-Iron: The diagram published by Wever and Jellinghaus[9] suggests a lower limit of just over 30 wt pct V and a wide range of homogeneity up to about 58 wt pct V for the σ phase, but these limits were determined from slow-cooled, unannealed alloys only. The more recent work of Martens and Duwez[10] shows that σ extends from 37 to 57 atomic pct V at 700°C.

The present work shows that the σ phase boundaries are located between 38.2 and 40.2 atomic pct V at the iron-rich end, and between 53.7 and 55.3 atomic pct V at the vanadium-rich end, for an annealing temperature of 1075°C. The σ phase field, therefore, ranges from about 39 to 54.5 atomic pct V at 1075°C. At higher temperatures, the phase appears to narrow rapidly.

Vanadium-Manganese: Pearson, Christian, and Hume-Rothery[11] first observed σ in this system, though no attempt was made to define its limits. An alloy containing 24.3 atomic pct V was observed to give a σ X-ray pattern though the microstructure was nonhomogeneous.

The present work defines the σ boundaries at 1000°C. Alloys containing 13.9 and 24.0 atomic pct V were homogeneous σ, while alloys with 25.5 and 12.9 atomic pct V contained a small amount of second phase. The σ field is therefore located between 13.4 and 24.5 atomic pct V at 1000°C.

Chromium-Iron: This diagram has been accurately determined by Cook and Jones.[12] The σ phase is shown to exist between 43 and 49 atomic pct Cr at 600°C.

Chromium-Cobalt: The σ limits in this system have been recently determined.[4] The phase was found to exist between 58.6 and 63 atomic pct Cr at 1200°C.

Chromium-Manganese: This system has been examined by Pearson and Hume-Rothery[13] and by Zwicker[14] with reasonable agreement in the σ region.

In the present work, alloys were annealed at 1000°C, and the results showed that the manganese-rich boundary lies between 15.7 and 16.7 atomic pct Cr, and the chromium-rich boundary between 23.5 and 24.5 atomic pct Cr. The σ phase exists, therefore, between 16 and 24 atomic pct Cr at 1000°C, in agreement with Hume-Rothery and Zwicker.

Molybdenum-Iron: Goldschmidt[15] first reported that the phase based on FeMo has the σ structure. It is stable only above 1180°C, and begins to melt at 1540°C.

In the present work, a series of specimens annealed at 1300°C showed that alloys containing 46.7 and 48.7 atomic pct Mo consisted of the $\sigma + \mu$ phases. An alloy containing 49.8 atomic pct Mo was homogeneous σ, while another alloy with 50.8 atomic pct Mo contained an appreciable amount of a molybdenum-rich phase. The σ phase field at 1300°C is therefore extremely narrow, existing around the FeMo composition.

Molybdenum-Cobalt: Goldschmidt[16] first reported this σ phase at the composition Co_2Mo_3, but it is stable only at high temperatures.

Alloys were annealed for a period of 10 days at 1300°C. Results showed that alloys containing 61 and 62 atomic pct Mo contained a molybdenum-rich second phase, while a specimen with 60 atomic pct Mo was almost homogeneous, except for a trace of the μ phase. The σ range is therefore very narrow, existing around 60.5 atomic pct Mo.

Molybdenum-Manganese: A σ phase was reported in this system by Kasper, Decker, and Belanger,[17] but no composition was mentioned.

In the present work, alloys ranging from 0 to 35 wt pct Mo were melted, and investigated as-quenched from 1000°C. At this temperature, a phase which has the typical microstructure of the σ phase, with numerous cracks, was found to extend from about 12 to 20 atomic pct Mo. However, X-ray

Table II. Deviations of Experimental Mean Compositions of Sigma Phases from Those Calculated from Eq. 1

System	Experimental Mean Composition, Atomic Pct	Mean N_v	Calculated Mean Composition from N_v = 6.93	Deviation in Calculated and Experimental Mean Composition, Atomic Pct
V-Ni	61.5 V	6.92	61.6 V	0.1
V-Co	50 V	7.0	51.7 V	1.7
V-Fe	47 V	6.58	35.6 V	11.4
V-Mn	19 V	6.62	3.5 V	15.5
Cr-Fe	46 Cr	7.08	53.5 Cr	7.5
Cr-Co	60.8 Cr	7.18	69.0 Cr	8.2
Cr-Mn	20 Cr	6.8	7.0 Cr	13.0
Mo-Fe	50 Mo	7.0	53.5 Mo	3.5
Mo-Co	60.5 Mo	7.17	69 Mo	8.5
		Average N_v = 6.93		Standard deviation = 9.1 pct

Table III. Deviations of Experimental Mean Compositions of Sigma and Mu Phases from Those Calculated from Eq. 2

System	Phase	Experimental Mean Composition, Atomic Pct	Mean N_v	Calculated Mean Composition from N_v = 3.41	Deviation in Calculated and Experimental Mean Composition, Atomic Pct
V-Ni	σ	61.5 V	3.50	59.1 V	2.4
V-Co	σ	50 V	3.18	57.6 V	7.6
V-Fe	σ	47 V	3.31	49.2 V	2.2
V-Mn	σ	19 V	3.48	14.4 V	4.6
Cr-Fe	σ	46 Cr	3.33	49.2 Cr	3.2
Cr-Co	σ	60.8 Cr	3.51	57.6 Cr	3.2
Cr-Mn	σ	20 Cr	3.49	14.4 Cr	5.6
Mo-Fe	σ	50 Mo	3.43	49.2 Mo	0.8
Mo-Co	σ	60.5 Mo	3.51	57.6 Mo	2.9
			Average N_v = 3.41		Standard deviation = 4.1 pct
				Calculated Mean Composition from N_v = 3.12	
Co-Mo	μ	46 Mo[20]	3.07	47.8	1.8
Co-W	μ	46 W[21]	3.07	47.8	1.8
Fe-Mo	μ	40 Mo[22]	3.18	37.4	2.6
Fe-W	μ	40 W[22]	3.18	37.4	2.6
			Average N_v = 3.12		Standard deviation = 2.2 pct

diffraction powder photographs taken at room temperature, and back-reflection Laue patterns using the actual microscopic specimen, showed that this phase does not have the σ structure. Further work on this system is being carried out at higher temperatures.

Tungsten-Cobalt and Tungsten-Iron: Goldschmidt[10] reported that high temperature σ phases are stable in both of these systems, but no composition limits were mentioned. No alloys in these systems have been examined in the present work.

Columbium and Tantalum Systems: A brief examination of compounds reported in the systems of columbium and tantalum with manganese, iron, cobalt, and nickel did not indicate the formation of the σ phase in any of these systems. Instead, Laves phases were found at the compositions $CbMn_2$, $TaMn_2$, $CbFe_2$ ($MgZn_2$ type) and at $TaCo_2$ and $CbCo_2$ ($MgCu_2$ type).[18, 28]

The data on the known binary σ phases are summarized in Table I.

Discussion

In one of the correlations discussed earlier in this paper, the composition of σ phases is characterized by a constant number of $3d + 4s$ electrons per atom. This number is calculated as follows:

$$N_v = 5(\text{V}) + 6(\text{Cr}) + 6(\text{Mo}) + 7(\text{Mn}) + 8(\text{Fe}) + 9(\text{Co}) + 10(\text{Ni}), \quad [1]$$

where the bracketed chemical symbols represent the atomic fractions of the corresponding elements in the alloy.

In the other proposed correlation, the σ phase composition is characterized by a constant number of $3d$ electron vacancies per atom, this number being calculated from the following formula:

$$N_v = 4.66\,(\text{Mo} + \text{Cr} + \text{V}) + 3.2(\text{Mn}) + 2.2(\text{Fe}) + 1.71(\text{Co}) + 1.6(\text{Ni}). \quad [2]$$

The values used here for manganese, iron, and nickel are not those of the Pauling theory. They are modified to some extent in order to fit better the experimental composition data for both the σ and μ phases. A lower value for manganese (in place of 3.66 in the Pauling theory) may be qualitatively justified on the basis of other known facts. As was noted by Hume-Rothery, Irving, and Williams,[29] manganese has an abnormally low melting point and a high compressibility, suggesting that the cohesive strength may be abnormally low. It is quite likely, therefore that, in the case of manganese, the bonding orbitals contain fewer electrons than the maximum permissible of 5.78 and, consequently, the atomic orbitals may well contain fewer vacancies than the theoretical number of $N_v = 3.66$. The changes for iron and nickel may be considered entirely empirical and justified mainly by the fact that they allow the treatment of certain ternary μ phase solid solutions in addition to that of the σ phase.[8]

If the μ phase is left out of consideration, the correlation for binary σ phases alone can be satisfactorily handled by using the Pauling vacancy numbers for all elements, except two. As shown above, the change for manganese may be qualitatively justified on the basis of other properties. The other case is that of vanadium, where the 5.78 bonding orbitals are not completely filled. As the atomic orbitals first fill with unpaired electrons, the latter represent the state of lowest free energy. For nickel and cobalt some pairing must take place, and it has been observed[19] that the ferromagnetic electrons in these metals are part of a relatively unstable group, which is readily changed in alloying. When these elements are alloyed with vanadium, the paired atomic electrons, which have relatively higher energy, may be assumed to help fill the 0.78 vacant bonding orbitals of vanadium. The effective N_v value for vanadium, when alloyed with nickel or cobalt, may therefore be 5.66. On the other hand, when alloyed with iron or manganese, which have no paired electrons in their atomic orbitals, vanadium may be assumed to have the conventional N_v value of 4.88. This would give

$$N_v = 5.66(\text{V when with Ni or Co}) + 4.88(\text{V when with Mn or Fe}) + 4.66(\text{Cr} + \text{Mo}) + 3.3(\text{Mn}) + 2.66(\text{Fe}) + 1.71(\text{Co}) + 0.61(\text{Ni}). \quad [3]$$

In the following, the relative merits of the two correlations (with constant total number of $3d$ and

Table IV. Deviations of Experimental Mean Compositions of Sigma Phases from Those Calculated from Eq. 3

System	Experimental Mean Composition, Atomic Pct	Mean N_v	Calculated Mean Composition from N_v = 3.61	Deviation in Calculated and Experimental Mean Composition, Atomic Pct
V-Ni	61.5 V	3.69	59.4 V	2.1
V-Co	50 V	3.68	48.1 V	1.9
V-Fe	47 V	3.70	42.8 V	4.2
V-Mn	19 V	3.60	19.6 V	0.6
Cr-Fe	46 Cr	3.58	47.5 Cr	1.5
Cr-Co	60.8 Cr	3.51	64.4 Cr	3.6
Cr-Mn	20 Cr	3.57	22.8 Cr	2.8
Mo-Fe	52 Mo	3.66	47.5 Mo	2.5
Mo-Co	60.5 Mo	3.54	64.4 Mo	3.9
		Average N_v = 3.61		Standard deviation = 2.8 pct

Table V. Atomic Sizes of Transition Elements

Element	V	Cr	Mn	Fe	Co	Ni
Interatomic distances	2.63	2.49	?	2.5	2.5	2.49
Goldschmidt atomic diameter	2.71	2.57	?	2.5	2.5	2.49
Element	**Cb**	**Mo**	**Pd**	**Ta**	**W**	**Pt**
Interatomic distances	2.85	2.72	2.745	2.85	2.73	2.769
Goldschmidt atomic diameter	2.94	2.80	2.745	2.94	2.82	2.769

4*s* electrons on the one hand and with constant number of 3*d* electron vacancies on the other) are compared on the basis of the composition data listed above, and using Eqs. 1, 2, and 3. From the values of the mean concentration for each of the binary σ phase fields, as shown in Table I, mean values of N_v can be obtained from Eq. 1. From these, an average value of $N_v = 6.93$ may be obtained for all σ phases.* This average value of N_v can be used to obtain values of the calculated mean concentration for each particular σ phase, and these can be compared with the experimental values. The results are shown in Table II. Similar results for Eqs. 2 and 3 are shown in Tables III and IV, respectively.

* Bloom and Grant[6] suggested that the σ phase is characterized by a value of $N_v = 7$. The fractional value here used should be more accurate, and its use should make the comparison more favorable for their proposal.

From the results it can be seen that the deviation between the calculated and experimental σ compositions is much less in the case of the electron vacancy correlation represented by Eqs. 2 and 3. The maximum deviation on the basis of Eq. 2 is 7.6 pct (vanadium-cobalt) and the standard deviation is 4.1 pct. The maximum deviation on the basis of Eq. 3 is 4.2 pct (vanadium-iron) and the standard deviation is 2.8 pct. The difference between calculated and experimental σ compositions is more marked for the correlation involving a constant total number of electrons per atom, as represented by Eq. 1. In this case a deviation of as much as 15.5 pct occurs for the vanadium-manganese system and the standard deviation is as high as 9.1 pct. It may be concluded, therefore, that the constant electron vacancy number is a more satisfactory criterion for the formation of the σ phase than the attainment of a constant total number of electrons per atom.†

† After completion of the manuscript, a private communication was received from Decker, Waterstrat, and Kasper[35] to the effect that the Mn-Mo σ phase has a narrow composition range at about 60 atomic pct Mn. This composition would exclude the correlation according to Eq. 1, and it could be reconciled with the correlation with the number of electron vacancies only if suitable assumptions are made. Similarly, a Ti-Mn phase at about 50 atomic pct Mn with a σ-like X-ray diffraction pattern was just reported by Elliott and Rostoker.[36] However, since at least three of the strongest diffraction lines characteristic of σ are missing, the interpretation of this phase as σ may be doubted.

Duwez and Baen[4] suggested that the difference in atomic sizes between the two components in a binary σ phase is limited to 8 pct. They stated that the formation of σ phases in alloys of tungsten with iron, cobalt, and nickel is prevented by this condition. Subsequent work by Goldschmidt[16] proved that tungsten does form binary σ phases with iron and cobalt, and that, therefore, Duwez and Baen's condition is not acceptable in the form originally proposed at a time when the data were insufficient. Nevertheless, the basic idea of those investigators that relative atomic sizes do play a role in determining the stability of the σ phase, appears to be supported by the data now available.

It is clear from Table I that the σ phases formed with vanadium have wider homogeneity ranges than the corresponding phases formed with chromium. It may well be that a certain difference in atomic sizes tends to make the σ phase more stable. Thus σ forms in the vanadium-nickel system, but not in chromium-nickel. It is significant that when a certain amount of chromium in the chromium-nickel system is replaced by molybdenum[4] or tungsten,[28] a ternary σ phase forms. The effect of molybdenum or tungsten is probably to increase the average size differences between atoms. Similarly, when molybdenum is added to any of the chromium-iron,[28] chromium-cobalt,[27] or vanadium-cobalt[27] binary σ phases, the phase field rapidly widens in the ternary system. On the other hand, when an element which will not effectively increase the difference in atomic sizes is added to these binary phases, the ternary fields often form narrow, elongated areas following lines of constant N_v.‡

‡ An exception to this is the ternary Fe-Cr-Co σ field, which also shows considerable widening.[4]

When the difference in atomic sizes is increased still more, as in the case of the binary σ phases of molybdenum and tungsten with iron and cobalt, the resulting σ phases are comparatively unstable, having narrow homogeneity ranges and decomposing at low temperatures.§

§ It should be noted, however, that such considerations do not adequately explain the rather large differences in regard to σ formation between the systems Cr-Fe (σ stable up to 825°C only), Cr-Co (σ stable up to 1310°C), and Cr-Ni (no σ phase).

It is significant that when the difference in atomic sizes becomes still larger than for molybdenum and tungsten, as in the case of columbium and tantalum with iron, cobalt, and nickel, no σ phases form at all, and Laves phases form instead. This leads to the prediction that σ may form when columbium and tantalum are alloyed with ruthenium, rhodium, and palladium, and that the composition ranges of the binary σ phases formed in alloys of the transition elements of the first long period may be considerably expanded in the corresponding ternary systems with tantalum and columbium (although the solubility of tantalum and columbium in these σ phases may be insufficient to show the effect). Another interesting question in this connection is whether or not the σ phase forms in binary alloys of chromium or vanadium with palladium or platinum. In these alloys the difference in atomic sizes is reversed in comparison with the σ phases so far investigated, in that of the two participating atoms the one with the larger *d*-shell electron vacancy number has the smaller size. It is planned to investigate these questions experimentally in the near future.

Conclusions

Of the two alternative criteria suggested for describing the composition of σ phases, the one based on *d*-shell electron vacancy numbers fits the data considerably better than the one based on the total number of *d* and *s* electrons. An important condition for the formation of the σ phase is then the attainment of constant electron vacancy number per atom of approximately 3.4 to 3.6.

Consideration of the temperature and composition ranges of stability of various σ phases suggests that the relative atomic sizes of the alloy components may also significantly affect σ formation. It appears likely that an intermediate difference in

atomic sizes is favorable, while too great difference restricts or even interdicts σ formation.

Acknowledgment

This work was supported by the Office of Ordnance Research, U. S. Army, Contract No. DA-11-022-ORD-1175.

References

[1] B. G. Bergman and D. P. Shoemaker: *Journal of Chemical Physics* (1951) **19**, p. 515.

[2] A. H. Sully: *Journal* Inst. Metals (1951-1952) **80**, p. 173.

[3] P. A. Beck: *Trans.* AIME (1952) **194**, p. 420; JOURNAL OF METALS (April 1952). See also: *Journal* Inst. Metals (1951-1952) **80**, p. 694.

[4] S. Rideout et al.: *Trans.* AIME (1951) **191**, p. 872; JOURNAL OF METALS (October 1951).

[5] D. K. Das, S. P. Rideout, and P. A. Beck: *Trans.* AIME (1952) **194**, p. 1071; JOURNAL OF METALS (October 1952).

[6] D. S. Bloom and N. J. Grant: *Trans.* AIME (1953) **197**, p. 88; JOURNAL OF METALS (January 1953).

[7] W. B. Pearson and W. Hume-Rothery: *Journal* Inst. Metals (1952) **80**, p. 641.

[8] P. Duwez and S. R. Baen: Symposium on the Nature, Occurrence and Effects of Sigma Phase. ASTM (1950) **50**, p. 48.

[9] F. Wever and W. Jellinghaus: *Mitt. K. W. Inst. Eisenforsch.* (1930) **12**, p. 317.

[10] H. Martens and P. Duwez: *Trans.* ASM (1952) **44**, p. 484.

[11] W. B. Pearson, J. W. Christian, and W. Hume-Rothery: *Nature* (1951) **167**, p. 110.

[12] A. J. Cook and F. W. Jones: *Journal* Iron and Steel Inst. (1943) **148**, p. 217.

[13] W. B. Pearson and W. Hume-Rothery: *Journal* Inst. Metals (1952-1953) **81**, p. 311.

[14] U. Zwicker: *Ztsch. Metallkunde* (1951) **42**, p. 277.

[15] H. J. Goldschmidt: *Research* (1949) **2**, p. 343.

[16] H. J. Goldschmidt: *Research* (1951) **4**, p. 343.

[17] J. S. Kasper, B. F. Decker, and J. R. Belanger: *Journal of Applied Physics* (1951) **22**, p. 361.

[18] Kehsin Kuo, Univ. of Upsala, personal communication, these structures were independently determined by him also. Dr. Kuo's forthcoming publication is entitled: "Ternary Laves and Sigma Phases of Transition Metals."

[19] W. Hume-Rothery, H. M. Irving, and R. J. P. Williams: *Proc.* Royal Soc. (1951) **A208**, p. 431.

[20] E. Henglein and H. Kohsok: *Revue de Metallurgie* (1949) **46**, p. 566.

[21] W. Arnfelt and A. Westgren: *Jernkontorets Ann.* (1935) **119**, p. 185.

[22] A. Magneli and A. Westgren: *Ztsch. anorg. allgem. Chemie* (1938) **238**, p. 268.

[23] B. F. Decker, R. M. Waterstrat, and J. S. Kasper: *Trans.* AIME (1953) **197**, p. 1476; JOURNAL OF METALS (November 1953).

[24] R. P. Elliott and W. Rostoker: *Trans.* AIME (1953) **197**, p. 1203; JOURNAL OF METALS (September 1953).

[25] K. Kuo: *Acta Metallurgica* (1953) **1**, p. 301.

[26] H. J. Goldschmidt: Symposium on High-Temperature Steels and Alloys for Gas Turbines. Iron and Steel Inst. Special Report No. 43 (1951) p. 249.

[27] Unpublished work, Univ. Illinois.

[28] H. J. Wallbaum: *Ztsch. Krystallogr.* Min. Petr. Abt. (1941) **103**, p. 391.

Annealing of a Cold Rolled Aluminum Single Crystal

by A. H. Lutts and P. A. Beck

IN the classical picture of recrystallization the growth of strain-free grains at the expense of a strained and work hardened matrix is responsible for the softening of cold worked metals on annealing. It has been commonly assumed that the release of the stored energy of cold work, softening, and reorientation take place simultaneously, as the high angle boundaries of the new recrystallized grains sweep over the cold worked matrix.

However, recent evidence indicates[1, 2] that, at least in some cases, considerable or even complete softening may take place essentially without reorientation (i.e., without the migration of ordinary high angle grain boundaries, or "recrystallization") and the release of most of the stored energy of cold work may precede softening. These cases suggest that the property changes, taking place during the annealing of cold worked metals, may be associated with various distinct processes. The study of such situations is of considerable interest, since quantitative data are still scarce.

In the present work, isothermal softening curves were determined for a heavily rolled aluminum single crystal, under such conditions that no "recrystallization" occurred until after complete softening. The hardness data were correlated with X-ray diffraction pinhole patterns in order to detect any reorientation that may occur and with measure-

A. H. LUTTS and P. A. BECK, Member AIME, are associated with the Dept. of Metallurgical Engineering, College of Engineering, University of Illinois, Urbana, Ill.

Discussion on this paper, TP 3697E, may be sent, 2 copies, to AIME by April 1, 1954. Manuscript, Aug. 20, 1953. New York Meeting, February 1954.

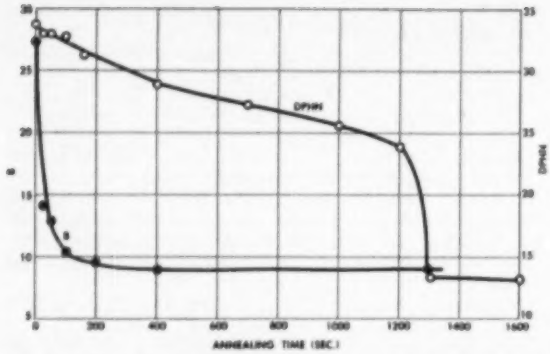

Fig. 1—Isothermal softening and recovery of line broadening at 350°C of pure aluminum single crystal rolled in the (110) [112] orientation at room temperature to 80 pct reduction. The microhardness (DPHN) values are averages of five readings with 200 gram load. The line broadening index (B) is defined as the ratio in percent of the intensity minimum measured between the two lines of the Cu Kα doublet, and of the intensity maximum of the Cu Kα_1 peak, both corrected for background intensity.

ments of X-ray diffraction line broadening. The various data were obtained with the same set of specimens, cut from a single crystal and annealed to various periods of time. The hardness measurements and the pinhole patterns were repeated with three sets of specimens originating from three different single crystals; all results were in good agreement.

Experimental Procedure

Single crystals of high purity aluminum,* approximately 0.1x1x6 in., were prepared by solidification according to Noggle's[3] procedure, oriented with (110) parallel to the large faces and [112] in the length direction, to an accuracy of about 1°. These crystals were rolled at room temperature to 80 pct R.A. in approximately 15 passes, with (110) in the rolling plane and [112] in the rolling direction. Confirming the findings of Barrett and Steadman[4] and of Liu and Hibbard[5] with copper, the rolled single crystals preserved their original orientation, showing remarkably little scatter. It was found that specimens cut from these rolled crystals could be annealed extensively without causing recrystallization to occur, provided that the cutting and all handling was done with great care and the cut edges of the specimens, as well as their rolled surfaces, were removed by etching. In these experiments the specimens, rolled to a thickness of 0.020 in., were etched on both sides prior to annealing until a thickness of about 0.010 in. was reached.

* Impurities in weight percent: Si 0.0009, Fe 0.0014, Cu 0.0018, Mg 0.0004, Ca <0.0002, and Na <0.0005.

Results

Fig. 1 shows (curve *DPHN*) the microhardness values (averages of five readings with the Tukon Microhardness Tester, using a Vickers Diamond Pyramid indenter and 200 gram load) for a series of specimens cut from the same rolled crystal, as a function of the annealing time (in salt bath) at 350°C. The kinetics of the isothermal softening might suggest that the mechanism was recrystallization. However, pinhole transmission patterns (taken with unfiltered copper radiation at 48 kv, specimen to film distance 5 cm, collimator length

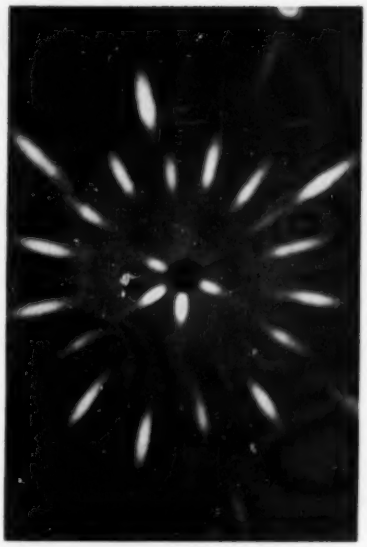

Fig. 2—Transmission pinhole pattern for the aluminum crystal as rolled. Unfiltered copper radiation at 48 kv, specimen to film distance 5 cm, collimator diameter 0.040 in., length 3 in., integrating by parallel displacement of the specimen.

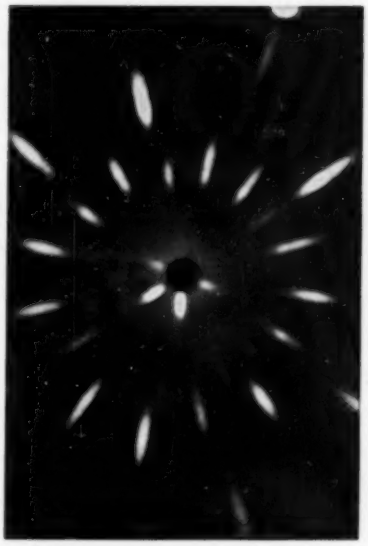

Fig. 3—Transmission pinhole pattern for the aluminum crystal annealed 1300 sec at 350°C after rolling. Conditions same as for Fig. 2.

Fig. 4—Transmission pinhole pattern for the aluminum crystal annealed 1600 sec at 350°C after rolling. Conditions same as for Fig. 2.

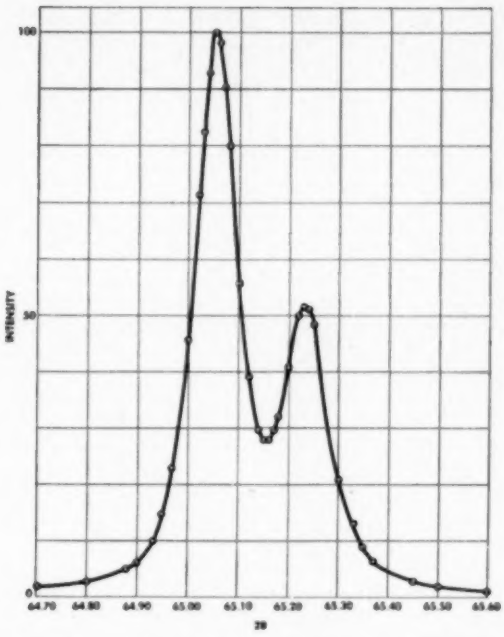

Fig. 5—Diffracted X-ray intensity as a function of Bragg angle for aluminum crystal as rolled. Unfiltered copper radiation, reflection from (220) plane. Receiving slit width 0.02° of arc.

3 in., pinhole diameter 0.040 in., using an integrating mechanism to cover a larger part of the specimen volume) of all specimens up to 1300 sec annealing period indicated no trace of reorientation. The pattern taken immediately after rolling (Fig. 2) was identical with the pinhole pattern (Fig. 3) of the specimen annealed for 1300 sec and completely soft. In preliminary experiments, the same results were obtained with two sets of similar specimens from another crystal, indicating good reproducibility of this behavior. The specimen annealed for 1600 sec partially recrystallized (Fig. 4), without further softening. No attempt was made to ascertain whether or not it would have been possible to anneal for this length of time without recrystallization, by using even more careful techniques.

Line broadening measurements were made with the same set of specimens, very carefully reproducing the alignment of each specimen with respect to the goniometer axis of the General Electric XRD-3 diffractometer used. The intensity of the beam diffracted by the (220) plane was measured point by point (slit width of 0.02° arc) as a function of 2θ by means of a GM counter and scaler. Fig. 5 shows the reflection of the Cu Kα doublet by the rolled specimen (within approximately 5 hr after rolling, stored at room temperature). Similar data for the specimen annealed 100 sec are shown in Fig. 6. The separation of the Cu Kα doublet was used as an index of line broadening, as suggested by Van Arkel and Burgers,[4] $B = (I_{min.} - I_b)/(I_{max.} - I_b)$ (where $I_{min.}$ is the intensity minimum measured between the two lines, $I_{max.}$ is the intensity of the Kα_1 peak and I_b is the background intensity measured at a 2θ value 2° higher than that of the Kα_1 peak). The results are shown in Fig. 1 (curve *B*). It is seen that the recovery of line broadening is essentially complete after 200 sec of annealing, when the hardness drop is only a small fraction of the total (curve *DPHN*). If the line breadth is plotted instead of the index *B*, the results are very similar, but the accuracy is smaller, so that the points show somewhat more scatter. In this connection, it is interesting to note that the line breadth values measured in the present work are somewhat less than one half of those reported by Williamson and Hall.[5] For instance, the breadth of the Cu Kα_1 line reflected by (220) of annealed pure aluminum is given by those investigators as 12 min of arc. As seen in Fig. 6, the present work results in a breadth at half the maximum intensity for the same line of about 5.8 min of arc. Presumably, the difference must be ascribed to smaller instrumental broadening in the present work.

Discussion

The results prove that under conditions where recrystallization, that is, the growth of new grains of a different orientation, is prevented, complete softening (to the hardness level of soft-annealed polycrystalline material) of a heavily rolled aluminum crystal may nevertheless take place by a different mechanism, not involving reorientation.† Since even the extent of the asterism in the pinhole patterns remains unchanged, it is clear that not only the principal orientation, but also the (relatively small) orientation scatter of the rolled crystal is essentially retained during softening. In view of information available from other work,[2] it seems likely that the mechanisms of softening without reorientation in a heavily deformed metal are recovery and subgrain growth (the latter being presumably identical with the process designated by Crussard as

† A similar observation with a Si-Fe crystal was mentioned in a discussion by Dunn.[6]

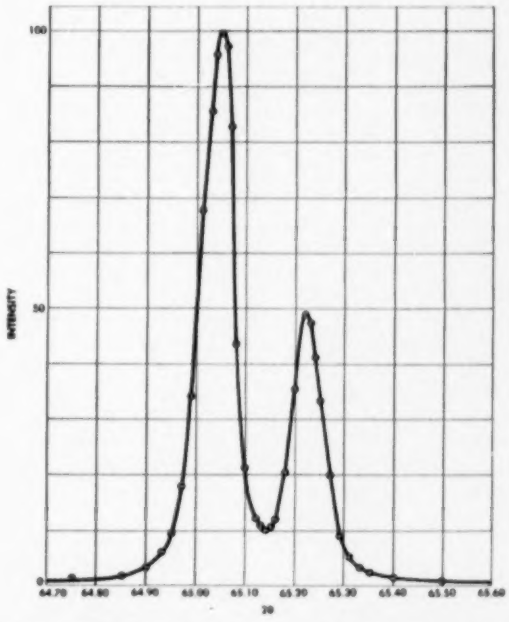

Fig. 6—Diffracted X-ray intensity as a function of Bragg angle for aluminum crystal, annealed 100 sec at 350°C after rolling. Unfiltered copper radiation, reflection from (220) plane. Receiving slit width 0.02° of arc.

"recrystallization in situ"). Work is now under way to check this point.

The disappearance of line broadening in the beginning phase of annealing of cold drawn tungsten wire was shown qualitatively in the early work of Goeler and Sachs.[7] Van Arkel and Burgers[8] found that line sharpening on annealing, at least in thoriated tungsten wire, distinctly precedes recrystallization. In a recent paper, Williamson and Hall[9] ascribed the process to recovery in aluminum and tungsten filings. However, the correlation of line sharpening with recovery and the lack of correlation with softening or recrystallization has not been convincingly demonstrated. Indeed, Averbach[10] indicated that the disappearance of line broadening on annealing of brass filings is a result of recrystallization. The present work demonstrates an example where not only the rate but also the kinetics of line sharpening is quite distinct from that of at least an important part of softening. Also, in the present case, the separation of line sharpening from "recrystallization" involving reorientation is more complete than in previously reported investigations. The experimental results on the kinetics of line sharpening (see curve *B*, Fig. 1) suggest strongly that the process is recovery, rather than one progressing by nucleation and the migration of interfaces. As found by Drouard, Washburn, and Parker,[11] isothermal recovery of work hardening takes place at a rate that is highest initially and then decreases. Borelius, Berglund, and Sjoberg[12] found the same kinetics for the low temperature release of the stored energy of cold work, and Eggleston[13] obtained similar kinetics for the low temperature recovery of the electrical resistivity. In contrast to these recovery processes, which do not involve interfaces, it is typical for the kinetics of recrystallization, and for that of any process which may be described in terms of nucleation and interface migration,[14] that the rate at first increases, then it passes through a maximum and finally decreases.

As shown in the case investigated, line sharpening goes to practical completion in an annealing period less than one-sixth of that necessary for softening. The present results indicate that the imperfections responsible for line broadening may account, at most, for a small fraction of the total work hardening. Whether or not in this case some of the line broadening is due to lattice strain is not yet known. But it is clear that a large part of the work hardening is retained after annealing treatments where the material is certainly strain free, as far as can be determined from the line broadening measurements.

On the basis of their recovery characteristics, the lattice imperfections responsible for line broadening may be clearly separated from the imperfections, also introduced by cold working, which account for the lattice disorientations causing Laue asterism. The present experimental observations appear to be consistent with the view that asterism, as well as a considerable part of the work hardening, are associated with the breaking up of the metal crystals during cold working into slightly disoriented domains, or subgrains, while line broadening may be caused by lattice imperfections within the individual subgrains. On this view, then, it would follow that the interlocking system of subboundaries is considerably more resistant to annealing than the imperfections dispersed inside the subgrains.

Conclusions

1—It is possible to attain complete softening in a heavily rolled aluminum crystal without any "recrystallization" involving the migration of high angle boundaries.

2—The isothermal X-ray line sharpening of a heavily rolled aluminum crystal may be shown, under suitable conditions, to proceed much faster than and to follow kinetics quite distinct from that of at least an important part of softening and of "recrystallization" involving lattice reorientation. The kinetics of line sharpening are similar to that of various known recovery processes, which proceed without interface migration.

3—In view of the significant differences in annealing behavior, it appears that the crystal imperfections which account for line broadening in aluminum are distinctly different from those responsible for the major part of work hardening.

Acknowledgments

The authors wish to express their appreciation to A. Merlini for his assistance with the measurements of line broadening and to J. S. Koehler and T. Noggle for the use of their equipment and for helpful advice in preparing single crystals. The work was supported by the U. S. Atomic Energy Commission, Contract No. AT(11-1)-67, Project No. 9.

References

[1] P. A. Beck: Do Metals Recrystallize? *Trans.* AIME (1952) **194**, p. 979; JOURNAL OF METALS (September 1952).

[2] P. A. Beck: Notes on Work Hardening and Recovery. *Acta Metallurgica* (1953) **1**, No. 4, p. 422.

[3] T. S. Noggle: A Soft Mold Technique for Growing Single Crystals of Aluminum. *Review of Scientific Instruments* (1953) **24**, p. 184.

[4] C. S. Barrett and F. W. Steadman: Structure of Copper after Rolling. *Trans.* AIME (1942) **147**, p. 57.

[5] Y. C. Liu and W. R. Hibbard, Jr.: Recrystallization of a Cold-Rolled Copper Single Crystal. *Trans.* AIME (1953) **197**, p. 672; JOURNAL OF METALS (May 1953).

[6] A. E. van Arkel and W. G. Burgers: Verbreiterung der Debye-Scherrerschen Linien von kaltbearbeitetem Wolframdraht und Wolframband als Funktion der Gluhtemperatur und Gluhdauer. *Ztsch. Physik* (1928) **48**, p. 690.

[7] V. Goeler and G. Sachs: Innere Spannungen im Rontgenbild. *Ztsch. Metallkunde* (1927) **19**, p. 410.

[8] G. K. Williamson and W. H. Hall: X-Ray Line Broadening from Filed Aluminium and Wolfram. *Acta Metallurgica* (1953) **1**, p. 22.

[9] C. G. Dunn: Discussion on Effect of Composition on Grain Growth in Al-Mg Solid Solutions, by L. J. Demer and P. A. Beck. *Trans.* AIME (1949) **185**, p. 309; JOURNAL OF METALS (May 1949).

[10] B. L. Averbach: Recovery and Recrystallization in Brass. *Trans.* AIME (1949) **185**, p. 491; JOURNAL OF METALS (August 1949).

[11] R. Drouard, Jack Washburn, and Earl R. Parker: Fundamental Studies Related to the Origin and Nature of Creep of Metals. ONR Report No. 5 (1952).

[12] G. Borelius, Stig Berglund, and Sven Sjoberg: Measurements on the Evolution of Heat during the Recovery of Cold-Worked Metals. *Arkiv for Fysik.* (1952) **5**, pp. 1-7.

[13] R. R. Eggleston: Cold Work Studies on Copper at Low Temperatures. *Journal of Applied Physics* (1952) **23**, No. 12, p. 1400.

[14] W. A. Johnson and R. F. Mehl: Reaction Kinetics in Processes of Nucleation and Growth. *Trans.* AIME (1939) **135**, p. 416.

An Investigation of the Systems Formed By Chromium, Molybdenum, and Nickel

by David S. Bloom and Nicholas J. Grant

An investigation of the Cr-Mo-Ni ternary system and attendant binaries has been completed. Some changes in the binary diagrams are shown to be necessary. The 1250°C section of the ternary and the liquidus surface have been delineated. A system of invariant reactions existing above 1250°C has been suggested.

BECAUSE chromium, molybdenum, and nickel are important not only as bases for alloying systems but also as major alloying additions for other refractory metals, a study of the phase diagrams is of great interest and importance. In addition there are interesting features of theoretical value, a number of which are of prime consideration in this work. The major aim was to determine the ternary phase diagram of these metals at and above 1250°C, with sufficient attention given to lower temperatures to permit an understanding of the conditions existing at 1250°C and above.

To understand ternary systems it is essential that accurate information concerning the binary systems be available, which in turn presupposes thorough knowledge of the constituent elements. On the basis of this investigation not only were significant inaccuracies indicated in the binary systems but much consideration had to be given to one of the elements, that is, chromium.

The observation has been made that chromium undergoes a crystal transformation at a temperature near its melting point. Much of the experimental data leading to the detection of this transformation and the effects of this hypothesis on the form of the Cr-Ni phase diagram have already been reported[1, 2] and will not be repeated here.

The experimental methods employed in the investigation have also been covered.[1-3] The purity of the molybdenum utilized in this work showed by qualitative spectrographic analysis that chromium, copper, iron, silicon, and tungsten were present in quantities of 0.1 to 0.001 wt pct.

During the course of the investigation more than 100 melts were made, weighing from 150 to 200 grams each. Each of these melts was sectioned for chemical analysis and for specimens for examination in the as-cast and various heat-treated conditions by X-ray and metallographic means.

All X-ray diffraction patterns reproduced here were made using chromium $K\alpha$ radiation although iron and copper targets were used on occasions during the investigation.

Experimental Results

Mo-Ni-System: The most recent comprehensive investigation of the Mo-Ni system was made by Ellinger[4] in 1942; the diagram as shown in the American Society for Metals Handbook is based on his work. The work done on the system in this investigation substantiated the general form of the diagram although some differences were observed. These are indicated by a comparison of Ellinger's diagram and Fig. 1, the latter showing the results of pertinent thermal analyses made in this research. It can be seen in Fig. 1 that the eutectic composition is

D. S. BLOOM, formerly Research Assistant, Dept. of Metallurgy, M.I.T., is now Research Metallurgist, Naval Ordnance Test Station, China Lake, Calif., and N. J. GRANT, Member AIME, is Associate Professor, Dept. of Metallurgy, Massachusetts Institute of Technology, Cambridge, Mass.

Discussion on this paper, TP 3703E, may be sent, 2 copies, to AIME by April 1, 1954. Manuscript, Sept. 18, 1953. New York Meeting, February 1954.

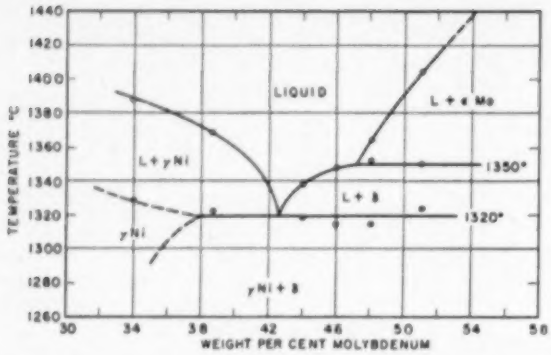

Fig. 1—Central region of Mo-Ni diagram based on thermal analysis data.

indicated to be approximately 57.5 pct Ni-42.5 pct Mo; this differs from Ellinger's value of about 54 pct Ni-46 pct Mo. Concomitant with the change in eutectic composition, a change in the liquidus curve was noted, as shown.

A second discrepancy was found in the peritectic temperature. The temperature as determined by thermal analysis is about 1350°C; the temperature given by Ellinger was 1370°C. The temperature of the eutectic reaction was found to be 1320°C, confirming Ellinger's results.

A third difference was found in the liquid composition in equilibrium with the molybdenum solid solution at the peritectic reaction temperature, 1350°C. Ellinger gave a value of about 48 pct Ni, whereas the best fit from this work is approximately 53 pct Ni.

It is difficult to decide which of the determinations is the more accurate. Ellinger made visual observations on solid samples as they were being heated, while the determinations reported here were developed from careful thermal analyses. Neither method can be claimed infallible, but it is felt that the values of the eutectic composition, the peritectic temperature, and the composition of the liquid at the peritectic temperature, which have been determined here, are more nearly correct than Ellinger's.

Recently, in unpublished work, the composition limits of the MoNi intermetallic compound have been questioned, but from the results observed in this research the equiatomic composition is to be included within the composition range, at 1250°C.

One further observation relative to the Mo-Ni system is that small additions of chromium raised the formation temperature of the compound Ni_4Mo. This point was not pursued in detail, but results leading to this observation were obtained in the pertinent thermal analyses. Presumably the Ni_4Mo field reaches a maximum temperature within the ternary system and then decreases, since the compound did not make its appearance in the 1250°C section of the ternary.

Cr-Ni System: Most of the results on the Cr-Ni system have been published.[8] Briefly, the diagram as presented showed a eutectoid reaction at about 1180°C with eutectoid composition of about 65 pct Cr-35 pct Ni; the phase above the eutectoid reaction was suggested to be a high temperature, face-centered cubic form of chromium labeled β Cr. In confirmation of this phase diagram and the mechanism of transformation in near-eutectoid alloys, one item of interest is presented.

It has been found that samples of near-eutectoid composition can transform from the high temperature β Cr phase to the low temperature α Cr and γ Ni by means of an intermediate structure. This has been suggested previously.[9] It has also been noticed that this transformation is strongly strain-sensitive. One rather interesting aspect of this transformation is revealed in Fig. 2. Fig. 2a shows the X-ray diffraction pattern obtained with chromium radiation on a 60 pct Cr-40 pct Ni sample as quenched from 1250°C. The lines due to the γ Ni phase are present, plus the lines ascribed to the β Cr phase. Fig. 2b shows a pattern from the same sample after the surface had been lightly cold worked by polishing on fine emery paper. A shift in the β Cr lines can be noticed, while the γ Ni lines have almost disappeared as a result of the distortion.

At this point it becomes necessary to consider the movements of lines of the chromium solid-solution

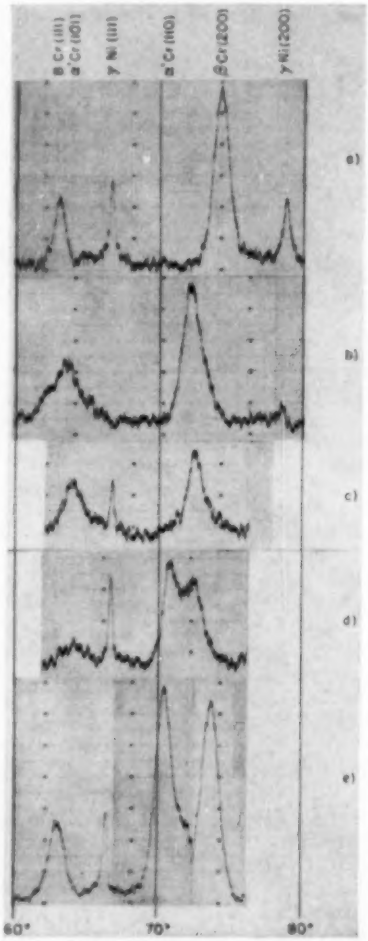

Fig. 2—Diffraction patterns from a 60 pct Cr-40 pct Ni alloy. Solid sample a—as quenched from 1250°C, electrolytically polished and etched; b—slightly cold worked by polishing; c—after annealing 30 min in boiling water; d—after an additional anneal of 15 min in lead at 360°C; e—after additional anneal of 15 min in lead at 500°C. The latter is a composite pattern combining the results of two different orientations of the specimen.

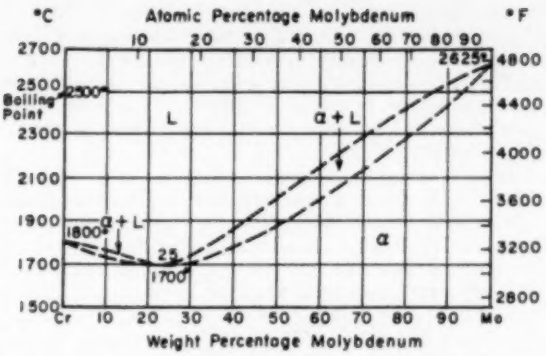

Fig. 3—Constitution diagram of Cr-Mo system from the Metals Handbook, ASM.

phase in Fig. 2 and the structures responsible for these lines. The lines in Fig. 2b which are produced by the chromium phase no longer fit the pattern of a face-centered cubic structure because of the shifting in opposite directions which they have experienced. The pattern which they do fit, however, is that of a body-centered tetragonal structure; and this intermediate, transitional tetragonal structure is called α' Cr. This follows of course because of the similarity between the body-centered cubic and body-centered tetragonal cells, and because the tetragonal structure apparently does collapse into the cubic structure under the appropriate conditions. It has been observed that the two α' Cr lines tend to approach each other (indicating a decreasing c/a ratio) and merge to form the α Cr (110) line of the normal body-centered cubic phase. In any event, as soon as the β Cr (200) line, for example, shifts (as long as the β Cr (111) line shifts a commensurate amount in the opposite direction), it can no longer be called the β Cr (200) line but becomes the α' Cr (110). Similarly, the β Cr (111) line becomes the α' Cr (101) line upon shifting. And these α' Cr lines ultimately become one α Cr line as the structural changes are completed.

Fig. 2c shows the pattern taken from the same surface after the sample had been annealed 30 min in boiling water. The only evident changes are the re-appearance of the γ Ni (111) line and a slight shift in the α' Cr lines. In Fig. 2d, the same sample, after being annealed an additional 15 min in molten lead at 360°C, shows an interesting development. The α' Cr (110) line has split off an additional line. A similar effect is not noticeable in the (101) line mainly because the specimen was oriented so as to maximize the (110) line and the effect there. In Fig. 2e the split of the line becomes more evident, and one leg of the diffraction line has practically resumed the β Cr (200) position, while the other leg is well on its way toward assuming the α Cr (110) position. This seemingly indicates that on relatively low temperature annealing the intermediate phase follows two tendencies: 1—to transform in part to the low temperature α Cr form, and 2—to revert to the undistorted high temperature β Cr form.

Cr-Mo System: The Cr-Mo system has been considered to consist of a complete series of solid solutions with a minimum in the liquidus curve near the chromium end of the system (see Fig. 3, which is from the 1948 American Society for Metals Handbook). Since the work on the Cr-Ni system had revealed that a transformation in pure chromium existed, it seemed advisable to examine the Cr-Mo binary more closely for evidence of the transformation in this system.

The point data from thermal analyses are shown in Fig. 4. These results indicated that the minimum in the liquidus curve is at a higher temperature and at a higher chromium composition than had previously been held. The minimum appears to be at about 1860°C and at a composition of about 80 wt pct Cr. This agrees extremely well with the earlier

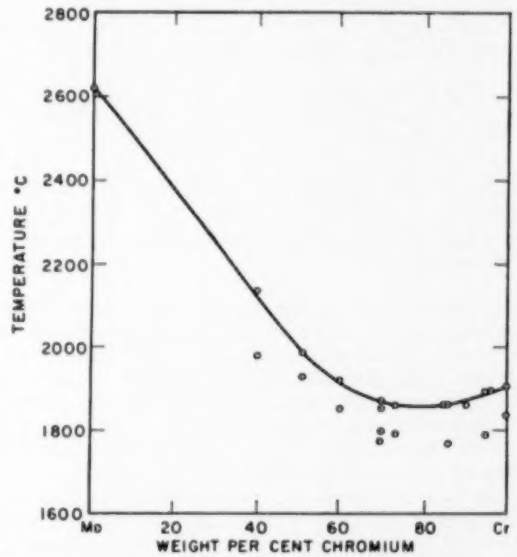

Fig. 4—Some results of thermal analyses in the Cr-Mo system showing the liquidus for the system. Solid-state reaction temperatures are developed from both heating and cooling curves.

work of Potter, Putnam, and Grant,[3] whose thermal analysis data for the liquidus are shown in Fig. 5.

It will be noted in Fig. 4 that reactions are indicated in the solid state. A satisfactory explanation of these points is not easily advanced. It should be noted further that the points shown in Fig. 4 were developed from both heating and cooling curves so that they cannot be imputed to nonequilibrium cooling conditions. Because of the presence of the points under the minimum of the liquidus it is difficult in this instance to see how these particular points can be connected in any way with the solidification or melting processes. Though the connection is not clear, they are considered to be derived from the transformation detected in the pure chromium.

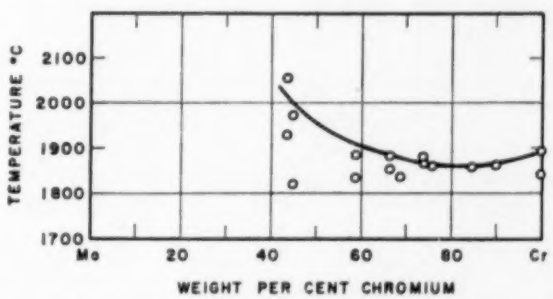

Fig. 5—Portion of the Cr-Mo liquidus from Putnam, Potter, and Grant.[3]

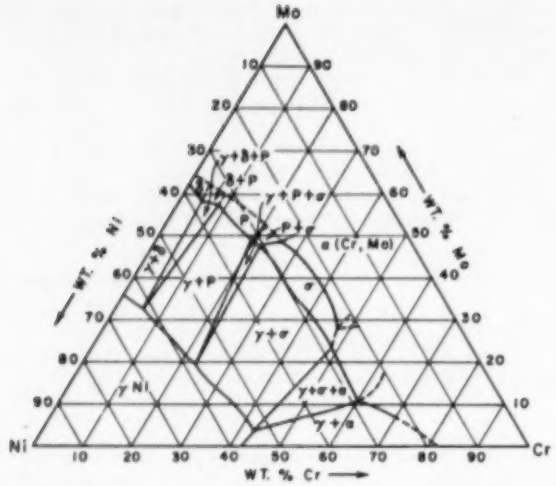

Fig. 6—1200°C section of the Cr-Mo-Ni system as developed by Rideout et al.[5]

A phase diagram for the Cr-Mo system which conforms to the thermal analyses and includes the chromium phase change is not easily constructed, nevertheless, it is clear that the Cr-Mo phase diagram as previously drawn (Fig. 3) cannot be considered to be complete or correct.

While many efforts were made to utilize the data to determine the diagram below the liquidus, all of them had a number of weaknesses. The data are thus presented without interpretation except for the drawing in of the liquidus surface showing the minimum in agreement with the liquidus of Potter, Putnam, and Grant.

Cr-Mo-Ni System: The scope of this portion of the investigation was to determine the liquidus surface of the Cr-Mo-Ni system as well as the 1250°C section. The examination of the binary systems was wider in scope, but only to afford an understanding of the conditions existing at 1250°C and above in the ternary system.

1250°C Section: Several previous investigations in this system have been made but the most pertinent one is that of Rideout, et al.[5] The presence in this system of the σ phase had first been reported by Putnam, Grant and Bloom[6] and also by Rideout et al.,[5] who also reported another ternary compound. This latter compound, of unidentified crystal structure, was called the "P" phase. These authors developed a portion of the 1200°C section of this system as shown in Fig. 6. The 1250°C section as developed in the present investigation is shown in Figs. 7 and 8, in weight percent and atomic percent, respectively.

Except for the region adjoining the Cr-Ni system the diagrams are fairly similar in outline and broadly indicate: 1—that the σ phase field diminishes with increasing temperature, and 2—that the ternary intermetallic compound P moves toward the Mo-Ni binary with increasing temperature. There are significant differences, however, in the extent of the σ fields.

The existence of the P phase was corroborated mainly on the basis of X-ray diffraction results, but a microstructure, one of many examined, of interest in this connection is shown. The diffraction lines as developed in this work are given in Table I in conjunction with the values of Rideout et al. (Some of the lines given by them but missing here may be β lines.) These values were obtained from powdered specimens of alloys which had been held

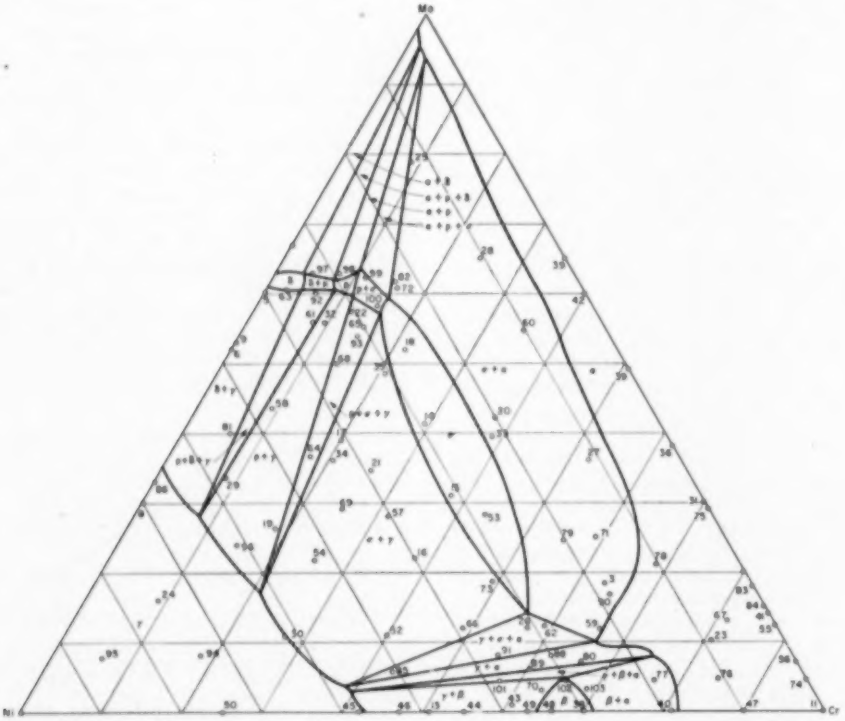

Fig. 7—1250°C section of the Cr-Mo-Ni system showing the heats which were used to determine the section. Values are in weight percent.

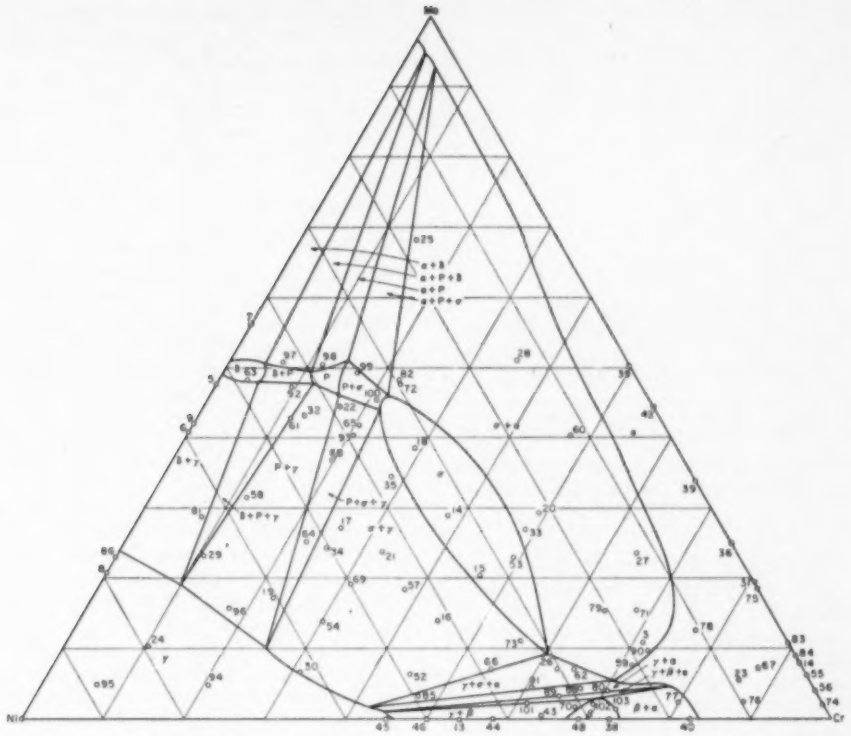

Fig. 8—Same 1250°C section as in Fig. 7, but with values in atomic percent.

for over 100 hr at 1250°C before powdering. The powders were then sealed in Vycor capsules and placed in a furnace at 1250°C, held there for 3 min and air cooled. Unfortunately the cooling took about 30 sec, and since the powder samples did not give exactly the same results as the lump samples, the method has been outlined. It was concluded that the cooling rate was not sufficiently fast for the powders to maintain the 1250°C equilibrium structure. The main difference was in the indicated location of the *P* phase; the powder samples indicated the *P* field to be at a slightly higher chromium content.

This shifting of the *P* phase field with temperature is further indicated by the microstructure of the as-cast 2 pct Cr-61 pct Mo-37 pct Ni alloy shown in Fig. 9. X-ray results show that at 1250°C the alloy consisted only of the δ phase, but the as-cast microstructure shows four phases to be present. These are identified provisionally as being α solid solution Mo in the center of the crosses, *P* phase surrounding the α Mo, δ phase surrounding the *P* phase, and the matrix which is a eutectic of δ and γ Ni. The identification of the *P* and the δ phases is of course difficult and is based in part on X-ray considerations which indicate that both phases are present.

This order of solidification leads to the conclusion that at a temperature of 1250°C the *P* phase extends even closer to the Mo-Ni binary. Extrapolating this trend to lower temperatures would mean that the *P*

Table I. 2θ Values of Lines of *P* Phase Using Chromium Radiation and Vanadium Filter

Values from Rideout et al.[5]	Values from Heat 61, This Investigation	Values from Rideout et al.[5]	Values from Heat 61, This Investigation
51.08	50.7	66.72	66.7
57.10		66.16	67.1
57.38	57.4	67.70	
58.72	58.2	68.08	68.1
59.96		68.52	68.65
62.80	62.85	70.28	
63.4		72.88	72.7
64.6	64.7	73.52	
65.86	65.8	74.14	74.9
65.94	66.1	77.38	77.4

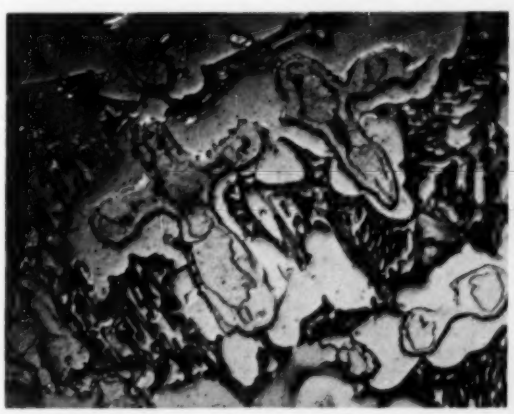

Fig. 9—2 pct Cr-61 pct Mo-37 pct Ni alloy as cast. The roughened material in the center of the crosses is α Mo surrounded by the P phase, which is in turn surrounded by the δ phase. The matrix is a eutectic consisting of δ phase and γ Ni. Electrolytic polish and etch. X750. Area reduced approximately 40 pct for reproduction.

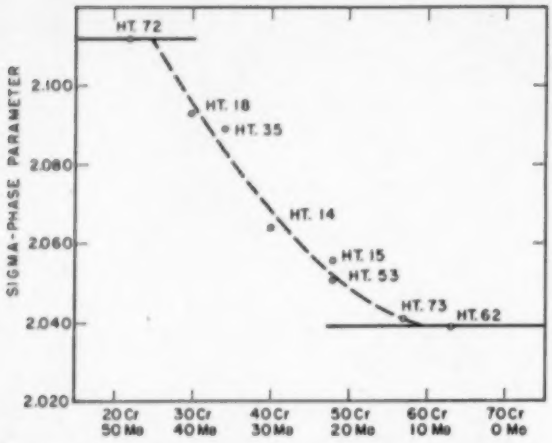

Fig. 10—σ phase parameter as a function of varying Cr-Mo composition at a constant 30 atomic pct Ni, at 1250°C.

phase would extend into the ternary system, and this is borne out by comparison of the two diagrams in Figs. 6 and 7.

In the central area of the 1250°C section are shown the ternary σ phase boundaries. From Fig. 7 it can be seen that the field has a rather long, slender shape. When plotted in atomic percent (Fig. 8) the field orients itself fairly closely along a line of constant nickel content, this axis being at about 32 pct Ni. Thus it can be considered that the nickel atoms are present in a proportion of about one-third, while the chromium and molybdenum proportions vary over a rather wide range. This is thought to be not without significance, particularly since the width of the field at this temperature in terms of nickel content is so restricted.

From theoretical considerations[7] there is reason to suspect that σ phase could form in binary Ni-Cr system at a composition near 67 pct Cr-33 atomic pct Ni, and this is substantiated by the position and shape of the σ phase field in the ternary system. Extensive tests over a wide range of compositions, temperatures and long holding times, however, failed to produce σ in the binary Cr-Ni alloys. Apparently molybdenum has a powerful effect of promoting σ formation as it is substituted for chromium.

Fig. 10 shows the variation of the average of the d values of six of the strongest lines in the σ phase pattern plotted as a function of chromium and molybdenum contents under the assumption that the nickel content is constant at 30 atomic pct. There is a near-linear relationship indicated, considering the scatter of the heats.

An additional point of interest is that the σ phase in this system is considered to form directly from the liquid through a ternary peritectic reaction; and the elongated shape of the field assumes added interest because of the proximity of the 1250°C section to the peritectic temperature. This will be discussed in further detail subsequently.

The work in the Cr-Ni binary system resulted in the acceptance of a eutectoid reaction in this system. This must of course be fitted into the ternary system. As was mentioned in the discussion of the Cr-Ni binary, the experimental difficulties involved in studying the high temperature phase were rather formidable. The presence of molybdenum in appreciable amounts does not, unfortunately, increase the ease with which the high temperature chromium phase can be retained.

From the study of the X-ray results and the pertinent microstructures it can be definitely established that the two-phase field, γ Ni plus α Cr, is the one which exists at 1250°C and not the alternative possibility, σ plus β Cr. Further, the extent of the three-phase field, γ Ni plus α Cr plus σ, can be laid out approximately by reference to the relevant alloys; the same applies to the two-phase field, γ Ni plus α Cr. Unfortunately the fields involving the β Cr phase cannot be laid down with accuracy. To illustrate this, two sample X-ray patterns are shown in Fig. 11 and are compared with a pattern of the two lower temperature phases, γ Ni and α Cr (Fig. 11a). Fig. 11b is from a 63.5 pct Cr-3.5 pct Mo-33 pct Ni alloy; here lines of the γ Ni phase and one line of the intermediate metastable α' Cr phase are identified. It is deduced from this that at 1250°C the sample had consisted of γ Ni plus β Cr, and that during the quench, or in preparation, the β Cr phase transformed to the α' Cr state. Fig. 11c is of a 66.5 pct Cr-3.5 pct Mo-30 pct Ni alloy; the lines present here are ascribed to the α Cr and α' Cr phases. However, to conform to other results it is necessary to conclude that at 1250°C this sample was mostly β Cr, but on cooling, or during preparation, the β Cr phase again had partially decomposed. Though these patterns and other similar patterns are not entirely satisfactory for delineating the fields at 1250°C, they do indicate conclusively that there

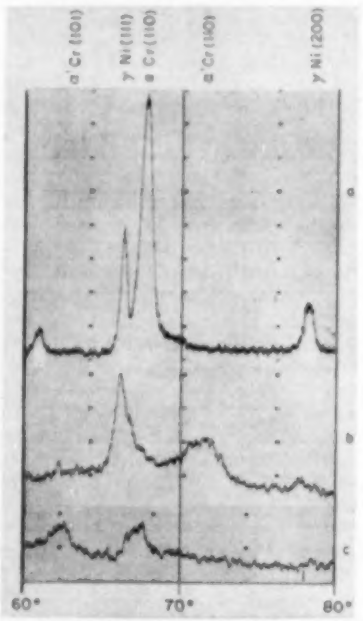

Fig. 11—a—Diffraction pattern of 60 pct Cr-40 pct Ni alloy as quenched from 1150°C, showing lines due to γ Ni and α Cr. b—63.5 pct Cr-3.5 pct Mo-33 pct Ni alloy after 21 hr at 1250°C, then quenched in water. Surface mechanically polished, deeply electrolytically etched; shows lines due to γ Ni and α' Cr. c—66.5 pct Cr-4.5 pct Mo-30 pct Ni alloy after 135 hr, at 1250°C, then quenched in water. Surface same as (b). Shows α Cr and α' Cr.

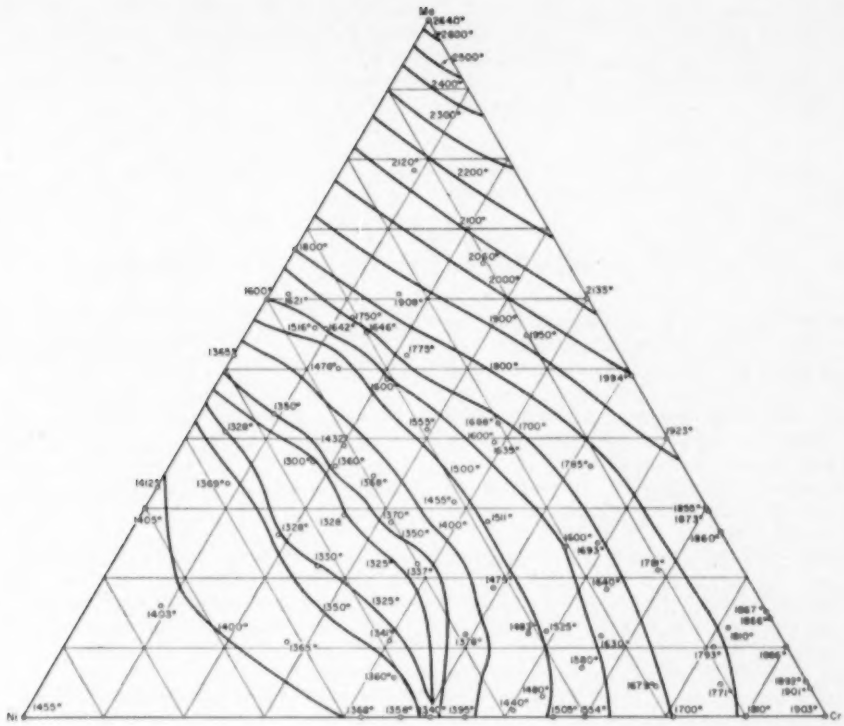

Fig. 12—Plot of liquidus temperatures and isotherms.

Fig. 13—Proposed system of high temperature invariant plane of the Cr-Mo-Ni system above 1250°C.

Fig. 14—Cooling curve of 9 pct Cr-79 pct Mo-12 pct Ni alloy. Time increases from right to left. The first change of slope is at about 2120°C, the second at about 2045°C.

does exist another phase at this temperature, located approximately as shown in Figs. 7 and 8.

The Liquidus Surface: The liquidus surface was developed from the liquidus temperatures as determined for each alloy by thermal analysis. The liquidus temperatures were taken to be the average of the cooling and heating values obtained at rather slow rates of temperature change. It was determined experimentally that for the particular experimental setup used, a cooling rate of 10°C per min would yield data with an accuracy commensurate with the accuracy of the W-Mo thermocouple. At more rapid cooling rates the accuracy became poorer. In actual practice cooling rates of about 5°C per min were maintained.

The liquidus surface as developed is shown in Fig. 12. No discontinuities are indicated in the isothermal lines, though in actuality some must exist. The minimum melting point found was about 1275°C in what is thought to be a ternary eutectic. The composition at this point is about 19 pct Cr-34 pct Mo-47 pct Ni. The maximum melting point found is that of pure molybdenum. There were no ternary compounds detected which melted with open maxima.

System of Invariant Planes: The development of the system of invariant planes existing about 1250°C has been undertaken and a construction developed which is at least compatible with all the data available. Since extensive work was not attempted involving reactions occurring between 1250°C and the liquidus temperatures, the synthesis must be accepted as somewhat provisional. The system as developed is reproduced in Fig. 13. In this construction the triangles and quadrilaterals representing the invariant planes are to be understood as being schematic rather than definitive. The scheme is reproduced mainly to assist others who may contemplate further exploration of the system.

It will be noted that there is no three-phase field coming down on to the invariant plane at 1500°C denoting the 3/1 (peritectic) reaction whereby the σ phase is formed. The phases which would be in coexistence in this field are the liquid plus α plus β phases. This field could be considered as originating in the Cr-Mo binary system and then moving with falling temperatures to the location as shown, but the thermal analyses and as-cast microstructures did not substantiate such a construction. The solution which did present itself, but is not shown because the evidence did not seem to warrant such a drastic innovation, was that there existed a three-phase field, α plus β plus liquid, which was based on a reaction occurring at very high temperatures in the Mo-Ni system. This would necessitate a high temperature transformation in molybdenum similar to the one which apparently occurs in chromium. In support of this hypothesis a cooling curve of an alloy of 9 pct Cr-79 pct Mo-12 pct Ni is shown in Fig. 14. The arrest occurring at about 2045°C indicates a more complicated solidification process than is involved in a mere liquidus-solidus type of solidification.

It is because of this indicated solid state change in the above alloy and the solid state change indicated with Cr-Mo binary system that no attempt was made to introduce a phase diagram, other than the liquidus curve, for the Cr-Mo binary (Fig. 4).

Summary

1—The investigation of the Mo-Ni system has resulted in some changes in the phase diagram in the regions of the eutectic and peritectic reactions.

2—The investigation of the Cr-Ni system has developed interesting phenomena concerning the intermediate structure associated with the eutectoid reaction. It has been shown that the retained high temperature phase can be decomposed by annealing or cold working near room temperature.

3—It has been concluded that the Cr-Mo system as presently accepted is incorrect, and while a definite revision has not been developed, suggestions have been advanced for possible changes of the diagram.

4—The 1250°C section of the Cr-Mo-Ni system has been developed, showing the rather interesting shape of the σ phase field at this temperature. The existence of another ternary compound called the P phase has been corroborated.

5—The liquidus surface of the ternary has been outlined.

6—A possible system of invariant planes for the ternary system Cr-Mo-Ni is suggested.

Acknowledgments

The authors wish to express thanks to Dr. J. W. Putnam for assistance and the Bureau of Aeronautics under whose sponsorship the work was performed.

References

[1] D. S. Bloom, J. W. Putnam, and N. J. Grant: Melting Point and Transformation of Pure Chromium. *Trans.* AIME (1952) **194**, p. 626; JOURNAL OF METALS (June 1952).

[2] D. S. Bloom and N. J. Grant: Chromium-Nickel Phase Diagram. *Trans.* AIME (1951) **191**, p. 1009; JOURNAL OF METALS (November 1951).

[3] J. W. Putnam, R. D. Potter, and N. J. Grant: The Ternary System Chromium-Molybdenum-Iron. *Trans.* ASM (1951) **43**, p. 824.

[4] F. H. Ellinger: The Nickel-Molybdenum System. *Trans.* ASM (1942) **30**, p. 607.

[5] S. Rideout, W. D. Manley, E. L. Kamen, B. S. Lement, and P. A. Beck: Intermediate Phases in Ternary Alloy Systems of Transition Elements. *Trans.* AIME (1951) **191**, p. 872; JOURNAL OF METALS (October 1951).

[6] J. W. Putnam, N. J. Grant, and D. S. Bloom: Sigma Phase in Chromium-Molybdenum Alloys with Iron or Nickel. *Symposium on the Nature, Occurrence and Effects of Sigma Phase.* ASTM, Spec. Pub. 110, June 1950.

[7] D. S. Bloom and N. J. Grant: Regarding Sigma Phase Formation. *Trans.* AIME (1953) **197**, p. 88; JOURNAL OF METALS (January 1953).

Solid State Bonding of Aluminum to Nickel

by S. Storchheim, J. L. Zambrow, and H. H. Hausner

The solid state bonding of aluminum to nickel was studied as a function of temperature, pressure, and time at pressure. The initial results indicated that as the reaction conditions were varied, marked changes in tensile strength occurred. Plots of the log penetration coefficient vs the reciprocal of absolute temperature for various isobars were straight lines displaced from each other.

THE techniques of bonding different metals to each other include brazing, welding, welding by application of a molten phase, and solid state welding without any molten phase present. This last technique, the pressing of metals either at room temperature or at some temperature below the melting point of the metals to be joined, seems to offer interesting possibilities for bonding purposes. However, this technique has not been completely investigated, and very little is known about the diffusion phenomena which occur during solid state welding. Some previous work on the effect of pressure on diffusion[1] was inconclusive.

This paper is concerned with an investigation regarding the effect that the processing variables, such as pressure, temperature, and time at pressure, have in solid state bonding. The tests were made with aluminum and nickel and special emphasis was given to the strength of the bond between these two metals and to the intermetallic penetration rate during the bonding process. It seems that the effect of pressure on the intermetallic penetration is of particular importance for practical purposes and this effect was therefore studied in detail.

Procedure

Apparatus: The means of solid state bonding used for this study was that of the hot-pressing technique.

S. STORCHHEIM, Junior Member AIME, J. L. ZAMBROW, and H. H. HAUSNER, Member AIME, are associated with the Atomic Energy Div., Sylvania Electric Products Inc., Bayside, N. Y.

Discussion on this paper, TP 3725E, may be sent, 2 copies, to AIME by April 1, 1954. Manuscript, July 16, 1953. New York Meeting, February 1954.

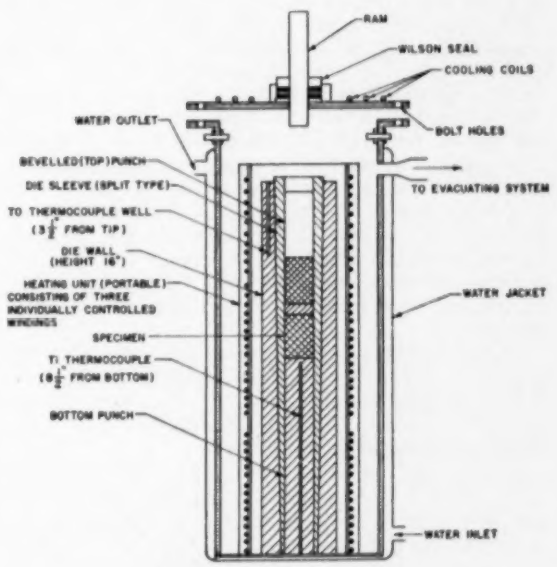

Fig. 1—Hot pressing apparatus.

This method requires the equipment pictured in Fig. 1 and involved the following procedure.

The two metals to be bonded were placed in an aquadag lubricated 18-4-1 tool steel die, 16 in. high by 1.440 in. ID, between punches of 1.366 in. diameter made of the same material. A thermocouple

[1] F. J. Radavich and R. Smoluchowski: Influence of Pressure on Intermetallic Diffusion. *Physical Review* (1944) 65, pp. 62, 248.

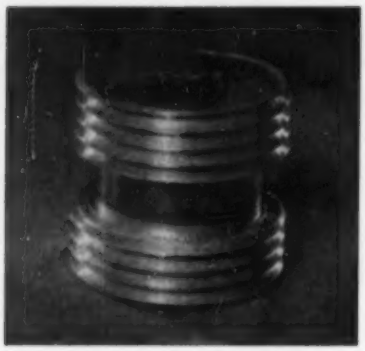

Fig. 2—Typical tensile test specimen, actual size.

well was located in the die body 3½ in. from the top of the die while another well was located centrally in the bottom punch 8½ in. from the bottom of the die. This die assembly was located in three cylindrical ceramic heating furnaces placed in tandem. Each furnace was individually controlled by a power transformer (Variac). The die and furnaces were in turn placed in a water-cooled, stainless steel pot which could be evacuated. On this was bolted a cover containing a centrally located Wilson seal with an 18-4-1 ram 1 in. in diameter running through it. After sealing, the pot was evacuated by a roughing pump to 200 microns pressure, after which a diffusion pump was used to bring the pressure down to 5 to 15 microns. At this pressure the furnaces were turned on. As soon as the furnaces started to heat up, out-gassing of the entire unit raised the pressure to 30 to 400 microns. By the time the specimens were at temperature ready to be pressed, approximately 30 min, the vacuum pumps had re-established the 5 to 15 micron pressure. Once the desired temperature was reached, the required pressure was applied for a predetermined length of time to the 1 in. ram through to the top punch and to the specimen. When the time had elapsed for keeping the specimen under pressure the pressure was released, the energizing coil current turned off, and the assembly allowed to cool. After cooling, the die was removed from the pot and the specimen was ejected.

Specimen Preparation: Two different types of specimens were made for this investigation. One was for subsequent tensile test while the other was for determination of intermetallic penetration. The specimens were prepared as follows:

Tensile Bars: Commercially rolled nickel pieces ¼ in. thick and 1.366 in. in diameter were placed between commercial rod of 2-S aluminum ½ in. thick and 1.366 in. diameter. This sandwich in turn was slipped into a 2-S aluminum sleeve 1.344 in. OD and 1.370 in. ID. This sleeve lined the couple up and prevented the aquadag lubricant from getting in between the Al-Ni interfaces. Immediately prior to the specimen assembly the nickel was abraded on its flat surfaces with 320 grit silicon carbide paper, producing clean, smooth surfaces. The aluminum was chemically cleaned just before assembly by: 1—degrease in acetone, 2—distilled water rinse, 3—immersion for 3 min in 5 pct NaOH at 70° to 80°C, 4—distilled water rinse, 5—immersion for 2 min in 50 pct HNO_3 solution at room temperature, and 6—distilled water rinse.

Once the sandwich was hot-pressed and ejected, the specimen was machined, such that the aluminum sleeve was removed and the nickel and part of the aluminum on both sides of it were taken down to a diameter of 1¼ in. The remaining aluminum was then threaded, see Fig. 2, and the bar so produced was tested for tensile strength. In all instances the specimens broke during the test at the Ni-Al interface and never within the aluminum or nickel. The ultimate tensile strength values at times showed considerable scatter for a set of given reaction conditions. Because of this, as many as three to five specimens were made for a particular set of conditions. The trend of the average tensile strengths obtained was not as conclusive as was the trend of the maximum tensile strengths, the latter values being obtained under optimum reaction conditions. Therefore, the values of ultimate tensile strength given in this report are maximum values.

Penetration Couples: The preparation of penetration couples was very similar to that of assembling the tensile bars; however, molybdenum strips ⅜ in. square and 0.001 in. thick were placed at the center of the Al-Ni interfaces as the couples were being assembled. The molybdenum strips were used as inert markers for they did not react with either the aluminum or nickel at the reaction conditions used. In addition, the molybdenum prevented Al-Ni interaction where it came between the aluminum and the nickel. In this manner, therefore, the molybdenum acted as reference lines for eventual penetration measurements, i.e., the extent of penetration was measured from both sides of the Al-Ni interface, as defined by the molybdenum strips, up through and to the deepest penetration of the Al-Ni intermetallic compounds formed.

Penetration Measurements and Methods of Calculating Penetration Constants: After the assembly was hot-pressed and ejected from the die, a quarter-pie shaped section was cut from it, mounted, and measurements of thirty of the deepest penetrations into the aluminum and into the nickel were determined microscopically. What was done was to project the image of the Al-Ni interface at 2000X magnification onto the screen of the metalloscope being used and measure the penetrations to the nearest 64th of an inch. The thirty measurements were averaged and this average was then converted to centimeters. Once this value was obtained, the pene-

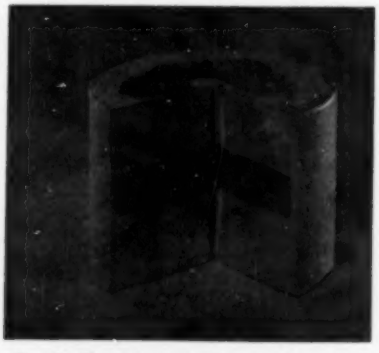

Fig. 3—Typical penetration couple, actual size.

tration data were calculated from the following formulas:

$$P = X^2/t$$

where X is the penetration in cm, t is time in seconds at temperature and under pressure, and P is the penetration coefficient in sq cm per sec.

$$P = P_o e^{-Q/RT}$$
$$\ln P = \ln P_o - Q/RT$$

where P_o is a temperature dependent constant, Q is the activation energy for penetration in cal per gram-atom, R is the universal gas constant, T is the absolute temperature of reaction, and ln P_o is the intercept on ln axis of ln P vs 1/T curve.

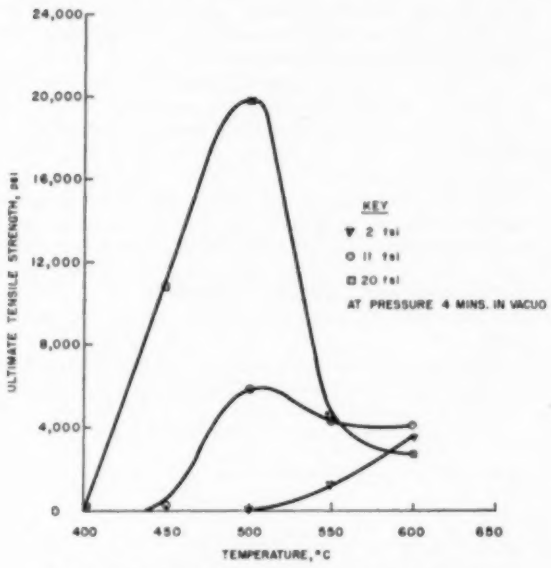

Fig. 4—Al-Ni tensile strength vs pressing temperature.

A typical view of a sectioned penetration couple is shown in Fig. 3.

Results

Ultimate Tensile Strength: Effect of Pressing Temperature: The effect of pressing temperature on the ultimate tensile strength of Al-Ni couples was first determined. Fig. 4 is a plot of the maximum ultimate tensile strength obtained vs varying pressing temperatures. Three curves are shown, each representing specimens pressed at different applied pressures, namely, 2, 11, and 20 tons per sq in. (tsi). In all instances pressure was applied for a period of 4 min. The curves show an increase in strength with increasing temperatures and specifically for the 11 and 20 tsi pressures; the curves reach a maximum, decline, and then indicate a leveling-off period at temperatures above approximately 550°C.

It is observed that as the pressure increases, the maximum tensile strength achieved also increases. Both the 11 and 20 tsi curves exhibit maximum strength at approximately 500°C. (Some work done at 5 tsi indicated that maximum tensile strength also occurred around 500°C.) Note that the initial rising and falling slopes of each curve decrease in rate of rise and fall, respectively, as the pressure used decreases. In addition, it is observed that the beginning of incipient bonding occurs at lower temperatures as the pressure is increased.

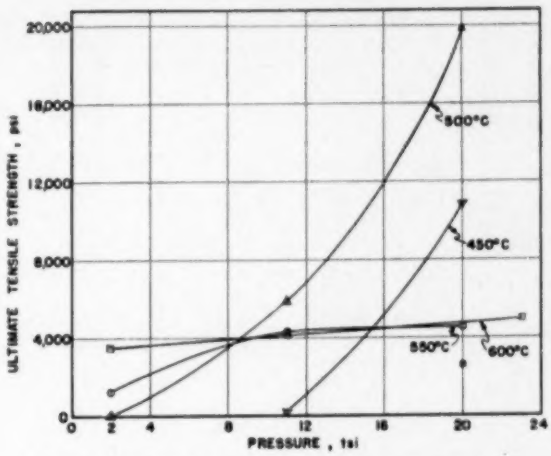

Fig. 5—Al-Ni tensile strength vs applied pressure held 4 min.

Effect of Applied Pressure: Fig. 5 shows the effect applied pressure held for 4 min has upon the maximum ultimate tensile strength of Al-Ni couples. These experiments were carried out at a series of isotherms, specifically, 450°, 500°, 550°, and 600°C. Incipient bonding was found to occur at 400°C for pressures of 11 and 20 tsi. This is not shown on the illustration.

At 450°C tensile strength is seen to increase rapidly while at 500°C the bonding increases even more rapidly, and to much higher values for increased applied pressure. At 550°C the increase of tensile strength with applied pressure is much more gradual than at 500°C, and the curve shows a leveling-off

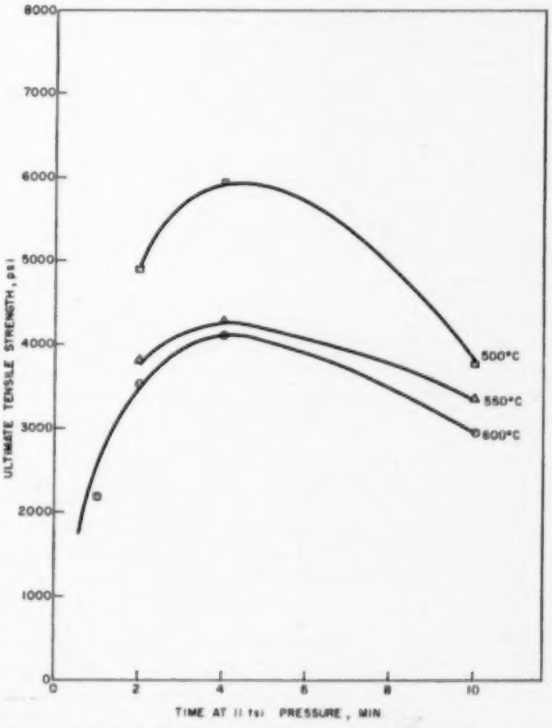

Fig. 6—Al-Ni tensile strength vs time at pressure (11 tsi) for various temperatures.

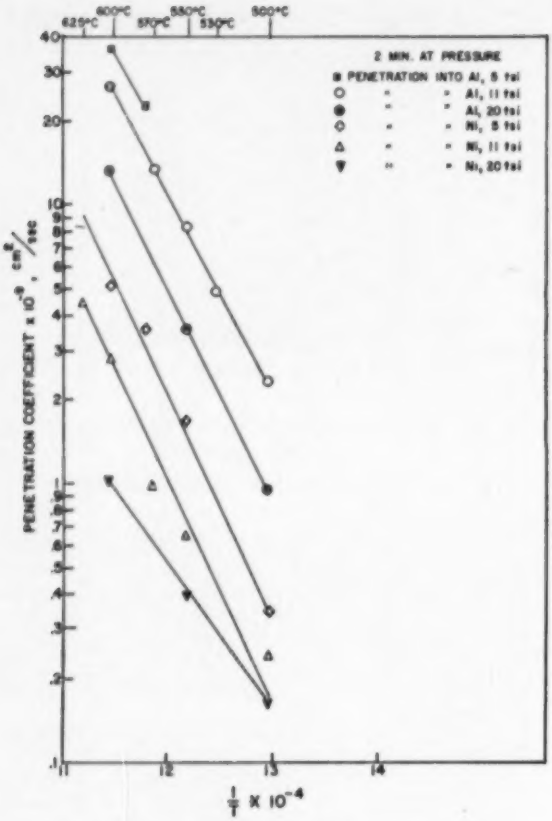

Fig. 7—Effect of temperature on Ni-Al penetration.

portion. At 600°C the tensile strength starts out at a moderately high level and then as the pressure increases to 23.5 tsi it increases slightly.

Effect of Time at Pressure: Fig. 6 is a plot of the maximum ultimate tensile strength vs time at 11 tsi pressure for a number of isotherms, namely, 500°, 550°, and 600°C. All curves exhibited the same tendency, that is they rise, reach a maximum, and then decline. It can be seen that maximum strengths are developed when the specimen is held at pressure for approximately 4 min. It can also be seen that once again maximum strengths occur at the 500°C isotherm.

Al-Ni Intermetallic Penetration: Effect of Pressing Temperature: Fig. 7 is a plot of the log of the penetration coefficients into aluminum and into nickel vs the reciprocal of the absolute pressing temperature. These specimens were reacted at various isobars, namely, 5, 11, and 20 tsi, all held at pressure for 2 min.

The upper three curves are for Al-Ni penetration into aluminum while the lower three are for Al-Ni penetration into nickel. (The top three curves are considered more accurate than the bottom three since the extents of penetrations were more readily measured.) Note that the curves are straight lines. This shows the penetration data of Al-Ni intermetallics conform to the equation $P = P_o e^{-Q/RT}$ and in turn shows the penetration effect is dependent upon the diffusion phenomenon.

In addition, it is seen that the curves are displaced from each other, indicating that the isobar used has a definite effect upon the penetration rate. Table I is a tabulation of the calculated activation energies and P_o values for the six curves presented.

The three top curves of Fig. 7 are approximately parallel and the activation energies calculated for the three curves are about the same. This fact indicates that the activation energy for the above penetration phenomenon is independent of pressure applied while penetration is occurring.

Fig. 8 is based on previously discussed tensile strength data and calculated penetration depths. Here the relationship between tensile strength and penetration is shown. Both curves are similar in general appearance in that they rise rapidly, decline, and then tend to level off. The greatest strength was attained when using 20 tsi although the decline in strength for this curve was much more rapid than for the 11 tsi isobar curve. In addition, the final strength of the level-off period, i.e., for greater penetrations, was lower for 20 than for 11 tsi.

Effect of Applied Pressure: Fig. 9 shows a plot indicating how the penetration coefficients of Al-Ni

Table I. Penetration Constants for Aluminum-Nickel Couples Hot-Pressed at Various Temperatures

	5 Tsi Penetration Into		11 Tsi Penetration Into		20 Tsi Penetration Into	
	Ni	Al	Ni	Al	Ni	Al
Activation energy, Q, cal/gram-atom	36,500	32,300	41,000	33,000	26,700	37,400
P_o, sq cm per sec	13.0	4.6	58.9	5.3	2.7	31.6

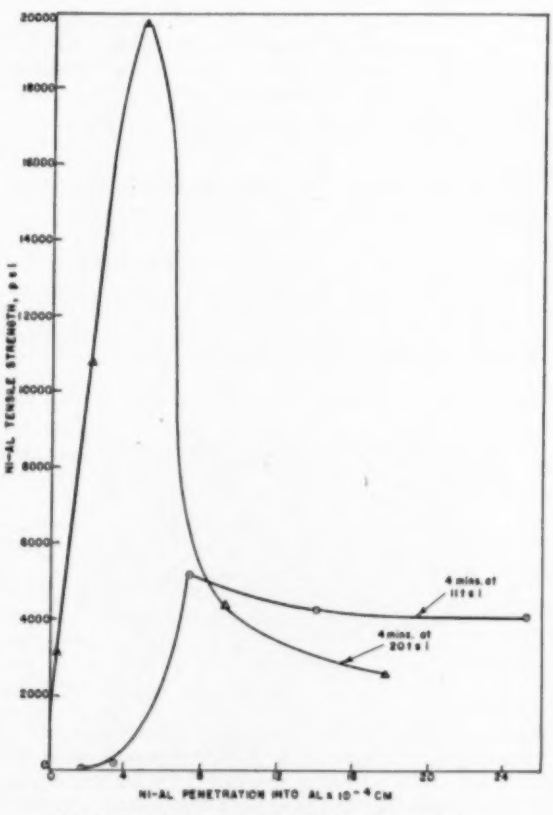

Fig. 8—Tensile strength vs penetration into aluminum.

intermetallics into aluminum are affected by pressure. This was done at various isotherms, namely, 500°, 550°, 575°, and 600°C. All the curves are observed to be straight lines with increasing slope as the temperature increases. It can be seen that the penetration rates decrease as the applied pressure is increased and that all the curves tend to approach a small range of pressures at "0" penetration rate.

Actual experiments conducted at 500°C at pressures close to and above that required for "0" penetration rate confirmed the finding. That is, no intermetallic formation was observed when sufficiently high pressure was used, as indicated in Fig. 10. Located on this figure are representative metallographic pictures of the bond interface. The dark zone disappears between 11 and 20 tsi pressures and the light colored zone continues to diminish and tends to become discontinuous even at higher pressures. Finally, at 34 tsi no trace of either alloy zone can be seen. Unfortunately, it was not possible to make tensile tests at all the investigated points because, as the pressure increased, exceptionally severe extrusion of the aluminum occurred in the already deformed die, and tensile bars were not readily hot-pressed. However, it should be pointed out that, with the disappearance of the dark zone, tensile strength rose over three times that obtained when both zones were present.

Metallographic Results: Fig. 11 shows the effect of temperature and pressure upon the extent of formation of intermetallic Ni-Al zone band widths. Fig. 11a and b represents the effect of temperature. Both specimens were pressed at 5 tsi for 2 min, one at 550°C, the other at 600°C. The zones for the 600°C specimen are much thicker than for the 550°C

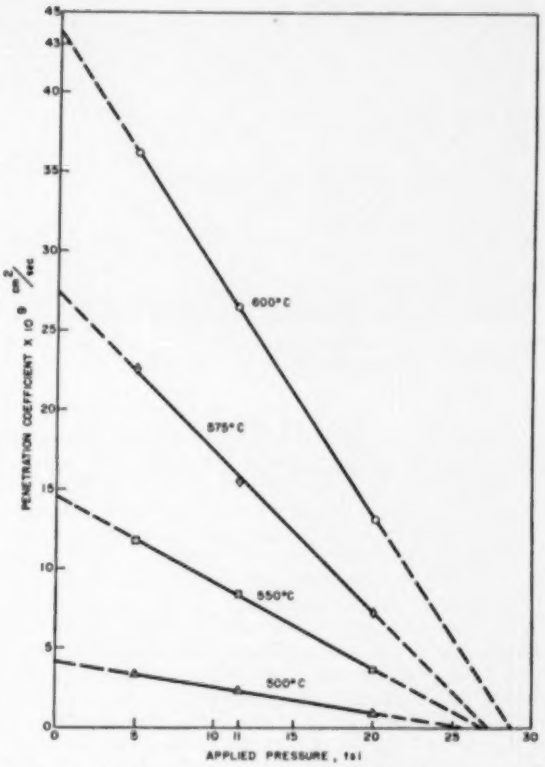

Fig. 9—Al-Ni into aluminum penetration coefficient vs applied pressure.

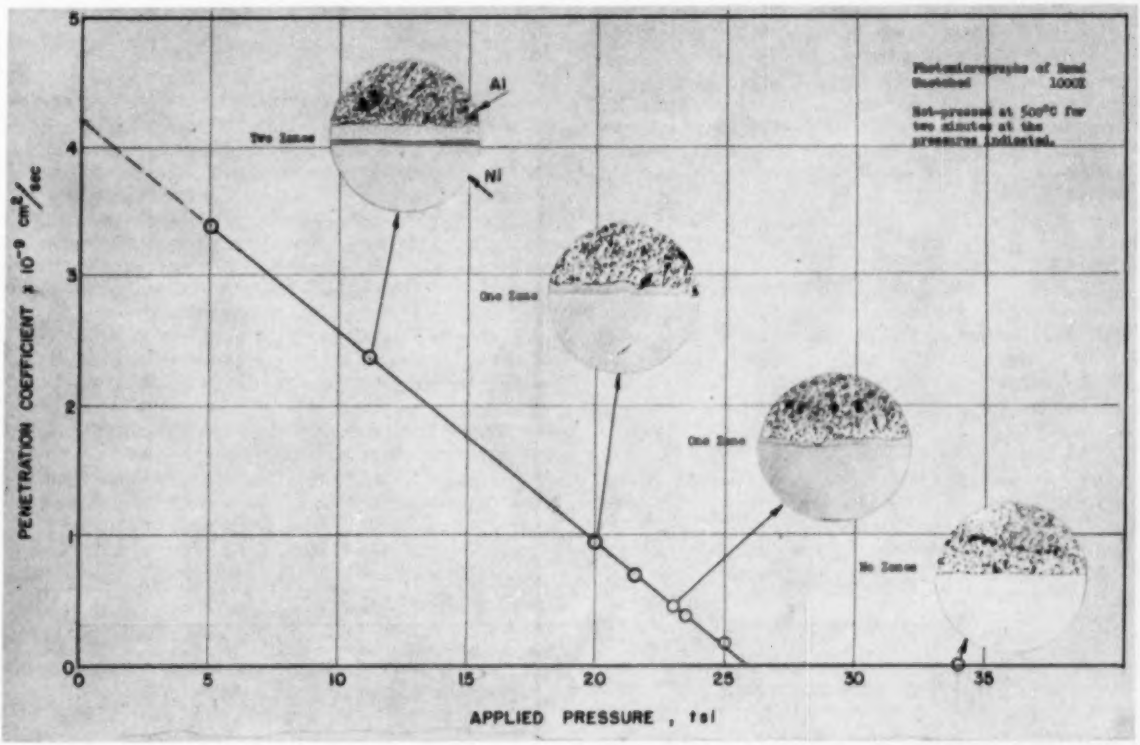

Fig. 10—Penetration coefficient into aluminum at 500°C vs applied pressure. Area reduced approximately 75 pct for reproduction.

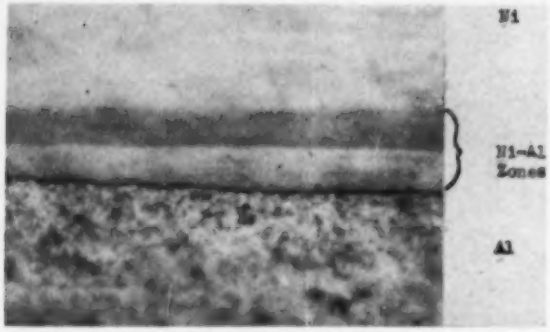

Fig. 11a—Unetched diffusion couple, 550°C, 5 tsi, 2 min. X1500. Area reduced approximately 25 pct for reproduction.

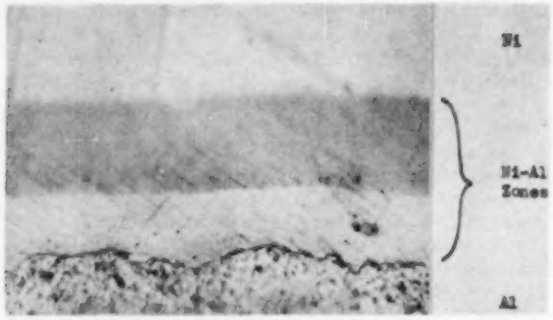

Fig. 11b—Unetched diffusion couple, 600°C, 5 tsi, 2 min. X1500. Area reduced approximately 25 pct for reproduction.

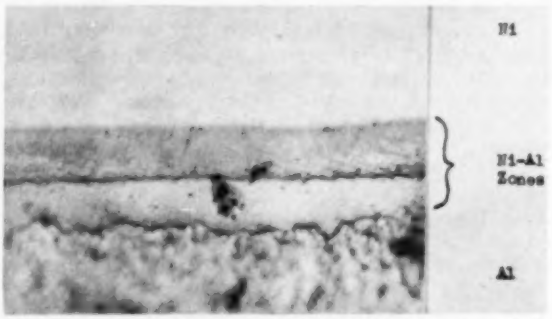

Fig. 11c—Unetched diffusion couple, 600°C, 20 tsi, 2 min. X1500. Area reduced approximately 25 pct for reproduction.

specimen. Fig. 11b and c shows the effect of pressure on zone thickness. Both specimens were pressed at 600°C for 2 min, Fig. 11b at 5 tsi and c at 20 tsi. The zones of the specimen pressed at 5 tsi are much thicker than those of the specimen pressed at 20 tsi.

In most cases the presence of two distinct intermetallic zones was seen, this for unetched specimen preparation. X-ray diffraction study suggests the dark zone, blue-gray, next to the nickel to be the γ phase, Ni_2Al_3. The other zone, next to the aluminum and light in color, has been tentatively identified by etching techniques as the β phase, Al_3Ni.

Practical Application of the Data Obtained: Fig. 12 is a practical application of the penetration information that was obtained. Here is a plot of the time for Ni-Al to penetrate through a given nickel thickness vs the pressing temperature at 11 tsi applied pressure. The lower curve is for nickel ¼ mil thick, while the upper curve is for nickel ½ mil thick. If a 4 min pressing time is taken, it can be observed that the curve for ¼ mil thick nickel is intersected at approximately 578°C. This means that a nickel film of this thickness would be just completely diffused through at approximately 578°C at a pressure of 11 tsi held for 4 min. A specimen was prepared and pressed under these conditions. Metallographic inspection showed that the nickel was just completely diffused through, which tends to confirm the data obtained. It can be seen that ½ mil nickel provides a much greater factor of safety as far as being penetrated by the Al-Ni intermetallics that form. In a like manner the time to penetrate a given aluminum thickness at various temperatures can be predicted.

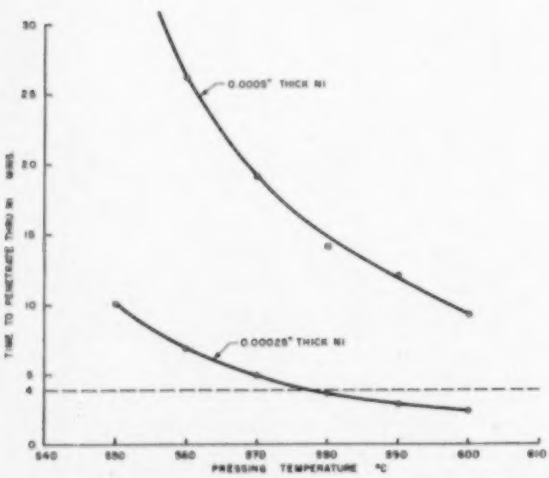

Fig. 12—Time for Ni-Al penetration through nickel vs pressing temperature.

Conclusion

It is possible, by use of the data obtained, to predict tensile strength and resultant penetrations for Al-Ni couples made by the solid state bonding technique used.

Perhaps the most important findings were those of the effect pressure had upon tensile strength and penetration rates. The fact that embrittling intermetallics can be prevented from forming by use of sufficiently high pressures is of paramount importance. It is now conceivable to reconsider the evaluation of the bonding of various metals which previously were rejected because of embrittling intermetallics.

This work has proved both of academic as well as of practical importance. Because of its potential meaning, a broad fundamenal program is being put into effect. This is being done in order to obtain a more basic theoretical understanding of the phenomenon discovered; i.e., the selective formation of alloys by proper pressure application during solid state bonding.

Acknowledgment

The work of A. Bartoszak and W. Marz in preparing all the hot-pressed specimens and of J. Nylin for his penetration measurements is hereby acknowledged. This work was done under AEC Contract AT-30-1 GEN-366.

Effect of Stress on the Creep Rates of Polycrystalline Aluminum Alloys Under Constant Structure

by O. D. Sherby, R. Frenkel, J. Nadeau, and John E. Dorn

A method is shown for the study of the creep rate dependence of metals on the applied stress under the condition of constant structure. The method was applied to pure aluminum and to dilute solid solution alloys of magnesium, copper, germanium, zinc, and silver in aluminum. A linear relationship was found to exist between the true stress and the logarithm of the creep rate.

ALTHOUGH extensive creep data are now available, the fundamentals of the creep phenomena are as yet only vaguely understood. Many attempts have been made to formulate theories for creep. But their agreement with fact has been disappointing. It appears that merely pyramiding more of the same type of data that is now available will not provide the essential aid toward formulating a better understanding of the complicated process of creep. Perhaps attempts to construct better models for the mechanism of creep might have to be tentatively abandoned until new types of definitive creep data are uncovered. The question therefore arises regarding what type of data might be needed to provide the essential knowledge for formulating better and more realistic theories of creep.

Perhaps one source of the failure to uncover an adequate theory arises from the fact that practically all theories for creep and nearly all analyses of experimental data on creep disregard the well-known fact that the structure of metals changes during creep. For example, it is customary in evaluating the effect of stress on the creep rate to correlate the secondary creep rate with the applied stress. But, as has been demonstrated recently,[1] the structures obtained during secondary creep tend to exhibit deformation banding at high stresses and polygonization at the lower stresses. Consequently the stress-secondary creep rate relationships found in this way are not fundamental, inasmuch as they reveal not only the effect of stress but also the effect of differences in structure on the secondary creep rates.

It is the purpose of the study reported here to isolate the effect of stress alone on the creep rate in an attempt to provide new data for possible formulation of a better theory of creep. In addition an attempt will also be made to ascertain how structure, temperature, and alloying might affect the stress-creep rate relationship.

The procedure that was adopted was simple: A specimen was precrept at a given engineering stress σ_e (initial engineering stress during creep under constant load, namely the load divided by the initial area of the specimen) and temperature T to a selected engineering strain, e (engineering strain, namely, the instantaneous gage length minus the initial gage length divided by the initial gage length), at which time the true stress was reduced to some lower value of the true stress, σ_1 (the true instantaneous stress, namely, the load divided by the instantaneous area). The instantaneous true creep rate, $\dot{\epsilon}_1$ (the true strain rate; with ϵ, the true strain, namely, the natural logarithm of the instantaneous over the initial gage length) following reduction of the true stress to σ_1 was then determined. Second, third, etc., tests were conducted under identical conditions except the stress was reduced to yet lower values, σ_2, σ_3, yielding yet lower instantaneous creep rates, $\dot{\epsilon}_2$ and $\dot{\epsilon}_3$. Inasmuch as the precreep conditions were identical in each series of tests, the instantaneous structures obtained immediately after reducing the stress were presumed to be identical.

O. D. SHERBY, Junior Member AIME, and R. FRENKEL are Research Engineers, Institute of Engineering Research, and J. E. DORN, Member AIME, is Professor of Physical Metallurgy, University of California, Berkeley, Calif., and J. NADEAU is Metallurgist, General Electric Co., Locomotive Laboratory, Erie, Pa.

Discussion on this paper, TP 3714E, may be sent, 2 copies, to AIME by April 1, 1954. Manuscript, Aug. 12, 1953. New York Meeting, February 1954.

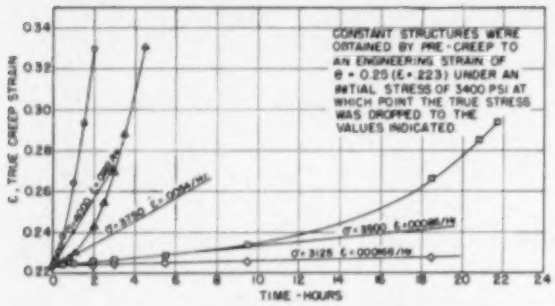
CONSTANT STRUCTURES WERE OBTAINED BY PRE-CREEP TO AN ENGINEERING STRAIN OF e = 0.25 (ε = .223) UNDER AN INITIAL STRESS OF 3400 PSI AT WHICH POINT THE TRUE STRESS WAS DROPPED TO THE VALUES INDICATED
ε, TRUE CREEP STRAIN
TIME - HOURS

Fig. 1—Typical creep curves for high purity aluminum showing creep rate dependence on the stress under constant structure conditions. $T = 422°K$.

This would not have been true, however, if the stresses were raised above the precreep stress because changes in structure would probably be introduced by the rapid additional straining occurring when the stress is raised.

Although the method is simple, certain factors need be considered in order to obtain accurate results: 1—It might be suspected that creep recovery immediately following the reduction in true stress might interfere with accurate evaluation of the instantaneous creep rate. But preliminary studies revealed that the coarse grained aluminum alloys investigated here did not exhibit any measurable creep recovery for the test conditions involved even upon complete removal of the stress. 2—If the stresses are reduced too much, long times will be required to get accurate creep rates. During such intervals of time the structure might differ from the instantaneous one generated during the precreep treatment. Consequently the range of stresses available for investigation are limited to those that give easily measurable instantaneous strain rates. 3—The major objection to the procedure arises from the fact that each point for the stress-creep rate relationship is obtained from a new specimen. Consequently sampling variations, which are known to be quite great for creep, are expected.

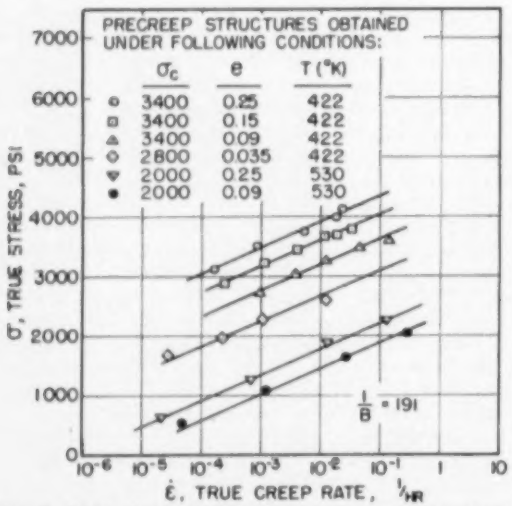

Fig. 2—Effect of true stress on the true creep rate at constant structure for high purity aluminum.

The solid solution aluminum alloys listed in Table I were used in the present investigation. Sheets of these alloys were homogenized, cold rolled from 0.100 to 0.070 in. in thickness and then recrystallized to about the same grain size. The creep specimens were selected with their tensile axes in the rolling direction. All creep tests were conducted under constant load conditions. The strain was measured to ±0.0001 and the initial creep stress was measured to ±20 psi.

Results

Effect of Structure on the Stress-Creep Rate Relationship for Aluminum: A typical example of one series of tests on high purity aluminum is shown in Fig. 1. Each specimen was precrept under constant load to an engineering strain of 25 pct at an initial stress of $\sigma_e = 3400$ psi. When an engineering strain of 25 pct was reached the load was reduced to give new reduced true stresses of 4000 psi, 3750 psi, etc., and the instantaneous true creep rates were measured as shown in the figure. Although difficulties were anticipated in determining the instantaneous creep rate immediately after reducing the stress, all of the creep curves exhibited rather good straight lines over the initial intervals of creep following reduction of the stress. Consequently fairly reliable initial creep rates could be obtained for the various reduced stresses. Only negligible transient effects were noted in these experiments.

Table I. Chemical Analyses and Grain Size of Alloys

Alloying Element	Atomic Pct	Grain Size Diameter, Mm	Chemical Analyses, Wt Pct Impurities Si	Fe	Cu	Mg	Mn
Al (99.987%)		0.21	0.003	0.003	0.006	0.001	
Mg	0.554	0.25	0.003	0.003	0.007		
	1.097	0.28	0.004	0.004	0.007		
	1.617	0.26	0.003	0.004	0.006		
Cu	0.101	0.29	0.003	0.003		0.0006	0.001
	0.232	0.30	0.003	0.004		0.0006	0.001
Zn	0.755	0.26	0.004	0.005	0.006	0.001	
	1.616	0.26	0.003	0.005	0.007	0.001	
Ge	0.082	0.27	0.003	0.005	0.007	0.001	
	0.145	0.26	0.003	0.006	0.007	0.001	
Ag	0.100	0.29	0.003	0.005	0.007	0.001	
	0.194	0.29	0.003	0.006	0.007	0.001	

The dependence of the true instantaneous creep rate on the true instantaneous stress for the structure developed for a strain e of 25 pct at 422°K under a stress of $\sigma_e = 3400$ psi is shown by the uppermost curve of Fig. 2. These data suggest that for this structure

$$\dot{\epsilon} = K' e^{B\sigma} \qquad [1]$$

where K' is a constant and $1/B$ is the slope of the uppermost curve in Fig. 2. But since the creep rate must vanish when the stress is zero, it is possible that the stress-creep rate relationship is given by

$$\dot{\epsilon} = \frac{K\,(e^{B\sigma} - e^{-B\sigma})}{2} = K \sinh B\sigma \qquad [2]$$

since $e^{-B\sigma}$ is known to be negligible for the relatively high stresses to which this study had to be limited.

The question now arises as to what effect the structural changes that attend creep straining might exert on the parameters K and B. The rapidly decelerating creep rate over the primary stage of creep suggests that those features of the structure that are

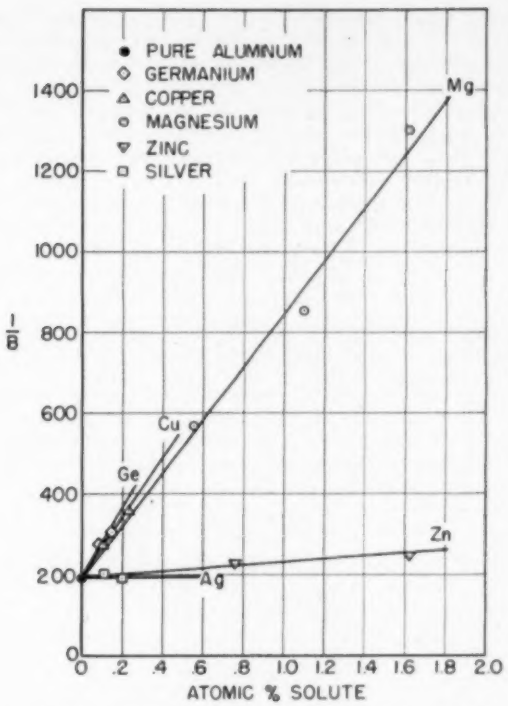

Fig. 3—Effect of alloying elements on the parameter $1/B$ for creep.

most pertinent to creep resistance are changing most rapidly in this range. This viewpoint has been confirmed by X-ray and metallographic investigations on the structures of metals following creep.[1, 2] Consequently if structure influences the parameters K and B this effect should be found over the primary range of creep. Therefore additional series of tests were made at precreep strains of $e = 0.09$ and 0.15 for the same conditions of temperature (422°K) and initial stress ($\sigma_o = 3400$ psi) as used previously for the tests precrept to $e = 0.25$. Whereas $e = 0.25$ refers to the beginning of tertiary creep, $e = 0.15$ refers to the beginning of secondary creep and $e = 0.09$ to about the middle of the primary stage of creep. As shown by the three upper curves of Fig. 2, the slope of the stress vs logarithm of the strain rate relationship is independent of the precreep strain and therefore of the structure developed during creep of annealed aluminum. On the other hand, K is found to be structure-sensitive, decreasing with increasing precreep strains analogous to the decrease in creep rate with strains for constant true stress-constant temperature creep tests.

In an effort to ascertain whether the precreep stress influences B, the stress-creep rate curve was obtained following prestrain of $e = 0.035$ at 2800 psi and 422°K as shown by the fourth curve of Fig. 2. The first four curves illustrate that B of Eq. 2 is practically constant, independent of the various structures that are developed over ranges of precreep conditions.

The factor B, which has been shown to be independent of structure, might depend on the creep temperature. In order to test this point two series of tests were conducted at 530°K at precreep stresses of $\sigma_o = 2000$ psi. As shown by the two lowest curves of Fig. 2, B also appears to be independent of the test temperature.

Effect of Alloying: The effect of alloying on B was evaluated by the procedures previously described for pure aluminum for the various alloys identified in Table I. The data of Fig. 3 reveal that $1/B$ increases almost linearly with the atomic percentage of the solute element. Furthermore those elements that were previously shown to have the greatest effect on solid solution strengthening at low temperatures[3] also appear to exhibit the greatest effect on inhibiting creep insofar as they exhibit the greatest value of $1/B$. The correlation between the tensile deformation strength at 5 pct strain at 194°K and $1/B$ for creep is shown in Fig. 4. Perhaps this correlation arises from the fact that $1/B$ as well as low temperature solid solution strengthening are both dependent on the strain-energy interactions and electronic interactions between solute atoms and dislocations.

Discussion

Most current theories for creep are predicated on the hypothesis that creep arises primarily from thermal activation of dislocations over a free energy barrier under the simultaneous action of an applied stress.[4-6] A typical example of the formal development of such models for creep suggests that the creep rate $\dot{\epsilon}$ is given by

$$\dot{\epsilon} = \frac{1}{2}\frac{N}{\lambda^2}\frac{kT}{h}e^{\Delta S/R}e^{-\Delta H/RT}\sinh\frac{A\lambda\sigma}{2kT} \qquad [3]$$

where λ is the displacement of a dislocation per activation (assumed to be the lattice spacing in the direction of slip); N is the number of active edge dislocations per sq cm; k is Boltzmann's constant; h is Planck's constant; T is the absolute temperature; ΔS is the entropy of activation; ΔH is the enthalpy of activation; A is the projected area of a dislocation on the slip plane; and σ is the applied stress.

Other theories for creep[7, 8] are based on the hypothesis that creep occurs when the localized stress over some arbitrary volume V exceeds an assumed yield strength σ_o. At high temperatures thermal fluctuations contribute to the local stress. The strain

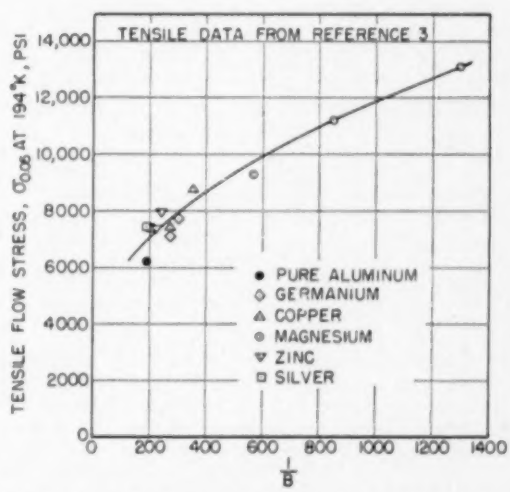

Fig. 4—Correlation between $1/B$ for the various solid solution alloys and the flow strength at 194°K.

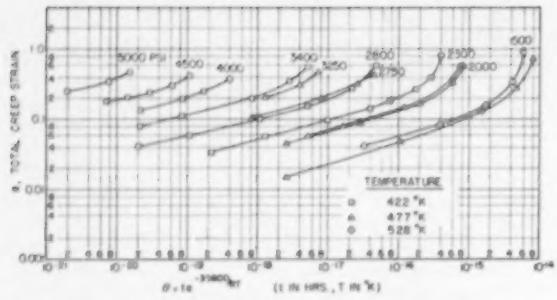

Fig. 5—Constant load creep tests for high purity aluminum.[1]

energy that must be supplied by thermal fluctuations when the applied stress is σ is then

$$\frac{(\sigma_a - \sigma)^2 V}{2G}$$

where G is the shear modulus of elasticity. Consequently the creep rate is thought to be given by

$$\dot{\epsilon} = \text{constant } e^{\frac{-(\sigma_a - \sigma)^2 V}{2GkT}}. \qquad [4]$$

Both of these popular theories for creep demand that the stress enter the creep rate relationship as stress (or some function of the stress) divided by the absolute temperature. The question arises as to whether these theoretical deductions agree with the facts.

Recent investigations[1] have shown that the structure developed during high temperature creep under a given stress σ_c depends only on the temperature-compensated time $\theta = te^{-\Delta H/RT}$ where t is the actual time, ΔH is the activation energy for creep, R is the gas constant, and T is the absolute temperature. Because the X-ray, metallographic, and mechanical testing techniques used to verify this conclusion have already been reported[1] they will not be repeated here. Since the structure depends on the temperature-compensated time it is not unanticipated that the creep strain was also found to be related to θ in accordance with the equation

$$\epsilon = f(\theta, \sigma_c) \qquad [5]$$

as shown by the typical example given in Fig. 5.

Extensive original research as well as reanalyses of data in the literature have verified the general validity of Eq. 5 for high temperature creep of non-precipitation hardening alloy systems.[9] The activation energies obtained by these analyses were found to be a fundamental property of the metal, being independent of the stress, temperature, grain size, structural changes occurring during creep, cold work or minor variations in composition. In fact the values of ΔH obtained from extant creep data for pure metals were found to equal the activation energies for self-diffusion.

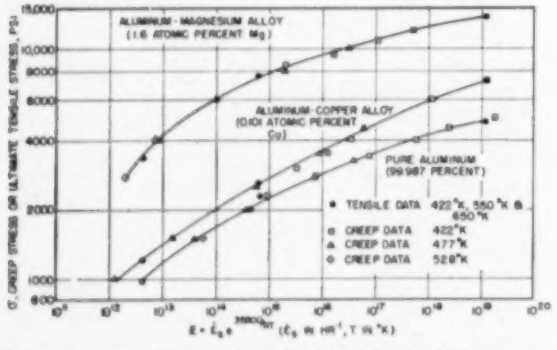

Fig. 6—Correlation between the initial creep stress and the parameter $\dot{\epsilon}_s e^{\Delta H/RT}$.[1]

Upon differentiating Eq. 5 with respect to time the creep rate is given by

$$\dot{\epsilon} = \frac{\partial f}{\partial \theta}\frac{d\theta}{dt} = F(\theta, \sigma_c)\, e^{-\Delta H/RT}. \qquad [6]$$

A preliminary check on the validity of Eq. 6 was obtained by its evaluation at the secondary stage of creep, where

$$\dot{\epsilon}_s = F(\theta_s, \sigma_c)\, e^{-\Delta H/RT}. \qquad [7]$$

But according to Eq. 5, or as shown by the data of Fig. 5, the value of θ_s is only a function of the creep stress σ_c. Consequently

$$Z = \dot{\epsilon}_s e^{\Delta H/RT} = \mathcal{F}(\sigma_c) \qquad [8]$$

where Z is the well-known Zener-Hollomon parameter.[10] The validity of this relationship is confirmed by the typical example shown in Fig. 6. This relationship has also been extensively verified.[9]

The evidence contradicting the validity of the two popular theories for creep as expressed by Eqs. 3 and 4 is therefore quite emphatic. The ϵ-θ relation and the Z parameter (as revealed by the evidence supporting the validity of Eqs. 5 and 8) are *not* functions of stress divided by temperature. Furthermore, as shown by the data reported here, B of Eq. 2 is independent of the temperature. The experimentally verifiable expression for the creep rate can now be obtained by combining Eqs. 2 and 6 to give

$$\dot{\epsilon} = Se^{-\Delta H/RT} \sinh B\sigma \qquad [9]$$

where ΔH and B are constants that depend on the metal. All effects of structural changes during creep are contained in the S parameter. And in view of the validity of Eq. 5, S depends on θ and σ_c. Therefore Eq. 9 is not a mechanical equation of state. Each new history of creep results in its unique value of S.

Early in the history of creep Andrade[11] revealed that the creep curve could be considered as the superposition of two curves. This fact suggested the possible existence of two mechanisms of creep, namely quasi-viscous and transient creep. Recent investigations by McLean on polycrystalline aggregates[12] have shown that grain boundary shearing and motion of dislocations account for all of the macroscopically measured creep. Consequently single crystals appear to creep by slip alone. Since single crystals also exhibit the so-called transient and quasi-viscous creep,[13, 14] the postulate that two mechanisms for creep exist will have to be abandoned. Apparently the changes in structure that attend creep are responsible for the decreasing creep rate over the primary stage of creep.

McLean's observations that the total creep strain of polycrystalline aggregates results from the sum of the contributions of dislocation motion and grain boundary shearing suggest that the creep rate equation should contain two additive terms. But for the coarse grained aluminum and the range of stresses that was investigated here, grain boundary shearing contributes only a few percent to the total creep strain.[13] Therefore the single term relationship given by Eq. 9 can yet be valid for the creep of polycrys-

talline aggregates over appropriate ranges of grain size and stress. Furthermore the activation energy for grain boundary relaxation of aluminum is equal to that for creep and self-diffusion.[9, 16] And recent studies[16] have also shown that the extent of grain boundary shearing in polycrystalline aggregates is a function of the same θ parameter as obtained for the total creep strain. This coincidence of the activation energies for slip and grain boundary shearing permits the use of single functional terms in Eqs. 5 and 6 for the total creep strain and the total creep rate of polycrystalline aggregates.

A satisfactorily detailed theory of creep cannot yet be formulated until more complete evidence is available on the kinds of structures that might influence the creep rate and their quantitative effect on the parameter S. Nevertheless the fundamentals for formulating the major structural units of a satisfactory model of creep are now believed to be known. The popular models for creep based on thermal activation of dislocations over free energy barriers might have to be discarded for creep at elevated temperatures because they predict that the creep rate is a function of stress divided by temperature, whereas the facts suggest that the creep rate is proportional to the hyperbolic sine of a constant times the stress. Obviously the free energy of activation for the rate-controlling process for creep is independent of the stress. Since the ΔH for creep is equal to the activation energy for self-diffusion, the rate-controlling mechanism for creep is probably a self-diffusion process.

One possible process for creep[17] is as follows: Under the action of an applied stress a dislocation moves up to a barrier which it cannot surmount. This barrier might arise from a number of structural factors such as grain boundaries, or dislocations trapped in block boundaries, etc. Both the barrier and the stopped dislocation might be modified by the diffusion of holes resulting in a decrease of their mutual interactions. As this process continues the strength of the barrier decreases to the value of the applied stress and thereupon releases the dislocation which then migrates to the next barrier. The distance of migration depends on the concentration of barriers which in turn increases with creep straining. Consequently the S-term of Eq. 9 is structure sensitive. Analysis reveals[17] that the B-term of Eq. 9 arises from the distribution of the fraction of the barriers having strengths σ^* to $\sigma^* + d\sigma^*$. In order that B be independent of structure the reasonable assumption must be made that the distribution of the barrier strengths is independent of creep straining and depends only on the type of alloy under consideration. This theory also satisfies the requirement that the activation energy for creep equals that for self-diffusion.

Conclusions

1—A method was developed for determining the effect of stress on the creep rate of metals at constant structures.

2—The equation for the creep rate was found to be

$$\dot{\epsilon} = Se^{-\Delta H/RT} \sinh B\sigma$$

where ΔH and B are independent of the creep structure and S is a parameter that depends on structure.

3—The value of $1/B$ increases almost linearly with the atomic percentage of solute atoms. Furthermore $1/B$ is a function of low temperature solid solution strengthening.

Acknowledgments

This investigation was sponsored by the Office of Naval Research. The authors wish to thank the O.N.R. staff for their continued interest and full cooperation throughout this and related studies on the plastic properties of metals. They wish especially to thank Mr. J. Harwood for his encouragement in all these research investigations. The materials used were supplied by the Aluminum Research Laboratories, Aluminum Company of America, together with their chemical analyses. In addition, the authors wish to thank A. Huie for his assistance in the creep testing program and to Mrs. G. Pelatowski sincere appreciation is extended for her preparation of the figures to this report.

References

[1] Oleg D. Sherby and John E. Dorn: Some Observations on Correlations Between the Creep Behavior and the Resulting Structures in Alpha Solid Solutions. *Trans.* AIME (1953) **197**, pp. 324-330; JOURNAL OF METALS (February 1953).

[2] W. A. Wood and R. F. Scrutton: Mechanism of Primary Creep in Metals. *Journal* Inst. Metals (1950) **77**, pp. 423-434.

[3] J. E. Dorn, P. Pietrokowsky, and T. E. Tietz: The Effect of Alloying Elements on the Plastic Properties of Aluminum Alloys. *Trans.* AIME (1950) **188**, pp. 933-943; JOURNAL OF METALS (July 1950).

[4] W. Kauzman: Flow of Solid Metals from the Standpoint of the Chemical-Rate Theory. *Trans.* AIME (1941) **143**, pp. 57-83.

[5] F. Seitz and T. A. Read: Theory of the Plastic Properties of Solids IV. *Journal of Applied Physics* (1941) **12**, p. 538.

[6] A. S. Nowick and E. S. Machlin: Dislocation Theory as Applied by N.A.C.A. to the Creep of Metals. *Journal of Applied Physics* (1947) **18**, pp. 79-87.

[7] R. Becker: Uber Plastizitat, Verfestigung und Rekrystallization. *Ztsch. Tech. Physik* (1926) **7**, p. 547.

[8] E. Orowan: Crystal Plasticity I, II, III. *Ztsch. Physik* (1934) **89**, pp. 605, 614, 634.

[9] Oleg D. Sherby, Raymond L. Orr, and John E. Dorn: Creep Correlations of Metals at Elevated Temperatures. *Trans.* AIME (1954) **200**, pp. 71-80; JOURNAL OF METALS (January 1954).

[10] C. Zener and J. H. Hollomon: Plastic Flow and Rupture of Metals. *Trans.* ASM (1944) **33**, pp. 163-235.

[11] E. N. Da C. Andrade: On the Viscous Flow in Metals, and Allied Phenomena. *Proc.* Royal Soc. (1910) **A84**, pp. 1-12.

[12] D. McLean: Creep Processes in Coarse-Grained Aluminum. *Journal* Inst. Metals (Sept. 1951-Aug. 1952) **80**, pp. 507-519.

[13] D. Hanson and M. A. Wheeler: The Deformation of Metals under Prolonged Loading, Part I, The Flow and Fracture of Aluminum. *Journal* Inst. Metals (1931) **45**, pp. 229-264.

[14] R. F. Miller and W. E. Milligan: Influence of Temperature on Elastic Limit of Single Crystals of Aluminum, Silver and Zinc. *Trans.* AIME (1937) **124**, pp. 229-251.

[15] C. Dean Starr, E. C. Vicars, A. Goldberg, and J. E. Dorn: Effect of Alloying Elements on Grain Boundary Relaxation in Alpha Solid Solutions of Aluminum. *Trans.* ASM (1953) **45**, pp. 275-285.

[16] B. Fazan, O. D. Sherby, and J. E. Dorn: Some Observations on Grain Boundary Shearing During Creep. Inst. of Engineering Research Report, Univ. of California, Berkeley, Series No. 22, Issue No. 32, November 15, 1953.

[17] J. E. Dorn and O. D. Sherby: A Model for the High Temperature Creep Process. Inst. of Engineering Research Report, Univ. of California, Berkeley, Series No. 22, Issue No. 30, August 15, 1953.

Plasticity of Molybdenum Single Crystals At High Temperatures

by R. Maddin and N. K. Chen

Single crystals of molybdenum were extended at temperatures from 1300° to 2500°C. It was found that with increasing temperatures, the yield becomes more pronounced and the number of slip bands for equal amounts of elongation decreases. Slip at high temperatures fragments the structure.

OTHER than the investigations on sodium and potassium by Andrade and Tsien,[1] the researches of Steijn and Brick[2] on α iron single crystals at low temperatures are about the only studies of the influence of temperature on glide of body-centered cubic single crystals. The effect of test temperature on glide has been rather widely investigated with hexagonal crystals[3] and less widely with face-centered cubic crystals.[4] As a result of these studies it can be said that, in general, the onset of plastic flow as measured by the initial rate of strain hardening becomes more abrupt with increasing temperature, and the value of the yield decreases with increasing temperature. Strain hardening, however, is markedly affected by changes in temperature except at very low and very high temperatures where the strain hardening rate becames constant.

In the present investigation it is shown that temperature affects the glide of molybdenum single crystals in much the same manner as crystals of other classes, i.e., for comparable strains the number of slip bands decreases with increasing temperature; shear along the slip bands increases with increasing temperature; the yield becomes more pronounced with increasing temperature of test; and the strain hardening approaches a constant at very high temperatures. In addition, it is shown that, in agreement with the work of Tsien and Chow,[5] slip occurs on {110} planes in <111> directions. It is further shown that slip at high temperatures fragments the structure into either irregular sized cells or bent atomic planes which are roughly aligned in crystallographic directions.

R. MADDIN, Member AIME, is Associate Professor of Metallurgy, and N. K. CHEN, Junior Member AIME, is Assistant Professor of Metallurgy, The Johns Hopkins University, Baltimore.

Discussion on this paper, TP 3718E, may be sent, 2 copies, to AIME by April 1, 1954. Manuscript, Sept. 28, 1953. New York Meeting, February 1954.

Experimental Procedure

Single crystals 3 mm in diameter by about 25 mm long were prepared using the technique previously described.[6]

The furnace in which the crystals were grown served as the extension apparatus for the tension tests. It consisted of a 4 in. water-cooled brass tube 20 in. long which was continuously evacuated at the bottom. Two water-cooled copper electrodes held the specimen by means of spherical collets secured in place in the electrodes by set screws. These electrodes served also to transmit power and stress to the specimen. The lower electrode was clamped to a stand, while the upper electrode was fastened to one side of a lever arm flexibly supported at the top through a slightly offset pinion. A metal bellows operating elastically was attached to the upper electrode to affect a vacuum seal and allow freedom of motion. The level of the arm was adjusted by rotating a graduated nut. Rotation of the electrode was prevented by a key fitted into a groove. After the specimen was mounted and the vacuum secured, the lever arm was adjusted so that the bellows was at its relaxed position. This insured that the total weight of the specimen, the upper electrode, and the downpull of the vacuum were balanced by the horizontal beam. Since the specimen was heated by its own resistance, expansion of the specimen proceeded freely by this arrangement. During the time of heating the specimen, the beam was maintained in a horizontal position by turning the nut at the top. By graduating the lever arm and using a known dead weight on the lever arm to supply a tensile stress, the graduated nut could be read to 0.0001 in. extension. Since

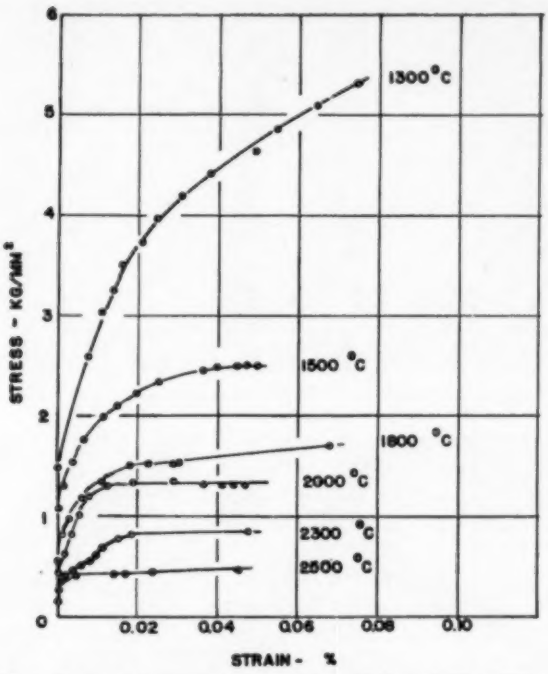

Fig. 1—Stress-strain curves for crystals extended at 1300°, 1500°, 1800°, 2000°, 2300°, and 2500°C.

the assembly acted in conjunction with an extension bellows, the absolute stress and strain were not known with certainty. However, the comparison of the stress-strain measurements for extension of crystals at different temperatures could be taken as real since the error introduced through the flexible bellows could be taken as constant for all crystals investigated.

The average integrated temperature of the specimen was measured from the change in its resistance with temperature based on a previous correlation.[6,9] At the desired average temperature, the current through and the voltage across the specimen were held constant during the extension. It should be emphasized that the "average" temperature referred to herein may vary as much as ±200°C.

Before load was applied, the current through and the voltage across the specimen were observed. Load was applied only after a constant resistance was obtained. All tests were conducted for values of elongation of 10 pct or less to avoid necking which would produce hot spots in the crystals. Since close tolerance was maintained between the upper electrode and its housing, a certain amount of axiality was assured. Tests in the elastic region at 1500°C gave reproducible curves.

The orientation of the crystals used were determined by the back-reflection Laue method and referred to a reference scratch at one of the ends of the specimen. The reference scratch was also used for later metallographic and X-ray examinations.

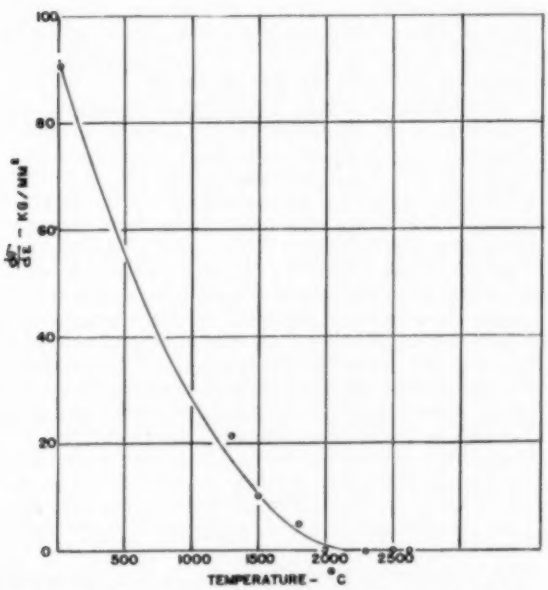

Fig. 2—Plot of the slope of the stress-strain curves $d\sigma/d\epsilon$ vs temperature.

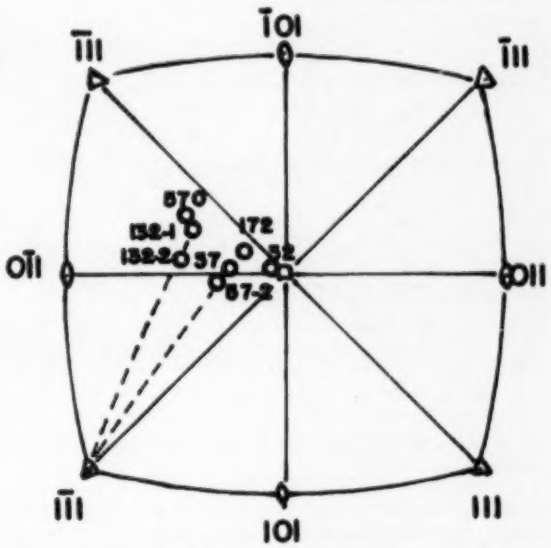

Fig. 3—Stereographic projection showing the initial and, in some cases, the final orientation of the crystals extended.

Results

Stress-Strain: The results of tensile tests at the integrated average temperatures 1300°, 1500°, 1800°, 2000°, 2300°, and 2500°C are shown in Table I and Fig. 1. The curves of Fig. 1 are plotted as unresolved stress vs strain. The orientation difference factor of all the crystals investigated is quite small if resolution of the stresses is made on the $(\bar{1}01)$ $[1\bar{1}1]$ system. (The ratio of the maximum to the minimum resolution factor is only 1.08, Fig. 3.) It can be seen (Fig. 1) that the yield becomes more pronounced with in-

Table I. Results of Tensile Tests

Specimen No.	Approximate Temperature, °C	Stress at Yield, Kg per Mm²	$\frac{d\sigma}{d\epsilon}$ (5-7%)
MR-6	20°	~5	91.2
Mo-57	1300	1.48	23
Mo-52	1500	1.08	10
Mo-570	1800	0.54	5
Mo-132	2000	0.44	0
Mo-172	2300	0.36	0
Mo-159	2500	0.22	0

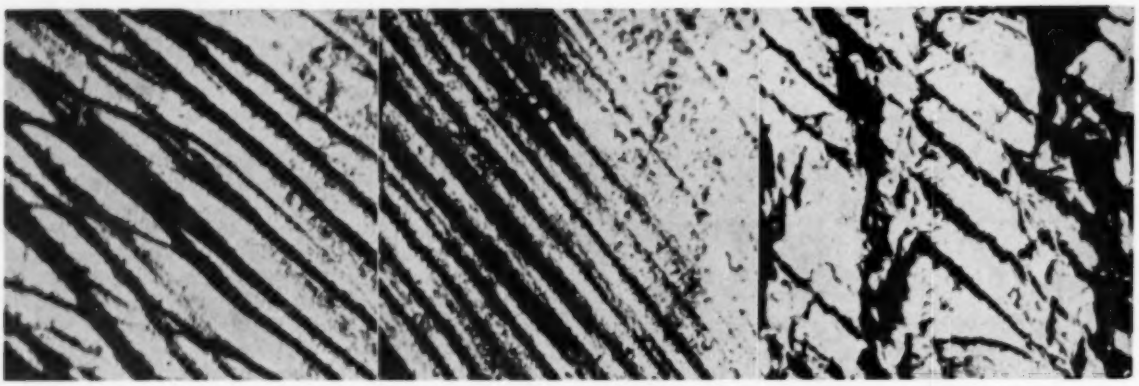

a—1800°C, at a position parallel to the reference mark.

b—1800°C, rotated 70° clockwise from position shown in a.

c—2000°C, at a position 45° from the reference mark.

d—2000°C, rotated 90° clockwise from position shown in c.

e—2300°C, at a position 22° from the reference mark.

f—2300°C, rotated 168° from position shown in e.

Fig. 4—Appearance of slip bands at 1800°, 2000°, and 2300°C. Stress axis is horizontal. X200. Area reduced approximately 50 pct for reproduction.

creasing temperature. The magnitude of the yield shows a 22 fold decrease with a temperature change of approximately 2500°C. These results can be compared with data for other metal single crystals shown in Table II. The ratio of the flow stress at various

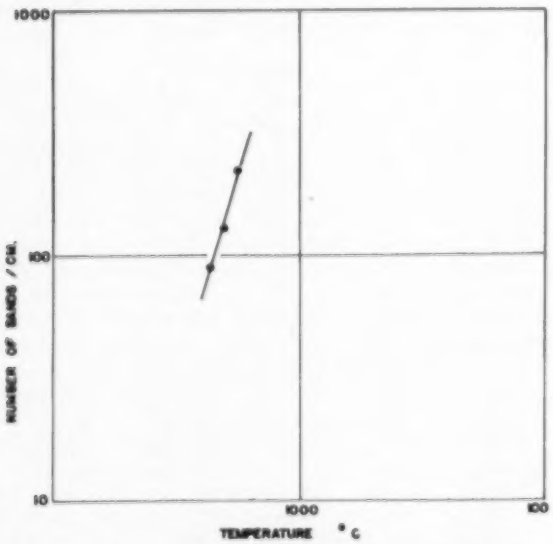

Fig. 5—Plot of log of the number of slip bands per centimeter vs the log of the temperature.

temperatures seems to approach a constant value for equal temperature increments. The data in Table II relate, for the most part, to the resolved shear stress values. For aluminum there may be an orientation factor which is not known; for molybdenum, the orientation resolution factor is, again, quite small and the *ratio* of the flow stresses would eliminate the need for the resolution.

The stress necessary to continue glide is markedly affected by temperature. In column 4, Table I, the slope of the stress-strain curves at 4 pct elongation is listed for the various tensile tests. The hardening coefficient (the slope of the stress-strain curve at 5 to 7 pct elongation) goes from zero near the melting point to about 91.2 kg per sq mm at 20°C. This is in agreement with results on other metal crystals. For example, the hardening coefficient for magnesium changes 400 fold within a temperature range of 485°C.[7] In the case of hexagonal metal crystals and one face-centered cubic metal (aluminum), the dependence of strain hardening on temperature is most marked at intermediate temperatures; the strain hardening coefficient becomes approximately constant near absolute zero and the melting point.[8, 9] In the present case of molybdenum, this also appears to be true, at least at high temperatures, as may be seen in Fig. 2 for temperatures from 20°° to 2500°C.

Slip Elements: The initial and, in some cases, the final orientation for the specimens investigated are shown in Fig. 3. Since the slip elements (the slip

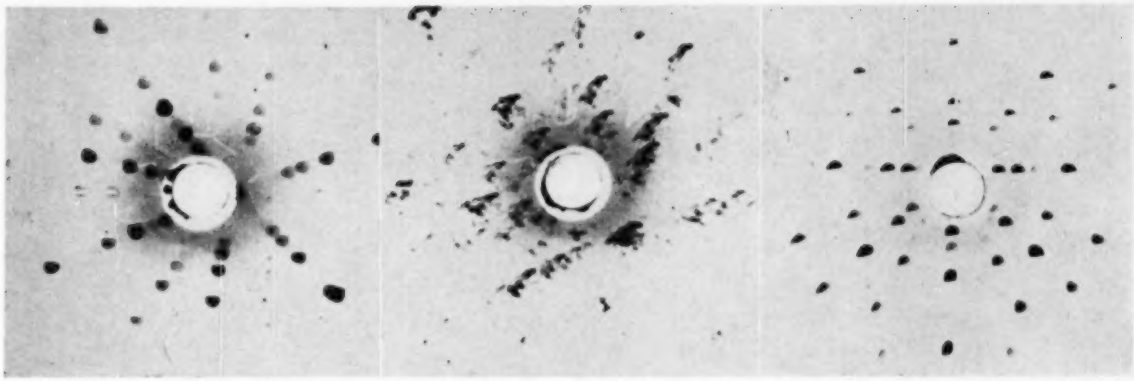

a—Before deformation at 1300°C. b—After deformation at 1300°C. c—Before deformation at 1500°C.

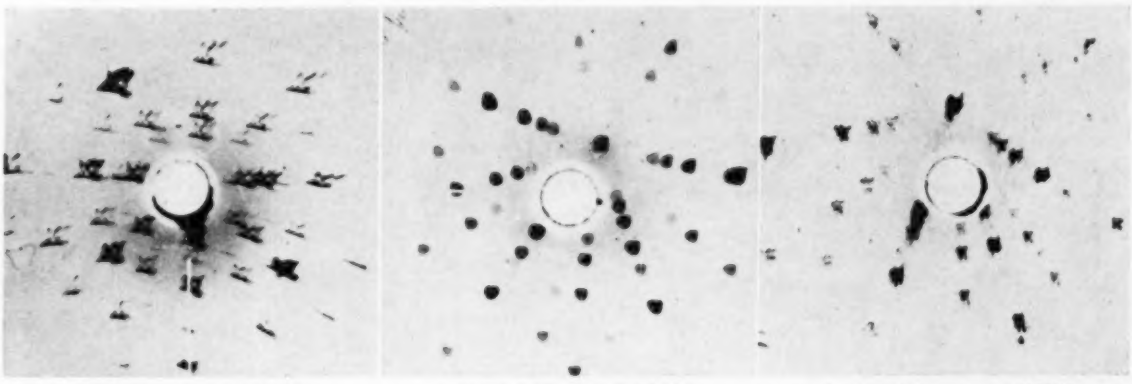

d—After deformation at 1500°C. e—Before deformation at 2000°C. f—After deformation at 2000°C.

Fig. 6—X-ray photograms before and after deformation.

plane and direction) for molybdenum at high temperatures were determined by Tsien and Chow[5] for seven crystals at 1000°C to be $(\bar{1}01)$ $[1\bar{1}1]$, further emphasis on determination of elements was considered unnecessary. However, the slip direction was checked in two cases (Mo-57 and Mo-132, Fig. 3) to be $[1\bar{1}1]$ and the slip plane was checked in two cases (Mo-172 and Mo-159) to be $(\bar{1}01)$.

With increasing temperature, the number of slip bands decreases and the shear along glide planes increases. This is illustrated in Fig. 4 which shows the appearance of slip bands at different positions around the specimens for tensile tests at 1800°, 2000°, and 2300°C for elongations of 7, 5, and 5 pct respectively. Although there still is present the forking of bands characteristic of the slip bands on body-centered cubic metals at room temperature, the bands are, in general, quite straight. A plot of the log of the number of slip bands per centimeter vs the log of temperature is shown in Fig. 5. Since the orientation resolution factor for all specimens is similar, no attempt has been made to calculate shear. Nevertheless, there may be a "shear" factor which might affect the results shown in Fig. 5. If this curve is assumed to continue along the same line, there should be about 100,000 bands per centimeter (or 0.01 micron apart) at room temperature for a crystal extended a comparable amount, i.e., 5 to 7 pct. It has been shown previously[6] that slip markings at room temperature appear as striae which cannot be resolved with the light microscope. Consequently, the spacing between slip bands at room temperature cannot be measured in order to check the value of 100,000 bands per centimeter at 5 pct elongation.

X-Ray: The X-ray reflections before and after deformation are shown in Fig. 6 for crystals extended at 1300°, 1500°, and 2000°C. It is apparent that the deformation at elevated temperatures fragments the structure. This becomes more apparent from the Laue photograms in Fig. 7 which were taken at different positions around the specimen axis of Mo-57 extended at 1300°C. Careful examin-

Table II.[3] Relation of Yield Stress with Temperature for Different Metals

Metal	Temperature, °C	Yield, Gram per Mm²	ΔT°C	Ymax./Ymin.
Cd	−250	75*	580	3.8
	330	20*		
Zn	−250	140*	530	4
	280	60*		
Mg	−230	175*	530	2.5
	300	76*		
Bi	0	230*	250	2.3
	250	100*		
Al	−185	1800	785	9
	600	200		
Mo	20RT	~5000*	2500	22
	2500	220		

* Resolved shear stress values.

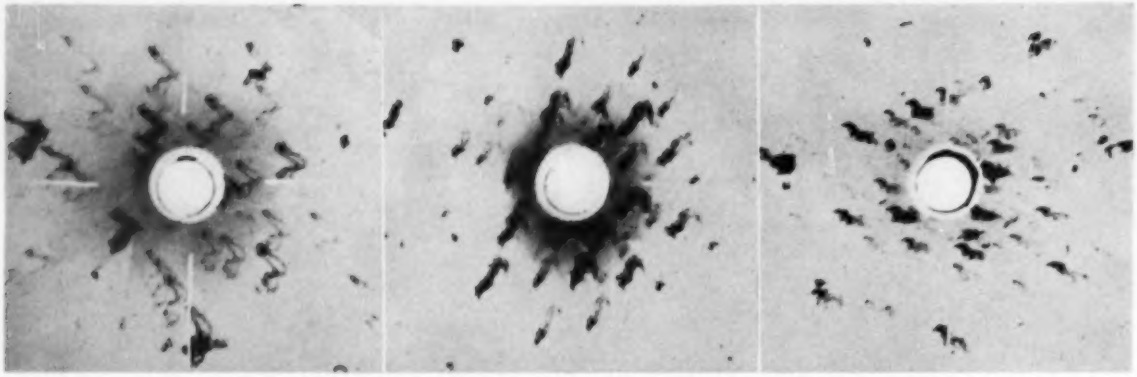

a—At a position 30° from reference mark. b—Rotated 60° clockwise from reference mark. c—Rotated 90° clockwise from reference mark.

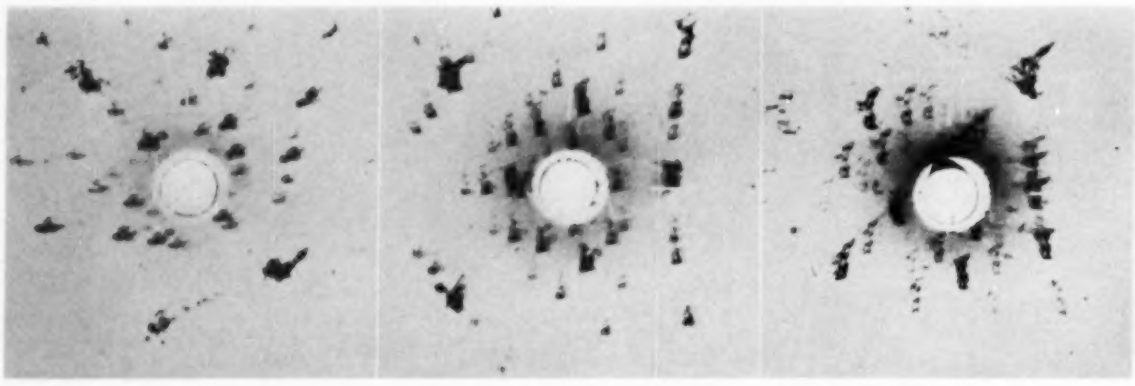

d—Rotated 120° clockwise from reference mark. e—Rotated 150° clockwise from reference mark. f—Rotated 180° clockwise from reference mark.

Fig. 7—X-ray photograms at different positions around the specimen axis of M-57 extended at 1300°C.

ation of the photograms indicates that there is a crystallographic order to this fragmentation since the spots are aligned in certain positions.

Summary

In the extension of molybdenum single crystals at high temperatures, it has been found that:

1—The number of slip bands at approximately equal amounts of elongation decreases with increasing temperature and the shear along the bands increases with increasing temperature.

2—The yield becomes more pronounced with increasing temperature of the tensile test. The strain hardening coefficient is greatly affected by temperatures up to about 2000°C; above this temperature it approaches zero.

3—Slip occurs on {110} plane in <111> directions.

4—Slip at high temperatures fragments the structure; however it is difficult to determine whether the fragmentation results from the formation of irregularly sized cells or polygonized bent atomic planes or both.

Acknowledgment

The authors would like to thank Dorothy Schaeffer for assisting in the tests. This work was supported by the Office of Naval Research under Contract Nonr 248(05), 039-004.

References

[1] E. N. daC. Andrade and L. C. Tsien: The Glide of Single Crystals of Sodium and Potassium, *Proc.* Royal Soc., London (1937) **163A**, p. 1.

[2] R. P. Steijn and R. M. Brick: Technical Report No. 2, Jan. 1, 1953, Contract AF 33(038)15889; Univ. of Pennsylvania, Philadelphia, Pa., to Flight Research Laboratory (WCRRL) Wright Air Development Center, Wright-Patterson Air Force Base, Ohio.

[3] E. Schmid and W. Boas: *Kristallplastizitat* (1935) Berlin. J. Springer.

[4] F. Rosi and C. H. Mathewson: A Study of the Plastic Behavior of High-Purity Aluminum Single Crystals at Various Temperatures, *Trans.* AIME (1950) **188**, p. 1159; JOURNAL OF METALS (September 1950).

[5] L. C. Tsien and Y. S. Chow: The Glide of Single Crystals of Molybdenum, *Proc.* Royal Soc., London (1937) **163A**, p. 19.

[6] N. K. Chen, R. Maddin and R. B. Pond: Growth of Molybdenum Single Crystals. *Trans.* AIME (1951) **191**, p. 461; JOURNAL OF METALS (June 1951).

[7] E. Schmid and G. Siebel: Magnesium. *Ztsch. Elektrochem* (1931) **37**, p. 447.

[8] W. Boas and E. Schmid: Aluminum. *Ztsch. Physik* (1931) **71**, p. 703.

[9] N. K. Chen and R. Maddin: The Plasticity of Molybdenum Single Crystals. *Trans.* AIME (1951) **191**, p. 937; JOURNAL OF METALS (October 1951).

[10] N. K. Chen and R. Maddin: Observations on Cleavage and Polygonization of Molybdenum Single Crystals. *Trans.* AIME (1951) **191**, p. 531; JOURNAL OF METALS (July 1951).

A Study of the Effect of Carbon Content on the Structure And Properties of Sintered WC-Co Alloys

by Joseph Gurland

The effects of variations of carbon content on the constitution and properties of sintered WC-Co alloys were studied. The grain growth of tungsten carbide during sintering was measured and it was shown that it takes place mainly by solution and reprecipitation of the carbide in and from the binder at the sintering temperature. It was found that the decomposition of W_3Co_3C by carburization during sintering is responsible for the formation of very large grains.

THE properties of sintered WC-Co alloys are critically dependent upon their final composition and structure. Slight changes of cobalt and carbon contents and small variations of grain size result in marked changes of mechanical properties and performance of products. Previous investigators have studied the microstructure as a function of composition[1] and have dealt with the influence of cobalt upon properties.[2] The present work is concerned with the effect of carbon content upon constitution, microstructure, and grain growth during sintering, as well as upon the physical properties of sintered compacts.

Phase Boundaries at the Sintering Temperature

The WC-Co section through the ternary diagram W-Co-C has been studied by Wyman and Kelley,[3] Takeda,[3] Sandford and Trent,[4] and Rautala and Norton.[5] Two phases, namely WC and a cobalt-rich solid solution (β), appear in the sintered structure if the carbon composition corresponds very nearly to the theoretical carbon content of WC (6.12 pct C). But small deviations from the ideal carbon content will bring about the occurrence of either graphite or the double carbide W_xCo_yC (η). The η phase was long believed to be metastable, this conclusion being based mainly on the work of Takeda. More recent studies have shown that it is a stable phase of the ternary system,[4, 5] but the actual phase boundaries have not been established and there has been some discussion as to whether or not the η phase occurs at some stage of sintering in the fully carburized alloys.[5] In view of this uncertainty it was thought advisable to undertake an investigation of the phases present during the sintering of WC-Co alloys.

J. GURLAND, Junior Member AIME, is Manager of Basic Research, Firth Sterling Inc., Pittsburgh.

Discussion on this paper, TP 3705E, may be sent, 2 copies, to AIME by April 1, 1954. Manuscript, Sept. 14, 1952. New York Meeting, February 1954.

Table I. Impurities in Sintered WC-Co Alloy

Fe — 0.20 pct	Ti — 0.007 pct
Mo — 0.023 pct	Si — Trace
S — 0.013 pct	Sn — Trace
Ta — 0.01 pct	

Commercially available tungsten, cobalt, and carbon powders were used in the present study. A typical analysis of impurities in a sintered compact is reported in Table I. The desired carbon compositions were attained by varying the amount of carbon added to the tungsten during carburization and controlling the composition during sintering by packing the compacts into beds of mixed alundum-carbon powders of suitably selected ratios. The alloys were sintered in a hydrogen tube furnace at 1400°C, then brought to equilibrium at the temperature under investigation and quenched in water. The high temperature phases were identified by metallographic and X-ray diffraction techniques. The samples were etched with a 10 pct solution of alkaline potassium ferricyanide.

The phase boundaries, established by metallographic examination, are shown in Fig. 1, which is a vertical section through the ternary diagram at 16 pct Co. The temperatures of the invariant planes at 1298° and 1357°C were established by Rautala and Norton. The vertical section shows that the three-phase field, WC + η + L, extends into the two-phase field, WC + L, but does not include the stoichiometric composition of WC. In practice this means that the η

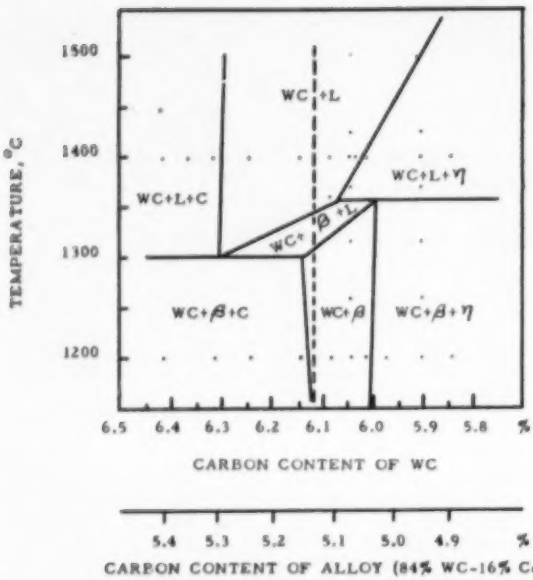

Fig. 1—Vertical section through ternary diagram W-Co-C at 16 pct Co.

phase will form during sintering, and will be present at room temperature if the tungsten carbide contains less than 6.00 pct C. If the carbon content of WC is between 6.00 and 6.06 pct, the η phase will occur in the equilibrium structure within a narrow temperature range and can be maintained at room temperature only by rapid cooling. Figs. 2 and 3 illustrate the difference in the appearance of the microstructure of two samples of 6.04 pct C cooled at different rates from 1370°C. The black η phase appears in the quenched specimen but not in the slowly cooled sample. If higher sintering temperatures are used, the η phase will precipitate during cooling through the critical temperature range and will decompose at lower temperatures if the cooling rate is slow enough. If, however, the sample is quenched from the critical temperature range, the double carbide will appear as a dark network around the carbide grains (Fig. 4).

Microstructure and Properties

Metallographic examination of slowly cooled samples indicates that in practice the composition range which will produce normal two-phase alloys of WC and Co at room temperature extends from 6.00 to 6.10 pct C in WC. Graphite or W_3Co_3C will appear in the microstructure if the carbon content falls outside this range. The microstructures of Figs. 5 and 6 are a result of carburizing and decarburizing a normal sample by a similar amount, as measured by the change of carbon content in weight percent. The initial carbon content of WC in the alloy was 6.08 pct; one sample was carburized to 6.40 pct (Fig. 5); the other was decarburized to 5.72 pct C in WC (Fig. 6). Whereas the particles of graphite are small and well dispersed, the double carbide is concentrated in patches and displaces a considerable area of the binder phase. On continued decarburization at high

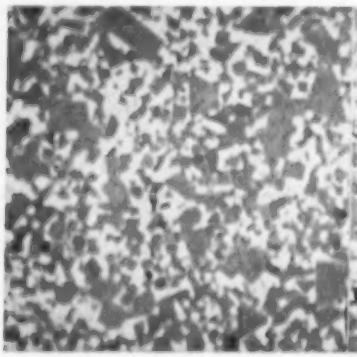

Fig. 2—84 pct WC-16 pct Co alloy. 6.04 pct C in WC. Slowly cooled from 1370°C. X1500.

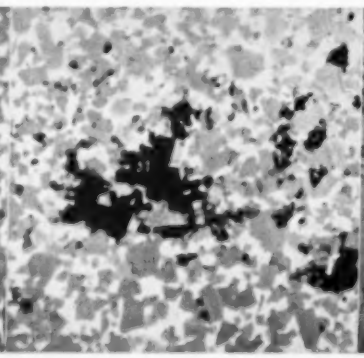

Fig. 3—Same alloy as Fig. 2. Quenched from 1370°C. X1500.

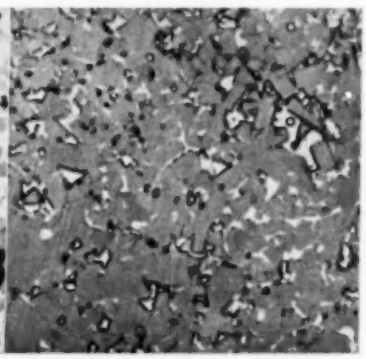

Fig. 4—Same alloy as Fig. 2. Slowly cooled from 1540°C and quenched from 1370°C. X1500.

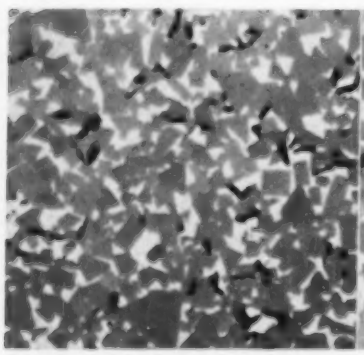

Fig. 5—Graphite formed as a result of carburizing a sintered alloy (84 pct WC-16 pct Co). X1500.

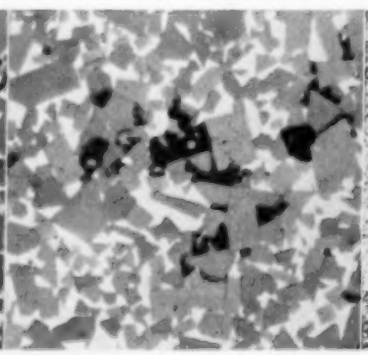

Fig. 6—W_3Co_3C formed as a result of decarburizing a sintered alloy (84 pct WC-16 pct Co). X1500.

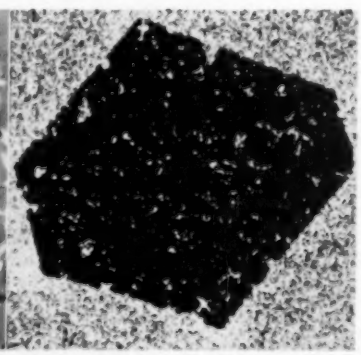

Fig. 7—Large grain of W_3Co_3C (η). X125.

temperatures, the η phase tends to grow into large regular grains such as shown in Fig. 7.

The effect of carbon content on the strength and hardness of an alloy of 84 pct WC-16 pct Co is plotted in Fig. 8. Graphite moderately decreases the strength and hardness. The double carbide brings about a drastic reduction of transverse strength. The hardness is reported as Rockwell A (60 kg load). The transverse rupture strength was determined by loading at the center of a 9/16 in. span. Each point represents the average of at least three measurements.

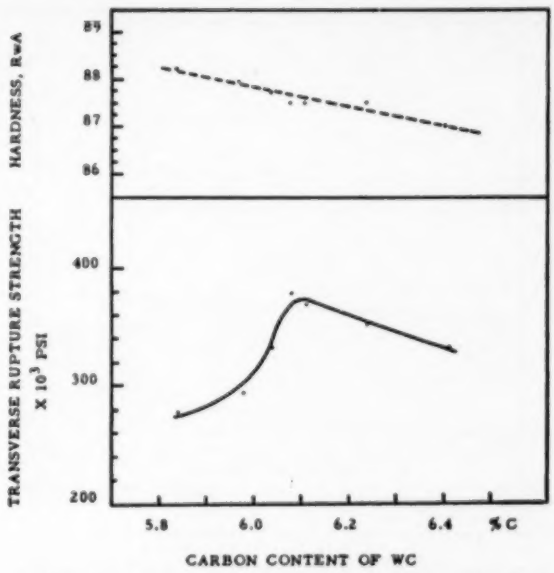

Fig. 8—Effect of carbon content of WC on strength and hardness of 84 pct WC-16 pct Co alloy.

Grain Growth

The grain size of the tungsten carbide constituent of sintered alloys is controlled in practice by the adjustment of a number of process variables extending back to the ore,[6] but it is finally determined by the extent of grain growth taking place during the sintering operation. Three mechanisms have been proposed for the increase of grain size during sintering: 1—solution and reprecipitation of tungsten carbide in and from the binder during the heating and cooling cycle,[8] 2—transfer of carbide from small to large grains by diffusion through the liquid binder at the sintering temperature,[1] and 3—coalescence of adjacent tungsten carbide grains.[7]

The last theory was first advanced to account for the occasional appearance of very large grains in localized areas of the microstructure.

In order to distinguish among these possibilities, a brief quantitative survey of grain growth during sintering was undertaken. The grain size of the sintered compacts was determined by a method of linear and planar sampling derived independently by a number of workers, among them F. N. Rhines, from whom the method was first obtained.[9] The underlying principles have been discussed by Smith and Guttman.[9] Both the number of dispersed grains per unit volume and their total surface area are derived from linear and planar grain counts on a metallographically prepared surface by the following relations:

$$N_v = \frac{\pi}{4}\frac{N_A^2}{N_L} \qquad [1]$$

$$S = 4N_L r^3 \qquad [2]$$

where N_v is the number of grains in a volume r^3; N_L is the number of grains along a line of length r; N_A is the number of grains within an area r^2; and S is the total surface area of grains in volume r^3.

An average diameter was calculated, assuming spherical grains. The last requirement is, of course, not satisfied by the angular tungsten carbide grains, but it was assumed that the error introduced by the shape factor is smaller than the reproducibility of the method, which is ± 5 pct. Approximately 1000 grains were counted on one field, at X1500, for each sample. The particle size of tungsten carbide powder was obtained by the same method from copper-infiltrated compacts or from powders mounted in bakelite. These measurements agreed, within 10 pct, with results from permeability measurements (Fisher Sub-Sieve Sizer) on the same powders.

For the purpose of evaluating the change of particle size distribution with sintering time, the grains on the polished surface of sintered compacts were classified into size ranges according to their largest visible dimension. This information was converted to particle size distribution by the statistical treatment of Scheil.[10] The distribution is reported on the basis of frequency.

1—Grain Growth in Two-Phase Alloys of Normal Carbon Content: The grain growth of normal WC-Co alloys was determined for a number of compositions, sintering temperatures, and sintering times. The effects of cobalt composition and temperature on final grain size are shown in Fig. 9. The effects of sintering time and initial particle size on final grain size are presented in Fig. 10. The grain growth was also found to be a function of the initial particle size distribution of the powder, as illustrated in Table II. The change of grain size distribution with sintering times is shown by the curves of Fig. 11.

On prolonged sintering, the tungsten carbide grains take on characteristic angular shapes. A plot of the frequency of angular measurements on the polished surface vs the angle (Fig. 12) has a decided maximum at 90°, indicating that the grains tend toward rectangular shapes. The major fraction of the measured values on the polished surface is as-

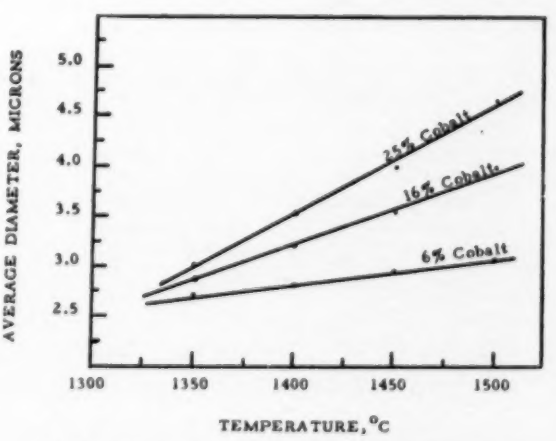

Fig. 9—Grain growth during sintering (1 hr at temperature).

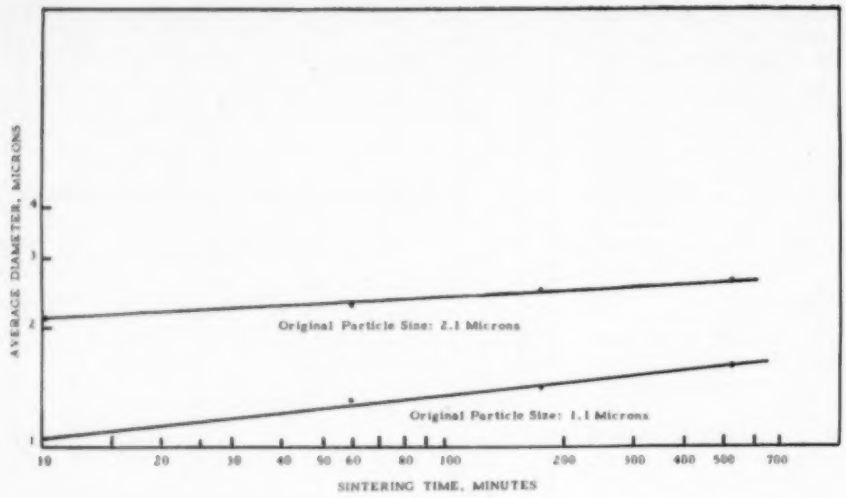
AVERAGE DIAMETER, MICRONS
Original Particle Size: 2.1 Microns
Original Particle Size: 1.1 Microns
SINTERING TIME, MINUTES

Fig. 10—Grain growth at 1400°C of 84 pct WC-16 pct Co alloys from fine and coarse WC powders.

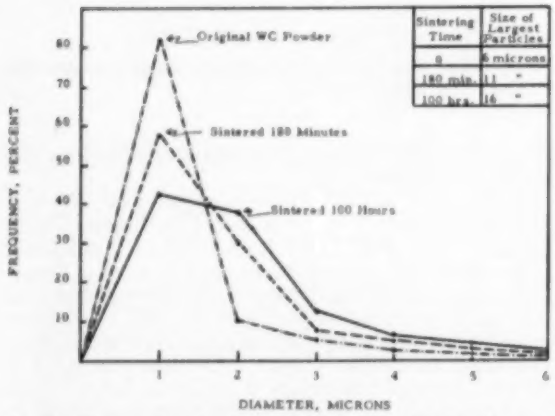

Fig. 11—Change of grain size distribution with sintering time at 1400°C.

sumed to correspond to the preferred range of the actual grain angles.[11] Approximately 1000 carbide grains were measured after sintering 100 hr at 1400°C.

2—Effect of Carbon Content on Grain Growth: The rate of grain growth increases with the carbon content of the alloys Three batches of tungsten carbide of 5.84, 6.04, and 6.14 pct C were mixed with 16 pct Co and sintered at 1400°C. The carbide powders were all initially of the same average diameter (1.33 micron). The grain size during sintering increased as shown in Fig. 13.

Table II. Effect of Particle Size Distribution of WC Powder on Grain Growth During Sintering (1 Hr at 1400°C)

Average Particle Diameter, Microns, Before Sintering	Particle Size Distribution* by Weight, Microns, Before Sintering			Average Grain Diameter After Sintering, Microns
	0-1	1-3	3-10	
2.3	42	49	9	2.4
2.4	44	47	9	2.7
2.4	30	54	16	3.3
2.5	31	54	15	3.1

* Particle size distribution of carbide powder determined by sedimentation technique.

3—Effect of a Change of Carbon Composition During Sintering: An increase of carbon content during sintering of a sample of normal composition also results in a larger grain size. For example, three compacts of normal carbon content, and 2.5 microns initial particle size, were sintered under carburizing, neutral, and decarburizing conditions. The grain sizes, after 8 hr sintering, were respectively 3.9, 3.7, and 2.8 microns. After these sintering treatments, the carburized sample had increased in carbon composition from 6.08 to 6.58 pct, whereas the decarburized sample had a final carbon content of only 5.77 pct C in WC.

A distinct effect was noticed when the alloy was initially deficient in carbon but carburized during sintering. Such conditions lead to the appearance of scattered large grains superimposed upon a more uniform and smaller grain structure. An extreme example of this effect is shown in Fig. 14, which illustrates the large grains formed by sintering a carbon-deficient alloy for 100 hr at 1400°, during which time the carbon content of the tungsten carbide increased from 6.03 to 6.30 pct. That this effect is dependent upon the rate of carburization is shown in Figs. 15 to 19. The carbon diffusion gradient from the surface to the interior of the compacts was varied by adjusting the composition of the packing

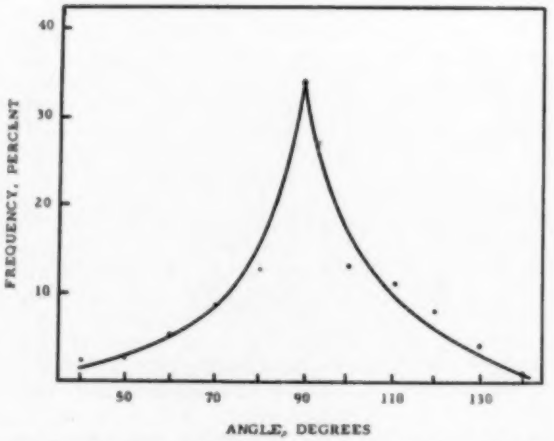

Fig. 12—Distribution of WC grain angles after 100 hr at 1400°C.

material. The number and size of the large grains increase with the carbon content of the packing material until the nonuniform grain growth is most pronounced with a 50 pct alundum-50 pct carbon mixture. Greater percentages of carbon bring about a reduction in the extent of nonuniform grain growth. The micrographs of Figs. 15 to 19 show increasing amounts of graphitic carbon as the carbon concentration in the packing material is raised. This nonuniform grain growth was only observed if the alloy composition was initially within the ternary field, WC + η + L. The large grains were not produced by carburizing an alloy of normal carbon content.

Discussion of Results

Although the η phase will not appear in fully carburized alloys, the location of the phase boundaries accounts for the decomposition of η on cooling observed by Takeda, if it is assumed that his compositions were slightly carbon deficient.

In agreement with industrial practice, it was found that the best properties are produced if the carbon content is as near as possible to that corresponding to a fully carburized WC. Even small deviations from the optimum carbon content strongly affect the physical properties because of the presence of undesirable phases in the microstructure. The effect of the double carbide W_xCo_yC is much more marked than that of graphite. The particles of graphite are small and relatively isolated, but a deficiency of carbon brings about the precipitation of W and Co as W_xCo_yC, which not only reduces the effective contribution of WC to the strength, but also embrittles the structure by replacing the binder with a brittle skeleton of η. The hardness of the double carbide is intermediate between that of WC and binder, it increases the hardness of the alloy only if it is present in small amounts and is well dispersed.

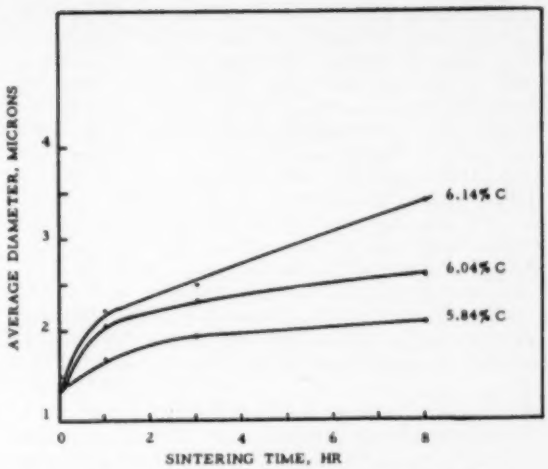

Fig. 13—Grain growth as a function of carbon content.

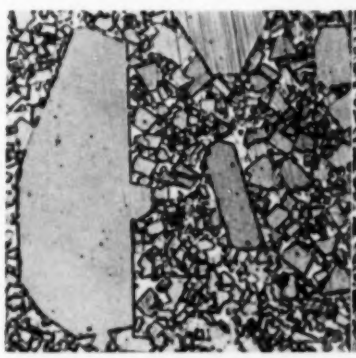

Fig. 14—Nonuniform grain growth after 100 hr sintering. X600.

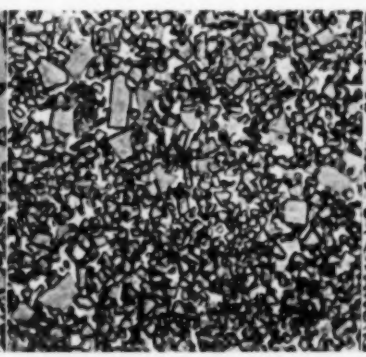

Fig. 15—84 pct WC-16 pct Co alloy of initially 5.84 pct C in WC. Sintered 3 hr at 1400°C. Packing material: 90 pct alundum-10 pct C. X1500.

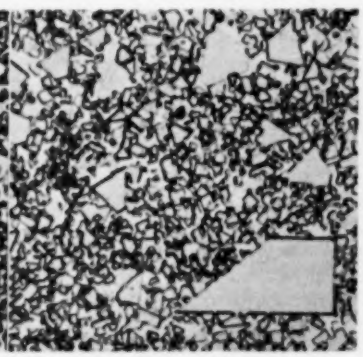

Fig. 16—Same alloy and sintering conditions as Fig. 15. Packing material: 75 pct alundum-25 pct C. X1500.

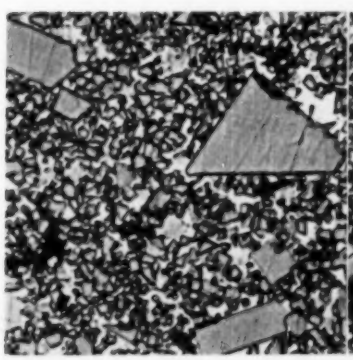

Fig. 17—Same alloy and sintering conditions as Fig. 15. Packing material: 50 pct alundum-50 pct C. X1500.

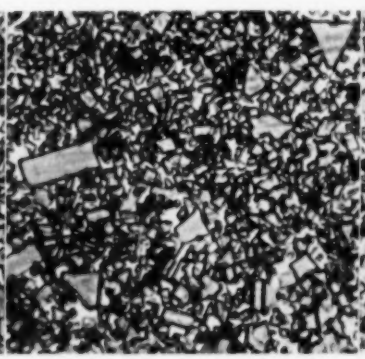

Fig. 18—Same alloy and sintering conditions as Fig. 15. Packing material: 25 pct alundum-75 pct C. X1500.

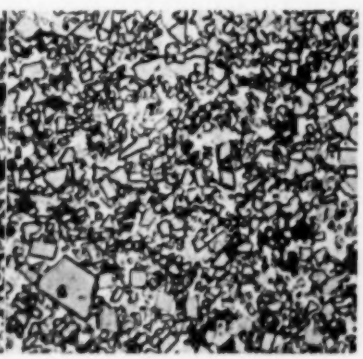

Fig. 19—Same alloy and sintering conditions as Fig. 15. Packing material: 10 pct alundum-90 pct C. X1500.

The grain size of tungsten carbide increases with sintering time, although the rate of increase slows down after prolonged sintering periods. The increase of average grain size on short time sintering (10 min) is so small that it falls within the experimental error (0.2 micron). The major part of the grain growth during sintering must therefore take place at the sintering temperature and not during the heating and cooling cycles. The increase of grain size as a result of solution of WC in the binder on heating, followed by subsequent precipitation on cooling, is estimated to be less than 0.1 micron for grains of 2.0 microns average diameter in an alloy of 84 pct WC-16 pct Co. This assumes that the carbide dissolves only from the smallest grain fraction and that precipitation occurs only on the largest grains.

The grain growth at temperature takes place mainly through the disappearance of the fine grains and the increase in number and size of the large ones. This process is accelerated by higher temperatures, greater binder contents, and smaller grain size. It is also influenced by the original particle size distribution of the powder, the most nonuniform powders showing the greatest increase of average grain size during sintering. With increased sintering times, the carbide grains tend to form rectangular parallelopipeds. The interfacial energy between tungsten carbide and binder is expected to be a function of surface orientation since hexagonal crystals are strongly anisotropic and certain crystallographic planes may be favored to form the grain surfaces. In the case of tungsten carbide, grain growth results in a decrease of interfacial energy not only by reduction of interfacial area, but also by the formation of low energy habit planes at the liquid-solid boundary.

In general, the rate of grain growth increases with carbon content. The smaller grain size of low carbon compositions may be caused by a reduction of the amount of liquid binder, which accompanies the formation of the double carbide, W_xCo_yC. But the η phase may also act as a grain growth inhibitor, especially since it forms preferentially at the carbide-binder interface.

The nonuniform grain growth seems to be definitely associated with the elimination of the η phase by carburization. The growth of the large grains may be visualized by assuming that the reaction

$$W_xCo_yC + 2C \rightarrow 3WC + 3Co$$

takes place at a few preferred locations in the microstructure, where the WC grains will start to grow preferentially at the expense of the disappearing double carbide. About 15 pct of the WC present takes part in the formation and decomposition of the double carbide in the alloy composition under discussion. The process is favored by a slow rate of carburization because the deposition of WC will occur in place if the composition changes drastically.

It is probable that the mechanism demonstrated above is not the only one which can bring about the formation of large grains. Other factors, such as impurities, trace elements, and temperature variations, may locally alter the liquid-solid interfacial equilibrium and result in nonuniform grain growth. Sometimes two or more grains show extensive areas of contact. Such grain boundaries must be of low interfacial energy so as not to be dissolved by the binder. This suggests that the crystallographic orientation of the adjacent grains are related by having nearly parallel or twinned orientations. Such relations have been observed with inorganic crystals and are brought about by either coalescence of existing grains of parallel or twinned orientations[12] or by the growth of crystals of twinned orientation from a common seed.[13] Unfortunately, the tungsten carbide grains are so small that orientation measurements on individual grains by X-rays are not possible.

Summary

1—A re-examination of the phase diagram in the sintering range indicates that the double carbide appears as a stable phase, in a narrow temperature range, during the sintering of slightly carbon-deficient WC-Co alloys.

2—The carbon content of WC-Co alloys very strongly influences the properties of sintered compacts. A deficiency of carbon will affect the properties much more drastically than an excess of carbon because of the formation of the double carbide W_xCo_yC. The η carbide reduces the strength by displacing the binder from the sintered structure.

3—The grain size of WC in the sintered structure increases with sintering time, sintering temperature, amount of binder, carbon content, and inhomogeneity of particle size distribution. The rate of grain growth decreases with larger initial grain size of the carbide powder.

4—The major part of grain growth takes place isothermally and is characterized by the disappearance of the smallest grains of WC and the increase in number and size of the largest ones.

5—Carburization of a carbon-deficient alloy during sintering results in nonuniform grain growth. This is associated with the disappearance of the η phase.

Acknowledgment

The author acknowledges the invaluable assistance of Paul Bardzil in carrying out the experimental work.

References

[1] L. L. Wyman and F. C. Kelley: *Trans.* AIME (1931) **93**, p. 208.

[2] E. W. Engle: *Powder Metallurgy.* Edited by J. Wulff. (1942) p. 436. Cleveland. ASM.

[3] S. Takeda: *Science Reports,* Tohoku Imp. Univ., Honda Anniversary Vol. (1936) p. 864.

[4] W. J. Sandford and E. M. Trent: Symposium on Powder Metallurgy. Iron and Steel Inst., *Special Report 28* (1947) p. 84.

[5] P. Rautala and J. T. Norton: *Trans.* AIME (1952) **194**, p. 1045; JOURNAL OF METALS (October 1952).

[6] E. Amman and J. Hinnuber: *Stahl und Eisen* (1951) **71**, p. 1081.

[7] E. J. Sandford: *Metal Treatment* (1947) **14**, p. 239.

[8] F. N. Rhines, Carnegie Institute of Technology, Pittsburgh, Pa., personal communication. Also discussed in part in: Symposium on Testing Metal Powders and Metal Powder Products. ASTM *Special Technical Publication No. 140* (1952) p. 86.

[9] C. S. Smith and L. Guttman: *Trans.* AIME (1953) **197**, p. 81; JOURNAL OF METALS (January 1953).

[10] E. Scheil: *Ztsch. anorg. allgem. Chemie* (1931) **201**, p. 259.

[11] D. Harker and E. A. Parker: *Trans.* ASM (1945) **34**, p. 156.

[12] G. Friedel: *Bull.* Soc. Franc. Mineral. (1933) **56**, p. 262.

[13] G. Deicha: *Experentia* (1949) **4**, p. 67.

Orientation Relationships in Cast Germanium

by W. C. Ellis and Jacqueline Fageant

All major regions in a progressively solidified germanium ingot were related through successive orders of octahedral twinning. The occurrence of lineage structure and the generation and survival of orientations are discussed.

WHEN metals solidify in a temperature gradient a preferred orientation, or casting texture, usually develops. For example, in face-centered and body-centered cubic metals, most of the solidifying crystals have a cube axis, <100>, aligned approximately in the freezing direction.[1] In the solidification of diamond cubic metals this is not the case, since there is a natural tendency to form twin orientations.[2, 3] In this paper, twinning relationships in cast germanium are described; some conclusions with respect to nucleation and survival of new orientations are discussed.

In the first experiment, an ingot of high purity germanium, ¾ in. in diameter and 1¼ in. in length, was formed by progressive solidification[4] from the bottom. The ingot was cut into 21 slices, each circular and about 0.030 in. thick. The top surface of each slice was polished and etched to reveal the regions of different orientations. Orientations were determined by the Laue X-ray back-reflection method. The uncertainty in the determined orientation relationships was 1° or 2° when separate slices and films were involved. Frequently, however, advantage was taken of illuminating across a boundary when the patterns of the two orientations were recorded on the same film. The uncertainty then was less than 1°. Often the twin relation was evident from common zones or individual reflections. Twin relationships were recognized through comparison of the values of the nine angles between cube poles of the two orientations with those calculated for successive orders of octahedral twinning.

The birth and survival of each region can be reconstructed by visual examination of the etched slices shown in Fig. 1. In slice 21, where solidification began, many regions are present; these regions were found to be twin-related. Solidification appears to have started from one nucleus formed probably at the wall of the crucible.* Subsequent orientations were developed by nucleation on existing solid surfaces, and only in the twin relationship. This is an example of a general process of nucleation on a surface of existing solid and may be descriptively termed oriented nucleation.† In germanium, and other diamond cubic substances, the orienting habit is that of twinning on an octahedral plane.[2, 3]

The prevalence of straight traces in the polished surfaces of succeeding slices (Fig. 1) suggests that the twinning observed in the first slice persisted throughout solidification. This was confirmed by X-ray determinations. The schematic diagram of Fig. 2 shows the twinning relationships of the major regions throughout the ingot. Since all observed relationships are describable as twinning, it is reasonable to conclude that no random nucleation occurred in the freezing of the ingot. An alternative possibility would be that nucleation of a random nature occurred, but only those nuclei in twin orientations survived in subsequent growth. This is unlikely for there would be as good a reason for the growth of randomly oriented nuclei as for the growth of the many different orientations present after several orders of twinning. The many twin components contain a wide distribution of orientations, and did grow. In fact, they are the only ones found in the solid.

The conditions of solidification of this ingot were such as to discourage nucleation of crystals wholly in the liquid. The rate of solidification was 0.125 in. per min. This slow rate of heat removal afforded but small opportunity for supercooling within the liquid —a condition needed to provide enough decrease in free energy for such nucleation.

When nucleation occurs on an existing solid surface, the interfacial energy between the existing and forming regions is important in determining the new stable orientation. The new orientation is expected to be one which minimizes this energy. In the diamond cubic structure, the interface for the

* The assumption is made that the observed twinning occurred during the solidification process rather than by subsequent transformation or recrystallization in the solid. There is substantial evidence in support of this assumption. Structural transformations have not been reported in solid germanium. E. S. Greiner in unpublished work has not found evidence, in careful thermal analyses, of transformations in the solid near to the melting point and for temperatures down to 500°C. Long annealing near the melting point by E. S. Greiner and these authors has not induced recrystallization in plastically deformed germanium other than that which may be described as polygonization. There remains a possibility that the twinning occurred in the cooling solid; but the discussion of nucleation and survival given applies substantially to this case as well.

† The term, oriented nucleation, has been used in connection with recrystallization[5] where the nucleus of a new orientation bears a unique relationship to a prior orientation.

W. C. ELLIS, Member AIME, and J. FAGEANT are associated with Bell Telephone Laboratories, Inc., Murray Hill, N. J.

Discussion on this paper, TP 3689E, may be sent, 2 copies, to AIME by April 1, 1954. Manuscript, Sept. 16, 1953. New York Meeting, February 1954.

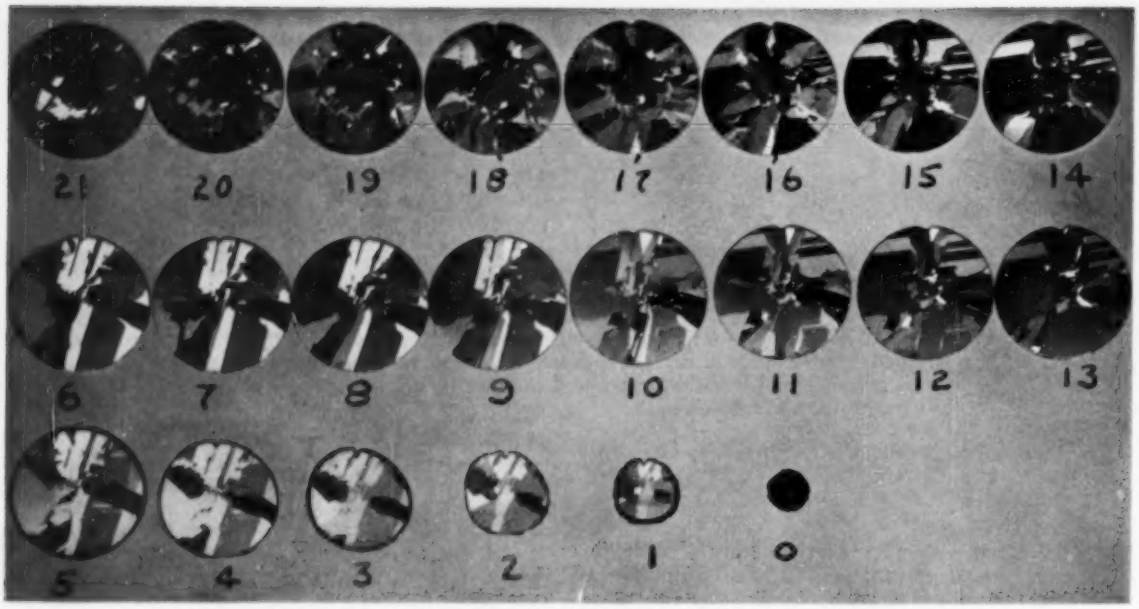

Fig. 1—Etched slices cut from a progressively frozen germanium ingot. Freezing began with slice 21.

twinned orientation is one of low energy.[6] A new layer of atoms on a {111} face sees little energetic difference between positions continuing the existing orientation and those initiating a twin relationship.

The interesting features of survival shown in Figs. 1 and 2 can be understood when the conditions of freezing and the orientations of adjacent regions are taken into account. Theuerer and Scaff[7] have shown by electrical measurements and by decanting a crucible containing a partially solidified ingot (frozen in the same thermal conditions as the ingot in this study) that the solid-liquid interface at the beginning of freezing is sharply concave upward. The growth direction, as inferred from the columnar structure shown by them, is normal to the freezing interface. In the present experiment, then, solidification originating near the periphery of the crucible proceeded rapidly toward the axis of the ingot, while the growth of material originating on the axis lagged that of the converging array. This follows from examination of the series of slices in Fig. 1. Orientations with axially directed growth failed to survive; the peripheral array converged at the ingot axis. The convergence was complete at about slice 10 when half of the ingot had solidified. To summarize, two of the conditions determining survival are the shape and the symmetry of the isothermal surfaces in the freezing system.

A third important condition in determining survival is simply that once a twin composition plane is formed, it is preserved as further solid is added from the liquid. In Figs. 1 and 2 freezing progressed from slice 13 to slice 7, the twin boundary between *B* and *G* persisted, but moved toward the top of the picture in each succeeding slice until it disappeared in slice 7. The reason for the final disappearance of the twin plane lies in its orientation with respect to the ingot axis. The plane, viewed along the axis in the growth direction, is inclined by 22° away from the axis and toward a 12 o'clock position (when the ingot slice is considered a clock face). This information comes from the stereographic projections (not shown) for the orientations of *B* and *G*. With these orientations the interface simply grew out of the ingot. The twinning composition plane was preserved without lateral shift. This preservation is further supported by the constant width of thin twin components during the progress of solidification to be observed in Fig. 1. It can be generalized that twin interfaces once formed, do not shift laterally‡ and only disappear by growing out of the ingot, or by interference with other growing regions due to the convergence at the axis discussed earlier.

‡ The preservation of the twin interface has been observed by Burke[8] in grain growth of α brass.

The preservation of interfaces was not limited to first-order twins: mirror planes that are physical junctures between higher order twinned regions are present in slices 9 and 7. The juncture plane between third-order twins *P* and *D* was preserved in these slices and disappeared in slice 6 as shown in Figs. 1 and 2. The evidence that this juncture is planar is the persistence of straight traces of the interface on successive ingot slices. The indices are (525) and since the plane is inclined 22° toward 9:30 o'clock, *D* grew at the expense of *P*.

Interfaces between high-order twins contain a large proportion of atoms common to the lattices of the adjacent regions.[6] It is suggested that they are of low energy as is the twin composition plane, and the crystal finds an inadequate motivation for a lateral shift or a disappearance of such an interface. To do other than continue the mirror interface would require the creation of new surfaces at a greater cost in energy. A consequence of the preservation of a twin interface or juncture is the selection of one of the bounding regions to survive in progressive freezing of an ingot. If the interface of low energy is parallel to the ingot axis, both regions survive.

Although no casting texture was observed in the sense of a preferred crystal direction aligned along the freezing axis, there is at least one direction of low Miller indices common to the observed several

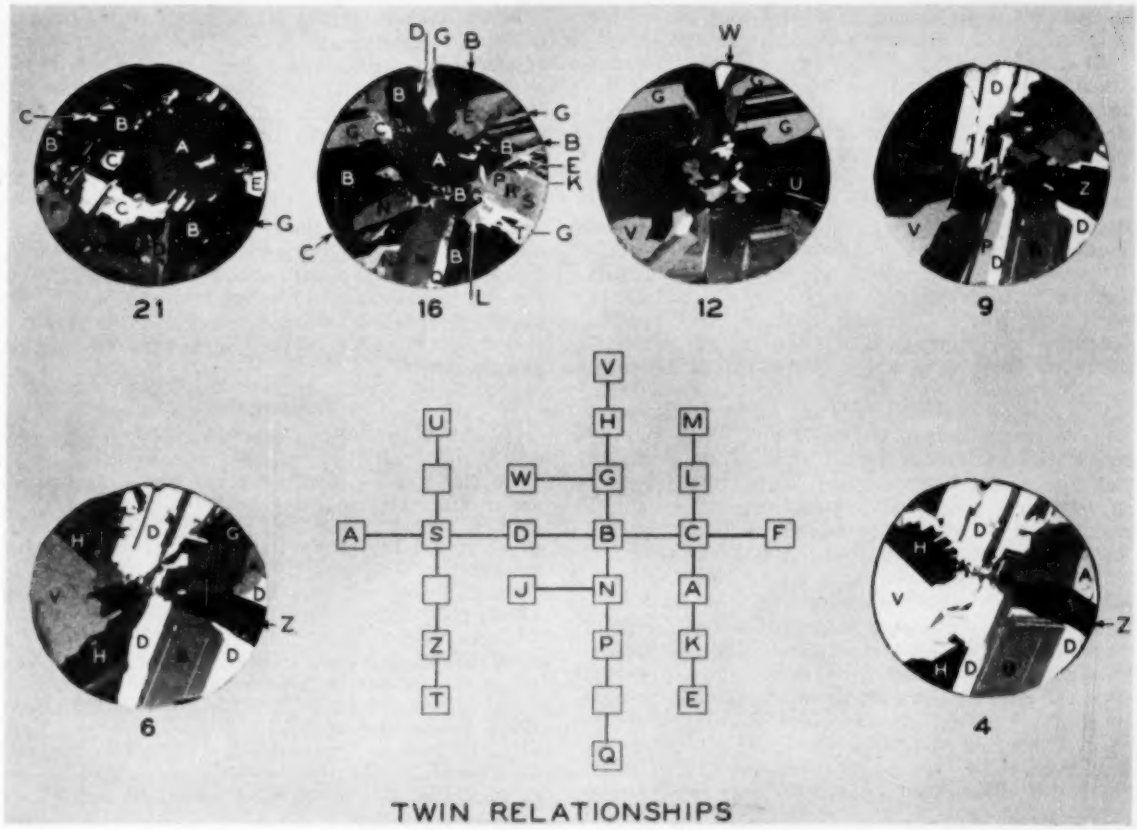

Fig. 2—Twin relationships in an ingot of germanium.

orders of twinning. For example, regions *V*, *H*, *G*, *B*, and *D* in slice 6 (Fig. 2) make up most of the section and have a common<113> crystallographic direction. The direction <113> is inclined about 45° away from the ingot axis toward 8 o'clock. No significance has been attached to this common direction.

New regions with orientations but 1° or 2° different from that of the parent region may form. The resulting lineage structure[9] is illustrated in Fig. 1. Region *B* was reasonably perfect at slice 12. At slice 11, however, a new orientation differing only 2° from *B* developed near the center. Upon further solidification, region *B* developed many additional small volumes of slightly differing orientations until it was replaced by orientation *V* growing in from the side. It is reasonable to conclude that the development of lineage retarded the growth of region *B* to permit region *V* and its twin *H* to take over in further solidification. The *V-H* region stopped growing laterally when it reached the more perfect part of crystal *B*. This portion still exists in slices 5 and 4 and presumably disappeared only because the ingot began to crown, reducing its cross section.

The nucleation of the lineage orientations is obscure: the orientation relationships among the regions in this and other cases, can be described by rotations but not always about an axis of small rational indices. Rotations have been observed about <110>, <112>, <113>, and also about an axis normal to the solidification interface. Teghtsoonian and Chalmers[10] have reported such structures in the solidification of tin and have offered an explanation in terms of the collection of vacancies to form dislocations. No final conclusions with respect to germanium can be drawn from the evidence thus far found.

A second experiment was performed in which an ingot was prepared by progressive solidification in a crucible designed to cause freezing, and therefore initial nucleation, in two physically separated locations. This was accomplished by providing the crucible cavity with two cylindrical extensions in its bottom so as to produce the ingot with legs shown in Fig. 3. Freezing proceeded from the bottom to the top, as in the first ingot, so that solid was

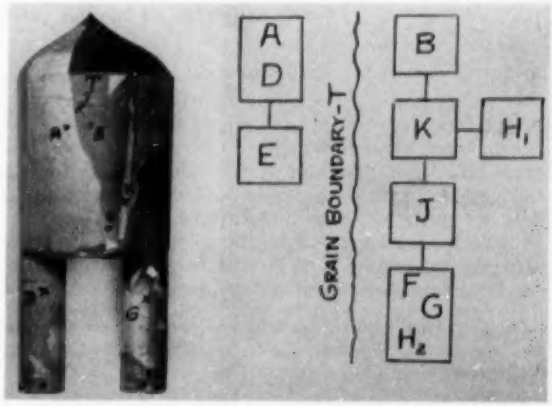

Fig. 3—Orientation relationships in an ingot in which nucleation occurred simultaneously in the two legs. Approximately full size.

nucleated nearly simultaneously in each leg before a bridge of solid formed in the main cavity.

The etching of the ingot revealed an irregular trace, labeled *T*, extending from the bottom of the larger section of the ingot to the last point to freeze at the top. A similar trace was found on the opposite side of the ingot. This suggests that the regions separated by the interface are not twin-related, and that the interface is the juncture of two main regions, each nucleated in one of the two legs. Further evidence was obtained by X-ray diffraction. The orientations of the etch-delineated regions were determined beginning at the base of each leg where freezing started. The specific locations and corresponding orientation relationships are depicted in Fig. 3. Twin-related domains exist throughout each leg and into the main ingot up to the irregular interface. Across this interface in two locations, (*A* to *B*) and (*A* to *F*), the orientation difference is not that of twin-related regions within four orders. Since this ingot is structurally simple with large regions of single orientation and but few orders of twinning, the finding further suggests that the two main regions are not twin-related.

Summary

All major regions in a progressively solidified ingot of germanium were related through successive orders of octahedral twinning. It is suggested that the entire ingot grew from one nucleus formed in initial freezing; all subsequent orientations originated through nucleation on the surface of existing solid. The new orientations are either twin-related or differ from a parent by only small angles of 1° to 2° or less. This special type of oriented nucleation does not lead to a casting texture.

In the growth of the ingot, survival of orientations was conditioned in part by the shape and symmetry of the solid-liquid interface. Twin composition planes and mirror composition planes of higher orders of twinning were preserved. This was another important factor in determining survival.

Acknowledgment

The authors are pleased to acknowledge the assistance of J. S. Doyle and D. Dorsi, who prepared the ingots and sections, and M. J. O'Brien, who did the photographs of ingots and sections. R. G. Treuting, H. C. Theuerer, and W. G. Pfann have added to the value of the paper through helpful discussions.

References

[1] C. S. Barrett: *Structure of Metals* (1952) 2nd Edition, p. 510. New York. McGraw-Hill Book Co.

[2] W. C. Ellis: *Trans.* AIME (1950) **188**, p. 886; JOURNAL OF METALS (June 1950).

[3] E. L. Salkovitz and F. W. Von Batchelder: *Trans.* AIME (1952) **194**, p. 165; JOURNAL OF METALS (February 1952).

[4] H. C. Torrey and C. A. Whitmer: *Crystal Rectifiers* (1948) p. 364. New York. McGraw-Hill Book Co.

[5] Ref. 1, p. 503.

[6] W. C. Ellis and R. G. Treuting: *Trans.* AIME (1951) **191**, p. 53; JOURNAL OF METALS (January 1951).

[7] H. C. Theuerer and J. H. Scaff: *Trans.* AIME (1951) **191**, p. 59; JOURNAL OF METALS (January 1951).

[8] J. E. Burke: *Trans.* AIME (1950) **188**, p. 1324; JOURNAL OF METALS (November 1950).

[9] M. J. Buerger: *Ztsch. Krist.* (1934) **89**, p. 195.

[10] E. Teghtsoonian and B. Chalmers: *Canadian Journal of Physics* (1951) **29**, p. 370.

Redistribution of Solutes by Formation and Solidification Of a Molten Zone

by W. G. Pfann

Formation and slow solidification of a molten zone in a homogeneous ingot produces a discontinuity in solute concentration at the boundary of the zone and a gradient of concentration within the zone. By using two solutes, one a donor, the other an acceptor, step or graded pn barriers can be produced.

EXPLOITATION of the difference in concentration between a molten solution and the solid which freezes from it is continued in this paper. The normal segregation which results from this difference has been used for purification[1, 2] and for pn barrier-formation in semiconductors.[3, 4] By means of *traveling* molten zones this difference has been used to effect multistage separations and to eliminate segregation in ingots.[5, 6] It will be shown here that by means of *stationary* molten zones this difference can be used to produce discontinuities in concentration. In particular it will be shown that a pn or npn barrier can be made by the simple act of melting and refreezing a portion of a block of semiconductor, provided that the block contains proper concentrations of a donor and an acceptor in solid solution.

W. G. PFANN, Member AIME, is associated with the Chemical and Metallurgical Research Dept., Bell Telephone Laboratories, Murray Hill, N. J.

Discussion on this paper, TP 3722E, may be sent, 2 copies, to AIME by April 1, 1954. Manuscript, Sept. 15, 1953. New York Meeting, February 1954.

Assumptions

The operation of melting and slow refreezing will be called *remelting* and the interface between liquid and solid at the start of refreezing will be called the *remelt boundary*. While remelting may be done for various shapes of starting crystal and remelt zone it will be assumed that the remelt zone is cylindrical, its length being measured in the direction of freezing, which is normal to the remelt boundary, and

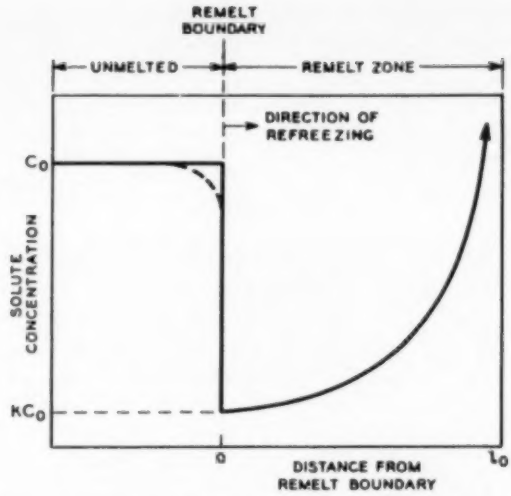

Fig. 1—Concentration of a single solute as a function of distance from remelt boundary. Remelting produces a step in concentration at the remelt boundary and a gradient in concentration in the remelt zone.

that the remelt boundary is planar, as in Fig. 1. The assumed conditions of freezing are: 1—diffusion in the solid is negligible; 2—diffusion (or mixing) in the liquid is complete, i.e., concentration in the liquid is uniform; 3—the distribution coefficient, k, defined as the ratio of the solute concentration in the freezing solid to that in the liquid is constant. Where electrical conductivity is discussed, it will be assumed to be proportional to the concentration of excess donors or acceptors. It will be assumed also that solute concentrations are in atomic units and that each solute atom contributes one carrier of electrical charge.

Simple Remelting with One Solute

In a block of material containing a uniform concentration C_0 of solute, melt a zone of length l_0 and freeze it back slowly, as in Fig. 1. Under the assumed conditions of freezing, the solute concentration in the first solid to form, at the remelt boundary, will be kC_0 and the solute concentration, C, in the remainder of the remelt zone after freezing will be given by the normal freezing equation[1]

$$C = kC_0(1-g)^{k-1} \qquad [1]$$

where g is the fraction of the remelt layer which has solidified. Thus, as shown in Fig. 1, remelting produces a discontinuity in concentration, of magnitude $C_0(1-k)$ at the remelt boundary and a gradient of concentration in the remelt layer. If k differs appreciably from unity, large percentage changes in concentration can be produced at the remelt boundary.

It is important in practice to consider the effect of diffusion in the solid during remelting, particularly in the period just before freezing begins. For $k < 1$ solute will tend to diffuse to the molten zone. If the diffusion coefficient, D, is small, but appreciable, then rounding of the step may occur as indicated by the dotted curve in Fig. 1. If D is large, and sufficient time elapses, the solid and liquid will attain concentrations C_l and C_l/k, respectively. C_l can be determined readily from a solute balance if the volumes of liquid, V_l, and solid, V_s, are known, as follows:

$$C_0(V_l + V_s) = C_lV_s + \frac{C_l}{k} V_l \cdot$$

(Even though a temperature gradient must exist, it is assumed to be small). If k is very small, most of the solute will eventually diffuse into the molten zone.

Formation of p-n Barriers by Simple Remelting with Two Solutes

Conditions for Barrier Formation: Consider a block of semiconductor containing uniform concentrations C_{01} and C_{02} of solutes, one of which is a donor, the other an acceptor. Let C_{01} be greater than C_{02} and let k_2 be greater than k_1. Upon remelting, a pn barrier may or may not form at the remelt boundary, depending on the k's and the C_0's. A barrier *will* form if $k_2C_{02} > k_1C_{01}$, which condition will be achieved only if

$$C_{01} > C_{02} > \frac{k_1}{k_2} C_{01}. \qquad [2]$$

Since $C_{01} > C_{02}$, the original material must be of conductivity type 1 and the material just inside the remelt boundary must be of type 2. Since there was an excess of solute 1 throughout the original material and since a deficit of solute 1 exists in the first-to-freeze portion of the remelt zone, the conductivity must revert to type 1 during the freezing of the remainder of the remelt zone. Hence, if the conditions of Eq. 2 are met, remelting produces two pn barriers, a "step" barrier at the remelt boundary and a "graded" barrier in the remelt layer. Fig. 2 illustrates their formation schematically. A unique and most significant feature of remelting is that the concentrations which freeze out at the remelt boundary are independent of the volume of the remelt zone. Thus step barriers of various shapes and sizes but of similar properties can be made from a given starting material by the simple steps of melting and slow refreezing.

Electrical Conductivities at the Step Barrier: The electrical conductivities, σ_a and σ_b, at the step bar-

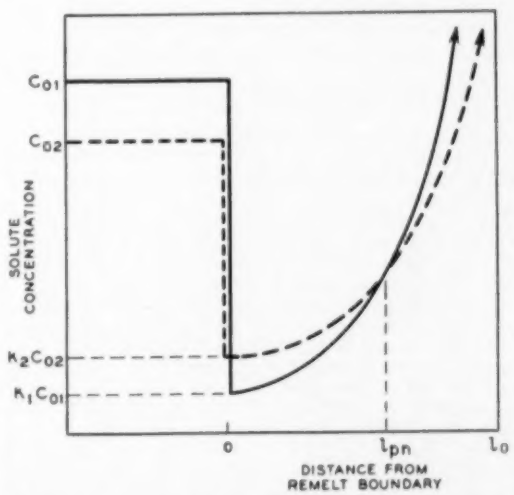

Fig. 2—Concentrations of two solutes, one a donor, the other an acceptor, after simple remelting. Remelting produces a step pn barrier at the remelt boundary and a graded pn barrier in the remelt zone.

Fig. 3—Radioautograph of a longitudinal section through the remelt zone of a germanium ingot containing radioactive antimony.

rier will be proportional to the difference concentrations $(C_{o1} - C_{o2})$ and $(k_2C_{o2} - k_1C_{o1})$ on the unmelted and remelted sides of the remelt boundary, respectively, and are given by

$$\sigma_a = (C_{o1} - C_{o2})e\mu_a \quad [3]$$

$$\sigma_b = (k_2C_{o2} - k_1C_{o1})e\mu_b \quad [4]$$

where the μ's are mobilities, e is the electronic charge, and subscripts a and b refer to the unmelted and remelted sides of the barrier, respectively. Solving Eqs. 3 and 4 for C_{o1} and C_{o2} to find the required initial concentrations to produce desired conductivities σ_a and σ_b at the step barrier gives

$$C_{o1} = \frac{1}{e(k_2 - k_1)}\left[\frac{k_2\sigma_a}{\mu_a} + \frac{\sigma_b}{\mu_b}\right] \quad [5]$$

$$C_{o2} = \frac{1}{e(k_2 - k_1)}\left[\frac{k_1\sigma_a}{\mu_a} + \frac{\sigma_b}{\mu_b}\right]. \quad [6]$$

While Eqs. 5 and 6 show that, in principle, any desired conductivities can be obtained for a given set of k's, in practice the solid solubilities of the components will be a limitation. Also, if both k's are small compared to unity it will not be practical to have $\sigma_b > \sigma_a$, as this would require that C_{o1} and C_{o2} be large and very nearly equal and hence the control of σ_a would be poor. For germanium a sufficient range of k's is available for both donors and acceptors[7] to permit n to p or p to n conversions at the remelt boundary.

Location and Concentration Gradient of the Graded Barrier: It is assumed that the remelt zone solidifies by normal freezing and that another pn barrier is formed in it by differential segregation. Equations for the location and concentration gradient of such a barrier have already been derived.[4] The location, in terms of g_{pn} the fraction solidified, is given by

$$g_{pn} = l_{pn}/l_o = 1 - r^{\frac{1}{(k_1 - k_2)}} \quad [7]$$

where

$$r = k_2C_{o2}/k_1C_{o1}. \quad [8]$$

The concentration gradient, $d(\Delta C)/dl$, is given by

$$\frac{d(\Delta C)}{dl} = \frac{k_1C_{o1}(k_1 - k_2)}{l_o} \cdot r^{\frac{(k_2 - 2)}{(k_1 - k_2)}}. \quad [9]$$

Hence, with the concentrations and k's of the solutes in the starting material and the length of the remelt zone known, the conductivities on either side of the step barrier and the location and concentration gradient of the segregation barrier can be computed.

Remelting with Additions

Many of the advantages of simple remelting will be retained, and others can be gained, if the addition to the remelt zone of solutes not present in the original material is permitted. Thus, whereas in simple remelting the concentrations in the remelt zone are entirely determined by those in the original block, in remelting with additions they are largely independent of those in the original block. One method of addition is to place solute on the surface of the block and subsequently to permit it to dissolve in the remelt zone when the latter is formed. Upon refreezing, the concentrations at the remelt boundary will be the sum of: those arising from simple remelting, which are independent of the volume of the remelt zone; and the concentrations of added solutes, which vary inversely with the volume of the remelt zone. Advantages of remelting with additions as compared with simple remelting are that greater control over the concentrations at the step barrier and the location of the graded barrier can be had.

Experimental Results

The redistribution of a single solute by remelting is rather strikingly illustrated by the following experiment. In a long ingot, containing a uniform distribution of solute, produce a stationary molten zone and then, by gradually reducing the temperature, cause the zone to freeze progressively from both ends toward the middle. The redistribution of radioactive antimony in a germanium ingot by this process, which will be named ingot-remelting, is shown in Fig. 3, which is a radioautograph of a longitudinal section through the remelt zone. The concentration of antimony is indicated by intensity, the lighter regions being richer in antimony. The sharp decrease in concentration at each remelt boundary and the increase in concentration in the last regions to freeze, at the center of the remelt zone, are quite apparent. The value of k for antimony in germanium is about 0.004.

Step and graded pn barriers have been made by ingot remelting of single crystal germanium using as solutes: gallium, an acceptor for which k is about 0.1, and antimony, a donor. These solutes correspond to solutes 2 and 1 respectively, in Fig. 2. Typical current-voltage curves for a step barrier and a graded barrier made from the same remelt zone are shown in Fig. 4. These exhibit certain

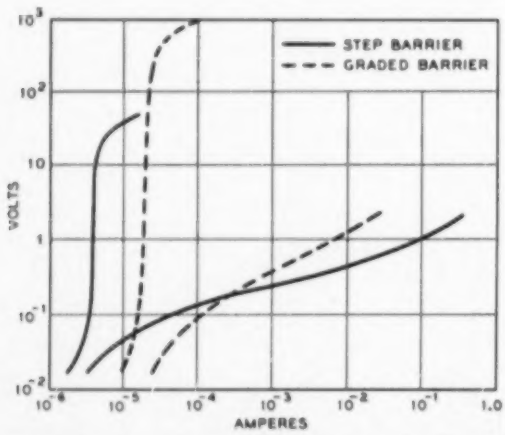

Fig. 4—Current-voltage characteristics of a step barrier and a graded barrier produced by simple remelting of a germanium ingot containing gallium and antimony.

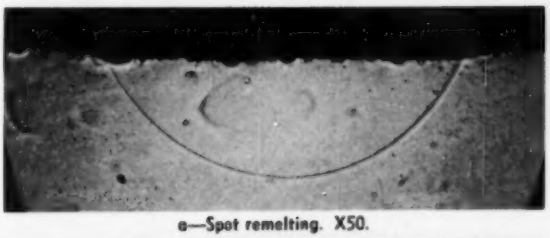

a—Spot remelting. X50.

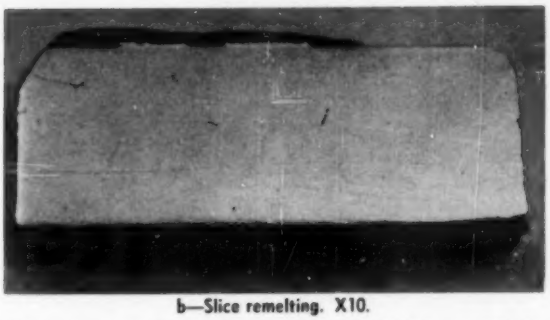

b—Slice remelting. X10.

Fig. 5—Cross sections showing remelt zones. Etching reveals the step barriers and thereby delineates the remelt zones.

typical characteristics which are in accord with pn barrier theory[6] and the known solute concentrations in the remelt zone, namely, that the saturation current and forward resistance are lower for the step barrier, and that the saturation extends to much higher reverse voltage for the graded barrier. The value of the saturation current for the step barrier agrees well with that computed from the measured conductivities and life-times, indicating that the barrier approximates an ideal step. The capacitance of the graded barrier agrees in order of magnitude with that computed from the calculated concentration gradient and varies quite accurately as the 1/3 power of the applied voltage, in accord with theory. The cross-sectional areas of the barriers of Fig. 4 are about 0.01 sq cm.

Step and graded barriers have also been produced in germanium by techniques of slice remelting and spot remelting. In slice remelting a slice of the order of 1x1x0.2 cm in dimensions is heated in a temperature gradient so as to produce a remelt boundary essentially parallel to the large faces. By lowering the temperature the solid-liquid interface is caused to advance in a direction normal to the large faces, producing a normal segregation of solutes in the remelt zone. (A heating technique of this general nature, used to produce pn barriers by a principle differing from that discussed here, has been described briefly elsewhere.[8])

In spot remelting a small hemispherical remelt zone is produced by heating a very small spot at the surface of a block or slice and back-freezing is made to occur in a radial direction by lowering the temperature. For a hemispherical remelt zone, the length of the intermediate region, l_{pn}, is $l_{pn} = r_o - r_{pn}$, where r_o is the radius of the remelt zone at the start of refreezing and r_{pn} is the radius of the graded barrier. It is readily shown that

$$l_{pn} = r_o [1 - (1 - g_{pn})^{1/3}]. \qquad [10]$$

Properties of pn barriers produced by slice and spot remelting were comparable to those shown in Fig. 4. Cross sections of slice and spot remelts appear in Fig. 5, the boundaries appearing therein being step barriers revealed by etching.

By suitable control of experimental conditions, by simple remelting, npn transistors have been produced in which α, the current multiplication factor, has been greater than 0.9 and collector resistance has been greater than one megohm.

Summary and Discussion

The formation and slow solidification of a molten zone in a homogeneous ingot results in a step in solute concentration at the remelt boundary and a gradient in concentration in the remelt zone. On the basis of simplifying assumptions the magnitudes of the step and the gradient have been expressed analytically. The magnitude of the step has been shown to be independent of the volume of the zone.

By using two solutes having unequal distribution coefficients, and properly chosen initial concentrations, remelting can produce step, graded, or npn barriers in a variety of shapes and sizes. Experimental results confirm simple theory for such barriers.

The remelt technique can have other applications. For example, it provides a means of producing a diffusion couple for the determination of diffusion constants. The crystal structure across such a couple would be essentially continuous, since the unmelted portion serves as a seed, and, in contrast to techniques such as welding, a minimum of faults would be produced at the junction. In general it provides a simple means of altering in discrete regions, such as surface layers, a composition-sensitive property of a substance. While this paper has been confined to starting materials of homogeneous composition and a particular direction of freezing of the remelt zone, such restrictions are unnecessary. Moreover, an additional degree of control of the concentrations in the remelt zone can be had by adding solutes before or during the remelt process.

Acknowledgments

The writer wishes to thank D. Dorsi for preparation of the germanium ingots, M. C. Waltz for electrical measurements and fabrication of the pn diodes, J. D. Struthers for help with the radioactive antimony, E. E. Thomas for photomicrographs, and J. H. Scaff and E. E. Schumacher for counsel and encouragement.

References

[1] P. W. Bridgman: *Proc.* Amer. Acad. Arts and Sciences (1925) **60**, p. 305.

[2] A. Weissberger: *Technique of Organic Chemistry.* Vol. III, Chap. VI.

[3] J. H. Scaff, H. C. Theuerer, and E. E. Schumacher: P-type and N-type Silicon and the Formation of the Photovoltaic Barrier in Silicon Ingots. *Trans.* AIME (1949) **185**, p. 383; JOURNAL OF METALS (June 1949).

[4] W. G. Pfann: Segregation of Two Solutes, with Particular Reference to Semiconductors. *Trans.* AIME (1952) **194**, p. 861; JOURNAL OF METALS (August 1952).

[5] W. G. Pfann: Principles of Zone-Melting. *Trans.* AIME (1952) **194**, p. 747; JOURNAL OF METALS (July 1952).

[6] W. G. Pfann and K. M. Olsen: Purification and Prevention of Segregation in Single Crystals of Germanium. *Physical Review* (1953) **89**, p. 322.

[7] J. D. Struthers, H. C. Theuerer, E. Buehler, and J. A. Burton: Paper presented at AIME Meeting, New York, Feb. 18, 1952.

[8] W. Shockley: The Theory of pn Junctions in Semiconductors. *Bell System Technical Journal* (1949) **28**, p. 335.

[9] K. Lehovec and E. Belmont: Preparation of Junctions in Single Crystals by Surface Melting. *Bull.* Amer. Phys. Soc. (1953) **28**, p. 68.

Hydrogen Embrittlement of Steels

by Jack T. Brown and William M. Baldwin, Jr.

The effect of hydrogen on the ductility, ϵ, of SAE 1020 steel at strain rates, $\dot{\epsilon}$, from 0.05 in. per in. per min to 19,000 in. per in. per min and at temperature, T, from +150° to —320°F was determined. The ductility surface of the embrittled steel reveals two domains: one in which $(\partial\epsilon/\partial\dot{\epsilon})_T > 0$, $(\partial\epsilon/\partial T)_{\dot{\epsilon}} < 0$, and the other in which $(\partial\epsilon/\partial\dot{\epsilon})_T > 0$, $(\partial\epsilon/\partial T)_{\dot{\epsilon}} > 0$. The usual "explanations" of hydrogen embrittlement are in accord with the first of these domains only.

THE purpose of this investigation was a fuller characterization of the effects of varying temperature and strain rate on the fracture strain of hydrogen-charged steel. To be sure, it is known that low and high temperatures remove the embrittlement that hydrogen confers upon steels at room temperature,[1-4] see Fig. 1a and b, and that high strain rates have a similar effect,[5-7] see Fig. 2a, b, and c. However, the general effect of these two testing conditions on the fracture ductility of hydrogen-charged steels is not known, i.e., the three-dimensional graphical representation of fracture ductility as a function of temperature and strain rate is not known—only two traverses of the graph are available. The need for such a graph is not pedantic. To demonstrate this point, Fig. 3a, b, and c shows three of many three-dimensional graphs, all possible on the basis of the two traverses at hand. The important point (as will be developed in the Discussion) is that each of them would indicate a different basic mechanism for hydrogen embrittlement.

It will be noted that the four types of ductility surfaces in Fig. 3a, b, and c may be characterized as follows:

Type a $\left(\frac{\partial\epsilon}{\partial\dot{\epsilon}}\right)_T > 0$, $\left(\frac{\partial\epsilon}{\partial T}\right)_{\dot{\epsilon}} < 0$

Type b $\left(\frac{\partial\epsilon}{\partial\dot{\epsilon}}\right)_T < 0$, $\left(\frac{\partial\epsilon}{\partial T}\right)_{\dot{\epsilon}} > 0$

Type c $\left(\frac{\partial\epsilon}{\partial\dot{\epsilon}}\right)_T < 0$, $\left(\frac{\partial\epsilon}{\partial T}\right)_{\dot{\epsilon}} < 0$

Type d $\left(\frac{\partial\epsilon}{\partial\dot{\epsilon}}\right)_T > 0$, $\left(\frac{\partial\epsilon}{\partial T}\right)_{\dot{\epsilon}} > 0$

Material and Procedure

Tensile tests were made at various temperatures and strain rates on a commercial grade of ¾ in. round SAE 1020 steel in both a virgin state and as charged with hydrogen. The steel was spheroidized at 1250°F for 168 hr to give the unembrittled steel the lowest possible transition temperature.

The steel was charged cathodically with hydrogen as follows: The specimen was attached to a 6 in. steel wire, degreased for 5 min in trichlorethylene, rinsed with water, and fixed in a plastic top in the center of a cylindrical platinum mesh anode. The assembly was placed in a 1000 milliliter beaker containing an electrolyte of 900 milliliters of 4 pct sulphuric acid and 10 milliliters of poison (2 grams of yellow phosphorous dissolved in 40 milliliters of carbon disulphide). A current density of 1 amp per sq in. was used which developed a 4 v drop across the two electrodes. All electrolysis was carried on at room temperature.

Temperatures for tensile tests were obtained by immersing the specimens in baths of water (+70° to +150°F), mixtures of liquid nitrogen and isopentane (+70° to −240°F), and boiling nitrogen (−240° to −320°F).

Specimens were tested in tension at strain rates of 0.05, 10, 100, 5000, and 19,000 in. per in. per min. The 0.05 and 10 in. per in. per min strain rates were obtained on a 10,000 lb Riehle tensile testing machine, the 100 in. per in. per min rate on a hydraulic-type draw bench with a special fixture, and the 500 and 19,000 in. per in. per min rates on a drop hammer.

The fracture ductility of hydrogen-charged steel at room temperature and normal testing strain rates (~0.05 in. per in. per min) is a function of electrolyzing time, dropping to a value that remains constant after a critical time.[7]* Under the conditions of this research the saturated loss in ductility occurred at approximately 30 min, see Fig. 4, and a 60 min charging time was taken as standard for all subsequent tests.

* The hydrogen content of the steel continues to increase with charging time even after the ductility has leveled off to its saturated value.[7]

After charging the steel with hydrogen, the surface was covered with blisters. These have been described by Seabrook, Grant, and Carney.[7] The original diameter of the specimen was not reduced by acid attack, even after 91 hr.

Results

The ductility of both uncharged and charged specimens is given as a function of strain rate in Fig. 5, and as a function of temperature at four different strain rates in Fig. 6. These results are assembled into a three-dimensional graph in Fig. 7. It is seen that the locus of the minima in the ductility curves of the charged steels divides the ductility surface into two domains. At temperatures below the minima,

$$\left(\frac{\partial\epsilon}{\partial T}\right)_{\dot{\epsilon}} < 0 \text{ and } \left(\frac{\partial\epsilon}{\partial\dot{\epsilon}}\right)_T > 0$$

J. T. BROWN, formerly graduate student, Case Institute of Technology, is now associated with Westinghouse Research Laboratories, Pittsburgh, and W. M. BALDWIN, JR., Member AIME, is Research Professor, Metals Research Laboratory, Case Institute of Technology, Cleveland.

Discussion on this paper, TP 5665E, may be sent, 2 copies, to AIME by April 1, 1954. Manuscript, July 27, 1953. New York Meeting, February 1954.

This paper is based on a thesis by J. T. Brown submitted in partial fulfillment of requirements for the degree of Master of Science to Case Institute of Technology.

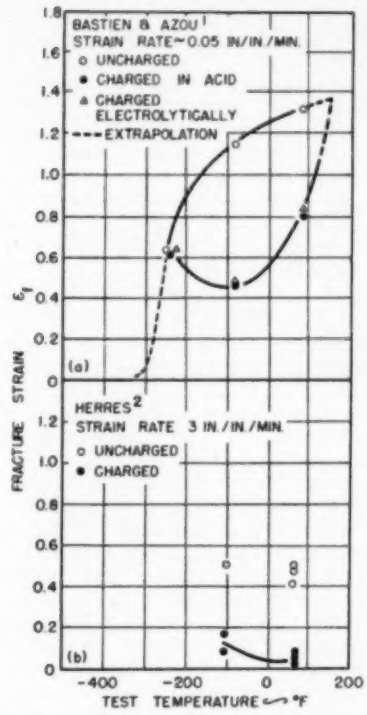

Fig. 1—Fracture strain as a function of testing temperature in steel.

(cf. for example, lines i and ii in Fig. 7); at temperatures above the minima,

$$\left(\frac{\partial \epsilon}{\partial T}\right)_{\dot{\epsilon}} > 0 \text{ and } \left(\frac{\partial \epsilon}{\partial \dot{\epsilon}}\right)_{T} > 0$$

(cf. for example, lines iii and iv in Fig. 7). These domains correspond to surfaces of types *a* and *d*, respectively, and the assembly corresponds to the prototype given in Fig. 3c.

Discussion

Of the two types of ductility surfaces which characterize hydrogen embrittlement only the type *a* surface has been rationalized. Zapffe and Sims[6] and Zapffe[3] picture hydrogen embrittlement to result from the precipitation of hydrogen in "substructure disjunctions" or "voids" at pressures sufficient to force the metal asunder. Straining is presumed to enlarge the imperfections, thus reducing the hydrogen pressure. Further precipitation of hydrogen is required to maintain or develop a disruptive pressure. With these premises, Zapffe proceeds to two conclusions: "If the rate of strain is increased . . . until the rate of decrease in P_{H_2} exceeds the rate of restoration through further precipitation of H, the apparent embrittlement should decrease." This prediction states that

$$\left(\frac{\partial \epsilon}{\partial \dot{\epsilon}}\right)_{T} > 0.$$

"The effect of temperature has an obviously similar relationship since the pressure of a gas phase likewise decreases with decreasing temperature. Thus there will be a critical temperature, also a critical rate of cooling, for any given set of conditions, such that the critical embrittlement pressure P_{H_2} is decreased more rapidly than it is replenished by precipitating H, and embrittlement is observed to decrease." This states that

$$\left(\frac{\partial \epsilon}{\partial T}\right)_{\dot{\epsilon}} < 0.$$

These two conditions are those characterizing a ductility surface of type *a*.

Petch and Stables[8] extend Orowan's rationalization of the delayed fracture of glass to the case of hydrogen embrittlement. They point out that if hydrogen gas is adsorbed on the internal surface of microcracks, the critical stress for extension of the crack in the Griffith relationship is lowered. "The extension of a crack under stress will take place in steps which occur when hydrogen solute atoms arrive at its edge in the course of diffusion." Since the proposed embrittling mechanism is diffusion-controlled, the authors point out that at high strain rates the metal should be ductile and adduced the data of Fig. 2c to support their conclusion. Again, this mechanism requires that

$$\left(\frac{\partial \epsilon}{\partial \dot{\epsilon}}\right)_{T} > 0.$$

Although the authors made no statement regarding the effects of temperature it follows that if the arrival of the hydrogen to the microcracks is diffusion-controlled, and since the diffusion rate decreases with decreasing temperature, then decreasing the test temperature at constant strain rate should increase the ductility, i.e.,

$$\left(\frac{\partial \epsilon}{\partial T}\right)_{\dot{\epsilon}} < 0.$$

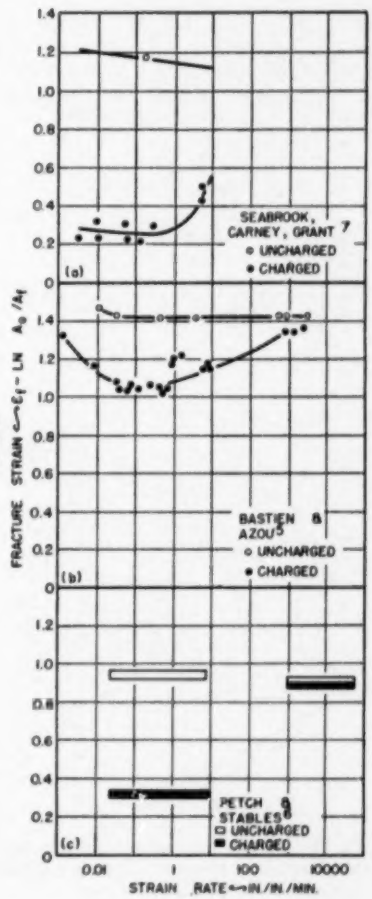

Fig. 2—Fracture strain as a function of strain rate in steel.

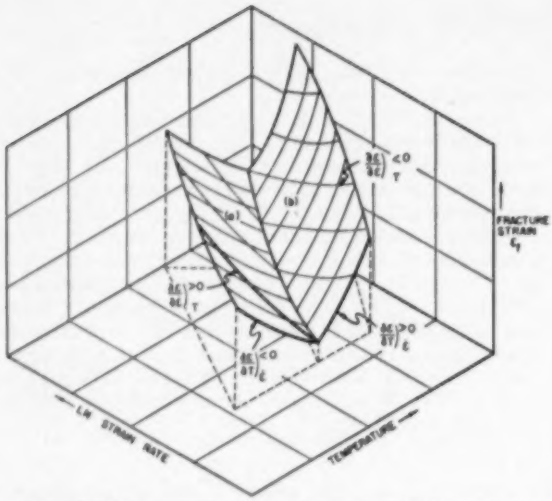

Fig. 3a—Possible construction of sheets type *a* and *b*. Dark lines indicate known traverses.

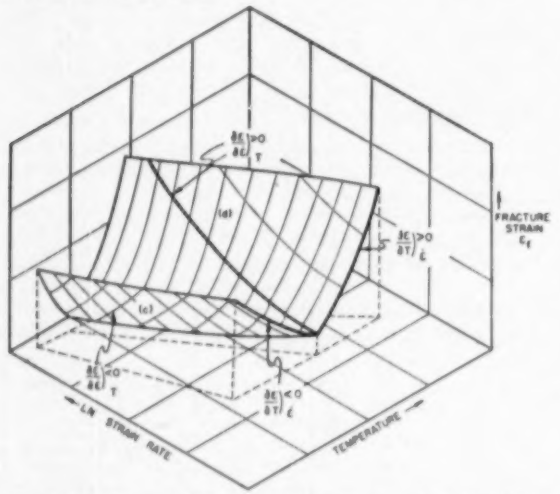

Fig. 3b—Possible construction of sheets type *c* and *d*. Dark lines indicate known traverses.

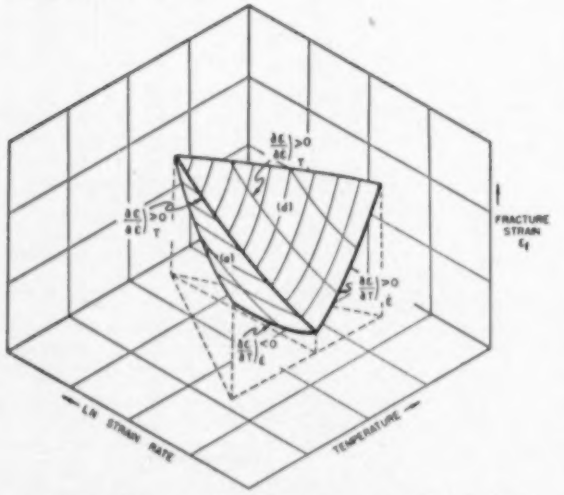

Fig. 3c—Possible construction of sheets type *a* and *d*. Dark lines indicate known traverses. This was actually how hydrogen embrittlement was observed to behave.

It is seen that the mechanism proposed by Petch and Stables, like Zapffe and Sims, corresponds to a ductility surface of type *a*.

Both these mechanisms are variations on a theme: hydrogen embrittlement is presumed to depend upon the competition of two rates, the one being the rate of straining of the metal, the second being the rate of the embrittling controlling process (diffusion or precipitation), the latter rate being presumed to increase with increasing temperature. If the first rate predominates the metal is ductile, if the latter predominates the metal is brittle.

Surfaces of types *b*, c, and *d* can be rationalized by extension of the competitive rate hypothesis. If competition exists between the rate of straining and the rate of some process which renders the metal *ductile*, the latter rate being presumed to increase with increasing temperature, a surface of type *b* will result. The behavior of an overaging alloy on deformation illustrates this situation. Here overaging is a process that renders the alloy more ductile; its rate increases with increasing temperature. The ductility of such alloys as a function of strain rate and temperature yields a surface of type *b* (cf., for example, Fig. 10 of ref. 9). At constant strain rate, the ductility increases with increasing temperature because the rate of overaging increases with increasing temperature. At constant temperature, the ductility decreases with increasing strain rate, since the benign effect of the overaging process is outstripped. Another example is the case of a hydrogen-charged steel in the process of degassing, since the degassification is a process rendering the metal ductile and its rate increases with increasing temperature.[5, 7, 8, 10, 11] The increase in ductility of charged steel at temperatures above the minimum has been attributed to degassing,[†] but such an explanation should not be indiscriminately put forward for such curves. The data in the present research represent a case in point, for the increase in ductility at temperatures above the minimum in Fig. 6, form a *d* surface and not the *b* surface that would be required, if degassing were the real explanation.[†] A description of hydrogen embrittlement based on the drag of a Cottrell atmosphere of hydrogen atoms on dislocations interfering with "normal" straining and leading to premature or brittle fractures also falls in this same class of theories and predicts a type *b* surface. In this case even though the drag of the Cottrell atmosphere itself is embrittling it is not the rate process that is pertinent to the problem. What is pertinent is the diffusion of the hydrogen which as it increases with increasing temperature decreases the drag and renders the metal more ductile, i.e., $(\partial\epsilon/\partial T)_{\dot{\epsilon}} > 0$. Conversely at constant temperature, the diffusion rate cannot keep pace with an increased strain rate, thus increasing the drag and embrittling the metal, i.e., $(\partial\epsilon/\partial\dot{\epsilon})_T < 0$.

To extend the competitive rate hypothesis to describe surfaces of type *c* and *d*, the nature of temperature-sensitive process must be changed from one which increases with temperature to one that decreases with temperature. Such rates are found in super-cooled reactions such as the isothermal austenite-pearlite reaction at temperatures above the pearlite nose. If the temperature-sensitive process

† The authors have no doubt that degassing is a factor in the hydrogen embrittlement of steels and suggest that a full characterization of the ductility surface of a charged steel would involve three domains instead of two, arranged in the manner of Fig. 8. Bastien and Azou's curve of Fig. 2b is quite probably a traverse across the type *a* and *b* or *d* and *b* surfaces of Fig. 8.

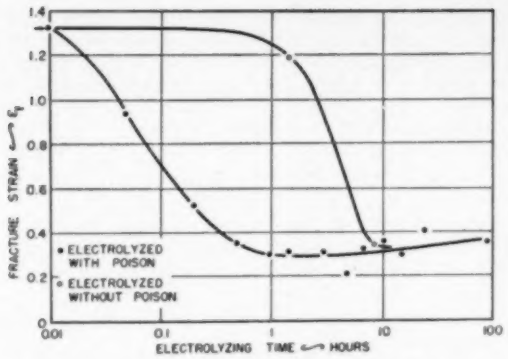

Fig. 4—Fracture strain of spheroidized SAE 1020 steel as a function of hydrogen charging time. Note accelerating effect of poison in electrolyte as well as gentle upswing of curves at long times.

renders the metal ductile, a ductility surface of type *c* results A type *d* surface results if the process is embrittling, since at constant strain rate an increase

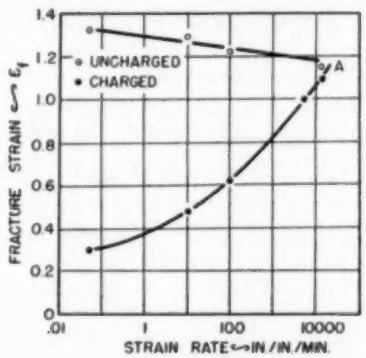

Fig. 5—Fracture strain as a function of strain rate in a charged and uncharged, spheroidized SAE 1020 steel at room temperature.

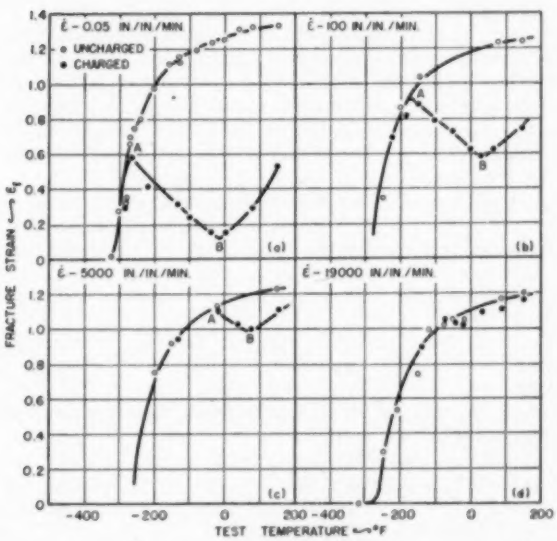

Fig. 6—Fracture strain of spheroidized 1020 steel with and without hydrogen embrittlement as a function of test temperature and strain rate. The two curves join at points *A*. A minimum in the curves exists at points *B*.

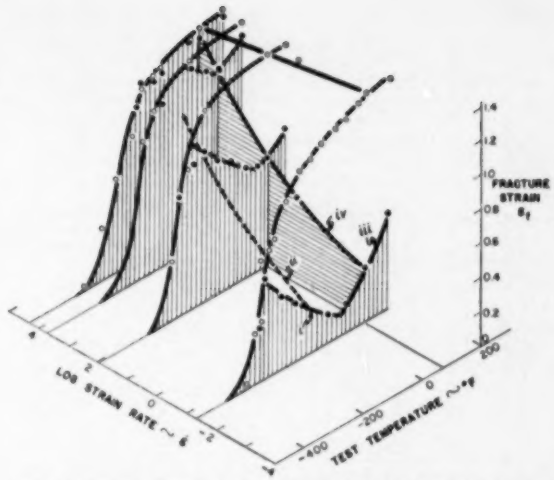

Fig. 7—Fracture strain of spheroidized SAE 1020 steel with and without hydrogen embrittlement as a function of temperature and strain rate.

in temperature decreases the rate of the embrittling process and thus increases the ductility, i.e.,

$$\left(\frac{\partial \epsilon}{\partial T}\right)_{\dot{\epsilon}} > 0,$$

while at constant temperature an increase in strain rate increases the ductility for the same reasons that it did in the case of the type *a* surface.

Undoubtedly there is significance in the fact that the two surfaces described by the present experimental results (types *a* and *d*) if they are to be rationalized by competitive rate mechanisms, have one feature in common; in competition with the strain rate is a rate of an embrittling process irrespective of whether the rate increases or decreases with temperature. Since an embrittling process is common to both ductility surfaces, types *a* and *d*, it may be the same physical reaction in both cases.

A physical reaction which increases in rate with increasing temperature at low temperatures and decreases in rate with increasing temperature at high temperatures is not uncommon in the general realm of kinetics. The logarithm of the rate of such re-

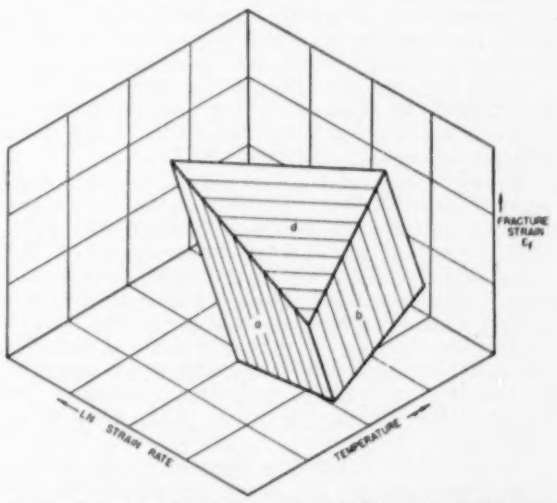

Fig. 8—Proposed full characterization of hydrogen embrittlement.

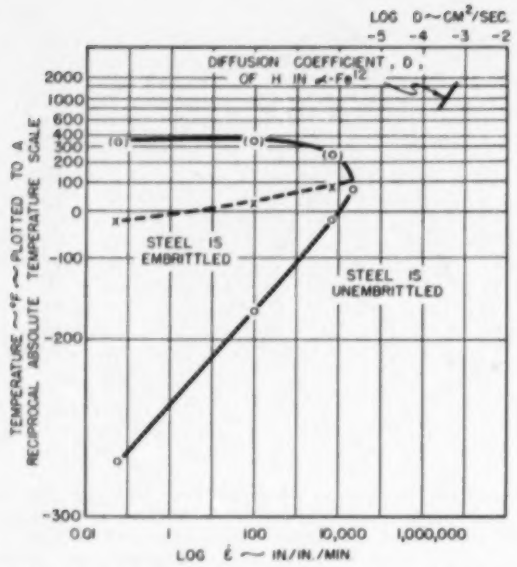

Fig. 9—A plot of temperatures at which ductility of charged steels returns to the ductility curve of uncharged steels as a function of strain rate. The circles plotted here are the points *A* of Fig. 6. Points in parentheses are extrapolated from Fig. 6. The crosses are the points *B* of Fig. 6, i.e., the temperatures and strain rates at which a minimum in the ductility curves occurred. The diffusion coefficient of hydrogen in α iron is plotted to the upper scale.

actions when plotted against the reciprocal of the absolute temperature appears as *c* curves—exemplified by the rate of growth curve of pearlite, or scaling rate curves in surface oxidation studies.

The shape of these overall rate curves is usually the product of two main factors. The first is a driving force (such as free energy) which is zero at an equilibrium temperature and which increases as reaction temperature is lowered from this point; the second is a mobility factor (such as diffusion or conductivity) which is generally of the form

$$D = D_o e^{-Q/RT}$$

such that the upper arm of the *c* curve approaches the equilibrium temperature asymptotically as the overall rate goes to zero (or log rate goes to minus infinity), and the lower arm of the *c* curve asymptotically approaches a straight line whose slope approximates the slope of the log mobility factor vs the reciprocal absolute temperature curve, i.e., $-Q/R$, as temperature goes to zero.

To obtain an approximation of the present overall rate curve, Fig. 9 is a plot of the temperature (on a reciprocal absolute temperature scale) at which the ductility of the charged steels returns to the ductility curve of the uncharged steels (points *a* in Figs. 5 and 6) as a function of strain rate (on a log scale). It is assumed that at these points there is some approximately fixed relationship between the strain rate and the rate of the embrittling reaction, so that the curve of Fig. 9 is an indication of the shape of the overall rate curve of the embrittling reaction.

There are two interesting features of the *c* curve. The upper arm of the curve asymptotically approaches a limiting temperature, and by analogy with the A_1 temperature of a pearlite curve, or the oxide dissociation temperature on a scaling rate curve, this would represent an equilibrium temperature above which hydrogen has no embrittling effect on steels. The authors know of no change in the physical state of iron-hydrogen alloys in this temperature range which would account for this behavior. The lower arm of the curve asymptotically approaches a sloping straight line. Again from the classical pattern of such curves it would be inferred that the slope of the line should approximate the slope of the diffusion coefficient of hydrogen in *a* iron. The diffusion data[12] are meager and involve large extrapolations but a rough parallelism is nevertheless observed.

It must be inferred from Fig. 9 that if a competitive rate mechanism is to explain hydrogen embrittlement, then the rate, β, of the embrittling process must in some measure depend upon strain rate, otherwise if

$$\epsilon = f_1(\dot{\epsilon}) - f_2(\beta)$$

then the minimum in the ductility curves would remain at a constant temperature which is not the case in Fig. 9.

Conclusions

1—Hydrogen depresses the ductility of mild steel within certain ranges of temperature and strain rate only.

2—Within this brittle range, a plot of the ductility vs strain rate and temperature reveals two domains, one at low temperatures in which

$$\left(\frac{\partial \epsilon}{\partial \dot{\epsilon}}\right)_T > 0, \qquad \left(\frac{\partial \epsilon}{\partial T}\right)_{\dot{\epsilon}} < 0$$

and another at high temperatures in which

$$\left(\frac{\partial \epsilon}{\partial \dot{\epsilon}}\right)_T > 0, \qquad \left(\frac{\partial \epsilon}{\partial T}\right)_{\dot{\epsilon}} > 0.$$

3—The first of these domains represents a behavior in accord with any theory—such as that of Zapffe and Sims[3] or Petch and Stables[4]—which basically hypothesizes that the ductility of steels depends upon two competitive rates: the strain rate and a rate of the embrittling reaction which increases with increasing temperature, the steel being ductile if the former rate predominates, and brittle if the latter does.

4—The second of these domains is not explained by theories of this type, nor by the assumption that the steels are degassing (though the authors feel that a third domain due to degassification of the steel in which

$$\left(\frac{\partial \epsilon}{\partial \dot{\epsilon}}\right)_T < 0 \text{ and } \left(\frac{\partial \epsilon}{\partial T}\right)_{\dot{\epsilon}} > 0$$

does exist in certain temperature and strain rate ranges).

5—If the general proposition of two competitive rates is to be applied to the second of these domains, the rate of the embrittling reaction must *decrease* with increasing temperature.

6—An approximate curve of the logarithm of the rate of the embrittling reaction as a function of the reciprocal of the absolute temperature follows the classical pattern of rate curves of reactions that

occur spontaneously below an equilibrium temperature, i.e., a *c* curve.

Acknowledgments

This work was conducted in cooperation with the Office of Naval Research, U. S. Navy. The advice and help of L. J. Ebert, I. Rozalsky and other members of the Metals Research Laboratory at Case Institute of Technology is greatly appreciated. T. S. Howald, Chase Brass and Copper Co., Inc., kindly loaned the platinum electrodes. The authors wish to thank the Westinghouse Electric Corp. for providing a Fellowship to one of us. (J.T.B.).

References

[1] P. Bastien and P. Azou: Effect of Hydrogen on the Deformation and Fracture of Iron and Steel in Simple Tension. *Proc.* World Metallurgical Congress. ASM (1951) pp. 535-552.

[2] S. H. Herres: Practical Importance of Hydrogen in Metal-Arc Welding of Steel. *Trans.* ASM (1947) **39**, pp. 162-192.

[3] C. Zapffe: Discussion to ref. 2. *Trans.* ASM (1947) **39**, pp. 190-191.

[4] J. D. Hobson and J. Hewitt: The Effect of Hydrogen on the Tensile Properties of Steel. *Journal* Iron and Steel Inst. (1953) **173**, pp. 131-140.

[5] P. Bastien and P. Azou: Influence de l'amptitude et de la vitesse des deformations plastiques sur la segregation de la hydrogene dans le fer et les aciers. *Comptes Rendues* (1951) **232**, pp. 69-71.

[6] N. J. Petch and P. Stables: Delayed Fracture of Metals under Static Load. *Nature* (1952) **169**, p. 842.

[7] J. B. Seabrook, N. J. Grant, and D. Carney: Hydrogen Embrittlement of SAE 1020 Steel. *Trans.* AIME (1950) **188**, pp. 1317-1321; JOURNAL OF METALS (November 1950).

[8] C. A. Zapffe and C. E. Sims: Hydrogen Embrittlement, Internal Stress and Defects in Steel. *Trans.* AIME (1941) **145**, pp. 225-259.

[9] S. Epstein: Aging of Iron and Steel. *Metals Handbook* (1948) pp. 438-443. Cleveland ASM.

[10] C. E. Sims, G. A. Moore, and D. W. Williams: The Effect of Hydrogen on the Ductility of Cast Steels. *Trans.* AIME (1948) **176**, pp. 283-308; METALS TECHNOLOGY (October 1948).

[11] C. E. Sims: Hydrogen Elimination by Aging. *Trans.* AIME (1950) **188**, p. 1321; JOURNAL OF METALS (November 1950).

[12] W. Geller and Tak-Ho Sun: Einfluss von Legierungszusätzen auf die Wasserstoffdiffusion im Eisen und Beitrag zum System Eisen-Wasserstoff. *Archiv Eisenhüttenwesen* (1950) **21**, pp. 423-430.

Technical Note

On the Temperature Range of the Martensitic Transformation In the Cu-Zn System

by A. L. Titchener and M. B. Bever

FROM their investigation of the martensitic transformation in Cu-Zn alloys, Greninger and Mooradian[1] concluded that there was no critical temperature at which martensite formation began in this system. Recent unpublished work by Genevray[2] with two compositions of brass revealed the existence of a critical temperature, which is a function of composition and stress. In the work reported here the temperature range of the martensitic reaction was studied as a function of composition in high purity Cu-Zn alloys.

The specimens were about 4 in. long with a diameter of 1/16 in.; their compositions are given in Table I. They were heated under vacuum for 5 min at 5° to 10°C below the temperature of incipient melting, and quenched into brine at about −10°C. Specimens of alloys C, D, E and F were obtained with little or no precipitated α phase. Many attempts yielded only three usable specimens of alloy B, and even these contained appreciable amounts of α. All efforts failed to preserve metastable β in alloy A (containing 38.02 pct Zn and 0.002 pct each of Pb and Fe).

A. L. TITCHENER is Lecturer, School of Engineering, Auckland University College, Auckland, New Zealand, and M. B. BEVER, Member AIME, is Associate Professor, Dept. of Metallurgy, Massachusetts Institute of Technology, Cambridge, Mass.

TN 199E. Manuscript, Oct. 7, 1953.

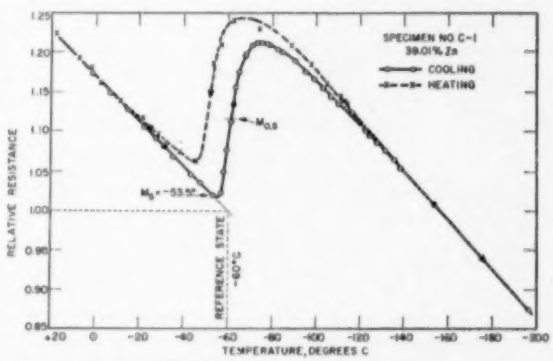

Fig. 1—Relative electrical resistance as a function of temperature in a typical experiment.

The transformation was studied by measuring the electrical resistance during continuous cooling and heating of each specimen at similar rates. The cooling media were alcohol with dry ice from room temperature to −78°C and a bath of petroleum ether and methyl cyclohexane (75:25), cooled by liquid nitrogen, from −78° to about −150°C. Readings were also taken at −195°C in liquid nitrogen.

Fig. 1 illustrates a typical experiment. The relative resistance is obtained by assuming the known

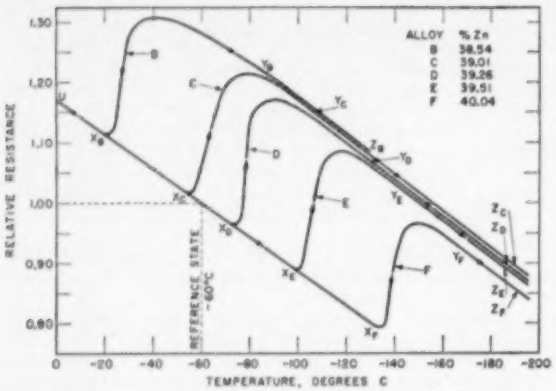

Fig. 2—Relative electrical resistance as a function of temperature during cooling of alloys B to F.

or extrapolated resistance of the parent β as unity at a reference temperature (e.g., −60°C), and expressing resistances at other temperatures as fractions of this reference value. The M_s temperature is taken at the point where the cooling curve first deviates from a straight line. The M_f temperature is taken at the point where the heating curve diverges from the cooling curve. Corresponding criteria are used for the reverse transformation during heating. Since they are fairly sharply defined, M_s temperatures are given to the nearest 0.5°C in Table I. The other phenomena, by comparison, are difficult to distinguish, and the respective temperatures are stated to the nearest 5°C.

The reversible nature of the transformation[1-3] was confirmed, and the hysteresis loops were studied. The relative resistance of different samples of a given composition is a unique function of temperature before and after transformation, but not within the transformation range. Here factors other than temperature apparently also enter. Grain size, grain orientation, and any α present are the most likely variables.

Because M_f and the temperatures for the beginning and end of the reverse transformation are not known precisely, the degree of hysteresis is expressed as the temperature difference between defined "50 pct transformation" points on cooling and heating. These points are the mean of maximum and minimum resistance during transformation. Such a point, labelled $M_{0.5}$, is indicated for cooling in Fig. 1. The hysteresis (Table I) decreases fairly consistently with increasing zinc content.

When M_s temperature is plotted against alloy composition, all points fall on a straight line with a minor deviation for alloy E. The slope of this line is −7.4°C per 0.1 pct Zn. This marked decrease of M_s with increasing zinc is consistent with a statement of Isaitschew, Kaminsky, and Kurdyumov.[2] Also a graph of M_s vs zinc content given by Kurdyumov[4] shows a slightly curved line sloping from 0°C at 38 pct Zn to −200°C at 42 pct Zn with an average slope of −5°C per 0.1 pct Zn. The absolute values of M_s found in the present investigation are comparable with those read from Kurdyumov's diagram at about 38.5 pct Zn, but at higher zinc contents the present values are lower than those given by Kurdyumov. Data for Cu-Al alloys[5] and for some binary alloy systems of titanium[6] give slopes of M_s comparable with those reported here.

The cooling curves for alloys B to F shown in Fig. 2 are averages for two or three specimens of each composition. Since relative resistances are plotted, the resistance-temperature relation of the untransformed β, regardless of composition, is described by a single straight line U-X_F. The curves X_B-Y_B, X_C-Y_C, etc., represent the progress of the transformation; Y_B-Z_B, Y_C-Z_C, etc., refer to the completely transformed alloys. Points X_B, X_C, etc., correspond to the M_s temperatures of the five compositions. The curves exhibit fairly consistent trends. The temperature coefficient of resistance of martensite differs little from that of the parent β, as demonstrated by the almost equal slopes of UX and YZ. That the portions YZ of the curves do not coincide presumably reflects an effect of composition on the difference between the resistivity of parent β and derived martensite. This difference decreases steadily as zinc content rises. The differences in slope and in general shape of the portions XY of the curves express geometrically two facts: the temperature difference between M_s and M_f depends on composition, and second, the transformation is affected to some extent by factors other than temperature and composition.

Table I. Composition of Alloys and Transformation Data

Alloy	Composition, Wt Pct Cu	Composition, Wt Pct Zn*	Transformation Temperature, °C: Cooling M_s	Cooling Mean M_s	Cooling M_f	Heating Start	Heating End	Mean Hysteresis, °C at $M_{0.5}$†
B	61.46	38.54	−18		−110	−35	−10	
			−23	−20	−70	—	—	14.5
			−23		−70	−40	−25	
C	60.99	39.01	−53.5		−130	?	+20	
				−54.5				9.5
			−55.5		−100	−70	−15	
D	60.74	39.26	−72.5		−130	−85	−50	
				−72.5				9.5
			−72.5		−125	−85	−30	
E	60.49	39.51	−98		−155	−115	−65	
				−97.5				8.5
			−97		−140	−110	−70	
F	59.96	40.04	−131.5		−180	−145	−105	
				−131				6
			−130.5		−185	−155	−115	

* Zinc by difference. Pb and Fe each 0.001 pct in alloys B and D, and 0.002 pct in alloys, C, E, and F.
† $M_{0.5}$ denotes "50 pct transformation" point as explained in the text.

Acknowledgment

This investigation is part of a program sponsored at Massachusetts Institute of Technology by the Office of Naval Research. The authors are greatly indebted to Professor Morris Cohen for his interest and advice. Thanks are due the American Brass Co., which supplied the alloys and their analysis. One of the authors (A. L. T.) thanks the Foreign Student Summer Project at the Massachusetts Institute of Technology for support during this work.

References

[1] A. B. Greninger and V. G. Mooradian: *Trans.* AIME (1938) **128**, p. 337.

[2] R. M. Genevray: The Martensitic Transformation in Muntz Metal. Master's Thesis, Dept. of Metallurgy, M.I.T., 1953.

[3] I. Isaitschew, E. Kaminsky, and G. V. Kurdyumov: Discussion of ref. 1. *Trans.* AIME (1938) **128**, p. 361.

[4] G. V. Kurdyumov: *Zhur. Tekhn. Fiziki* (1948) **18**, p. 999.

[5] V. Gawranek, E. Kaminsky, and G. V. Kurdyumov: *Metallwirtschaft* (1936) **15**, p. 370.

[6] P. Duwez: *Trans.* ASM (1953) **45**, p. 934.

On the Torsional Deformation and Recovery Of Single Crystals

by S. S. Hsu and B. D. Cullity

The stress distribution at the surface of a twisted cylinder is analyzed along the boundary of a slip plane of arbitrary orientation and this analysis is applied to the torsion of cylindrical crystals of magnesium. A criterion for slip is developed and the critical resolved shear stress of magnesium in torsion is found to be 0.038 kg per sq mm. The mechanism of torsional deformation in magnesium and aluminum is described, as well as the relaxation of a twisted crystal at elevated temperatures.

THERE has been considerable fundamental study of the mechanism of slip occurring during deformation in tension and compression but comparatively little attention has been paid to the mechanism of torsional deformation. This paper is concerned with the way in which a single crystal deforms in static torsion and with the phenomenon of untwisting which a twisted crystal undergoes during annealing. Particular attention is paid to the application of the critical resolved shear stress law to torsional deformation.

Probably the most likely mode of torsional deformation that can be imagined consists of rotation of one part of the crystal relative to another on the active slip plane. Here the most interesting feature is the slip direction. If a cylindrical single crystal is twisted about its axis and if, to consider the simplest case, the active slip plane is normal to the specimen axis, then the direction of gross slip at any point must always be at right angles to the radius drawn to that point. It follows that the crystallographic direction of slip must be continually changing, in sharp contrast to slip in tension which occurs in a crystallographically constant direction.

Extensive investigations of slip in torsion have been made by Gough and his associates.[1] They made torsional fatigue tests on metal single crystals belonging to a number of different crystal systems and observed, with a microscope, the appearance of slip lines on the surface and of strain markings on the transverse cross section of cylindrical specimens. They concluded that the critical resolved shear stress law was just as valid in torsion as in tension, in the sense that slip occurred on that plane and in that direction in which the resolved shear stress was a maximum. They also established that the operative slip planes and directions were the same as in tension. They did not, however, measure the critical resolved shear stress in torsion nor, in fact, did they establish that a *critical* value of the resolved shear stress was necessary for the initiation of slip. Their investigations were, moreover, restricted to torsional fatigue tests which necessarily involve small strain amplitudes.

Wilman,[2] studying crystal growth and the abraded surfaces of crystals, observed crystal fragments

S. S. HSU, formerly graduate student, Dept. of Metallurgy, University of Notre Dame, is now with the Division of Chemical Engineering, University of Illinois, Urbana, Ill., and B. D. CULLITY, Member AIME, is Associate Professor of Metallurgy, University of Notre Dame, Notre Dame, Ind.

Discussion on this paper, TP 3719E, may be sent, 2 copies, to AIME by April 1, 1954. Manuscript, Sept. 14, 1953. New York Meeting, February 1954.

This paper is based on a dissertation by S. S. Hsu submitted in partial fulfillment of the requirements for the degree of Doctor of Philosophy to the Engineering Div. of the Graduate School of the University of Notre Dame.

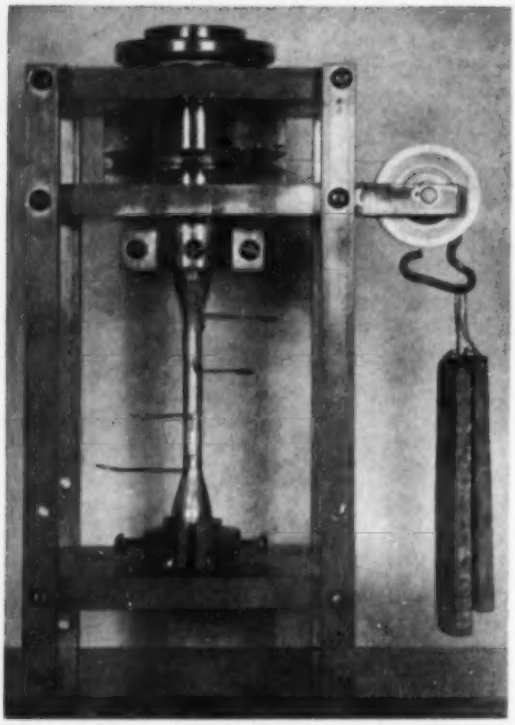

Fig. 1—Torsion machine with specimen in place and strain gages mounted on specimen.

rotated relative to one another and was apparently the first to suggest the notion of "rotational slip." The connection between rotational slip and slip in torsion will be discussed later in this paper.

Mechanical methods of measuring torsional strain were supplemented in the present work by the X-ray diffraction method devised by Cullity and Julien[5] for measuring the torsion of a crystal lattice. Since this method requires specimens highly transparent to X-rays, magnesium and aluminum were the chief crystals investigated. Magnesium was chosen for most of the deformation studies since the fact that it normally has only one slip plane simplified the interpretation of the results; aluminum was used for the recovery (untwisting) experiments in order to avoid any oxidation that might occur during the long annealing periods.

Torsional Deformation

Procedure: Cylindrical single crystal specimens of high purity aluminum and magnesium were used in the torsion experiments. They had a reduced center section (Fig. 1), ¼ in. in diameter over a 2 in. gage length, and large end sections ½ in. in diameter. They were grown from aluminum stated to contain 0.004 pct total impurities and from magnesium stated to contain less than 0.024 pct total impurities.

Table I. Critical Torque and Rigidity Modulus

Specimen	ϕ, Degrees	r, Mm	T_c, Kg-Mm	G, Kg per Sq Mm
Mg-9	30	3.09	2.21	1700
Mg-1	32	3.03	2.23	1530
Mg-8	38	3.11	2.80	1650
Mg-6	45	3.10	4.06	1690
Mg-3	52	3.18	7.03	1760

The single crystal specimens were prepared by the Bridgman method in a split graphite mold, and were examined both by X-ray diffraction and by macroetching. Only fairly perfect crystals were chosen for the experimental work, namely, those showing no more than 0.5 degree of disorientation as measured by spread of Laue spots. Their orientations were determined by the back-reflection Laue method.

Specimens were twisted in the torsion machine shown in Fig. 1, which also illustrates the appearance of a specimen after considerable torsion. The lower end of the specimen was fixed tightly into the base of the machine and the upper end was clamped into a rotatable shaft at the upper part of the machine. The specimen was twisted by allowing known loads to rotate the shaft through the attached pulley. Friction between moving parts of the machine was minimized by using ball bearings. The load required to overcome the remaining frictional forces was determined before each experiment by a blank test without the specimen.

This torsion machine was bolted on the table of a disassembled transit and could be rotated freely about a vertical axis. Two or four stiff metal wires with bent sharp tips were cemented normal to the surface of each specimen usually one day before testing, along an approximately vertical line, to serve as strain gages. The amount of torsional strain in terms of angle of twist betwen gages was obtained by observing the initial and final angular positions of the transit table when the tips of the gages had been brought into the same vertical reference plane. This plane, parallel to the specimen axis, was defined by the transit telescope which was mounted near the torsion machine and was free to rotate only about a horizontal axis. With this arrangement, an angular displacement of ½ min of arc on the specimen surface could be accurately detected.

The torsion machine was so designed that the specimen could be examined by X-rays before, during, or after the deformation process. A General Electric CA-7 X-ray tube was used: its fine line source permitted patterns to be made either by the ordinary Laue or focusing Laue techniques.

Critical Resolved Shear Stress: Some magnesium crystals were given a careful metallographic polish in order that any surface markings produced by

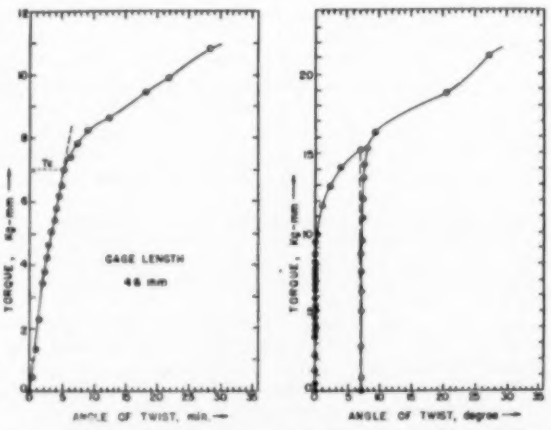

Fig. 2—Curve of torque vs angle of twist for magnesium crystal. $\phi = 52°$.

torsion could be observed. After moderate torsion, macroscopically visible slip traces appeared on the surface of these specimens and the direction of these traces, together with the known orientation of the crystal, showed that slip was occurring on the basal plane and only on the basal plane, just as in tension.*

* Pyramidal slip can occur in magnesium in tension at room temperature under special circumstances,[5] but the basal plane is the usual slip plane.

Fig. 2 is typical of the "stress-strain" curves obtained from magnesium crystals. Actually these curves were not plotted in these units but in terms of torque T vs the angle of twist in the given gage length. The specimen has clearly behaved elastically up to the critical torque T_c, which is the torque required to start plastic deformation on the surface of the crystal. Beyond this point the deformation is plastic. If the specimen is unloaded in the plastic region and then reloaded immediately, the specimen twists elastically almost up to the point of the previous highest torque as shown in Fig. 2. If the reloading is delayed, however, the yield point on reloading becomes lower. The analogous effect in tension has been observed for a number of metals and is due to recovery at room temperature.

As shown in Table I, the critical torque T_c was found to increase as the angle ϕ, between the torsion (specimen) axis and the slip plane normal, increased. Table I also lists the radius r of each specimen and the modulus of rigidity G, as calculated from the slope of the torque vs the angle of twist curve in the elastic region. These results show that G is almost completely insensitive to crystal orientation.

In order to explain the variation of T_c with ϕ, it is necessary to analyze the stresses acting on the slip plane. When ϕ is zero, the problem is simple since the slip plane then intersects the surface of the cylinder in a circle lying in the XY plane of Fig. 3. In this case the shear stress acting on the slip plane is a maximum at the surface of the cylinder, acts in a direction tangential to the circular boundary of the slip plane, and is given at any point on the surface by

$$\tau_0 = \frac{2T}{\pi r^3} \qquad [1]$$

where T is the applied torque, and r the specimen radius.

In the general case, when ϕ is not zero, the boundary of the slip plane is an ellipse as shown in Fig. 3. Whatever the orientation of the crystal, the slip plane normal N can always be brought into the YZ plane by a suitable rotation of the specimen about its axis. The semiminor axis of the ellipse OA then coincides with the X axis and the semimajor axis OB lies in the YZ plane. The location of any point P on the ellipse can be described, for a given value of ϕ, by the angle θ between OA and OP' where P' is the projection of P on the XY plane. In this general case, the distribution of shear stress on the slip plane is rather complicated. The various stresses resulting from the applied torque are evaluated in the Appendix, where it is shown that the resultant shear stress parallel to the slip plane at a point on the specimen surface does not act in a tangential direction but at a definite angle to the tangent, except for the special cases of $\theta = 0°$ or $90°$.

At this point a decision must be made as to the proper direction in the slip plane in which to resolve

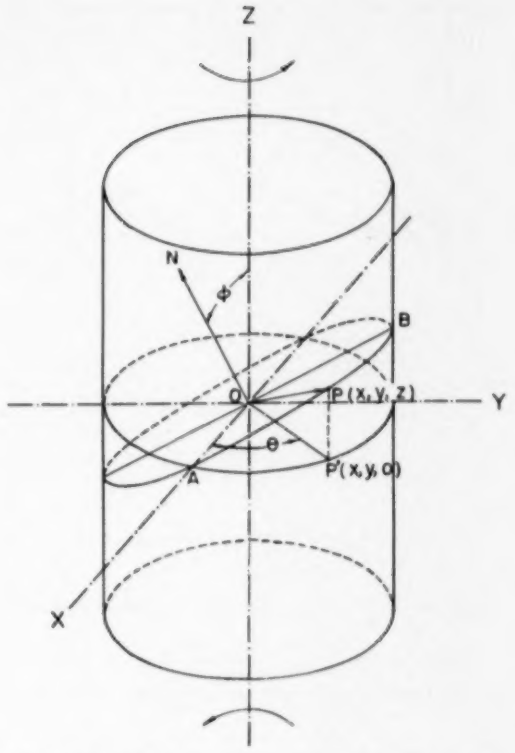

Fig. 3—Cylindrical torsion specimen in relation to rectangular axes X, Y, and Z.

this resultant stress in order to find the critical resolved shear stress. In a metal having a close-packed hexagonal structure like magnesium, there are three crystallographically equivalent slip directions 60° apart. None of these slip directions need be specifically considered, however, since macroscopic slip in torsion occurs in such a way that the effect of slip direction is averaged out. Experimentally, T_c measures the onset, not of microscopic slip, but of a considerable amount of plastic flow and this macroscopic slip must occur predominantly in a tangential direction. To accomplish this, slip at various points on the surface must proceed, on a microscopic scale, in a zig-zag fashion in the three crystallographically defined slip directions, and in such a way that the gross, macroscopic direction of slip is tangential.

It is therefore assumed that the only effective stress acting is τ_t, the tangential component of the resultant shear stress parallel to the slip plane. As shown in the Appendix, this stress is given by

$$\tau_t = \tau_0 \frac{\cos\phi\,(1 - \cos^2\theta\tan^2\phi)}{\sqrt{1 + \cos^2\theta\tan^2\phi}} \,. \qquad [2]$$

This relation is plotted in Fig. 4 for $\theta = 0°$ to $90°$ and for a number of ϕ values, including those particular values of ϕ possessed by the crystals which were tested. When $\phi = 0°$, the tangential shear stress τ_t is independent of θ but, as ϕ increases, τ_t becomes larger at the end of the major axis ($\theta = 90°$) than at the end of the minor axis ($\theta = 0°$). At $\phi = 45°$, the shear stress at the end of the minor axis becomes zero and then reverses its direction for larger values of ϕ.

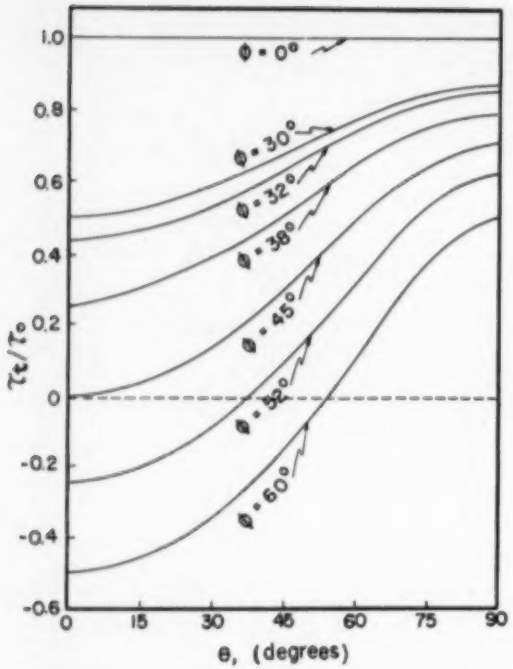

Fig. 4—Variation of resolved tangential shear stress τ_t, in units of τ_o, with θ and ϕ.

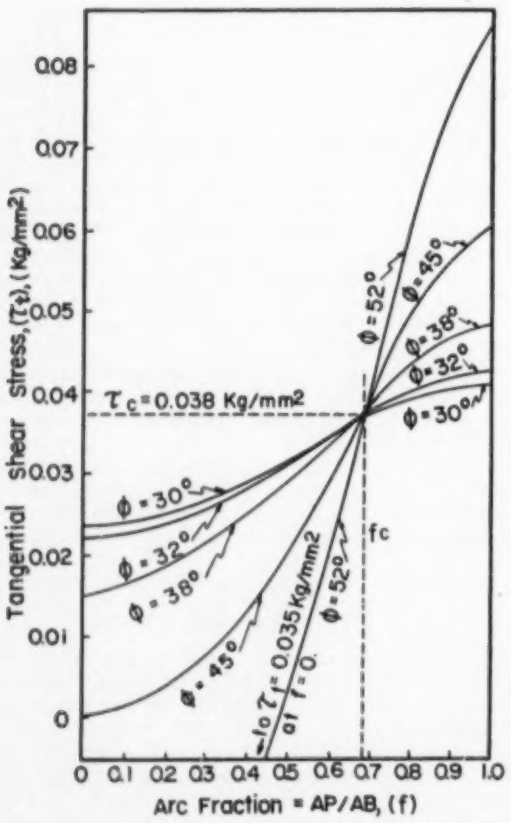

Fig. 5—Variation of resolved tangential shear stress τ_t with arc fraction f.

For crystals with ϕ between 0° and 45°, τ_t is everywhere positive and always a maximum at the end of the major axis and a minimum at the end of the minor axis. Slip must therefore begin at the ends of the major axis but it will not be macroscopically detectable in a stress-strain test until it has extended all around the elliptical perimeter of the slip plane. Two extreme criteria might be assumed for the occurrence of this macroscopic slip: 1—It occurs when τ_t at the ends of the major axis becomes equal to τ_c, the critical resolved shear stress. This assumption implies that slip at the ends of the major axis so alters the stress distribution in the unslipped region that the stress at various points in the latter is successively raised above τ_c so that slip can extend over the whole perimeter. 2—It occurs when τ_t at the ends of the minor axis becomes equal to τ_c. This implies that slip at all other points on the perimeter, at which τ_t exceeds τ_c, has no effect on the value of τ_t at the ends of the minor axis. Neither of these extreme criteria seem very reasonable and neither leads to a constant value of τ_c for various values of ϕ. An intermediate criterion was therefore assumed, namely, that macroscopic slip occurs when τ_t at all points on a fixed fraction of the slip plane perimeter has been raised above τ_c, the value of this fraction and of τ_c to be determined from the experimental data.

Fig. 5 shows the curves of Fig. 4 replotted in a somewhat different form. The ordinate is now τ_t, obtained from Eqs. 1 and 2, and the abscissa is the fraction f of one quadrant of the elliptical perimeter given by AP/AB in Fig. 3. Within experimental error the curves all intersect at $\tau_t = 0.038$ kg per sq mm and $f = 0.68$. These particular values are τ_c, the critical resolved shear stress, and f_c, the fixed fraction of the elliptical perimeter already referred to. The quantity $(1 - f_c)$ is the fraction of the elliptical perimeter in one quadrant on which τ_t is greater than the critical value τ_c. The value of this quantity is about one-third, from which it may be concluded that microscopic slip extending around one-third of the slip plane perimeter provides sufficient slip stimulation, in the form of a change in the stress distribution in the unslipped region, to cause macroscopic slip around the whole perimeter. This is true even for the two specimens having ϕ equal to 45° and 52°.

For given values of ϕ and θ, the exact values of f used in plotting Fig. 5 were obtained by elliptic integration. When this was done, it was found that f was almost equal to $\theta/90°$, for a given value of ϕ, even when ϕ was as large as 60°.

When ϕ exceeds 45°, some parts of the slip plane perimeter are subjected to negative shear stress. When a considerable portion of the perimeter is in this condition and, in particular, when the maximum negative stress is greater numerically than the maximum positive stress ($\phi > 60°$), then it seems likely that a condition of elastic instability will result and that the specimen will deform in some other manner, such as by bending or twinning, rather than by torsion. Support for this view is given by a specimen with $\phi = 64°$, whose deformation is discussed in the next section.

The critical resolved shear stress for magnesium in torsion (0.038 kg per sq mm) is roughly half of that for magnesium in tension, as determined by Bakarian and Mathewson[4] who found 0.0778 kg per sq mm for material containing less than 0.02 pct impurities and by Burke and Hibbard[5] who found

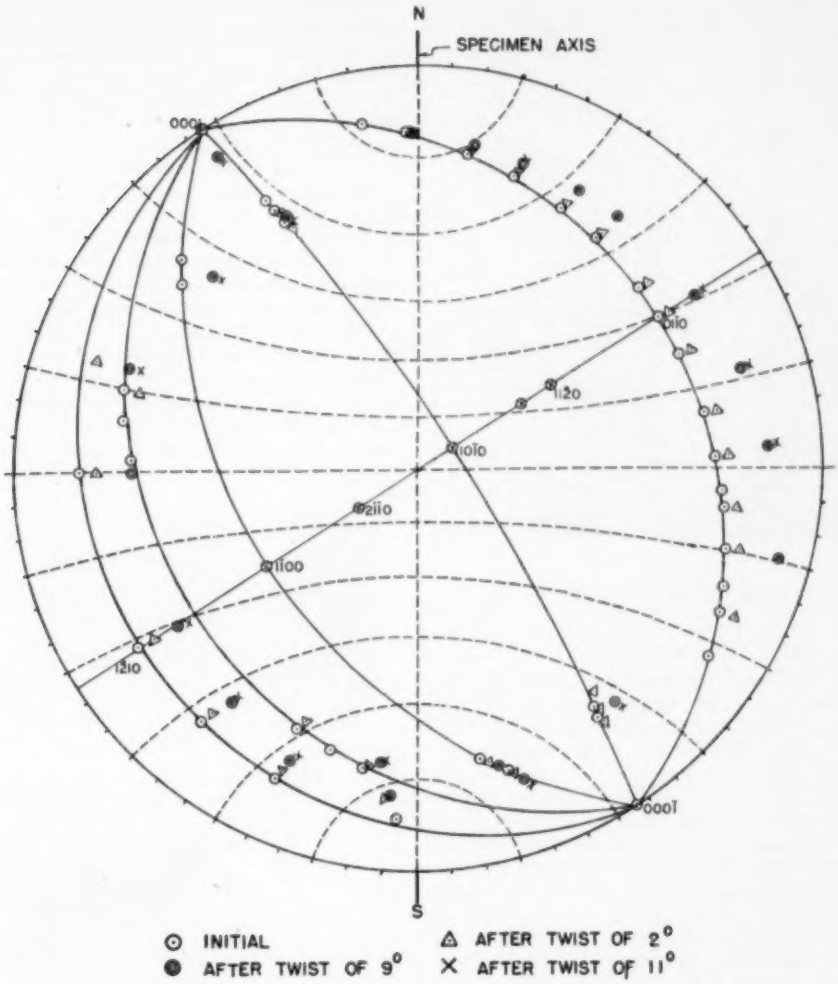

Fig. 6—Stereographic projection of magnesium crystal at various stages during torsion.

0.046 kg per sq mm for material containing less than 0.05 pct impurities. To establish that this difference between torsion and tension was genuine and not due to differences in chemical composition, the critical resolved shear stress in tension was redetermined in this laboratory on magnesium crystals prepared in the same way and from the same material as the torsion specimens. The average of four determinations was 0.066 kg per sq mm.

Flow Mechanism: Transmission Laue patterns were made at intervals during the torsional deformation of magnesium crystals in order to follow changes in lattice orientation. Each pattern was recorded with the lower end of the crystal rotated back to its initial position before deformation; any change in lattice orientation shown in these patterns was therefore due to deformation alone. The way in which the poles of various crystal planes move during torsion is illustrated stereographically in Fig. 6.

This projection shows that poles move on small circles of a stereographic net whose north-south axis coincides with the specimen axis, i.e., plane normals rotate, not about the slip plane normal, but about the axis of torsion. The angular distance which each pole moved on the projection was found to be in very good agreement with the measured angle of twist of the specimen at the point of incidence of the X-ray beam.

The mechanism of torsional deformation in magnesium can be visualized as follows. As soon as the critical resolved shear stress is exceeded, slip begins at the crystal surface on the basal planes. The interior of the crystal is still only elastically strained, however, and acts as a comparatively rigid core. This core is surrounded by rings of material which have slipped on their basal planes. As torsion proceeds, these rings rotate with respect to one another but they cannot do so freely, since they are held to the rigid core and must, moreover, rotate so that their basal planes (and all other planes, for that matter) make a constant angle with the torsion axis. The result is a tendency for the crystal to separate or break apart on its basal planes.

This behavior is illustrated by the model shown in Fig. 7. It is composed of a set of elliptical rings surrounding a rigid core so as to form a cylindrical rod. These rings are initially in contact on inclined planes representing the basal slip planes of a crys-

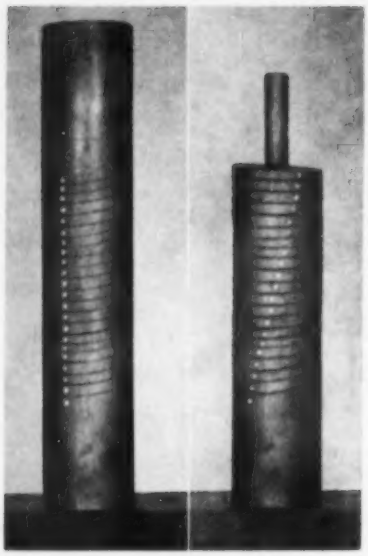

a b

Fig. 7—Model illustrating torsional deformation.

tal. When a torque is applied to the surface of the upper end of the rod, these rings rotate relative to one another as shown by the relative positions of the white dots before and after twisting. Since these layers are constrained to rotate about the central rod, they cannot remain in complete contact on their basal planes, as shown in Fig. 7b.

The greater the angle ϕ, the more difficult will this kind of rotation become and the greater will be the tendency to separation of a crystal on its basal planes. This tendency manifests itself in one side of the crystal being in tension and the opposite side in compression and a real crystal, as opposed to a mechanical model, adapts itself to these stresses by bending rather than by separation on its basal planes. Fig. 8 shows an example of a magnesium crystal bent as a result of torsion: ϕ had a value of 64° for the specimen shown, which was twisted by 50° per in. Slip alone seemed to operate, even in severely twisted crystals with large values of ϕ; twinning was not observed macroscopically.

Is the slip which occurs in torsion the equivalent of Wilman's rotational slip? The answer to this must be no if rotational slip is defined as relative rotation about the slip plane normal, since such rotation occurs in torsion only when $\phi = 0$, i.e., when the torsion axis coincides with the slip plane normal. Rotational slip is thus only a special case of torsional slip.

The torsion of magnesium crystals is not uniform along their axes. Measurements of torsional strain made in the center of the gage length by an X-ray method[8] yielded considerably higher strains than mechanical measurements based on gages at each end of the gage length (the two extreme gages in Fig. 1). When two other gages were mounted closer to the center of the specimen, the X-ray and mechanical measurements of strain agreed very well, showing that there was a real gradient of strain in the specimen. The smaller strain at the ends of the gage length are doubtless due to the restraint of the adjoining thick sections.

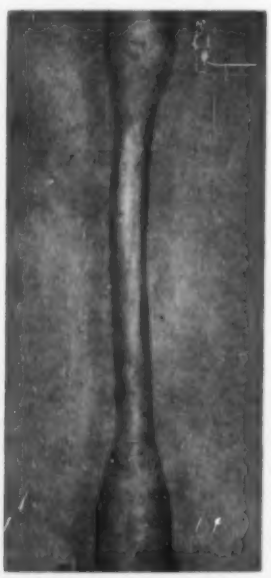

Fig. 8—Magnesium crystal after torsion.

a—Before torsion.

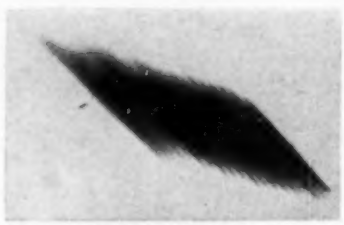

b—After torsion.

Fig. 9—Focused Laue reflections from an aluminum crystal. Soller slit in primary beam. X1.5. Area reduced approximately 40 pct for reproduction.

Some experiments were made with aluminum crystals to see how a cubic metal would behave in torsion. These experiments are very incomplete: the slip plane was not identified, nor was the critical resolved shear stress measured. However, it was established that lattice plane normals rotate about the torsion axis just as they do in magnesium. Some X-ray evidence was also obtained for lattice bending, probably elastic, in the interior of the crystal. However, no appreciable bending of the specimen itself was observed and, compared to magnesium, the torsional strain in aluminum crystals was found to be much more uniform along the specimen axis, presumably because aluminum has more available slip systems.

Julien and Cullity[6] compared the elastic torsion of quartz with the plastic torsion of aluminum and concluded that the latter was extremely nonuniform on a fine scale. However, the plastic torsion of aluminum may be surprisingly uniform if the crystal has, initially, a high degree of perfection. Fig. 9a is a focused Laue reflection, obtained by the method of Guinier and Tennevin,[7] of a plate-shaped aluminum crystal grown by the strain-anneal method: the fine focused line to the right of the primary beam spot indicates a rather high degree of perfection. Fig. 9b shows the same reflection after torsion of 0.19° per mm. The striations in this reflection are the result of torsion of the crystal and the inclination of the striations is a measure of the degree of torsion,[8] while the fact that the striations are so very straight and evenly spaced indicates that the torsion of this crystal is extremely uniform.

Recovery of Torsional Deformation

The term "recovery" is here used to mean the process by which a plastically twisted crystal partially relaxes or recovers from its twisted position on annealing. Cylindrical crystals of aluminum, about ⅛ in. in diameter and grown by the strain-anneal method, were annealed in a salt bath furnace after torsional deformation and the untwisting of the lattice was measured by an X-ray method. The specimen was annealed for a given time, removed for X-ray examination, and then returned to the furnace for further annealing. Guinier and Tennevin[8] have shown that such intermittent annealing produces the same effects as continuous annealing.

Fig. 10a is a typical focused Laue reflection from a twisted and annealed aluminum crystal. A Soller slit was used in the incident beam and striations indicating torsion are visible at one end of the reflection. (They slope in the opposite direction to those in Fig. 9b because of a difference in the direction of twist.) The tangent of the angle γ between these striations and the vertical is proportional to the degree of torsion, measured in degree per mm.[8] However, the specimen is highly polygonized in addition to being twisted, as evidenced by the fine vertical lines crossing the reflection, and these lines due to polygonization so obscure the inclined striations that a measurement of γ is made impossible. On the other hand, the angle α between the vertical and the diagonal of the whole image, Fig. 10b, is readily measurable and it may be shown than tan α is directly proportional to tan γ. A measurement of α thus leads to a value for the degree of torsion in arbitrary units.

Table II shows the results of annealing an aluminum crystal at 600°C for a total period of 404 hr. In this table, t' is the actual annealing time. Polygonization was observed after the first 1.5 hr of annealing. In order to formulate the relation between torsional strain and time at constant temperature, the following assumptions were made: 1—After 1.5 hr of annealing at 600°C, the specimen should be completely polygonized. Any residual stress still remaining in the specimen due to previous torsion in the crystal becomes the driving force for untwisting. The period of 1.5 hr is therefore regarded as a preannealing period as far as torsional recovery is concerned and the values of t in Table II measure the time of annealing after the first 1.5 hr. 2—The untwisting is viscous, i.e., it proceeds at a rate proportional to the stress. 3—In the absence of an applied torque and after polygonization is complete, the stress at any time is proportional to the strain.

Table II. Untwisting of Aluminum at 600°C

Annealing Time, Hr			
t'	t	α, Degrees	$\epsilon = \tan \alpha$
0	—	55	1.43
1.5	0	54	1.38
44	42.5	53	1.33
62	60.5	52	1.28
81	79.5	51	1.23
108	106.5	50.5	1.21
150	148.5	50	1.19
220	218.5	47.5	1.09
321	319.5	46	1.04
404	402.5	45	1.00

a—Actual reflection from an aluminum crystal.

b—Schematic drawing of reflection to show angles α and γ.

Fig. 10—Focused Laue reflections from twisted crystals.

Making these assumptions and putting tan α = ϵ = effective torsional strain in arbitrary units, we can write

$$-\frac{d\epsilon}{dt} = K_1\tau = K_2\epsilon \qquad [3]$$

where τ is the stress and K_1 and K_2 are constants. Integration of Eq. 3 gives

$$\epsilon = \epsilon_0 e^{-K_2 t}. \qquad [4]$$

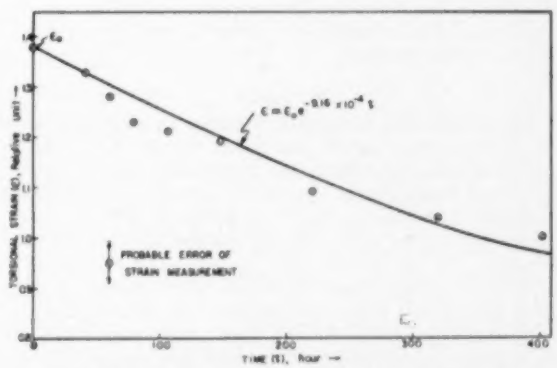

Fig. 11—Relaxation of effective torsional strain with time at 600°C for aluminum.

The constant K_s was evaluated by least squares from the data in Table II as 9.16×10^{-4} hr^{-1}. Eq. 4 therefore becomes

$$\epsilon = 1.38\, e^{-9.16 \times 10^{-4} t}. \qquad [5]$$

This equation, plotted in Fig. 11, fits the experimental data fairly well.

In another experiment an aluminum crystal in the form of a rectangular plate was twisted about its longitudinal axis and annealed for various periods of time at 650°C, which is only some 10°C below the melting point. Polygonization occurred rapidly and the torsional strain gradually relaxed and, at the end of about 50 hr, almost disappeared. Then, after 72 hr, the Laue spot was observed to contain a set of striations of opposite slope to the initial ones, indicating that a part of the crystal had not only untwisted completely but had started to twist in the *opposite direction* to the original twist. Leschen[9] describes this plastic after effect as follows: "In the torsion of a rod, for instance, the outer layers are under greater stress than the interior portions and deform plastically while the interior is still only elastically stressed. If the external load is removed, the rod partially untwists, but there remains an internal distribution of balanced elastic stresses: the inner layers have not been entirely relieved of stress while the outer portions have been somewhat twisted in the opposite, or negative, direction."

Conclusions

1—The critical resolved shear stress of magnesium in torsion is 0.038 kg per sq mm at room temperature.

2—The torsional deformation of both magnesium (hexagonal) and aluminum (cubic) is accompanied by rotation of lattice planes about the axis of torsion. As a result, magnesium crystals of particular orientations become considerably bent after torsion.

3—Twisted aluminum crystals untwist at elevated temperatures at a rate which suggests viscous flow. At temperatures near their melting point, twisted aluminum crystals can become twisted, at least in part, in the opposite direction to the original twist.

Acknowledgments

This work was performed under ONR contract N7onr-43905 and the writers wish to express their thanks to the Office of Naval Research for making this investigation possible. They are also grateful to Dr. R. L. Fullman, of the Research Laboratory, General Electric Co., and Professors L. Lee and M. O. Peach, of the Dept. of Engineering Mechanics, University of Notre Dame, for many helpful discussions of the stress analysis.

Appendix

The torsion of a circular cylinder of radius r about its axis is considered here with reference to Fig. 3. As Wright[10] has shown, the material of the cylinder may be isotropic or anisotropic, with any crystal symmetry whatever, without affecting the final result. In either case the stress distribution is the same.

At any point P on the elliptical boundary of the slip plane, let σ be the normal stress (parallel to plane normal N), τ be the shear stress (parallel to slip plane), and s be the resultant stress. These stresses are evaluated below in a RVZ coordinate system, where R is parallel to OP', V is tangential to the circular cross section at P', and Z is the axis of the cylinder (Fig. 3).

$$\sigma = \sigma_{RR}l^2 + \sigma_{VV}m^2 + \sigma_{ZZ}n^2 + 2\tau_{RV}lm + 2\tau_{VZ}mn + 2\tau_{ZR}nl$$

where l, m, and n are the cosines of the angles which N makes with R, V, and Z, respectively. $l = -\sin\theta \sin\phi$; $m = -\cos\theta \sin\phi$; and $n = \cos\phi$.

$$\sigma_{RR} = \sigma_{VV} = \sigma_{ZZ} = \tau_{RV} = \tau_{VR} = \tau_{RR} = \tau_{RZ} = 0$$

and

$$\tau_{RV} = \tau_{VR} = \frac{2T}{\pi r^3} = \tau_o$$

where T is the applied torque.

Therefore, $\sigma = -\tau_o \cos\theta \sin 2\phi$

$$\sigma_R = \sigma l = \tau_o \sin 2\theta \sin^2\phi \cos\phi$$
$$\sigma_V = \sigma m = 2\tau_o \cos^2\theta \sin^2\phi \cos\phi$$
$$\sigma_Z = \sigma n = -2\tau_o \cos\theta \sin\phi \cos^2\phi.$$

The components of the resultant stress are:

$$s_R = -(\sigma_{RR}l + \tau_{VR}m + \tau_{ZR}n) = 0$$
$$s_V = -(\tau_{RV}l + \sigma_{VV}m + \tau_{ZV}n) = -\tau_o \cos\phi$$
$$s_Z = -(\tau_{RZ}l + \tau_{VZ}m + \sigma_{ZZ}n) = \tau_o \cos\theta \sin\phi.$$

The components of the shear stress are:

$$\tau_R = s_R - \sigma_R = -\tau_o \sin 2\theta \sin^2\phi \cos\phi$$
$$\tau_V = s_V - \sigma_V = -\tau_o \cos\phi\,(1 + 2\cos^2\theta \sin^2\phi) \qquad [6]$$
$$\tau_Z = s_Z - \sigma_Z = \tau_o \cos\theta \sin\phi\,(1 + 2\cos^2\phi). \qquad [7]$$

Let τ_t be the component of the shear stress in the slip plane and tangential to its boundary at P, and δ be the angle between τ_t and the V axis. Then

$$\tau_t = \tau_Z \sin\delta - \tau_V \cos\delta \qquad [8]$$

$$\text{where } \delta = \cos^{-1}\frac{1}{\sqrt{1 + \cos^2\theta \tan^2\phi}}. \qquad [9]$$

Eqs. 6 to 9 combine to give

$$\tau_t = \tau_o \frac{(\cos^2\theta \tan^2\phi - 1)\cos\phi}{\sqrt{(\cos^2\theta \tan^2\phi + 1)}}. \qquad [10]$$

This expression gives the tangential shear stress component acting on the material below the slip plane. Eq. 2 refers to τ_t above the slip plane and is obtained by changing the sign of the above expression.

References

[1] This work is summarized in a long review paper, the 1933 Edgar Marburg Lecture of the ASTM: Crystalline Structure in Relation to Failure of Metals—Especially by Fatigue, by H. J. Gough. *Proc.* ASTM (1933) **33**, Part II. The paper gives extensive references to original work.

[8] H. Wilman: *Nature* (1950) **165**, p. 321.

[8] B. D. Cullity and C. A. Julien: *Journal of Applied Physics* (1953) **24**, p. 541.

[4] P. W. Bakarian and C. H. Mathewson: *Trans.* AIME (1943) **152**, p. 226.

[5] E. C. Burke and W. R. Hibbard: *Trans.* AIME (1952) **194**, p. 295; JOURNAL OF METALS (March 1952).

[6] C. A. Julien and B. D. Cullity: *Acta Metallurgica* (1953) **1**, p. 588.

[7] A. Guinier and J. Tennevin: *Acta Crystallographica* (1949) **2**, p. 133.

[8] A. Guinier and J. Tennevin: *Progress in Metal Physics.* (1950) Vol. 2. New York. Interscience Publishers.

[9] J. G. Leschen: *Cold Working of Metals.* (1949) p. 197. Cleveland. ASM.

[10] S. J. Wright: Reports and Memoranda No. 1031. Aeronautical Research Committee of Great Britain (1926).

AVAILABLE IN FEBRUARY 1954

DISLOCATIONS IN METALS

Based On An Institute of Metals Div. Symposium

Edited by

Morris Cohen
Massachusetts Institute of Technology
Cambridge, Mass.

Chapter Headings and Authors:

The Nature of Dislocations in Ideal Single Crystals, by

J. S. Koehler and F. Seitz
University of Illinois
Urbana, Ill.

Role of Dislocations in Crystal Growth and Grain Boundary Phenomena, by

W. T. Read, Jr., and W. Shockley
Bell Telephone Laboratories
Murray Hill, N. J.

Dislocations and Mechanical Properties, by

E. Orowan
Massachusetts Institute of Technology
Cambridge, Mass.

1954 **$5.00**

AIME Members will receive a
30 pct discount on the book

Published By
The American Institute of Mining & Metallurgical Engineers, Inc.
Institute of Metals Div.
29 West 39th St.
New York 18, N. Y.

Use coupon on reverse side for ordering.

MODERN USES OF NONFERROUS METALS

Edited by C. H. Mathewson

Price: $4.90 to AIME Members; $7.00 to Nonmembers

MODERN USES OF NONFERROUS METALS, edited by C. H. Mathewson, paints on a broad canvas progress in the field of utilization of nonferrous metals. Many radical changes have taken place since the first edition of this book. In essence, this second edition is a completely new work. Every chapter has been rewritten or added to, and in all cases brought up to date. The 26 chapters were written by leading authorities in their fields. Laboratory and production men have made giant strides in developing new alloys to meet man's needs in an ever changing world. Thus, MODERN USES OF NONFERROUS METALS is a work which will find wide acceptance among both technical and nontechnical readers. For the young engineer, it contains a graphic picture of how nonferrous metals are used, while for others it embodies much that is new. The book is written in nontechnical language. Approach in many chapters is narrative. Where illustration is required, tables, graphs, and other devices are used.

Published through the Seeley W. Mudd Fund by

The American Institute of Mining and Metallurgical Engineers, Inc., 29 West 39th St., New York 18, N. Y.

Solidification of Metals and Alloys . . .

A Symposium by the AIME's Institute of Metals Division

A publication on the subject of major significance to metallurgists, by four of the nation's outstanding authorities. Three papers cover ferrous and nonferrous metals solidification and discuss many of the phenomena of metal freezing.

1951 • 75 Pages • $3.00

Nucleation of Solids, J. H. Hollomon and D. Turnbull

Growth of Metal Crystals, R. F. Mehl

Solidification of Steel Ingots, B. R. Queneau

Preface, Cyril Stanley Smith

OTHER METALS BRANCH BOOKS

Transactions, Vols. 185 ('49), 188 ('50), 191 ('51)	$7.00
75 Years of Progress in Iron and Steel, 1948	1.50
Bergwerk und Probierbuchlein, 1949	5.00
Stress Corrosion Cracking of Metals, 1944	5.00
Nonferrous Rolling Practice, 1948	4.00
Rod and Wire Production Practice, 1949	3.00
Proceedings	
Electric Furnace Steel, 1947-1951	$10.00 Ea.
Blast Furnace, Coke Oven and Raw Materials, 1946, 1947, 1951, 1952, 1953	10.00 Ea.
Open Hearth 1944-1947, 1952, 1953	10.00 Ea.
Dislocations in Metals, 1954	5.00
Tube Producing Practice, 1951	3.00

AIME 29 W. 39th St., New York 18, N. Y.
Please send me the books listed below. Enclosed is Check ☐; Money Order ☐ for $..... (AIME members may be billed.)
• AIME Members, 30% Discount on All Books.

1. ..... 3. .....

2. ..... 4. .....

Name .....

Address .....

City and Zone ..... State .....

Nonmember Foreign Orders, Add 50c for Mailing.